

Laboratory for Particle Engineering and Technology

File No. IR/S3/EU-04/2006

A Project Completion Report Submitted to SERC-DST

by

SANJEEV KUMAR, V. KUMARAN and S. VENUGOPAL

DEPARTMENT OF CHEMICAL ENGINEERING



**INDIAN INSTITUTE OF SCIENCE
BANGALORE 560012, INDIA**

April, 2014

1. *Title of the project:* Laboratory for Particle Engineering and Technology
2. *Principal Investigator(s) and Co-Investigator(s):* Sanjeev Kumar Gupta, V. Kumaran, and S. Venugopal
3. *Implementing Institution(s) and other collaborating Institution(s):* Indian Institute of Science
4. *Date of commencement:* 01-04-2007
5. *Planned date of completion:* 31-03-2012
6. *Actual date of completion:* 31-03-2013
7. *Objectives as stated in the project proposal:*
 - To develop quantitative understanding of synthesis of nanoparticles in bulk precipitation and reverse micellar routes
 - Development of flexible wall micro-channels which can mix and pump fluids simultaneously
 - Investigate particle synthesis in rigid wall and flexible wall microchannels of various configurations to develop a robust continuous process for nanoparticle synthesis, which permits control of particle size and polydispersity
 - Quantitative understanding of formation of monolayer of particles and development of a robust process for monolayer formation.
 - Development of nanoparticle based chemiresistive gas/vapour sensor
8. *Deviation made from original objectives if any, while implementing the project and reasons thereof:*

Given the magnitude and scale of the project, and associated laboratory set-up and synchronization issues, the objectives were modified as given below to harness new discoveries made during the course of the project and optimize the technical and scientific reach of the project. The modified objectives are as follows:

1. To develop quantitative understanding of bulk synthesis of nanoparticles
2. Development of robust continuous processes for nanoparticle synthesis
3. Development of a robust process for formation of ordered nanoparticle arrays
4. Development of nanoparticle array based floating gate memory devices
5. Development of a nanoparticle based catalyst layer for fuel cells to reduce mass transfer limitations and cost
6. Nanostructured films on paper using inkjet printing for low-cost sensing/diagnostic applications
7. Enhancing mixing in micro channels using soft surfaces to trigger instability of the laminar flow
8. Examining the effect of enhanced mixing on nanoparticle synthesis

9. *Experimental work giving full details of experimental set up, methods adopted, data collected supported by necessary table, charts, diagrams & photographs. Detailed analysis of results indicating contributions made towards increasing the state of knowledge in the subject:*

9.1 Quantitative understanding of the bulk Synthesis of gold nanoparticles:-

Both experimental and modelling studies were carried out to understand the factors involved in the synthesis of monodisperse noble metal nanoparticles. The experimental findings on aqueous-based protocols are presented first followed by a description of the models developed for both aqueous and organic based protocols followed by novel algorithms developed to solve multi-dimensional population balance equations.

9.1a Experimental studies of batch protocols

Tannic acid, a plant based polyphenol, was used to rapidly (on the order of minutes) synthesize size-controlled gold and silver nanoparticles under ambient conditions. We systematically investigated the effect of pH on the size distribution of nanoparticles synthesized. Based on induction time and ζ -potential measurements, we show that particle size distribution is controlled by a fine balance between the rates of reduction (determined by the initial pH of reactants) and coagulation (determined by the pH of the reaction mixture) in the initial period of growth.

The Turkevich method for synthesizing gold nanoparticles, using sodium citrate as the reducing agent, is renowned for its ability to produce biocompatible colloids with mean size >10 nm. Here we show that monodisperse gold nanoparticles in the 5-10 nm size range can be synthesized by simply reversing the order of addition of reactants, i.e. adding chloroauric acid to citrate solution. Kinetic studies and electron microscopic characterization revealed that the reactivity of chloroauric acid, initial molar ratio of citrate to chloroauric acid (MR), and reaction mixture pH play an important role in producing monodisperse gold nanoparticles. Reversing the order of addition also enhanced the stabilization of nanoparticles at high MR values. Remarkably, the system exhibits a ‘memory’ of the order of addition, even when the timescale of mixing is much shorter than the timescale of synthesis.

Typically, aqueous phase synthesis result in particle size distribution that exhibit high polydispersity while organic phase synthesis involve high temperature processing to achieve lower polydispersity. PEGylation of gold nanoparticles is commonly used to enhance biocompatibility of gold colloids. Interestingly, we found that addition of excess PEG molecules and ageing results in “digestive ripening” and enhanced monodispersity of citrate stabilised colloids. The amount of adsorbed carboxylate-PEG mixture was found to be critical for particle ripening.

9.1a.1 Experimental details

Hydrogen tetrachloroaurate trihydrate (Sigma Aldrich), silver nitrate (Merck) trisodium citrate (Sigma Aldrich), tannic acid (Acros), potassium carbonate (Merck), polyvinylpyrrolidone (Average M.W. 10,000, S. D. fine chemicals), and hydrochloric acid (S. D. fine chemicals) were used as obtained without further treatment. Deionized water obtained from a MilliQ® system was used in all the experiments. All chemicals were used as received.

Prior to use, Teflon® parts and glassware were cleaned with aquaregia and rinsed with deionised water and dried in a laminar hood. A home built turbine and baffle system, made of Teflon®, designed to fit a 100 mL beaker, was used to provide a standardised mixing environment for tannic acid reduction method (macroscopic blending time of 2s). A 100 ml beaker with magnetic stirrer on hot plate was used for the synthesis of gold nanoparticles by citrate reduction method.

9.1a.1.1 Synthesis of silver nanoparticles by tannic acid reduction

Typically, 20 mL of required concentration of aqueous tannic acid at pH 8.0 (adjusted by adding K_2CO_3) was taken in the beaker. Then, 5 mL of 2.95 mM silver nitrate was added as one portion into the tannic acid solution, while stirring. A pale yellow colour appeared almost instantaneously indicating the formation of silver nanoparticles, and the stirring was continued till there was no perceivable change in colour. The nanoparticles were synthesised over a wide range of values of the initial molar ratio of tannic acid to silver nitrate (MR). Experiments were performed in stop flow reactor to obtain the kinetic data of the synthesis.

9.1a.1.2 Synthesis of gold nanoparticles by tannic acid reduction

For the preliminary investigations and experiments ‘A’ – ‘F’, the precursor solutions were prepared as follows. 0.25 mL of 25.4 mM chloroauric acid solution was made up to 22 mL using DI water. 3 mL of the desired concentration of tannic acid solution was prepared. 150 mM potassium carbonate solution was used to adjust the pH of tannic acid and/or chloroauric acid solution. If necessary, 0.1 N hydrochloric acid was used to adjust the pH of chloroauric solution.

Typically, chloroauric acid solution was taken in the stirred vessel and the reducing agent was added as one portion (within 1 second). The reaction mixture was stirred till the colour of the colloidal solution did not appear to change.

For stop flow module studies (experiment 'H'), stock solutions of chloroauric acid and tannic acid were prepared as follows. Briefly, 0.25 mL of 25.4 mM chloroauric acid was made up to 20 mL using DI water. 2.25 mL of 5.9 mM tannic acid was made up to 5 mL using DI water.

Experiment 'I' was carried out by adding 10 mL of 0.64 mM chloroauric acid solution (pH-3.2) slowly (dropwise, ~ 1 mL/min) into 15 mL of 0.89 mM tannic acid solution (pH-7.1) that was being stirred. The total volumes and amounts of reagents used were kept at the same value as experiment 'B' and 'G'. For seeded growth experiment reported in figure 6f, 2.5 mL (from a total of 25 mL) of the solution formed in experiment 'I' was made up to 15 mL using DI water and 10 mL of 0.32 mM chloroauric acid solution was added slowly (dropwise) into it. The pH was adjusted to be above 6.4 by intermittently adding required quantities of 150 mM potassium carbonate solution.

9.1a.1.3 Synthesis of gold nanoparticle by citrate reduction method

Gold nanoparticles were synthesized, following 'Turkevich method', as follows: The initial molar ratio of citrate to chloroauric acid (MR) was adjusted to the desired value by adding required amount of trisodium citrate (136 mM concentration, 4% w/v solution) to boiling chloroauric acid solution. The total reaction volume was maintained at 25 mL and the concentration of chloroauric acid in the reaction mixture was 0.254 mM (measured pH of 3.2). For analyzing the effect of reversing the reactant addition (i.e. adding chloroauric acid into citrate at same final chloroauric acid concentration), 0.25 mL of 25.4 mM of chloroauric acid (measured pH of 1.6) was added to 24.75 mL of boiling citrate solution of required concentration. The volume of chloroauric acid added was chosen to minimize its initial pH, as it varies with concentration. Increasing the initial chloroauric acid concentration further did not result in a measurable change in pH.

A further set of experiments, also involving the two alternative modes of addition, were performed at different MR values but with fixed citrate concentration of 5.2 mM. Higher concentrations of citrate caused excessive coagulation and precipitation, which was attributed to the high ionic strength. For experiments involving addition of citrate to chloroauric acid (Turkevich method), 1 mL of 136 mM citrate solution was added into 24 mL of chloroauric acid of desired concentration. For experiments carried out using the alternative mode of addition, desired volume of 25.4 mM chloroauric acid solution (measured pH of 1.6) was added to boiling citrate solution. The total reaction mixture volume was maintained at 25 mL. If necessary, the pH of reactants was changed using hydrochloric acid (1 N) or potassium carbonate (150 mM) solutions. For the experiment involving PVP as a stabilizer, the concentration used was chosen to maximize the stabilization strength, while taking care to avoid affecting the reduction rate. Higher concentrations were found to affect the reaction rate, and also did not enhance the stabilization (as inferred from the size dispersion).

Kinetic studies were performed, as per established protocol, by removing two aliquots of sample from the reaction mixture at desired time intervals. Almost immediately, the sample was cooled in an ice-bath to stop the progress of the redox reaction. The absorbance value of the surface plasmon peak was recorded directly from one aliquot. The pH of the second aliquot was adjusted to 1.5, a value at which the colloidal particles precipitated out, and the absorbance at 315 nm was measured. The chloroauric acid concentration was obtained from a calibration curve.

9.1a.2 Rapid green synthesis of silver nanoparticles

9.1a.2.1 Tannic acid as reducing agent

Tannic has been used as reducing and stabilizing agent for the synthesis of gold and silver nanoparticles. It is essential to understand the structure of tannic acid to evaluate the potential of tannic acid as reducing and stabilizing agent. Figure 1 shows the representative structure of tannic acid, corresponding to its average formula weight.

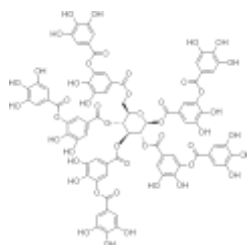
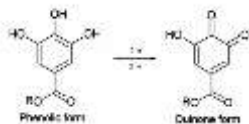


Figure 1. Representative structure of tannic acid ($C_{76}H_{52}O_{46}$).

It consists of a central core of glucose that is linked by ester bonds to polygalloyl ester chains. Tannic acid has 25 phenolic–OH groups in its structure; but, only ten pairs of o-dihydroxyphenyl groups are capable of taking part in redox reactions to form quinones and donate electrons, because of the chelating action of adjacent hydroxyl groups and constraints on carbon valency. Scheme 1 shows the oxidation reaction of phenolic form. So, each tannic acid molecule is capable of donating twenty electrons.



Scheme 1. Oxidation of phenolic group into ketones.

Tannic acid at its natural acidic pH is known to be a weak reducing agent that can only grow seeds into nanoparticles at room temperature. Tannic acid has a pKa value between seven and eight, depending on its extent of dissociation, and is known to partially hydrolyse under mild acidic/basic conditions into glucose and gallic acid units. Gallic acid at alkaline pH reduces silver nitrate into silver nanoparticles rapidly at room temperature, but the particles form aggregates in solution as gallic acid is a poor stabilising agent. Glucose is a weak reducing agent at room temperature, but it is an excellent stabilising agent at alkaline pH. These findings suggest that tannic acid could be an ideal reducing and stabilising agent under alkaline conditions at room temperature.

9.1a.2.2 Tuning of redox potential of tannic acid via pH

Tannic acid solution's natural pH is acidic in nature. Typically, the reduction of silver nitrate with tannic acid is carried at high temperatures. The reduction of silver nitrate with tannic acid, with a molar ratio of 0.5, was carried at room temperature. The natural pH of the reaction mixture is 3.2 and the reaction mixture remained colorless even after few weeks indicating the necessity to accelerate the reaction by increasing the temperature. Figure 2a shows the hydrodynamic diameter of silver nanoparticles synthesized with change in the pH of reducing agent used in the reaction. The increase in pH of the reducing agent reduces the induction time period, time required for the color appearance after mixing reactants, and reduces the size of nanoparticles synthesized. The hydrodynamic size of silver nanoparticles synthesized at pH of reducing mixture 8 is 23.9 ± 3.9 nm. Further increase in the pH does not cause a significant decrease in the hydrodynamic size but leads to polymerization of tannic acid. Hence, further experiments were performed with the pH of reducing agent at 8. The efficiency of tannic acid as a reducing agent was characterized by investigating the redox potential of tannic acid solution at different pH. Figure 2b shows the change in redox potential of tannic acid solution with pH. The change in redox potential of tannic acid with the pH follows the same trend as that of hydrodynamic diameter with the pH of reducing agent. These experiments clearly demonstrate that the reduction of silver nitrate at room temperature is plausible by altering the pH of tannic acid.

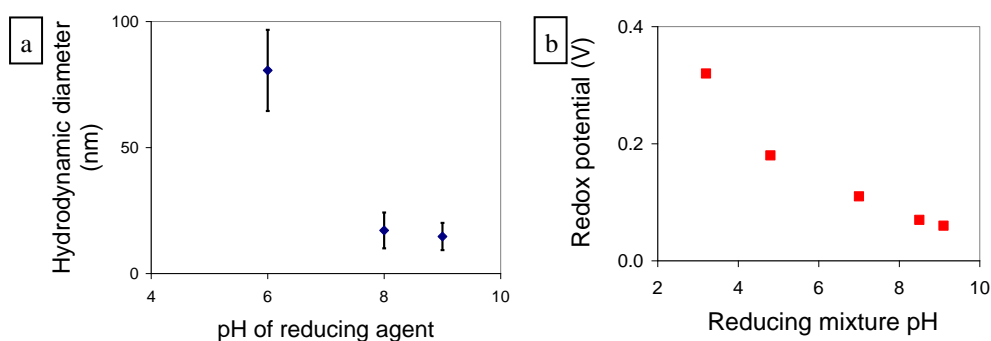


Figure 2 (a) The change in hydrodynamic diameter of silver nanoparticles with pH of reducing agent. The reaction doesn't takes place at pH 4. (b) The variation of redox potential of tannic acid solution with pH of reducing agent.

9.1a.2.3 The effect of molar ratio of tannic acid to silver nitrate

Generally, in the synthesis of nanoparticles, the size control of nanoparticle is achieved by tuning the molar ratio of reactants which in turn alters the reduction and nucleation rate. To achieve size control, the molar ratio of tannic acid to silver nitrate was varied from 0.05 to 1. In all experiments, the pH of reducing agent, tannic acid solution, was adjusted to 8. Figure 3a shows the variation in hydrodynamic size of silver nanoparticles with the molar ratio of tannic acid to silver nitrate. Unlike the expected trend, the increase in the molar ratio increases the hydrodynamic diameter of silver nanoparticles. Figures 3b-d show representative electron microscopy images (FESEM and TEM) for these samples. The

insets represent the part of the UV-Vis spectrum that corresponds to the surface plasmon resonance (SPR) band of silver nanoparticles, and the measured particle size distribution of these samples. To analyse the role of molar ratio in the synthesis, the nanoparticle synthesis was monitored by studying the evolution of absorbance with millisecond resolution in stop flow module.

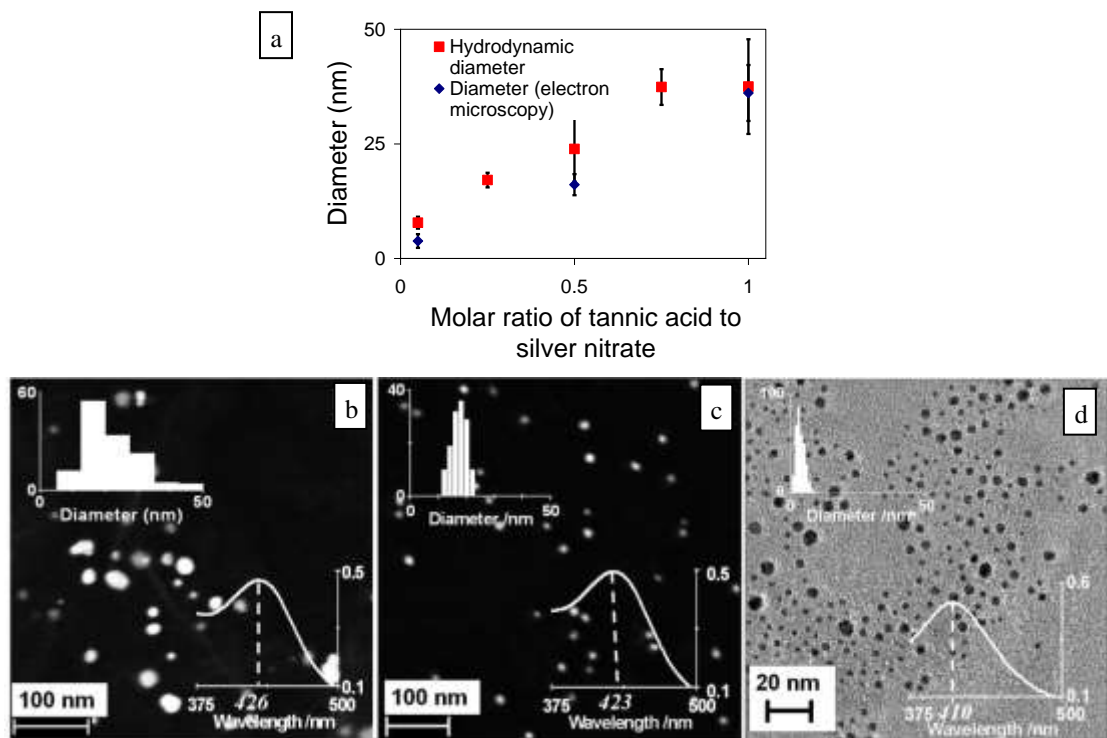


Figure 3 (a) The change in the hydrodynamic diameter of silver nanoparticles with molar ratio of tannic acid to silver nitrate. Representative electron microscopy images of silver nanoparticles synthesised at various initial molar ratios of tannic acid to silver nitrate (MR). (b) MR = 1 (FESEM), (c) MR = 0.5 (FESEM), (d) MR =0.05 (TEM). The inset graphs in (b) – (d) depict the corresponding particle size distribution and UV-Vis spectrum, with ordinates representing the actual number of particles counted and absorbance (a.u.) respectively.

Table 1. Variation of induction time for nanoparticle formation and average particle size with the molar ratio of tannic acid to silver nitrate.

Molar ratio of tannic acid to silver nitrate (MR)	Induction time (s)	Nanoparticle diameter (nm) ($\mu \pm \sigma$)
0.05	0.008	3.3 ± 1.2
0.5	0.158	14.3 ± 2.1
1	1.52	22.1 ± 5.9

Table 1 summarizes the results of particle size characterisation and induction time measurements. Figure 4a shows the time evolution of absorbance measured using a stop flow module, at the wavelength corresponding to SPR peak for these samples. From Mie theory, the absorbance is directly proportional to volume of nanoparticles (for diameters < 20 nm). The slope of the absorbance profiles at the early stages is higher for smaller molar ratio values indicating that the growth rate is higher at smaller molar ratio values. Figure 4b highlights the variation in induction time, which is the time elapsed between mixing of reactants and formation of detectable particle, with the molar ratio values.

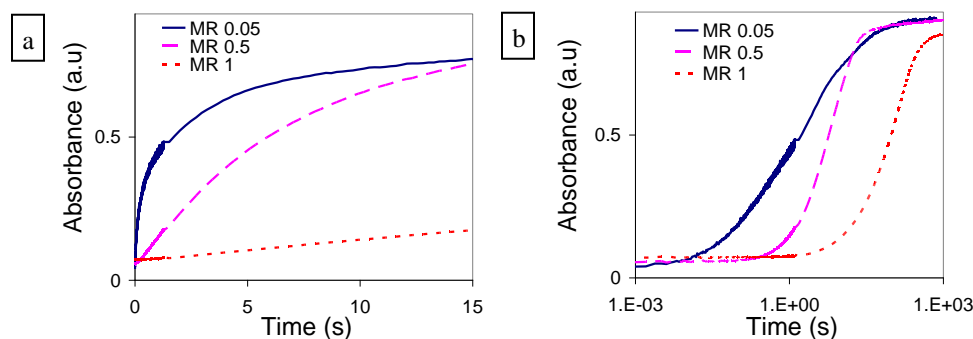


Figure 4. Time evolution of absorbance at SPR peak wavelength for different initial molar ratios of tannic acid to silver nitrate (MR). (a) Normal scale. (b) Logarithmic scale. The absorbance rises faster for lower MR values.

The trends of lower growth rate, and increasing nanoparticle size and induction time with increasing molar ratio is opposite to that expected based on an assumption that increasing reagent concentration should increase reaction rates; thereby, resulting in higher monomer concentration leading to faster growth and nucleation. These trends cannot be interpreted in terms of the role of tannic acid as a stabiliser, as increasing stabiliser concentration is also expected to result in smaller sizes. This implies that the role of tannic acid is not limited to that of reducing/stabilising agent; as, even at alkaline pH, tannic acid has only moderate redox potential and should not nucleate silver nanoparticles at room temperature, just like hydroquinone. To understand the process involved in synthesis that leads to unexpected results, the reaction between tannic acid and silver nitrate was studied.

Knowledge of stoichiometric ratio of the desired reaction is essential to understand the effect of concentration of tannic acid on the synthesis of nanoparticles. The stoichiometric ratio required for the completion of the reaction between tannic acid and silver nitrate was investigated. To a known molar solution of silver nitrate, tannic acid was added in aliquots, and the concentration of unreacted tannic acid was determined from UV visible spectroscopy. Figure 5 shows UV-Vis spectra of 0.25 mL aliquots sampled during the stepwise addition (corresponding to MR values) of tannic acid solution, maintained at a pH of 8, to 5 mL of 2.95 mM silver nitrate solution. It is seen that the surface plasmon peak of silver nanoparticles at 420 nm increases steadily and then saturates at an MR value of 0.05, indicating that silver nitrate is completely reduced. Also, for MR values ≥ 0.05 , a small shoulder at 270 nm is seen that is attributed to the presence of excess tannic acid. The spectrum of a concentrated solution of pure tannic acid at pH 8 is also shown for comparison. If stoichiometric ratio of tannic acid to silver nitrate is 0.05, it shows that one mole tannic acid can react with 20 mole of silver nitrate. These results validate the expected redox stoichiometry of tannic acid and are in concord with previous results on the chelating capability of tannic acid.

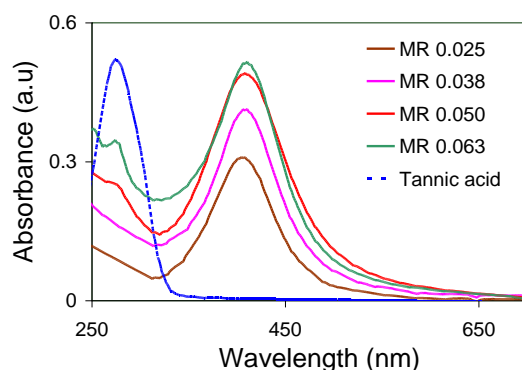
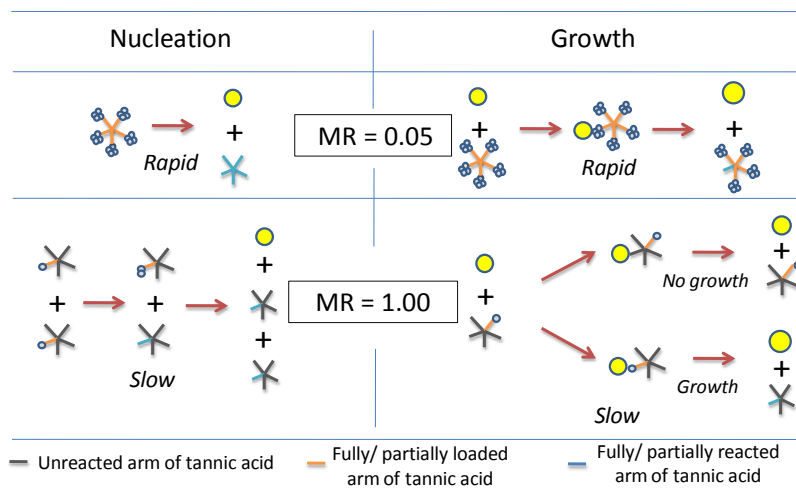


Figure 5. UV visible spectra of silver nanoparticle solutions as a function of the initial molar ratio of tannic acid to silver nitrate (MR). The spectrum of a concentrated (2x original) tannic acid solution is also shown for comparison.

9.1a.2.4 Tannic acid as organizer

Tannic acid has five units of gallic acid and each gallic acid unit can combine with 4 silver ions. Each tannic acid molecule can be thought of as a five-armed chelator. The atomic reorganisation occurs within such complexes facilitating nucleation. Thus, at a MR of 0.05, tannic acid complexes will be saturated with 20 silver atoms enabling rapid nucleation (faster induction time) that results in smaller particle size.



Scheme 2. Schematic representation of organizer based nucleation and growth processes at MR values of 0.05 and 1. Tannic acid is represented as a five armed molecule with each arm capable of reducing and chelating with four silver atoms. Both nucleation and growth processes are faster at MR value of 0.05 as compared to MR value of 1 resulting in the rapid formation of smaller nanoparticles at the lower MR value. Note: the number of loaded atoms depicted is representative of the mean value, given that all the silver ions are reduced and chelated.

At MR of 1, each tannic acid is on average ligated to only one silver atom and so, the nucleation rate will be decided by the interaction of such “unsaturated” compounds in solution leading to slower nucleation rate (larger induction times) that results in larger particle sizes. The role of tannic acid as an organiser during nucleation was first proposed by Chakraborty to model the observed size variation of gold nanoparticles synthesised using Slot and Geuze protocol, which couldn't be explained by homogeneous nucleation models. Turkevich et al. also assigned a similar role to acetone dicarboxylic acid in the formation of gold nanoparticles using citrate as the reducing agent. The decrease in the initial growth rate with an increase of MR value can also be accounted for by considering that growth occurs due to collision of nuclei/particles with chelated silver atoms.

On an average, the rate of collision between chelated silver atoms and nuclei/particle will be similar in all cases due to opposing effects of increasing concentration and decreasing ligation; however, the probability of incorporation per collision will be higher for compounds ligated with more number of silver atoms. Thus, at smaller MR values, the incorporation efficiency of atoms onto nuclei/particles (i.e. growth) will be higher per collision resulting in higher growth rates. Scheme 3.2 illustrates these concepts at MR values of 0.05 and 1. These investigations show that it is plausible to synthesis silver nanoparticles within seconds at room temperature.

Further experiments were performed to investigate the synthesis gold nanoparticles by tannic acid reduction at room temperature.

9.1a.3 Synthesis of gold nanoparticles

9.1a.3.1 Effect of molar ratio of tannic acid to chloroauric acid

Slot and Geuze synthesized gold nanoparticles of varying size, ranging from 12 nm to 3.5 nm, simply by increasing the molar ratio of tannic acid to chloroauric acid in the presence of sodium citrate. Although this protocol has been widely used in the last three decades, there is no report on the use of higher amounts of tannic acid to form nanoparticles of even smaller sizes. Preliminary experiments, aimed at understanding this aspect, showed that the addition of only tannic acid in amounts higher than the maximum value reported by Slot and Geuze resulted in the formation of gold sols even at room temperature (24-28 °C), on a timescale of minutes. So, gold colloids were synthesized at various MR values

without altering the natural pH of the solutions. All the MR values chosen were greater than the stoichiometric requirement for complete reduction of gold salt. A few experiments carried out at different overall concentrations of gold chloride and tannic acid (varied from 25% to 200% of the standard value used) also yielded the same final nanoparticle size distribution as the samples reported herein for the corresponding MR values.

Figure 6a shows the variation of UV-Vis spectra as a function of the MR value. The surface plasmon resonance (SPR) peak in the UV-Vis spectra of gold nanoparticle solutions formed at the molar ratio values higher than 2.08 were red shifted with respect to those formed at lower molar ratio values, indicating the presence of large particles, while those formed at the molar ratio values below 2.08 exhibit increased absorbance in the NIR region indicating the presence of anisotropic and faceted particles. Figure 6b shows the variation of hydrodynamic diameter with the molar ratio; the trend is in accord with that observed in UV-Vis spectra, with a minimum at the molar ratio value of 2.08. Representative TEM images of a few of these samples are also shown in figures 3.6c-e, and the trend in the mean size is in agreement with UV-Vis and DLS data.

The TEM image of the sample prepared at the molar ratio value of 0.69 shows that many particles are highly faceted with triangular or bipyramidal shapes, while the sample prepared at MR value of 2.08 shows predominantly quasispherical particles and a smaller fraction of particles with triangular/bipyramidal shapes. The TEM image of the sample prepared at MR value of 5.2 has several branched flower-like particles along with flocculates and irregular shaped nanoparticles. Further increase in the molar ratio to 45 results more uniform flower like nanoparticles.

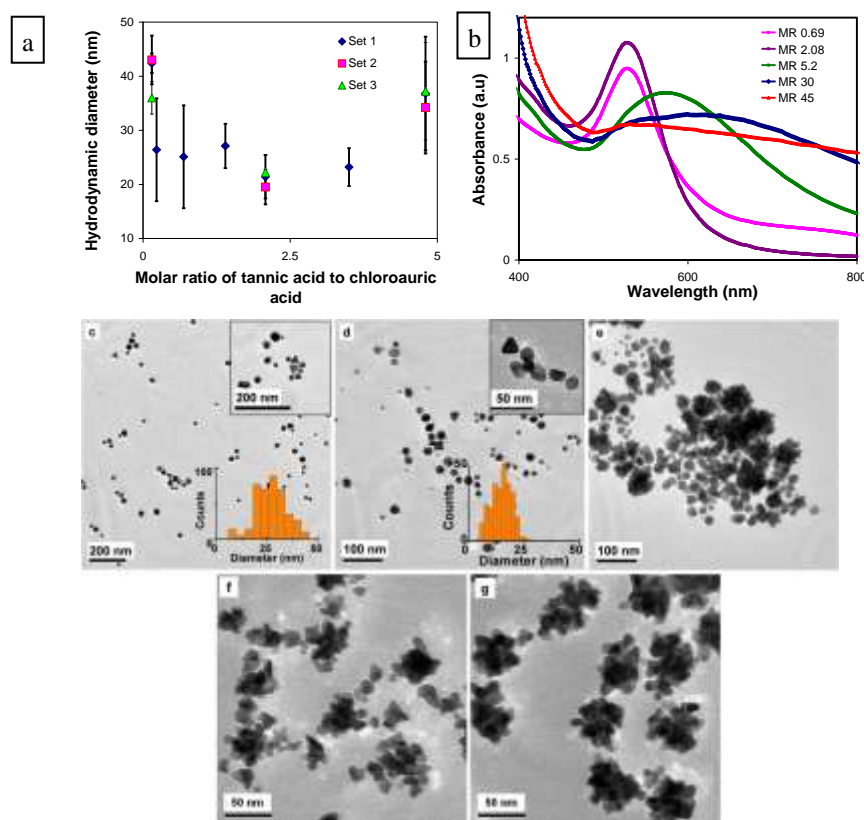


Figure 6. Effect of varying the molar ratio of tannic acid to chloroauric acid (MR). (a) UV visible spectra of colloids synthesized at different MR values. A red shift is observed in the surface plasmon peak beyond MR value of 2.08. (b) Variation of hydrodynamic diameter with MR. The error bars represent the standard deviation of the estimates of mean size obtained from six repeated measurements. (c) – (e) Representative TEM image of nanoparticles synthesized at different MR values. Insets show higher magnification images and size distribution histograms. (c), MR 0.69. Diameter = 25.3 ± 8.0 nm. (d) MR 2.08. Diameter = 14.1 ± 4.8 nm. (e) MR 5.2 (f) MR 30 (g) MR 45.

These flower like nanoparticles are similar to the ‘nanoroses’ described in a recent report, which are ideal candidates for biomedical applications. The mean size (diameter of an equivalent circle having the same projected area) is not reported due to the highly irregular shape of the particles. The atomic absorption spectroscopy analysis of the sample prepared with the molar ratio 2.08 indicated that the yield was 90.8 ± 5.6 % (95% confidence limits), and that there was no gold remaining in the supernatant (within detectable limits, i.e. >3.07 %). This proves the quantitative conversion of gold present as ions in the precursor into atoms constituting the nanoparticles. The non-monotonic variation with molar of

the size and shape of nanoparticles cannot be explained by simple arguments based on increased reactivity and stabilization.

The synthesis of gold nanoparticles with the molar ratio was studied by using stop flow module. Figure 7a-b shows the change in absorbance of nanoparticles with time for experiments with different molar ratio. Unlike silver nanoparticle synthesis, where nanoparticles have induction time followed by growth, the gold nanoparticle synthesis has two step process of change in absorbance.

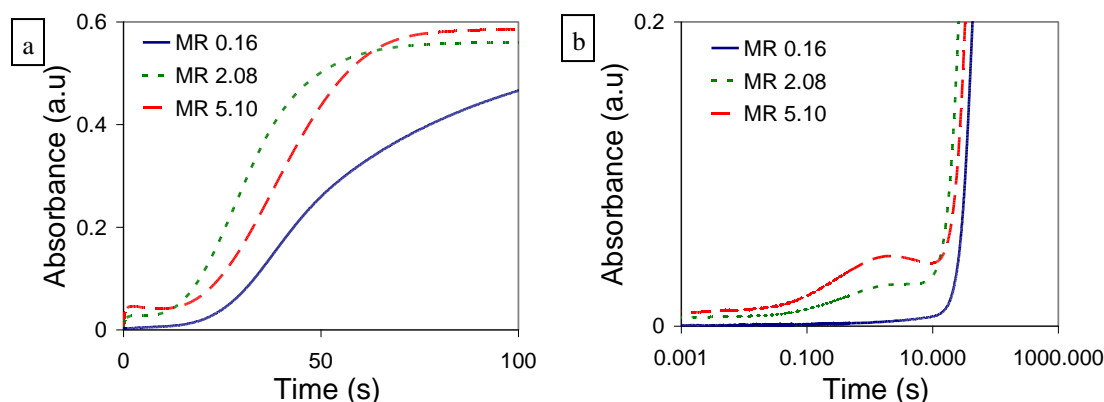


Figure 7. The variation of absorbance of nanoparticles with time for synthesis with different molar ratio, monitored with stop flow reactor in linear scale (a) and logarithmic scale (b).

Initially, after mixing reactants, the absorbance at 520 nm increases rapidly without any induction time period. The spectra of nanoparticles at the initial stage show that the increase in absorbance at 520 nm is due to the increase in overall background. The absorbance remains stable for few minutes which is followed by the gradual increase of absorbance at 520 nm. As molar ratio increases, initial increase in absorbance is rapid but growth at a later stage slows down. The time evolution spectra of nanoparticles show that the synthesis involves complicated pathway suggesting the role of tannic acid as organizer. Further detailed examination along with modeling is essential to understand the process involved in the synthesis. As the objective is to synthesize spherical gold nanoparticles rapidly, further experiments were all carried out at an overall MR value of 2.08.

9.1a.3.2 Effect of reducing mixture pH

The changes in gold nanoparticle size or shape distributions resulting from a change in pH of the reaction mixture are ascribed to either a variation in the reactivity of the precursors and/or the strength of stabilization of nanoparticles. Tannic acid exists in more dissociated form in basic pH, and hence acts as better stabilizer and ionic form increases its reactivity. A series of experiments were carried out under ambient conditions, by varying the pH and characterized the resulting colloidal samples using TEM, induction time, and ζ -potential measurements. Experiments performed with reducing mixture 3.2 and 7.1 are labeled as experiment 'A' and 'B'. Figure 8a shows the variation of hydrodynamic diameter with the change in pH of reducing mixture. The hydrodynamic diameter of nanoparticles decreases significantly with the increase in the pH of reducing mixture and saturates after pH 7.1. Figure 8b shows the TEM image of nanoparticles synthesized with reducing mixture pH 7.1. The measured lattice spacing (0.232 ± 0.008 nm) of the fringes seen in the inset of figure 8b corresponds to the value expected for gold (111). It is seen that both the nanoparticle mean diameter and polydispersity reduces upon an increase in tannic acid pH.

Figure 8c shows the change in absorbance of nanoparticles in the millisecond time scale monitored with SFR. The increase in the pH of reducing mixture from 3.2 to 7.1 reduced the induction time period from 3 s to 1.5 s. Since the reduction in induction time (a measure of reactivity) is moderate while the ζ -potential changes significantly from -20 mV to -49 mV, the observed decrease in mean size and polydispersity is mainly attributed to a decrease in coalescence caused by increased strength of stabilization in experiment 'B'.

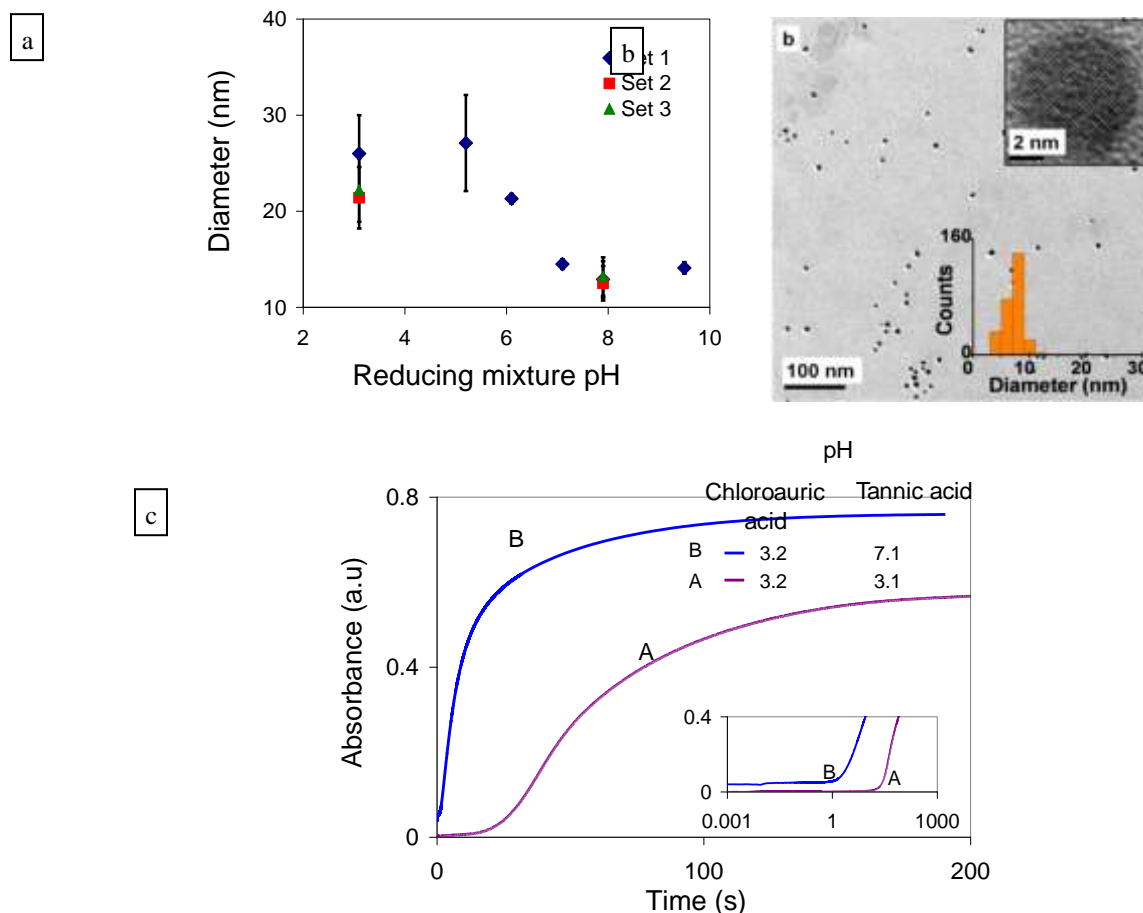


Figure 8. (a) The variation of hydrodynamic diameter of nanoparticles with the pH of reducing mixture. (b) Representative TEM image of nanoparticles synthesized with reducing mixture pH 7.1 and MR 2.08. Inset shows the high resolution image of nanoparticles with lattice fringes. Diameter = 7.1 ± 1.6 nm. (c) Stop flow reactor characterization of growth of nanoparticles with different pH of reducing mixture.

Given that both these samples were stable upon storage for more than a year, coalescence is inferred to occur mainly during the initial period of nanoparticle growth. This supposition, i.e. that the value of ζ -potential measured in experiment A (-20 mV) is below the threshold for stabilizing small (< 2 nm) nanoparticles, is in accord with earlier reports.

9.1a.3.3 Interplay between pH dependent reactivity and stabilization

The chloroauric acid exists with chloride ligand and remains highly reactive at acidic form. But, experiments prove that tannic acid behaves as good stabilizer at basic pH. As the pH values required for maximizing precursor reactivity and nanoparticle stabilization differ significantly, different conditions under which both reactivity and stabilization could be optimized were explored. The experimental conditions used, and the results of sample characterizations are presented in table 3.2.

9.1a.3.4 Effect of initial pH of chloroauric acid

To study the effect of precursor reactivity on nanoparticle synthesis, experiments 'C' and 'D' were conducted by varying the pH of reagents while ensuring that the resultant reaction mixture pH was the same as in experiment 'B'. Figure 9a-b shows the TEM image of nanoparticle synthesized with different initial pH of chloroauric acid but with same reaction mixture pH. It is observed that the nanoparticle size and polydispersity increase with an increase in the initial pH of the chloroauric acid solution. The ζ -potential values measured in experiments 'B', 'C', and 'D' are sufficiently above the threshold value to preclude coalescence as the major factor responsible for the observed changes in nanoparticle size distribution amongst these three cases. Figure 9c shows the change in absorbance of nanoparticles during synthesis obtained from SFR. The large increase in induction time clearly indicates that it is the decrease in chloroauric acid reactivity at higher pH values that results in small nucleation rates and prolonged nucleation periods (as nucleation will continue till sufficient nanoparticle surface area is generated for growth to dominate), thereby accounting for the observed changes in nanoparticle size distribution at the same overall reaction mixture pH.

Table 2. Summary of experimental conditions and characterization results.

Label	Initial pH of chloroauric acid solution	Initial pH of tannic acid solution	pH of reaction mixture	Particle diameter ($\mu \pm \sigma$), nm	Induction time ^b , s	ζ -potential ^c , mV
A	3.2	3.1	3.2	14.1 ± 4.8	3	-20 ± 2
B	3.2	7.1	6.4	7.1 ± 1.6	1.5	-49 ± 2
C	7.0	6.3	6.4	10.7 ± 3.8	66.8	-69 ± 2
D	9.1	3.1	6.4	14.2 ± 5.4	163.5	-60 ± 2
E	2.1	7.1	5.0	10.0 ± 2.9	0.9	-18 ± 7
F	2.1	9.0	7.1	5.8 ± 1.0	0.5	-35 ± 7

a – based on TEM images. b – determined using a stop-flow module (SFM) as the time taken from mixing the reagents to the appearance of surface plasmon peak corresponding to gold nanoparticles. c – ζ -potential values were obtained using a Brookhaven Zetaplus ('A' – 'D') or a Malvern Zetasizer ('E' and 'F').

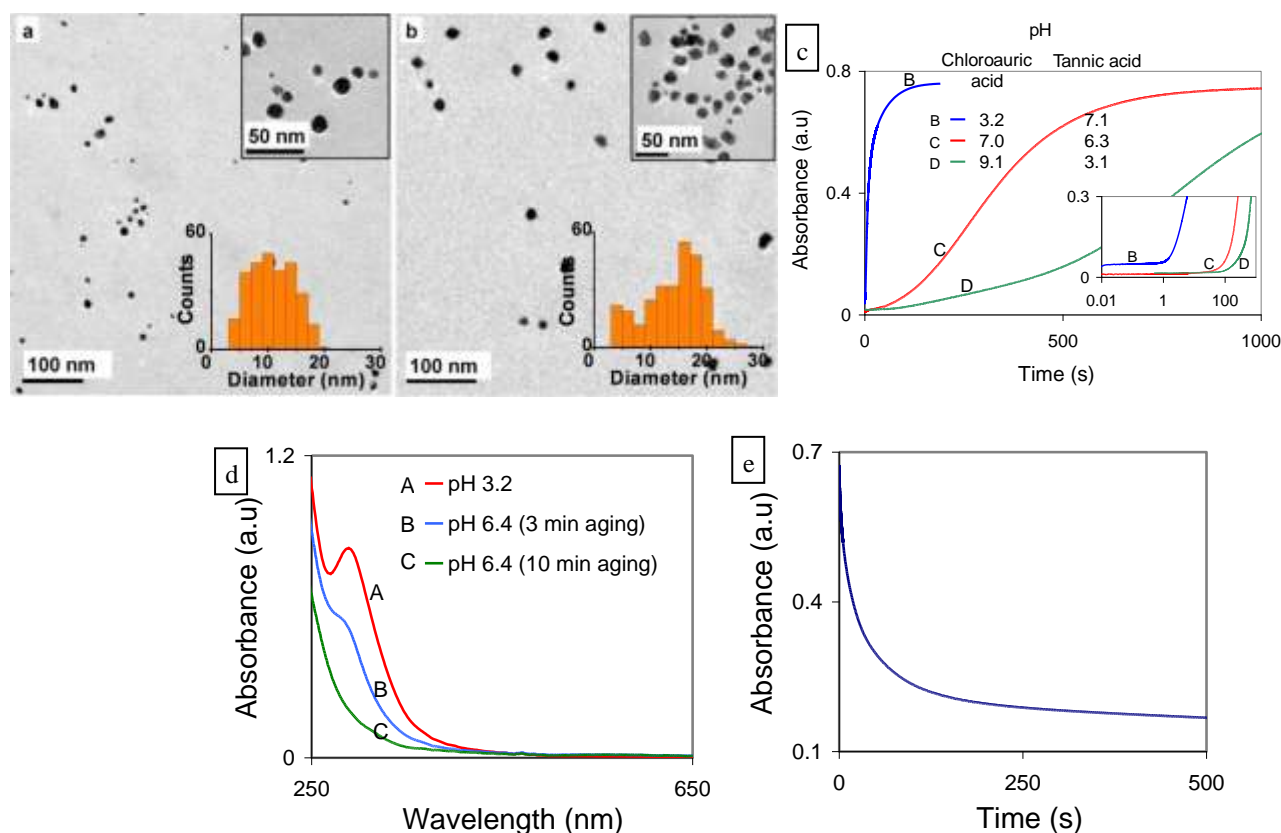


Figure 9. Representative TEM images of gold nanoparticles. (a) Tannic acid at pH 6.3 was added to chloroauric acid at pH 7.0. Nanoparticle diameter ($\mu \pm \sigma$) = 10.7 ± 3.8 nm. (b) Tannic acid at pH 3.1 was added to chloroauric acid at pH 9.1. Nanoparticle diameter ($\mu \pm \sigma$) = 14.2 ± 5.4 nm. (c) Stop flow reactor characterization of growth of nanoparticles showing the effect of initial pH of chloroauric acid pH with same reaction mixture pH. (d) The dynamics of absorbance at 315 nm monitored using an SFM at ms resolution, after rapidly mixing chloroauric acid solution at pH 3.2 with K₂CO₃ solution to change the pH to 6.4. The inset shows UV-Vis spectra (measured ex-situ) of a similar solution at various time intervals after increasing the pH from 3.2 to 6.4.

However, this deduction presumes that the reactivity of chloroauric acid is dependent on its initial pH and not on the reaction mixture pH. It is reported that chloroauric acid is present mainly as a combination of gold chloro-hydroxyspecies in aqueous solutions, and that the reactivity decreases as the chloride ligands are displaced by hydroxyl ligands at higher pH values. It is also known that the absorbance at 315 nm corresponding to the charge transfer to solvent (CTTS) absorption band depends on the number of chloride ligands present.

So, SFR experiments were conducted to study the effect of a sudden change in pH on the transformation of chloroauric acid species from one form into another, by monitoring the CTTS band of gold chloride at 315 nm. Figure 9d shows that the response time for chloroauric acid species transformation is of the order of 3-4 minutes, for a change in pH from 3.2 to 6.4. As this timescale is larger than the timescale for completion of reaction in experiment 'B', it indeed establishes that the reactivity of chloroauric acid solution is controlled by its initial pH and not the reaction mixture pH.

9.1a.3.5 Effect of pH of reaction mixture on stabilization and particle size

To delineate the effect of the reaction mixture pH from that of precursor reactivity, experiments 'E' and 'F' were conducted with chloroauric acid maintained at pH 2.1 and tannic acid at pH 7.1 and 9, this resulted in final reaction mixture pH values of 5.0 and 7.1 respectively. Figure 10a-b shows the TEM image of nanoparticles synthesized with highly reactive chloroauric acid and different reaction mixture pH. Figure 10c shows the change in absorbance of nanoparticles during synthesis with different reaction mixture pH. The redox potential of tannic acid increases only slightly over this range, while chloroauric acid is expected to be in a more reactive state than in experiment 'B'. The measured values of induction time (0.9 and 0.5 s) are in agreement with these expectations. However, the observed value of nanoparticle size distribution (10.0 ± 2.9 nm) in experiment 'E' is larger than that in experiment 'B' (7.1 ± 1.6 nm), while that observed in experiment 'F' (5.8 ± 1.0 nm) is smaller.

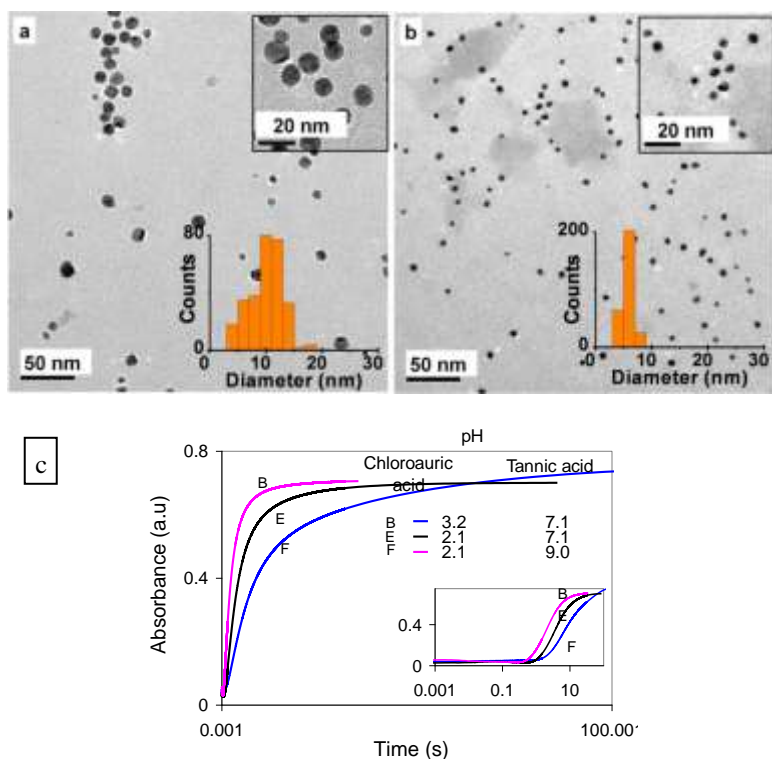
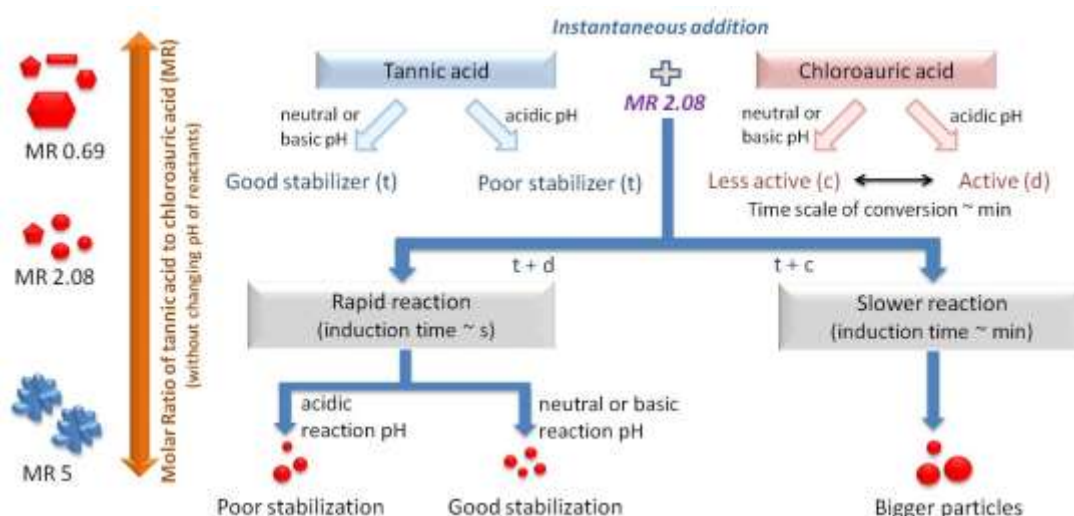


Figure 10. Representative TEM images of gold nanoparticles. (a) Tannic acid at pH 7.1 was added to chloroauric acid at pH 2.1. Nanoparticle diameter ($\mu \pm \sigma$) = 10.0 ± 2.9 nm. (b) Tannic acid at pH 9.0 was added to chloroauric acid at pH 2.1. Nanoparticle diameter ($\mu \pm \sigma$) = 5.8 ± 1.0 nm. (c) Stop flow reactor characterization of growth of nanoparticles showing the effect of reaction mixture pH.

The ζ -potential values measured in experiments 'E' and 'F' (-18 and -35 mV) clearly indicate that the strength of stabilization has substantially decreased in the case of experiment 'E', signifying that coalescence was the reason for the observed larger size and polydispersity.

Overall, these results show that gold nanoparticle size distribution is determined by a fine balance between the reactivity of precursors and coalescence in the initial period, which can be manipulated by controlling the initial pH of reactants and reaction mixture pH respectively. Scheme 3.3 illustrates the various pathways described earlier. An important outcome is that independent control over reactivity and stabilization can be achieved by manipulating the pH of the precursor solutions.



Scheme 3. Schematic summary of the effect of MR and the roles of reagent and reaction mixture pH in determining nanoparticle size and shape.

9.1a.3.6 Effect of mode of mixing reactants

As the objective is to achieve size-control, further attention was focused on experiment 'B', which exhibited the desirable characteristics of rapid nucleation and high stability. Experiment 'F' was not considered because of the need to add both an acid and a base for adjusting pH, which can lead to large variations in ionic strength and affect colloidal stability. In experiment 'B', tannic acid was added as one portion into chloroauric acid solution and so, during the initial period of mixing (mixing timescale ~ 2 s) an acidic environment was present around the growing nanoparticles possibly leading to coalescence.

Hence, an experiment ('G') was carried out to minimize coalescence during mixing by altering the order of addition such that the growing nanoparticles were typically in alkaline medium. This was achieved by simply reversing the order of addition (i.e. chloroauric acid into tannic acid), while maintaining the initial pH of reagents, overall amount of reagents, the volume of the added reagent, and the volume of the total reaction mixture at values used in experiment 'B'. For comparison, a 1 mL sample was prepared by rapidly mixing (\sim in 3 ms) the two reagents in SFM (experiment H), while maintaining the concentration, initial pH and volumetric ratio similar to experiment 'B'. Figure 11a and 3.11b show representative TEM images of nanoparticles formed in experiments 'G' and 'H', and their corresponding size distributions are determined to be 5.9 ± 1.6 nm and 6.2 ± 1.9 nm respectively. The effect of mode of mixing on diameter and standard deviation is however minimal, even in the case of rapid mixing, indicating that stabilization of nanoparticles by adsorption of tannin requires a finite time during which particles may coalesce. Attempts to ameliorate this situation by using an excess of tannic acid did not yield the desired result. So, the next best strategy was to add diluted chloroauric acid slowly into tannic acid to result in an optimal particle number density, which would suppress coalescence in the initial period and provide adequate time for adsorption of tannin.

Experiment 'I' was conducted by adding chloroauric acid at a rate of ~ 1 mL/min into a pool of tannic acid, while maintaining overall concentration and total volume of the reaction mixture constant as in experiment 'G'. For comparison, experiment 'J' was conducted by adding tannic acid slowly into a pool of chloroauric acid, keeping volume added, overall amounts and total volume same as in experiment 'G' and 'I'. Figures 3.11c and 3.11d show representative TEM images of nanoparticles formed in experiments 'I' and 'J'; their corresponding size distributions were determined to be 5.3 ± 0.7 nm and 15.8 ± 11.6 nm respectively. The narrow standard deviation observed in experiment 'I' confirms that it is the dynamics of tannin adsorption that controls coalescence in the initial period.

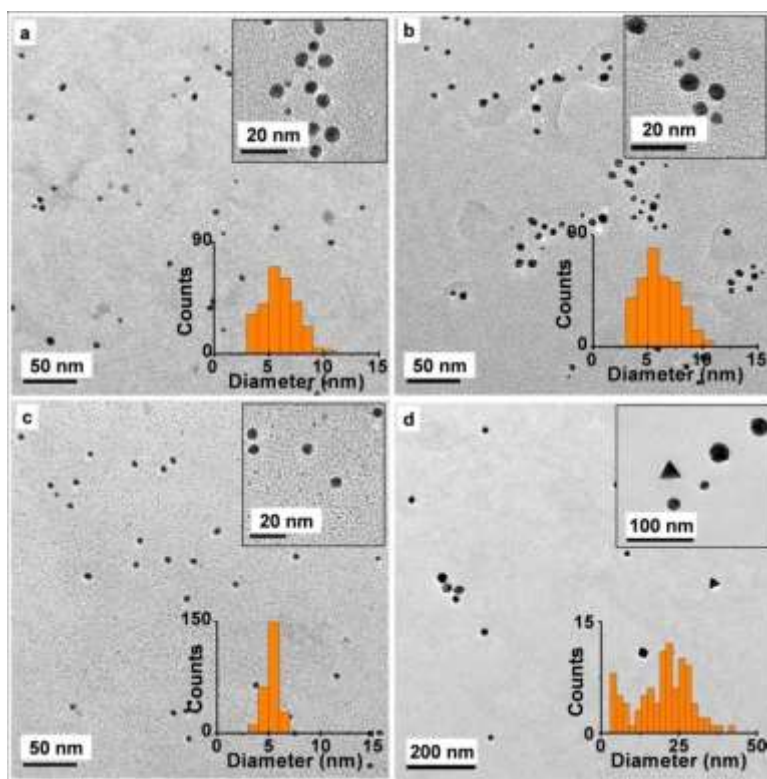


Figure 11. Representative TEM images highlighting the effect of order of addition, and rate of addition. Insets show higher magnification images and size distribution histograms. (a) Chloroauric acid added as one portion into tannic acid. Diameter = 5.9 ± 1.6 nm. (b) Chloroauric acid and tannic acid were rapidly mixed using SFM. Diameter = 6.2 ± 1.9 nm. (c) Chloroauric acid added slowly (1 mL/min) into tannic acid. Diameter = 5.3 ± 0.7 nm. (d) Tannic acid added slowly (1 mL/min) into chloroauric acid. Diameter = 15.8 ± 11.6 nm.

Considering that the mean size is smaller than in experiment ‘G’ for the same amount of gold atoms used, it is clear that the nanoparticle number density obtained ($\sim 6.4 \times 10^{13}$ particles/mL) is higher than those obtained using the fast addition protocol. In the case of experiment ‘J’, the rather large size and polydispersity are attributed to the presence of nanoparticles with different shapes and morphology. The observed faceted nature of nanoparticles is in agreement with that reported for nanoparticles growing in an environment of excess chloride at acidic pH.

9.1a.3.7 Size control by slow addition

Given that the slow dropwise addition method for a rapid precipitation reaction is akin to a seeded growth approach after an initial period, it was conjectured that smaller sized nanoparticles would be formed by simply adding lesser amount of chloroauric acid to the mixture. Figures 12a-d summarizes the results of such a set of experiments wherein particles ranging from 1.7 nm to 3.8 nm have been synthesized at room temperature within a matter of minutes. The constant value of standard deviation estimates (0.6-0.8 nm), limited by errors associated with thresholding of TEM images for particle size analysis, indicates that the growth is surface reaction controlled (i.e. the growth rate is independent of particle size). This process can be easily extended to form size-controlled nanoparticles with larger mean size, if care is taken to ensure that the reaction mixture pH never falls below 6.4. Figure 12e shows one such result obtained after the addition of 4x the amount of chloroauric acid used in experiment ‘I’.

The nanoparticle size distribution is found to be 7.4 ± 0.6 nm, which reaffirms the surface-reaction controlled nature of the growth mechanism. The processing time required to form size controlled nanoparticles in the range of 2-10 nm can be further reduced by maximizing the amount of chloroauric acid for a given volume and number density of seeds. Table 3.3 shows the various experiments performed with different conditions to optimize seeded growth. In seeded growth, the concentration of Au⁰ in the reaction mixture should be very less to avoid secondary nucleation. This can be achieved by providing more surface area for growth or by reducing the rate of production of Au⁰. For seeded growth, the chloroauric acid (0.254 mM) has to be added slowly at the rate of 1 ml/min to suppress secondary nucleation.

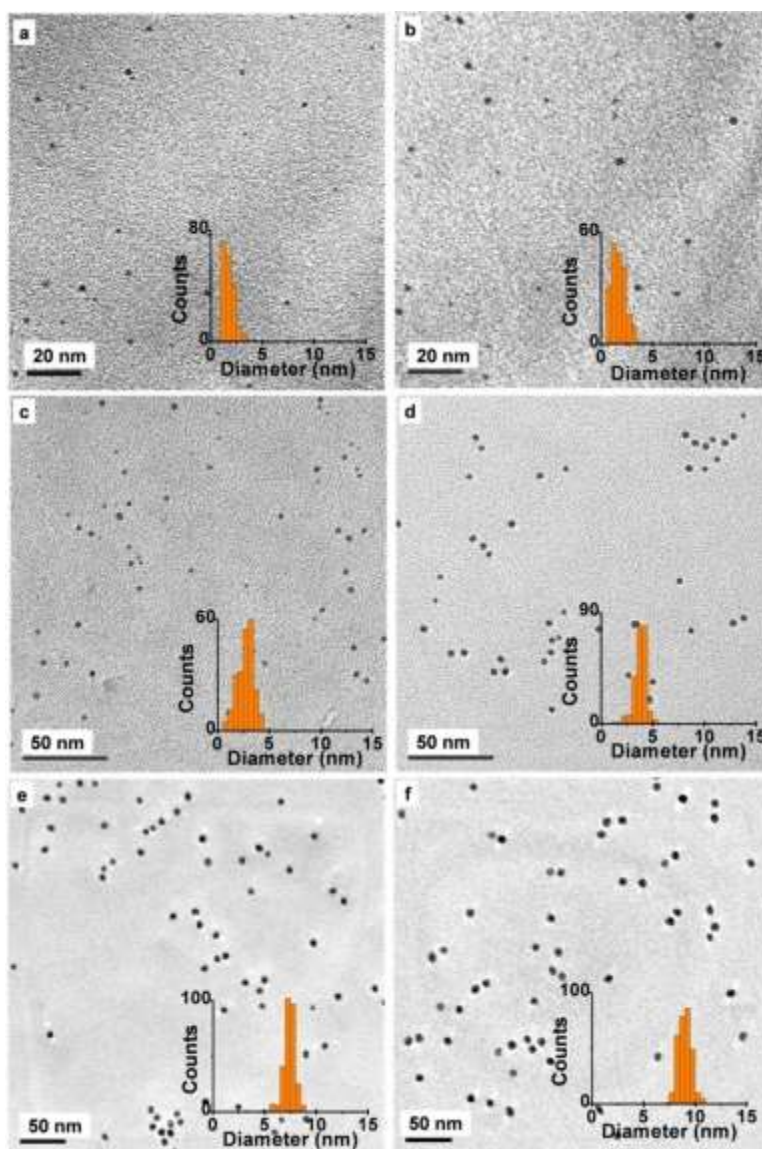


Figure 12. Representative TEM image of size-controlled nanoparticles formed by slow (dropwise) addition protocol. Insets show size distribution histograms. Nanoparticles were synthesized by slow ($\sim 1\text{ mL/min}$) addition of (a) 0.2 mL, (b) 0.4 mL, (c) 2 mL, (d) 5 mL, (e) 40 mL, of 0.64 mM chloroauric acid into 15 mL of 0.89 mM tannic acid, while maintaining reaction mixture pH above 6.4. The nanoparticle size distributions are (a) 1.7 ± 0.5 nm, (b) 1.8 ± 0.7 , (c) 2.7 ± 0.8 nm, (d) 3.8 ± 0.6 nm, (e) 7.4 ± 0.6 nm. In (f) nanoparticles were synthesized by slow (dropwise) addition of 10 mL of 0.32 mM chloroauric acid solution into 15 mL of diluted gold colloid formed in experiment T'. Diameter = 9.1 ± 0.7 nm.

Table 3. Effect of seed concentration and chloroauric acid addition rate on seeded growth of gold nanoparticles

Seed concentration (numbers/mL)	Addition rate of chloroauric acid (mL/min)	Expected size (nm)	Obtained final particle size (nm)
10^{14}	Instantaneous	7.7	5.3 ± 1.7
10^{14}	2	7.7	5.9 ± 1.7
10^{14}	1	7.7	7.4 ± 0.7
10^{13}	1	9.4	9.1 ± 0.7
10^{12}	1	12.3	6.2 ± 1.9

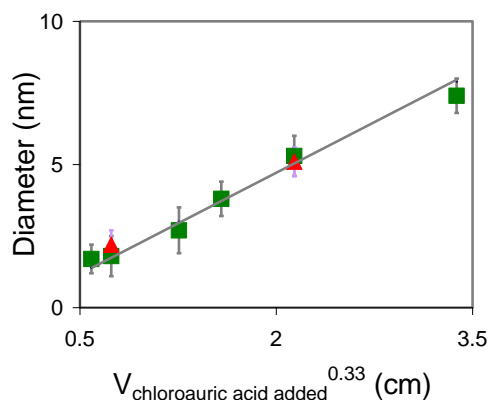


Figure 13. A plot of expected and observed nanoparticle diameter as a function of the amount of the 1/3rd power of the moles (equivalent to volume) of chloroauric acid added. The agreement between the predicted and observed diameters indicates that the slow (dropwise) addition process is akin to a one-shot nucleation-seeded growth process.

Adding chloroauric acid instantaneously or at a rate higher than 1 ml/min results in secondary nucleation. Seeded growth experiments performed with different number density of seeds show that a minimum of 10^{13} seeds/ml is required to avoid secondary nucleation. Figure 12f shows particles with a size distribution of 9.1 ± 0.7 nm that were formed within 10 minutes by optimizing the concentration of chloroauric acid for a seed density of 6.4×10^{12} particles/mL.

A simple mass balance for seeded growth shows that increase in mean nanoparticle diameter must be proportional to 1/3rd power of the moles (equivalent to volume at constant temperature) of chloroauric acid added. Figure 13 shows a plot of the predicted and the observed mean diameters as a function of the 1/3rd power of the volume of chloroauric acid added. The observed values (including a few replicate samples) are seen to agree very well with the predicted values, which is a clear indication that the slow (dropwise) addition protocol is akin to one-shot process for seed formation followed by their controlled growth into nanoparticles.

9.1a.4 Insights into synthesis of smaller gold nanoparticles by citrate reduction method

9.1a.4.1 Role of molar ratio and pH in the synthesis of citrate stabilised gold nanoparticles

Ji et al. showed that changing the molar ratio in classical citrate method changes the pH of the reaction mixture and hence the particle size. It is essential to delineate effects of parameters, namely citrate concentration and pH, to analyze and understand the citrate reduction protocol. To analyze the effect of molar ratio and pH, independent of one another, experiments were performed at different molar ratio and pH. Table 4 shows the diameter of nanoparticles synthesized at different molar ratio and pH. Figure 14 shows the FESEM images of nanoparticles synthesized at different molar ratio and pH. The effect of molar ratio at reaction mixture pH 6.7 was investigated. The change in the molar ratio from 0.5 to 20.8 results in variation of the size of nanoparticles from 27.2 ± 6.3 nm to 18.1 ± 7.3 nm. The variation of size obtained is significantly lower than that reported by Frens.

Table 4. Effect of MR and reducing mixture pH on the diameter of nanoparticles.

pH Molar ratio (MR)	3.3	5.0	6.7
20.8	61.0 ± 26.2	24.3 ± 5.3	18.1 ± 7.3
5.2	51.3 ± 17.2	22.6 ± 4.6	16.2 ± 3.1
0.52	55.2 ± 15.3	35.5 ± 8.4	27.2 ± 6.3

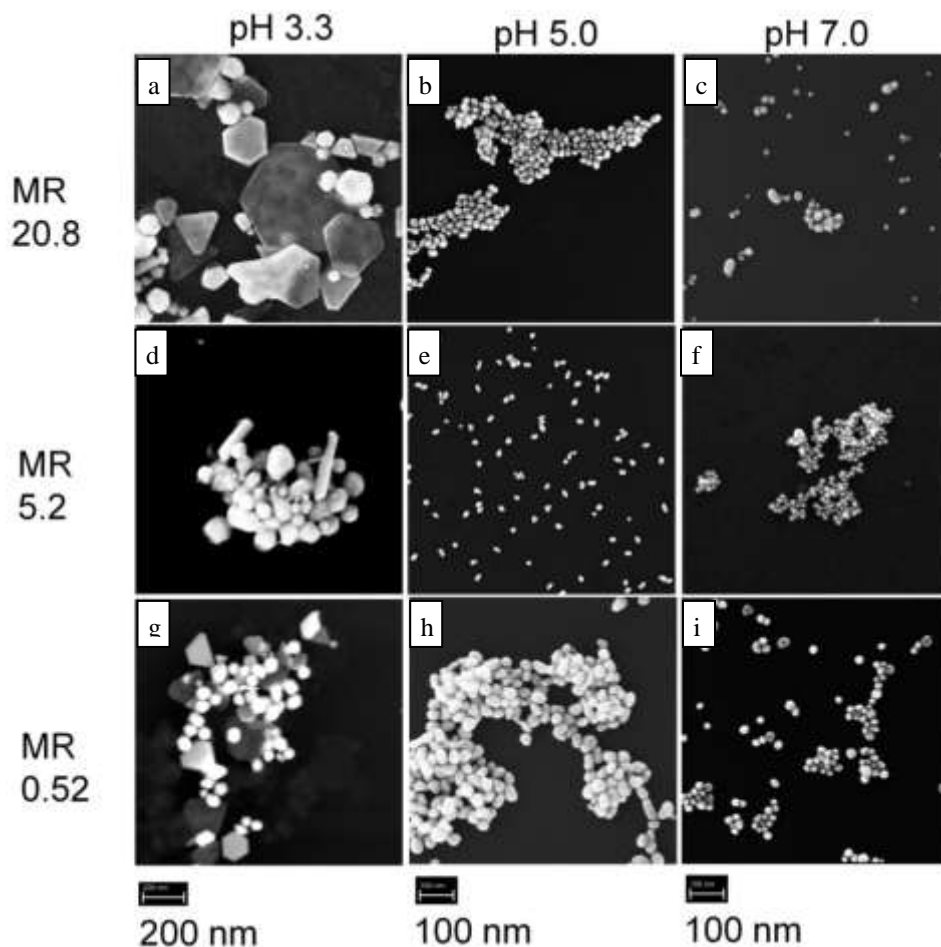


Figure 14. Representative FESEM images of nanoparticles synthesized at (a) MR 20.8 and pH 3.3 (b) MR 20.8 and pH 5.0 (c) M 20.8 and pH 6.7 (d) MR 5.2 and pH 3.3 (e) MR 5.2 and pH 5.0 (f) M 5.2 and pH 6.7 (g) MR 0.52 and pH 3.3 (h) MR 0.52 and pH 5.0 (i) MR 0.52 and pH 6.7.

In classical citrate reduction protocol, both molar ratio and pH of the reaction mixture varies and hence it is difficult to attribute the change in the particle size to one of the parameter. Decoupling the effect of molar ratio and pH and show that the change in size of nanoparticles caused by the variation of molar ratio is less compared to citrate reduction protocol. The effect of molar ratio on the reduction rate of chloroauric acid was analyzed. Figure 15a shows the concentration of chloroauric acid with time at different molar ratio. At reaction mixture pH of 6.7, increase in the molar ratio results in the increase of rate of reduction. Unlike the reduction rate trend in classical citrate reduction, which gives faster reduction rate for lower molar ratio, here expected trend is obtained. The increase in concentration of citrate results in higher reduction rate and nucleation rate, thus resulting in smaller nanoparticles.

Further, the effect of molar ratio at a reaction mixture pH of 3.3 was investigated. The poor stabilization of nanoparticles at acidic pH leads to a higher extent of coagulation of nuclei and smaller nanoparticles during the initial growth phase. At reaction mixture pH 3.3, significant amount of gold nanoplates is present along with nanoparticles. The size of nanoparticles synthesized, excluding nanoplates, is similar irrespective of molar ratio. The average size of nanoplates present along with nanoparticles increases with the molar ratio. A similar trend of increase in size of nanoplates with the molar ratio is also reported in synthesis of silver nanoplates by citric acid. The effect of molar ratio on reduction rate was studied and the effect of molar ratio on reduction rate is negligible. Figure 15b shows the concentration of chloroauric acid with time at different molar ratio and the reaction mixture pH 3.3.

The effect of reaction mixture pH on the size of nanoparticles and the reduction rate was investigated. At molar ratio of 0.5, the size of nanoparticles varies from 45.2 nm to 27.6 nm for the change in pH from 3.3 to 6.7. At molar ratio of 20.8, the size varies from 61 nm to 19.2 nm for change in pH from 3.3 to 6.7. The effect of pH on the size and shape is in accordance with the results reported in literature. The effect of reaction mixture pH on the rate of reduction of chloroauric acid was investigated. Figure 15c shows the change in the concentration of chloroauric acid with time at

different reaction mixture pH and at a molar ratio of 5.2. The size of the nanoparticles synthesized decreases with the increase in reaction mixture pH.

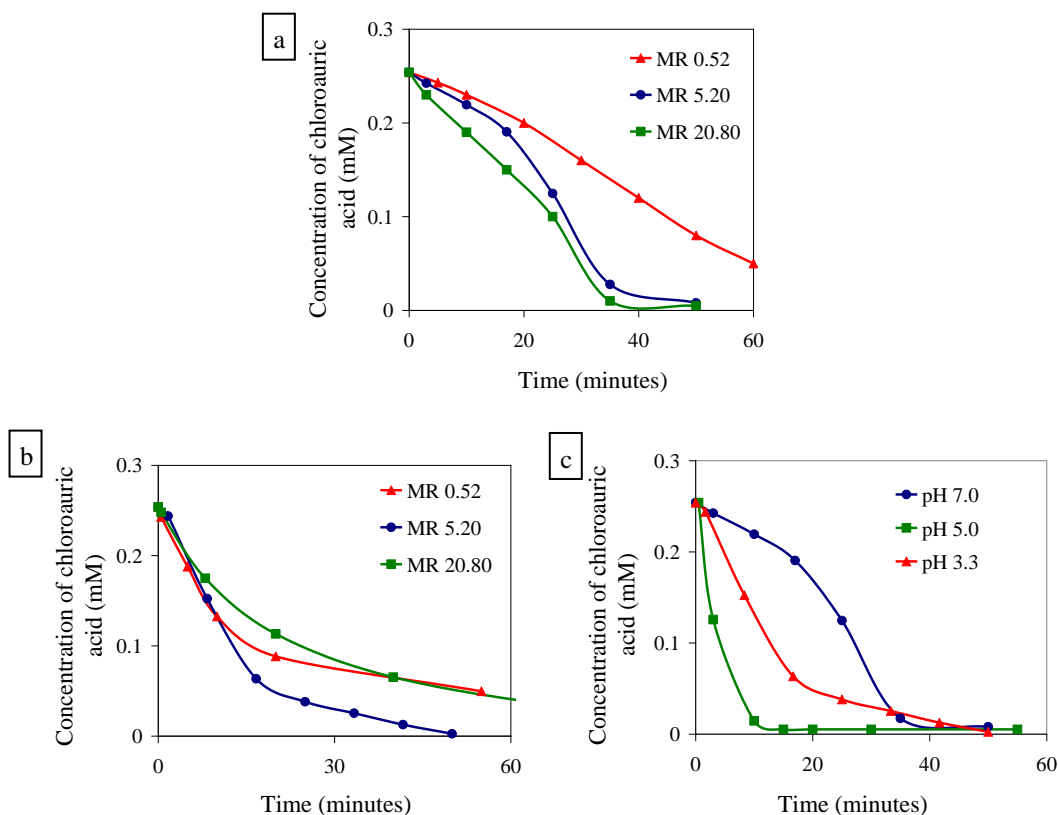


Figure 15. (a) Concentration of chloroauric acid with time at molar ratio (MR) 0.52, 5.2 and 20.8. The reaction mixture pH is 7.0. (b) Concentration of chloroauric acid with time at molar ratio (MR) 0.52, 5.2 and 20.8. The reaction mixture pH is 3.3. (c) Concentration of chloroauric acid with time at reaction mixture pH 7.0, 5.0 and 3.3. MR = 5.2.

But, the trend in reduction rate is different from the trend observed in the size of nanoparticles. As the pH of the reaction mixture reduces from 7.5 to 5.5, the rate of reduction of chloroauric acid increases. But, further decrease in the pH to 3.2 results in slower reduction. Eventhough the rate of reduction passes through maxima with pH, the size of nanoparticles decreases monotonically with pH. Initial reduction in pH increases the reactivity of chloroauric acid and hence results in faster reduction. Further reduction in pH to 3.3 decreases the concentration of ionized form of citrate ($pK_a - 3.2$) and reduces the reactivity of citrate and hence reaction slows down. Hence, there is an optimum pH where the rate of reduction is maximum.

The reduction of chloroauric acid is fast at acidic pH of 5, but higher extent of coagulation during the growth phase due to poor stabilization leads to reduction in number of particles and hence results in bigger particles. A combination of fast reduction (pH – 5) and good stabilization (pH > 7) of particles during the growth phase never occurs together in the standard citrate reduction protocol.

9.1a.4.2 Effect of reaction temperature on synthesis of gold nanoparticles

The effect of reaction temperature on the size and shape of nanoparticles synthesized was investigated. In all experiments conducted at 100°C, the time period of induction and the color saturation time was lesser than the experiments conducted at 60°C. For example, at MR 5.2, induction time period is 600 s at 60 °C and 50 s at 100 °C. Eventhough the induction time decreases by a factor of 10, the size of nanoparticles does not reduce significantly. Figure 16a-c shows the FESEM image of nanoparticles synthesized at different reaction mixture pH and MR 20.8. Figure 16d shows the rate of reduction of chloroauric acid at different reaction mixture pH. The trend remains similar to that at 60 °C. The observations indicate that the rate of reduction of chloroauric acid is faster at 100°C. But, the size of nanoparticles, synthesized at 100 °C, remains comparable with that synthesized at 60 °C.

As a result of pH optimization for faster reduction, we show that citrate reduction takes place even at room temperature. We conducted the experiments at reaction mixture pH 4.7, where the rate of reduction is maximum.

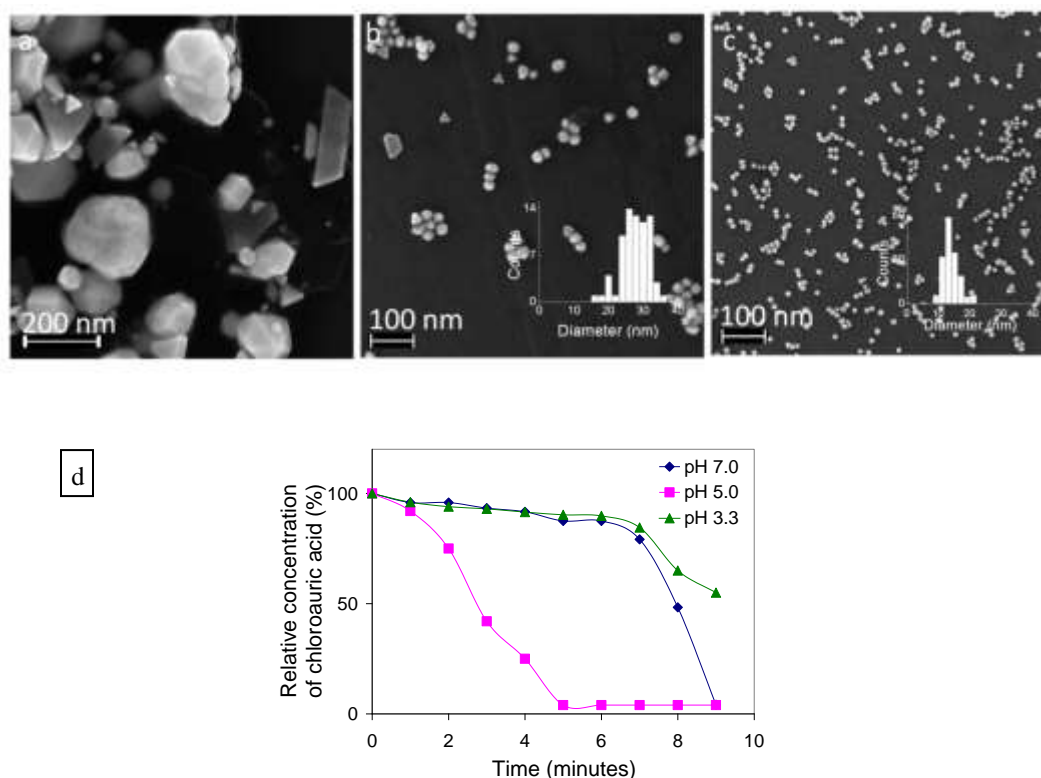


Figure 16. Representative FESEM images of nanoparticles synthesized at different reaction mixture pH and at reaction temperature of 100°C. (a) reaction mixture pH 3.2. Diameter = 123 ± 36 nm. (b) reaction mixture pH 5.0. Diameter = 27.5 ± 5.5 nm. (c) reaction mixture pH 7.5 Diameter = 13.6 ± 2.8 nm. (d) Change in concentration of chloroauric acid with time at different reaction mixture pH.

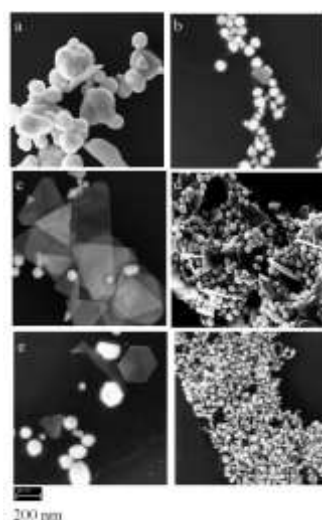


Figure 17. Representative FESEM images of nanoparticles synthesized at room temperature and the following conditions. (a) Reaction mixture pH = 3.3, MR = 20.8. (b) Reaction mixture pH = 4.7, MR = 20.8. (c) Reaction mixture pH = 3.3, MR = 5.2. (d) Reaction mixture pH = 4.7, MR = 5.2. (e) Reaction mixture pH = 3.3, MR = 0.52. (f) Reaction mixture pH = 4.7, MR = 0.52.

Depending on the molar ratio of the reaction mixture, the induction time period varies between 45 minutes to 180 minutes. Figure 17 shows the FESEM images of nanoparticles synthesized at room temperature and at different molar ratio and pH. It is clear that by adjusting the reaction mixture pH to obtain maximum reduction rate, we can achieve the synthesis of nanoparticles by citrate reduction even at room temperature. The nanoparticles obtained at room temperature are a mixture of nanoparticles and nanoplates. The synthesis at room temperature, with the molar ratio of 5.2 and pH 3.3, results in high yield of nanoplates.

9.1a.4.3 Tuning synthesis with the presence of stabilizer in fast reduction

Synthesis of smaller monodisperse particles requires a burst of nucleation, generally a result of fast reaction, and better stabilization. Kinetic studies of the synthesis of nanoparticles at different pH clearly shows that a combination of fast reduction (pH 4.5) and good stabilization (pH > 7) can never occur together. Here, we propose two different strategies to synthesis monodisperse and smaller nanoparticles. To reduce the size of nanoparticles, an additional stabilizer can be added in the fast reduction of chloroauric acid to reduce coalescence of during synthesis or the rate of reduction of chloroauric acid can be increased at higher pH range can be increased by introducing organizer.

In order to minimize the extent of coagulation during a fast reaction, synthesis with a molar ratio of 5.2 and pH 4.7, an additional stabilizer was added during the synthesis. It was ensured that the stabilizers examined did not react with chloroauric acid. Sodium dodecyl sulphate is a widely used surfactant for stabilizing nanoparticles. Sodium dodecyl sulphate, with pKa 2, is a suitable stabilizer at acidic pH range. Figure 18a shows the change in peak wavelength of absorbance with respect to concentration of sodium dodecyl sulphate. Initial increase in the concentration of sodium dodecyl sulphate results in the decrease in the diameter of nanoparticle. Sodium dodecyl sulphate reduces the coagulation of nanoparticles during the initial phase of synthesis and thus results in smaller nanoparticles. But further increase in sodium dodecyl sulphate concentration increases the particle size. Higher concentration of sodium dodecyl sulphate, an ionic stabilizer, increases the concentration of counterion (Na^+ ions) and hence increases the diameter of nanoparticles synthesized. The mean diameter of nanoparticles synthesized at 4 mM concentration of sodium dodecyl sulphate is 13 ± 3.1 nm. Figure 18b shows electron microscopy image of nanoparticles synthesized at 4 mM concentration of sodium dodecyl sulphate. In ionic stabilizer, the concentration of stabilizer that can be added to the system is limited by ionic concentration. Hence, polyvinylpyrrolidone (PVP), a water soluble polymer, was used to stabilize gold nanoparticles.

The effect of concentration of PVP on the size of nanoparticle was studied. Figure 19a shows the variation in diameter and peak wavelength of nanoparticle absorbance with concentration of PVP. As the concentration of PVP increases, the diameter of nanoparticle decreases. At the concentration of 0.2 mM of PVP, the diameter of nanoparticles, obtained from TEM images, is 6.1 ± 1.6 nm. Figure 19b shows the TEM image of nanoparticles synthesized with 0.2 mM PVP. Further increase in the concentration of PVP did not result in the decrease in the size of nanoparticles. Eventhough the size of nanoparticles synthesized decreases significantly; the polydispersity of nanoparticles remains higher. The rate of reduction of chloroauric acid and formation of nanoparticle with and without PVP was analyzed to study the effect of PVP. Figure 19c shows the reduction in absorbance of chloroauric acid with respect to time with and without PVP.

The rate of reduction of chloroauric acid remains same with and without PVP, at 60 °C and 100 °C, indicating that PVP does not react with chloroauric acid. Figure 19d shows the change in absorbance of nanoparticle at 520 nm with time. With the presence of PVP, the induction time period in the synthesis of gold nanoparticle increases. The induction time period is the time period for which the reaction mixture remains colorless. The gold nanoparticles remain colorless until a size of 2 nm. The appearance of the color indicates the time at which the size with significant absorbance ($\sim 2\text{nm}$) begins. In the presence of PVP, the induction time period increase to 6 minutes from 4 minutes. Due to the presence of stabilizer, PVP, the coagulation of smaller nanoparticles are reduced and hence the induction time period is delayed.

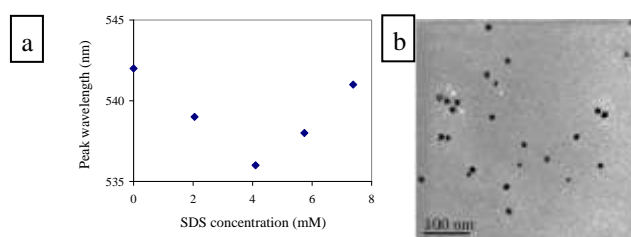


Figure 18. (a) Effect of sodium dodecyl sulphate on the diameter and peak wavelength of absorbance of gold nanoparticles. (b) TEM image of nanoparticles synthesized at molar ratio of 5.2, pH 5.5 and 4 mM sodium dodecyl sulphate. Diameter = 13 ± 3.1 nm.

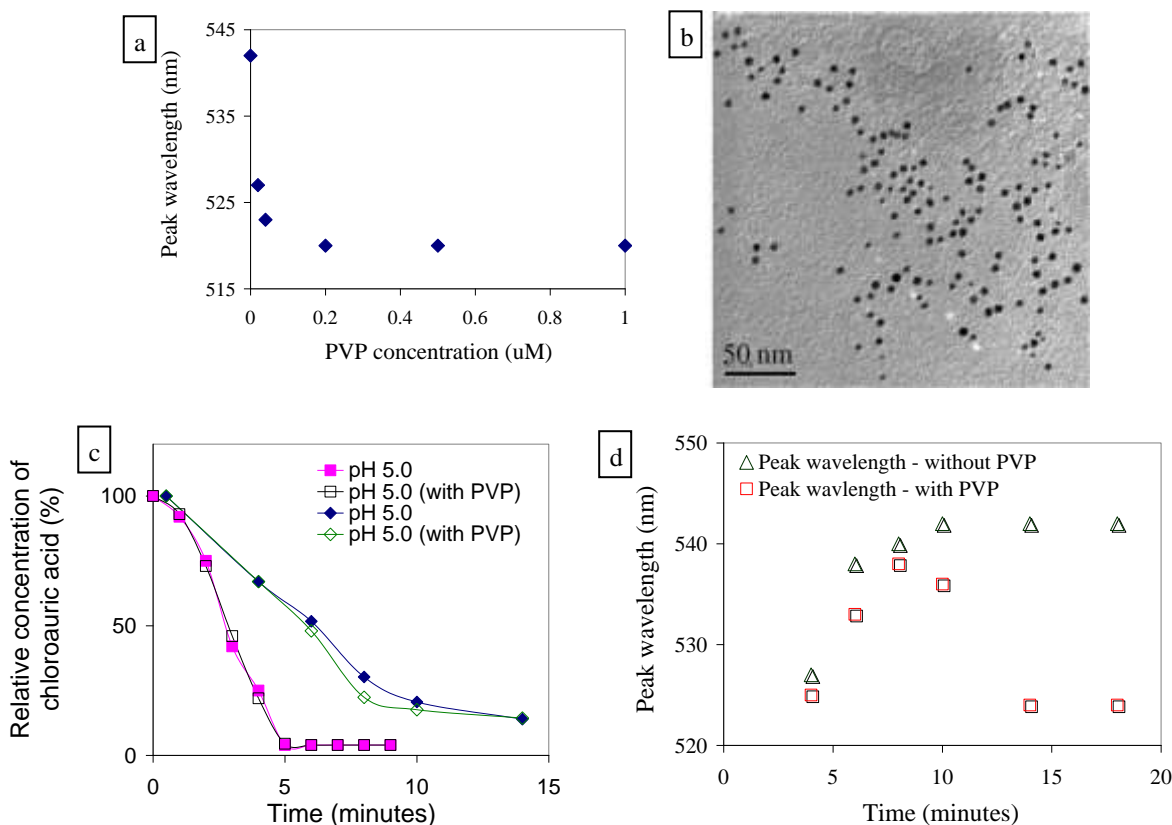


Figure 19. (a) Effect of polyvinylpyrrolidone on the diameter and peak wavelength of absorbance of gold nanoparticles. (b) TEM image of nanoparticles synthesized at MR 5.2, pH 5.5 and without PVP. Diameter = 6.1 ± 1.6 nm. (c) Reduction of absorbance of chloroauric acid with time in absence and presence of 0.2 mM PVP, molar ratio of 5.2 and pH 5.5. Square and circle symbol represents experiments performed at 100°C and 60°C respectively. (d) The variation of peak wavelength of nanoparticles during synthesis of nanoparticles with and without PVP.

During the synthesis of nanoparticles in the presence of PVP, the solution remains colorless initially, turns blue, and then wine red. Figure 19d shows the peak wavelength of nanoparticle solution with and without PVP. The formation of nanoparticles at pH 4.7 and in the presence of PVP is similar to that in the classical citrate reduction. The size of nanoparticles can be simply tuned from 30 nm to 6 nm by changing the concentration of PVP.

9.1a.4.4 Effect of mode of addition of reactants

The effect of mode of mixing reactants on the synthesis of gold nanoparticles, adding chloroauric acid into citrate vs adding citrate into chloroauric acid, was studied at different molar ratio. Figure 20a shows the effect of mode of addition at different molar ratios on diameter and figure 20b-g shows electron microscopy images of nanoparticles synthesized by a different mode of addition and at different molar ratio. At MR > 5, addition of chloroauric acid into citrate solution results in smaller nanoparticles than adding the other way. The time required for the synthesis of nanoparticles is faster while adding chloroauric acid into citrate solution. Figure 21a and b shows the digital image of the reaction mixture during the synthesis. At MR 20.8, addition of chloroauric acid into citrate took 180 seconds for the completion of the reaction and resulted in nanoparticles of size 7.2 ± 0.8 nm. At same molar ratio, addition of citrate solution into chloroauric acid took 10 minutes for the completion of the reaction and resulted in nanoparticles of size 13.6 ± 2.7 nm. At MR < 5, the mode of addition of reaction does not affect the diameter significantly. The effect of order of addition of reactants, which results in sub 10 nm nanoparticles, was systematically investigated.

Turkevich et al. have shown that the presence of acetone dicarboxylic acid eliminates the induction time period in the synthesis of gold nanoparticles by citrate reduction method. The change in order of addition of reactants too reduces the induction time period. Unlike classical citrate reduction, where citrate solution at room temperature is added to the reaction mixture, here, boiling citrate solution is used. Thermal oxidation of citrate solution by dissolved oxygen can result in formation of acetone dicarboxylic acid and lead to faster reaction.

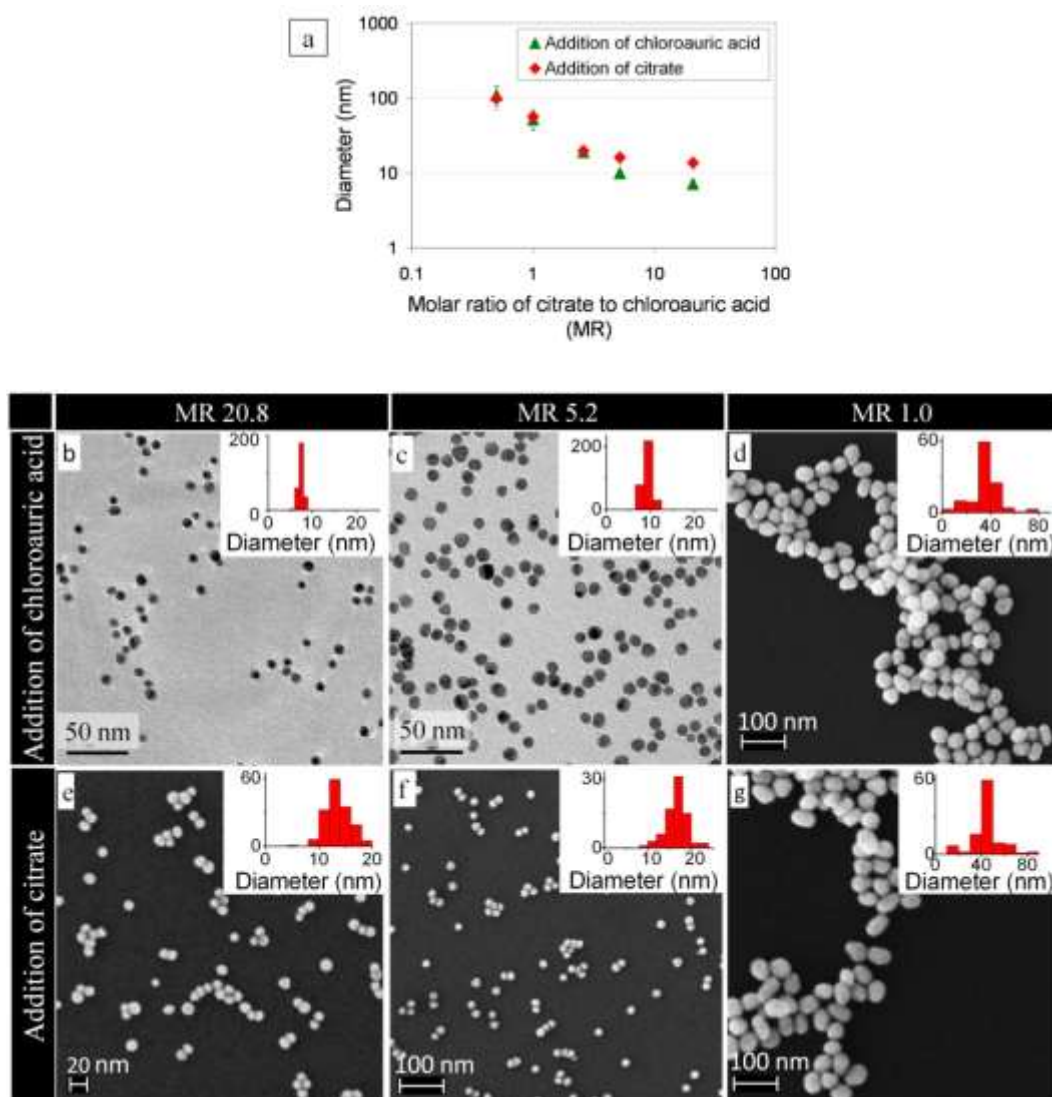


Figure 20. Effect of reversing the order of addition of reactants. (a) Plot showing the variation of the mean particle size with molar ratio for the two different modes of addition. The error bars represent one standard deviation. H_{Au}Cl₄ concentration was maintained constant at 25.4 mM. (b) – (g) Representative Field Emission Scanning Electron Microscope (FESEM) images with particle size histograms as insets are shown for colloids synthesized at three different molar ratios (MR) by the two different modes of addition of reactants. (b) MR=20.8, gold chloride into citrate, Diameter = 7.2 ± 0.8 nm. (c) MR=5.2, gold chloride into citrate, Diameter = 10.0 ± 1.0 nm. (d) MR=2.6, gold chloride into citrate, Diameter = 52.0 ± 15 nm. (e) MR=20.8, citrate into gold chloride, Diameter = 13.6 ± 2.7 nm. (f) MR=5.2, citrate into gold chloride, Diameter = 16.1 ± 3.3 nm. (g) MR=2.6, citrate into gold chloride, Diameter = 56.0 ± 15 nm.

To eliminate the possibility of use of citrate solution at 100 °C causing smaller nanoparticles, an experiment was performed by adding boiling 1% w/v citrate solution into boiling chloroauric acid. The citrate solution was boiled for 10 minutes prior to addition. Figure 21c shows the digital images of the reaction mixture during the synthesis. Figure 22c shows the FESEM image of nanoparticles synthesized by adding boiling citrate into boiling chloroauric acid. The time taken for the formation of gold nanoparticles was similar to classical citrate method and it resulted in nanoparticles of size 14.0 ± 2.2 nm indicating that use of citrate solution at 100 °C does not affect the synthesis.

Further experiment was performed by adding concentrated reactants into boiling water rather than diluting one of reactant prior to reaction. Addition of citrate solution into boiling water followed by chloroauric acid resulted in shorter induction time and smaller nanoparticles (8.1 ± 1.1 nm) while adding chloroauric acid into boiling water followed by citrate solution resulted in slower reaction and bigger nanoparticles (13.5 ± 2.3 nm). Figure 22a-b shows FESEM image of nanoparticles synthesized by adding reactants into boiling water in a different order. These experiments clearly show that thermal degradation of citrate into acetone dicarboxylic acid can not account for the change in the size of nanoparticles. We further investigated the role chloroauric acid reactivity and the initial pH of chloroauric acid.

In the classical citrate method, required volume of 1% w/v (34 mM) of citrate solution is added to 25 ml of 0.01% w/v (0.254 mM) of chloroauric acid solution. The pH of chloroauric acid is 3.2 and after addition of citrate (MR 20.8) into chloroauric acid, the pH of resultant reaction mixture changes to 7.5. While changing the order of mixing reactants, concentrated chloroauric acid at pH 1.6 (25.4 mM) is added into citrate solution of desired concentration and the reaction mixture pH remains the same irrespective of order of addition. In these experiments, after mixing reactants, the pH of the reaction mixture is 7.5. The chloroauric acid remains with chloride ligands at acidic pH and has hydroxide ligands at neutral or basic pH. The change in pH after mixing reactants causes the change in speciation of chloroauric acid. The change in pH is instantaneous but the change in speciation of chloroauric acid is slow.

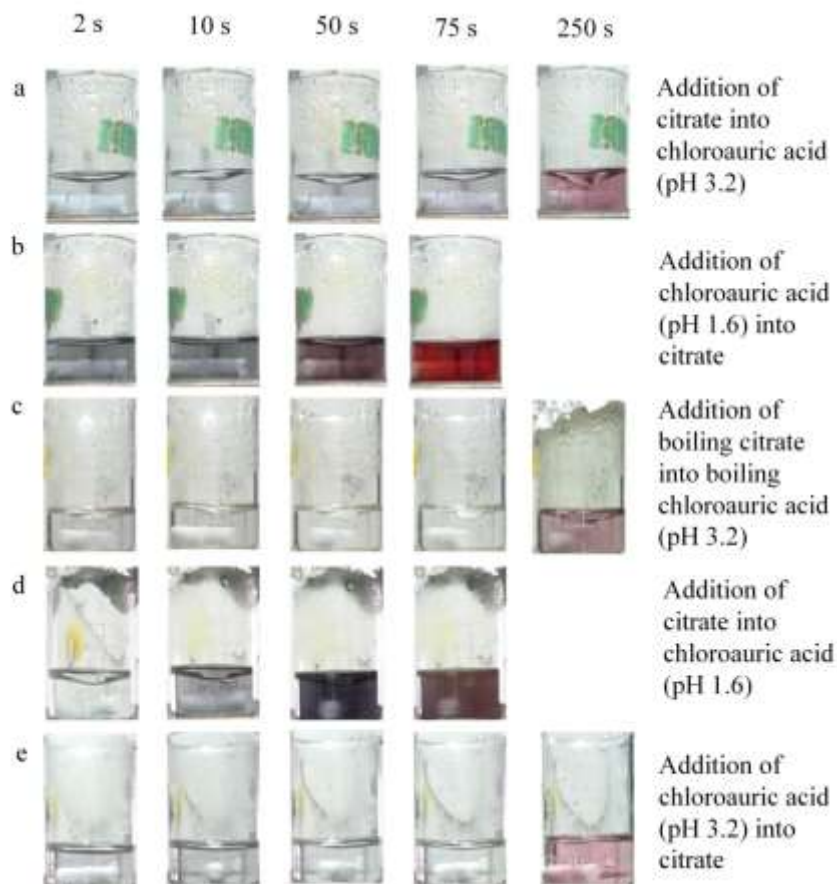


Figure 21. Digital images of reaction mixture taken during the course of nanoparticle synthesis. The MR value was 20.8 in all the above experiments. (a) addition of citrate into boiling chloroauric acid (pH 3.2), standard Turkevich method. (b) addition of chloroauric acid (pH 1.6) into boiling citrate. (c) addition of citrate solution boiled for 10 minutes prior to addition into chloroauric acid (pH 3.2). (d) addition of citrate into boiling chloroauric acid (pH 1.6). (e) addition of chloroauric acid (pH 3.2) into boiling citrate.

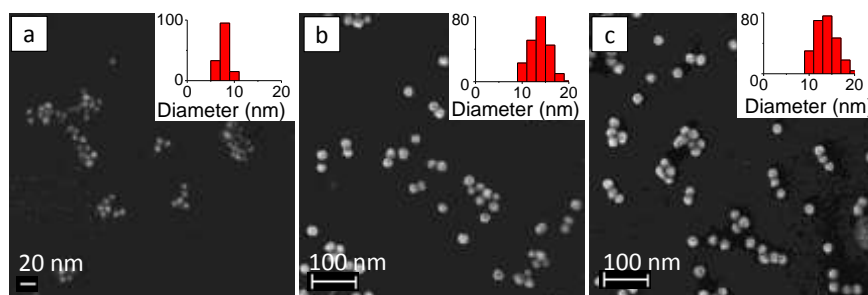


Figure 22. (a) FESEM image of nanoparticles synthesized by adding citrate followed by chloroauric acid into boiling water. MR = 20.8 (classical citrate method). Diameter = 8.8 ± 1.1 nm. (b) FESEM image of nanoparticles synthesized by adding chloroauric acid followed by citrate into boiling water. MR = 20.8 (classical citrate method). Diameter = 13.5 ± 2.3 nm. (c) FESEM image of nanoparticles synthesized by addition of boiling citrate into boiling chloroauric acid. MR = 20.8. Diameter = 14.0 ± 2.2 nm.

Hence, a highly acidic chloroauric acid with active chloroauric acid can take longer time for conversion and can result in higher time scale available for faster reaction. Thus, initial pH of chloroauric acid can affect the synthesis of gold nanoparticles.

Further experiments were carried out by changing the initial pH of chloroauric acid in the synthesis of gold nanoparticles by classical citrate reduction method and by adding citrate in chloroauric acid. The pH of chloroauric acid was tuned to 1.7 and the pH of citrate was changed to 8.5 such that the pH of the reaction mixture remains same at pH 7.5. Here, the chloroauric acid at pH 1.7 exists as highly reactive species than at pH 3.2. Due to the higher time window of availability of active species, the reaction must be faster while using highly acidic chloroauric acid. As expected, the chloroauric acid at pH 1.7 results in faster reduction than the chloroauric acid at pH 3.2. Figure 20d shows the digital image of the reaction mixture with time. Figure 23a shows the change in concentration of chloroauric acid with time for experiments conducted with chloroauric acid with initial pH 1.7 and 3.2. Figure 23b shows the change in absorbance of nanoparticles with time.

The prominent induction time period which is present in the classical citrate reduction method is absent in the case where the initial pH of chloroauric acid is 1.7. Figure 23c shows the FESEM image of nanoparticles synthesized with chloroauric acid at initial pH 1.7. The size of nanoparticles synthesized with chloroauric acid with initial pH is 19.6 ± 8.8 nm while classical citrate reduction method results in nanoparticles of size 13.6 ± 2.8 nm. The nanoparticles, synthesized with initial pH of chloroauric acid 1.7, turned into blue color after a day and crashed. Addition of hydrochloroauric acid and potassium carbonate to the system to change pH also increases the salt content in the reaction mixture. The presence excess amount of salt in the citrate synthesis screens the double layer and results in coagulation of nanoparticles. These results indicate that eventhough the increase in reduction rate is achievable by tuning reactivity, the size of nanoparticle remains higher than that synthesized by classical citrate reduction method. Another experiment was performed by adding chloroauric acid into citrate solution, but the pH of chloroauric acid was reduced to 3.2 from 1.6.

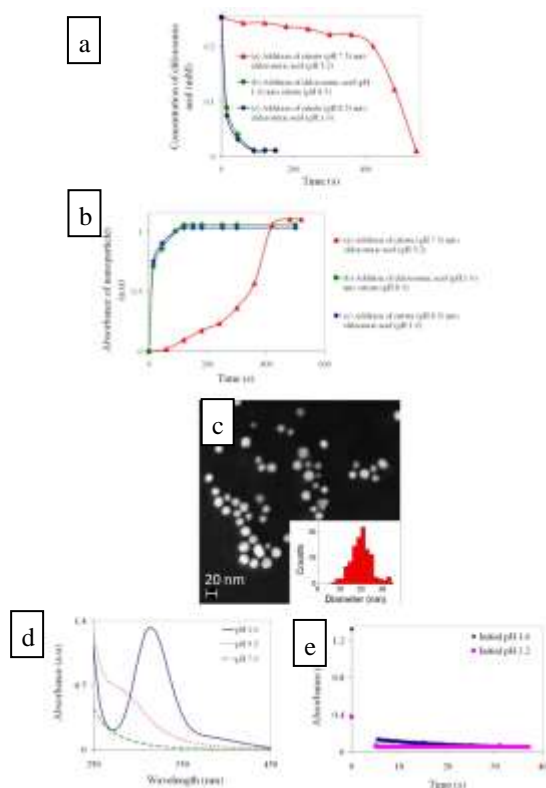


Figure 23. (a) The concentration of chloroauric acid with time during reaction at different modes and initial pH. (b) The absorbance of nanoparticles with time for different modes and initial pH. (c) FESEM image of nanoparticles synthesized by adding citrate with pH 8.5 into chloroauric acid with pH 1.6. MR = 20.8. Diameter = 19.6 ± 8.8 nm. (d) UV visible spectroscopy of chloroauric acid at different pH. (e) The change in absorbance at wavelength 315 nm with time on change in pH.

Due to the reduction in the initial pH of chloroauric acid, the available time window of active species during transformation decreases and results in slower reaction. Figure 23e shows the digital image of the reaction mixture during the synthesis.

We further investigated the rate of change of species of chloroauric acid on the change in the pH. The UV visible spectroscopy of the chloroauric acid solutions shows a distinct peak for auric ions with chloride ligands at 315 nm due to CTTS and hence it is easy to monitor the reactive form of chloroauric acid. Experiments were performed at $\sim 95^\circ\text{C}$ where the pH of chloroauric acid was changed from its initial pH to pH 7.5 by adding potassium carbonate and the change in absorbance was monitored with time. Figure 24a shows chloroauric acid at different pH and Figure 24b shows the change in peak wavelength at 315 nm corresponding to auric chloride. The equilibration time is in order of 5 seconds and hence can react significantly during this time scale resulting in acetone dicarboxylic acid which further accelerates the reaction.

The effect of concentration of chloroauric acid on the mode of addition and the diameter of nanoparticle was investigated. The concentration of citrate was maintained at 5.2 mM for all the experiments. Figure 24a shows the change in diameter of nanoparticles synthesized for different mode of addition of reactants and at different concentration of chloroauric acid. At higher concentration of chloroauric acid, 2.54 mM, irrespective of mode of addition the size of nanoparticles remains same. The time taken for completion of the reaction also was similar. The initial pH of chloroauric acid is 1.6 and 2.2 for addition of chloroauric acid into citrate and addition of citrate into chloroauric acid respectively.

At lower concentration of chloroauric acid, 0.04 mM, addition of chloroauric acid into citrate results in nanoparticles of size 5.9 ± 1 nm and addition of citrate into chloroauric acid results in nanoparticles of size 35.3 ± 6.1 nm. The initial pH of chloroauric acid is 1.6 and 6.4 for addition of chloroauric acid into citrate and addition of citrate into chloroauric acid respectively. The large difference in the initial pH results in the change in size of nanoparticles.

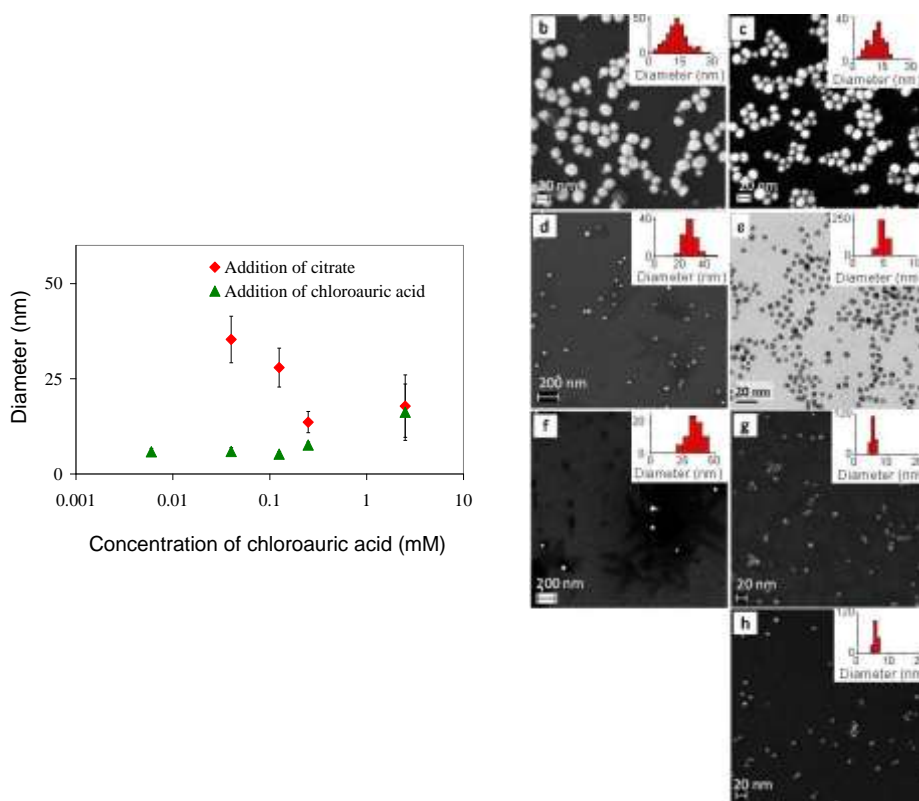


Figure 24. (a) Variation of nanoparticle size with chloroauric acid concentration for the two alternative orders of addition. (b)-(h) Representative electron microscopy images of nanoparticles synthesized by (b) addition of citrate into chloroauric acid. Chloroauric acid concentration = 2.5 mM. Diameter = 17.8 ± 8.2 nm. (c) addition of chloroauric acid into citrate. Chloroauric acid concentration = 2.5 mM. Diameter = 16.2 ± 7.4 nm. (d) addition of citrate into chloroauric acid. Chloroauric acid concentration = 0.125 mM. Diameter = 27.9 ± 5.1 nm. (e) addition of chloroauric acid into citrate. Chloroauric acid concentration = 0.125 mM. Diameter = 5.2 ± 0.7 nm (f) addition of citrate into chloroauric acid. Chloroauric acid concentration = 0.04 mM. Diameter = 35.3 ± 6.1 nm. (g) addition of chloroauric acid into citrate. Chloroauric acid concentration = 0.04 mM. Diameter = 5.9 ± 1.0 nm. (h) addition of chloroauric acid into citrate. Chloroauric acid concentration = 0.006 mM. Diameter = 6.1 ± 1.1 nm.

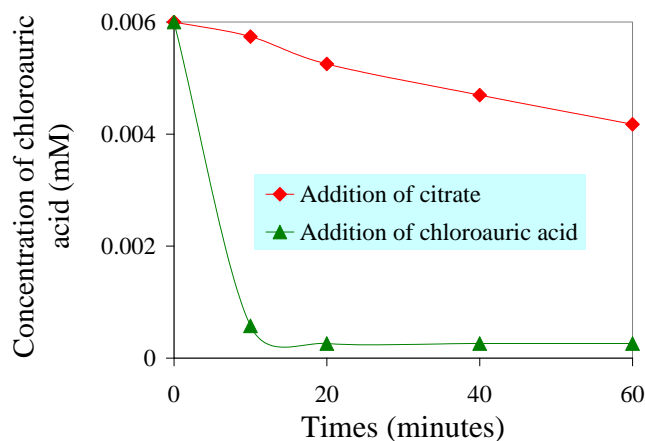


Figure 25. The change in chloroauric acid concentration with time for the two alternative modes of addition at a chloroauric acid concentration of 0.006 mM.

On further reducing the reaction concentration of chloroauric acid to 0.006 mM, the addition of chloroauric acid into citrate results in nanoparticles of size 5.8 ± 0.9 nm but the addition of citrate into chloroauric acid did not give any nanoparticles. The change in concentration of chloroauric acid with time for different mode of addition, at the lower concentration of chloroauric acid, was analyzed. Figure 25 shows the concentration of chloroauric acid with time for different mode of addition. The addition of citrate into chloroauric acid results in a negligible amount of reaction even after 1 hour of reaction, but the addition of chloroauric acid into citrate results in faster reaction. The induction time period involved in the faster reaction was 100 s. An autocatalytic step in the oxidation of citrate by chloroauric acid is speculated to be responsible for this ‘memory effect’. The presence of reactive chloroauric acid for short duration of 5 s during initial blending is sufficient to yield some acetone dicarboxylic acid which sustains reaction.

9.1a.5 Effect of addition of thiol-functionalized PEG molecules on citrate-stabilized metal nanoparticles

An interesting phenomenon leading to narrower particle size distributions was observed when an excess of poly (ethyleneglycol, PEG-300) was added to citrate stabilised solutions of metal nanoparticles. A systematic investigation of this phenomenon was carried out.

9.1a.5.1 Gold

5 mL of freshly prepared citrate capped gold nanoparticles of size 14.0 ± 3.1 nm ($\mu \pm \sigma$; Fig. 5.1a,b) were mixed with 5 μ L of thiol-functionalized polyethylene glycol (PEG-thiol, molecular weight: 356 g/gmol) and aged overnight (~ 16 hours) at 25 °C. The molar ratio of PEG-thiol to gold corresponds to 10. To image the particles after PEG capping, a 5 μ L aliquot was drop-cast on silicon substrate, and surprisingly, the size was found to be 11.0 ± 0.7 nm (Fig. 5.1c,d). Digestive ripening of particles using excess ligands by heating, for one or two hours, the colloidal solution near the boiling point of the solvent is well established. However, here, it was observed that focusing of particle size occurs at room temperature.

Thermogravimetric analysis (TGA) data of PEG-thiol capped gold nanoparticle suggests degradation of PEG-thiol around 300 °C (Fig. 5.2). Citrate capped gold nanoparticles show 16.8 % weight loss at 600 °C. For PEG-thiol capped gold nanoparticles, the weight loss was found to be 79.8 % at 600 °C. Also, the major weight loss was found to occur between 280 and 320 °C, correlating with the thermal degradation temperature of polymer.

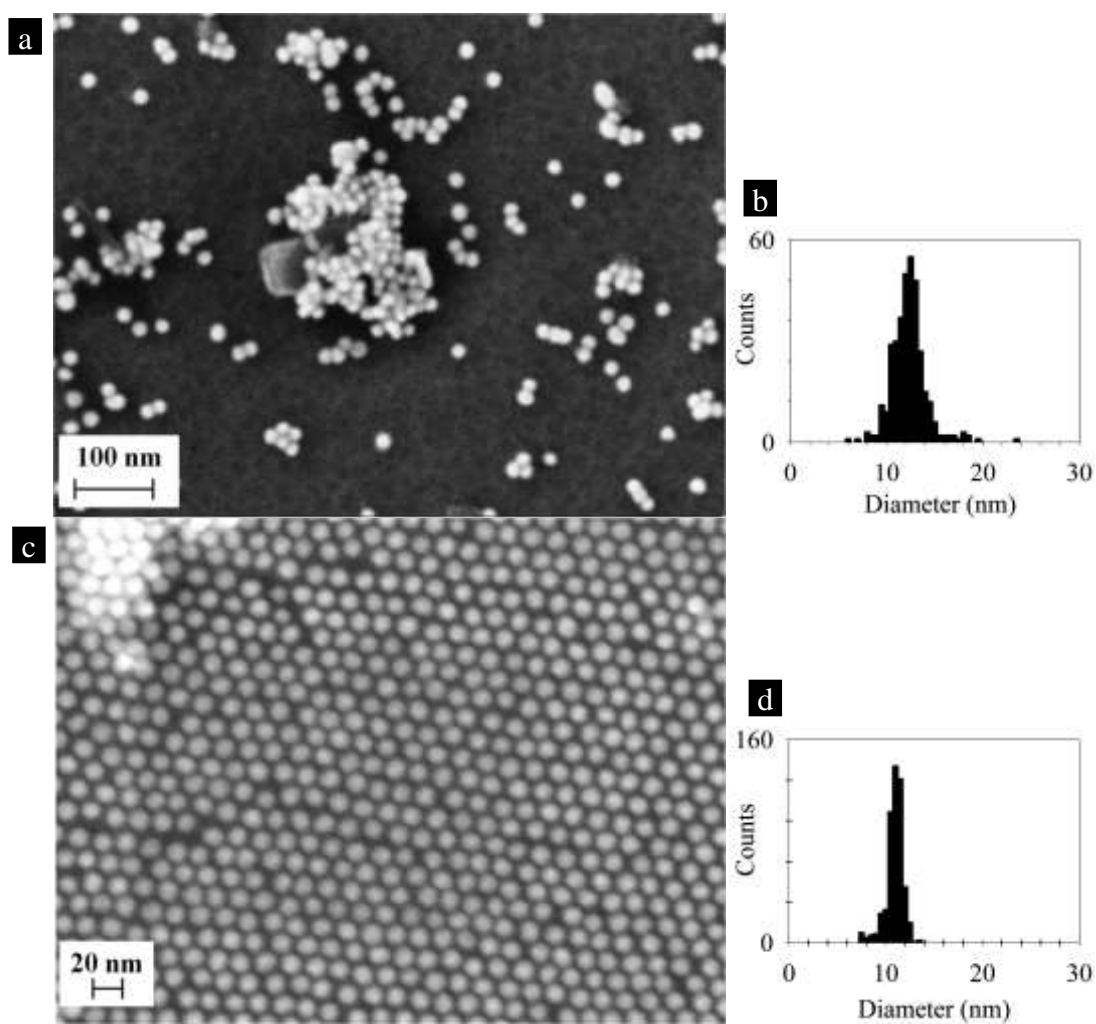


Figure 5.1: Representative FESEM image of (a) citrate capped gold nanoparticles (b) thiol-functionalized polyethylene glycol capped gold nanoparticles and their respective size histograms (c and d). The molar ratio of PEG-thiol to gold is 10:1 and the PEG-thiol capped gold nanoparticles were drop-cast on silicon substrate after ageing the colloidal solution for ~16 hours at 25 °C.

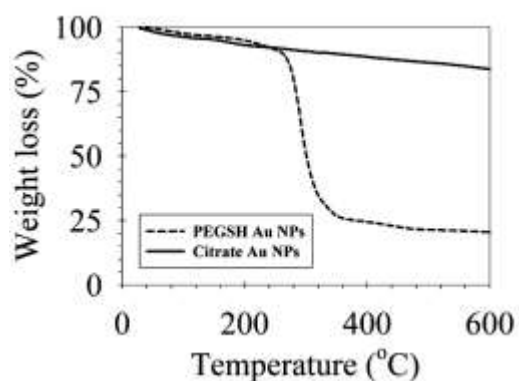


Figure 5.2: Thermogravimetric analysis (TGA) of citrate capped and PEG-thiol capped gold nanoparticles.

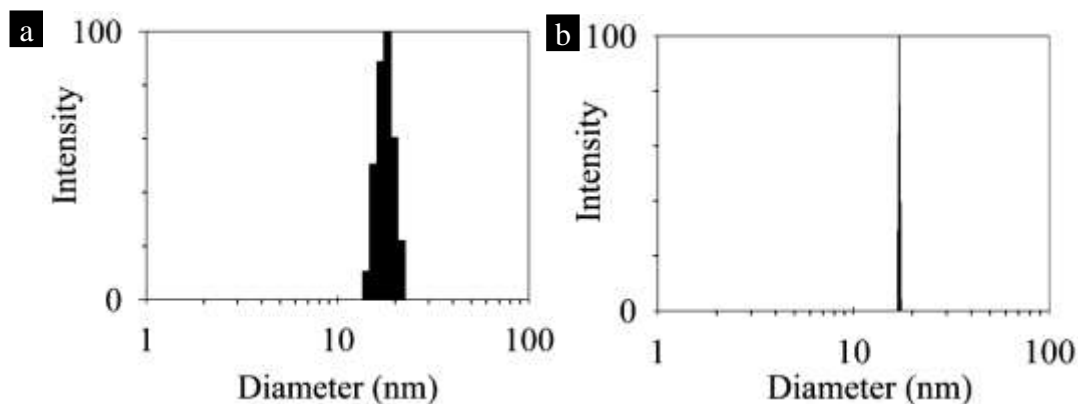


Figure 5.3: Representative DLS size histograms of (a) citrate capped and (b) PEG-thiol capped gold nanoparticles. The molar ratio of PEG-thiol to gold is 10:1 and the PEG-thiol capped gold nanoparticles were analyzed after ageing the colloidal solution for ~16 hours at 25 °C.

Dynamic Light Scattering measurements (DLS) corroborate the FESEM result of decrease in polydispersity before and after addition of PEG-thiol (Fig. 5.3). The DLS mean hydrodynamic diameters before and after PEG-thiol addition were 17.8 ± 2.0 nm and 17.1 ± 0.2 nm. As the chain length of the PEG-thiol molecule is 2.8 nm, the gold core diameter, after addition of PEG-thiol is deduced to be 11.5 nm ($=17.1 - 2 \times \text{PEG-thiol chain length}$), which is in concord with FESEM data (Fig. 5.1c,d). To investigate whether this is a generic phenomenon or system specific, the process of addition of PEG-thiol was extended to other metal nanoparticles, namely, citrate capped- palladium, silver and platinum nanoparticles.

9.1a.5.2 Palladium

The use of concentration ratios of sodium citrate to palladium (5.2, similar to gold nanoparticle synthesis) did not result in nanoparticle formation. In fact, there was no notable color difference even after heating the solution for four hours. Based on the report, that reverse addition of gold salt increases the reaction rate, an experiment was carried out using the reverse mode of addition, i.e., adding palladium chloride to boiling citrate solution. However, no discernible reaction occurred, and the color of the solution remained pale yellow. The UV-Vis spectrum of the solution (Fig. 5.4) after reaction showed a peak at 250 nm, which is characteristic of palladium chloride in water.

Citrate capped palladium nanoparticles were then successfully synthesized. Briefly, 4.125 mg of palladium chloride (PdCl_2) mixed with 0.5 mL of 1 N HCl was diluted to 25 mL, followed by the addition of 50 mL of 34 mM sodium citrate solution. The solution was heated to its boiling point in a beaker, which was attached with a reflux condenser, for 4 hours (Fig. 5.5a) After 1 hour, the initial pale yellow color started to change to dark brown (Fig. 5.5b). With continued heating, the color of the solution turned to intense brown. The particles were found to be highly polydispersed, with size ranging from 5 to 30 nm (Fig. 5.6a). After adding excess PEG-thiol (PEG to Pd molar ratio of 10) and heating to 74 °C (using a Peltier bath) for duration of 9 days, the size of the nanoparticle decreased to 4.7 ± 1.1 nm (Fig. 5.6b). The UV-Vis spectra showed significant spectral change immediately after the addition of PEG-thiol (Fig. 5.6c,d). The palladium nanoparticles do not show any absorption features, while after PEG-thiol addition, a couple of peaks at 270 nm and 310 nm appeared immediately, which is attributed to the possible formation of palladium complexes. X-ray photoelectron spectroscopic (XPS) analysis suggests the presence of palladium in Pd^{2+} form (may be palladium oxide) based on the location of binding energy peak of Pd 3d_{5/2} and 3d_{3/2} peaks at 337.8 and 342.9 eV respectively (Fig. 5.7), whereas pure palladium peak corresponds to 335.2 and 341.1 eV respectively²²⁰. However, the size and polydispersity of the nanoparticles were found to increase upon further storage, for another 15 days at room temperature, to around 39.2 ± 7.9 nm (Fig. 5.8).

9.1a.5.3 Silver

Citrate-capped silver nanoparticles were synthesized as follows. A mixture of 1 mL of 30 mM sodium citrate and 2 mL of 5 mM silver nitrate solution was made up to 98 mL using DI water. Upon boiling of this mixture, 1 mL of freshly prepared, ice-cold 50 mM NaBH_4 solution was added. The reaction was carried out under argon atmosphere in a Schlenk flask. Upon ageing at 4 °C (inside refrigerator), the as-synthesized citrate capped silver nanoparticles transformed into rods, cubes etc. (Fig. 5.9). So, in this study, only freshly prepared citrate capped nanoparticles were used.

With the addition of PEG-thiol to the freshly prepared citrate-capped silver nanoparticles, the color of the solution transformed from pale yellow to transparent, after being stored for 1 day at 25 °C. As there was no evidence of precipitate in the vial or any aggregated particles in FESEM image of the sample obtained by drop-casting the colloidal solution on to a silicon substrate, it was speculated that the nanoparticles were transformed into small nanoclusters (Fig.

5.10). The film-like features seen in the FESEM image is attributed to the presence of an organic layer, possibly excess PEG-thiol (Fig. 5.10). The size of these clusters could not be determined using FESEM.

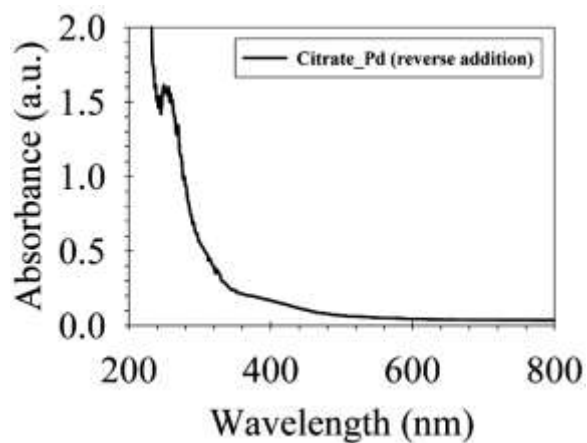


Figure 5.4: UV-Vis spectrum of a palladium chloride solution that was boiled with citrate solution.

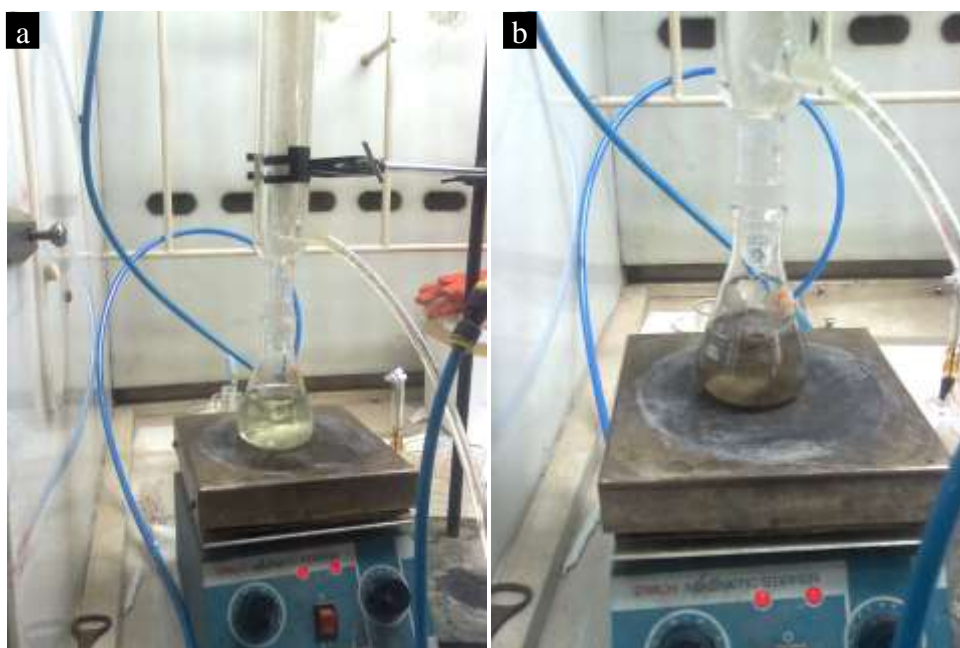


Figure 5.5: Digital photographs taken during the process of synthesizing citrate-capped palladium nanoparticles, (a) at the start of the reaction and (b) after boiling for 1 hour.

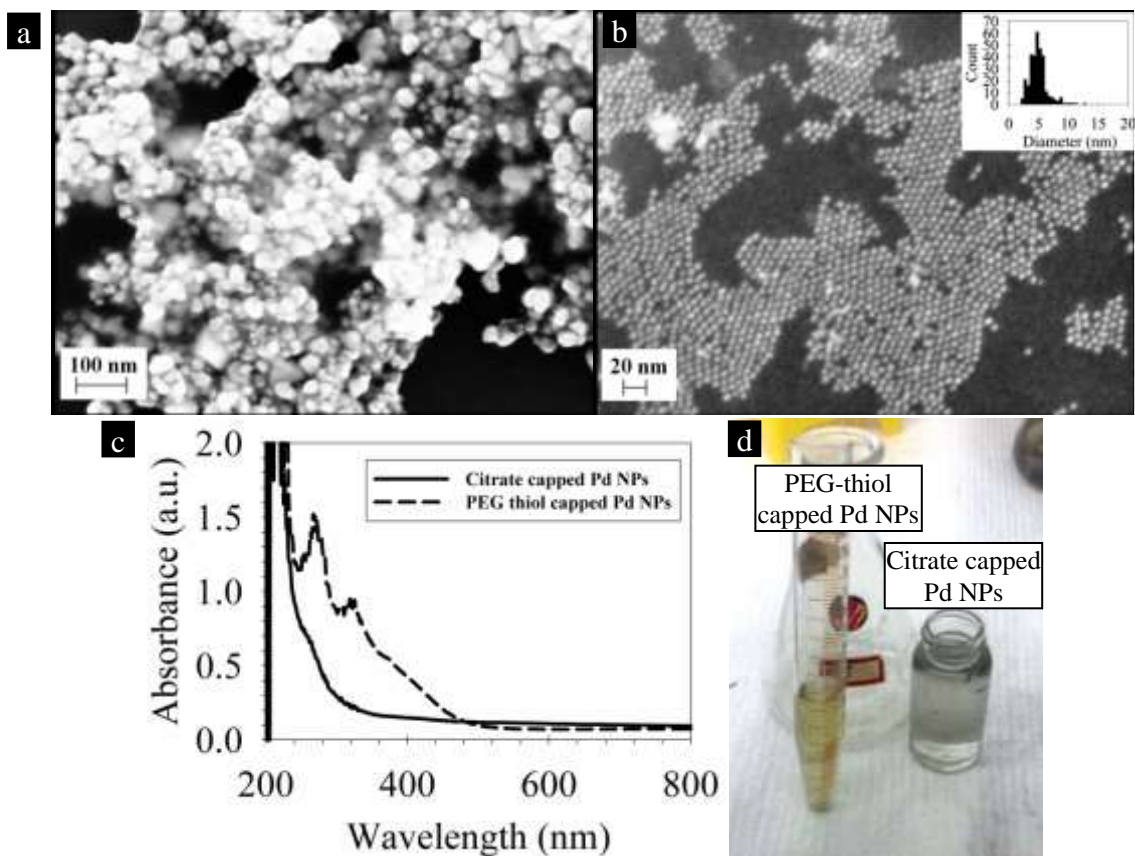


Figure 5.6: Representative FESEM image of (a) citrate capped palladium nanoparticles and (b) aged PEG-thiol coated gold nanoparticles after 9 days. (c) UV-Vis spectra of palladium nanoparticles before and after addition of PEG-thiol. (d) Digital photograph of citrate capped palladium nanoparticles before (left) and after addition of PEG-thiol (right). 5 μ L of PEG-thiol was added to 5 mL of colloidal solution and the PEG-thiol capped gold nanoparticles were drop-cast on silicon substrate after ageing the colloidal solution for 9 days at 74 $^{\circ}$ C.

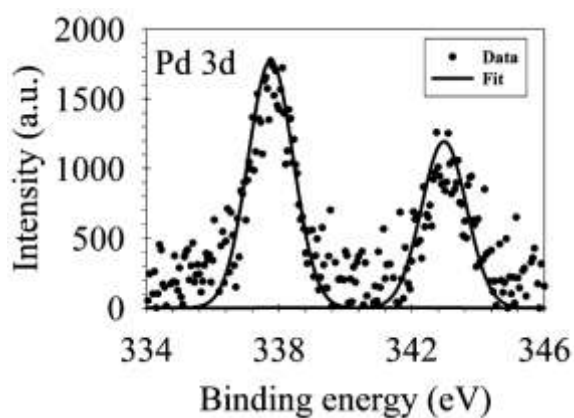


Figure 5.7: X-ray photoemission spectra of PEG-thiol capped palladium nanoparticles, after ripening.

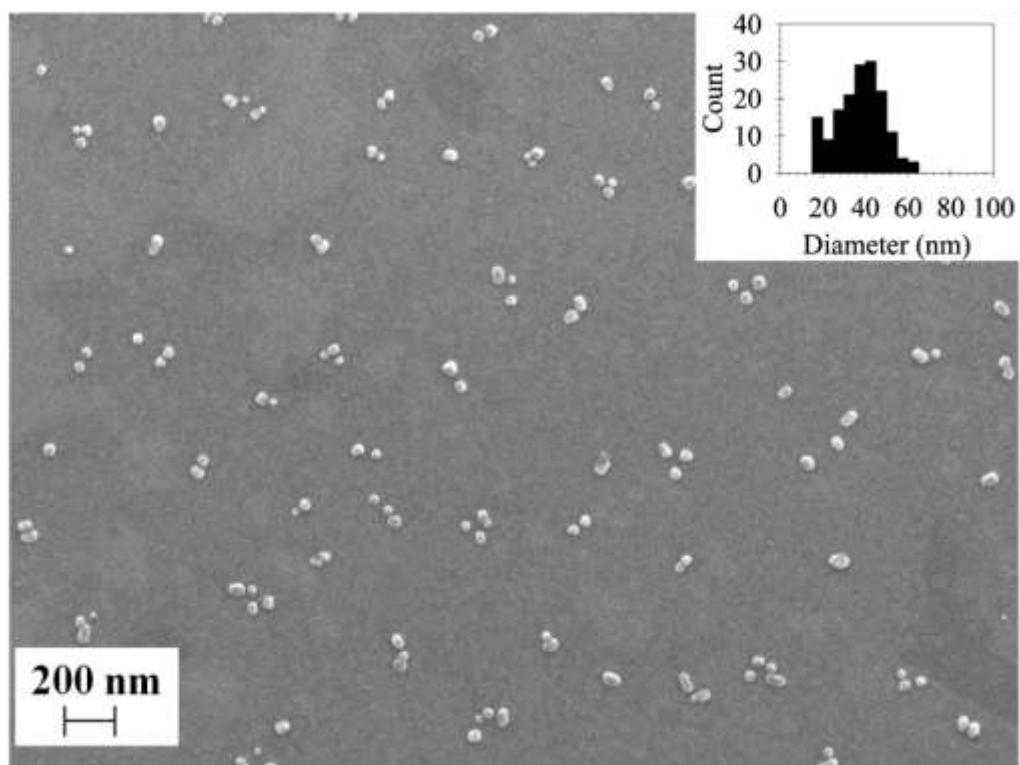
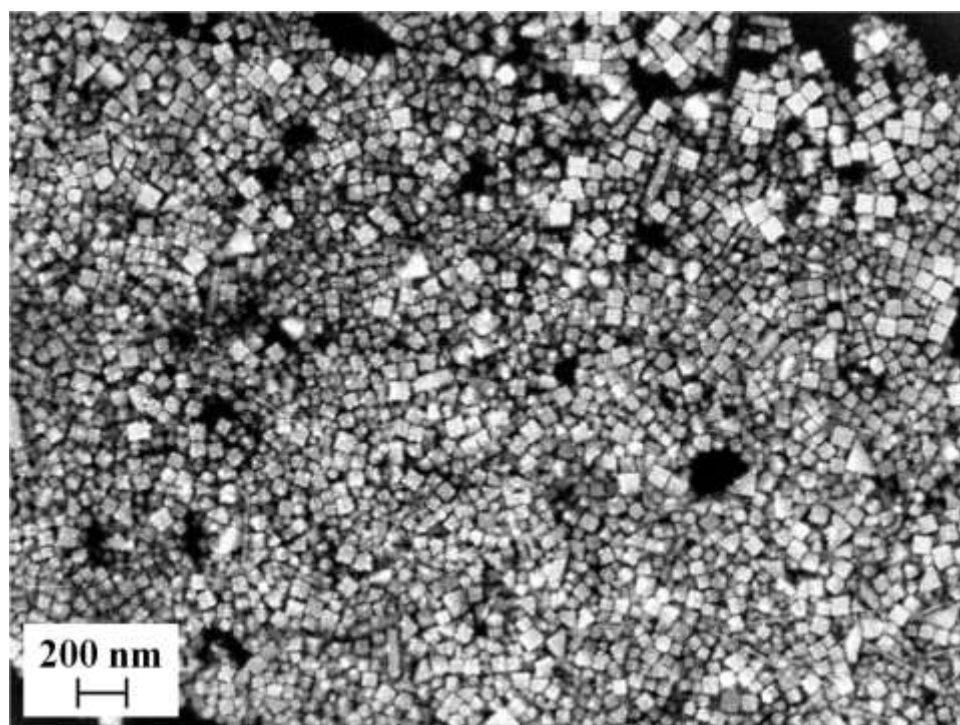


Figure 5.8: Representative FESEM image of aged PEG-thiol capped palladium nanoparticles after 15 days from particle ripening.

a



b

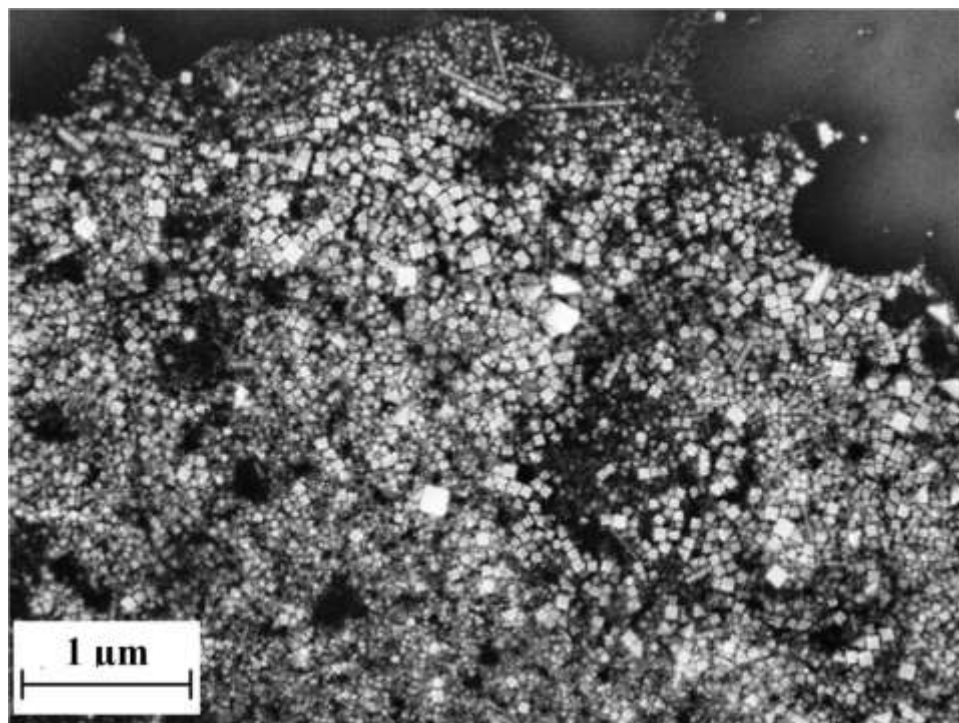


Figure 5.9: Representative FESEM images of citrate capped silver nanoparticles, after ageing at different magnifications.

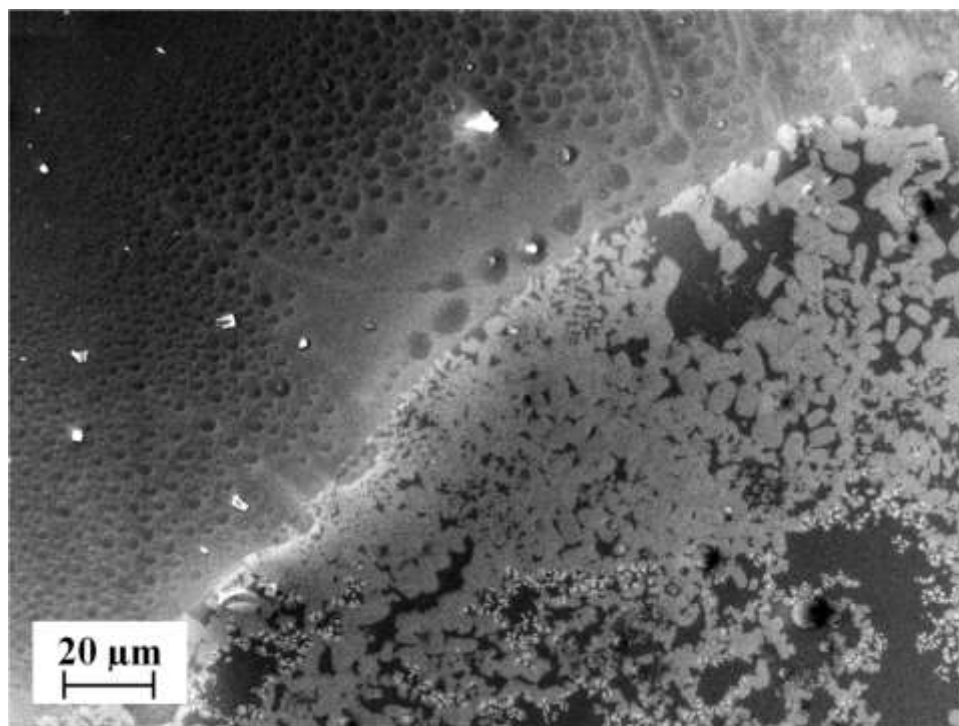


Figure 5.10: Representative FESEM image of PEG-thiol capped silver nanoparticles, after ageing at 25 °C for 1 day.

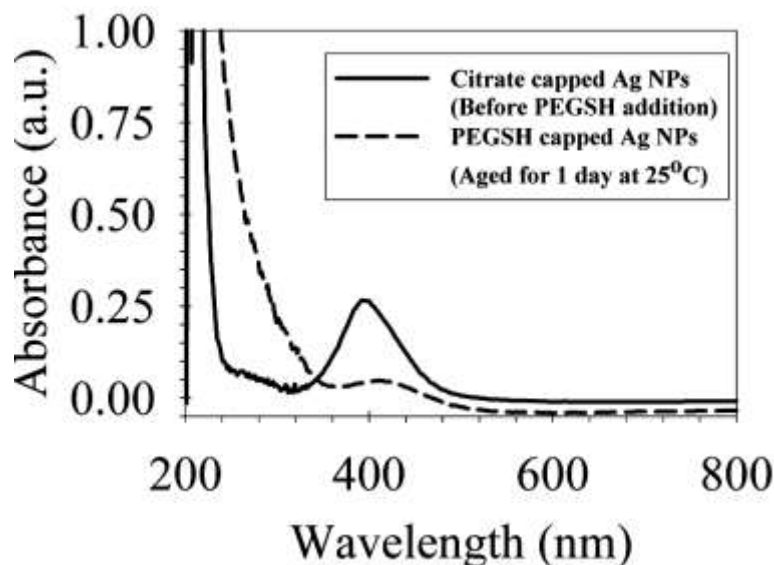


Figure 5.11: UV-Vis spectra of (a) citrate capped silver nanoparticles and (b) aged PEG-thiol capped silver nanoparticles after 1 day at 25 °C.

The UV-Visible spectra of citrate capped silver nanoparticles before and after addition of PEG-thiol molecules show a significant decrease in absorbance at 400 nm after PEG addition, which can be attributed to either a plausible change in number concentration of particles or a change in their size (Fig. 5.11). Photoluminescence spectra of PEG-thiol capped silver nanoparticles shows greater enhancement when compared to original citrate-capped silver nanoparticles (Fig. 5.12). The particles were excited at 320 nm and the spectra were collected from 350 nm to 600 nm. The citrate capped silver nanoparticles (>5 nm) showed very little photoluminescent activity, the response being similar to water (Fig. 5.12). The dotted lines represent the repeated measurement without altering the parameters, clearly showing that there is negligible effect of laser excitation on the citrate colloids. PEG-thiol capped silver nanoclusters, showed photoluminescent enhancement and their spectra were blue-shifted, which can be attributed to the metal-ligand charge transfer absorption as reported earlier. Note, both citrate capped silver nanoparticles and PEG-thiol capped silver nanoparticles were used as is without any dilution. However, with repeated measurement (dotted line and dashed line), photobleaching was found to occur in the case of PEG-thiol capped nanoparticles. Photobleaching is a phenomenon where in the absorption of photon degrades the polymer and causes a reduction in photoluminescent intensity with time. Use of a fresh solution of PEG-thiol capped silver nanoparticles yielded the original result (unbleached). All these experiments suggest the presence of silver nanoclusters as hypothesized using UV-Vis spectra. These observations are similar to the recently observed effect of treatment of mercapto-succinic acid (MSA) with citrate capped silver nanoparticles above 70 °C by Dhanalakshmi and co-workers. However, in this study the etching effect was also observed at room temperature. With an increase in temperature to 74 °C, particle etching occurred within two hours. Also, similar reports of ligand based etching of silver nanoparticles have been reported using Glutathione. In addition to various reports of thiol based etching of silver nanoparticles with different backbone, Radziuk et al., have reported a reduction in polydispersity of silver nanoparticles by the addition of PEG molecules followed by thermal treatment at 90 °C for 2 hours. The ratio of PEG to silver used was 0.1 in their study, which is much lower than that used in our study.

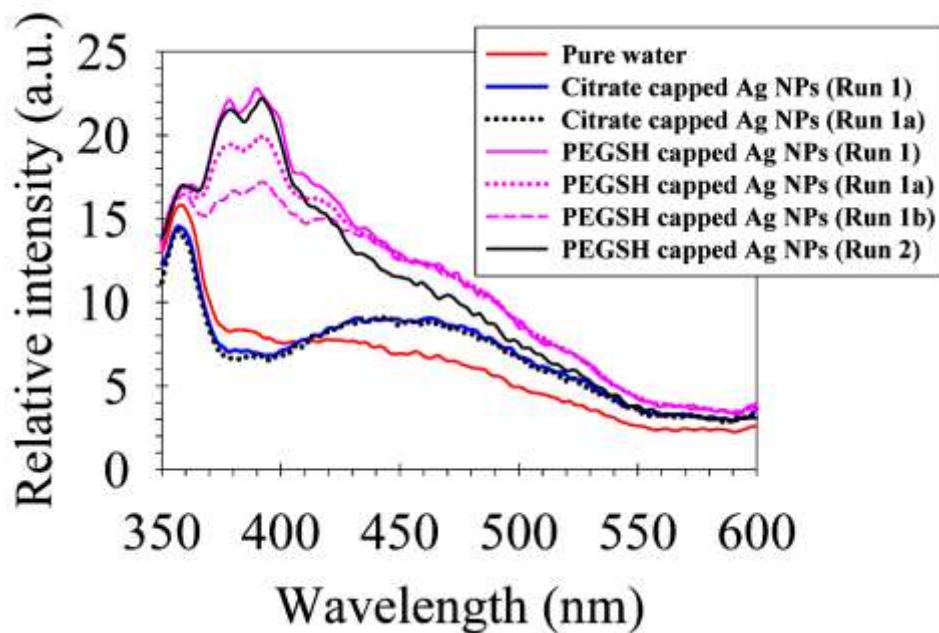


Figure 5.12: Photoluminescence spectra of citrate capped silver nanoparticles and PEG-thiol capped silver nanoparticles, excited at 320 nm. Upon continued excitation, the intensity of the PEG-thiol capped sample decreases, which is attributed to photobleaching. The dotted lines represent the repeated measurement of the corresponding sample without altering the parameters.

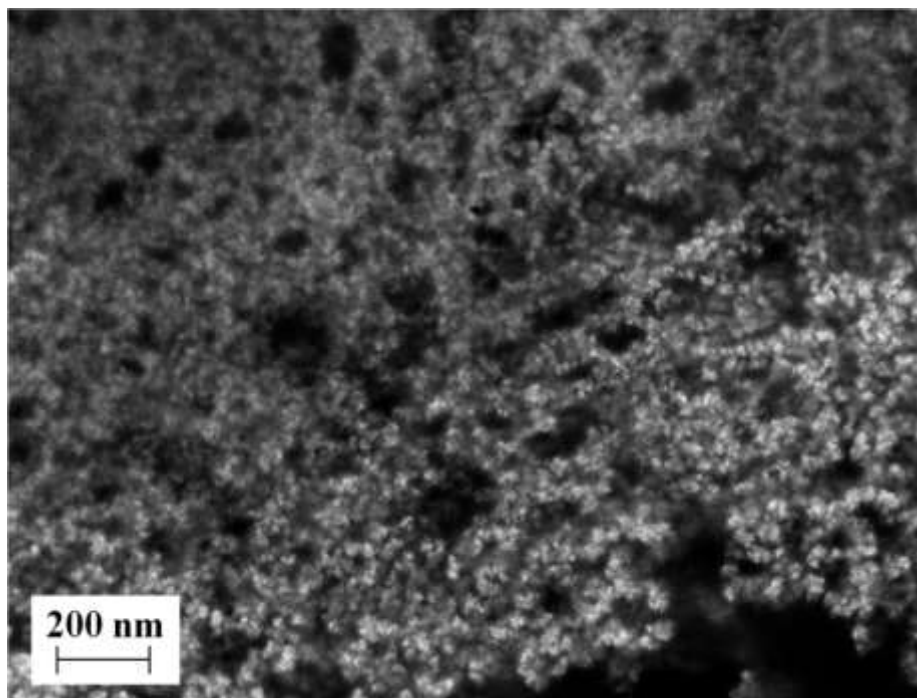


Figure 5.13: Representative FESEM image of citrate capped platinum nanoparticles

9.1a.5.4 Platinum

Citrate capped platinum nanoparticles were synthesized based on a modification of the recipe of Harriman et al²²⁷. The standard mode of addition of citrate to platinum precursor was reversed, so as to facilitate faster reduction and lower polydispersity. This mode of addition was adopted based on the report of Sivaraman et al. 25 mL of water was mixed with 1 mL of sodium citrate solution (1% w/v) and allowed to boil for few minutes. After that, 0.33 mL of H_2PtCl_6 solution (1% w/v) was injected into the boiling solution. The amount was chosen such that the molar ratio of platinum to citrate is equal to that used for the case of gold, i.e., 5.2. The color of the solution changed from yellow to light brown in 30 minutes. The reaction was allowed to continue for another 3 hours. The FESEM image shows clustering of particles (Fig. 5.13), which were difficult to resolve individually. 5 μL of PEG-thiol was added to 5 mL of freshly prepared citrate

stabilized platinum nanoparticles. The sample was kept in a water bath maintained at 74 °C using Peltier stage. In contrast with the earlier systems, the size of citrate capped platinum nanoparticles was found to increase after PEG-thiol addition (molar ratio of PEG-thiol to platinum was 10) and ageing for 12 days ($\sim 6.3 \pm 1.2$ nm, Fig. 5.14). X-ray photoelectron spectroscopic (XPS) analysis confirms the presence of platinum in metallic form based on the location of binding energy peaks of Pt 4f_{5/2} and 4f_{7/2} peak at 71.2 and 74.6 eV, respectively 228(Fig. 5.15). The presence of platinum in oxide form with peaks at 72.6 and 76.3 eV was also observed. This is most likely due to oxidation of the atoms at the surface of the nanoparticles. All these experiments suggest that addition of PEG-thiol molecules to citrate capped metal nanoparticles results in changes to the particle size distribution, the extent of which depends on the nature of the metal. This point will be revisited in a later section (see sec.5.16) of this chapter. To further understand the phenomena involved, a detailed study of the factors responsible for the reshaping of gold nanoparticles was then carried out.

9.1a.5.5 Effect of vacuum on PEG coated gold nanoparticles

When the PEG-thiol coated gold nanoparticle samples were imaged in TEM, a significant fraction of the particles were odd shaped and polydispersed, similar to as-synthesized citrate capped gold nanoparticles with a size of 17.6 ± 2.7 nm (Fig. 5.16). A region of thick organic film in the shape of open-ended wrench can be seen in Figure 5.17. Efforts to image at higher magnifications in this region were not successful, due to charging effects. Furthermore, domains of monodisperse particles (size: 15.9 ± 1.4 nm) that appear to be embedded in an organic film were sometimes observed (Fig. 5.18). Further, the particles (region marked with an oval) were found to be more spherical than the particles found away from this region (Fig. 5.19). In fact, the contrast between the particles and the substrate was found to be less in the region marked with an oval, as compared to regions away from this. Mixed regions of particles assembled in both ordered and disordered manner were also observed (Fig. 5.20). Also, the particle size is significantly different to the sizes obtained using FESEM, and this discrepancy cannot be simply attributed to the higher resolutions associated with TEM, as the FESEM also has the required resolving power at the 10 nm lengthscale. In addition, sub-2 nm clusters were also observed (Fig. 5.21). These nanoclusters were observed at very low magnifications, so it can be surmised that these may not be due to the impingement of electron beam (Fig. 5.21a). In fact, the sizes of these clusters increased during imaging at higher magnifications similar to the recent report of impact of electron beam on particle size²²⁹ (Fig. 5.21b). The change in nanoparticle size, shape and polydispersity observed in TEM measurements suggests two possibilities: (a) higher vacuum in the TEM chamber ($\sim 10^{-9}$ mbar) when compared to FESEM ($\sim 10^{-6}$ mbar) leading to ligand desorption, (b) bombardment with higher electron energies (~ 200 kV) as compared with FESEM (~ 10 kV) leading to particle reshaping. To discern between these two factors, it was decided to carry out a couple of experiments: (i) to place the sample in TEM chamber for one hour without opening the column valve that connects the electron gun to the chamber (chamber vacuum: $\sim 10^{-9}$ mbar) followed by imaging it in FESEM (chamber vacuum: $\sim 10^{-6}$ mbar; lower by 3 orders of magnitude) and (ii) to place the sample in FESEM for prolonged periods of time (chamber vacuum: $\sim 10^{-7}$ mbar, which is achieved after few hours). The colloidal solution was drop-cast on silicon nitride TEM substrate to mimic the nature of the silicon substrate used in FESEM imaging, as well as to facilitate handling in both TEM and FESEM.

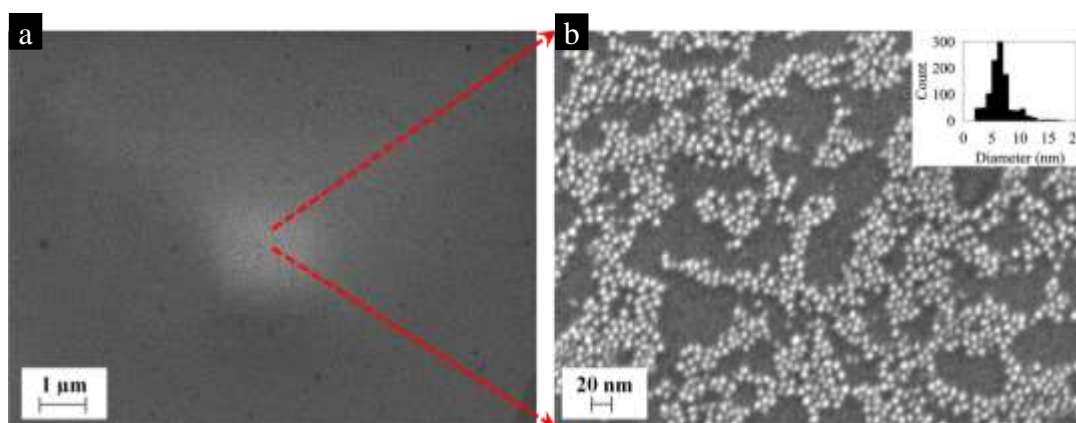


Figure 5.14: Representative FESEM image of PEG-thiol coated platinum nanoparticles, after ageing for 12 days at different magnifications.

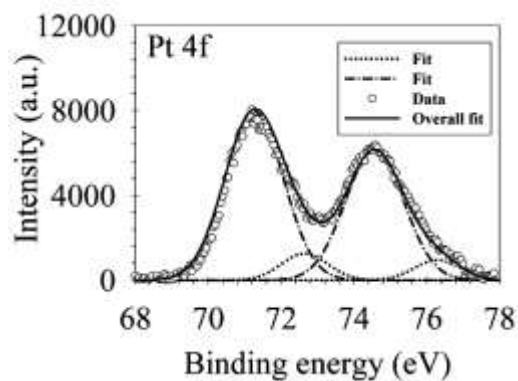


Figure 5.15: X-ray photoemission spectra of PEG-thiol capped platinum nanoparticles, after ageing for 12 days

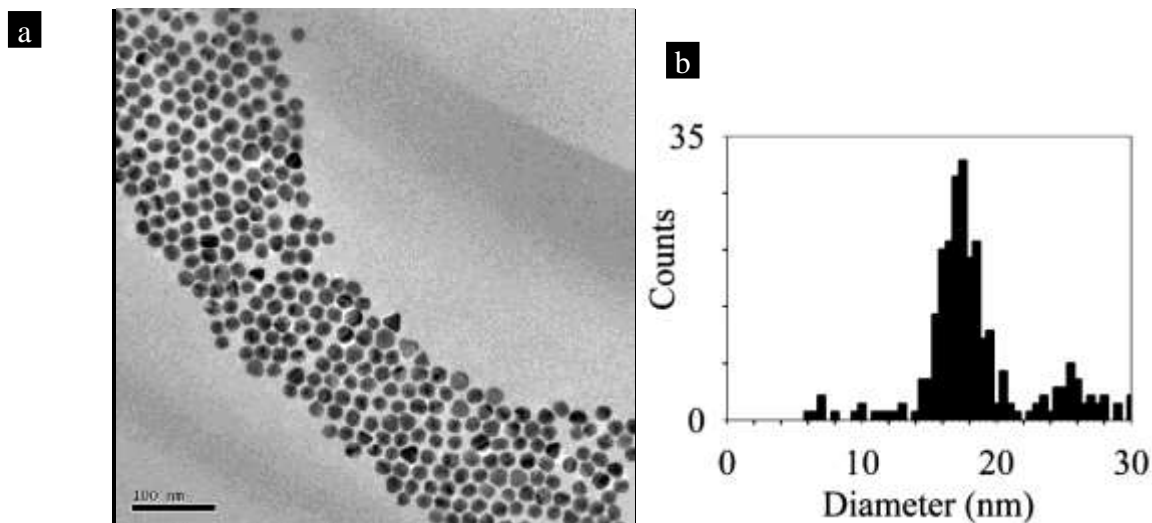


Figure 5.16: (a) Representative TEM image of PEG-thiol capped gold nanoparticles and (b) corresponding size histogram. The molar ratio of PEG-thiol to gold was 10 and the PEG-thiol capped gold nanoparticles were drop-cast on TEM grid after ageing the colloidal solution for ~ 1 day at 25°C .

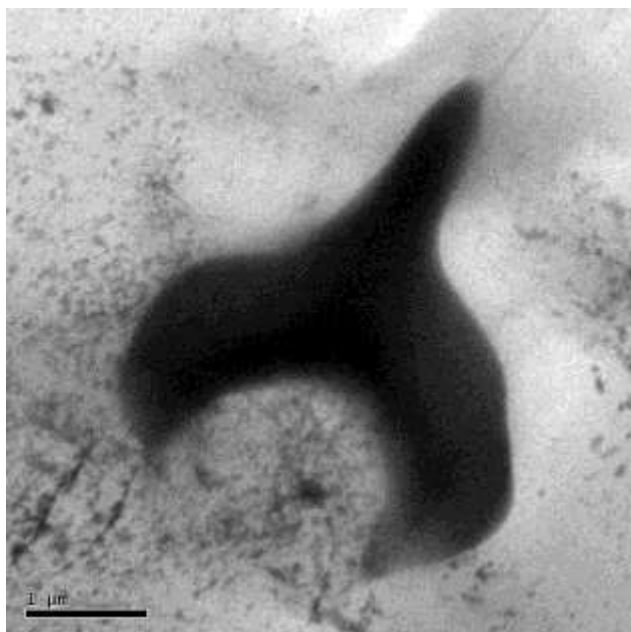


Figure 5.17: Representative TEM image during imaging thiol-functionalized PEG capped gold nanoparticles, highlighting thick organic film in the shape of open-ended wrench.

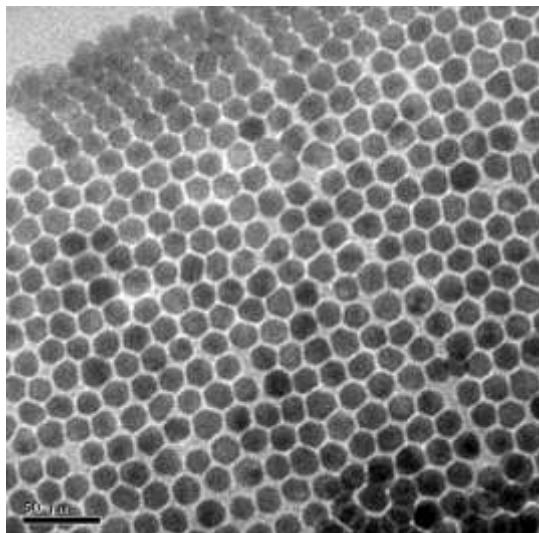
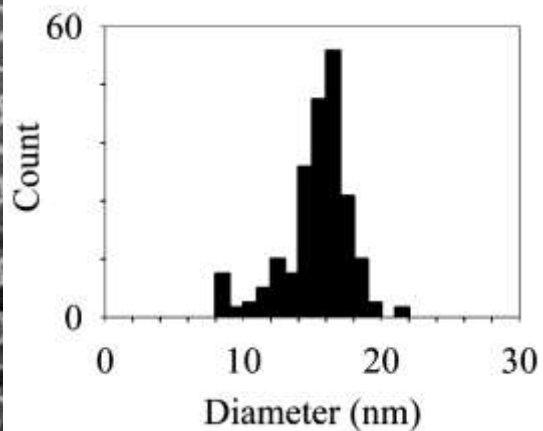
a**b**

Figure 5.18: (a) Representative TEM image of thiol-functionalized PEG capped gold nanoparticles near organic film and (b) respective size histogram.

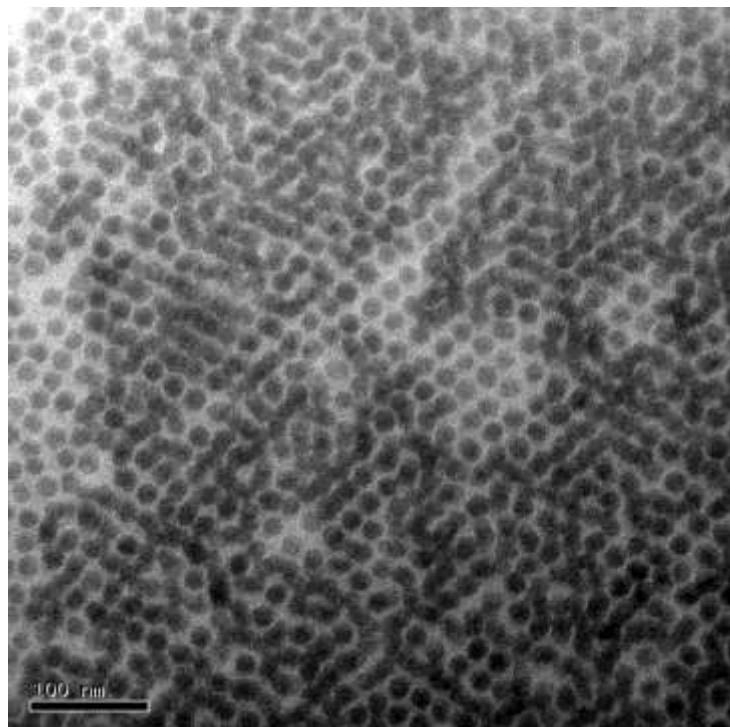
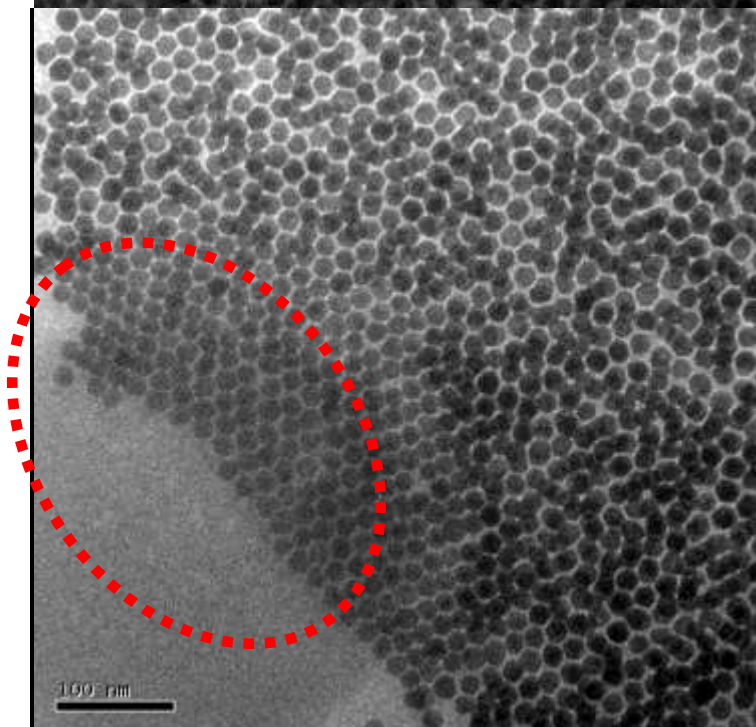
a**b**

Figure 5.19: TEM images of thiol-functionalized PEG capped gold nanoparticles, highlighting low polydispersity, obtained at different locations. Images show particles with two contrasts, suggesting possible presence of organic film. The particles inside the region marked with a dotted oval (b) were found to be more spherical than the particles found away from this region

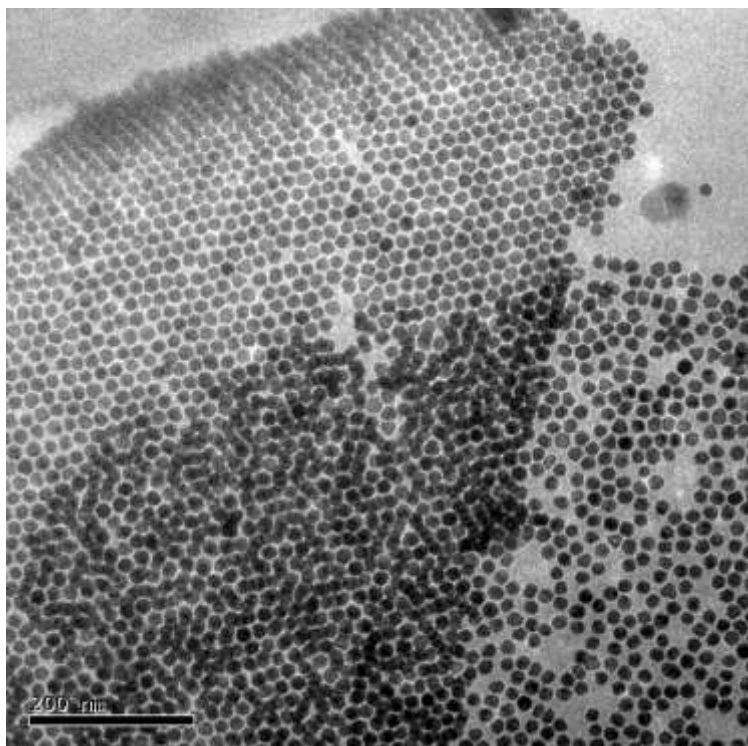


Figure 5.20: Representative TEM image of thiol-functionalized PEG capped gold nanoparticles, highlighting particles assembled in ordered and disordered fashion, next to each other.

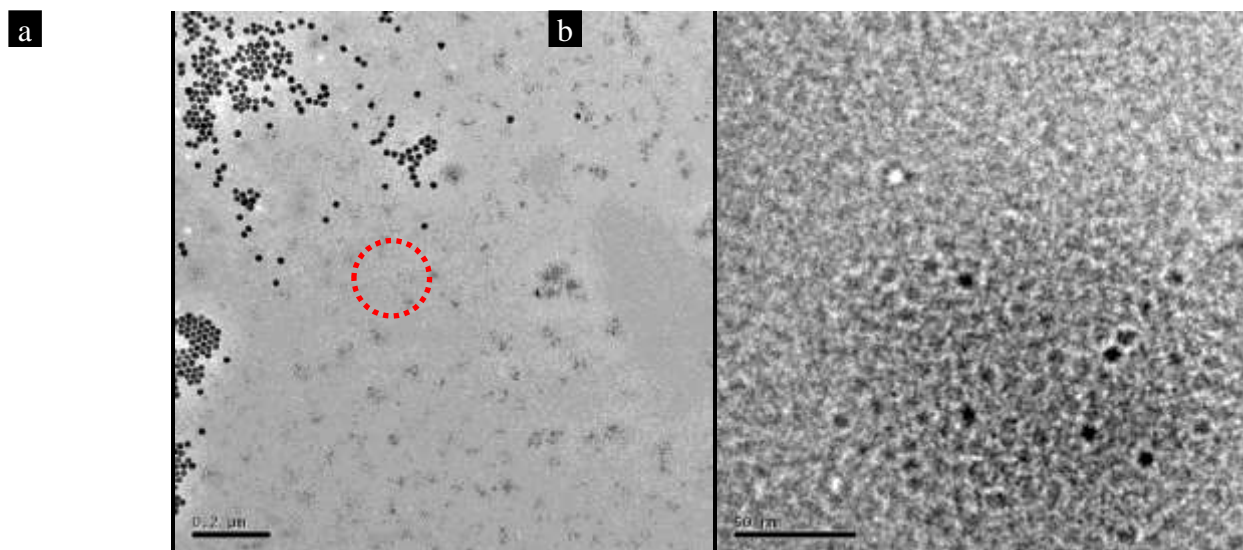


Figure 5.21: Representative TEM images of PEG-thiol-functionalized gold nanoparticles obtained at (a) low and (b) high magnification. These sub-2 nm clusters were found to increase in size during the course of imaging.

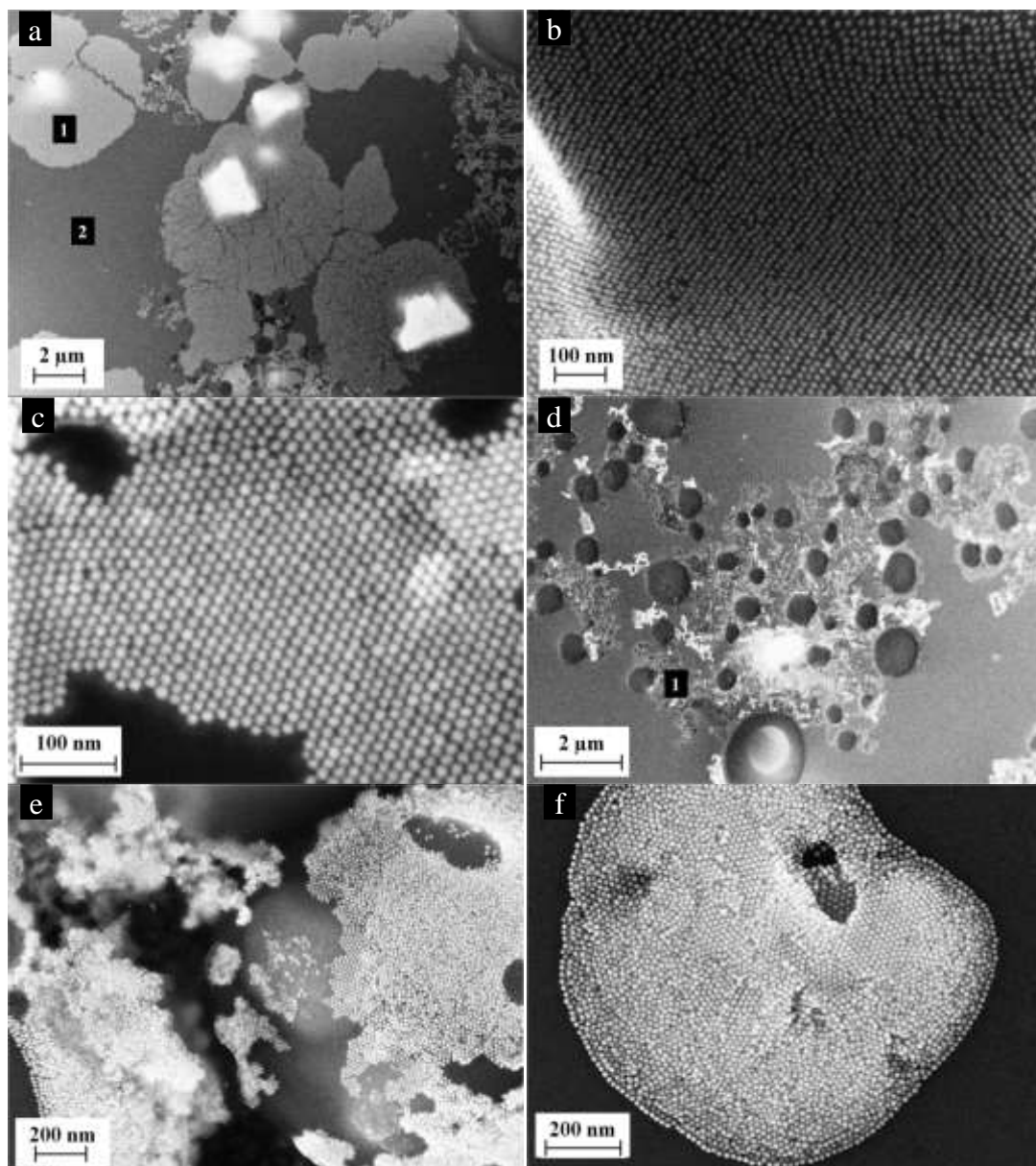


Figure 5.22: Representative FESEM images of thiol-functionalized PEG capped gold nanoparticles at different magnifications before (a-c) and after treating the sample in TEM chamber for 1 hour, without switching on the electron beam (d-f). The regions marked 1 and 2 (in a) represent nanoparticle array and substrate respectively. Clearly, the higher vacuum in the TEM chamber has affected the size distribution of the particles.

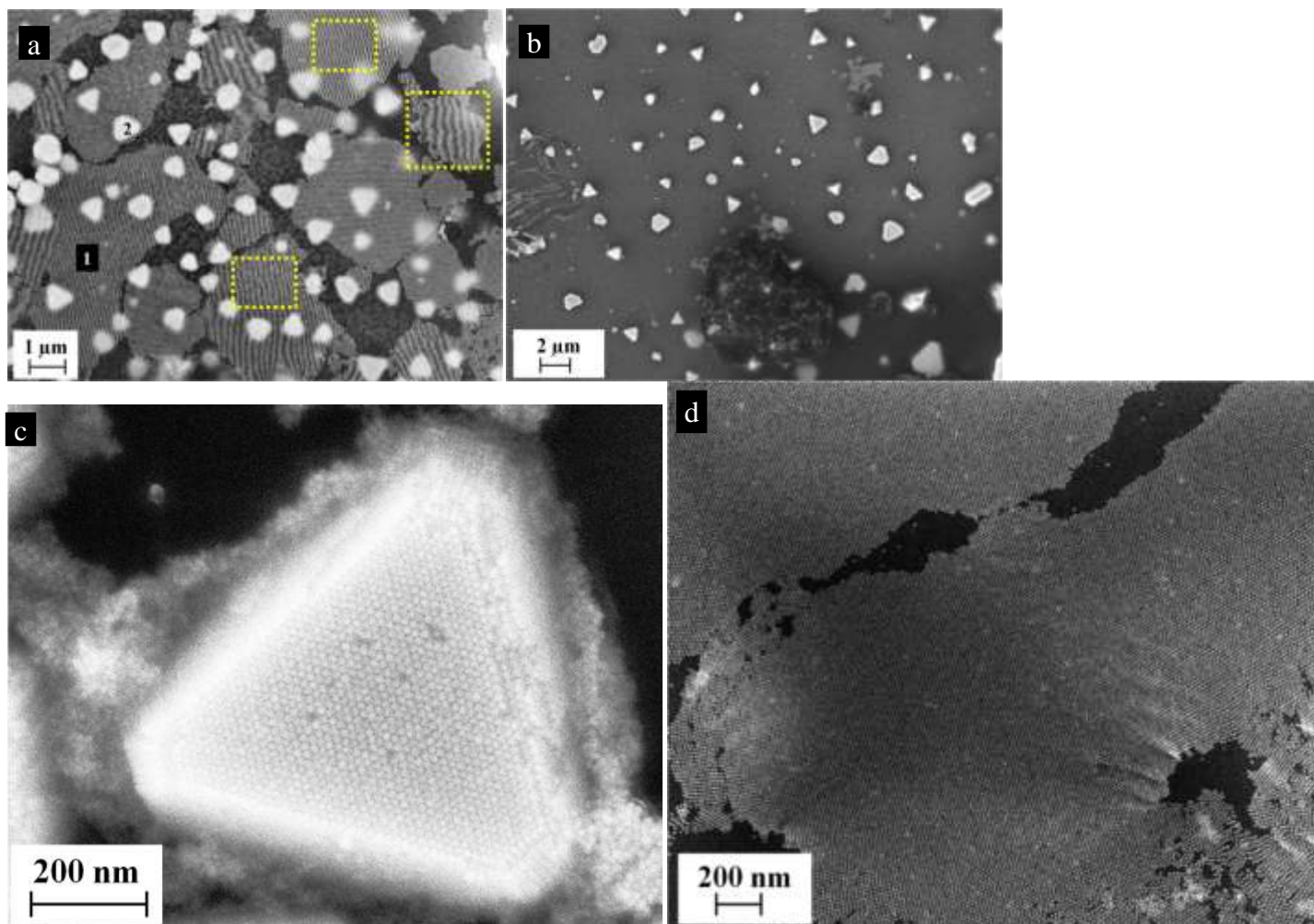


Figure 5.23: Representative FESEM images by drop-cast of either (a) concentrated PEG-thiol capped gold nanoparticle solution (~ 20 times the original concentration) or (b) freeze-drying the standard colloidal solution was found to result in formation of supracrystals, a 3D assembly of PEG-thiol coated gold nanoparticles. The dotted rectangles (in a) represent Moiré patterns due to two ordered pattern, namely, ordered array and SEM scan line. The regions marked 1 and 2 represent monolayer array (shown in d) and supracrystal (shown in c).

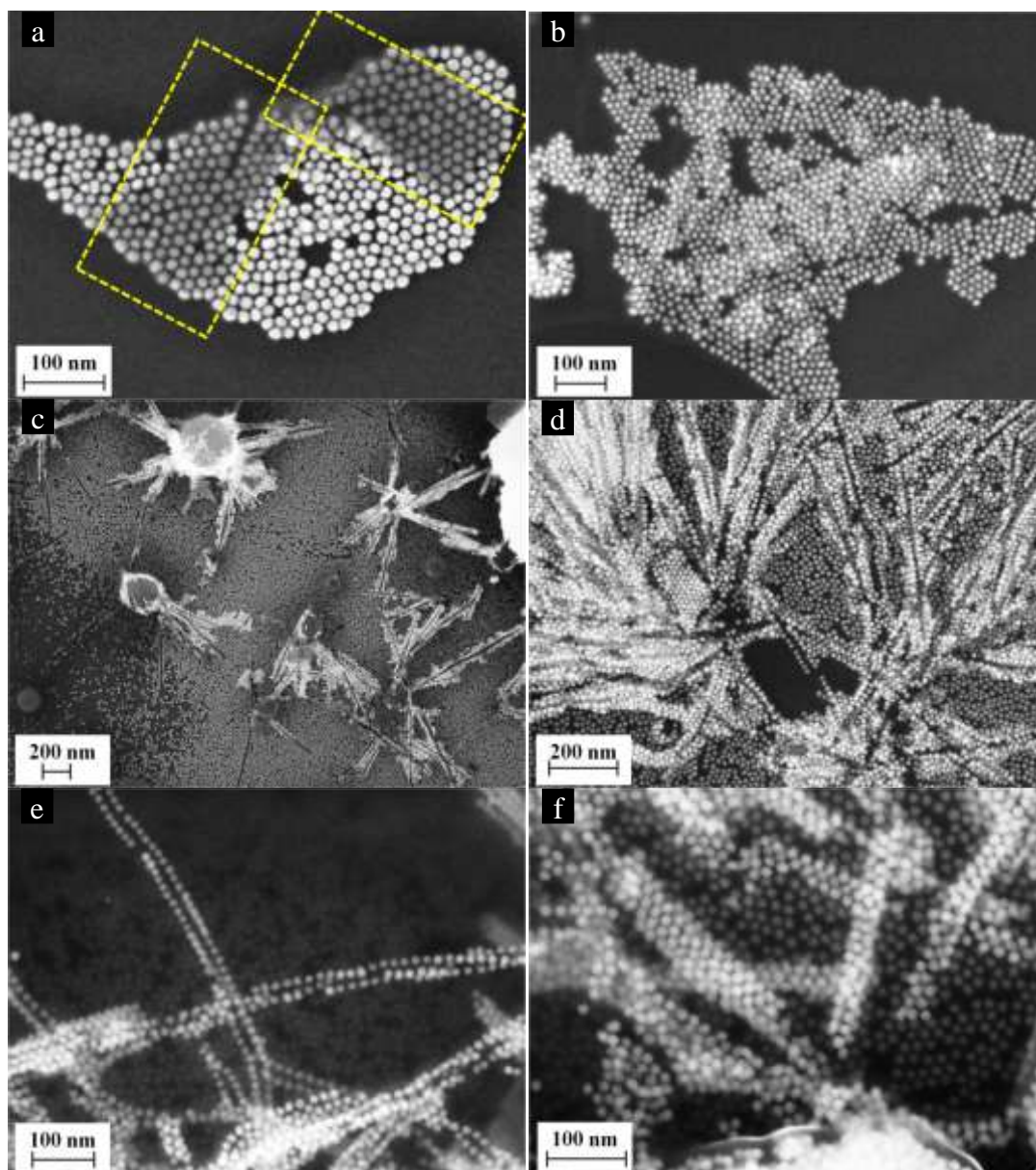


Figure 5.24: (a-f) Representative FESEM images of thiol-functionalized PEG capped gold nanoparticles at different magnifications after leaving the sample imaged in Fig. 5.23c inside the FESEM chamber for 1 day. The dotted rectangles highlight regions of different contrast due to the possible partial removal of PEG molecules under vacuum. Clearly, the transformation of supracrystals into linear assemblies, as well as changes in size distribution can only be attributed to the effect of vacuum on the organic film.

Before the sample was placed in high vacuum chamber in TEM, the sample was imaged in FESEM which highlights highly, ordered array of monodispersed nanoparticles (Fig. 5.22a-c). Typically, the particles were found in patches of highly ordered arrays, which appear to behave like an organic film, in that their spacing and ordering were altered upon prolonged e-beam exposure as if a thin piece of cotton cloth was being pulled apart in tension (also seen in Fig. 5.23d). Notably, the particles exhibit a monodisperse size distribution. After placing in the high vacuum chamber of a TEM for 1 hour without opening the column valve that connects electron gun to the chamber, the sample was again analyzed in FESEM. The images clearly indicate both loss of size and ordering after being placed in high vacuum chamber (Fig. 5.22d-f). Interestingly, drop-casting either concentrated PEG-thiol capped gold nanoparticles (~ 20 times the original concentration) or freeze-drying the colloidal solution was found to result in formation of supracrystals, a 3D assembly of PEG-thiol coated gold nanoparticles (Fig. 5.23a-c). When this sample was placed in FESEM chamber for prolonged periods of time (~ 1 day, without e-beam exposure), transformation of supracrystals into linear assemblies of particles was observed along with a broadening of particle size distribution (Fig. 5.24). Cheng and Cao²³⁰, in a recent simulation study, have theoretically found that beyond a critical concentration of nanoparticles in solution, PEG grafted gold nanoparticles aggregate into nanowires.

9.1a.5.6 Evolution of particle size distribution in chloroform/water mixture

PEG molecules have good solubility in chloroform, and so a small aliquot of chloroform (0.2 mL) was added to ripened, aqueous PEG-thiol coated gold nanoparticles (5 mL). Upon heating, the color of the colloid changed from red to blue to light brown. Upon subsequent cooling, the color of the solution reverted back to red. FESEM images indicate the formation of rods and other odd-shaped particles at the higher temperature (the colloidal solution was drop-cast when the color of the solution was blue), and the size change was reversible upon cooling (Fig. 5.25). This clearly suggests that PEG grafted gold nanoparticle can reshape and resize depending on the solvent and temperature conditions.

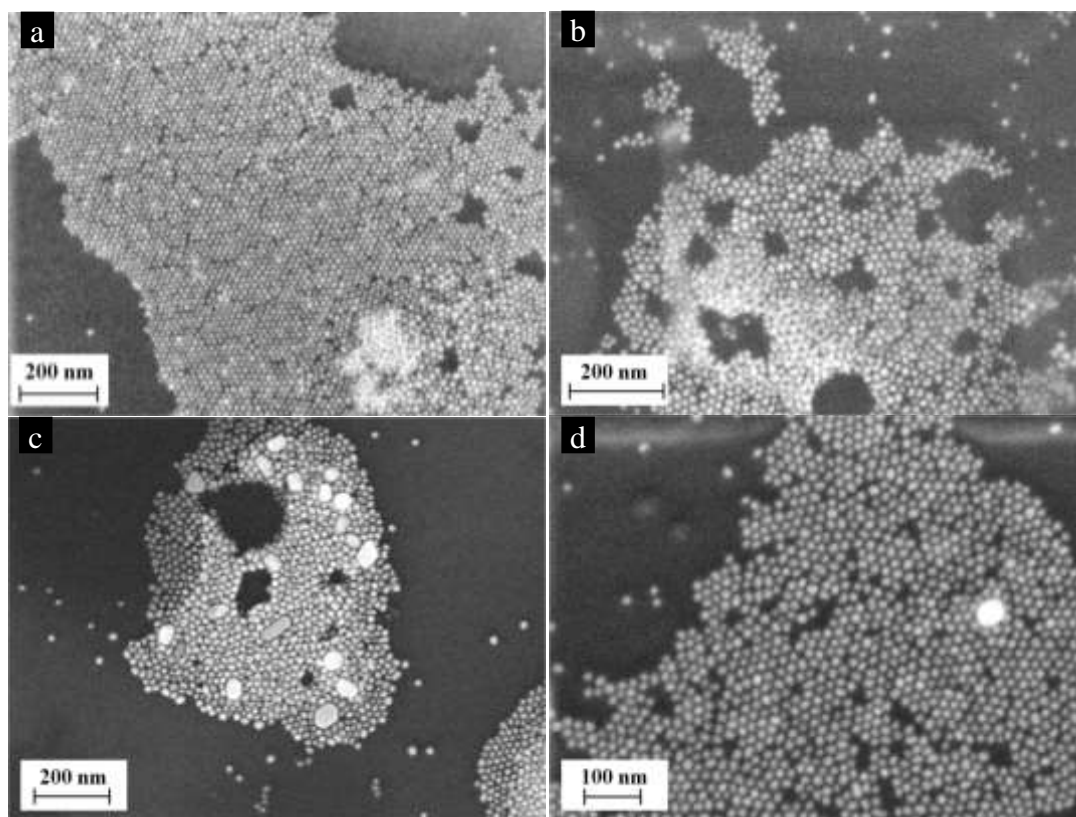


Figure 5.25: Representative FESEM images of (a) PEG-thiol coated gold nanoparticles, (b) PEG-thiol coated gold nanoparticles (5 mL) after addition of small amounts of chloroform (0.2 mL), (c) boiled PEG-thiol coated gold nanoparticles dispersed in water and chloroform, and (d) the colloidal solution after being cooled back to room temperature.

9.1a.5.6 Role of excess PEG-thiol molecules on ripening of gold nanoparticles

To understand further the role of free PEG-thiol molecules, freshly prepared citrate capped gold nanoparticles (14 ± 3.1 nm) were mixed with different amounts of PEG-thiol molecules, namely, PEG/Au ratio of 0.15 (which is equivalent to surface atoms of gold present in the solution, assuming a uniform size of 14 nm), 1 and 10. After ageing the sample for 1 day at 25 °C, the mean sizes were found to be 13.3 ± 2.1 nm, 13.0 ± 0.8 nm, and 11.0 ± 0.7 nm for PEG/Au ratio of 0.15, 1 and 10 respectively (Fig. 5.26a-f). Low magnification FESEM images at different PEG/Au ratios clearly show that Moiré patterns appear for arrays with higher amounts of PEG-thiol, i.e., for the case of 1 (Fig. 5.27). Moiré patterns appear due to the interference between two regular patterns. In this study, SEM scan lines act as one of the reference pattern, while the ordered nanoparticle array forms the second pattern. Such Moiré patterns have been reported for dodecanethiol capped gold nanoparticles³¹. Similar Moiré patterns were also reported for block copolymer monolayer structure.

9.1a.5.7 Removal of excess PEG molecules from ripened nanoparticles

In order to further understand the role of excess free PEG in solution in enhancing the monodispersity of PEG-thiol grafted gold nanoparticles, monodisperse PEG-thiol coated gold nanoparticles (molar ratio of PEG to gold of 10) were boiled with small aliquots of hydrogen peroxide (2 mL peroxide was added to 5 mL of colloid), as peroxides are known to degrade PEG molecules²³². Excess sodium citrate (2 mL of 1 % (w/v) solution) was also added to the solution to ensure the presence of adequate stabilizers. After a couple of minutes of boiling, an aliquot from the solution was drop-cast on silicon substrate. Circular domains (marked 1) of 2D nanoparticle arrays were found in a layer of organic film (marked 2); the region marked 3 corresponds to silicon (Fig. 5.28). Such contrast in FESEM images of molecular films have been ascribed to the differing electron affinities of the materials involved²³³. A higher magnification FESEM image

of the regions marked as 1 and 2 in the Fig. 5.29 a and b revealed highly ordered and disordered nanoparticle arrays respectively. The mean size of the particles in the ordered region was found to be 8.6 ± 1.7 nm (Fig. 5.29c,d), which is about 2 nm lower than that of the mean size of the particles, before adding peroxide. In the circular domains two characteristic features were observed, namely, (1) white bright spots (marked with a circle) and (2) ripple like features (marked with an oval), as shown in Fig. 5.30. To understand those features further, high-magnification images were taken using both secondary electron and backscattered electron detector. The angle selective backscattered (AsB) electron image and secondary electron (SE) images shed light on a couple of issues, (a) presence of organic film around the gold nanoparticles, as ripple in SE image was not translated in AsB image (Fig. 5.31a) and (b) possible presence of gold as some gold-rich complex as the bright spots encircled in Fig. 5.31b are visible in AsB as such. These results indicate that, given the absence of any noticeable deposition of metallic gold on the containers, the gold atoms have been redistributed onto other nanoparticles or form complexes upon oxidation of PEG/organic film by peroxide. After the solution was boiled for 20 minutes, SEM and DLS results (Fig. 5.32) indicate that the particles have fused and that they are electrostatically stabilized (zeta potential changed from -0.2 ± 2 mV to -46 ± 3 mV). These results show that the PEG molecules have been oxidized by peroxide boiling for 20 minutes and that the citrate molecules are adsorbed onto the particle surfaces. Further, the primary particles have clustered into small aggregates. DLS size histogram also corroborate these findings, as the size distribution shows two modes in the 10-100 nm size range that are attributed to the primary particles and their agglomerated clusters respectively.

Alternatively, instead of boiling ripened PEG-thiol coated gold nanoparticles with hydrogen peroxide, excess PEG molecules were removed by high speed centrifugation or membrane filtration. Excessive washing resulted in irreversible aggregation of particles. These observations are consistent with the recent reports of Shon et al., wherein when the excess PEG molecules were removed from the solution, the stability of nanoparticles decreased and also there were signs of aggregation. Interestingly, these complexes are labile enough to desorb under ambient

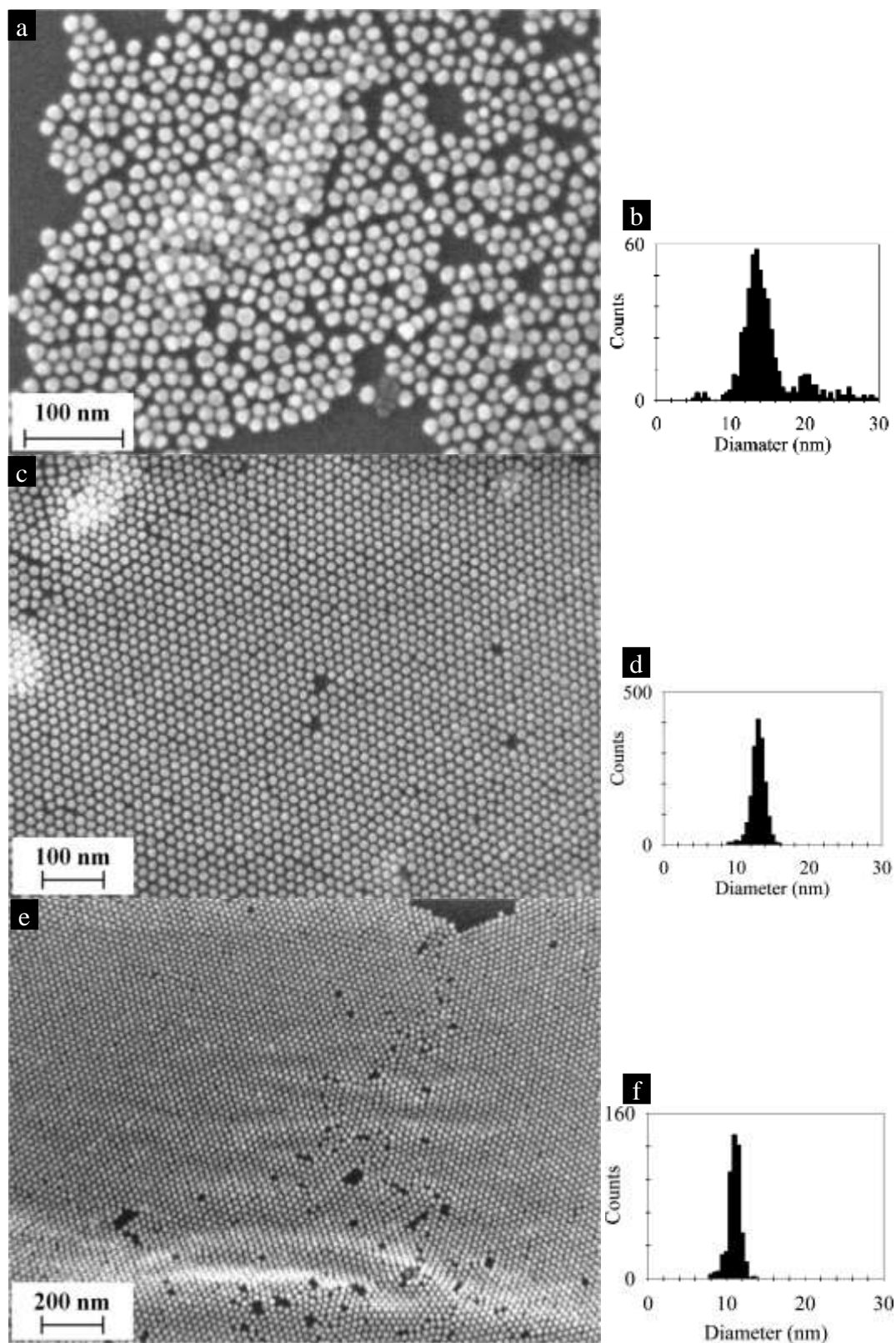
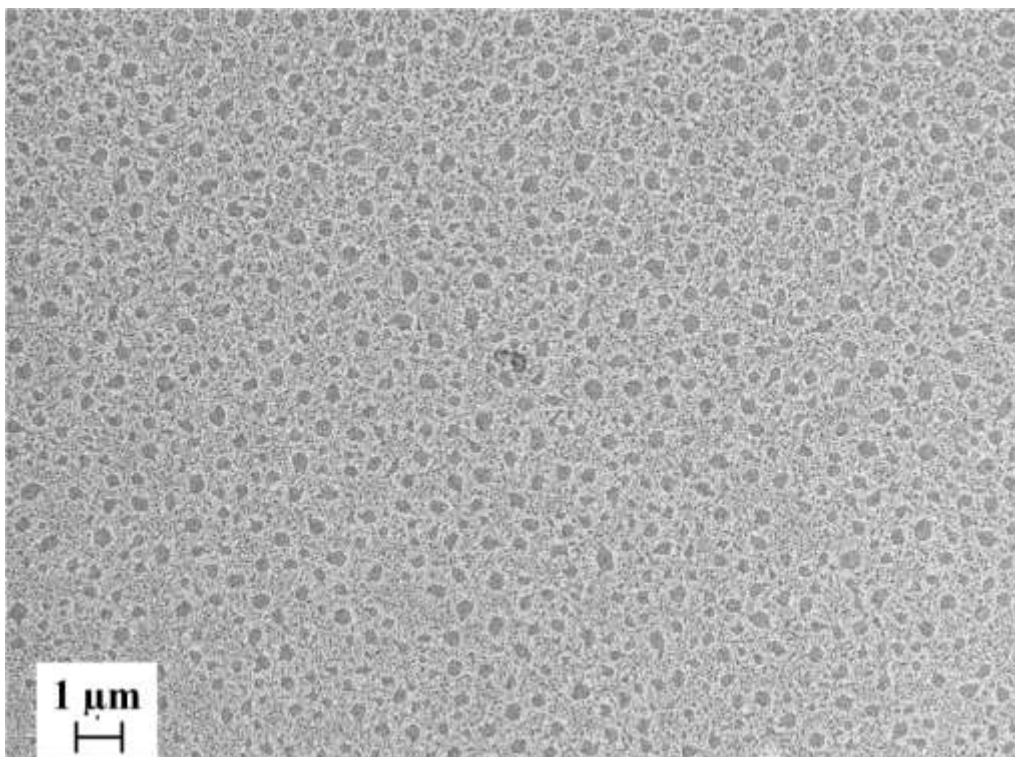
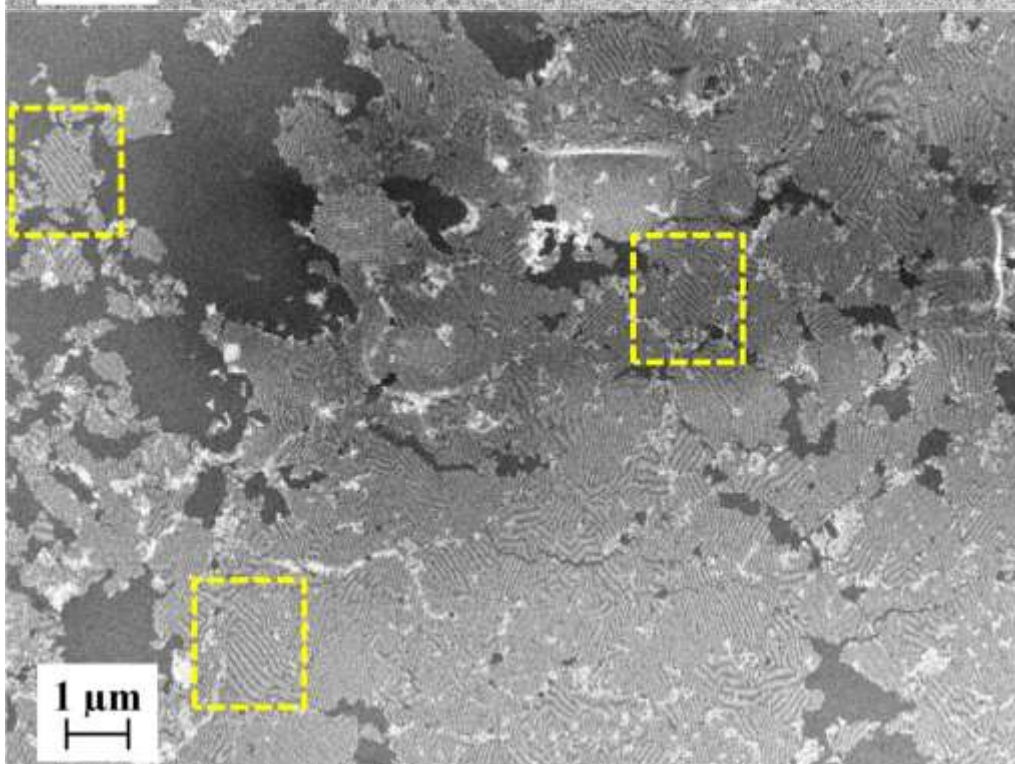


Figure 5.26: Representative FESEM images of PEG-thiol coated gold nanoparticles with the ratio of PEG-thiol to Au, (a) 0.15, (b) 1, (c) 10, and (d-f) their respective size histograms. PEG-thiol coated gold nanoparticles were drop-cast on silicon substrate, after ageing the colloidal solution for 1 day at 25 °C.

a



b



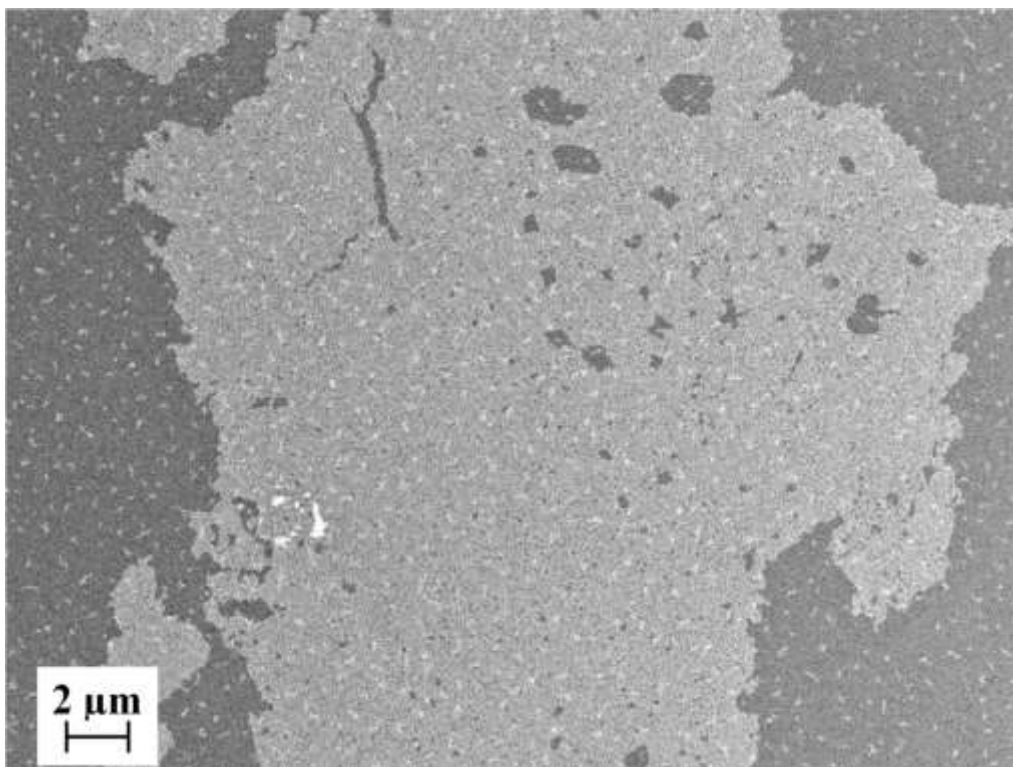
c

Figure 5.27: Representative low magnification FESEM images of PEG-thiol coated gold nanoparticles with the molar ratio of PEG-thiol to Au of, (a) 0.15, (b) 1, (c) 10, highlighting Moiré patterns. The dotted rectangles (in b) represent regions of Moiré pattern. Moiré patterns can appear due to the interference between two regular patterns. Here, SEM scan lines act as reference pattern, while the ordered nanoparticle array forms the second pattern. PEG-thiol capped gold nanoparticles were drop-cast on silicon substrate after ageing the colloidal solution for 1 day at 25 °C.

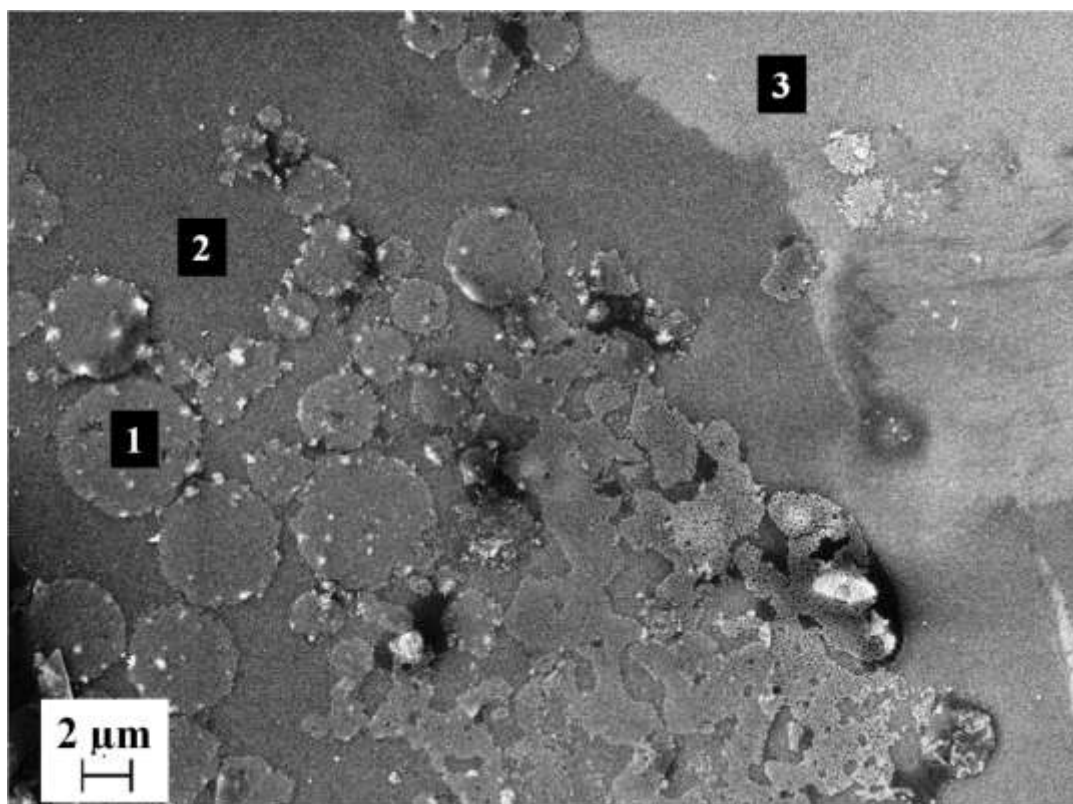


Figure 5.28: Representative low-magnification FESEM image of PEG-thiol coated gold nanoparticles mixed with excess hydrogen peroxide and sodium citrate and boiled for 2 minutes. The region marked 1, 2 and 3 correspond to circular domains of 2D nanoparticle array, organic film and bare silicon respectively.

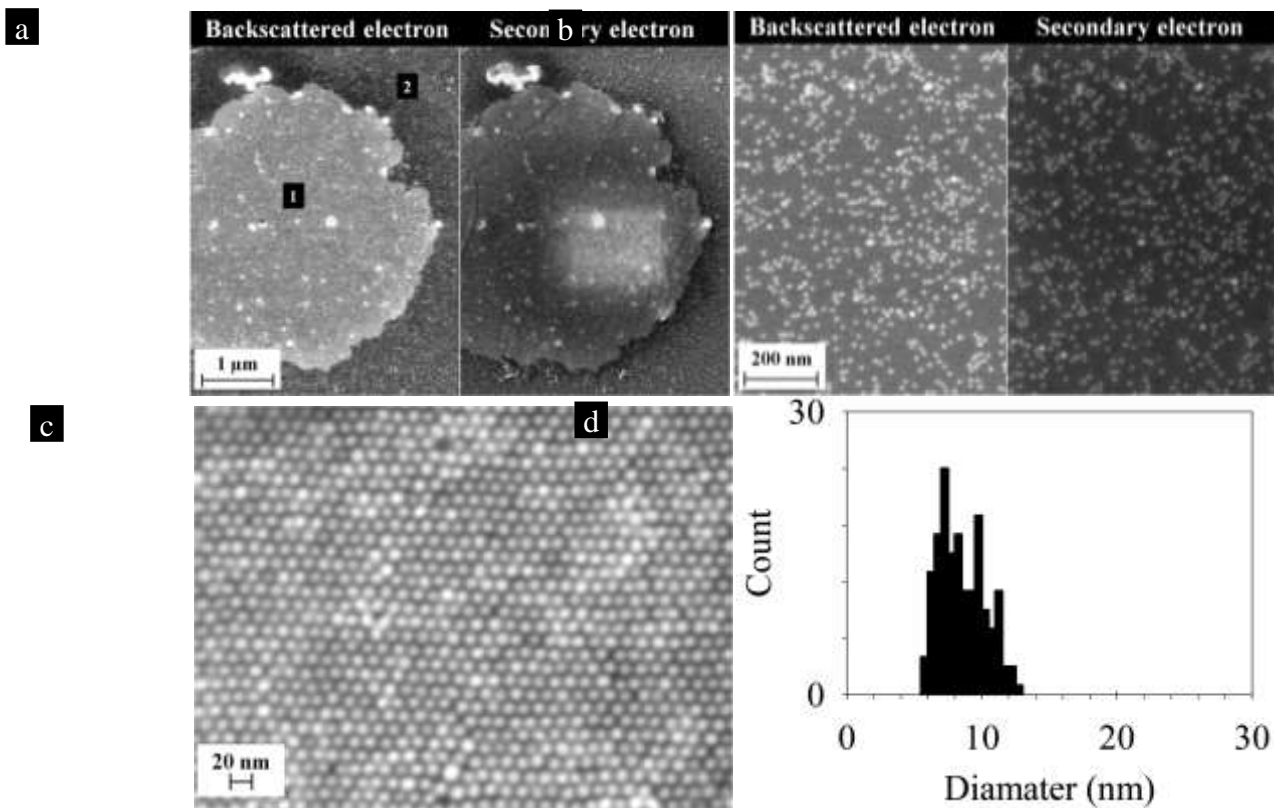


Figure 5.29: (a) Representative FESEM images of PEG-thiol coated gold nanoparticles mixed with excess hydrogen peroxide and sodium citrate after boiling for 2 minutes, showing regions of (b) highly disordered nanoparticle array (region marked 2 in a), (c and d) highly ordered nanoparticle array. The left hand side and right hand side images in a and b were obtained using backscattered electron and secondary electron detector respectively. (c) High magnification FESEM image of circular regions reveal highly ordered array with their corresponding size histogram (d).

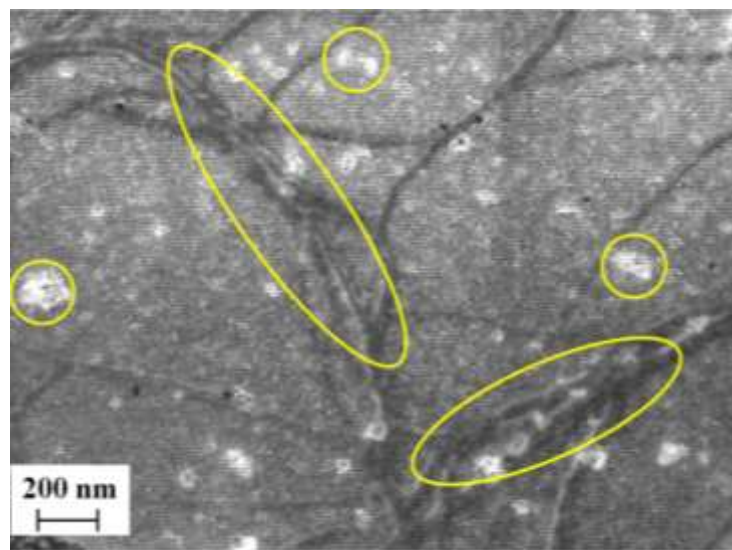


Figure 5.30: Representative FESEM image of PEG-thiol coated gold nanoparticles mixed with excess hydrogen peroxide and sodium citrate after boiling for 2 minutes.

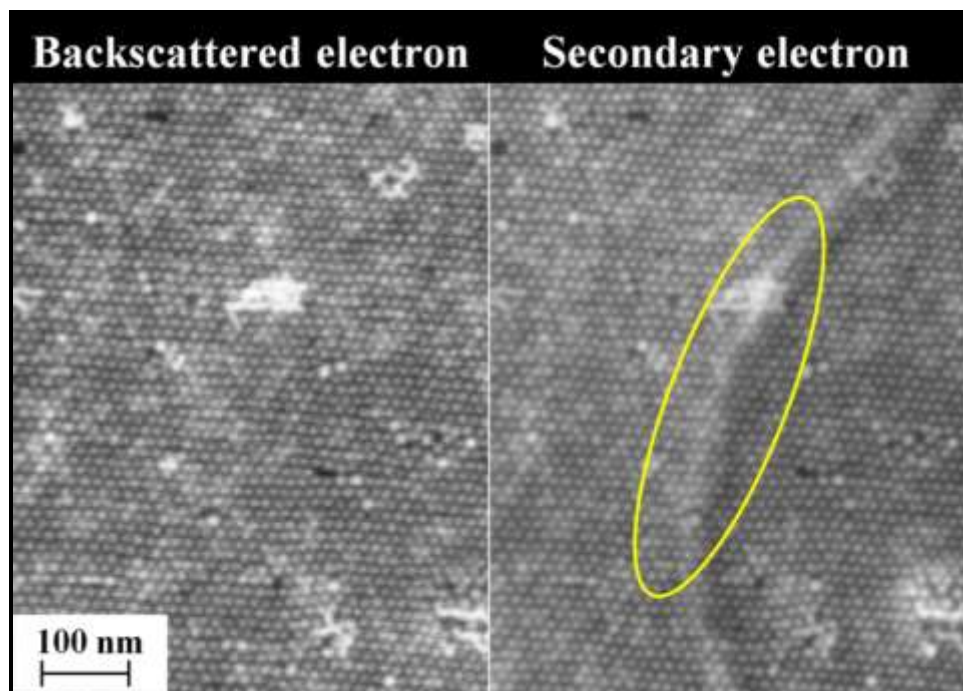
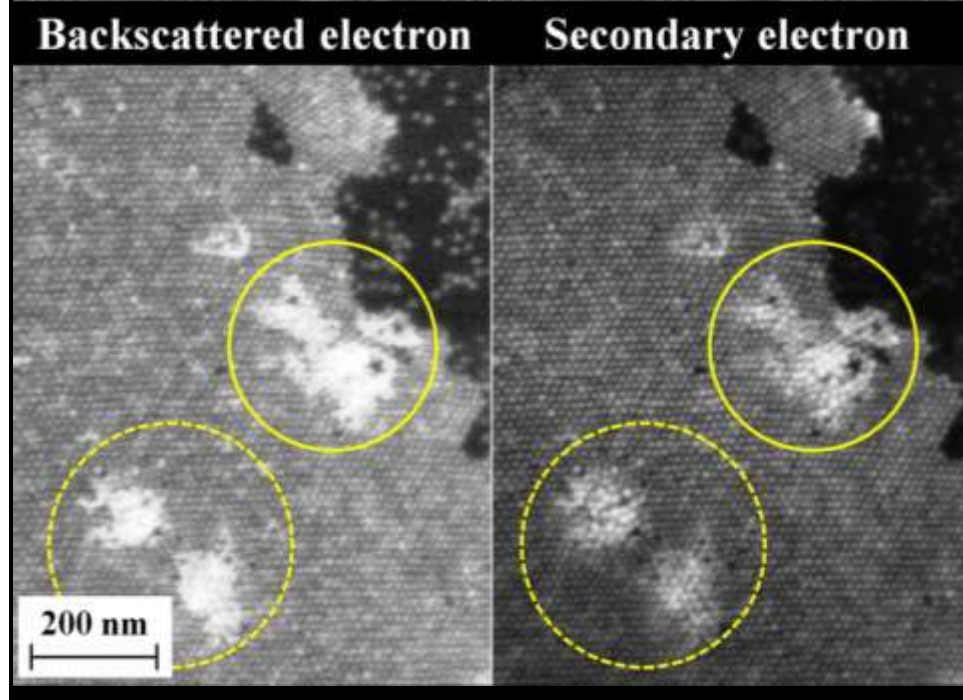
a**b**

Figure 5.31: Representative high-magnification FESEM images, obtained using both secondary electron and backscattered electron detector, of boiled PEG-thiol coated gold nanoparticles mixed with excess hydrogen peroxide and sodium citrate at different locations; (a) region of organic PEG film (as region marked by the oval in secondary electron detector was not translated onto the backscattered electron image) and (b) region of gold-rich complex (as regions marked with circles in secondary electron image also appear as very bright spots in backscattered electron image).

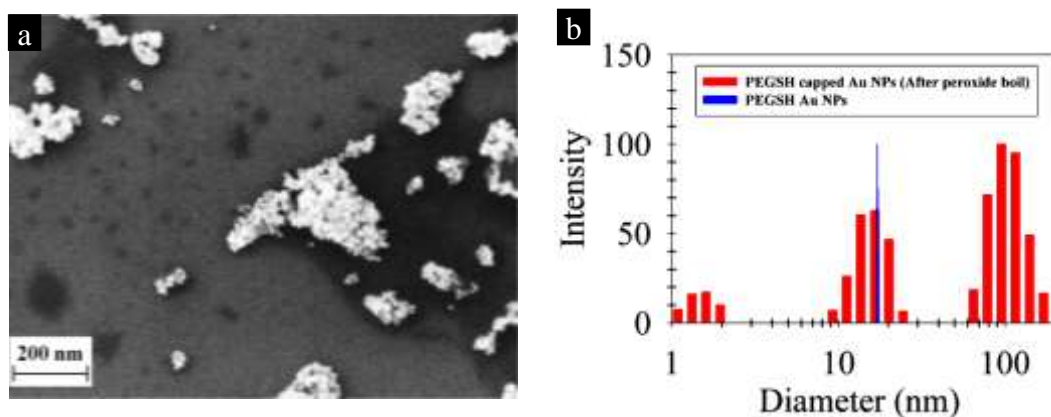


Figure 5.32:(a) Representative FESEM image of thiol-functionalized PEG capped gold nanoparticles boiled with a mixture of hydrogen peroxide and sodium citrate after boiling for 20 minutes, suggesting fusion of nanoparticles due to removal of ligands and the (b) representative DLS size histogram.

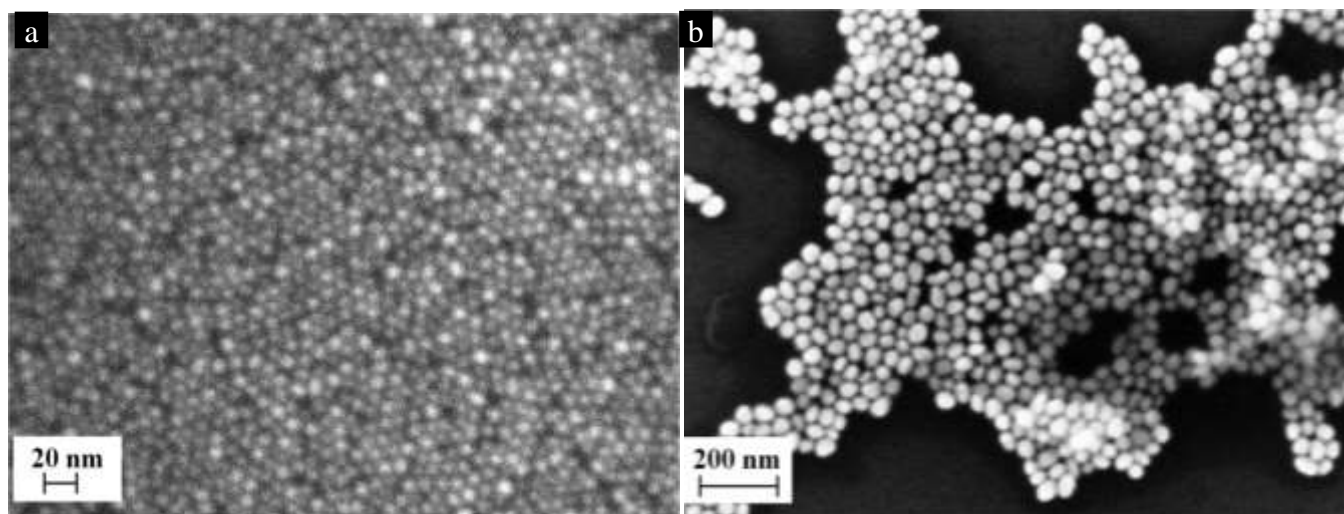


Figure 5.33: (a) Representative FESEM images of (a) PEG-thiol coated gold nanoparticles derived from 5 nm citrate capped gold nanoparticles and (b) PEG-thiol coated gold nanoparticles derived from ~ 40 nm citrate capped gold nanoparticles (Frens method).

conditions from a substrate after several months. On the contrary, ageing of colloidal solution for several months did not result in any changes to particle size distribution, as the results of DLS measurements were identical to the initial value of 17.1 ± 0.2 nm.

All these results suggest that excess ligand molecules/complexes are in equilibrium with the adsorbed molecules/complexes on the surface of gold nanoparticles, and as far as this equilibrium is maintained, particles exhibit very narrow size distributions. Very recently, Tantakitti and co-workers, have reported nanoscale clustering of carbohydrate thiols in mixed self-assembled monolayers on gold²³⁶. They have also reported that during storage, sugar and oligo(ethylene glycol) thiols can laterally diffuse, facilitating intermolecular interactions between the components leading to nanoscale clustering. Further, AFM measurements suggest gel like structure. Hence, it can be surmised that, excess PEG molecules are essential even when the particles are drop-cast on the substrate. With the removal of PEG molecules either through vacuum or ageing in the ambient atmosphere, the particles restructure and reshape. However, similar rapid ripening process was neither observed starting from smaller nanoparticles⁶² (< 5 nm) synthesized through citrate (Fig. 5.33a) nor starting from larger-size particles, synthesized using Frens protocol⁶⁸ (Fig. 5.33b), despite waiting for reasonable time intervals (4 days) or using higher temperatures (~ 100 °C for 10 minutes). As the pH of the colloidal solution containing larger-sized particles was acidic and also the amount of sodium citrate added was minimal, it could have affected the ripening process. So, additional sodium citrate was added to this solution to make the amount equivalent to the standard Turkevich protocol. Evidence for ripening process was seen through the formation of small sized particles (Fig. 5.34), although complete ripening was not observed even after a matter of weeks. It is surmised that enough steric repulsion might not be in place to overcome the van der Waals attraction between particles, as the FESEM images reveal flocculation of particles unlike uniform 2D assembly observed in smaller size particles earlier. So, the use of

longer chain PEG-thiol ligand molecules, viz. 1000 and 5000 g/mol molecular weight molecules was attempted to provide appropriate steric repulsion.

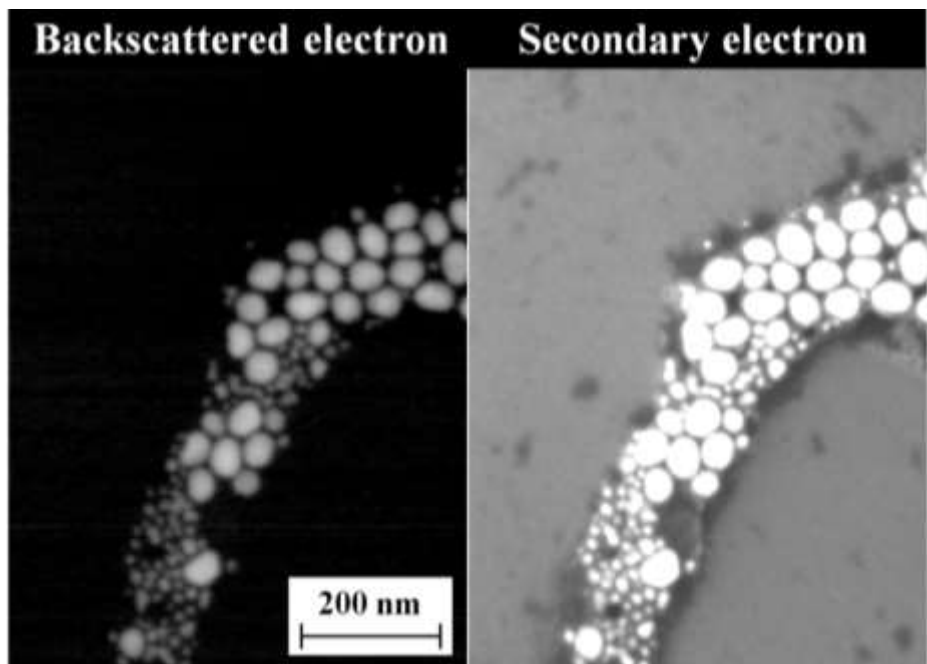


Figure 5.34: Representative FESEM image of ~ 40 nm citrate capped gold nanoparticles after changes in pH through the addition of sodium citrate (such that the final molar ratio of citrate to gold reached 5.2), highlighting ripening process through the formation of small sized particles using two detectors, namely, backscattered electron (left) and secondary electron (right) detectors.

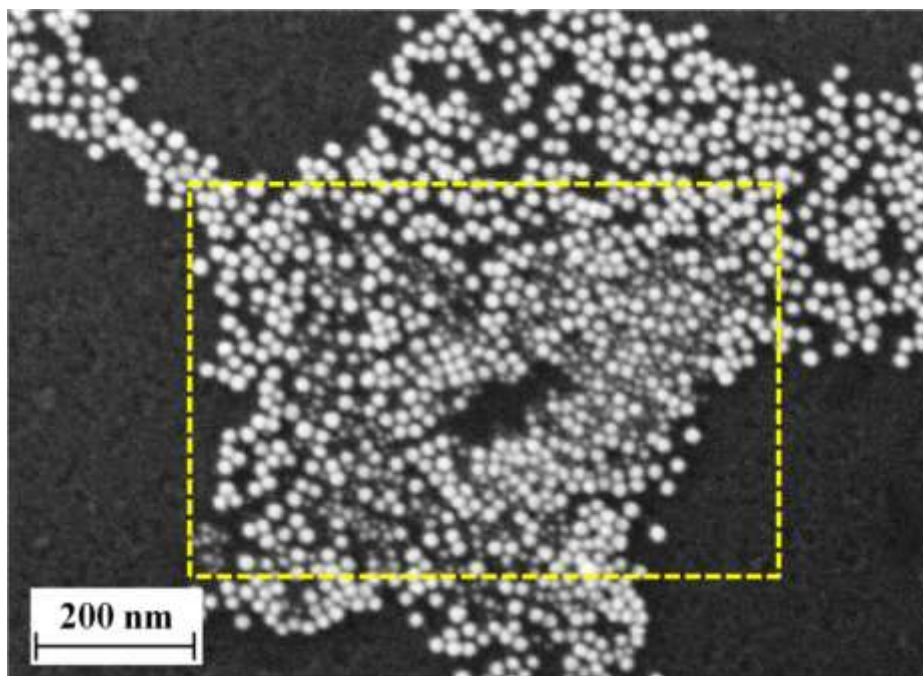


Figure 5.35: Representative FESEM image of citrate capped gold nanoparticles after immediate addition of PEG-thiol molecules of molecular weight 5000 g/mol; highlighting possible ripening process through the formation of etching of larger particles (dotted rectangle).

9.1a.5.8 Effect of molecular weight of PEG-thiol

In view of varying the final size of ripened particles from 11 nm, longer chain length PEG-thiol molecules (molecular weight: 1000 and 5000 g/mol) were employed. The molar ratio of PEG to gold was maintained at 10. Standard citrate colloid of mean size 14 nm was employed for this study. Even after two days, significant reduction in particle size was not observed. Nevertheless, with PEG 5000, drop-casting of colloidal solution, immediately after PEG-thiol addition showed formation of extremely small particles of sizes less than 5 nm (Fig. 5.35). This suggests that particle ripening should be indeed possible. With appropriate activation, size focusing of particles could occur as observed for lower molecular PEG-thiol (356 g/mol). Experimental observations show particle sizes of $\sim 10.7 \pm 2.3$ nm and 14.1 ± 2.4 nm for PEG-thiol molecules of molecular weight 1000 and 5000 g/mol respectively (Fig. 5.36a-d). DLS measurements confirm changes in both the particle size and reduction in polydispersity with boiling (Fig. 5.36e,f). However, the extent of monodispersity is poorer when compared to particle ripened using PEG-thiol molecules of molecular weight 356 g/mol. At this juncture, it is speculated, distribution in molecular weight of PEG-thiol used could be the reason for observed variation in polydispersity using different molecular weight PEG molecules. Surprisingly, zeta potential measurements showed -14 ± 3.3 mV and -16.8 ± 2.0 mV for particles capped with PEG-thiol 1000 and 5000 molecules, thereby suggesting that some of the citrate molecules are still adsorbed and retain their charge even after addition of the PEG-thiol molecules. To understand the effect of ligand length, experiments were carried out where in PEG-thiol molecules of molecular weight 5000 (molar ratio of PEG-thiol to gold: 10) was added to ripened gold nanoparticles capped with PEG-thiol molecules of molecular weight 356 and vice-versa. Addition of PEG-thiol 5000 molecules to highly monodispersed PEG-thiol 356 molecules capped gold nanoparticles of size (11.0 ± 0.7 nm) resulted in loss of monodispersity and also an increase in mean size to 13.2 ± 1.9 nm (Fig. 5.37a), while the addition of PEG-thiol 356 molecules to particles capped with PEG-thiol 5000 capped gold nanoparticles resulted in a reduction of mean size to 11.9 ± 1.6 nm (Fig. 5.37b). On the contrary, with further increase in chain length (molecular weight: 20000 g/mol) for PEG-thiol coated gold nanoparticles (molar ratio of PEG-thiol to gold: 10), there were clear indications of linear assembly of nanoparticles (Fig. 5.38b), unlike the preference of hexagonal close-packed assembly observed earlier, for lower chain length PEG ligands. The size distribution was narrower as compared to the original citrate-stabilized colloidal solution, but was not as monodisperse as those particles obtained using PEG 356.

9.1a.5.9 Absence of gold thiolates in PEG-thiol coated nanoparticles

Based on the results of peroxide boiling experiment in section 5.6, it can be surmised that size focusing of particles might occur through etching of larger particles into smaller particles via the formation of soluble gold complexes. To test the hypothesis of presence of gold complexes, Matrix Assisted Laser Desorption Ionization (MALDI) measurements were carried out. MALDI spectra showed no characteristic peaks corresponding to gold thiolates for PEG-thiol coated gold nanoparticles at two different ratios of PEG/Au, 0.15 and 10 (Fig. 5.39). Negative and positive ion MALDI spectra were collected for both the samples for m/z values ranging from 50 to 100000. For the m/z values ranging from 50 to 1000, there were 4 multiplet peaks occurring with a periodicity of 224 (Fig. 5.39a,b). The molecular weight of PEG-thiol is 356 g/mol, while that of single gold atom attached to PEG-thiol corresponds to 553 ($=197+356$). So the peaks correspond to neither pure PEG-thiol nor gold-PEG-thiol complex but rather to the molecular mass of 224, which corresponds to Sinapic acid, the matrix material (Fig. 5.39c-f). Furthermore, there were no significant peaks observed for m/z values ranging from 1000 to 100000 in both the samples (Fig. 5.40). This suggests the absence of gold complexes or gold nanoclusters less than 2 nm size²³⁷ in the aged sample. Therefore, the bright films (i.e., electron rich domains) seen in Fig. 5.31b could have occurred during the process of drying on a substrate, as part of the sample preparation of precursor due to the effect of peroxide. Although there is no evidence for presence of gold complex in the aged solution, the possibility of their formation immediately after PEG-thiol addition cannot be ruled out.

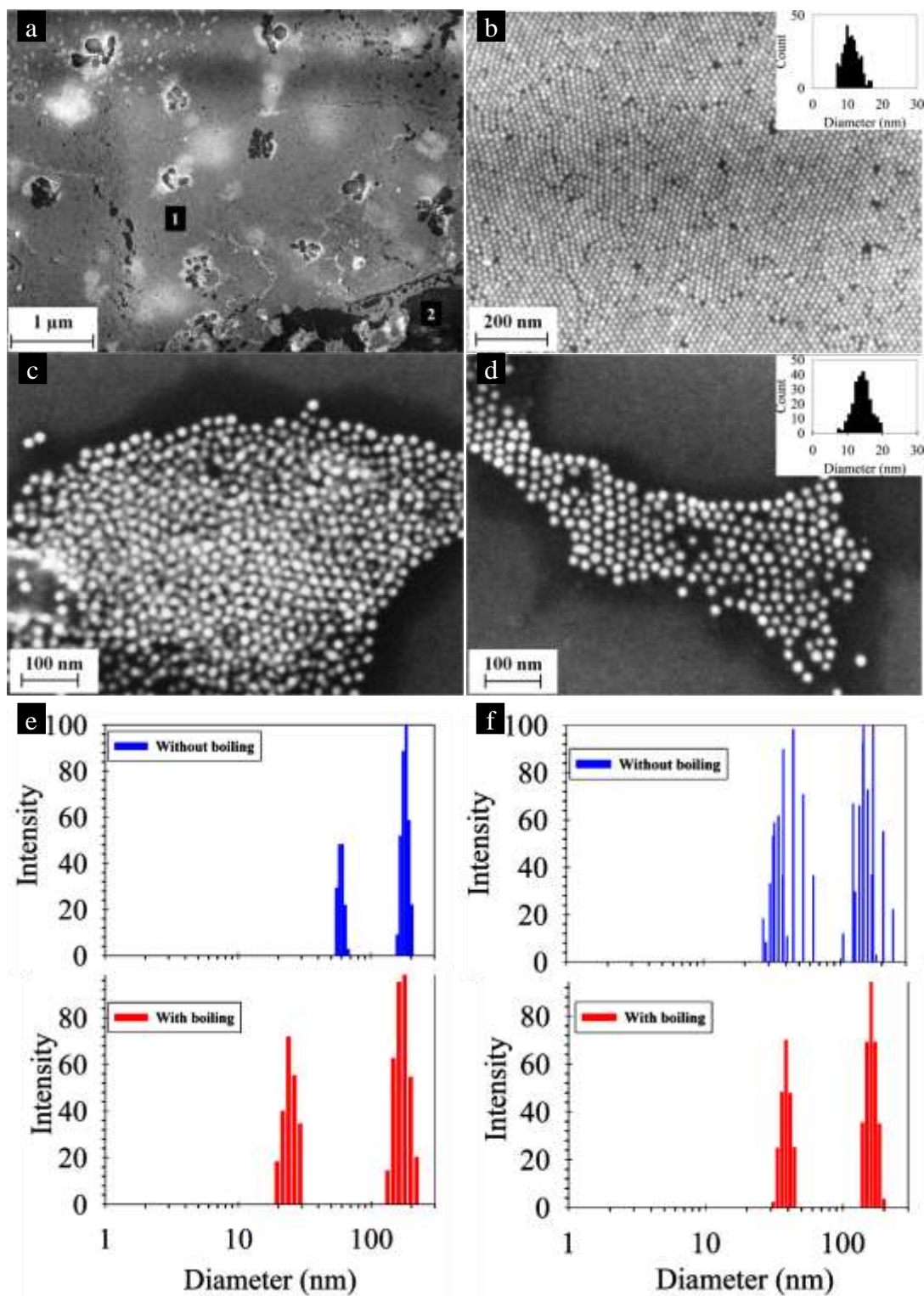


Figure 5.36: Representative FESEM images of ripened gold nanoparticles using PEG-thiol molecules having molecular weight of (a-b) 1000 g/mol, and (c-d) 5000 g/mol. The insets in b and d represent respective size histograms. DLS measurements of PEG-thiol coated gold nanoparticles with and without boiling for different molecular weights, (e) 1000 g/mol, and (f) 5000 g/mol. The molar ratio of PEG-thiol to gold was maintained 10 for both the cases and the sample was boiled for 10 minutes before analysis.

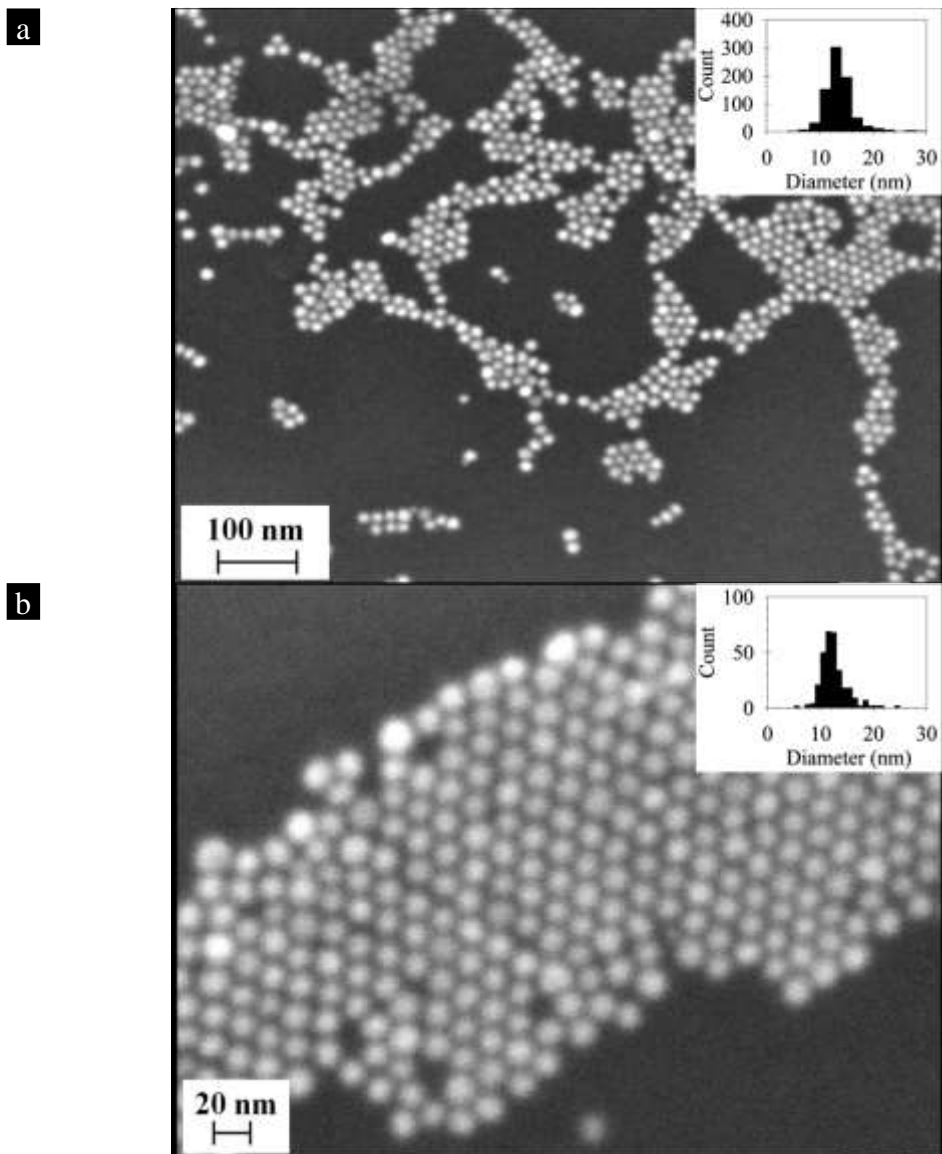


Figure 5.37: (a) Representative FESEM images of addition of PEG-thiol 5000 molecules to ripened particles using PEG-thiol 356. (b) Representative FESEM images of addition of PEG-thiol 356 molecules to ripened particles using PEG-thiol 5000. The insets represent respective size histograms.

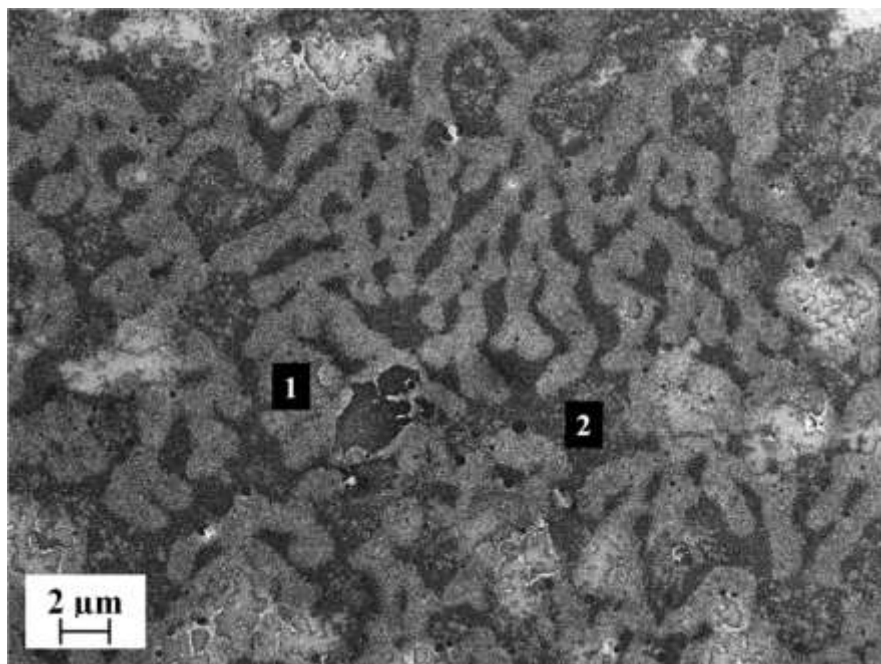
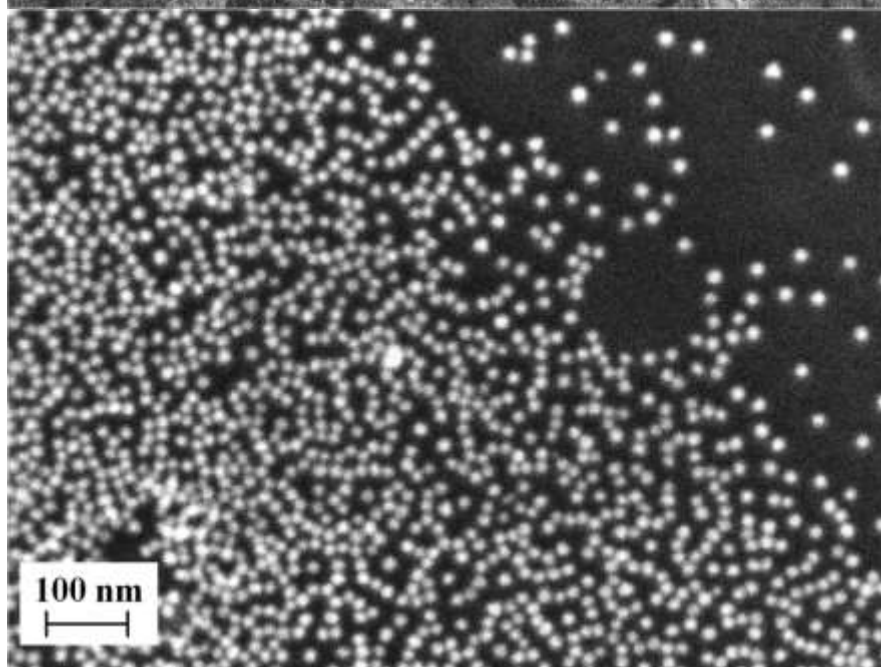
a**b**

Figure 5.38: Representative FESEM images of ripened gold nanoparticles using PEG-thiol molecules of molecular weight 20000 g/mol at (a) low and (b) high magnification. The molar ratio of PEG to gold is 10 and the sample was aged for 1 day at 25 °C. The regions marked 1 and 2 (in a) represent close-packed and non-close packed arrays respectively.

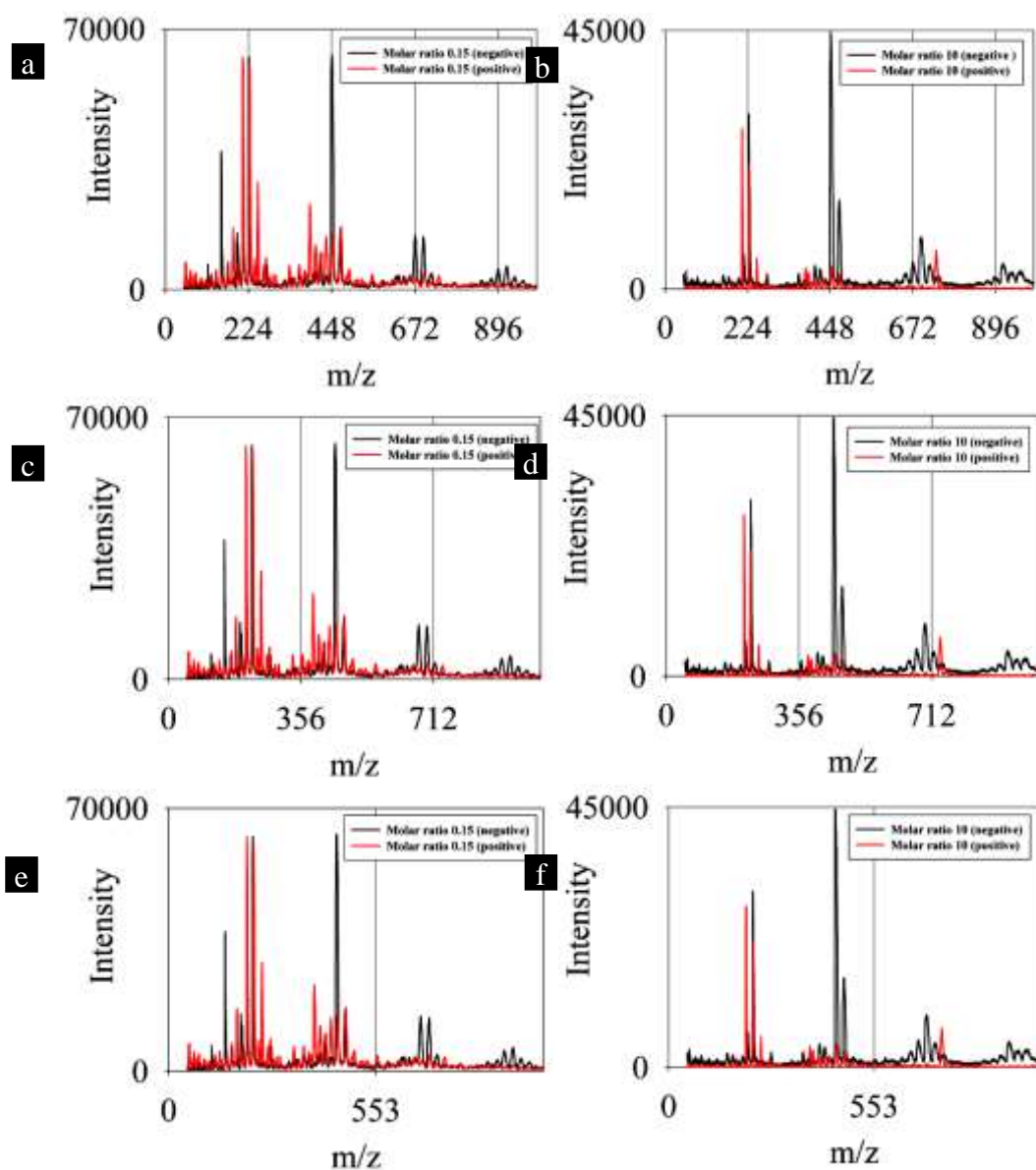


Figure 5.39: Low m/z range, MALDI spectra of PEG-thiol capped gold nanoparticles ionized both negatively and positively, at different ratios of PEG-thiol to gold of 0.15 and 10 plotted with different grid lines (a-f). The molecular weight of Sinapic acid (matrix), PEG-thiol, Au1-PEG-thiol is 224, 356 and 553 respectively. It can be seen that peaks coincide well with the Sinapic acid and not with gold thiolates or any complex.

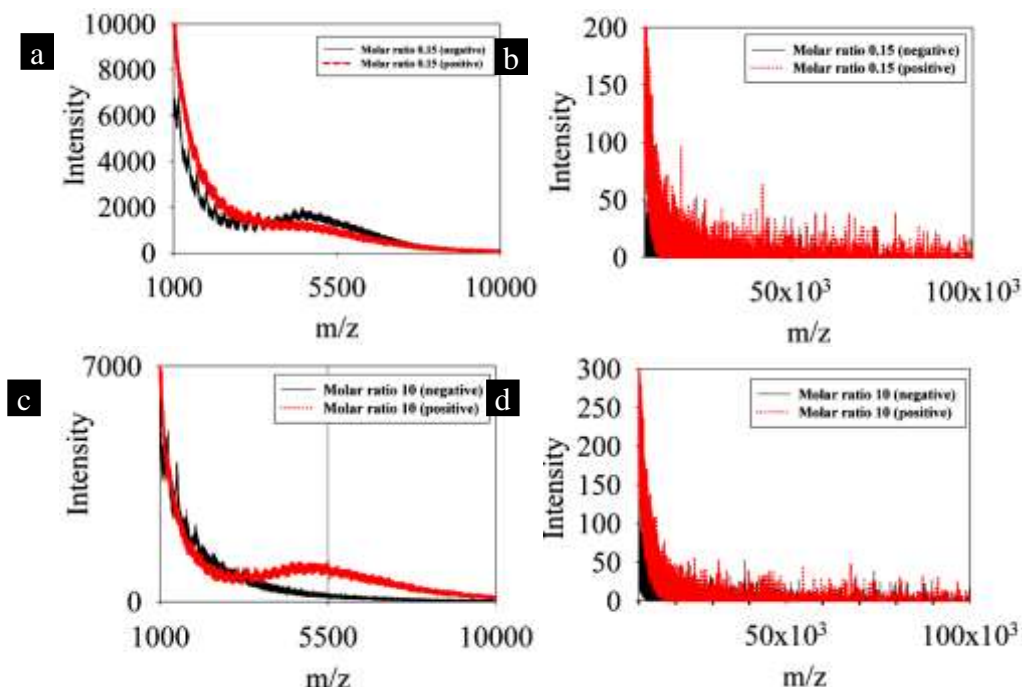


Figure 5.40: High m/z range, MALDI spectra of PEG-thiol capped gold nanoparticles ionized both negatively and positively, at different ratios of PEG-thiol to gold of 0.15 and 10.

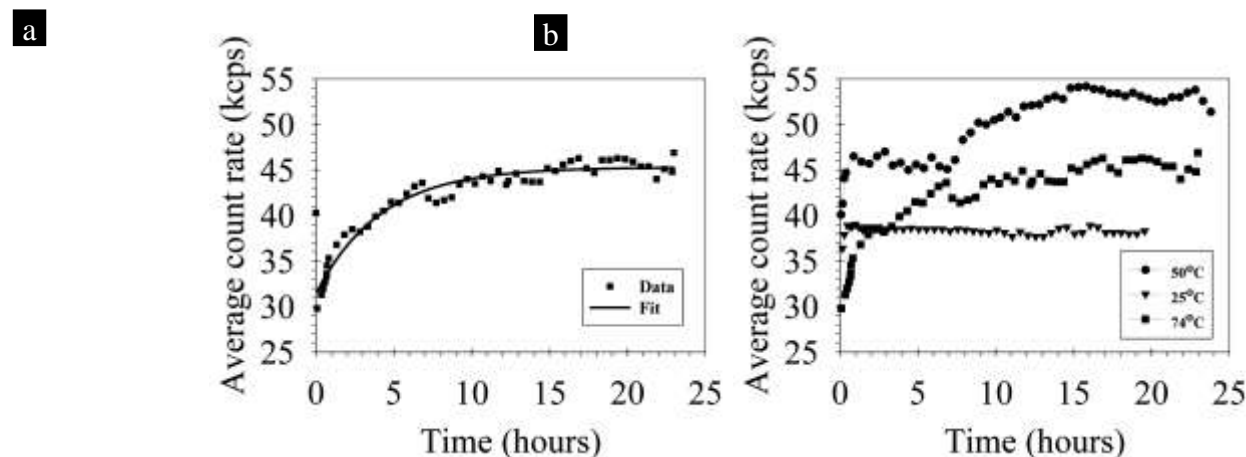


Figure 5.41: (a) Time-dependent average DLS photon count intensity after addition of PEG-thiol (PEG/Au: 10) and aged the sample at 74 °C. Extraction of time constant (~ 4.1 hours) based on the time-dependent average DLS photon count intensity at 74 °C. There is a sudden drop in DLS photon count intensity from 40 to 30 kpks after the addition of PEG-thiol to citrate capped gold nanoparticles. (b) Time-dependent average DLS photon count intensity with respect to temperature, after addition of PEG-thiol (PEG/Au: 10). It can also be that there is a significant batch to batch variation.

9.1a.5.10 DLS photon counts

In addition to particle size and polydispersity, Dynamic Light Scattering measurements can provide vital information on the number density of particles, provided the scattered signal is only from the single scattering events. The average photon count intensity (I) is dependent on both number density (n) and particle size (d), as any slight variation in either of these parameters can significantly affect the photon counts as

$$I \propto d^6$$

In the current study, there was a sudden drop in DLS count rate, immediately after the addition of the excess PEG-thiol molecules to the citrate capped gold nanoparticles (PEG/gold: 10) as shown in Fig. 5.41a. Remarkably, the DLS count rate was also found to be dependent on temperature. With an increase in temperature from 25 °C to 74 °C, the ageing time for observing monodispersity decreased from ~ 16 hours to 4.1 hours, based on the time dependence DLS photon counts (obtained by fitting a time constant to the time-dependence of DLS photon count at 74 °C) as shown in Fig.

5.41a. However, there was significant batch to batch variation in photon counts of citrate capped gold nanoparticles, i.e., the initial photon count of citrate capped gold nanoparticles varied from 30 to 45 kcps between batch to batch as seen from the values at time = 0 in Fig. 5.41b. To overcome the issue of the batch to batch variation, PEG capping experiments were conducted from the same batch of citrate capped gold nanoparticles (as the ageing of citrate capped gold nanoparticles for 1 day did not affect their size or photon counts), as shown in Fig. 5.42. Still a significant jump was observed from 23.6 kcps to 42.6 kcps and 56.9 kcps after addition of PEG-thiol molecules (molar ratio of PEG to gold corresponds to 10) at temperatures of 25 °C and 74 °C respectively. Neither drift in the equipment at 25 °C nor at 74 °C can be attributed to this sudden jump in photon counts. Also, at 74 °C, there was a steady increase of photon counts to 37 kcps after 5 hours in pure citrate capped gold nanoparticles, which can be attributed to the slight fusion of particles as determined from changes in particle size distribution (Fig. 5.42). As the mean hydrodynamic size remains constant before and after PEG-thiol addition, only an increase in number density of particles (leading to multiple scattering events) can explain the sudden drop of photon counts. The increase in number density of particles can be explained based on the argument that the gold nanoparticles capped with different chain length have different photon count rate, even though the gold core sizes are comparable (molecular weight: 356, 1000 and 5000 g/mol yielded 10.8, 39.8 and 43.2 kcps). This suggests that while considering the intensity, the hydrodynamic diameter must be taken into account not just the core diameter, even though scattering from pure polymers is negligible in comparison to metal atoms. Further, the values are obtained after diluting the sample with water to ensure that multiple scattering effects are avoided and not for time dependence measurements.

As SAXS intensity at low q values before and after addition of PEG-thiol molecules remains the same, the amount of gold atoms contained within the sample is deemed to be equal (Fig. 5.43). The SAXS equipment does not have the resolution to go to q values closer to zero, and so parameters such as number density, mean size and polydispersity cannot be estimated with precision and so, are not reported here.

9.1a.5.11 PEG-citrate complexation

Zeta potential measurements showed a decreasing trend from -54, -35, to -0.2 mV as the PEG-thiol/Au molar ratio changed from 0, 0.15 to 10 respectively. This suggests that at PEG-thiol to gold ratio of 10, the particles are sterically stabilized, unlike the other two cases which are electrostatically stabilized. To understand this aspect further, Nuclear Magnetic Resonance (NMR) measurements were carried out. ^1H NMR of free PEG-thiol in solution shows characteristic peak values at 2.7 (-SH, labelled 1), 2.9 (-S-CH₂, labelled 2), 3.3 (-OCH₃, labelled 3), 3.5 and 3.6 (hydrogen from ethylene glycol chain, labelled 4 and 5) ppm respectively (Fig. 5.44). ^1H NMR of citrate capped gold nanoparticles shows a characteristic peak at 2.6 ppm corresponding to -CH₂ protons of citrate (Fig. 5.45a). ^1H NMR of PEG-thiol capped gold nanoparticles shows all the peaks corresponding to PEG-thiol molecules (Fig. 5.45b). Surprisingly, there is an additional peak attributed to bound citrate that is also present at 2.6 ppm. This is counterintuitive because zeta potential after addition of PEG-thiol molecules was found to be only -0.2 mV, so a complete replacement of

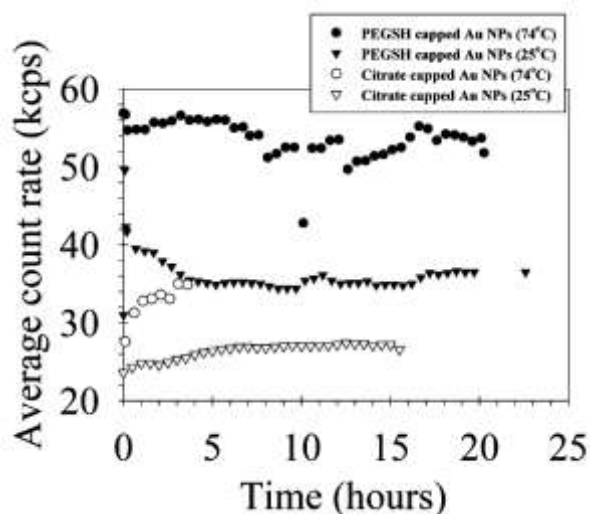


Figure 5.42: (a) Time-dependent average DLS photon count intensity with respect to temperature for the same batch of citrate capped gold nanoparticles, after addition of PEG-thiol (PEG/Au: 10). It can also be seen that the photon count intensity of citrate capped gold nanoparticles at 25 °C does not increase much while at 74 °C, the increase is attributed to the fusion of particles.

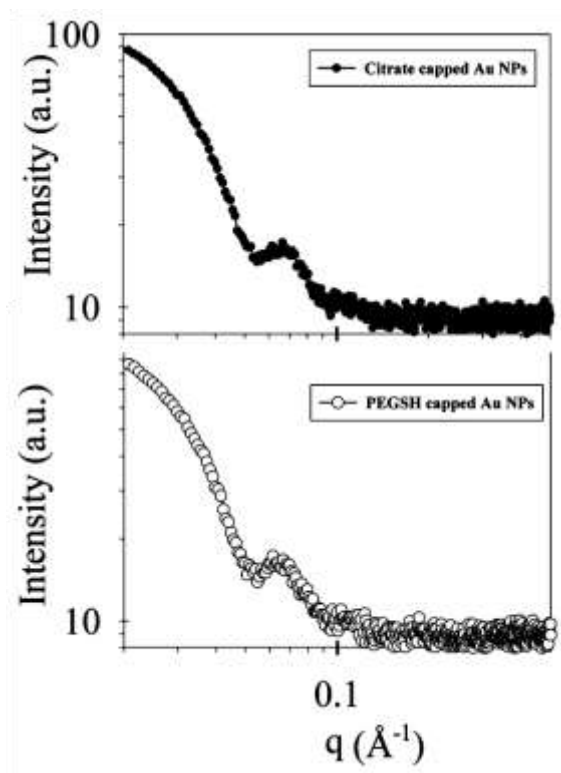


Figure 5.43: Small-Angle X-ray Scattering (SAXS) spectra of citrate capped and PEG-thiol capped gold nanoparticles. As the intensity at low q values remains the same, the amount of gold contained in the two samples can be considered equal.

citrate ions with PEG molecules was expected. However, ^1H NMR data clearly shows this is not the case. To understand this aspect further, Raman measurements were carried out in solution. The signals arising from the solution are weak as the amount of molecules present in the sample is equivalent to the amounts present in the final colloid. The Raman spectra of pure PEG-thiol in water did not show any characteristic peak (Fig. 5.46). Typically, the carboxylate peaks of citrate appear between 1380 to 1600 cm^{-1} . More specifically, the symmetric and asymmetric stretching modes of carboxylate anion appear in the range of 1414 - 1425 cm^{-1} and 1560 - 1580 cm^{-1} respectively. The intensity ratio and the wavenumber difference between symmetric and asymmetric modes can be used to determine the structure of adsorbed carboxylate ion. The wavenumber difference between the ionic carboxylate symmetric and asymmetric stretching is 145 - 164 cm^{-1} . If the wavenumber difference between stretching modes is higher than the ionic value, then the presence of citrate as unidentate complex is indicated, otherwise a bidentate complex is expected to be formed. From the intensity ratio between different stretching modes, one can estimate relative amounts of bidentate and unidentate complexes present in the sample. The Raman spectra of pure sodium citrate in water showed the presence of peaks at 1400 , 1440 , 1558 and 1566 cm^{-1} , as shown in Fig. 5.46. This suggests the presence of carboxylate anion in ionic state, as the wavenumber difference between the symmetric and asymmetric modes is around 158 - 166 cm^{-1} . After the addition of PEG-thiol to sodium citrate in water, the difference between the symmetric and asymmetric modes decreased to 85 cm^{-1} , suggesting the presence of carboxylate as bidentate complex (as shown in Fig. 5.46). The Raman spectra of citrate capped gold nanoparticles showed peaks at 1558 and 1604 cm^{-1} , suggesting only asymmetric stretching mode of carboxylate ion (Fig. 5.46). Also, as the intensity ratio between $I(1604)$ to $I(1558)$ is greater than 1, only bridging bidentate complexes of carboxylate ions are formed. This observation is in contrast to the observation reported earlier in the literature, where in the 60 nm citrate capped gold nanoparticles gave rise to Raman signals that showed the presence of unidentate and ionic complexes, in addition to bidentate complexes. The observation of only bidentate complex in the present study can be attributed to the reduced size of the nanoparticle ($\sim 15\text{ nm}$), which has higher radius of curvature, thereby favoring the formation of bidentate carboxylate complex.

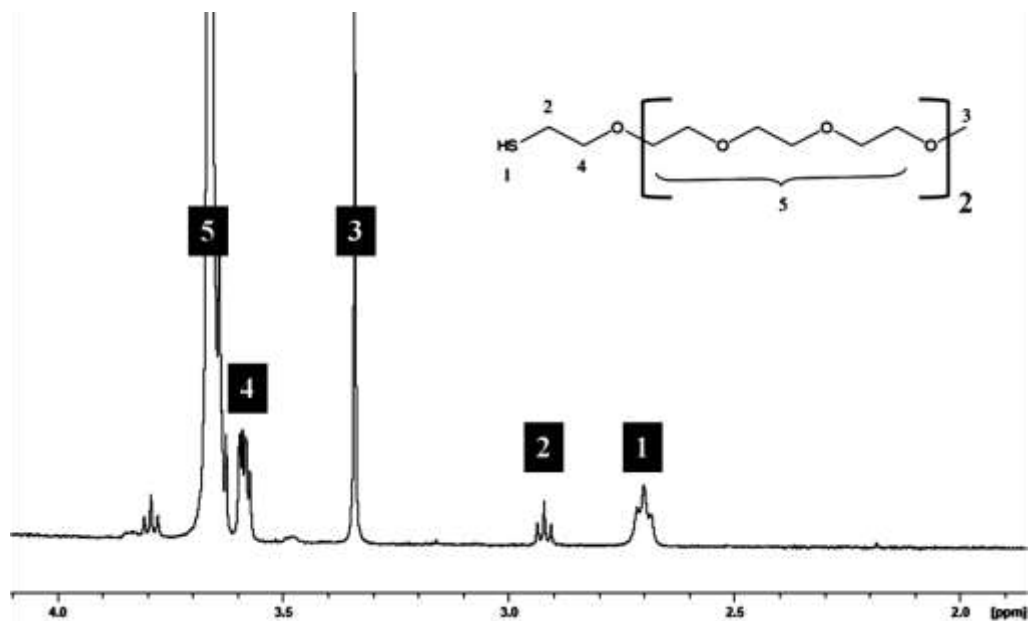
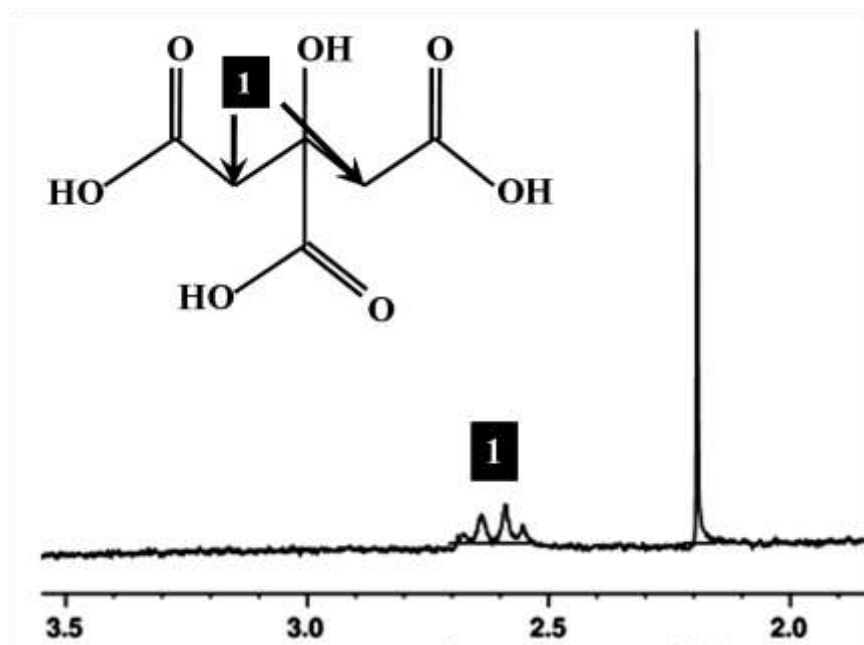


Figure 5.44: ¹H Nuclear Magnetic Resonance (NMR) of PEG-thiol dispersed in D₂O. The numbers embedded with the NMR data correspond to the respective numbers marked in PEG molecular structure (as inset). The characteristic peak values at 2.7 (-SH, labelled 1), 2.9 (-S-CH₂, labelled 2), 3.3 (-OCH₃, labelled 3), 3.5 and 3.6 (hydrogen from ethylene glycol chain, labelled 4 and 5) ppm.

a



b

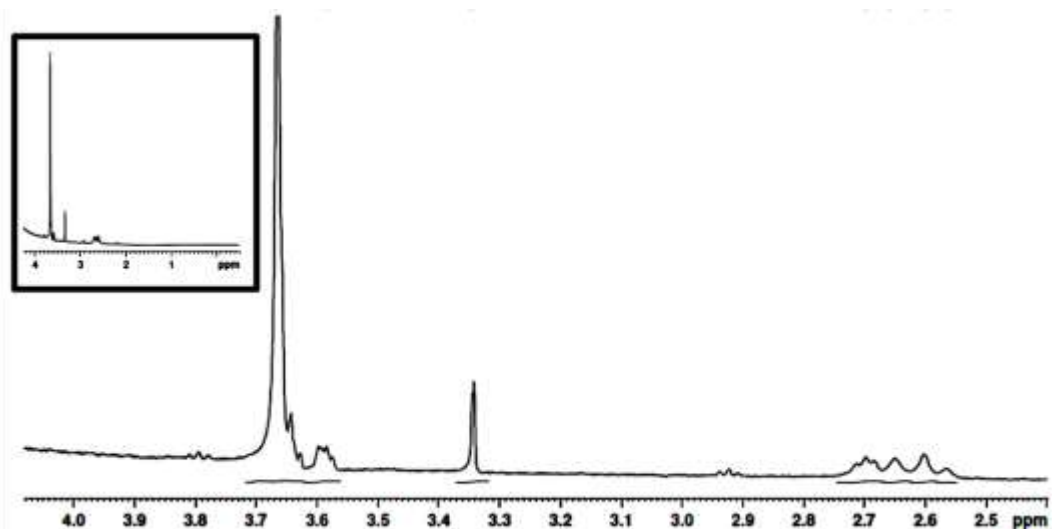


Figure 5.45: (a) ^1H Nuclear Magnetic Resonance (NMR) of citrate capped gold nanoparticles dispersed in D_2O . The number embedded with the NMR data corresponds to the respective numbers marked in PEG molecular structure (as inset). (b) ^1H Nuclear Magnetic Resonance (NMR) of PEG-thiol capped gold nanoparticles dispersed in D_2O . The inset represents the full spectrum scan. The peak at 2.7 ppm suggests that there is a significant presence of bound citrate present in the PEG capped gold nanoparticle.

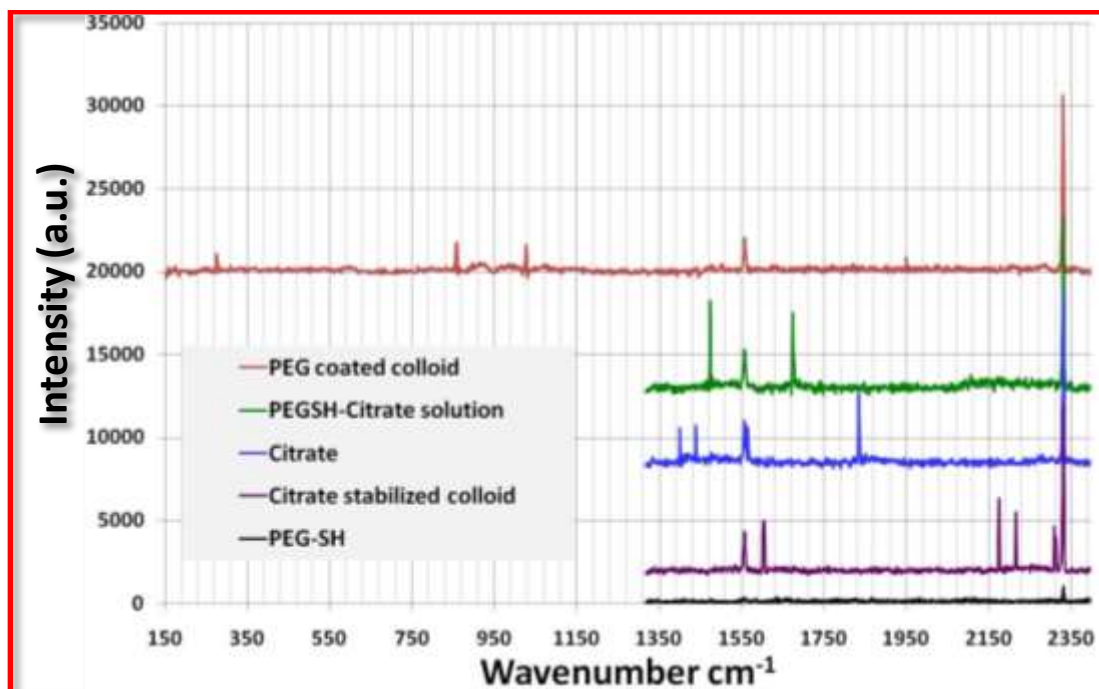


Figure 5.46: Raman spectra of PEG-thiol, sodium citrate and PEG-thiol-sodium citrate solutions in water. The sample concentrations correspond to the respective amounts in PEG-thiol capped gold nanoparticles. Raman spectra of citrate capped gold nanoparticles, with the characteristic carboxylate peaks at 1558 and 1604 cm^{-1} ; thereby suggesting the presence of only bridging bidentate complex. Raman spectra of PEG-thiol coated gold nanoparticle indicating negligible presence of Au-S peak $\sim 300 \text{ cm}^{-1}$.

Raman spectra of PEG-thiol capped gold nanoparticle showed the presence of bound citrate (1560 cm^{-1}) and a weak signal corresponding to Au-S at $\sim 300 \text{ cm}^{-1}$. This result is in concord with NMR measurements (Fig. 5.45b) that citrate is still bound to the gold surface and that the gold-thiol bonds are not present in significant numbers.

9.1a.5.12 Role of PEG backbone

Raman measurements and ^1H NMR spectra of PEG-thiol capped gold nanoparticles suggest that the presence of PEG backbone is critical, while thiol group is not critical for the observed size changes. This is in contrast to all earlier reports on “digestive ripening” of gold nanoparticles that were shown to occur through the formation of gold-thiolate complexes. To test this hypothesis, an additional experiment was performed where PEG molecules of molecular weight 300 g/mol without any thiol functionalization were added to a solution of freshly prepared citrate capped gold nanoparticles and aged for 1 day. The molar ratio of PEG to gold was maintained at 10. A low magnification FESEM image of the PEG capped gold nanoparticles shows Moiré patterns similar to the PEG-thiol capped gold nanoparticles (Fig. 5.47). After focusing on the particles at high magnification (200kx) and then obtaining image at low magnification (19 kx) shows image distortion due to the possible presence of organic/PEG film (Fig. 5.47). The FESEM images obtained at high magnification clearly show enhanced monodispersity of gold nanoparticles (Fig. 5.48). The size of the particle is $10.3 \pm 1.4 \text{ nm}$, which is similar to the value obtained using PEG-thiol. These results suggest that, after the addition of excess PEG molecules, the gold nanoparticles are covered with citrate molecules, which are, in turn, crowned with PEG molecules. Such crowning by PEG molecules has been attributed to the interactions of lone pairs of electrons present on the oxygen atoms of PEG molecules. It is also believed that by varying the molecular weight of PEG molecules without thiol group should enable to alter the particle size. As the polydispersity is higher in the case of higher molecular weight (5000 g/mol) PEG molecules, this will not enable to improve the polydispersity of initial citrate capped gold nanoparticles. Hence it was decided to carry out the experiments only with lower molecular weight (300 g/mol) PEG molecules.

9.1a.5.13 Role of bound carboxylate ion

As NMR and Raman measurements showed the presence of bound citrate, the role of sodium citrate in particle ripening was investigated next. The gold nanoparticles with and without bound citrate, of similar size range were synthesized using different approaches. The results of these experiments are presented next.

Tannic acid method

Tannic acid capped gold nanoparticles of mean size 13.8 ± 4.3 nm were prepared as reported earlier⁶³ (Fig. 5.49a). After adding PEG-thiol molecules (molar ratio of PEG to gold: 10:1), there was no evidence of change in particle size distribution after ageing the sample for 16 hours. The mean size was found to be 14.5 ± 2.1 nm (Fig. 5.49b). Also, addition of premixed solutions of PEG-thiol and sodium citrate to tannic acid capped gold nanoparticles did not show evidences of size focusing, thereby indicating the importance of adsorbed citrate ions. The mean size was found to be 10.4 ± 4.9 nm (Fig. 5.49c,d).

Ascorbic acid method

Flower like nanostructures of varying size from 10 to 40 nm were prepared based on the report of Boca and coworkers (Fig. 5.50a), using ascorbic acid as the reducing agent. Adding excess PEG-thiol molecules (molar ratio of PEG to gold: 10:1) did not result in significant changes in particle size distribution (Fig. 5.50b).

Ethylene glycol protocol

Standard Turkevich protocol was modified by replacing water with ethylene glycol as solvent (Fig. 5.51a). After addition of excess PEG-thiol molecules (molar ratio of PEG/Au: 10:1), and aging for 1 day, particle ripening was clearly observed (Fig. 51b,c). Next, as ethylene glycol can act as both reducing and stabilizing agent, the nanoparticle synthesis was carried out without the addition of citrate (Fig. 5.51d).

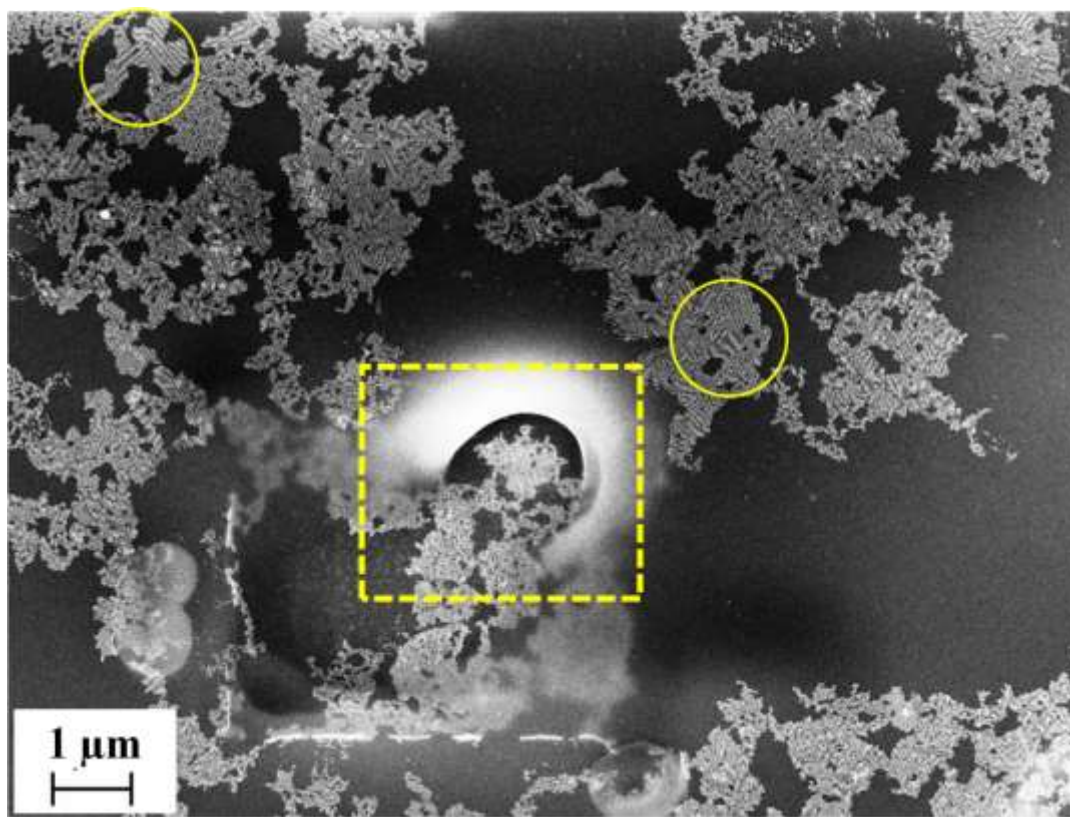


Figure 5.47: Representative low magnification FESEM image of PEG capped gold nanoparticles (without any thiol moiety). This was formed after addition of PEG molecules of molecular weight 300 g/mol without any thiol functionalization to citrate capped gold nanoparticles and aged for 1 day. The molar ratio of PEG to gold is 10. The regions marked with solid circles represent Moiré patterns while the dotted rectangle represents image distortion due to the possible presence of organic film.

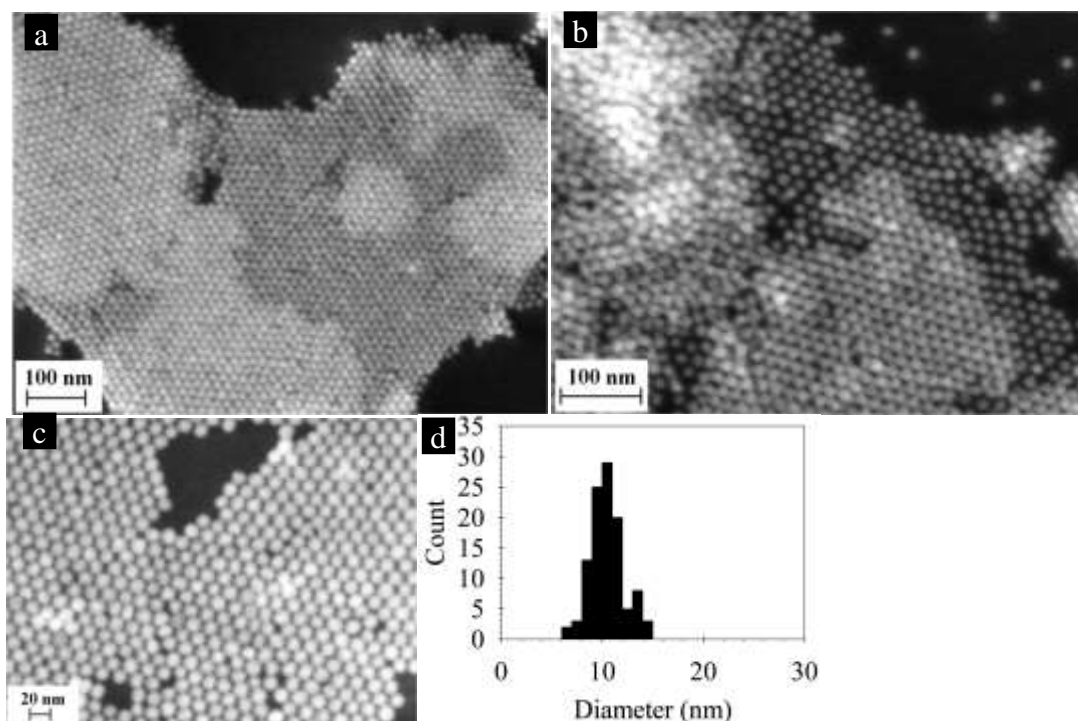


Figure 5.48: (a-c) Representative high magnification FESEM image of PEG capped gold nanoparticles (without any thiol moiety) obtained at different locations and magnifications. This was formed after addition of PEG molecules of molecular weight 300 g/mol without any thiol functionalization to citrate capped gold nanoparticles and after being aged for 1 day. The molar ratio of PEG to gold is 10. (d) Size histogram of PEG capped gold nanoparticles.

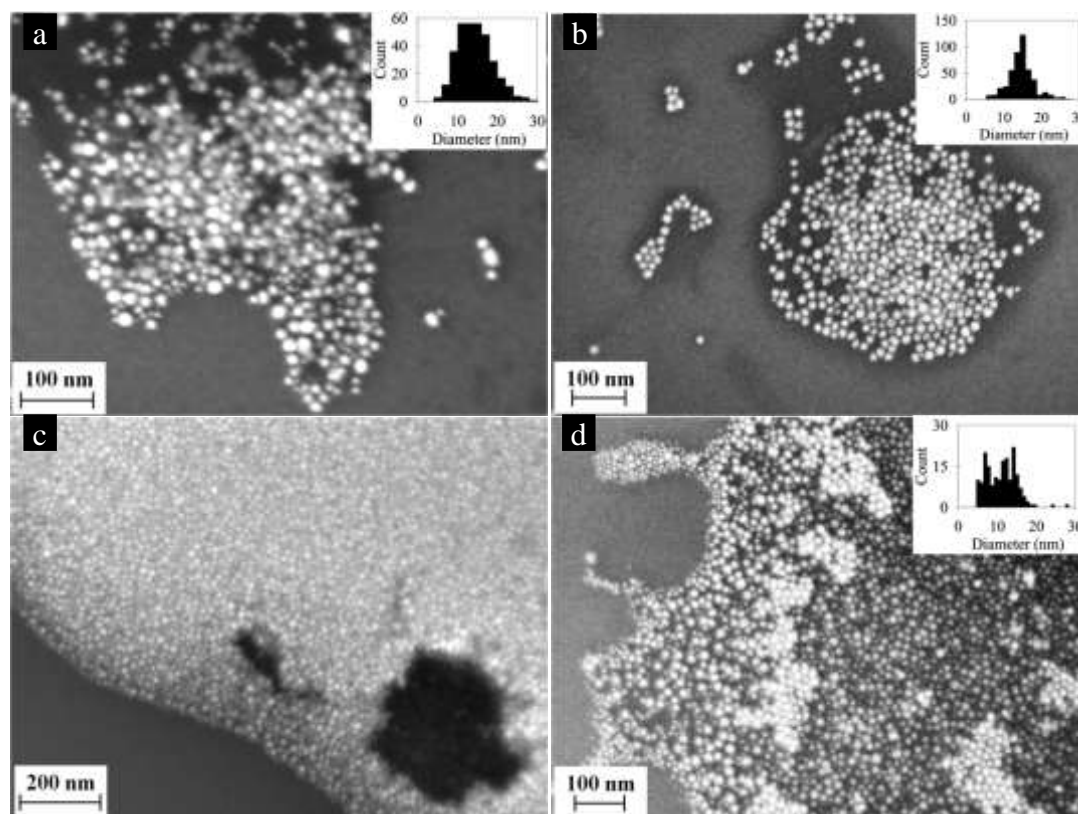


Figure 5.49: Representative FESEM image of (a) polydispersed tannic acid capped gold nanoparticles (13.8 ± 4.3 nm), (b) after addition of PEG-thiol and ageing for 16 hours (14.5 ± 2.1 nm) and (c) after post-factorial addition of sodium citrate to one day aged tannic acid-PEG-thiol capped gold nanoparticles (d) after one week (10.4 ± 4.9 nm)

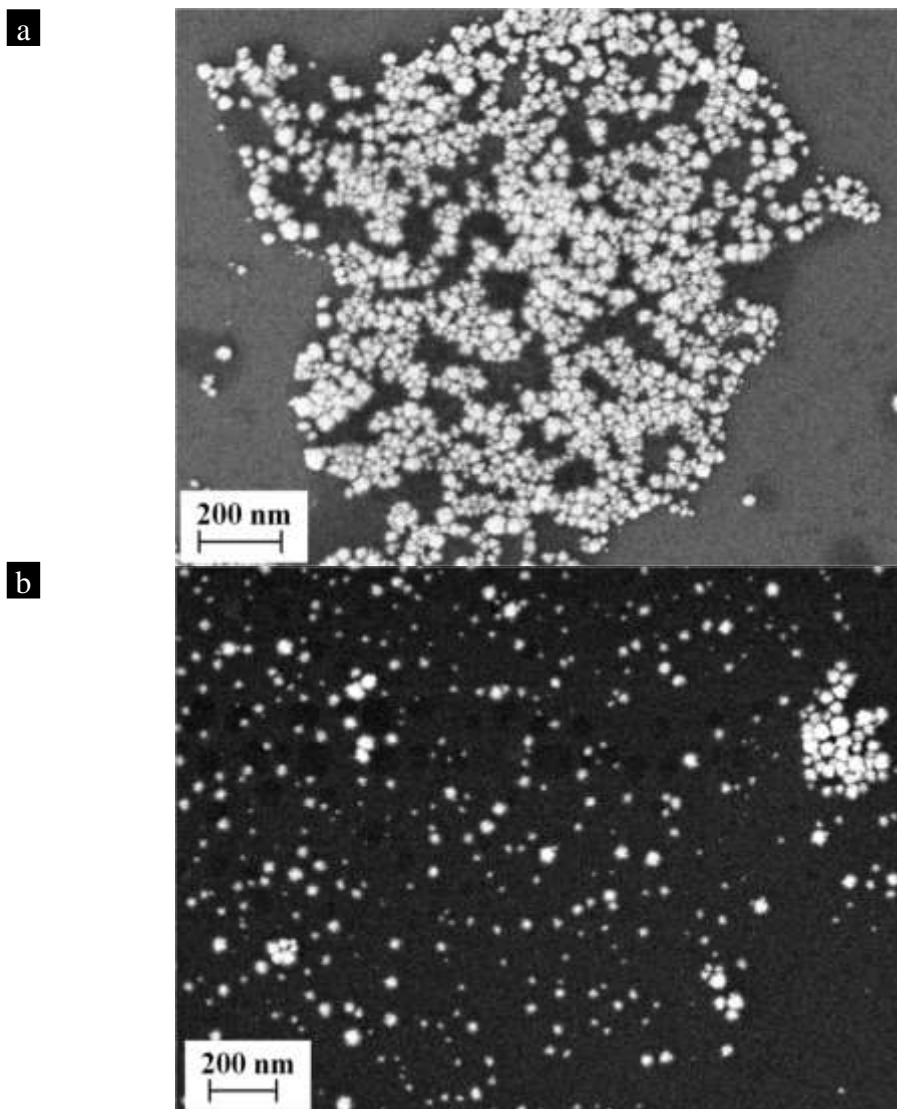


Figure 5.50: (a) Representative FESEM image of ascorbic acid capped gold nanoflowers. (b) Representative FESEM image of gold nanoflowers after addition of PEG-thiol and ageing the sample for 1 day at 25 °C.

When PEG-thiol was added to this solution, there was no evidence of ripening even after waiting for prolonged durations (2 days) (Fig. 5.51e). This experiment again highlights the role of adsorbed citrate in particle ripening.

Sodium acrylate protocol

Gold nanoparticles of size 10.0 ± 2.3 nm were synthesized using sodium acrylate as reducing and stabilizing agents based on an earlier report (Fig. 5.52a). Upon addition of excess PEG-thiol molecules (molar ratio of PEG/Au: 10:1), there was no significant evidence of size focusing as the mean particle size was found to be 13.4 ± 3.7 nm (Fig. 5.52b). This is surprising because both sodium acrylate and sodium citrate have the same functional unit, carboxylate ion. The only notable difference between the Turkevich protocol and the sodium acrylate protocol is the amount of the free carboxylate ions. So, the Turkevich protocol was also modified by increasing the molar ratio of sodium citrate to gold from 5 to 20 (mean size of particle remains same, i.e., 16.0 ± 3.4 nm, as shown in Fig. 5.52c). In the Turkevich protocol

with excess citrate, there was no evidence of ripening even after waiting for prolonged periods of time (2 days), the mean size was found to be 16.8 ± 4.1 nm (Fig. 5.52d).

9.1a.5.14 Phase-space of ripening

A phase-space of ripening was constructed in concentration domain (citrate, gold and PEG concentration) (Fig. 5.53). The black closed circles represent instances of particle ripening, while the red closed circles correspond to instances where ripening didn't occur. To demarcate the 'zone of ripening', additional experiments were carried out and are marked as points with closed half red and black circles. There were signs of particle ripening, but the process did not proceed to completion. Based on this phase-space of particle ripening, it becomes evident that the amount of citrate, PEG and gold is critical for particle ripening to be observed. To test this further, a modification of sodium acrylate protocol was carried out such that the amount of free carboxylate ions in the colloidal sample remains the same as standard Turkevich protocol where ripening was observed (Fig. 5.54a). As surmised, enhancement of monodispersity was observed in the modified sodium acrylate protocol, as shown in Fig. 5.54b-d with the addition of PEG-thiol molecules (molar ratio of PEG to gold is 10) and after being aged for 18 hours at 25 °C. This experiment clearly highlights the role of excess carboxylate ion in the colloidal solution and its implications on particle ripening.

9.1a.5.15 Pechini process

All the aforementioned experiments suggest that presence of carboxylate ions and PEG molecules is critical for observing particle ripening. These observations are analogous to one of the widely-used process for synthesizing multi-component oxide powders, polymerizable complex method, which is also known as Pechini process. It involves the formation of polymeric resin by gelation of the reaction mixture consisting of desired metal ions, chelating agent (citric acid, EDTA) and polyol (ethylene glycol). The metal ions are trapped inside the organic matrix. Control of particle size and shape of metal oxide nanoparticles can be achieved, albeit moderately, through calcination of polymeric resin at higher temperature (~ 300 - 500°C). Kim and co-workers have synthesized monodispersed barium ferrite nanoparticles (4.7 ± 0.8 nm) without calcination, through the formation of metal-citrate complexes. Until now, the Pechini process has been widely used to synthesize metal oxide nanostructures only. In addition, in the Pechini process, the molar ratios of citric acid and ethylene glycol, has been reported to affect the chain size of the polymer and its cross-linking degree while the amount of metal ions determine the polymerization rate. Our experiments, in fact, do suggest particle ripening only in the small zone of the ratio of citrate, PEG and gold. Particle ripening process through addition of PEG-thiol was neither observed for smaller particles (< 5 nm) nor for larger size particles (> 30 nm). It is pertinent to note that these particles were obtained by varying the amount of citrate. Furthermore, the order of addition of precursors, ethylene glycol and citric acid has been found to significantly affect the formation of barium titanium citrate gel using the Pechini process. Similarly, it has been highlighted earlier that post-factorial addition of citrate does not result in particle ripening.

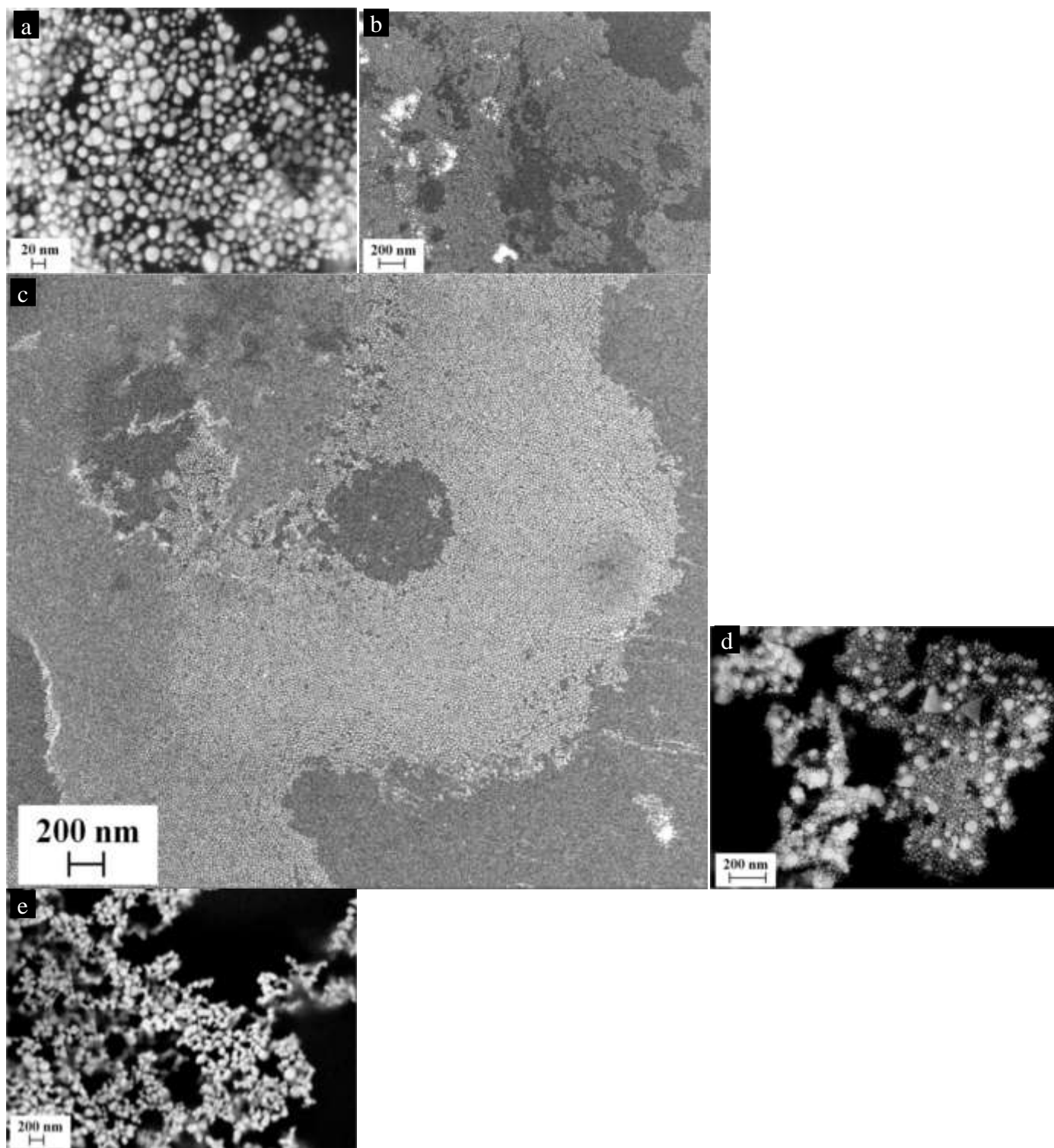


Figure 5.51: Representative FESEM image of citrate capped gold nanoparticles synthesized with ethylene glycol as solvent (instead of water) before (a) and after addition of PEG-thiol (b,c). Fig d represent the FESEM image of gold nanoparticles synthesized with ethylene glycol as both reducing agent and stabilizing agent without citrate while e represents gold nanoparticles after capping with PEG-thiol molecules. The molar ratio of PEG to gold was maintained at 10 and the sample was aged at 25 °C for 1 day.

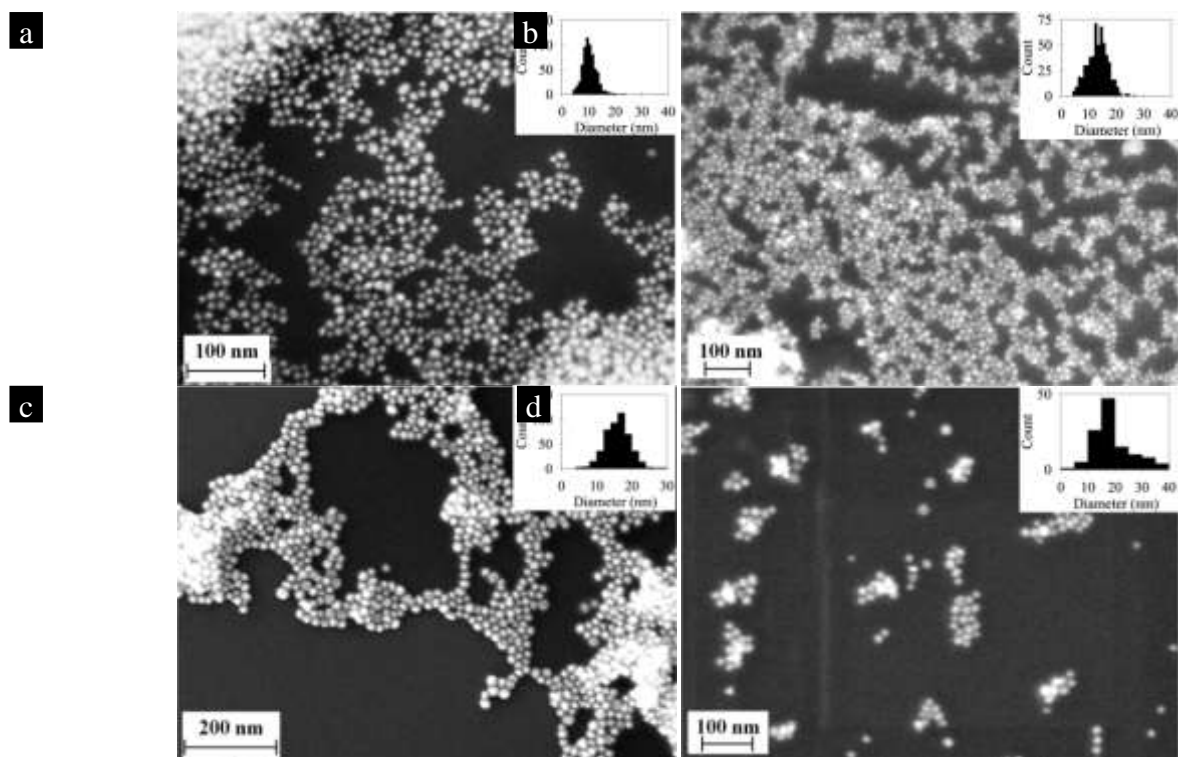


Figure 5.52: Representative FESEM images of sodium acrylate capped gold nanoparticles (a) before and (b) after addition of PEG-thiol molecules and aged for 1 day. Representative FESEM image of citrate capped gold nanoparticles with citrate to gold nanoparticles (c) before and (d) after addition of PEG-thiol and aged for 2 days. Clearly excess citrate prevents ripening of particles. The molar ratio of PEG to gold is 10.

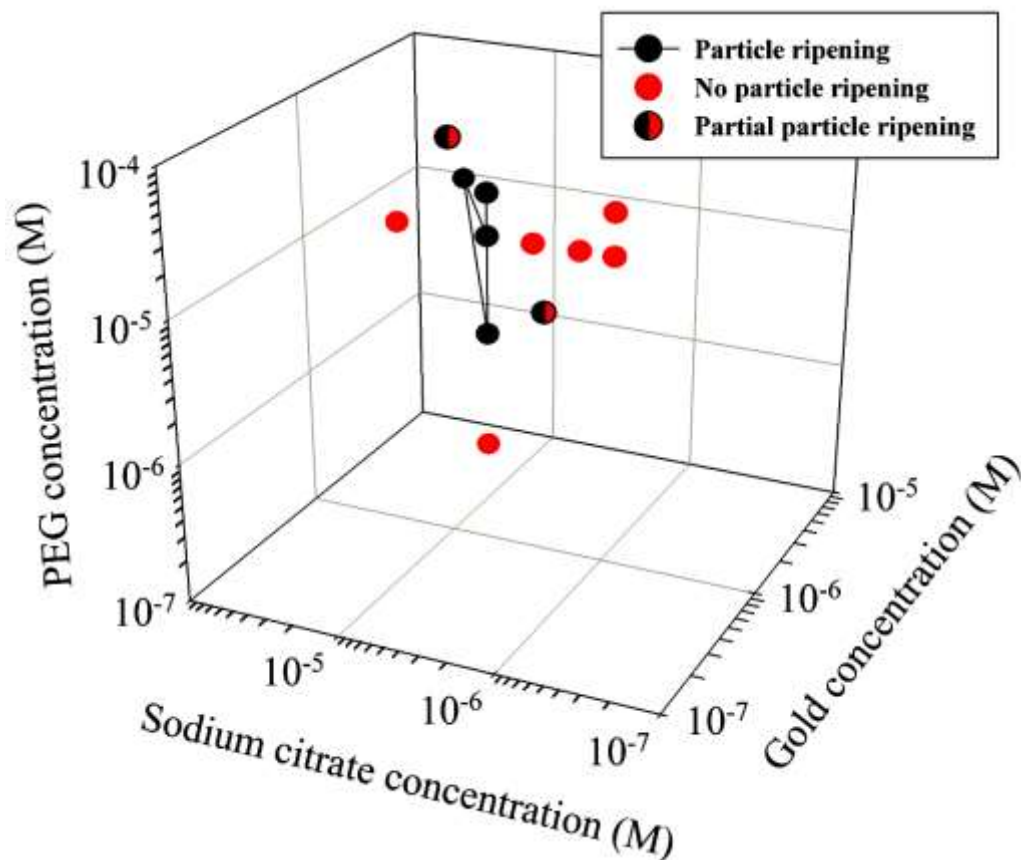


Figure 5.53: Phase space of PEG-thiol, gold, sodium citrate highlighting the regions of particle ripening. The black closed circles are the ones at which particle ripening occurred while the red closed circles are the points correspond to conditions of no evident particle ripening. Couple of experiments marked as points with closed half red and black circles were carried to identify the limits of boundary lines for particle ripening. There were only indications of particle ripening.

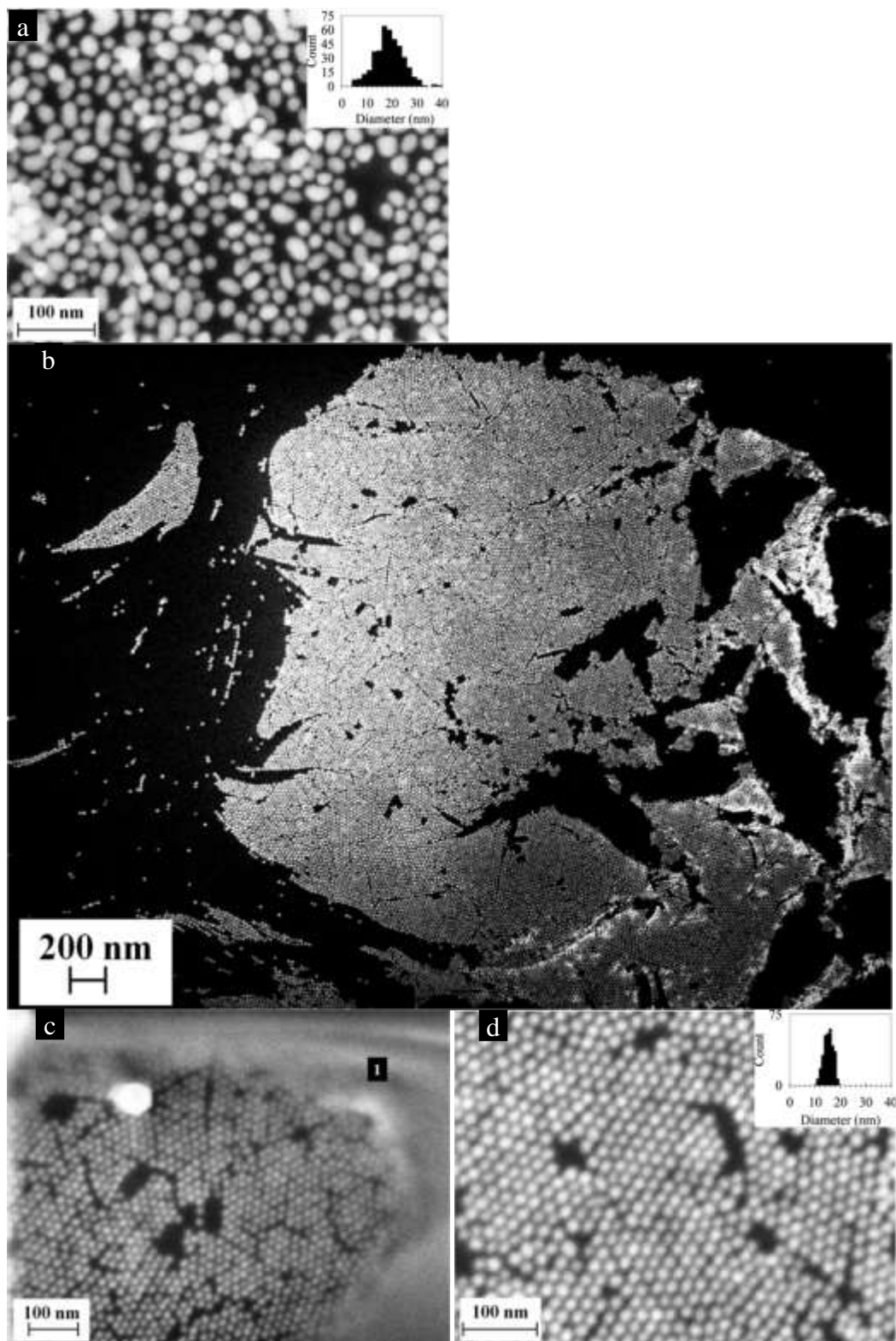


Figure 5.54: Representative FESEM images of gold nanoparticles synthesized using modified sodium acrylate protocol, (a) before and (b-d) after addition of PEG-thiol at different magnifications. The region marked 1 (in c) represent due to the possible presence of organic film. The molar ratio of PEG to gold is 10 and the sample was aged for ~ 18 hours at 25°C .

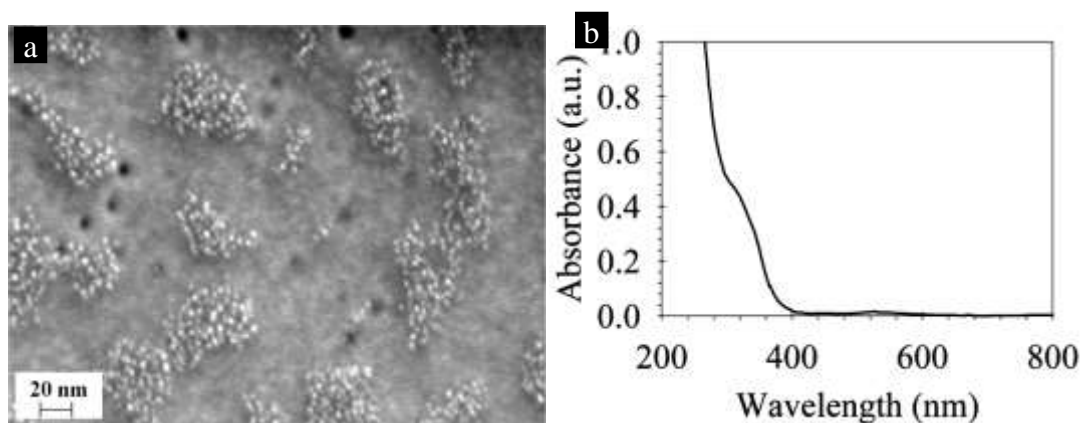


Figure 5.55: (a) Representative FESEM image of gold nanoparticles synthesized using Pechini process with the addition of PEG-thiol molecules (molecular weight: 356 g/mol) a priori. (b) UV-Vis spectra of as-synthesized gold nanoparticles (as shown in a) indicate suppression of the characteristic gold SPR peak at 520 nm, indicating sub-3 nm particles.

In order to test whether all these process are thermodynamically controlled, an additional experiment was conducted where in a mixture of PEG-thiol and sodium citrate (24 mL of water + 1 mL of 1 % sodium citrate + 25 μ L PEG-thiol, molecular weight 356 g/mol) was taken to boiling followed by the addition of gold chloride solution (0.25 mL of 1 % HAuCl₄). The color of the solution remained colorless even after 30 minutes of continued boiling. FESEM image of solution showed the presence of sub-3 nm particles (Fig. 5.55a). UV-Vis spectra also corroborated the presence of sub-3 nm particles as the characteristic Surface Plasmon Resonance (SPR) peak of gold nanoparticle at 520 nm was not prominent. This suggests that thiol group prevents growth of particle. To overcome the issue of thiol binding, PEG molecules without thiol moiety were added instead of PEG-thiol molecules. In this case, the color of the solution turned light blue almost immediately, and turned to wine red after 8 minutes. This is interesting because in the experiment carried out without the addition of PEG molecules, the color of the colloidal solution changed to wine red in less than 2 minutes⁶². More interestingly, the particles are highly polydisperse (Fig. 5.56a-b). However, with ageing of the colloidal solution at 25 °C for 12 hours, the particles become monodisperse with mean size of 12.1 ± 1.8 nm (Fig. 5.56c-f). The same sample aged at 4°C (kept in a refrigerator) does not undergo similar transformation (Fig. 5.56g-h), clearly highlighting the role of temperature.

Halving the gold concentration yielded particles of size 9.0 ± 1.2 nm, while doubling the gold concentration yielded 10.7 ± 1.8 nm. At this juncture, it is difficult to explain the trend of particle size with gold concentration. There could be interplay of both pH and variation of the initial number of nuclei which can cause this variation.

To understand the pH effect, two more experiments were carried out: (1) the gold concentration was increased to 10 times and (2) reduced 10 times of the standard concentration, keeping all other precursor concentration same. With increased gold concentration to 10 times, the FESEM images showed presence of hexagonal plates in addition to large size particles (Fig. 5.57a-b). On the contrary, lowering the gold concentration by 10 times, the size of the particles increased to ~ 30 nm, and the spread of the size distribution was high (Fig. 5.57c-d). With ageing of the colloidal solutions at 25°C, the size of the particles did not alter in both cases. All these experiments suggest that optimum amounts of PEG-citrate-gold (“sweet zone”) are critical to observe size focusing.

In parallel, to understand the role of temperature, an additional experiment was conducted where in a mixture of PEG and sodium citrate (24 mL of water + 1 mL of 1 % sodium citrate + 25 μ L PEG, molecular weight 300 g/mol) was taken to boiling and cooled to room temperature. After 10 minutes, the gold chloride solution (0.25 mL of 1 % HAuCl₄) was added to the above mixture maintained at room temperature and stirred for 30 minutes. The color of the solution remained colorless for few hours and a faint blue color started to appear after 4 hours. The solution color did not change even after ageing the solution for 1 week.

It is well known that acetone dicarboxylic acid is an intermediate in the citrate protocol^{62,251,252} that is responsible for autocatalytically reducing gold ions to metallic form. So, the aforementioned experiment was modified such that instead of sodium citrate, acetone dicarboxylic acid was used to initiate the reduction at room temperature, i.e., gold chloride solution (0.25 mL of 1 % HAuCl₄) was added to a mixture of PEG and sodium citrate (24 mL of water + 0.5 mL of 1 % sodium citrate + 25 μ L PEG-thiol, molecular weight 300 g/mol). The color of the solution turned purple-red in a couple of minutes. The FESEM images showed presence of spherical size particles (~ 30 -200 nm) in addition to nanoplates (Fig. 5.58a-b).

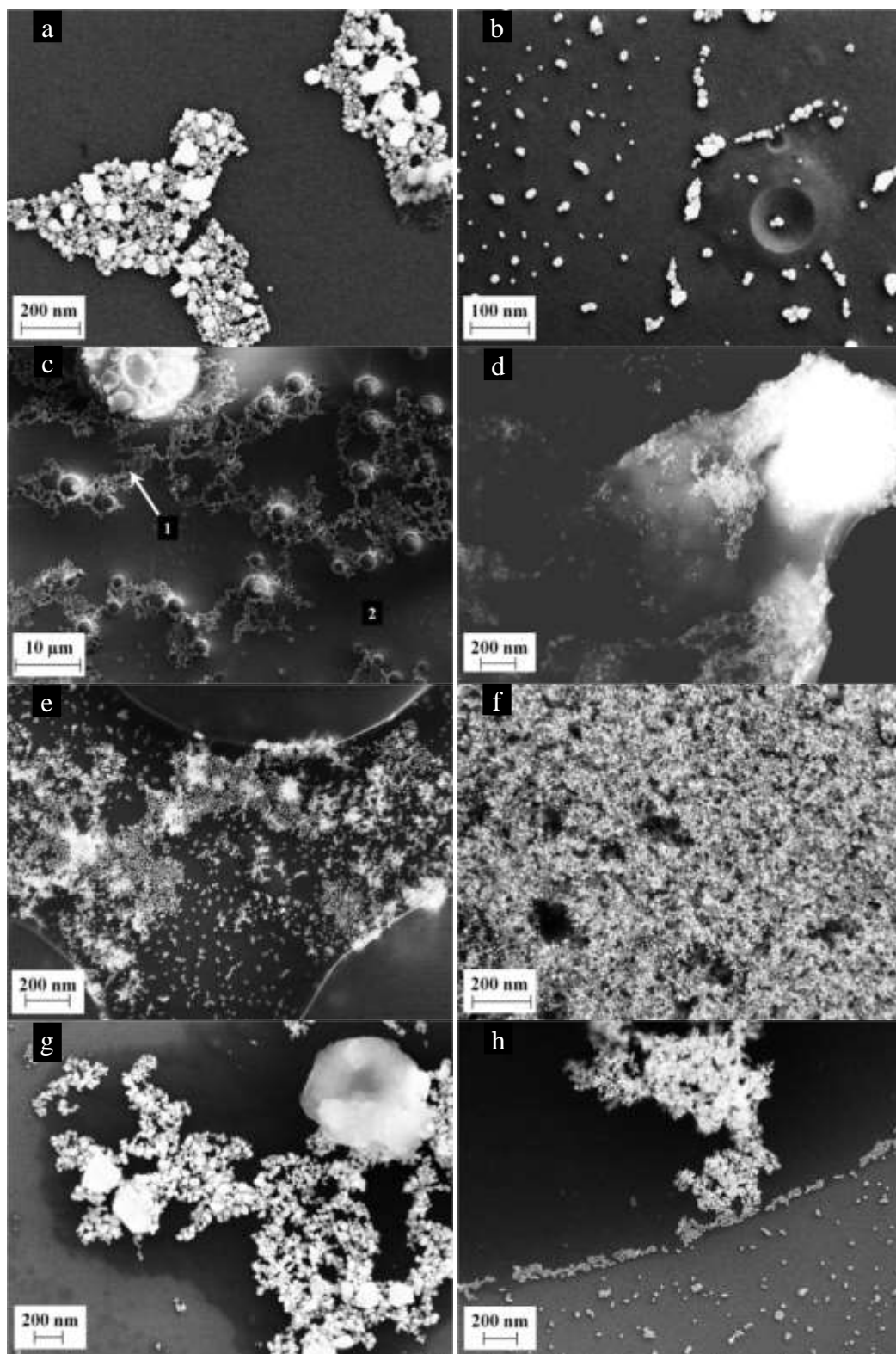


Figure 5.56: Representative FESEM image of gold nanoparticles synthesized using citrate reverse protocol, with the a priori addition of PEG molecules (molecular weight: 300 g/mol); without ageing (a-b), with ageing for 12 hours at 25 °C (c-f), and with ageing for 1 day at 4 °C (g-h). The molar ratio of PEG to gold is 10. The regions marked 1 and 2 in c represent array and bare substrate respectively.

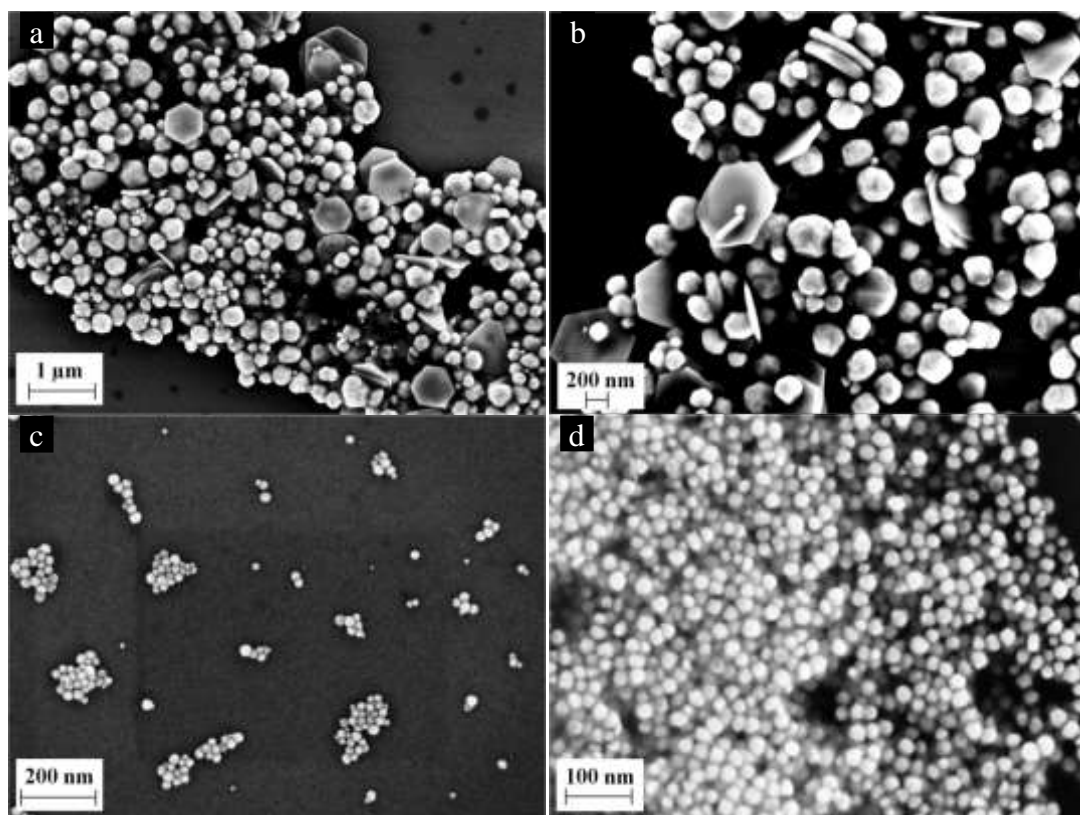


Figure 5.57: Representative FESEM images of gold nanoparticles formed using the standard Pechini process with increasing the gold concentration 10 times (a-b) and decreasing the gold concentration 10 times (c-d) when compared to standard concentration. The molar ratio of PEG to gold is 1 and 100 respectively.

To understand the effect of reverse mode of addition (addition of gold precursor to reducing agent; the standard mode of addition is addition of reducing agent to gold precursor), the above experiment was repeated without any PEG molecules. Interestingly, the concentration of nanoplates increased in the colloidal sample (Fig. 5.58c-d). Earlier, it was shown that pH of the reaction mixture can induce nanoplate formation (Fig. 5.57a-b), and it was found here that the final colloidal solution pH was 4.5. So to overcome the pH effect, the experiment at room temperature using acetone dicarboxylic acid was modified with a priori addition of requisite amounts of sodium hydroxide solution, so as to maintain final pH of 6.5. As surmised, only nanoparticles were found (Fig. 5.58e). The particles were found to be more than 30 nm and the color of the colloidal solution remained purple even after 1 week.

Very recently, Muhammed and co-workers have observed size focusing of polydisperse silver nanoparticles by using reducing agent and excess ligands made of poly (ethylene glycol) appended with lipoic acid at one end and a reactive (-COOH/NH₂) or inert (-OCH₃) functional group at the other end. The authors have hypothesized that the free thiols in solution can etch the nanoparticles, progressively leading to nanoclusters. In parallel, Shiers and co-workers have also reported thiolate driven etching of silver nanoparticles. The authors have reported tiopronin (C₅H₉NO₃S, carboxylic acid and thiol containing biomolecule) as ligand which has been found to form Ag(I)-tiopronin polymer chains arranged into layers. Also, Shiers et al. have reported that these layers form into 2D polymeric nanosheets which can engulf polydisperse nanoparticles and transform them into monodisperse nanoparticles. In the current study, it is surmised similar phenomenon could be occurring where in PEG and sodium citrate form a complex, which can transform polydisperse gold nanoparticles into monodisperse nanoparticles.

To study the feasibility of the formation of an organic complex between PEG and citrate, an additional experiment was conducted wherein aqueous solution of PEG and sodium citrate was heated to boiling for 30 minutes, cooled to room temperature and then drop-cast on silicon substrate. Polymeric nanostructures were observed (Fig. 5.59a-b). Electron beam was found to damage these nanostructures, while focusing in FESEM. All these evidences suggest particle ripening due to PEG-citrate complexation.

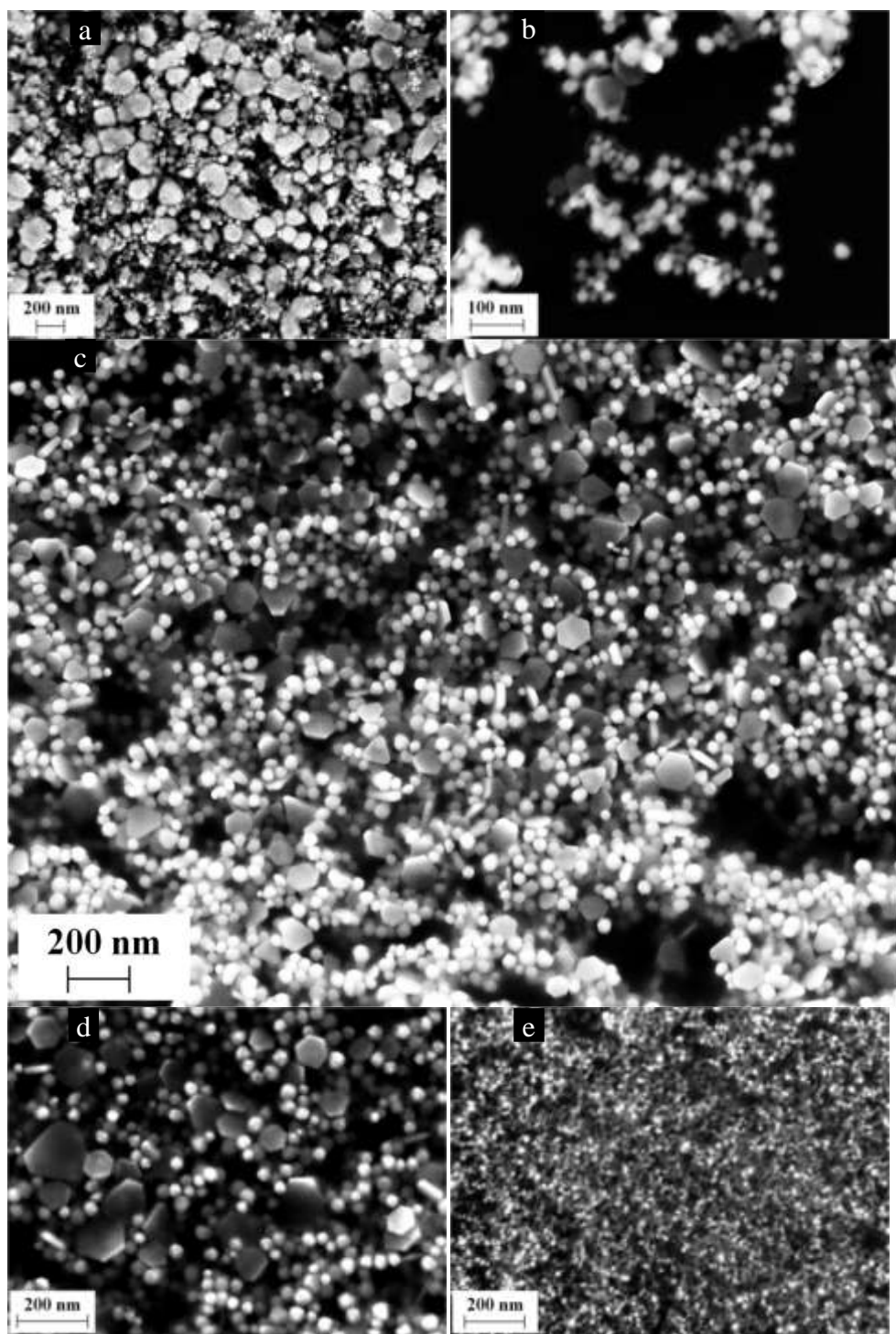


Figure 5.58: (a-b) Representative FESEM image of gold nanoparticles synthesized using acetone dicarboxylic acid and PEG molecules (molecular weight: 300 g/mol). Both nanoparticles and nanoplates were observed. (c-d) Representative FESEM images of gold nanoparticles synthesized using acetone dicarboxylic acid alone. The concentration of nanoplates increased without the addition of PEG molecules. (e) Representative FESEM images of gold nanoparticles synthesized using acetone dicarboxylic acid and PEG molecules (with final pH modified to 6.5 using sodium hydroxide solution a priori). The molar ratio of PEG to gold was maintained at 10.

Network of polymeric pseudocrown ethers (cyclic polyethers with the repeating unit of $(-\text{CH}_2-\text{CH}_2-\text{O}-)_n$, $n > 2$) can be formed by photopolymerization of poly(ethylene glycol) diacrylate (PEGDA)/metal complexes. Crown ethers are also formed by linking PEGDA monomers with metal ions through the ether oxygen complexation resulting in bridging acrylate groups. This eventually increases the possibility of cyclopolymerization which can result in a cross-linked network with crown ether structures. The process, suggested by Elliot and co-workers, is schematically illustrated in Fig. 5.60a. The mesh size of crown ethers is found to be controlled through molecular weight of polymers, cross-linking agent etc. Also, ethylene glycol-citrate complexes through chelation of metal-carboxylate-ethylene oxide (in the PEG backbone) have been reported to form chain networks. It is surmised that the formation of thin sheets or complex 3D networks of PEG-citrate-gold to be the plausible structure which can aid in particle ripening as shown in Fig. 5.60b. However, the exact details of this size transformation process could not be unveiled.

To test the generality of the “Pechini-type” process for forming monodisperse metal nanoparticles, the process was carried out using silver salt instead of gold salt. Surprisingly, in addition to spherical particles, significant fraction of silver nanorods was observed (Fig. 5.61a-c). More interestingly, the size of some of the nanorods exceeded a length of $2\ \mu\text{m}$ (Fig. 5.61d). UV-Vis spectrum shows a small hump near $280\ \text{nm}$ (Fig. 5.61e), which is characteristic of silver nanorods. To verify whether the formation of nanorod is due to the reverse addition of precursor solution or presence of PEG molecules, an additional experiment was conducted wherein the process was repeated without the addition of PEG molecules. Silver nanorods were observed in this case as well, but not with similar density or aspect ratio (Fig. 5.61f). UV-Vis spectra also corroborated the FESEM result (Fig. 5.61e).

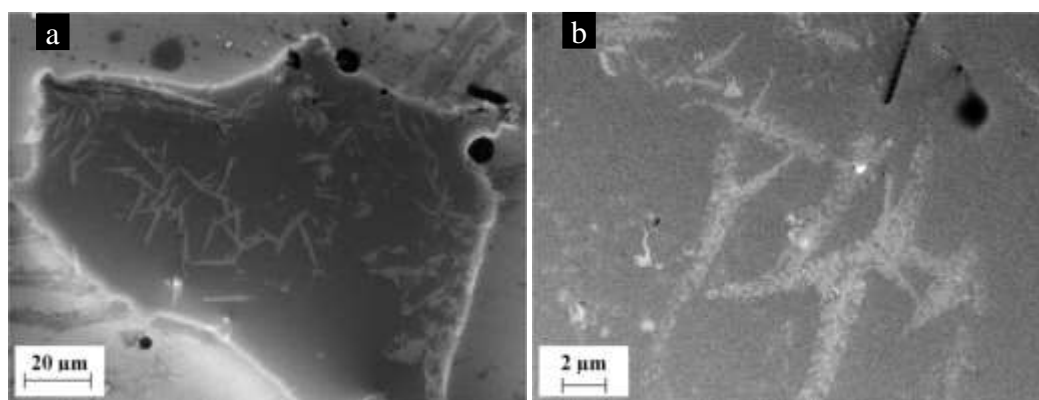
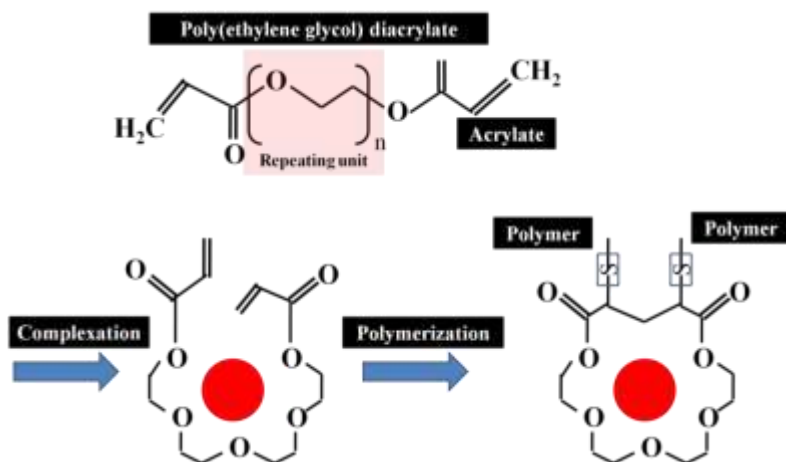


Figure 5.59: (a-b) Representative FESEM images of boiled aqueous mixture of PEG and sodium citrate drop-casted on silicon substrate.

a



b

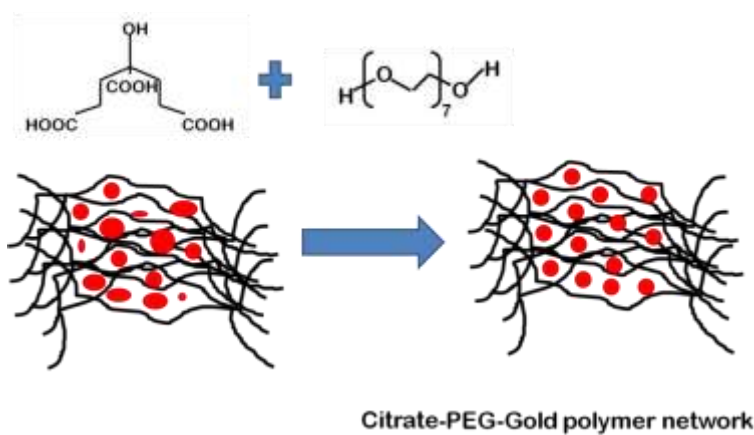
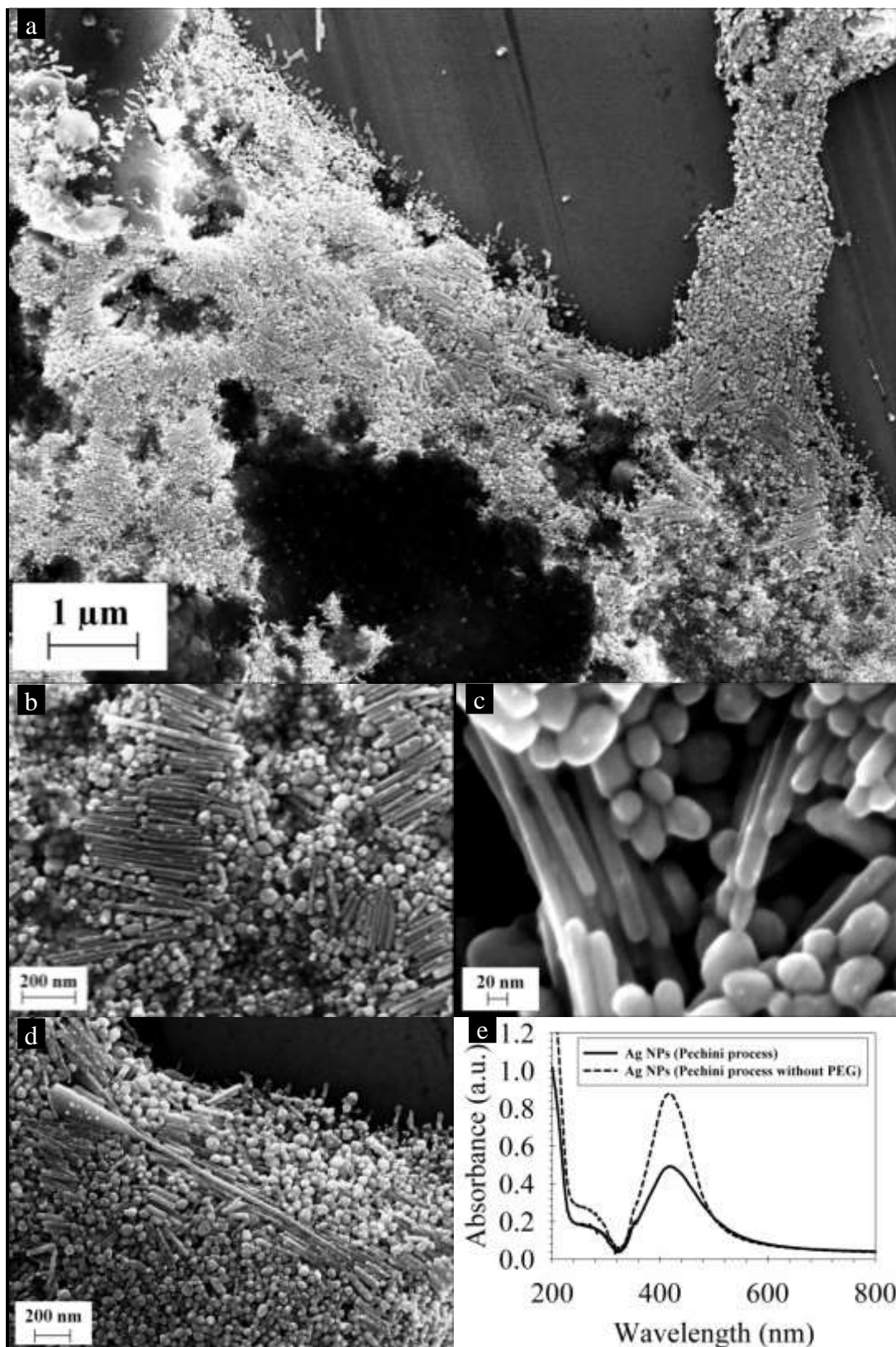


Figure 5.60: (a) Schematic of formation of pseudocrown ether of poly(ethylene glycol) diacrylate (PEGDA)/metal complexes
 (b) Schematic of formation of 3D complex network of citrate and PEG, through chelation of metal nanoparticle or metal ions.



f

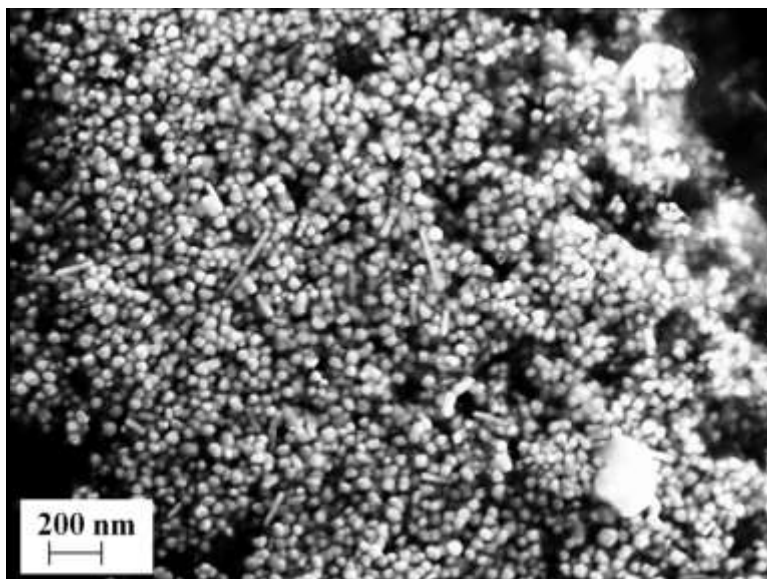


Figure 5.61: (a-d) Representative FESEM images of silver nanoparticles and nanorods prepared through standard Pechini process. (e) UV-Vis spectra of as-synthesized silver nanocolloid; shoulder at ~ 280 nm indicates the presence of silver nanorods in solution. (f) Representative FESEM image of silver nanorods prepared through Pechini process, without the addition of PEG molecules. The molar ratio of PEG to silver is 10.

9.1a.5.17 Thermal stability of PEG capped gold nanoparticles

When the PEG-thiol coated gold nanoparticles (derived from citrate, molar ratio of PEG to gold is 10) were heated to boiling, the color of the colloidal solution turned blue after heating. More remarkably, when the colloidal solution was cooled to room temperature, the color of the solution reverted to red color (Fig. 5.64). This color transition can be exploited for miniaturized sensing applications. More interestingly, this phenomena was observed even after multiple heating-cooling cycles (7 cycles were conducted). Couple of reasons can be envisaged for the color transformation due to the thermal cycling, (1) change in particle size and shape and (2) dipolar coupling due to the reduction in interparticle spacing between the particles. As discussed in Section 5.4, it is believed the color transition is to do more with morphological change of particles in this case. On the contrary, when the thermal cycling experiments were repeated with PEG-thiol coated gold nanoparticles derived from tannic acid molecules (monodisperse particles of size 7 nm, and molar ratio of PEG to gold is 10), nanopouches were observed (Fig. 5.65a-c). This can be attributed to the possible reaction of tannic acid with PEG molecules.

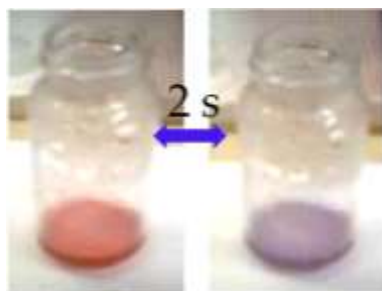


Figure 5.62: Digital photograph demonstrating reversible transformation of red to blue colour of the PEG-thiol coated gold nanoparticle solution, with temperature.

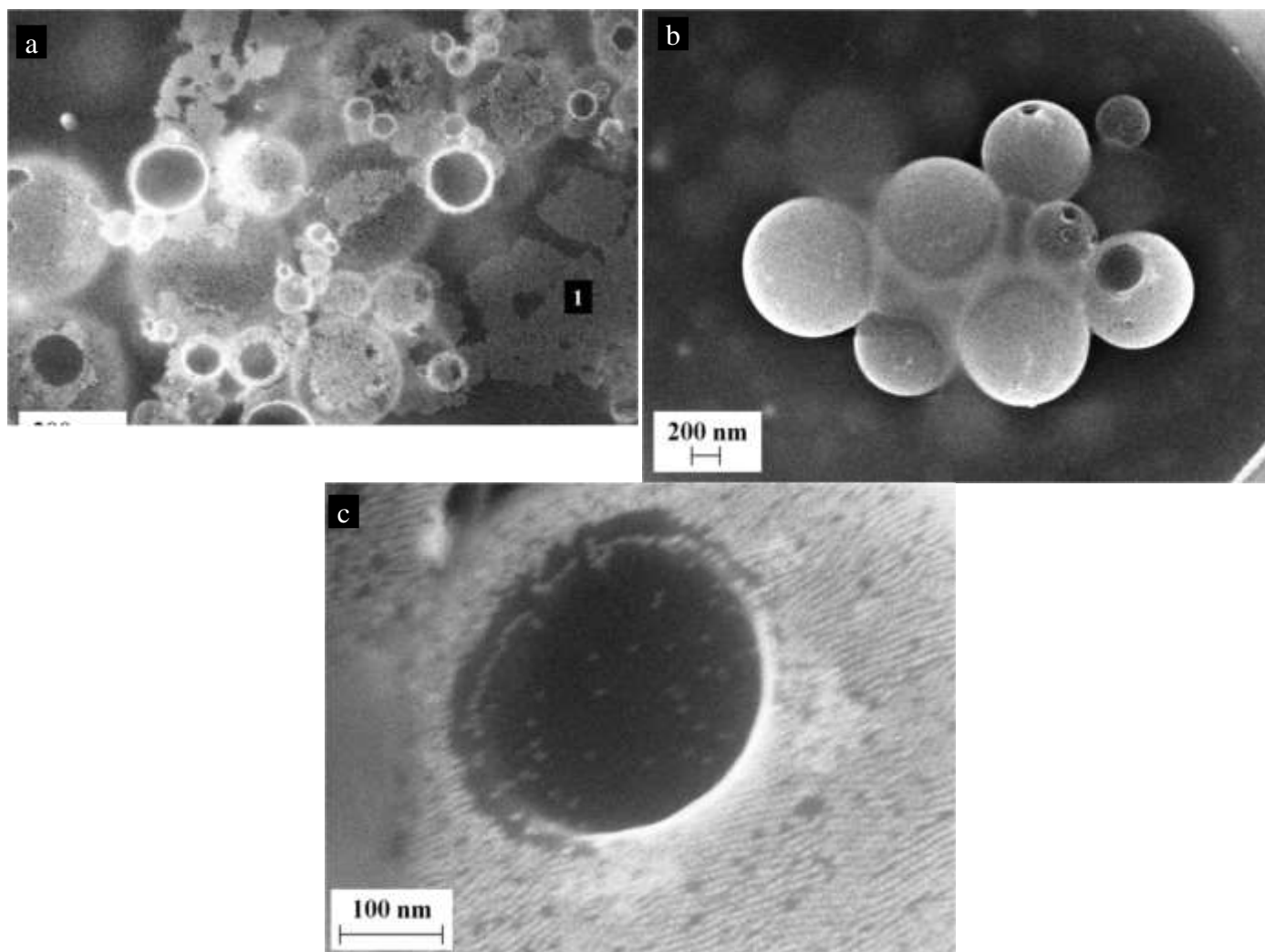


Figure 5.63: (a-c) Representative FESEM images after thermal cycling of PEG-thiol coated gold nanoparticles derived from tannic acid capped gold nanoparticles. The formation of nanopouches can be attributed to the possible side reaction of tannic acid with PEG molecules.

9.1a.6 Conclusions

A systematic investigation of various process involved in the synthesis was performed. As the result of detailed study, a new protocol was developed for the room temperature synthesis of gold and silver nanoparticles. A modified citrate reduction method, capable of synthesizing nanoparticles in size range 5 - 10 nm, was developed.

Tannic acid has been used as a reducing and stabilising agent to synthesize silver nanoparticles on a timescale of seconds through a simple, green, room temperature protocol. Tannic acid has been previously utilized as a reducing agent in the presence of additional stabilizers¹⁹ or as both the reducing and stabilizing agent; but the reaction times reported are 2 hours at room temperature and 30 minutes at 80°C, while the particle sizes reported are >15 nm. The crucial difference between the present study and the earlier reports is that the pH of the tannic acid solution was adjusted prior to the addition of metal salt. The alkaline pH environment enhanced the reducing and stabilizing capability of tannic acid allowing room temperature synthesis of silver nanoparticles in seconds, while also enabling variation of the mean size from 3 to 22 nm. The increase in particle size with increasing molar ratio of tannic acid to silver nitrate indicates a third role for tannic acid as an organiser for facilitating nucleation. This concept of using tannic acid at alkaline pH as a reducing, organising, and stabilising agent is easily extendable to other elements that are known to chelate with the tannic acid.

The tannic acid reduction method was extended to synthesize gold nanoparticles. Unlike silver nitrate, chloroauric acid possesses pH dependent form and reactivity. The pH of precursor solutions, mode of contacting, and the dynamics of stabilizer adsorption vis-à-vis Brownian collision frequency are shown to be critical for tuning nanoparticle formation, growth, and coalescence. The competition between the change in speciation of chloroauric acid and the reaction with

tannic controls the diameter of nanoparticles. The initial pH of chloroauric acid must be acidic but the reaction mixture pH must be greater than 7 for fast reduction and good stabilization. Various mode of mixing reactants was investigated. The slower addition of chloroauric acid solution into tannic acid resulted in reduced polydispersity as compared to faster addition protocols. The slow (dropwise) addition protocol was utilized to synthesize size-controlled gold nanoparticles in the range of 2-10 nm within minutes at room temperature. The optimal process is shown to be similar to a one-shot nucleation-seeded growth technique and the growth mechanism is identified to be surface-reaction controlled under these conditions. These insights on independently manipulating reactivity and stabilization can be extended to other redox reactions for rapidly synthesizing size-controlled metal nanoparticles, as most systems exhibit pH dependent reactivity and stabilization.

The effect of molar ratio of citrate to chloroauric acid and pH on the synthesis of nanoparticles was investigated. At pH 6.7, the change in the molar ratio from 0.5 to 20.8 results in size variation of 32 nm to 16 nm and the size variation is less compared to that obtained by classical citrate reduction protocol. In the synthesis of gold nanoparticles by citrate reduction, the reactivity of reactants and stabilization of nanoparticles are pH dependent. The faster reduction of chloroauric acid at reaction mixture pH of 4.7 is accompanied by poor stabilization of nanoparticles and hence results in bigger nanoparticles. The presence of an additional stabilizer during fast reduction the size of nanoparticles synthesized reduced the particle size to 6.1 nm. By altering the mode of addition, i.e. adding chloroauric acid into citrate rather than citrate into chloroauric acid, the initial pH of chloroauric acid was decreased and the reduction was faster resulting in smaller nanoparticles. By changing concentration of chloroauric acid and citrate, nanoparticles from size range 5 nm to 15 nm (coefficient of variation – 10%) were synthesized. A confluence of conditions conducive to nucleation and effective stabilization, resulting from the change in order of addition, is the reason behind this effect. The concentration of reactive chloroauric acid species is the critical factor controlling the oxidation of citrate to form acetone dicarboxylic acid, which facilitates nucleation. The process exhibits a ‘memory’ of the order of addition, even when the timescale of mixing is much faster than the timescale of particle formation.

A simple process for generating monodispersed metal nanoparticles in aqueous phase was developed. A systematic study was conducted in order to understand the role of excess ligand in enabling size focusing. PEG-carboxylate interaction is found to be critical for observing particle ripening. Also, the presence of thiol moiety was not critical for the phenomena to be observed. Finally, as a proof of concept, PEG-thiol coated gold nanoparticles were drop-cast on PDMS, which enables transfer of arrays to any desired substrate.

9.1b Modelling studies of batch protocols

9.2 Development of robust continuous processes for nanoparticle synthesis:-

A primary objective of our project was to synthesize sub-10 nm metal nanoparticles in a continuous fashion using aqueous-phase processes. Based on our understanding of the tannic acid process, we designed both microchannel reactors as well as macro-scale reactors to synthesize nanoparticles, and understand the effect of flow parameters on particle size distribution.

9.2.1 Microchannel reactors

Controlled mixing of precursors can be accomplished through diffusion by reducing dimensions of microreactors. Fouling is one of the main disadvantages of micro reactors, which hinders the scale-up of synthesis process. It can be overcome by either modifying the walls of the reactors or developing new designs. In the present study, we have developed a 3-D coaxial flow microreactor (CFMR) to avoid the particle deposition.

9.2.1.1 Fabrication of CFMR using capillary/glass tubes

Polymer and glass capillary tubes were used as material for fabricating CFMR and the reactor set up consists of two concentric tubes; namely inner tube (50 μm ID, 360 μm OD, PFA tube) and outer tube (2.4 mm ID, 4 mm OD, glass tube). Micropipette tips were used for precise centering of PFA tube in outer tube (Fig 6.1). Inlet port for the outer fluid was designed such that it was perpendicular to the main flow direction (Fig 6.1). COMSOL multi physics software was used to perform numerical simulations of Navier-Stokes equation to determine ratio of volumetric flow rates between inner and outer flows required in order to maintain fully developed coaxial laminar flow. Simulation results showed that outer fluid flow rates should always be greater than ten times of inner fluid flow rates to maintain inner fluid core diameter as thin as possible.

Initially, Flow visualization experiments were conducted with dye and water maintaining a flow rate ratio of 1:12 (Inner: Outer) at a total volumetric flow rate of 39 mL/h in CFMR. Homemade syringe pumps were used for pumping liquids through inlets of the reactor. Initially, the flow was observed to be coaxial in nature. After some time, a shifting of dye stream from the point of confluence and oscillations at the point of confluence were recorded (Fig 6.2). The plausible reason for this behavior may be instabilities related to the tangential velocity component of the fluid fed in the inlet for outer fluid flow.

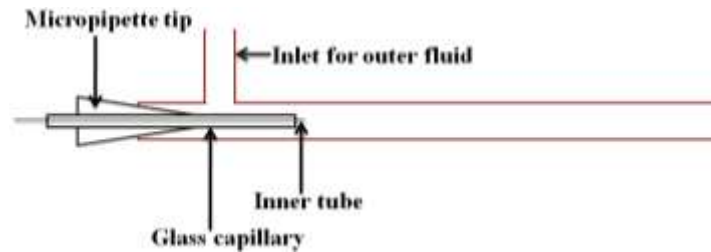


Figure 6.1: Schematic showing CFMR-I fabricated using a PFA capillary as an inner tube and glass tube as the outer tube. Set up consists of three fluidic ports; two of them were inlets for inner and outer fluid, while another one was for the outlet.

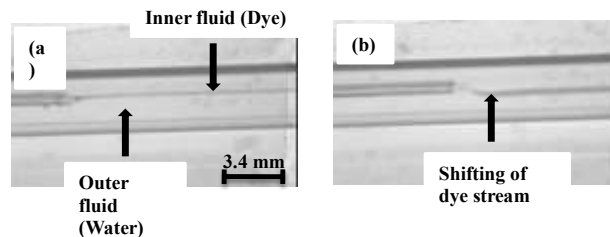


Figure 6.2: Digital micrographs of flow visualization experiments conducted in CFMR-I (a) at $t = 0$ (b) $t = 5$ min. Displacement of dye stream from point of confluence was observed after a certain time possibly, due to instabilities associated with outer tube fluid.

To avoid this, the inlet of outer fluid was modified by providing a bulb (25 mm diameter) between inlet of outer fluid and outer glass tube (Fig 6.3). Flow visualization experiments carried out in CFMR-II again at same operating conditions mentioned earlier. Surprisingly, same kind of flow behavior (oscillations) was observed and even a change in operating conditions (0.6 mL/h for inner fluid and 36 mL/h for outer fluid) did not result in a change of the observed phenomena. We surmised that oscillations of syringe pumps may be responsible for this observed behavior. Gravity flow to CFMR rather than syringe pumps was employed to pump the liquids in further experiments. The inner diameter of inner tube was increased from 50 μm to 400 μm in order to track the disturbances easily. Oscillations were again observed at the point confluence. This observation clearly confirmed that, this behavior is due to external vibrations and not because of syringe pumps. To avoid this noise, all further experiments were carried out in a relatively quiet corner of Lab 2 and visualization experiments (Fig 6.4) confirmed the steady nature of flow.

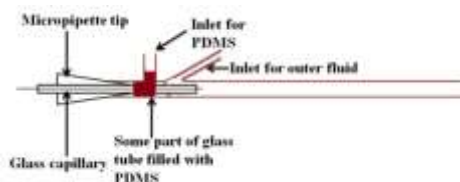


Figure 6.3: Schematic diagram of CFMR-II. Conical shape of micropipette tip allows for the precise centering of inner tube in outer tube. Additionally, embedding the micro pipette tip in PDMS enhanced its mechanical strength. The Inlet of outer fluid was modified by providing a bulb (25 mm diameter) between inlet of outer fluid and outer glass tube in order to enable proper converging flow through outer tube.

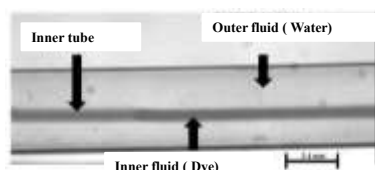


Figure 6.4: Snapshot of dye flowing in CFMR-II. Dye stream flowed steadily through the inner tube without any oscillations. Inner diameter of inner tube is around 400 μm , flow rates were used 3 mL/h for inner fluid and 36 mL/h for outer fluid.

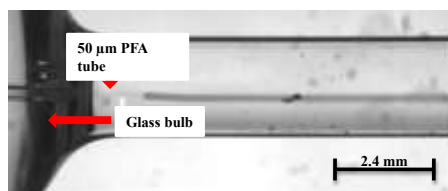


Figure 6.5: Snapshot of CFMR-Design 2 at the entrance. Co axial flow was maintaining up to certain length in CFMR.



Figure 6.6: Flow visualization experiments in CFMR-Design 2. Coaxial flow maintained up to certain distance only. Dye is expected to flow in center but it flows like a jet to the bottom (due to inaccurate centering of inner tube).

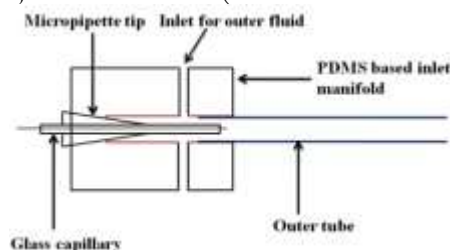


Figure 6.7: Schematic diagram PDMS module-CFMR.

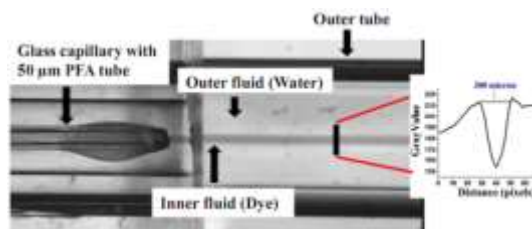


Figure 6.8: Snapshot of flow visualization experiment in coaxial flow microreactor. The inset shows the grayscale profile ($1\ \mu\text{m} = 0.06\ \text{pixels}$) along the black line shown in Fig 4.8.

Another important aspect of the fabrication process was the need for precise centering of the inner tube. Fig 6.5 and 6.6 shows that the inner flow behaves like a jet and hit the bottom of the capillary tube, if it is not properly centered. To avoid this issue, a polydimethylsiloxane (PDMS) based inlet manifold (Fig 6.7, See appendix A.2 for details) was designed to allow precise centering of the inner tube and provide sufficient mechanical strength. Figure 6.8 shows that the flow is now coaxial as expected. The width of inner flow (dye appears as black) was measured using the grey scale profile (Fig 3.8 inset) along the line shown in Fig 6.8 and compared to the value expected based on coaxial laminar flow, neglecting diffusion. The measured width was $300\ \mu\text{m}$, while the calculated value was $200\ \mu\text{m}$. This discrepancy is attributed to inevitable errors associated with the imaging and image analysis processes. We note that the inner core diameter is the relevant diffusion length scale in our reactor.

9.2.1.2 Gold nanoparticle synthesis

Synthesis of gold nanoparticles was carried out in CFMR-III (PDMS inlet manifold) by using tannic acid protocol at room temperature. Aqueous chloroauric acid ($0.6\ \text{mL/h}$) at a concentration of $0.25\ \text{mM}$ was fed through inner tube, while reducing agent (tannic acid) at a concentration of $0.09\ \text{mM}$ was fed ($36\ \text{mL/h}$) through outer tube in this reactor. Initially, tannic acid fills the entire tube, while gold chloride is separated from the contents of the outer tube by a small plug of water, pumped just prior to injection of chloroauric acid. The reaction between two reactants results in formation of gold nanoparticles. Overall molar ratio of tannic acid to gold salt (based on final collected volume) was maintained at 2.08 in CFMR, similar to the batch process to compare the results. Gold nanoparticles were collected in petri dish at different time intervals to examine the dynamics of the reactor. Visible spectra (Fig 6.9) showed the presence of gold nanoparticles exhibiting surface plasmon resonance at $528\ \text{nm}$.

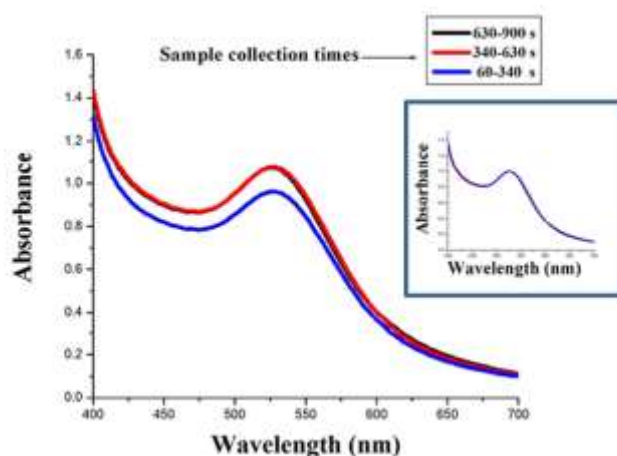


Figure 6.9: Visible spectra of gold nanoparticles synthesized in CFMR. Gold nanoparticles samples were collected to check the dynamics of the reactor. Coincidence of normalized visible (as shown in inset) spectra of gold nanoparticle samples confirms the steady state nature of the process.

Visible spectrum of gold colloid is identical for samples collected between $630\text{--}900\ \text{s}$ and $340\text{--}630\ \text{s}$. Visible spectrum of gold colloid sample collected between $60\text{--}340\ \text{s}$ has lower absorbance than the other samples; the reason for this behavior is possible dilution of gold nanoparticles with excess tannic acid during the startup phase. The normalized plots shown in the inset confirms the steady state nature of the process. We note that this is the first report of steady state continuous flow synthesis of gold nanoparticles. Tannic acid charge stabilized gold nanoparticles are difficult to image with FESEM (Field emission scanning electron microscopy) because of organic contamination. It is necessary to stabilize gold nanoparticles with alkane thiol and to transfer to organic phase. $5\ \text{mL}$ of the product gold nanoparticles, $5\ \text{mL}$ of ethanol

and 1 μL of dodecanethiol were mixed in a centrifugal tube and centrifuged for 30 min to obtain a precipitate after two hours. Ethanol was used to wash this precipitate to remove excess surfactants and then it was allowed to dry overnight in the laminar hood. The dried thiol-capped gold nanoparticles were redispersed in 0.5 mL chloroform. 2 μL of this concentrated gold nanoparticle sample was placed on a cleaned silicon wafer piece for analysis under FESEM. A further experiment was carried out at a chloroauric acid concentration of 0.05 mM (MR-10.4) to understand the role of concentration of precursors. Figure 6.10 shows that steady state is achieved for these conditions also. To compare these results with batch reactors, two controlled experiments were carried out in batch reactors with and without mechanical agitation. We expect the batch process (without agitation) in which a jet of chloroauric acid is injected into a stationary pool of tannic acid to mimic the mixing present in the continuous flow reactor. Overall molar ratio and volume of reactants were maintained same as CFMR for direct comparison.

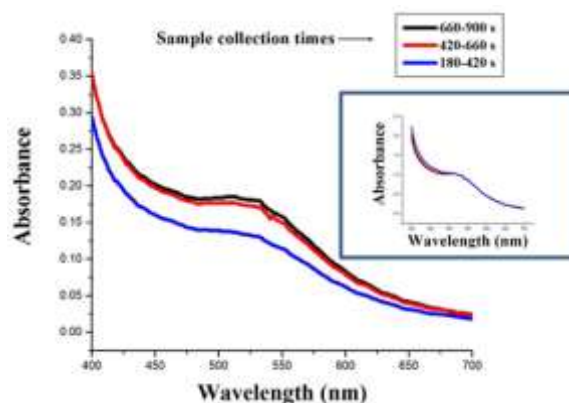


Figure 6.10: Visible spectra of gold nanoparticles synthesized in CFMR (MR 10.4). Gold nanoparticles samples were collected at different time intervals to verify the dynamics of the process. Coincidence of normalized plots confirms the steady state nature of the process (inset).

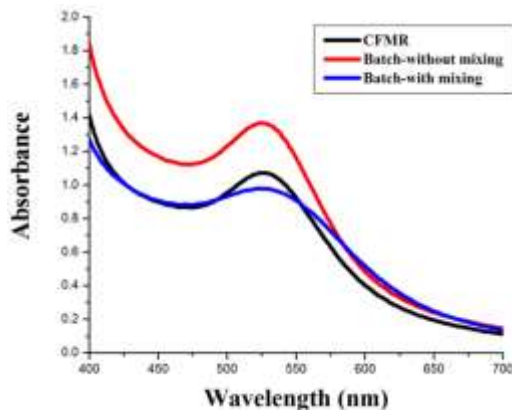


Figure 6.11: Visible spectra of gold nanoparticles synthesized through different contact modes namely CFMR, batch without agitation and batch with agitation for comparison at MR 2.08. Difference in visible spectrum clearly indicates that difference in gold nanoparticles size distribution.

Distinctive difference in UV-Vis spectra for different contact modes confirms that variation in mean size (Fig 6.11). Size distribution of nanoparticles synthesized in CFMR, batch-with agitation and batch-without agitation were found to be 10.2 ± 4 nm, 10.4 ± 3.8 nm and 6.5 ± 1.5 nm (Fig 3.12) at MR 2.08 and 5 ± 1.5 nm, 5.8 ± 1.9 nm and 4.8 ± 1.7 nm (Fig 6.13) at MR 10.4. These results are summarized in Table 6.1.

Gold nanoparticles were synthesized at two different molar ratios. Triangular nanoparticles and wide size distribution was observed when chloroauric acid concentration 0.25 mM. The plausible reason for this behavior is that nanoclusters, which are produced near the contact region, can diffuse either in basic medium or acidic medium. Decomposition of unreacted chloroauric acid results into formation of chloride (Cl^-) ions and they can etch the surface of gold nanoclusters, which are growing in acidic medium leading to formation of triangular nanoparticles³⁹ (Fig 6.14). The spherical shape of nanoparticles observed when gold concentration was 0.05 mM to support this hypothesis.

The particle size distribution results (table 6.1) indicate that bulk mixing plays an important role at higher chloroauric acid concentrations (and low MR values) and that mean size and distribution can be controlled by changing the precursor concentrations. From a production stand point, the processing rates were in the range of 1-10 mg/h of gold, which is comparable to those reported in the literature. During the preliminary experiments, the overall flow rates were constrained due to the flexible nature of PFA (inner tube). So, a further modification was made in the fabrication process, wherein silica capillary tube was used for inner tube in conjunction with a PDMS input manifold and tube for the outer flow. These experiments are discussed in the next chapter.

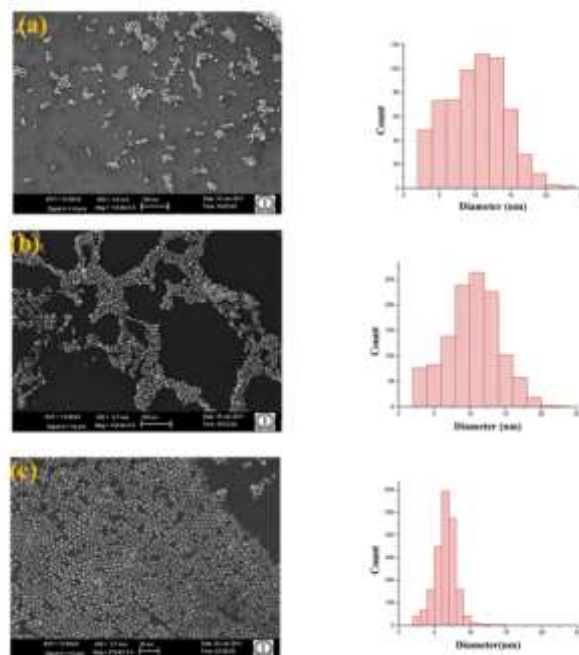


Figure 6.12: Representative FESEM images of gold nanoparticles synthesized through different contact modes (Left) and size distribution histogram of nanoparticles obtained using Clemex@ software (right). (a) CFMR, Nanoparticle diameter 10.2 ± 4.2 nm. (b) batch-without agitation, Nanoparticle diameter 10.4 ± 3.8 nm. (c) batch-with agitation, Nanoparticle diameter 6.5 ± 1.5 nm. pH of chloroauric acid was 1.4 and pH of tannic acid solution used was 7.1 in all these experiments.

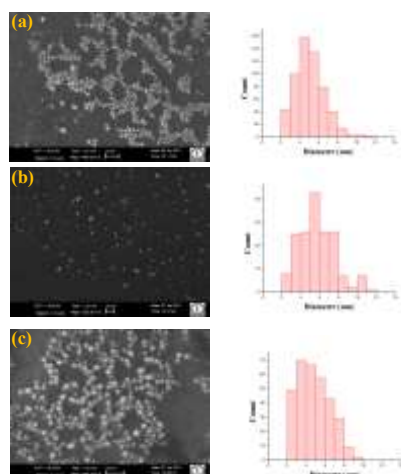


Figure 6.13: Representative FESEM images of gold nanoparticles synthesized through different contact modes at molar ratio (tannic acid/chloroauric acid) 10.4 (Left) and corresponding size distribution histogram of nanoparticles obtained using Clemex software (right). (a) CFMR, Nanoparticle diameter 5 ± 1.5 nm. (b) batch-without agitation, Nanoparticle diameter 5.8 ± 1.9 nm. (c) batch-with agitation, Nanoparticle diameter 4.8 ± 1.7 nm. pH of chloroauric acid at 2.5 and pH of tannic acid at 7.1 maintained in all these experiments.

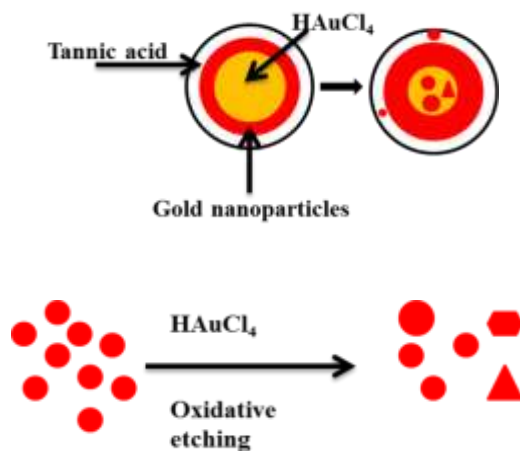


Figure 6.14: Schematic illustrating the reason for triangular nanoparticles when chloroauric acid concentration 0.25 mM (MR-2.08). (a) Nanoclusters, which are formed during initial stage, can diffuse either into acidic or basic medium and nanoparticles which are in basic medium are better stabilize by tannic acid. (b) Oxidative etching gold nanoclusters by chloride ions leads into formation of triangular nanoparticles.

Table 6.1: Size distribution of gold NPs synthesized in CFMR at two different molar ratios

Molar ratio	Contact mode	Size distribution (nm)	Coefficient of variance (COV)	Remarks
2.08	CFMR	10.2 ± 4.2	41%	Triangular nanoparticles (few)
	Batch-with agitation	6.5 ± 1.5	23%	
	Batch-without agitation	10.4 ± 3.8	37%	Triangular nanoparticles (few)
10.4	CFMR	5.0 ± 1.5	33%	
	Batch-with mixing	4.8 ± 1.7	35%	
	Batch-without mixing	5.8 ± 1.9	30%	

9.2.1.3 PDMS based coaxial flow microreactor

Polydimethylsiloxane (PDMS) is soft and flexible polymer widely used for fabricating microchannels. Fabrication of microchannels with PDMS has received wide attention due to their optical properties, ease of bonding, good thermal and oxidative stability etc. Soft lithography based on the PDMS is one of the emerging cost effective technologies for micro fabrication. A rapid PDMS microchannel fabrication method was developed by molding PDMS around nylon threads.

Different diameters of microchannels were fabricated by glass rods with different diameters and needles with various sizes as a channel molds (Fig 6.15). Glass rods (needles) were kept between the two rigid supports in microchannel mold. Bubble free PDMS, which is the mixture of SYLGARD 184 silicone elastomer base and curing agent (10:1 by weight), was poured in the microchannel mould. It was then kept in an oven for curing at 60°C for four hours. After curing, Hexane and heptane were used to swell the PDMS cross linked network to remove the glass rod or needle from it. PDMS block was allowed to deswell in ethanol and followed by five hours of continuous heating in oven at 60°C to evaporate ethanol and heptane solvents from it.

Coaxial flow microreactor consists of two concentric tubes namely inner and outer tube (Fig 6.16) and the mixing of two miscible fluids performed through diffusion. Outer tube with 1.1 mm ID was fabricated by molding PDMS around 1.1 mm glass rod. Inner tube with 150 μm ID and 360 μm OD is made out of fused silica was inserted in the center using two concentric micro pipette tips, which are attached to the outer capillary. Flow visualization experiments (Fig 6.17) were carried out to visualize flow patterns in CFMR with dye as inner fluid and water as outer fluid. Volumetric flow rates of outer and inner tube maintained at 60:1, 30:1, 12:1 ratios in these experiments.

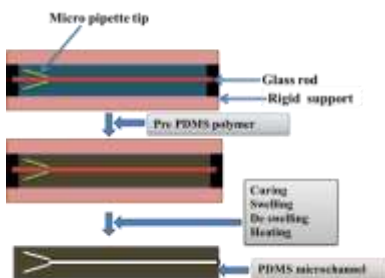


Figure 6.15: Schematic illustrating the procedure for fabrication of microchannel through PDMS as a material. Glass plate (3 cm width and 20 cm length) was used as a rigid support and two glass plates with 1cm width, 1.5 cm thickness and 20 cm length kept apart with distance of 1 cm on the top of it to create space to hold desired molded shape. Pre polymer liquid was poured around a glass rod; curing, swelling, de swelling and heating is the next steps to fabricate microchannel with 1mm diameter.

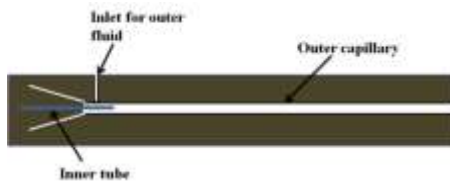


Figure 6.16: Schematic showing the PDMS based coaxial flow microreactor.

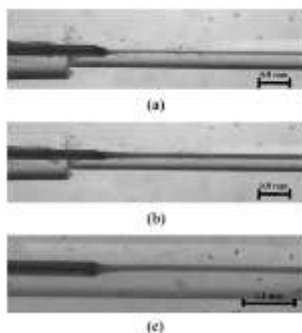


Figure 6.17: Snapshots of flow visualization experiments conducted in 0.9 mm and 1.1 mm CFMR. Experiments were carried out at different volumetric flow ratios. Experimental core diameter of inner fluid calculated from by Image J software. (a) 0.9 mm microchannel at 60:1(O/I) flow rate ratio, Inner core diameter 100 μm . (b) 0.9 mm microchannel at 30:1 flow rate, Inner core diameter 150 μm . (c) 1.1 mm microchannel at 60:1 flow rate, 120 μm .

Silver nanoparticles were synthesized in CFMR (1mm ID outer tube, 0.15 mm ID inner tube and 135 mm length) at overall molar ratio of tannic acid to silver nitrate of 0.068 at different flow rates. Volumetric flow rates of two reactants were maintained at 60:1 (Outer: Inner) in order to reduce the core diameter (0.12 mm) of inner fluid in coaxial flow to decrease the diffusion timescales of both the reactants. Silver nitrate (0.423 mM) fed through inner tube whereas tannic acid (0.093mM, pH 8) through outer tube at different overall flow rates ranging from 30.5 mL/h to 91.5 mL/h. Reaction between silver nitrate and tannic acid results in formation of silver nanoparticles. Yellow color appearance of silver nanoparticles (grey line) was observed in CFMR (Fig 6.18).

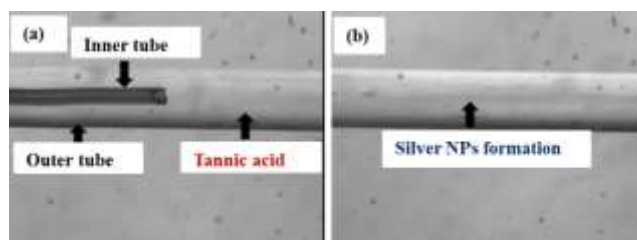


Figure 6.18: (a) Snapshot of coaxial flow micro reactor, which is used for synthesizing silver nanoparticles. (b) Silver nanoparticles (grey line) are formed due to interfacial reaction between tannic acid and silver nitrate. Appearance of yellow color within the reactor starts after 3 cm distance from the point of confluence, corresponds to the residence time of 1 s (91.5 mL/h flow rate).

The appearance of color starts at a length (measured from point of confluence), which corresponds to a residence time of 1 s. This time correlates well with time scales of reaction measured in batch reactors³⁶. The samples were collected in petridish at different times to verify the dynamics of the reactor as well as for further characterization techniques (Fig 6.19). UV-Visible spectra of silver nanoparticles showed the presence of silver nanoparticles by exhibiting the surface plasmon resonance in the visible region at 410 nm (Fig 6.20). Two more peaks were observed along with silver corresponded to the tannic acid at 205 nm and 260 nm. Coincidence of normalized plots (UV-Vis spectra) confirmed the steady state nature of the process (Fig 6.20 inset). Experiments were repeated for reproducibility of the results. Samples were analyzed with UV- Spectrophotometer. It showed that UV-Vis spectrum was similar for both trials (Fig 6.21). There is no significant difference in the UV-Visible spectra of silver nanoparticles synthesized in CFMR at different flowrates (Fig 6.22). Size distribution of silver nanoparticles samples obtained by DLS (Dynamic Light Scattering) is show in Fig 6.23. These results show that particle size distribution is independent of flow rate (Fig 6.24). Size distribution of silver nanoparticles samples obtained by DLS (Dynamic Light Scattering) is show in Fig 6.23. These results show that particle size distribution is independent of flow rate (Fig 6.24). This is advantageous for scheduling different production rates and in simplifying the control equipment required, as the quality of colloidal solution is mainly related to the nanoparticle size distribution.

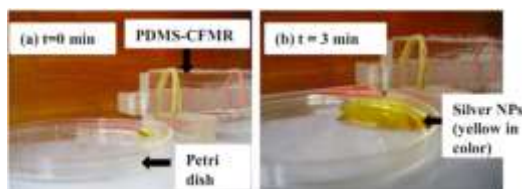


Figure 6.19: Snapshots of silver nanoparticles synthesized in CFMR. Samples of silver nanoparticles collected in petridish at different times to verify the steady state of continuous flow process.

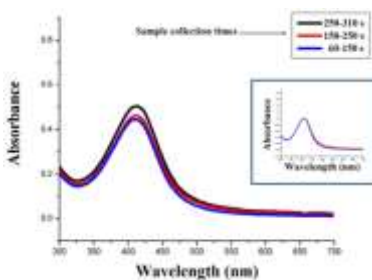


Figure 6.20: UV-Visible spectra of silver nanoparticles synthesized in PDMS based CFMR (inner tube 150 micron). Silver nanoparticles samples were collected to check the dynamics of the reactor. The inset shows normalized plots. The overlapping of normalized UV-Vis spectra of samples collected at various time intervals verifies the steady state nature of the process.

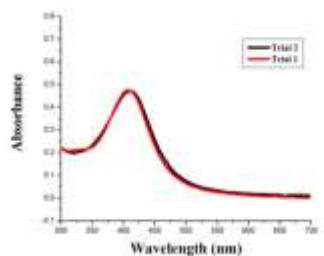


Figure 6.21: UV-Visible spectra of silver nanoparticles synthesized in CFMR by maintaining tannic acid at 54 mL/h flow rate whereas silver nitrate at 0.9 mL/h and similar concentrations employed in both the cases. Both the experiments were conducted to verify the reproducibility of experiments. Overlapping of UV-Visible spectrum of both trials indicates that experiments are reproducible.

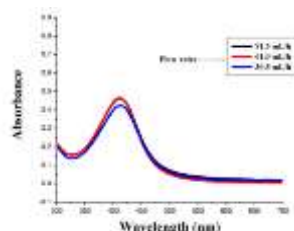


Figure 6.22: UV-Vis spectra of silver nanoparticles synthesized in CFMR at different flow rates. Surface Plasmon resonance of silver showed at 410 nm. These spectra show that particle mean size remains same because there is no significant difference in spectra.

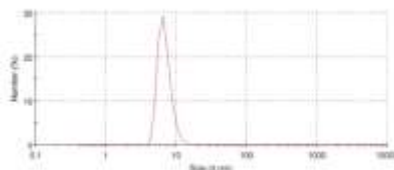


Figure 6.23: Size distribution of silver nanoparticles synthesized in CFMR (90 mL/h flow rate - tannic acid and 1.5 mL/h flow rate - silver nitrate) obtained by Zetasizer in terms of number (%). It found to be 6.9 ± 1.6 nm.

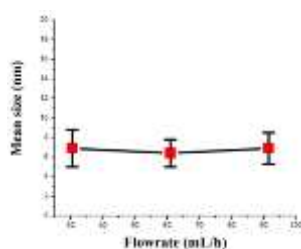


Figure 6.24: Variation of hydrodynamic diameter of silver nanoparticles synthesized in CFMR with different flow times. The error bars represent standard deviation.

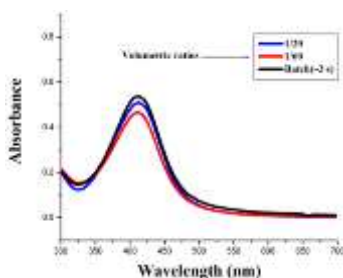


Figure 6.25: UV-Visible spectra of silver nanoparticles synthesized in CFMR at different volumetric ratios.

Mixing is completely driven by diffusion in coaxial flow microreactor and diffusion time scales can be controlled through varying the flow ratios in CFMR. Inner fluid core diameter was increased to 180 μm from 120 μm by varying the volumetric flow ratio from 1:60 to 1:20 in order to increase the diffusion time (3.6 s-9 s). Silver nanoparticles were

synthesized by maintained at molar ratio of tannic acid to silver nitrate at 0.068 for easy comparison with batch. UV-Visible spectrum confirms that there is no significant difference in particle size (Fig 6.25) and particle characterization with DLS was also shows that mean size of nanoparticle remain constant (summarized in Table.4.1). The size of particles synthesized was similar to the batch process indicating that diffusion time scales are not critical.

Table 6.1: Particle size distribution at different mixing times

Contact mode	Mixing time (s)	Particle size distribution (nm)
Batch	3 s	5.6 ± 1.8
CFMR (1/20)	9 s	7.7 ± 2.2
CFMR (1/60)	3.6 s	6.4 ± 1.4

Gold nanoparticles were synthesized in coaxial flow microreactor (1mm ID outer tube, 0.15 mm ID inner tube and 135 mm length) using chloroauric acid as a precursor and tannic acid as reducing and stabilizing agent. Molar ratio of tannic acid to chloroauric acid was maintained at 2.08 for easy comparison with batch. Chloroauric acid (0.25 mM) was fed through inner tube with 0.75 mL/h and whereas tannic acid (0.05 mM pH 7) was fed through the outer tube with 45 mL/h. Chloroauric acid pH was maintained between 1.8-2.4 and tannic acid pH at 7 in order to maintain overall reaction mixture pH above 6 to minimize coalescence. UV-Visible spectrometer and scanning electron microscopy were used for particle characterization. Gold nanoparticle samples were collected at different time levels to verify the dynamics of the reactor (Fig 6.26). Overlapping of UV-Vis spectra of samples collected at various time intervals (300-500 s, 500-700 s) verifies the steady state nature of the process. The size distribution of gold nanoparticles were found to be 10 ± 3.9 nm, 8.2 ± 3.4 nm, 6.5 ± 3.0 nm when overall concentrations of gold salt were 0.05 mM, 0.25 mM, 0.5 mM respectively (Fig 6.28). Mass balance of gold nanoparticles based on mean diameter, which is obtained from SEM images (Fig 6.28), indicates that the number of nanoparticles are more in the case of higher concentrations compared to lower concentrations. It is also well known that initial nucleation rate is high for higher concentrations and rate of coalescence of initial nuclei is more in the case of higher concentration compared to lower concentration. These facts suggest that coalescence play key role in determining the particle size (Fig 6.27).

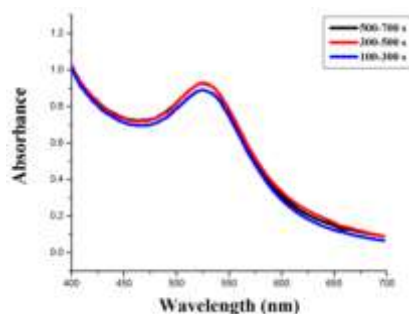


Figure 6.26: Visible spectra of gold nanoparticles synthesized in CFMR made of PDMS. Gold nanoparticle samples collected at different times to check the dynamics of reactor. The overlapping of UV-Vis spectra of samples collected at various time intervals (300-500 s, 500-700 s) verifies the steady state nature of the process.

Similar to the results obtained for silver nanoparticle synthesis, the effect of varying the flow rate ratio is insignificant on particle size distribution of the synthesized collides (Fig 6.29, 6.30) (summarized in Table 6.2). Finally, Fig 6.31 shows the FE-SEM image of gold nanoparticles synthesized using a batch reactor. The size of the particles is measure to be 6.5 ± 1.5 nm. At the lower mean size and polydispersity of the colloids synthesized in batch process shows that the differing pH environment in inner core of outer fluid plays a key role in determining particle size distribution of gold colloids synthesized by reduction of chloroauric acid. Also, the time taken for chloroauric acid species equilibration upon change in pH of environment is large and thus leads to coalescence irrespective of the core diameter. This suggests that the optimal value of the initial pH of chloroauric acid solution needed to minimize coalescence different for batch and continuous process.

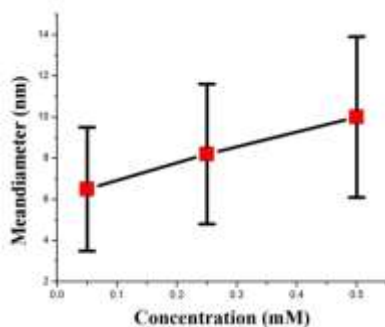


Figure 6.27: Schematic showing the variation of mean diameter of gold nanoparticles with overall concentration of gold synthesized in CFMR.

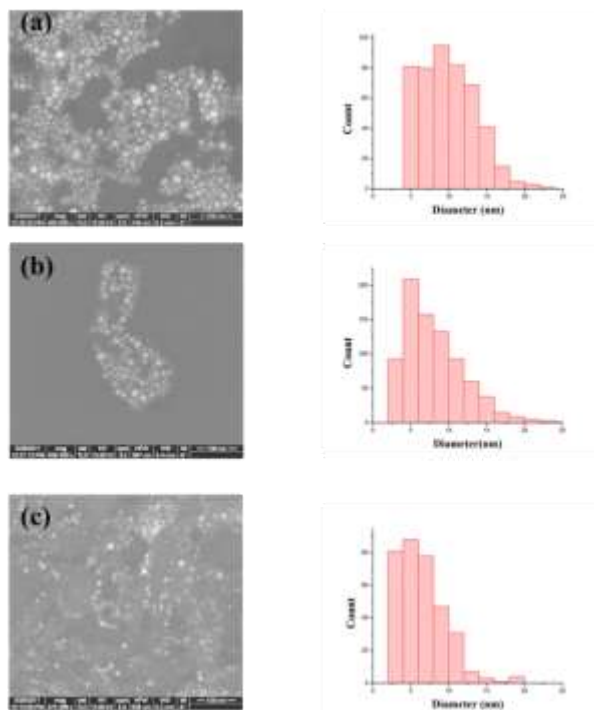


Figure 6.28: Representative FESEM images and histograms of gold nanoparticles synthesized in CFMR by varying overall concentrations of gold salt (a) 0.5 mM, Particle size distribution 10 ± 3.9 nm (b) 0.25 mM, Particle size distribution 8.2 ± 3.4 nm (d) 0.05 mM, Particle size distribution 6.5 ± 3.0 nm.

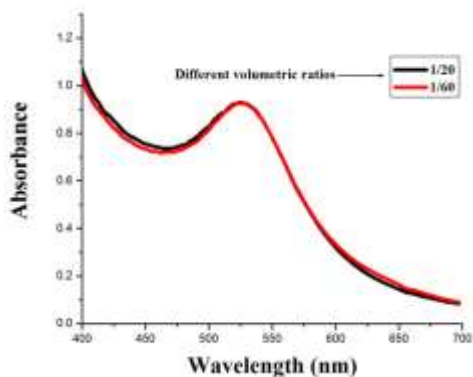


Figure 6.29: UV-Visible spectrum studies of gold nanoparticle synthesized in CFMR at different volumetric flow ratios to vary the diffusion times. Coincidence of UV-Visible spectrum of both diffusion times confirms that mean size and particle distribution remains same.

9.2.2 Macroscale reactors

9.2.2.1 Side-feed reactor

Microchannel flows can provide uniform and repeatable heat and mass transport conditions, which is purported to help in enhancing the reproducibility of nanoparticle synthesis; however, the widespread use and ‘numbering-up’ of microchannels is hindered by large pressure drops due to small channel sizes, leading to very high power requirements for pumping the reagents. As our earlier results suggested that speed of mixing and flow conditions had very little effect on the nanoparticle size distribution, as long as their reactivity was tuned by choosing appropriate feed conditions, we designed a simple gravity fed open channel reactor with multiple feed inlets to mimic the drop-wise addition protocol for synthesizing monodisperse gold nanoparticles (figure 6.32). Salient features of our process design are the very high throughput (g/hr) vis-à-vis typical throughput values of microchannel reactors (mg/hr) and the negligible power-requirements for pumping liquids.

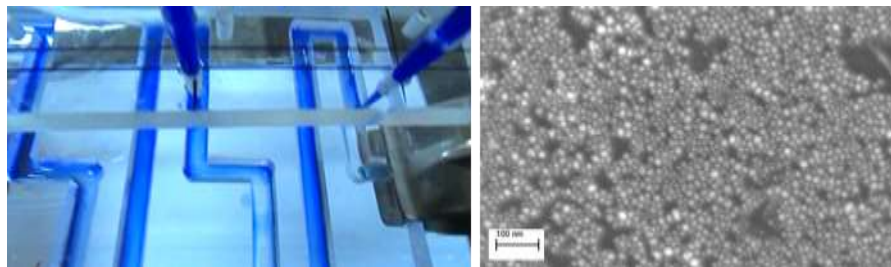


Figure 6.32. (a) Photograph of a novel flow reactor for metal nanoparticle synthesis. The channels were formed by cutting 2 mm wide x 2mm deep slots into a PMMA sheet. The blue colour is due to the dye used for visualisation of the flow pattern in the reactor. During nanoparticle synthesis, tannic acid flows through the channels, while metal salt is added drop-wise at selected points using syringes. A representative FESEM image of gold nanoparticles synthesized using the reactor is shown. The throughput in terms of gold was 1 g/hr, and the average size of the gold nanoparticles was ~10 nm.

9.2.2.2 Spinning bowl reactor

There currently exist barriers to high throughput production by chemical means of uniformly-sized gold/other nanoparticles, with wide-ranging applications in the electronic storage and nanosensor industry.

Several types of reactors are known and are in use for mixing and reacting reagents. Stirred tank reactors, tubular reactors, and microchannel reactors with radially interdigitated, Y, and T mixers are employed for facilitating precipitation for production of nanoparticles. These reactors produce gold particles with high polydispersity and/or suffer on account of choking of channels due to the deposition of nanoparticles on channel walls. Microchannel reactors also suffer from large pressure drops required to maintain a reasonable processing rate. Another known reactor is a spinning disk reactor (SDR) employed for process intensification in precipitation reactions. They are more energy efficient as compared to microchannel reactors at a given throughput and are easier to fabricate and operate. Once the disk is in motion a relatively small amount of energy is required to keep the disk rotating due to high inertia exhibited by the disk. Also, the SDR requires lower pumping energy than continuous flow mixing devices because the liquid film does not experience any pressure drop on the surface of the disk. Spinning disk reactors have been used for synthesis of nanoparticles of silver, barium sulphate, barium carbonate, magnesium hydroxide and zinc oxide. Synthesis of gold nanoparticles using this reactor, with two precursor streams introduced on the spinning disk, however leads to formation of quite large size aggregated particles.

It is therefore desirable to design a high-yield reactor, free from wall deposition related problems, for synthesis of uniformly-sized nanoparticles. So, a novel technique for rapid synthesis of gold nanoparticles in a continuous fashion using a spinning disk- spinning bowl (SD-SB) reactor that results in smaller and more uniform particles as compared to the conventional continuous stirred tank reactor and spinning disk reactors was developed. HAuCl_4 is dispersed as fine micron-sized non-interacting droplets into a film of tannic acid for forming the gold nanoparticles. The SD-SB reactor can be operated in traditional vertical configuration. The use of novel horizontal/inverted mode of operation allows large throughputs to be realized without any loss of performance, by enlisting gravity to pump the reactants.

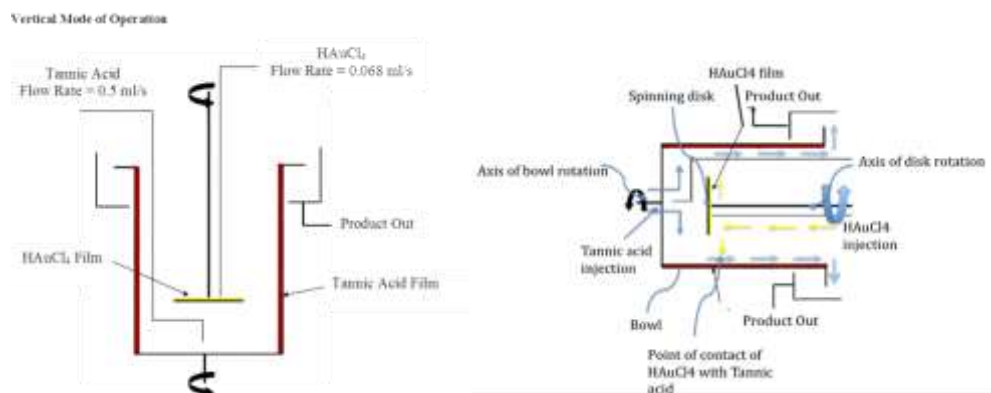


Figure 6.33: Spinning bowl spinning disk reactor set-up in vertical and horizontal mode of operation.

CSTR *v/s* SB-SD Reactor

Continuous stirred tank reactors are the most commonly used type of reactors in industrial processing. CSTR is operated under steady state conditions and is usually well mixed. Thus the concentration in the exit stream is same as everywhere within the reaction vessel. However, in the case of precipitation reactions it is reported that CSTR shows multiple steady states and cyclic behavior in concentration. In order to confirm this trend in nanoparticle synthesis a CSTR of volume 50 ml was designed with rushton turbine as the stirrer and gold nanoparticle synthesis was carried out. The flow rate of tannic acid and HAuCl₄ was 0.5 ml/s and 0.068 ml/s respectively. This was identical to the flow rates in SB-SD reactor so that a direct comparison of the two reactors could be made. The residence time in the reactor was 88 s and the reaction was carried out for 16 min. Though no multiple steady states were observed under given conditions the mean size of the gold nanoparticles synthesized in the CSTR kept increasing with time. Table 6.3 gives the time evolution of gold nanoparticles synthesized in CSTR. It is seen that the particle size increased from 5.3 nm to 6.2 nm and the standard deviation increased from 1.2 to 2.1 in the course of 16 min. It is possible that the initial gold nanoparticles formed in the reactor might act as seeds and lead to formation of larger particles as time evolves. In order to reduce this effect, seeds were introduced along with tannic acid by adding two drops of HAuCl₄ (conc. 2.12 mM) into 50 ml tannic acid. However, the particles formed were still polydisperse and the mean size increased with time. Figure 6.34 shows the time evolution of absorbance in UV-visible spectra at 530 nm for gold nanoparticles synthesized in CSTR with and without the presence of seed particles. The FE-SEM images and the particle size distribution of this experiment are shown in Figure 6.35.

Transient studies of gold nanoparticles synthesis in SB-SD reactor was conducted with all the parameters like flow rate, concentration of HAuCl₄ and tannic acid and time of collection kept same as that of CSTR. Figure 6.36 shows the transient behavior of peak absorbance of gold nanoparticles synthesized in the SB-SD reactor. Two trials are conducted to check for repeatability and the experiment is found to be repeatable. It is seen that the reactor takes 2 min to attain steady state under these conditions. Also, the SEM images of these nanoparticles do not show any change in the mean size and size distribution with time. It is seen that the steady-state absorbance values of gold nanoparticles in CSTR is twice that of gold nanoparticles from SB-SD reactor. This is because the UV-visible spectra of the two samples are taken from different instruments and this discrepancy has been verified by taking UV-visible spectra in the same instrument and the absorbance from the two samples matched.

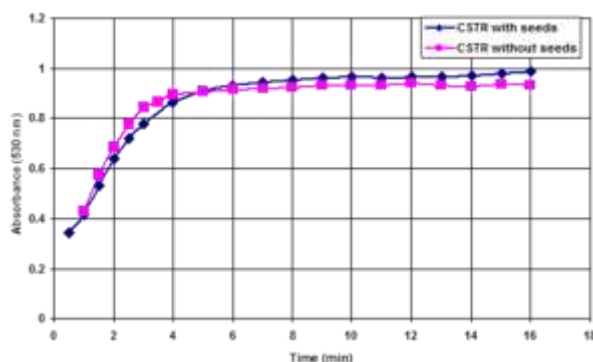


Figure 6.34: Comparison of transient studies of gold nanoparticles formed in CSTR with and without the presence of seed particles. [Tannic Acid] = 0.5 mM, [HAuCl₄] = 0.25 mM, Tannic Acid Flow Rate = 0.5 ml/s, HAuCl₄ Flow Rate = 0.068 ml/s.

Table 6.3: Time evolution of particle diameters of gold nanoparticles in CSTR.
 [Tannic Acid] = 0.5 mM, [HAuCl₄] = 0.25 mM, Tannic Acid Flow Rate = 0.5 ml/s, HAuCl₄ Flow Rate = 0.068 ml/s.

Time (min)	Particle Diameter (nm)	Standard Deviation
5	5.3	1.2
10	5.6	1.3
16	6.2	2.1

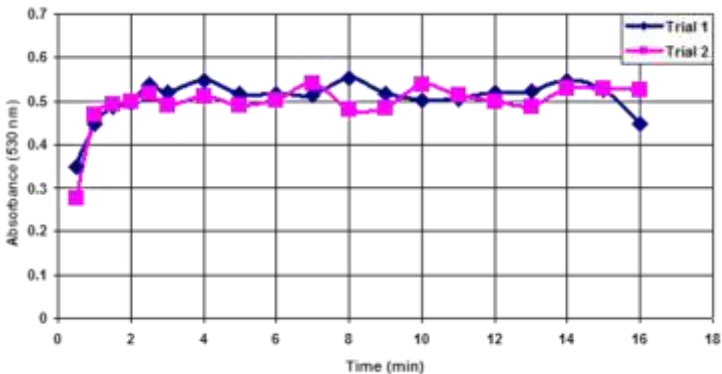


Fig 6.35: Repeatability of transient studies of gold nanoparticles formed in spinning disk reactor. [Tannic Acid] = 0.5 mM, [HAuCl₄] = 0.25 mM, Tannic Acid Flow Rate = 0.5 ml/s, HAuCl₄ Flow Rate = 0.068 ml/s.

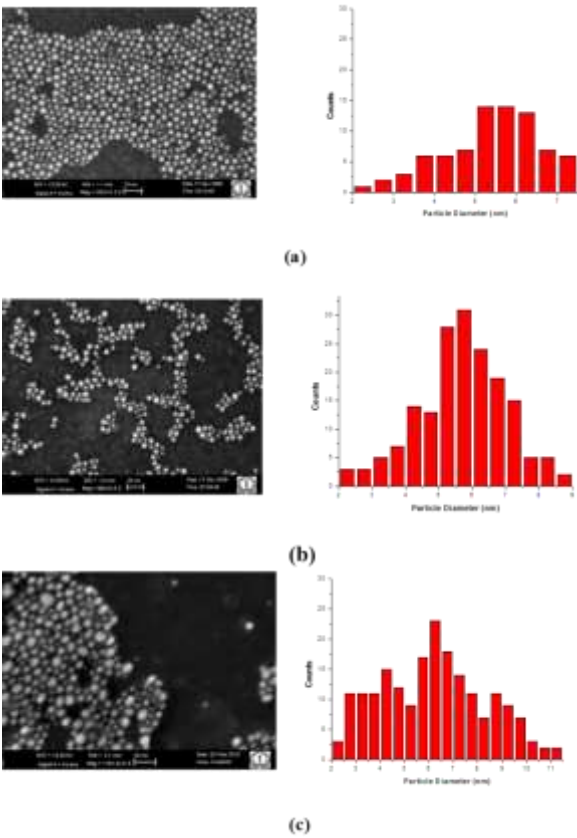


Figure 6.36: SEM image and histogram of gold nanoparticles formed at (a) 5 min, (b) 10 min and (c) 16 min in CSTR. [Tannic Acid] = 0.5 mM, [HAuCl₄] = 0.25 mM, Tannic Acid Flow Rate = 0.5 ml/s, HAuCl₄ Flow Rate = 0.068 ml/s.

Gold nanoparticle synthesis was carried out at different bowl speeds and consequently different film thickness. Table 6.4 and Figure 6.37 show the variation of particle size and size distribution with bowl speed as all the other conditions are kept constant. For bowl speeds 1500 rpm, 2000 rpm, 3000 rpm and 4000 rpm the particle size and size distribution does not vary with bowl speed. In the case of bowl speed of 800 rpm, back flow of tannic acid film was observed. Also the thickness of tannic acid film is such that splashing occurs ($H > 2$) with the formation of Worthington jet and secondary droplets leading to smaller particle size and larger standard deviation. At 5000 rpm bowl speed splashing of tannic acid onto the disk was observed. This is because under these conditions $H < 0.2$ at which surface effects induces splashing and forms secondary droplets. It is observed that the particle size becomes 6.1 ± 1.7 nm under these conditions. Thus, it can be concluded that apart from the extreme conditions, bowl speed and film thickness had no effect on mean size and particle distribution and it is important to work in the no-splashing regime. Figure 6.38 shows the UV-visible spectra of gold nanoparticles synthesized at different bowl speeds. Figure 6.39 to Figure 6.43 show the FE-SEM images and their corresponding threshold images and size distribution of gold nanoparticles synthesized at different bowl speeds keeping other parameters constant. IgorPro software is used to analyze the SEM images and obtain data about the mean size and particle distribution.

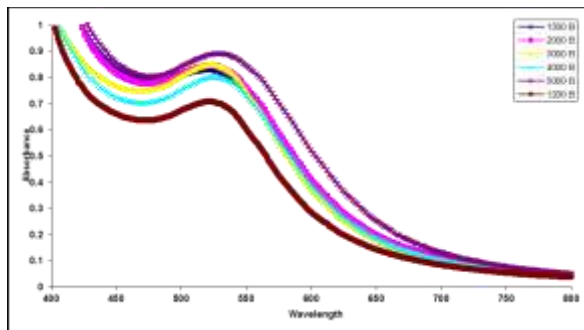


Fig 6.37: UV-visible data of gold nanoparticles formed under different bowl speeds.

Table 6.4: Variation of particle size with bowl speed in vertical mode. Disk Speed = 2000 rpm. Drop Size = 600 μm . $[\text{HAuCl}_4] = 0.25$ mM $[\text{Tannic Acid}] = 0.5$ mM HAuCl_4 flow rate = 0.068 ml/s, Tannic Acid flow rate = 0.5 ml/s.

Bowl Speed (rpm)	Film Thickness (μm)	Residence Time (s)	Molar Ratio	Particle Size (nm)	Standard Deviation	Remarks
800	2600	40.8	2	3.2	1.9	Back Flow. Deep pool Impact.
1500	900	14.2	2	4.9	1.4	
2000	515	8.1	2	4.8	1.4	
3000	300	4.72	2	5	1.6	
4000	200	3.14	2	4.9	1.4	
5000	109	1.71	2	6.1	1.7	$H=0.12$ Splashing on Disk

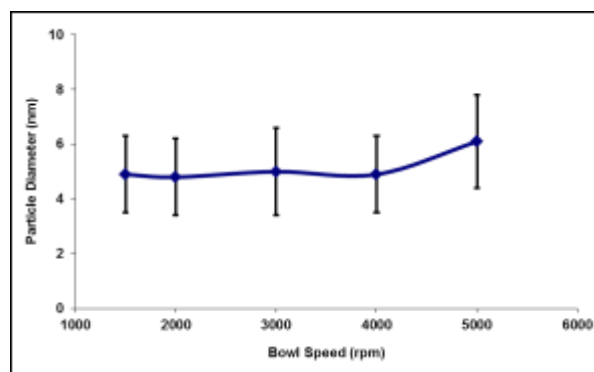


Figure 6.38: The relationship between gold nanoparticle size and bowl speed along with their standard deviations. Disk Speed = 2000rpm. Drop Size = 600 μm . $[\text{HAuCl}_4] = 0.25\text{mM}$ $[\text{Tannic Acid}] = 0.5\text{mM}$ HAuCl_4 flow rate = 0.068 ml/s, Tannic Acid flow rate = 0.5 ml/s.

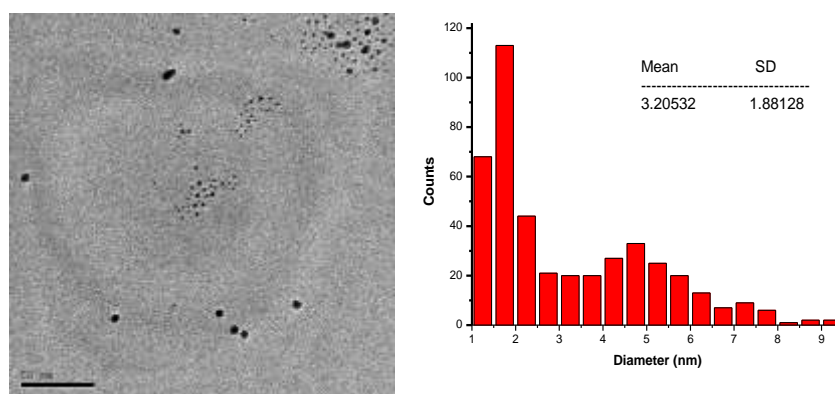


Figure 6.39: TEM of gold nanoparticles synthesized at 800 rpm Bowl Speed and the corresponding particle size distribution. Disk Speed = 2000 rpm.

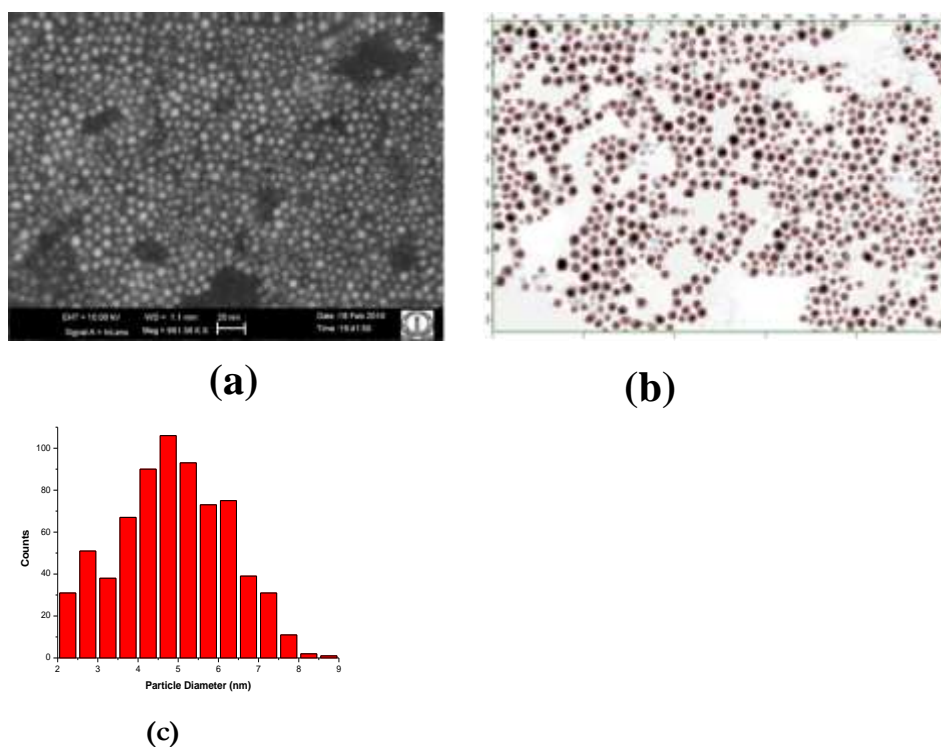
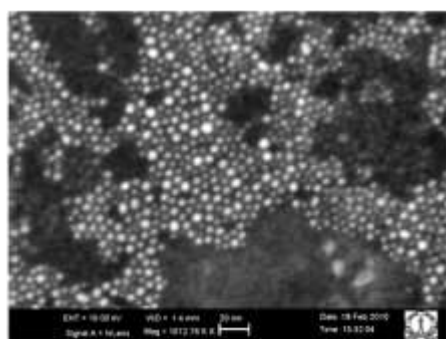
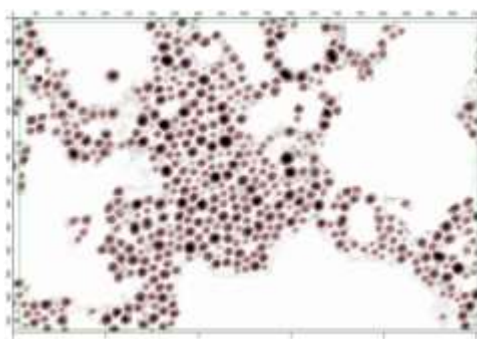


Figure 6.40: (a) SEM of gold nanoparticles synthesized at 1500 rpm Bowl Speed. (b) Threshold image of (a) using IgorPro. (c) Particle size distribution of (a). Disk Speed = 2000 rpm.



(a)



(b)

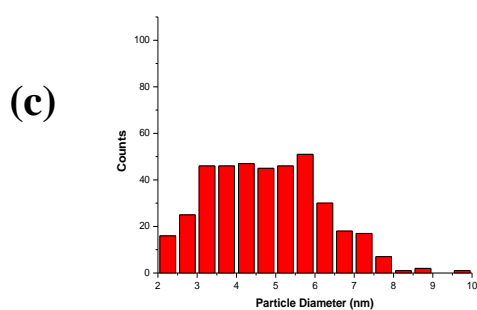
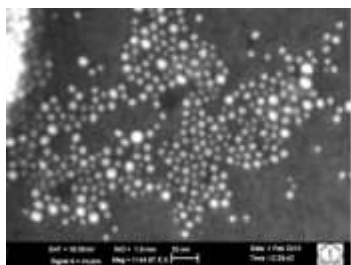
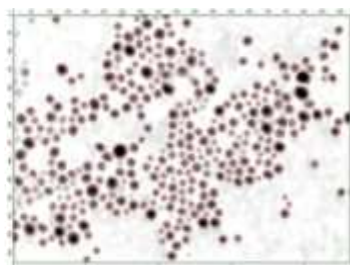


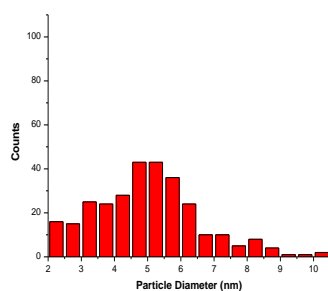
Figure 6.41: (a) SEM of gold nanoparticles synthesized at 2000 rpm Bowl Speed. (b) Threshold image of (a) using IgorPro. (c) Particle size distribution of (a). Disk Speed = 2000 rpm.



(a)



(b)



(c)

Figure 6.42: (a) SEM of gold nanoparticles synthesized at 3000 rpm Bowl Speed. (b) Threshold image of (a) using IgorPro. (c) Particle size distribution of (a). Disk Speed = 2000 rpm.

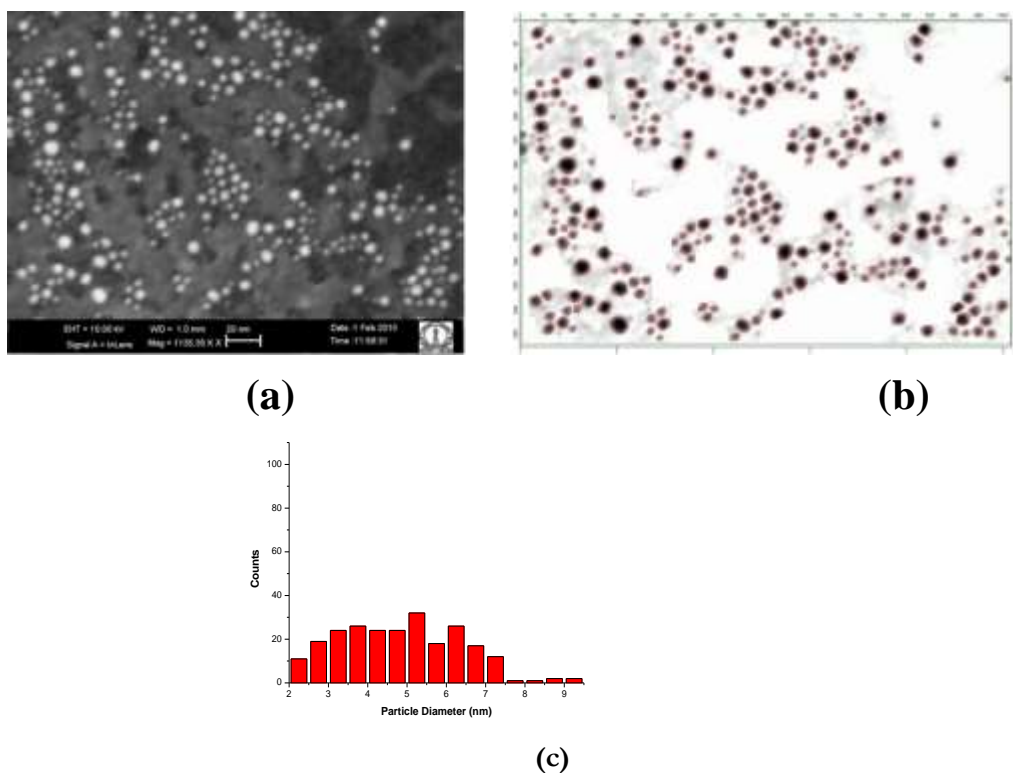


Figure 6.43: (a) SEM of gold nanoparticles synthesized at 4000 rpm Bowl Speed. (b) Threshold image of (a) using IgorPro. (c) Particle size distribution of (a). Disk Speed = 2000 rpm.

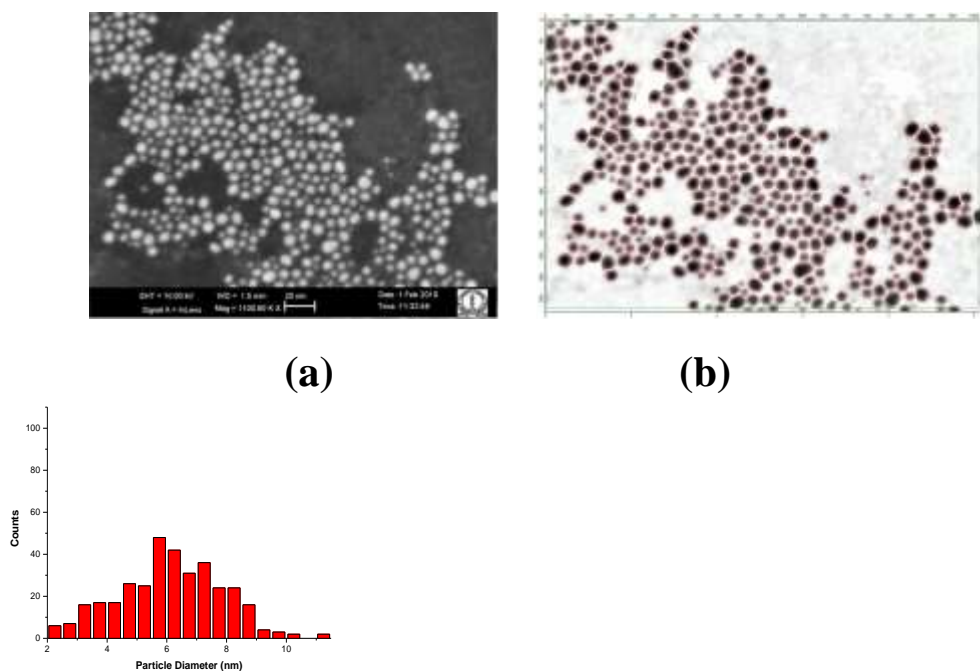


Figure 6.44: (a) SEM of gold nanoparticles synthesized at 5000 rpm Bowl Speed. (b) Threshold image of (a) using IgorPro. (c) Particle size distribution of (a). Disk Speed = 2000 rpm.

6.1.2. Effects of disk speed on particle size and size distribution.

Gold nanoparticle synthesis was carried out at different disk speeds by keeping bowl speed as 1500 rpm and all the other parameters constant. Table 6.5 and Figure 6.44 show the variation of particle size and size distribution of gold nanoparticles with disk speed (drop size). It is seen that the drop size has no effect on the particle size and polydispersity. Figure 14 shows the UV-visible spectra of gold nanoparticles synthesized at different disk speeds. All the three peaks overlap showing that the particle sizes are identical. Figure 15- Figure 17 show FE-SEM images, their corresponding threshold images using IgorPro and the particle size distribution of gold nanoparticles synthesized at different disk speeds. It is seen that the particle size and distribution are identical in all the three disk speeds. However, it is not possible to conclude that the drop size has no effect on particle size since the drop size was varied over a short range (450 μ m - 900 μ m) due to limitations in the equipment.

Table 6.5: A comparison of variation of gold nanoparticle size with disk speed. Bowl Speed = 1500 rpm. Film Thickness = 900 μ m. Residence Time = 14.2 s. [HAuCl₄] = 0.25 mM [Tannic Acid] = 0.5 mM. HAuCl₄ Flow Rate = 0.068 ml/s. Tannic Acid Flow Rate = 0.5 ml/s.

Disk Speed rpm	Drop Size μ m	Frequency of Drops Drops/mm/s	Particle Size nm	Standard Deviation
2000	900	2	4.9	1.4
3000	600	6	4.5	1.2
4000	450	15	4.9	1.4

Spinning bowl-spinning disk/atomizer was used to synthesis silver nanoparticles, with AgNO₃ and tannic acid as precursors. AgNO₃ was dispersed as fine droplets into a film of tannic acid. It is expected that each non-interacting AgNO₃ droplet when in contact with tannic acid acts as a micro-reactor and the nanoparticles formed has lesser chances of collision and agglomeration leading to more uniform particles. The effect of concentrations of AgNO₃ and tannic acid, atomizer (in place of spinning disk to feed AgNO₃) and its different positions (with respect to the bowl) on the silver nanoparticles' size and size distribution was studied. The experiments were done in vertical mode (easy to handle) of operation as it was learnt from previous studies that horizontal mode of operation has no effect on particle size, only production rate.

Table 6.6: Variation in system used and concentration in vertical mode of operation.

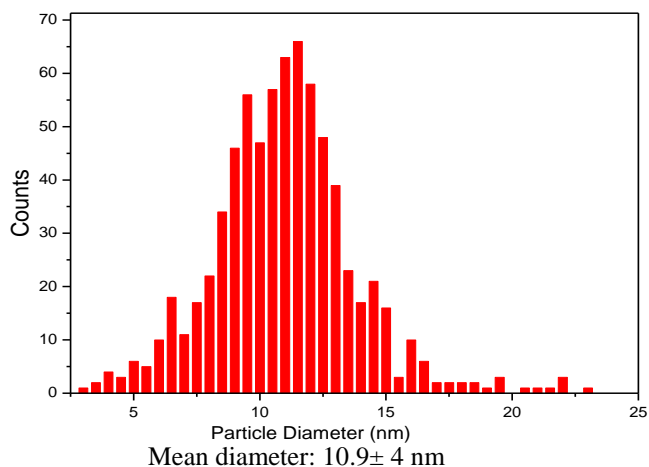
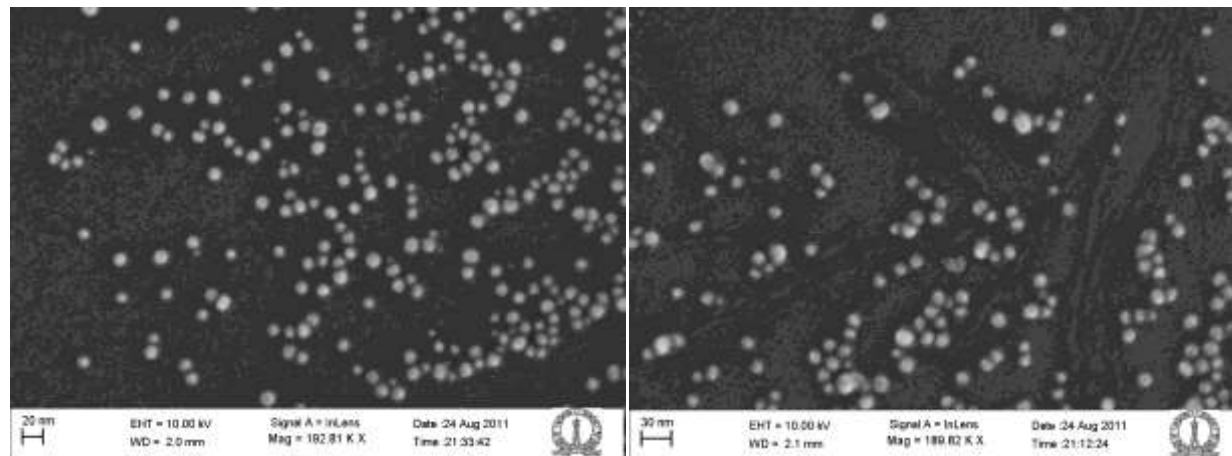
System	[AgNO ₃] mM	[TA] mM	Molar Ratio	AgNO ₃ flow rate (ml/min)	TA flow rate (ml/min)	Bowl speed (RPM)	Disk speed (RPM)
SB-SD	49.058	0.334	0.05	4	30	1500	2000
Batch dumping	49.058	0.334	0.05	-	-	-	-
Batch dropwise addition	49.058	0.334	0.05	-	-	-	-
SB-atomizer at center	49.058	0.334	0.05	4	30	1500	-
SB-atomizer closer to bowl wall	49.058	0.334	0.05	4	30	1500	-
SB-atomizer at center	20	0.334	0.125	4	30	1500	-

Concentration of AgNO₃ was 49.058 mM and tannic acid was 0.334 mM, which is 10 times the concentration previously studied using turbine and baffle system. Tannic acid pH was adjusted to 8.0 using K₂CO₃. AgNO₃ was dispersed as tiny droplets emerging from spinning disk or atomizer into a thin film of tannic acid flowing continuously on the bowl

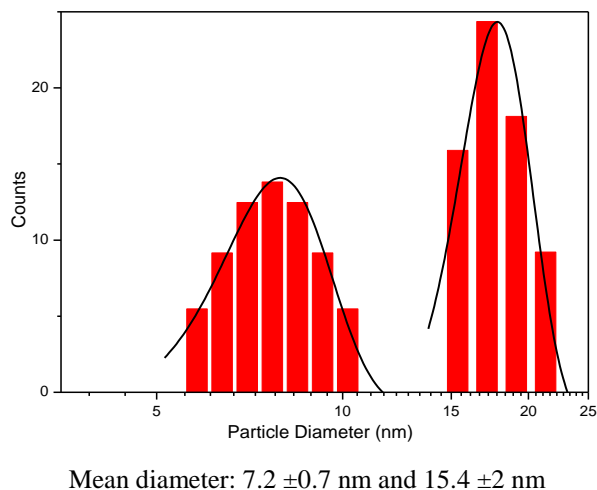
surface. Bowl and disk were rotated at the speed of 1500 rpm and 2000 rpm respectively. Atomizer was operated at 90% probe frequency. The flow rates of AgNO_3 and tannic acid was 4 ml/min and 30 ml/min. The silver nanoparticles thus formed were characterised using DLS and SEM.

Characterisation of synthesised nanoparticles using DLS and SEM:

Sample - SB-SD:



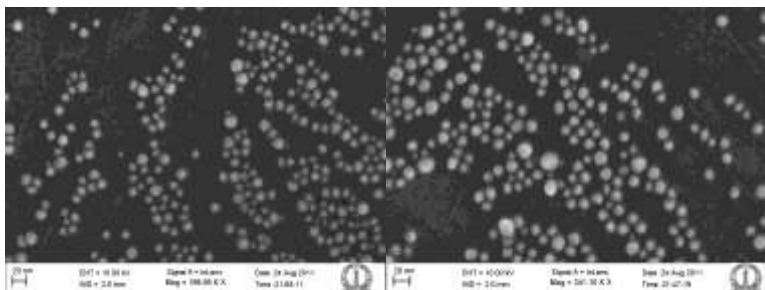
Particle size distribution obtained from SEM



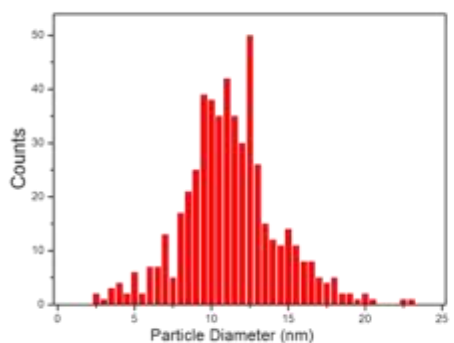
Particle size distribution obtained from DLS

Sample - Batch dumping:

To study the effect of SB-SD system, the above experiment was repeated in turbine-baffle system. The concentrations and pH were maintained constant. AgNO_3 solution was added to tannic acid and stirred until no further color change was observed.

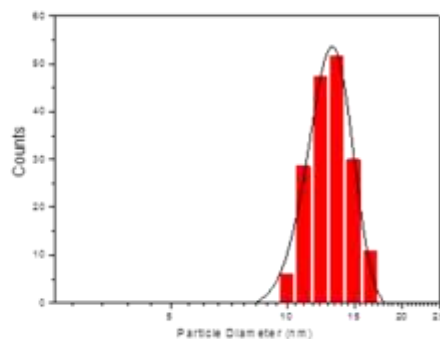


Particle size distribution obtained from SEM



Mean diameter: 11 ± 4 nm

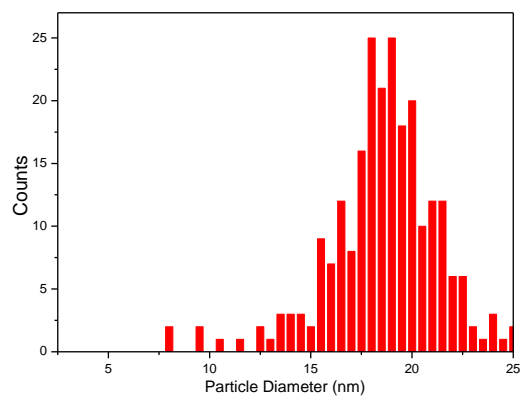
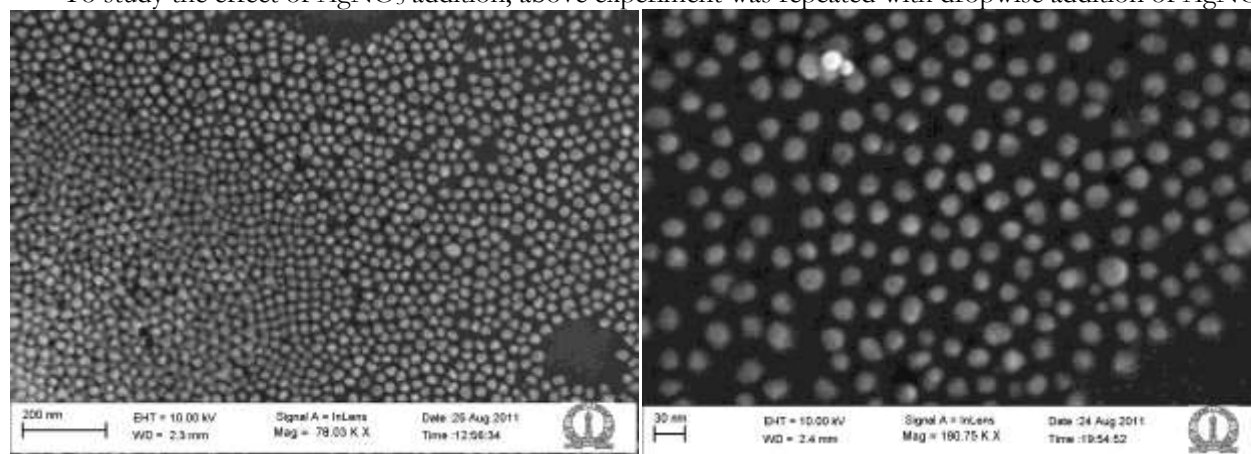
Particle size distribution obtained from DLS



Mean diameter: 16.4 ± 1.8 nm

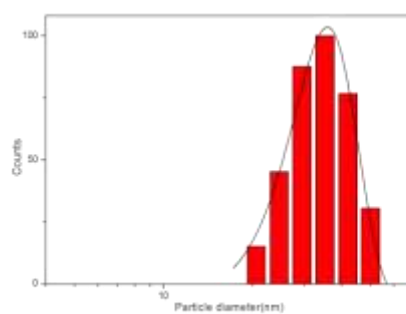
Sample - Batch dropwise addition:

To study the effect of AgNO_3 addition, above experiment was repeated with dropwise addition of AgNO_3 to tannic acid.



Mean diameter: 18.8 ± 3.5 nm

Particle size distribution obtained from SEM

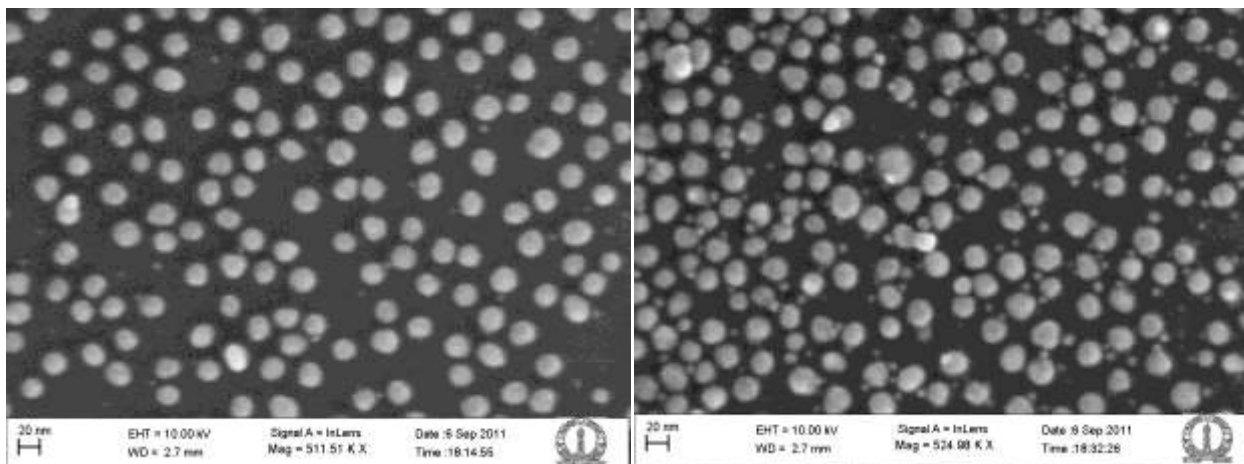


Mean diameter: 35.8 ± 3 nm

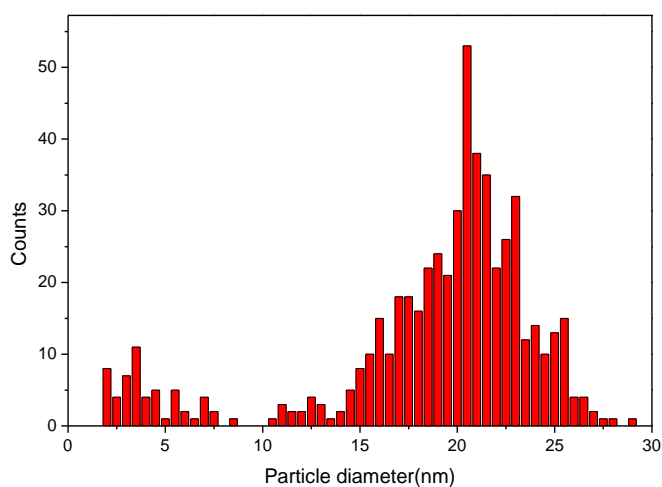
Particle size distribution obtained from DLS

Sample- SB-atomizer at center:

To study the effect of smaller AgNO_3 drop size on the nanoparticles size and size distribution, atomizer was used in place of spinning disk to feed AgNO_3 solution. Unlike spinning disk which disperses AgNO_3 drops on to the bowl surface within specific region (forms a band), atomizer creates a fine spray of AgNO_3 drops which reaches bowl surface at different points. The concentration and pH were maintained constant.

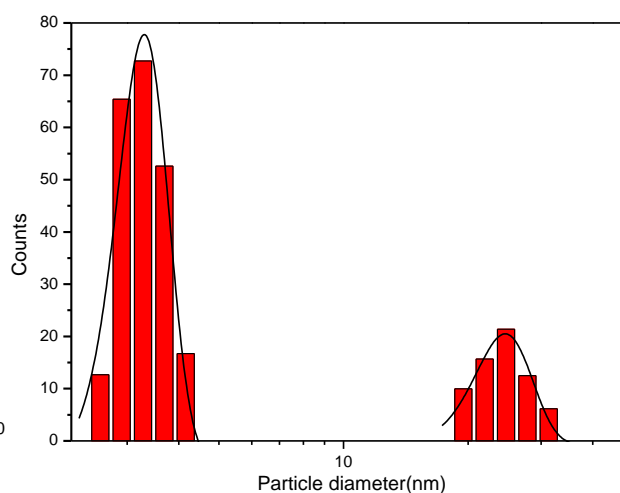


Particle size distribution obtained from SEM



Mean diameter: 3.2 ± 1.8 nm and 20.7 ± 5.2 nm

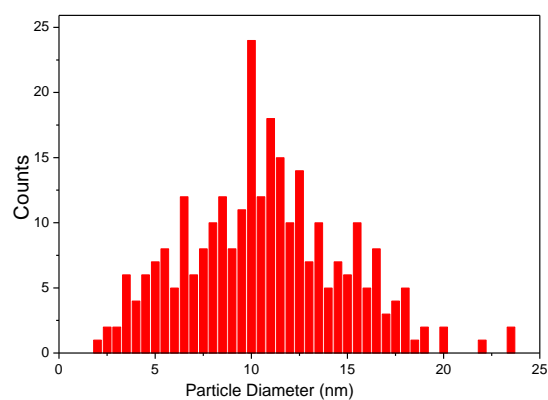
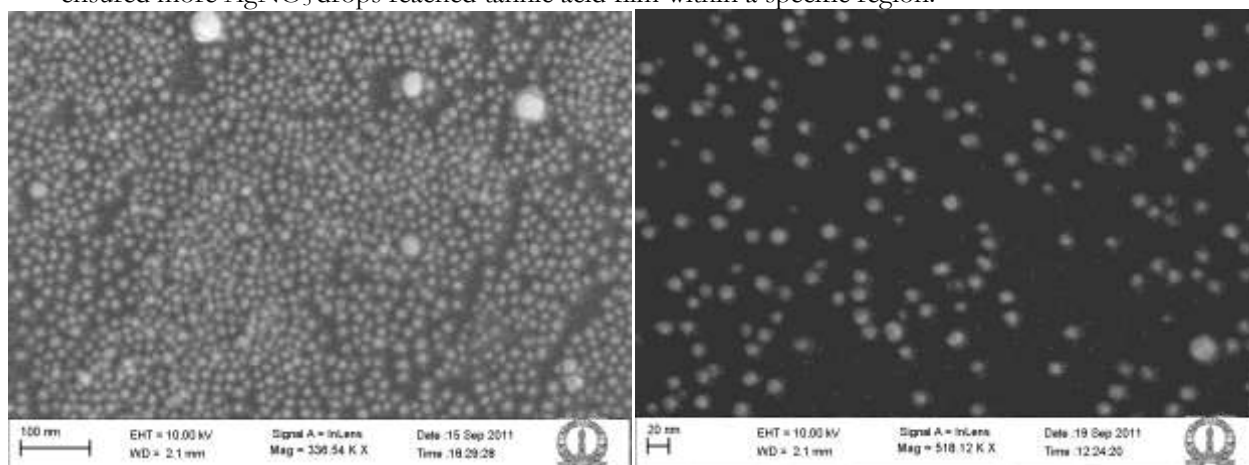
Particle size distribution obtained from DLS



Mean diameter: 4.7 ± 1.6 nm and 20.6 ± 3.6 nm

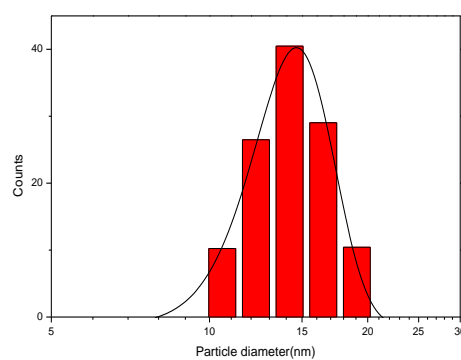
Sample- SB-atomizer closer to bowl wall:

To study if nanoparticles' size was affected by atomizer position, the atomizer was placed closer to the bowl wall, which ensured more AgNO_3 drops reached tannic acid film within a specific region.



Mean diameter: 10.5 ± 8 nm

Particle size distribution obtained from SEM

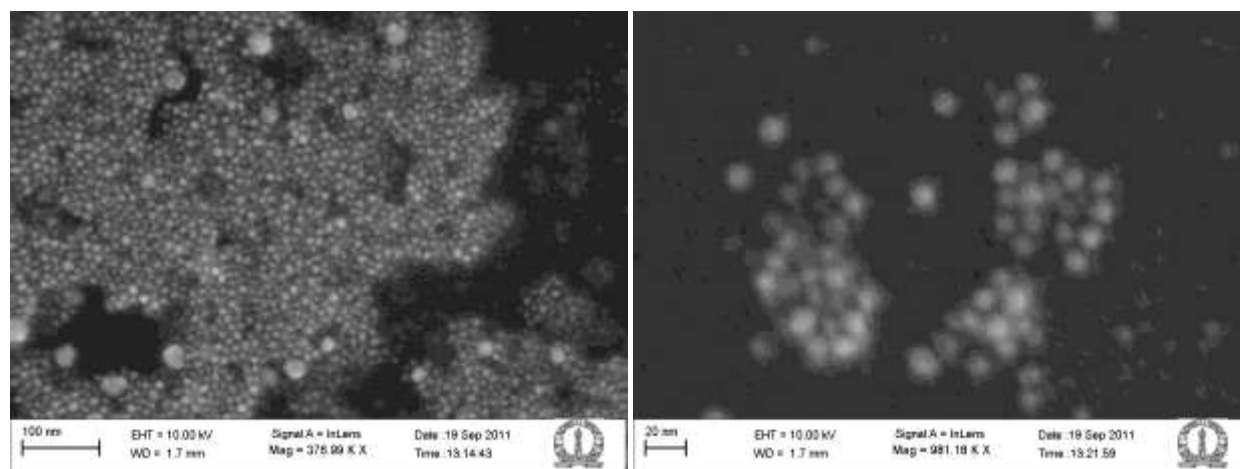


Mean diameter: 13.8 ± 4 nm

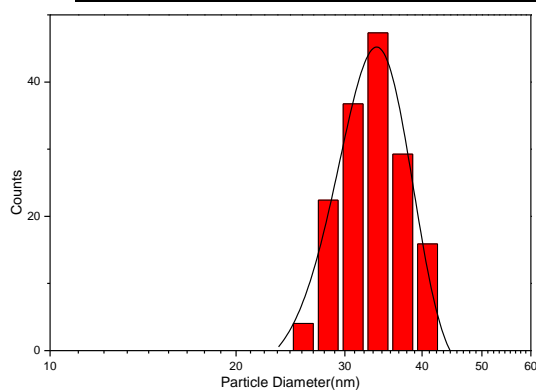
Particle size distribution obtained from DLS

Above sample with PEG-thiol

To study the effect of PEG-thiol on silver nanoparticles synthesised, 1 μ l of PEG-thiol was added to 1ml of as synthesised silver nanoparticles, mixed well and kept aside for 12-15h. The sample was then characterised using DLS and SEM for possible change in size and shape of nanoparticles.



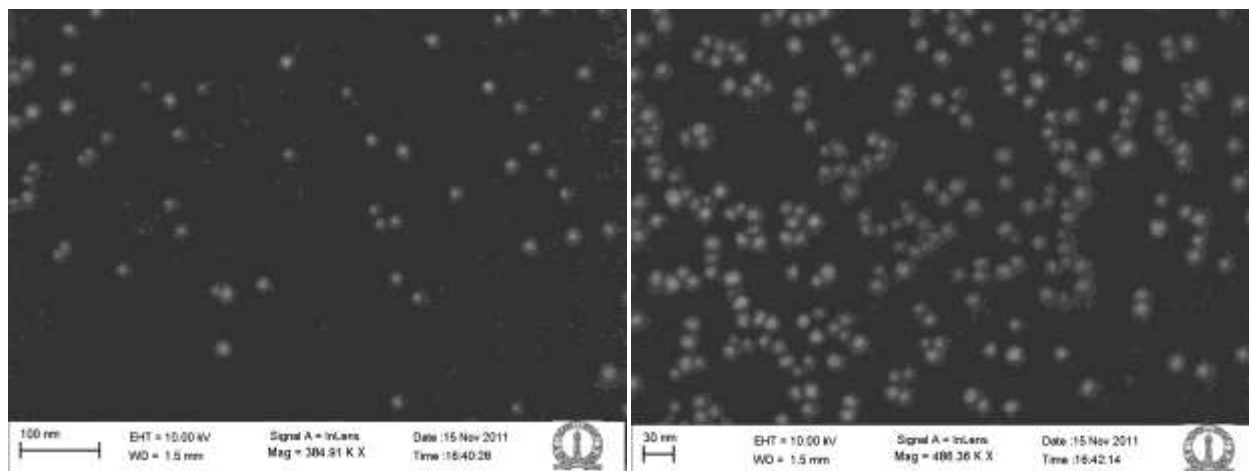
Particle size distribution obtained from DLS



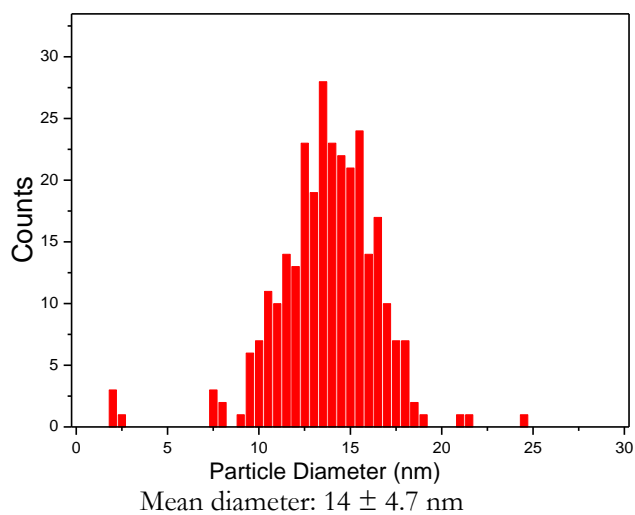
Mean diameter: 31.3 ± 2.3 nm

Sample- SB-atomizer at center (reduced AgNO₃ concentration):

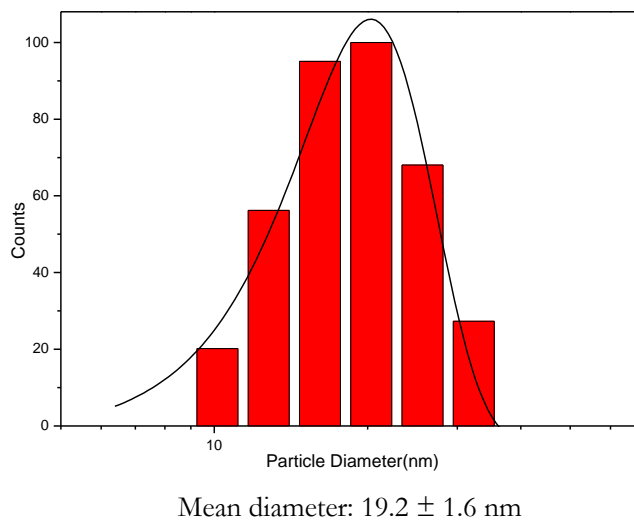
To examine if lower concentration of AgNO₃ affects size or size distribution of the nanoparticles formed, AgNO₃ concentration was reduced from 44.058 mM to 20 mM while the tannic acid concentration was maintained at 0.334 mM.



Particle size distribution obtained from SEM



Particle size distribution obtained from DLS



Results and discussion:

The silver nanoparticles formed showed bimodal size distribution.

System	Particle size-distribution		Remarks
	SEM image analysis	DLS	
SB-SD (Vertical mode)	10.9 ± 4 nm	7.2 ± 0.7 nm, 15.4 ± 2 nm	Bimodal distribution, nanoparticles of size < 5 nm present.
Batch dumping	10 ± 4 nm	16.4 ± 1.8 nm	Nanoparticles size < 5nm are lesser in number compared to SB-SD, no substantial change in larger nanoparticle size distribution
Batch dropwise addition	18.8 ± 3.5 nm	35.8 ± 3 nm	Does not represent/reproduce SB-SD size distribution
SB-atomizer at center (Vertical mode)	3.2 ± 1.8 nm, 20.7 ± 5.2 nm	4.7 ± 1.6 nm, 20.6 ± 3.6 nm	Distribution different from SB-SD, with more nanoparticles < 5nm and larger nanoparticle size increased to ~20 nm from 16 nm
SB-atomizer closer to bowl wall (Vertical mode)	10.5 ± 8 nm	13.8 ± 4 nm	No substantial change in smaller nanoparticle size, larger nanoparticle size decreased to ~ 11 nm
SB-atomizer at center (reduced AgNO ₃ concentration)	14 ± 4.7 nm	19.2 ± 1.6 nm	Single size distribution ~ 15 nm, with very few nanoparticles < 5 nm.

9.3 Development of robust processes for formation of nanoparticle arrays:-

The emergence of novel electronic, optical and magnetic properties in ordered two-dimensional (2D) nanoparticle ensembles, due to collective dipolar interactions of surface plasmons or excitons or magnetic moments, and the appeal of cost-effective nanostructure fabrication have motivated intense research efforts into fabricating self-assembled nanostructures. Several applications of nanoparticle arrays, viz. as catalysts for templated nanowire growth for dye sensitized solar cells, as catalyst layers in fuel cells, as electrical transducers of chemical or biological binding events etc., require control over interparticle spacing in the 10-50 nm regime. In addition, few applications such as magnetic recording media demand nanostructures in a square pattern, as opposed to the ubiquitous hexagonal pattern. Thus, there is a demand for a scalable approach to control particle arrangement in 2D nanoparticle arrays. Nanoparticle ensembles can be obtained through two approaches, namely, top-down and bottom-up. For nanostructure fabrication in the sub 50 nm regime, top-down lithography based approaches are hampered due to both economic and fundamental limitations while the bottom-up self-assembly based processes are hindered due to two serious problems, namely, (a) scalability and (b) control over particle arrangement in arrays. Of the several bottom up approaches proposed so far in the literature, many such as dip-pen lithography, molecular assembler etc., are time consuming; in contrast, self-assembly of ligand protected nanoparticles offers an attractive avenue for cost-effective large scale fabrication of nanostructures.

To date, several approaches have been proposed for fabricating large scale 2D arrays using self-assembly of ligand protected nanoparticles. Significant ones include: (i) self-assembly on a solid substrate by drop-casting, (ii) self-assembly at fluid interfaces such as air-water or air-toluene interface in conjunction with microcontact printing which enables transfer of arrays to any desired substrate and (iii) convective assembly of particles on solid substrate. Self-assembly on a solid substrate is driven by wetting properties and limited by issues related to substrate compatibility while the self-assembly at fluid-fluid interfaces has been demonstrated only over small domains (few cm scale). Convective based assembly has so far been demonstrated only for larger size particles. Moreover, a detailed understanding of the process involved is not generally available, and scale up of these self-assembly processes is yet to begin in any serious way. Self-assembly of ligand protected nanoparticles or the use of diblock copolymer micelles as templates are the most preferred routes for fabricating ordered 2D arrays with precise particle arrangement. Self-assembly of ligand protected nanoparticles is a simple technique, wherein the interparticle spacing is typically tuned by changing ligand molecules; Self-assembly of diblock copolymer templates offers the possibility of tuning nanoparticle array packing and spacing using different substrates. However, ligands based on alkane chains that are most commonly used only vary the interparticle spacing in the sub-5 nm range, whereas the diblock copolymer method is restricted to substrates on which the polymer can form micelles with well-defined shape and, typically, the spacing is controllable only above 25 nm. Grafting polymeric ligands directly onto nanoparticles using functionalized end-groups is an attractive avenue for controlling the order and spacing of nanoparticle arrays in the 5–50 nm range.

In this chapter, first a simple process for fabricating wafer scale arrays in few minutes by adding excess surfactant is presented. The role of excess ligand and its implications during solvent drying and array fabrication is studied using complementary measurement techniques namely, SEM and ellipsometry, i.e., SEM provides topography of the film after drying while the ellipsometric data provides details on film formation during drying. Then, the study was extended to arrays fabricated using gold nanoparticles capped with thiol-terminated polystyrene of different molecular weights. Large scale arrays were found to form by simple drop-casting technique by controlling the effects of solvent dewetting. Next, a systematic study involving the effect of substrate on the interparticle spacing in monolayer arrays formed by self-assembly of polymer grafted nanoparticles is discussed. Finally, a process to fabricate arrays with square packing based on convective shearing at a liquid surface induced by miscibility of colloidal solution with the substrate is proposed. Fabrication of 3D aggregates of polymer-nanoparticle composite by manipulating solvent-ligand interactions is also discussed.

Significant efforts in making large scale array fabrication using ligand protected gold nanoparticles include:

Drop-casting colloidal solutions with excess ligand on a solid substrate

Jaeger's group has developed a simple drop-coating technique to assemble particles over cm scale on a smooth solid substrate (Fig. 3.1). They demonstrated their concept by drop-casting 5 nm dodecanethiol capped gold nanoparticles with excess dodecanethiol, on silicon nitride surface. The success of the process depends on finding a right balance between the rate of solvent evaporation and nanoparticle diffusion. They conjectured that a decrease of the solvent evaporation rate in a controlled manner occurs with the addition of excess dodecanethiol molecules, thereby leading to large scale assembly. This technique is limited to the use of ultra-smooth solid substrates for spreading colloidal solutions.

Drop-casting colloidal solution on curved or flat water substrate

Santhanam and coworkers have developed a simple and scalable technique by evaporating nanoparticles suspended in organic solvent on a curved water surface (Fig. 3.2a). This process was inspired by the work of Nagayama and coworkers,

wherein a curved mercury surface was used to fabricate single domain of highly ordered protein crystals. This technique in conjunction with microcontact printing enables the transfer of arrays from the water surface onto any desired substrate, overcoming the major limitation of the process of assembling particles directly on a solid substrate. Many variations to this approach have been reported in the literature. The significant ones include: (i) Pang et al. formed free-standing films by evaporating gold nanoparticles in toluene with poly methylmethacrylate (PMMA) on flat water surface (Fig. 3.2b), (ii) Eah has extended the approach of particle drying from air-toluene interface to air-water interface to increase the 2D superlattice domain area (Fig. 3.2c,d), and (iii) Wen and Majtech have reported a large scale assembly technique by controlling the evaporation of the nanoparticles in a binary solvent mixture of toluene and hexane. They have also reported that in the case of dodecanethiol coated gold nanoparticles, use of excess ligand is necessary to form large scale arrays, unlike the case of iron oxide nanoparticles.

Doctor-blade/roll-to-roll processing of 2D assembly of particles

A potential industrial technique for roll-to-roll assembly of nanoparticles is the technique of doctor-blade casting. Recently, a large-scale monolayer of 11 nm sized Wustite/Cobalt core-shell particles was fabricated. The ordering was uniform with the exception of few defects and irregularities (Fig. 3.3). Along similar line is the work of Malaquin and coworkers, which involves convective assembly of 100 nm gold nanoparticles or 500 nm latex particles on plasma treated PDMS substrate by controlling evaporation rate indirectly by manipulating temperature, relative humidity etc. Self-assembly of particles on PDMS substrate enables direct transfer of arrays to any desired substrate. However, this comes with the cost of substrate compatibility, and as the PDMS is incompatible with organic solvents, this technique is limited to self-assembly of aqueous based colloids. Thus, it can be realized that there is no single robust technique for large-scale self-assembly of nanoparticles in the size range of 2-20 nm. More importantly, the process needs to be compatible with different substrates. It is imperative to understand the mechanisms that dictate self-assembly process before venturing out into scale-up. The directed self-assembly scheme of alkanethiol encapsulated gold nanoparticles on a water surface is attractive due to its capability of transferring the arrays that are floating on the water surface to any desired substrates (eg. flexible or rigid) using soft-lithographic techniques. In the following section, a process to fabricate large scale arrays of dodecanethiol coated gold nanoparticles and thiol-terminated polystyrene capped gold nanoparticles will be discussed.

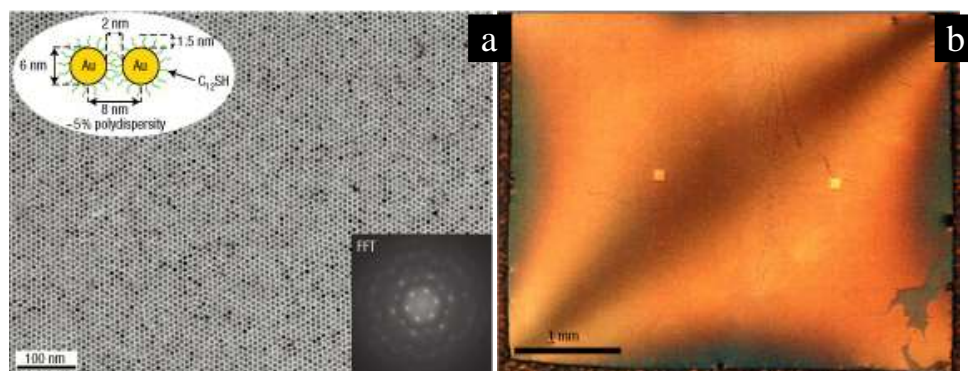


Figure **Error! No text of specified style in document..1**: (a) Transmission electron micrograph of monolayer of dodecanethiol capped gold nanoparticles produced by drop-casting gold colloid solution (containing excess dodecanethiol) dispersed in toluene onto silicon nitride substrate. The top inset represents schematic of dodecanethiol capped gold nanoparticles. The bottom inset represents fast Fourier transform of the image highlighting good order. (b) Optical photograph of compact monolayer of gold nanoparticles formed on silicon nitride substrate. (Reproduced with permission from Bigioni et al.²⁸ Copyright (2006) Nature Publishing Group).

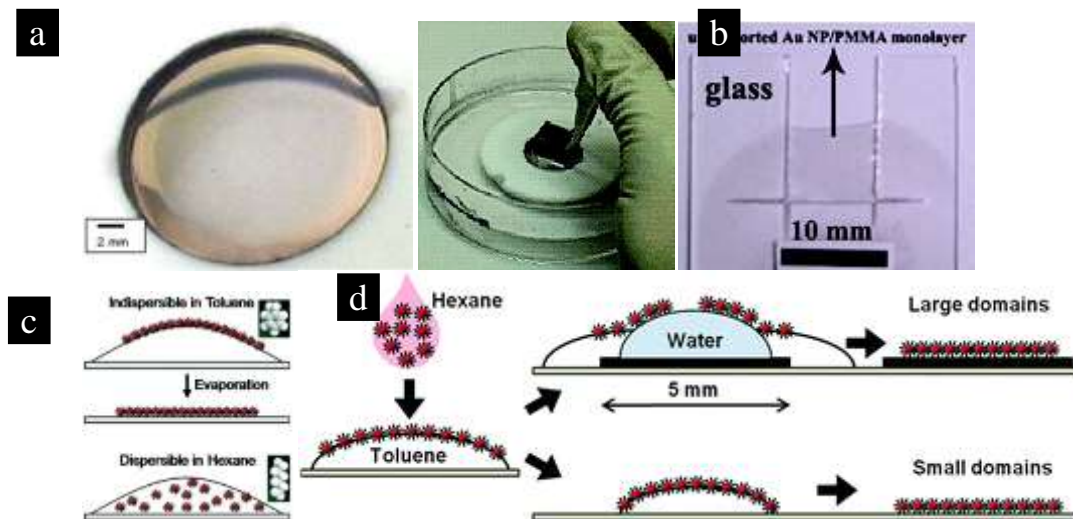


Figure **Error! No text of specified style in document..2**: (a) Optical photograph of gold nanoparticle array floating on water surface and inking the PDMS stamp pad with nanoparticle array self-assembled at the curved air-water interface (Reproduced with permission from Santhanam and Andres. Copyright (2003) American Chemical Society). (b) Optical image of nanoparticle/poly (methacrylate) film transferred to glass; the arrow represents the free-standing film (Reproduced with permission from Pang et al.. Copyright (2008) American Chemical Society). (c) Schematic representation of monolayer formation by drop-casting dodecanethiol capped gold nanoparticles dispersed in hexane onto toluene surface (Reproduced with permission from Martin et al.. Copyright (2010) American Chemical Society and (d) Schematic representation of array formation wherein the assembly at the air-toluene interface is transported onto an air-water interface (Reproduced with permission from Eah. Copyright (2011) Royal Society of Chemistry).

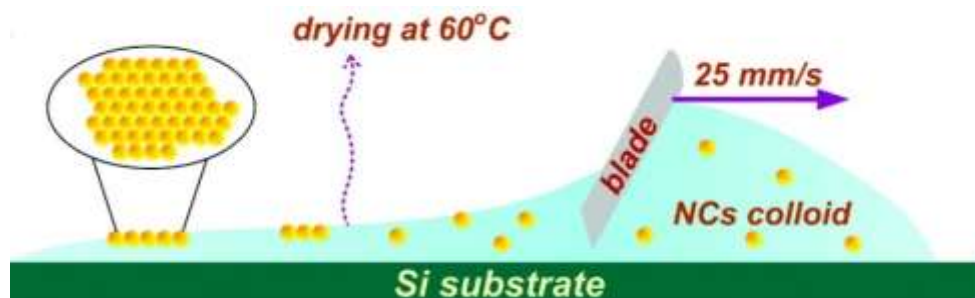


Figure **Error! No text of specified style in document..3**: Schematic representation of large scale assembly of nanoparticles through doctor-blade casting (Reproduced with permission from Bodnarchuk et al. Copyright (2010) American Chemical Society).

Large-scale self-assembly of gold nanoparticles

In the study of Santhanam et al., it has been highlighted that the curvature of water surface is critical for obtaining large scale monolayer devoid of macroscopic holes. As an exploratory work, a rectangular cell of dimensions 2 x 10 cm is fabricated thereby ensuring the same water curvature as reported earlier (Fig. 3.4a). Monolayer of dodecanethiol capped gold nanoparticles was fabricated over large area in the rectangular cell (see Fig. 3.4b,c). However, this process is inefficient as more than 90 % of particle were lost to the Teflon walls. Further, non-uniform, local nanoscale ordering of nanoparticles was observed. Furthermore, in the Teflon cell approach, the array is pinned to the wall, thereby resulting in residual stress in the film. The stresses in the film are more evident when the capping ligand is changed from dodecanethiol to thiol-terminated polystyrene of molecular weight 3000 g/mol (Fig. 3.5a). Also, unlike dodecanethiol capped gold nanoparticles, centimeter-scale gold nanoparticle array capped with thiol-terminated polystyrene could be obtained only by using a narrow range of concentration by using a circular Teflon cell approach. Typically, either finger-like pattern having inter-connected nanoparticle array or large circular holes surrounded by nanoparticle arrays, as shown in Fig. 3.5b, were formed. These observations suggested that stresses in the film must be avoided to form large scale array.

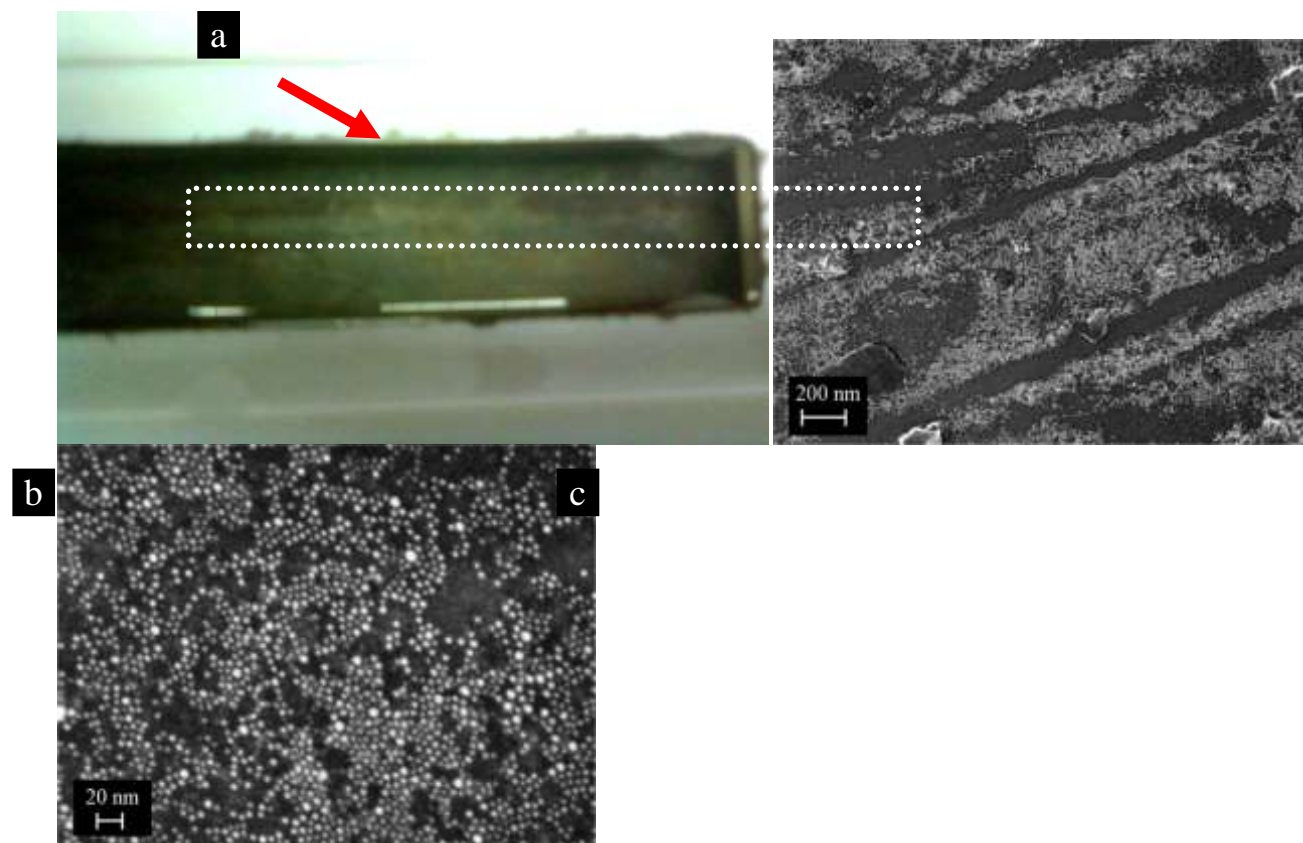


Figure **Error! No text of specified style in document..4**: (a) Digital photograph of gold nanoparticles dispersed in chloroform/hexane mixture on curved water surface in rectangular Teflon cell (2x10 cm). The outlined region, dotted square box used to highlight the presence of monolayer gold nanoparticle film on the water surface while the arrow indicates the particle lost to the Teflon walls. (b-c) Representative FESEM image of sub-monolayer gold nanoparticle array formed using the rectangular Teflon cell at different magnifications. Increasing the concentration should yield monolayer gold nanoparticle array.

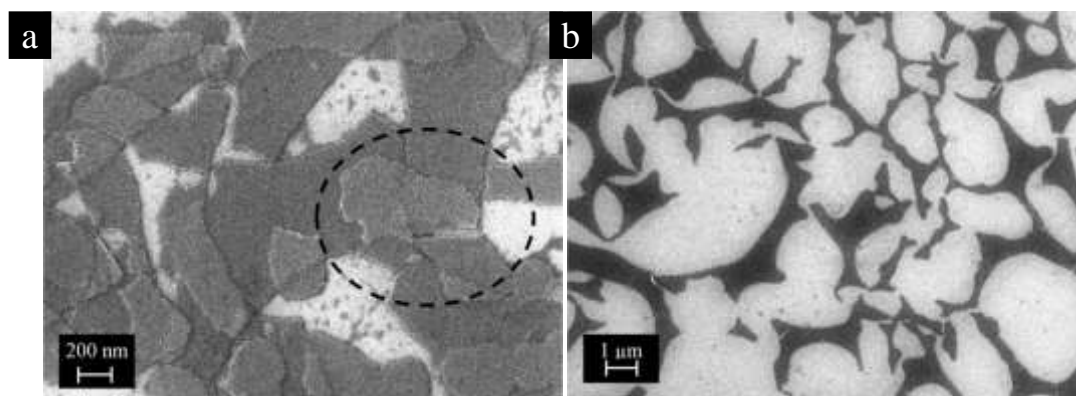


Figure **Error! No text of specified style in document..5**: Representative FESEM images showing polymer/solvent dewetting occurring while floating thiol-terminated polystyrene (molecular weight: 3000) capped gold nanoparticles on the water surface at (a) low nanoparticle concentration ($< 10^{14}$ particles/ml) and (b) high particle concentrations ($> 10^{14}$ particles/ml). At low particle concentration, parts of arrays due to residual stresses, portion of arrays flip on top of neighbouring domains as shown in the outlined region in a (dotted circle) while at high concentrations, multilayer is formed with larger holes (bright regions in b, corresponds to holes).

Effect of excess ligand on self-assembly of DDT capped gold nanoparticles

The Teflon cell approach is not easily scalable to the wafer-scale due to losses associated with adsorption of nanoparticles on the walls, while the array formation by drop casting on a solid substrate is controlled by the topography and wetting properties of the system, and is limited by issues related to material compatibility. In order to overcome the residual stress in the film, 0.4 mL of 5 nm dodecanethiol capped gold nanoparticles dispersed in toluene was drop-cast on free water surface in a petridish (Tissue culture, 900030A). The colloidal solution does not spread uniformly leading to multiple lens-like formations, which affected uniformity over large scale (Fig. 3.6a). This non-uniform spreading led to the formation of

monolayer/multilayer of gold nanoparticle arrays as shown in Fig. 3.6b. The key to any successful self-assembly approach is to allow the colloidal solution to spread uniformly. The use of excess ligands to form ordered arrays have been reported for various systems, with the actual mechanism yet to be identified. Some proposed explanations are: (i) the role of excess ligand acting as high boiling point solvent, (ii) the alteration of contact line motion of solvent and dynamics of dewetting, (iv) excess ligands form a monolayer on the subphase which enables rearrangement of nanoparticles, in addition to reducing the attractive forces between the particles.

Herein, a hybrid approach comprising of utilizing excess ligands to facilitate the spreading of colloidal solution on water surface was employed. The nanoparticle array was formed by drop casting 0.4 mL of 5 nm gold nanoparticles dispersed in toluene (containing 5 μ L dodecanethiol) on the water surface (9 cm diameter, petridish), as shown in Fig. 3.7a. Almost, the entire surface of water was covered with a nanoparticle array within a few minutes, resulting in large area close-packed monolayer (Fig. 3.7b). To understand the role of the nature of the surfactants, several surfactants like SPAN 20, TWEEN 20, TRITON-X 100 were also tried. The water soluble surfactants, namely, Tween 20 and Triton-X 100, engulfed the nanoparticles into the water phase while the SPAN 20 resulted in large area monolayer (Fig. 3.8).

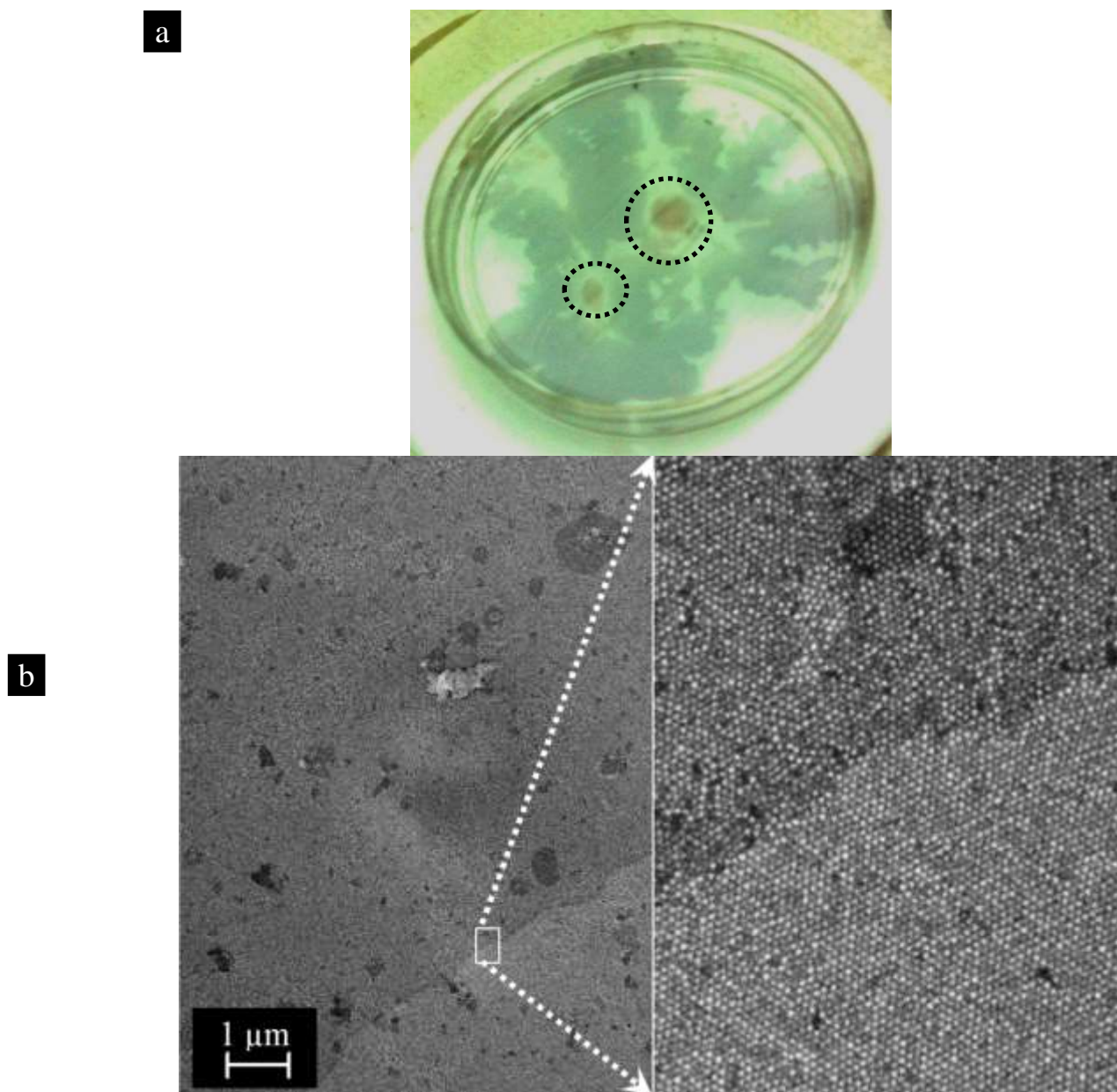


Figure **Error! No text of specified style in document..6:** (a) Digital photograph of dodecanethiol capped gold nanoparticle array formed by drop casting gold nanoparticles dispersed in toluene without excess dodecanethiol molecules. The outlined regions (two circles) in a are used to highlight the occurrence of multiple nucleation events during monolayer formation. (b) Dual-magnification FESEM image of dodecanethiol capped gold nanoparticle array formed by drop casting gold nanoparticles dispersed in toluene without excess dodecanethiol molecules.

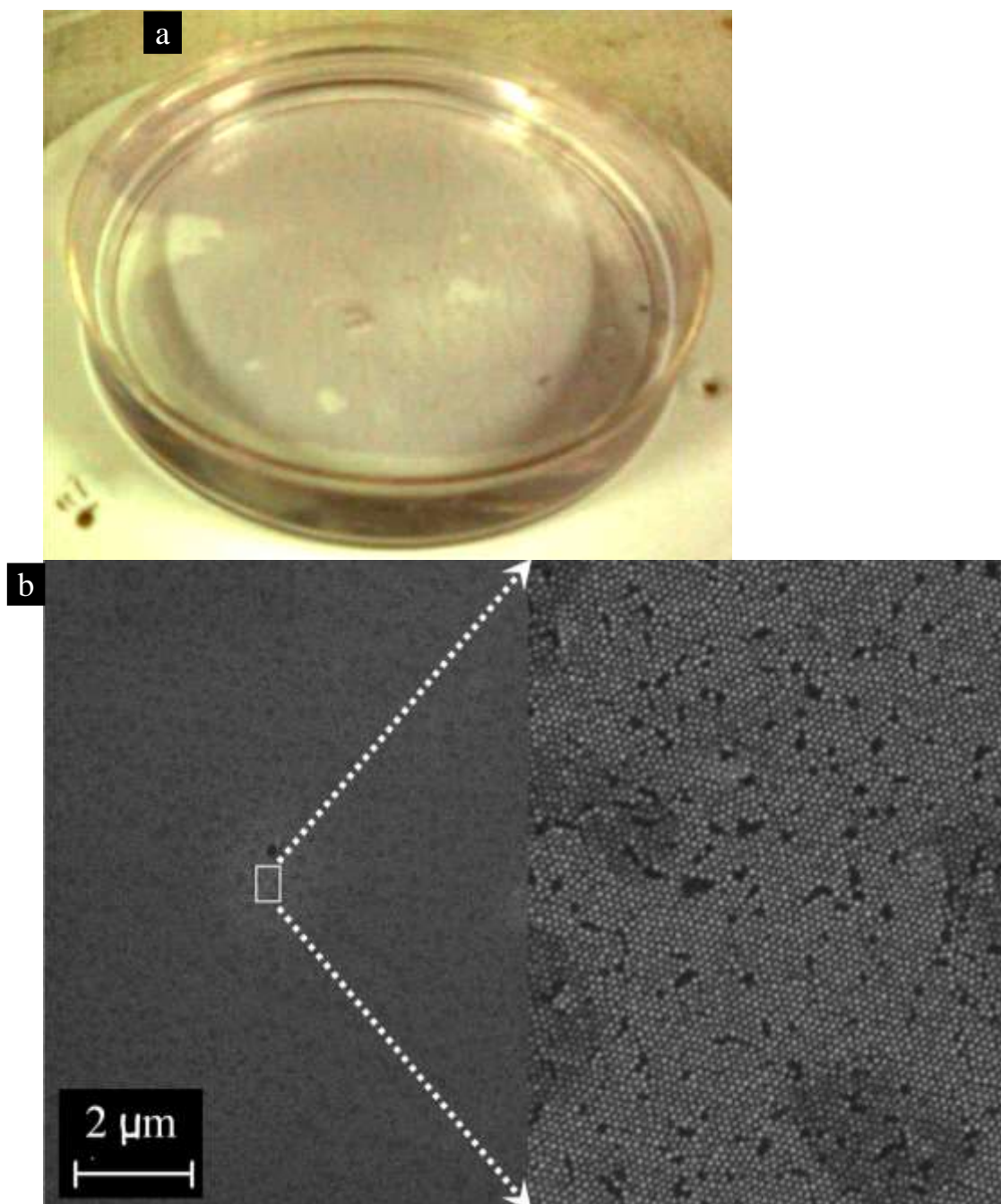


Figure **Error! No text of specified style in document..7**: (a) Digital photograph of dodecanethiol capped gold nanoparticle array formed by drop casting gold nanoparticles dispersed in toluene with 5 μL excess dodecanethiol molecules. It can be seen that the entire petridish is filled with gold nanoparticle array. (b) Dual-magnification FESEM image of dodecanethiol capped gold nanoparticle array formed by drop casting gold nanoparticles dispersed in toluene with 5 μL excess dodecanethiol molecules.

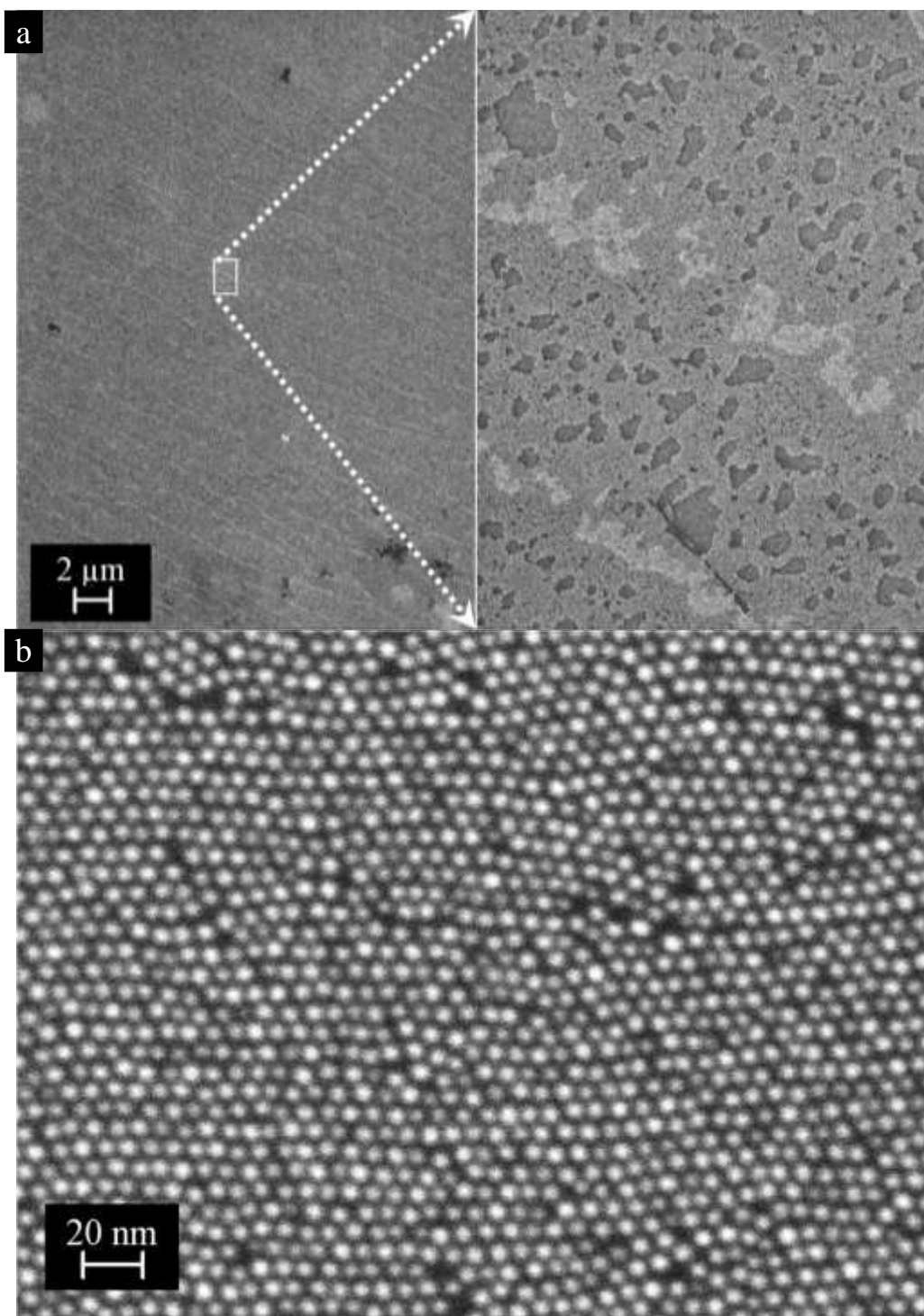


Figure **Error! No text of specified style in document.**8: Representative FESEM image of monolayer gold nanoparticle array formed by spreading toluene-hexane mixture, with SPAN 20 (sorbitan monolaurate) as surfactant on the water surface in a petridish at (a) low and (b) high magnifications.

Ellipsometric study of formation of 2D nanoparticle arrays

Nanoparticle self-assembly is a process wherein the interaction between nanoparticles results in final structure. As a result of evaporation induced dewetting, various structures such as isolated islands, labyrinthine structures, fractal structures, circular rings etc. have also been observed. Thus, it becomes imperative to understand the differences in the self-assembly of dodecanethiol capped gold nanoparticles with and without addition of excess surfactant. Both modeling and experimental approaches have been employed to investigate the self-assembly of nanoparticles into 2D arrays. Rabani and co-workers have employed coarse-grained lattice models to explain how solvent fluctuations during the evaporation affect the final nanostructure, with many of their predictions yet to be corroborated. In-situ studies using tools such as AFM, SAXS, optical microscopy have also been used to understand the nucleation and growth behavior during self-assembly of 2D nanoparticle arrays. Very recently, Park and co-workers have used in-situ TEM measurements, to understand the drying mediated self-

assembly of platinum nanoparticles in real time. Based on their observation, they propose an important role of capillary forces developed in the evaporating solvent front, in addition to lateral immersion forces. The aforementioned techniques used for investigating self-assembly are limited to nanoscale or at the most microscopic level in their spatial resolution. Recently, an alternate measurement technique, ellipsometry (Fig. 3.9), has generated a lot of attention for in-situ characterization of polymer nanostructures, as it provides information both at macroscopic and microscopic levels. In the following, the use of ellipsometry to analyze the effect of excess surfactant on the self-assembly of dodecanethiol coated gold nanoparticles at the air-water interface is presented. Dodecanethiol capped gold nanoparticles dispersed in toluene were drop-cast on the water surface, and ellipsometric data were collected at various incident angles during the evaporation of solvent. The optical images obtained during the process of array formation as the solvent evaporates for the case without excess thiol is presented in Fig. 3.10 and with excess thiol is presented in Fig. 3.11. Without the addition of excess surfactant, the initial pattern is similar to the islands of particles, which eventually aggregate to form large scale monolayer arrays with multiple voids. Also, multiple nucleation events can be observed visually during self-assembly of nanoparticles. On the contrary, self-assembly of dodecanethiol capped gold nanoparticles containing excess dodecanethiol resulted in labyrinthine structure, which eventually form large scale array without any voids. This is surprising because labyrinthine structures have been observed in simulations after complete evaporation of solvent.

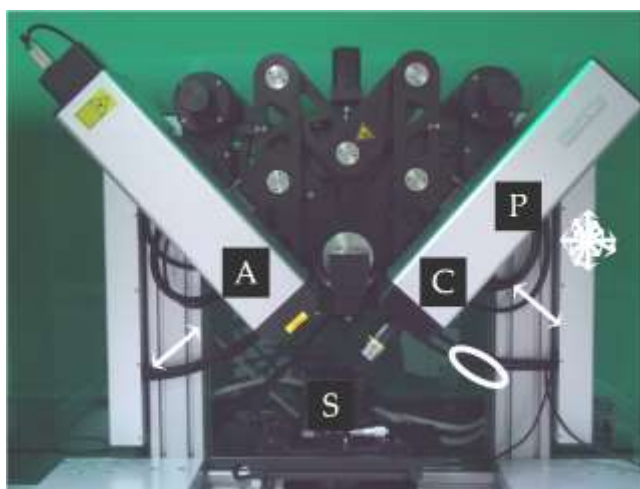


Figure **Error! No text of specified style in document.**9: Digital photograph of general ellipsometer set-up. Light emitted from the source, first passes through the polarizer (P), and the compensator (C) before it is reflected at the sample (S). The polarizer converts the unpolarized light into linearly polarized light. After reflection the light again passes a linear polarizer denoted the analyzer (A) before it reaches the detector.

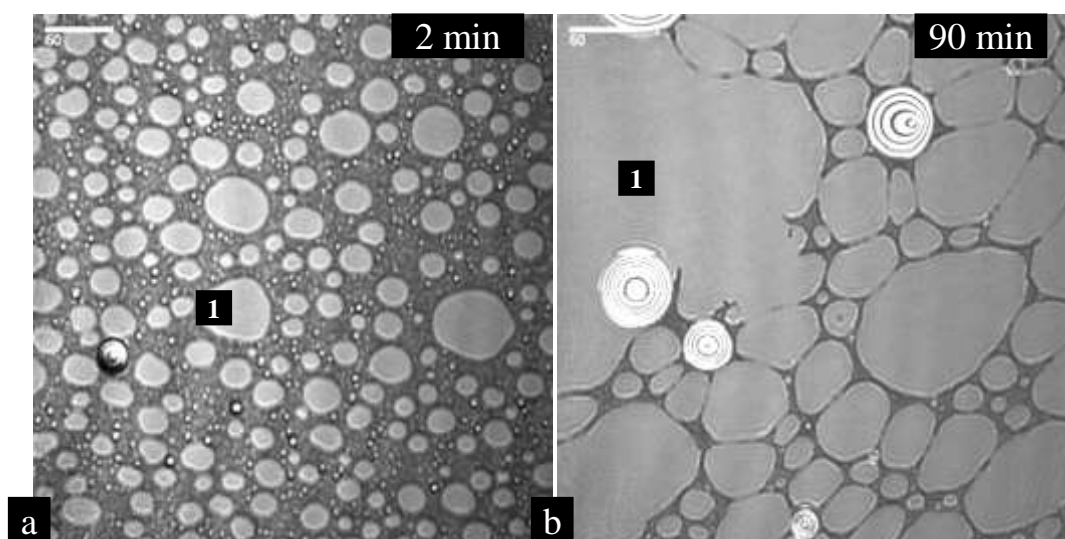


Figure **Error! No text of specified style in document.**10: Optical photograph during self-assembly of dodecanethiol gold nanoparticle array without addition of excess dodecanethiol to the colloidal solution at different times after drop-casting of colloidal solution (a and b). The initial patterns represent island formation, and even after 90 minutes, arrays with microscopic holes are formed. The scale bar represents 50 μm . The regions marked 1 represent the array.

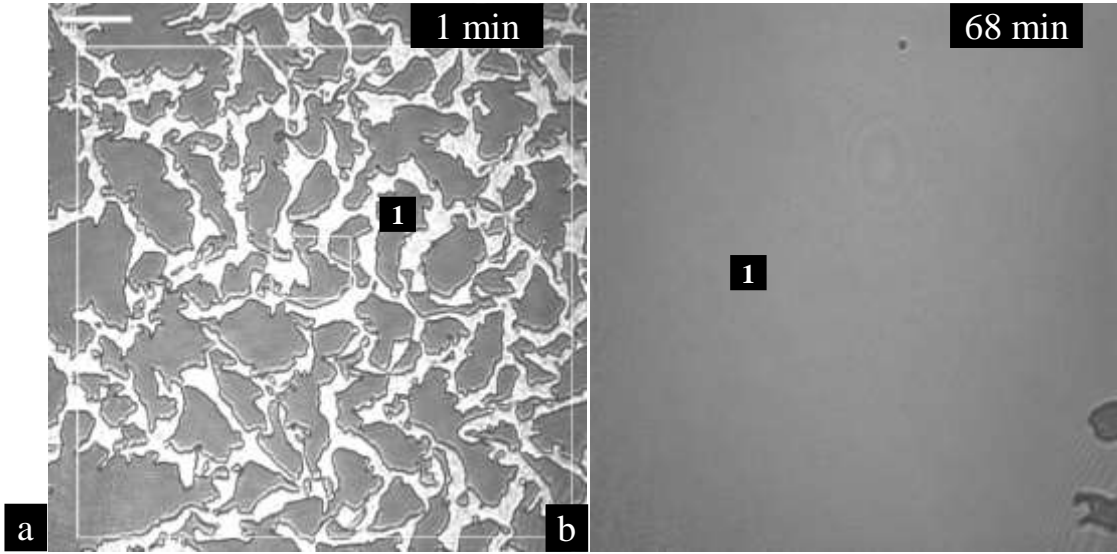


Figure **Error! No text of specified style in document..11**: Optical photograph during self-assembly of dodecanethiol gold nanoparticle array with the addition of excess dodecanethiol to the colloidal solution at different times after drop-cast of colloidal solution (a and b). The initial patterns represent labyrinthine-like structures, enabling large scale array formation. The scale bar in a represents 50 μm , and the same magnification is used for obtaining Fig. b. The regions marked 1 represent the array. The two concentric boxes (white line in a) represent the region of interest (ROI), where the ellipsometric data is measured.

Modelling of optical constants

The data from ellipsometry were modeled based on air-film-substrate three layer structures with water and gold film as substrate and layer stack respectively (Model 1). As long as the films are uniform, with known n and k (refractive and extinction index) values, finding the root of the quadratic equation as explained in the experimental section of ellipsometry in the previous chapter (see sec. 2.5.6) becomes trivial. However, “the gold film layer”, considered in this study is a highly inhomogeneous medium whose refractive indices cannot be determined directly. Alternatively, to treat the problem of macroscopically inhomogeneous medium, i.e., a medium in which bulk properties such as dielectric function, elastic modulus, conductivity etc. is varying in space, an effective medium approximation is employed. For example, in a metal-dielectric composite, consisting of collection of metallic and dielectric grains in a particular arrangement, the effective function is obtained by utilizing the component fractions. The derivation of effective dielectric constant involves solving equations for the electric field and dipole moment per unit volume and then volume-averaging. Depending on the direction of electric field, i.e., parallel or perpendicular, the averaging leads to optical equivalent of capacitors in parallel or in series,

$$\varepsilon = f_a \varepsilon_a + f_b \varepsilon_b \quad (3.1)$$

$$1/\varepsilon = f_a/\varepsilon_a + f_b/\varepsilon_b \quad (3.2)$$

where, ε represents dielectric constant of the medium and f represents volume fraction. The corresponding subscripts a and b represent respective properties of the two phases a and b , in the system. These expressions represent very crude approximations, because it represents two extreme cases, where either the local fields are parallel to the surface (no screening of charges) or perpendicular to the surface (maximum screening of charges). Modifications to this equation are accomplished by inclusion of a screening parameter, s , which is given by ($s = 1/\tilde{\alpha} - 1$, $0 < \tilde{\alpha} < 1$). In this equation, $\tilde{\alpha} = 0$ represents no screening while $\tilde{\alpha} = 1$ represents maximum screening.

$$\frac{\varepsilon - \varepsilon_h}{\varepsilon + s\varepsilon_h} = f_a \left(\frac{\varepsilon_a - \varepsilon_h}{\varepsilon_a + s\varepsilon_h} \right) + [1 - f_a] \left(\frac{\varepsilon_b - \varepsilon_h}{\varepsilon_b + s\varepsilon_h} \right) \quad (3.3)$$

Various models such as Maxwell-Garnett, Bruggeman, Lorentz-Lorenz etc. have been proposed in the literature depending on the way the host medium is accounted for in 3.3. In the Maxwell-Garnett model, the host medium is treated as one of the phases ($\varepsilon_h = \varepsilon_a$ or ε_b), while in the case of Bruggeman approximation, host medium is equated to the effective dielectric constant ($\varepsilon_h = \varepsilon$). In Lorentz-Lorenz approximation, host medium is equated to empty space ($\varepsilon_h = 1$). Lorentz-Lorenz approximation is used as the effective medium approximation in this study similar to an earlier report. The gold film is modeled (Model 1) as linear mixture composed of dodecanethiol capped gold nanoparticles dispersed in toluene matrix with an initial volume fraction of 0.01 (based on volume fraction of particle in the initial colloidal

solution). The value of 0.01 is used after rounding off the actual value 0.0065, as this is the least value which the EP4 software can accept as input. The dodecanethiol capped gold nanoparticles are treated as gold dispersed in dodecanethiol matrix with a volume fraction of 0.24 (obtained based on calculation of the ratio of average volume of gold core to the volume of dodecanethiol capped gold particle). The dispersion coefficients of standard gold and dodecanethiol were taken from the literature. Representative screen shots of the model fit to the ellipsometric data of phase change and amplitude ratio between the p- and s-polarized light data obtained 15 minutes after drop-casting of dodecanethiol gold nanoparticles on the water surface are shown in Fig. 3.12. During the data fit, “*unwrap delta*” option was used which essentially adds or subtracts 360° to the data to obtain a better fit. Ellipsometric data shows a decreasing trend of film thickness for both with and without excess surfactant (Fig. 3.13). The first data point could only be collected after 6 minutes due to the time associated with the focusing procedure. At 6 minutes, the thickness was 80 and 65 nm for the case of without and with excess dodecanethiol respectively, followed by a decrease to 50 nm after 1 hour. At the later stages, the replacement of toluene with air in the model did not fit the data well. This suggests the presence of toluene even though the film visually appears to be dry. Also, a different model is assumed, wherein gold film in the Model 1 was replaced with pure dodecanethiol capped gold nanoparticles (Model 2), a discernible difference of 20 and 7 nm was found at 6 minutes between the two cases with a final saturated film thickness of 6 nm (remarkably similar to the measured height by AFM, of 8 nm, shown later in the Chapter 4, Section 4.5.1).

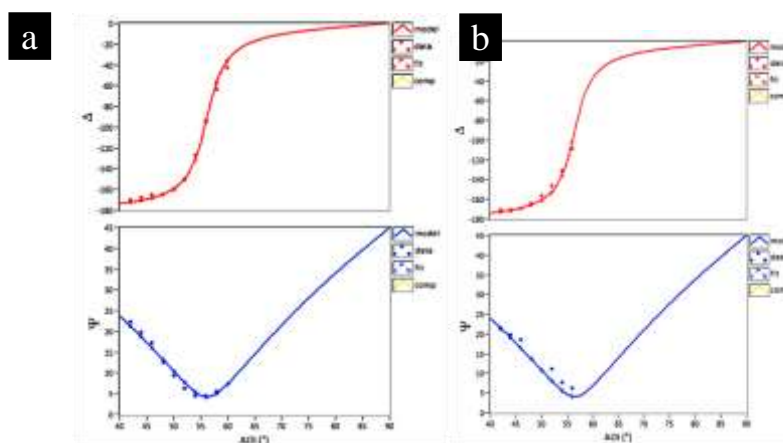


Figure **Error! No text of specified style in document..12**: Representative screen shots of EP4 model fit of ellipsometric data obtained after 15 minutes of drop-cast of dodecanethiol capped gold nanoparticles on the water surface containing, (a) without excess thiol and (b) with excess thiol to the colloidal solution.

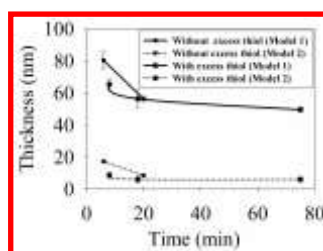


Figure **Error! No text of specified style in document..13**: Evolution of film thickness obtained using ellipsometry during self-assembly of dodecanethiol capped gold nanoparticles for both with and without addition of excess dodecanethiol. The exact thickness was found to depend on the model; however, the absolute difference of initial film thickness was observed in both cases. The points represent the mean of experimental data and the error bars represent 95 % confidence interval ($n=4$).

Thus, the evaporation rate is faster for the arrays fabricated with excess surfactant as a result of better spreading of the colloidal solution on the water surface. These results are contrary to the earlier report of delayed drying in the excess surfactant case. Also, the first data point was obtained after 6 minutes (time needed to focus the array and image collection), during which most of the possible intriguing aspects of self-assembly of nanoparticles might have taken place. A simple volume balance shows that 0.4 mL of colloidal solution if spread on the entire petridish of 9 cm diameter, will have a thickness of $\sim 80 \mu\text{m}$. The highest initial film thickness obtained from ellipsometric data is 80 nm, which is at least 3 orders of magnitude lower than the earlier computed value of $80 \mu\text{m}$. So, it can be surmised that the drastic changes in the film thicknesses can possibly occur in first few minutes and at even faster rate for self-assembly of dodecanethiol

capped gold nanoparticles containing excess dodecanethiol. At present, there is very little scope for further reduction of the time required for focusing; and thus, limits our ability to probe the dynamics of drying.

Large scale arrays of thiol-terminated polystyrene capped gold nanoparticles

In the results described thus far, the interparticle spacing in the 2D nanoparticle array was 2 nm, equivalent to chain length of dodecanethiol molecule (assuming interdigitation between the ligands on neighboring particles). Several applications demand tunable interparticle spacing in the nanoparticle arrays. Recently, thiol-functionalized polystyrene ligands with varying molecular weights were used to tune the interparticle spacing of self-assembled gold nanoparticle arrays over the range of 10–30 nm. Until now in our group, polystyrene capped gold nanoparticles were dispersed in a solvent mixture of chloroform-cyclohexane (50:50 by volume). The solvent mixture is selected based on their boiling point, density and miscibility of water in addition to solubility of nanoparticles in the organic solvent. The requirements include low boiling point (or vapor pressure) to aid faster evaporation, lower density and immiscibility with water so that it floats over the water surface (Table 3-1).

Recently, Yim and co-workers suggested toluene as a better solvent based on both the physical properties of the system and wettability of solvent on the substrate for placement of alkanethiol capped gold nanoparticles. For polystyrene, good solvents are chloroform, toluene, tetrahydrofuran; while dodecane, hexane, water are few bad solvents. Due to large spreading coefficient toluene on water in addition to favorable solubility parameter and physical properties, thiol-terminated polystyrene coated gold nanoparticles were dispersed in toluene instead of chloroform-cyclohexane mixture. The spreading coefficient is given by $S_{\text{solvent on water}} = \gamma_{\text{water-air}} - (\gamma_{\text{solvent-air}} + \gamma_{\text{solvent-water}})$, where γ denotes surface tension. For toluene on water, $S_{\text{toluene on water}} = 8.3 \text{ mN/m}$ ($\gamma_{\text{water-air}} = 72.8 \text{ mN/m}$; $\gamma_{\text{toluene-air}} = 28.4 \text{ mN/m}$; $\gamma_{\text{toluene-water}} = 36.1 \text{ mN/m}$), is positive which indicates toluene spreads on water better than hexane. Mukherjee et al. had shown when gold nanoparticles embedded in polystyrene matrix were spin-coated on silicon wafer, complete dewetting to absolute stability of the thin film were observed depending on the nanoparticle concentration. This indicates that colloidal particles can counteract the dewetting effects of polymer-solvent interactions. To counter the effects of polymer dewetting during array formation, 5 μL dodecanethiol was mixed with 0.4 mL toluene solution containing $\sim 10^{14}$ particles/mL of thiol-terminated polystyrene capped nanoparticles and drop-cast on petridish, along the lines of dodecanethiol experiments. Remarkably, dodecanethiol molecules replaced thiol-terminated polystyrene molecules, as seen from the range of interparticle spacing in Fig. 3.14. This result appears remarkable as dodecanethiol displaced thiol-terminated polystyrene groups within 5 minutes, the time taken for drying, as determined visually. However, it is conjectured that the presence of thin layer of toluene, as deduced from the results of ellipsometry, leads to this observation, as thin films of organic can also be transfer-printed along with the array onto the silicon substrate. To circumvent the ligand exchange problem, dodecanethiol was first drop-cast on the water surface before spreading thiol-terminated polystyrene (molecular weight: 20000) capped gold nanoparticles. Close-packed nanoparticle arrays were formed over the entire substrate, as shown in Fig. 3.15.

Table **Error! No text of specified style in document.-1**: Physical and chemical properties of commonly used solvents and ligands.

Material	Density	Solubility parameter (MPa ^{1/2})	Boiling point (°C)	Dielectric constant	Solubility in water (g/100g)
Toluene	0.87	18.2	110.6	2.38	0.05
Chloroform	1.5	19.0	61.7	4.81	0.795
Hexane	0.66	14.9	69	1.89	0.014
Cyclohexane	0.78	16.8	80.7	2.02	<0.1
Dichloromethane	1.33	20.2	39.8	9.08	1.32
Tetrahydrofuran	0.89	18.6	66	7.6	30
Ethanol	0.79	26.0	78.5	24.6	Miscible
Acetone	0.79	19.7	56.2	20.7	Miscible
Dodecane	0.75	16.2	216.3	2.0	Immiscible
Dodecanethiol	0.85	17.0	266-283	2.1	Immiscible
Polystyrene	1.06	21.3	Not available	2.6	Immiscible
Polystyrenethiol	0.9	~17-18	Not available	Not available	Immiscible

The values in the table have been extracted from

(a) MSDS compilations (see section II-B-4 of the Chemistry Webexercises Directory)

- (b) Tarasov, V. "Control of the self-assembly of alkanethiol-coated gold nanoparticles in the solid state.", BS Thesis, Massachusetts Institute of Technology, 2008.
- (c) Sherrington et al.
- (d) From chemical book database.

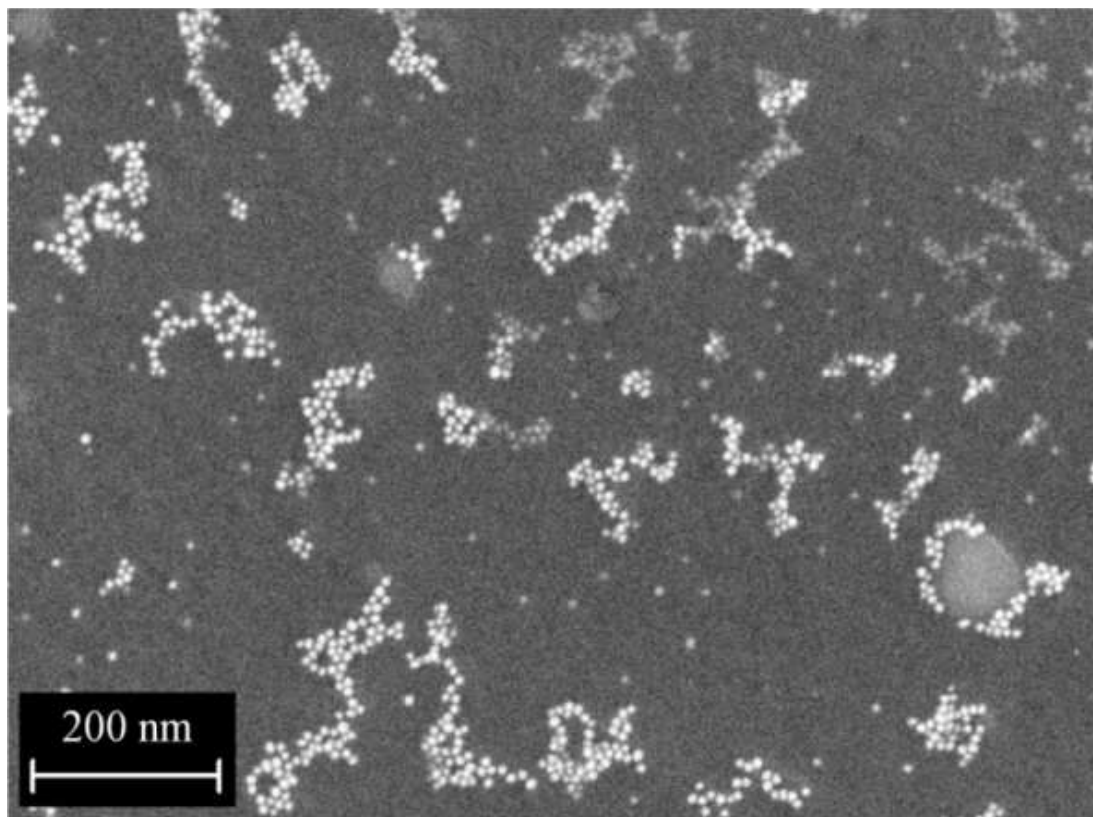


Figure **Error! No text of specified style in document.**14: Representative FESEM image of thiol-terminated polystyrene (molecular weight: 20000) capped gold nanoparticles dispersed in toluene (with 5 μ L dodecanethiol), floated on the water surface. The distance between particles is approximately 2 nm, corresponding to dodecanethiol chain length and not thiol-terminated polystyrene (molecular weight: 20000). This suggests that small molecule (DDT) had replaced long chain molecule (PSSH) within the time scale of minutes. Nevertheless, it can be seen that polymer/solvent dewetting is minimized.

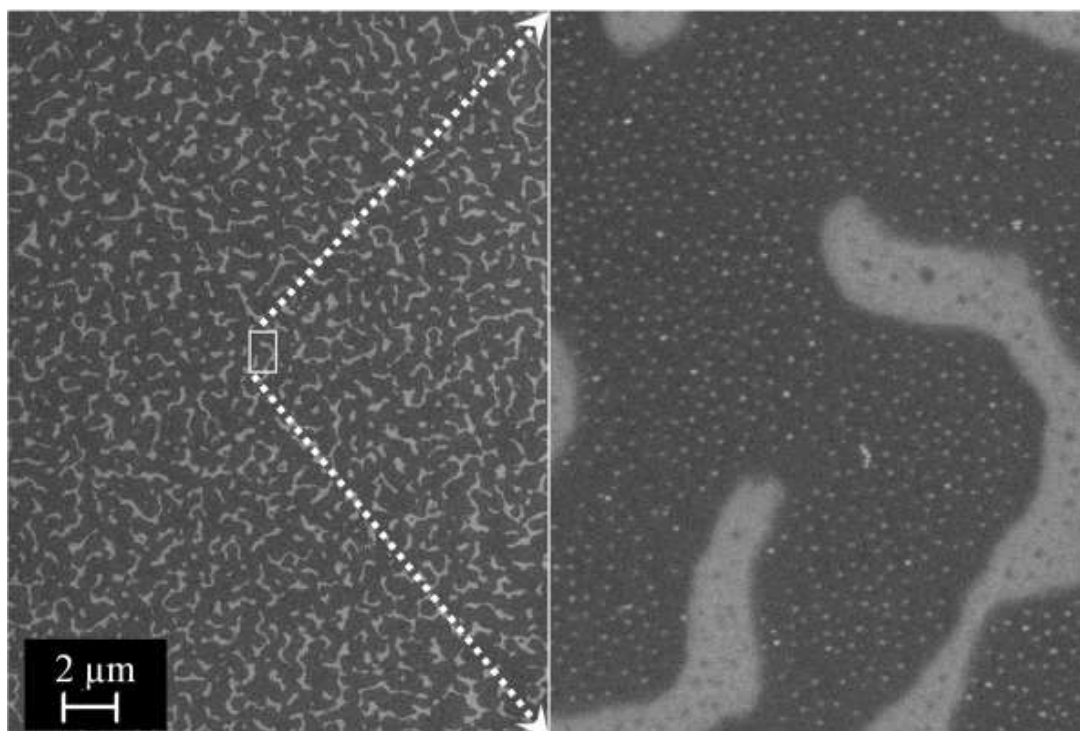


Figure **Error! No text of specified style in document.**15: Dual-magnification FESEM image of thiol-terminated polystyrene (molecular weight: 20000) capped gold nanoparticles dispersed in toluene floated on the water surface modified with 5 μL of dodecanethiol (Scale bar: 2 μm). The right side image represents the zoomed portion of the small box on the left side.

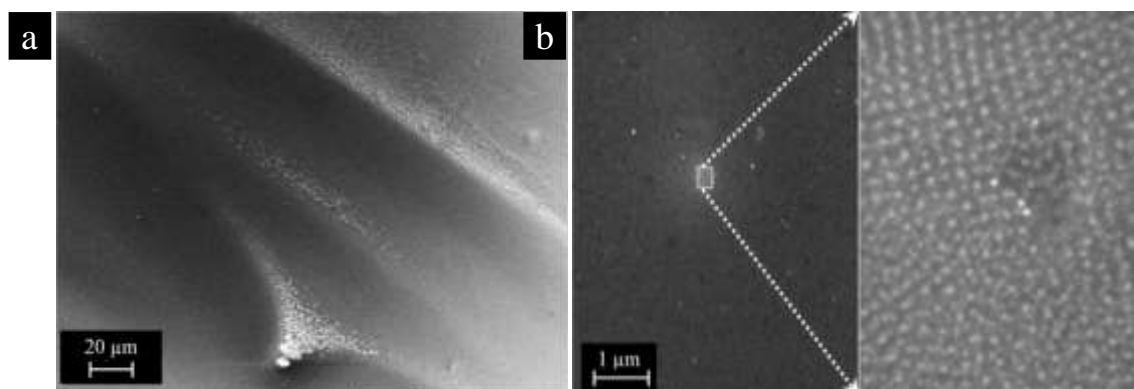


Figure **Error! No text of specified style in document.**16: (a) FESEM image of thiol-terminated polystyrene (molecular weight: 20000) capped gold nanoparticles dispersed in toluene drop-cast on Si/SiO₂ substrate (Scale bar: 20 μm). The bright regions represent bare silicon substrate while the dark regions correspond to array. It can be clearly seen that polymer/solvent dewetting is completely negated. (b) Dual-magnification FESEM image of thiol-terminated polystyrene (molecular weight: 20000) capped gold nanoparticles dispersed in toluene drop casted on Si/SiO₂ substrate (Scale bar: 1 μm). The right side image represents the zoomed portion of the small box on the left side. Most of the places, it can be seen on the right hand side of the image b, multilayer is formed.

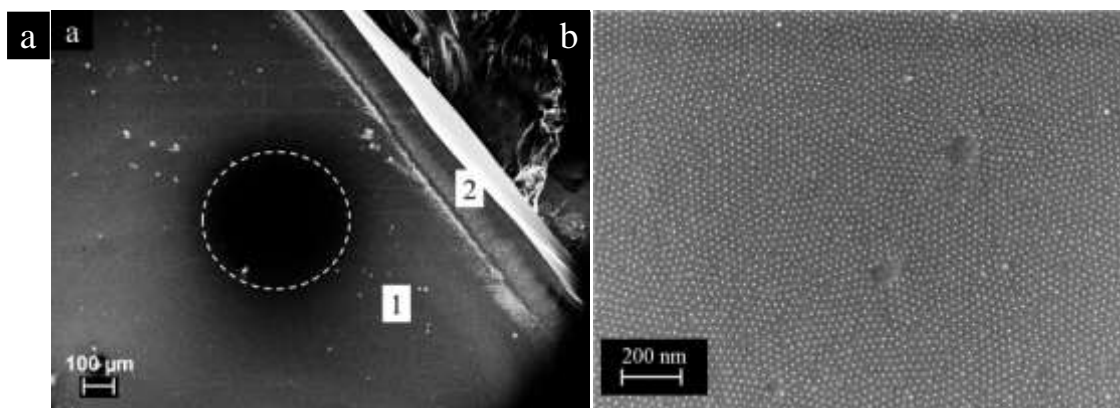


Figure **Error! No text of specified style in document.**17: (a) Low magnification FESEM image of thiol-terminated polystyrene (molecular weight: 20000) capped gold nanoparticles dispersed in toluene drop-casted on 10 minutes ozone treated Si/SiO₂ substrate (Scale bar: 100 μm). The two regions marked 1 and 2 represent array and bare silicon substrate respectively. The outlined region (circle) is attributed to the blind spot of the Inlens detector used for detecting secondary electrons. It can be clearly seen that polymer/solvent dewetting is completely negated. (b) High magnification FESEM image of thiol-terminated polystyrene (molecular weight: 20000) capped gold nanoparticles dispersed in toluene drop-cast on 10 minutes ozone treated Si/SiO₂ substrate (Scale bar: 200 nm).

Further, to completely avoid dewetting problem, thiol-terminated polystyrene (molecular weight: 20000) capped gold nanoparticles in toluene was drop cast on Si/SiO₂ (~10 nm oxide) substrate instead of dodecanethiol modified water surface. In fact, the contact angle hysteresis (difference between the advancing and receding contact angle) for polystyrene dispersed in toluene on silicon was found to be 2°, indicating a high degree of spreading¹²⁶. As surmised, no dewetting of nanoparticle array was observed, as shown in Fig. 3.16. However, the assemblies were found to be multilayer of nanoparticles which can be attributed to the drying of drop in a localized position. Next, silicon wafer was treated with UV-Ozone (Jelight 42, UVO cleaner) for 10 minutes so that the droplet can spread into a uniform thin film. As expected, the drop-casting resulted in uniform monolayer of nanoparticle arrays, as shown in Fig. 3.17. In summary, polymer dewetting can be completely avoided depending on the substrate affinity towards nanoparticles. Also, monolayer can be formed without losing particles. Thus, a simple and scalable process for fabricating large-scale, ordered, 2D arrays of gold nanoparticles upon drop-casting the colloidal sample was developed.

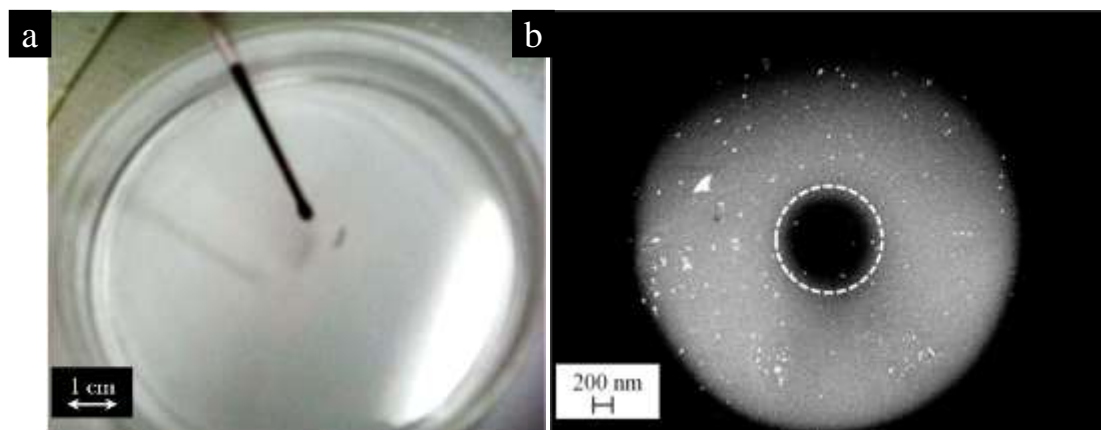


Figure **Error! No text of specified style in document.**18: (a) Digital photograph of drop-cast of thiol-terminated polystyrene capped gold nanoparticles dispersed in toluene on flat water surface in a petridish. (b) Low magnification FESEM image of the self-assembled 2D arrays formed by drop-casting gold nanoparticles dispersed in toluene onto a silicon substrate. The outlined region (dotted circle) in b is the blind spot of the in-lens detector used for detecting secondary electrons.

Tunable interparticle spacing in nanoparticle arrays

Polymer grafted nanoparticle self-assembly combines the benefits of ligand protected nanoparticle self-assembly with that of diblock copolymer micelles self-assembly, i.e. the ease and versatility of processing with that of tunable interactions with the environment. The self assembly of ligand protected nanoparticles from an evaporating colloidal solution is shown to occur at the solvent-air interface, and the substrate roughness, but not its other physico-chemical properties, is

reported to affect the particle ordering in the dried film. In contrast, the self-assembly of diblock copolymer micelles is reported to be affected by polymer-substrate interactions leading to controllable changes in particle spacing and the ordering. Given the versatile and 'hybrid' nature of polymer grafted nanoparticles, it is vital to understand the mechanism as well as various factors affecting their self-assembly into ordered arrays. However, until now there are only a few relevant reports on self-assembly of polymer grafted nanoparticles wherein the interparticle spacing in arrays is tuned by altering the ligand length, but none on the effect of substrate.

To elucidate the mechanism of self-assembly, the effect of substrate on the ordering of nanoparticle arrays formed by drop casting from a polymer grafted nanoparticle solution was studied. In the following, the results of characterization, using the complementary techniques of atomic force microscopy (AFM) and field-emission scanning electron microscopy (FESEM), of nanoparticle arrays formed by polystyrene thiol (average molecular weight 20000 g/mol) grafted gold nanoparticles (7 nm diameter) on three different substrates and also using different solvents is presented.

Substrate effects

Thiol-functionalized polystyrene grafted gold nanoparticles were dispersed in toluene, and 5 μ L drops were cast on three different substrates, namely, silicon, graphite and water (Fig. 3.18). The toluene drops spread rapidly into a uniform thin film (due to favorable vdW interactions and large spreading coefficients), and resulted in the formation of a monolayer of gold nanoparticles after solvent evaporation (~ 1 min), over macroscopically large areas. The monolayer formed on the water surface was transferred onto a silicon substrate by microcontact printing for further characterization.

Representative FESEM images are shown in Fig. 3.19a-f. The average interparticle spacing (edge to edge distances) were determined to be 20.0, 14.5 and 10.0 nm on silicon, graphite and water, respectively (Fig. 3.19g). Shoulders in the histograms are observed due to presence of doublets (formed by particle aggregation during phase transfer of particles from aqueous to organic medium) that are manually removed after thresholding leading to vacant sites and concomitantly to larger estimates of interparticle spacing. The average thicknesses of the thin films were found to be 23.0 ± 1.1 , 21.0 ± 0.9 and 23.3 ± 1.1 nm, respectively (Fig. 3.20a-c). The respective histogram values over the entire AFM scan area were found to be 21.7 nm, 19.3 nm and 23.7 nm (Fig. 3.20e-g). These values can be considered equal to each other. The measured height is lower than the mean hydrodynamic size (d_h) of thiol-functionalized polystyrene grafted gold nanoparticles in toluene (29 nm based on DLS measurement, Fig. 3.20h). This difference could be attributed to the dry state of the films compared to solvated conditions under which hydrodynamic diameter are measured. Also, the interactions of the polystyrene ligand with the substrate can account for the observed reduction in the height of the nanoparticle films, in comparison with the corresponding hydrodynamic diameters. So, it can be surmised that the height of the nanoparticle film is determined only by the hydrodynamic diameter of the colloidal nanoparticles in solution, which implies that the polymer configuration in the vertical plane will be similar to that adopted in a good solvent, i.e. a slightly extended brush configuration. Furthermore, based on the interparticle spacing data, the polymer chains tethered on adjacent nanoparticles and facing each other barely touch on a silicon substrate, whereas for arrays formed on graphite and water they are compressed by 25% and 50%, respectively, assuming very little interdigitation.

Solvent effect

To ascertain the generic nature of these observations, a further three experiments were carried out, namely, thiol-functionalized polystyrene grafted gold nanoparticles: i) were dissolved in tetrahydrofuran and then spread on a silicon substrate, ii) were dissolved in a 50 % (v/v) mixture of chloroform/cyclohexane and spread on water, iii) were dissolved in toluene and spread on a water surface, modified *a priori* by casting a thin layer of low molecular weight (3000 g mol⁻¹, Polymer source Inc.) thiol-functionalized polystyrene to mimic a floating graphite film (Fig. 3.21a-f). The average interparticle spacing (edge to edge distances) were 16.7, 13.3 and 13.1 nm for these three cases, respectively (Fig. 3.21g). The heights of the nanoparticle monolayer films were 13.4 ± 0.8 , 29.1 ± 1.5 and 22.0 nm respectively (Fig. 3.22a-c), while the corresponding film thickness from the histogram maps were found to be 14.0 nm, 27.9 nm and 20.4 nm (Fig. 3.22d-f); these values correlate well with the corresponding mean hydrodynamic diameters of the gold colloids in solution, viz. 16 nm (Fig. 3.22g), 35 nm (Fig. 3.22h) and 29 nm (Fig. 3.20h), respectively. Therefore, these results unequivocally demonstrate that the nature of the substrate only affects the compression of polystyrene ligands in-plane and thereby the particle spacing, whereas solvent-polystyrene interactions alone control the height as well as the uncompressed spacing of the self-assembled 2D arrays (Fig. 3.23). In arriving at these conclusions, the vdW interactions of the gold core with substrate and between two gold cores were not considered as the separation distances are typically greater than 10 nm.

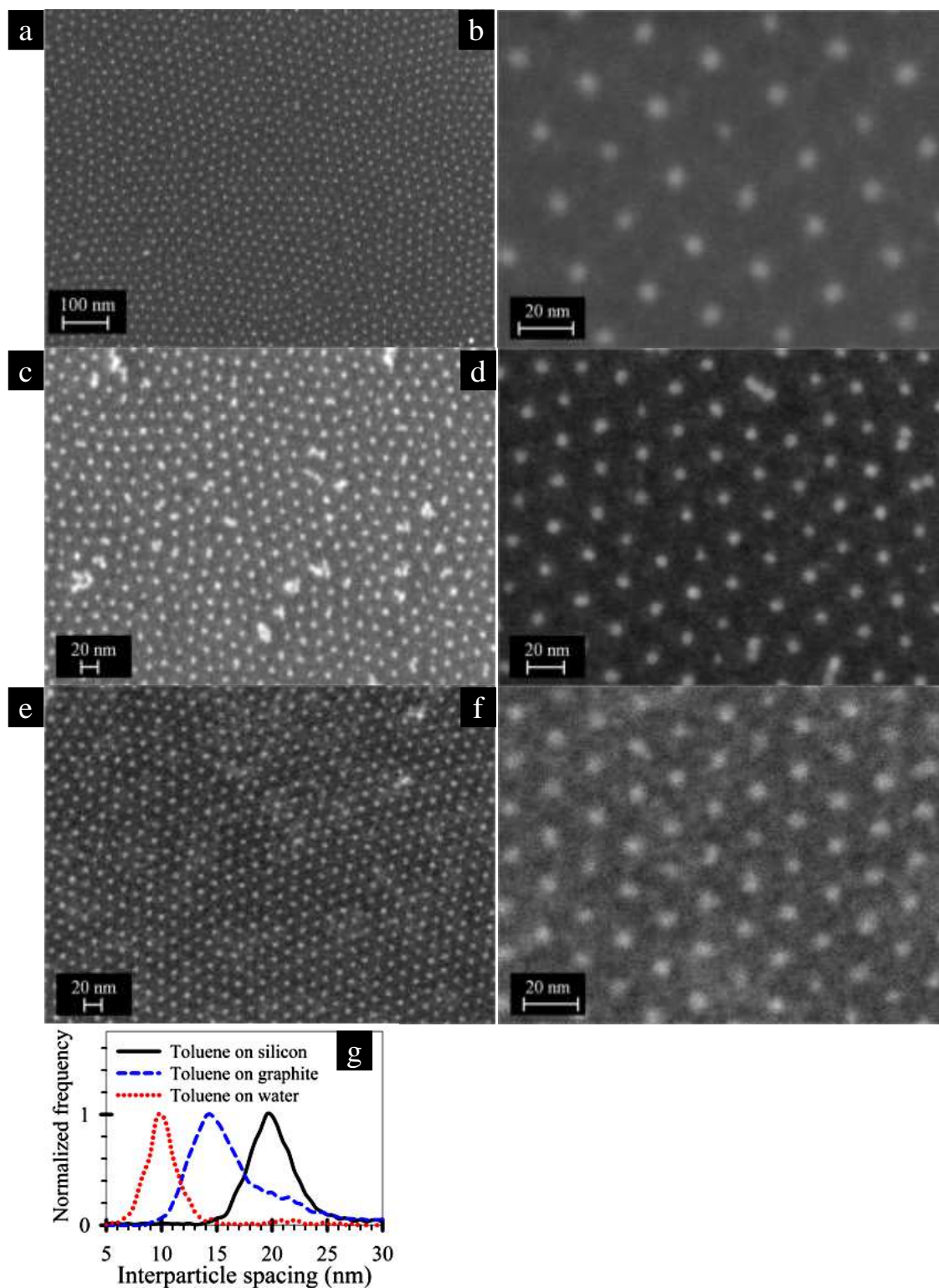


Figure **Error! No text of specified style in document.**19: Representative FESEM images of self-assembled 2D arrays of thiol-functionalized polystyrene grafted gold nanoparticles (a–f) and their corresponding interparticle spacing distributions (g). These 2D arrays were formed by drop-casting gold nanoparticles from: a,b) toluene solution onto a UVO treated silicon substrate (with native oxide), c,d) toluene solution onto freshly cleaved graphite, e,f) toluene solution onto water.

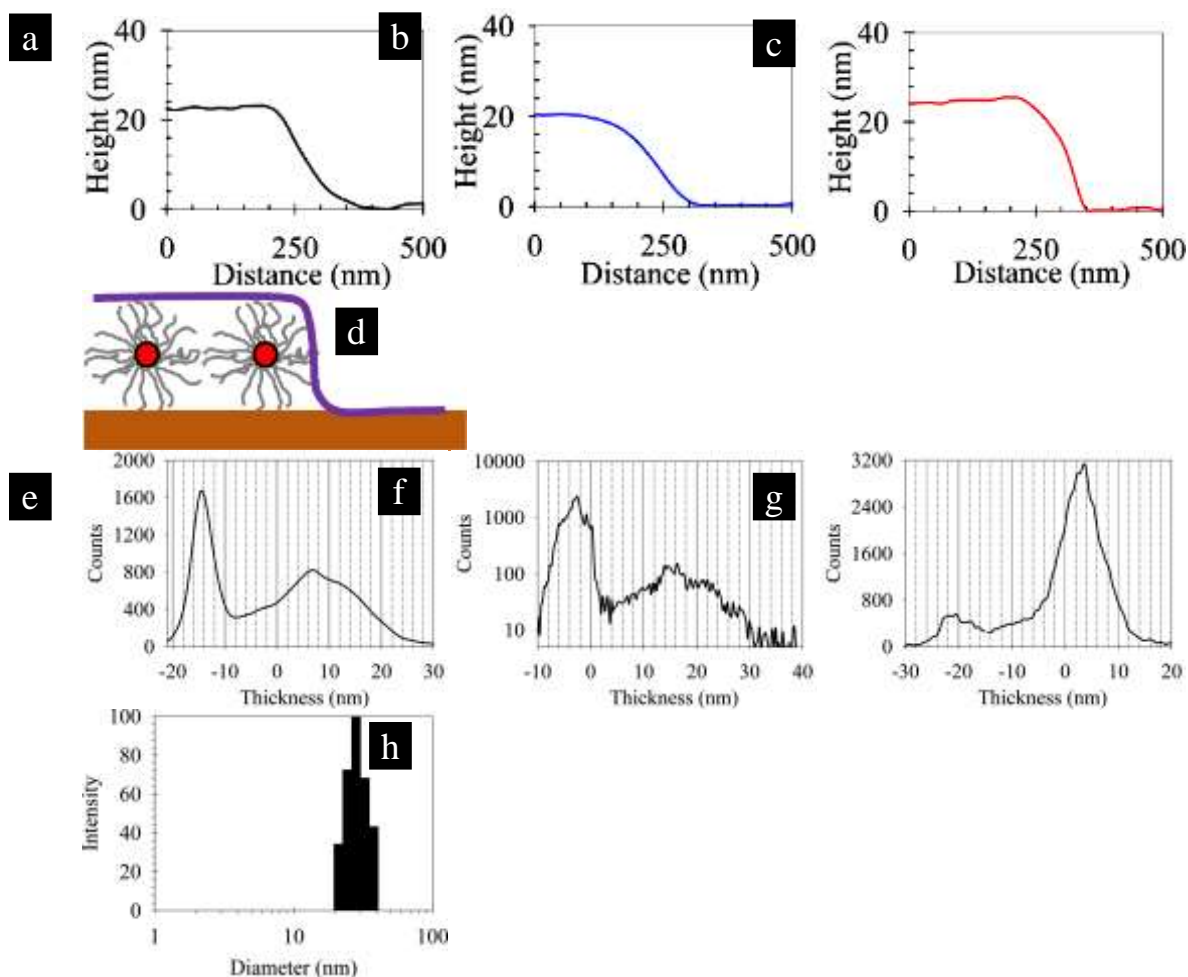


Figure **Error! No text of specified style in document..20**: AFM cross-section profiles across arrays formed by drop-casting gold nanoparticles from: a) toluene solution onto a UVO treated silicon substrate (with native oxide), b) toluene solution onto freshly cleaved graphite, c) toluene solution onto water. (d) Schematic representation of AFM cross-section profile across nanoparticle array. AFM histogram map of the thickness profile of the array over the entire area for colloidal solution drop-cast onto a (e) silicon substrate (with native oxide), (f) freshly cleaved graphite and (g) water. The respective thicknesses are 21.7 nm, 19.3 nm and 23.7 nm, which are in agreement with the AFM line thickness values of 23.0 nm, 21.0 nm and 23.0 nm. (h) DLS size histogram of thiol-terminated polystyrene capped gold nanoparticles dispersed in toluene.

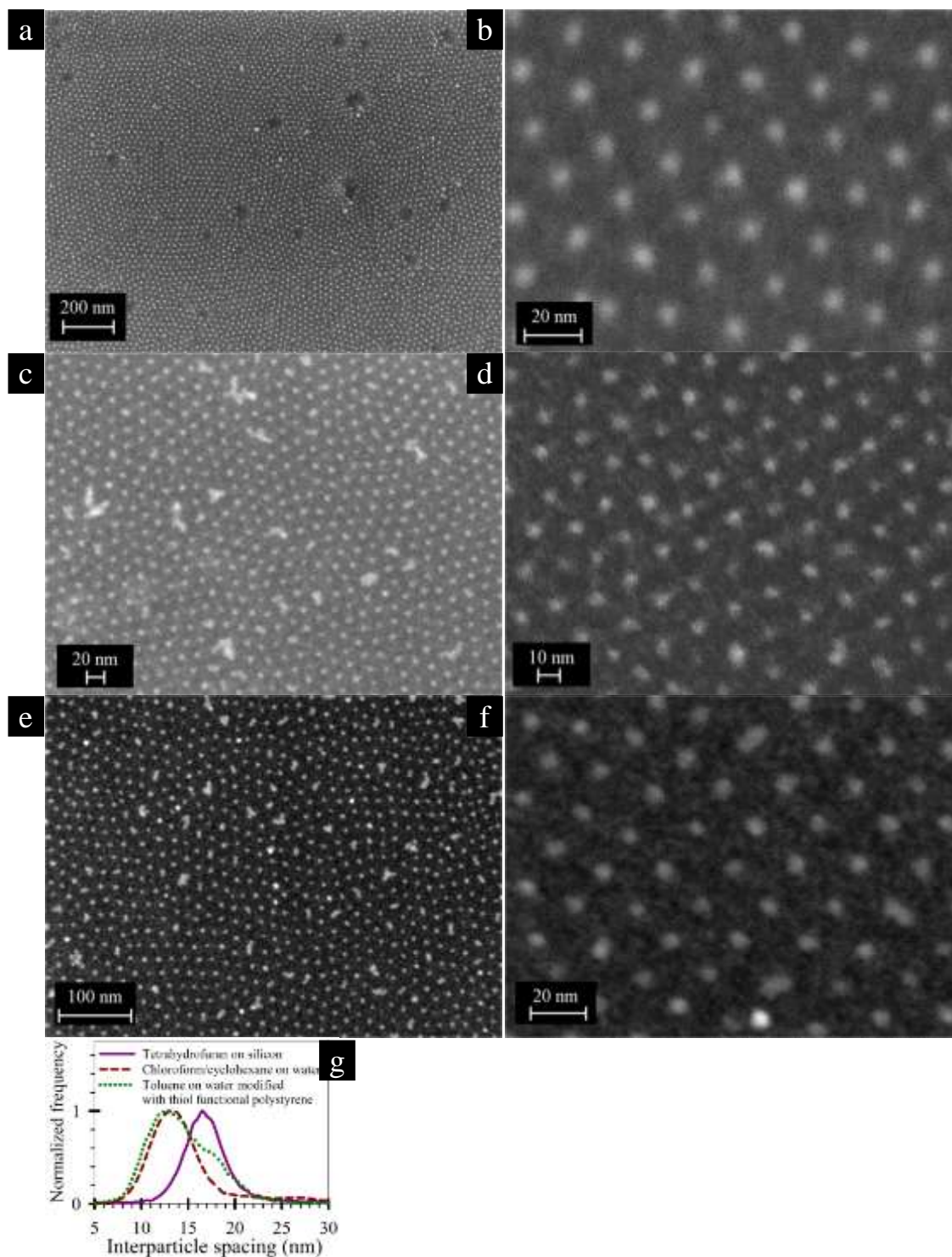


Figure **Error! No text of specified style in document.**21: Representative FESEM images of self-assembled 2D arrays of thiol-functionalized polystyrene grafted gold nanoparticles (a–f) and their corresponding interparticle spacing distributions (g). These 2D arrays were formed by drop-casting gold nanoparticles from: a,b) tetrahydrofuran solution onto silicon (with native oxide), c,d) 50% (v/v) chloroform/cyclohexane solution onto water, and e,f) toluene solution onto a water surface that was *a priori* modified with a thin film of thiol-functionalized polystyrene.

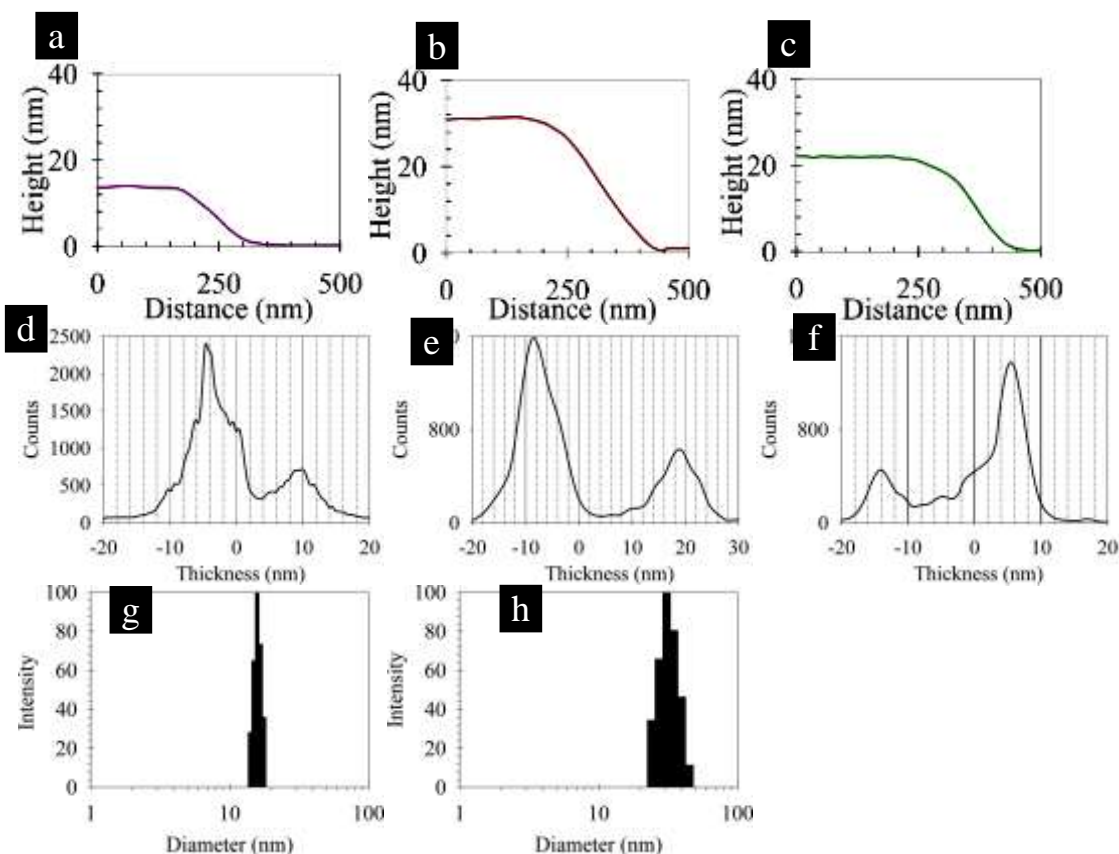


Figure **Error! No text of specified style in document..22**: AFM cross-section profiles across arrays formed by drop-casting gold nanoparticles from a) THF solution onto silicon, b) 50% (v/v) chloroform/cyclohexane solution onto water, and c) toluene solution onto a water surface that was *a priori* modified with a thin film of thiol-functionalized polystyrene. AFM histogram map of the thickness profile of the array over the entire area for colloidal solution drop-cast using d) THF solution onto silicon, e) 50% (v/v) chloroform/cyclohexane solution onto water, and f) toluene solution onto a water surface that was *a priori* modified with a thin film of thiol-functionalized polystyrene. The respective thicknesses are 14.0 nm, 27.9 nm and 20.4 nm, which are in agreement with the AFM line thickness values of 13.4 nm, 29.1 nm and 22.0 nm. DLS size histogram of thiol-terminated polystyrene capped gold nanoparticles dispersed in (g) THF and (h) 50% (v/v) chloroform/cyclohexane.

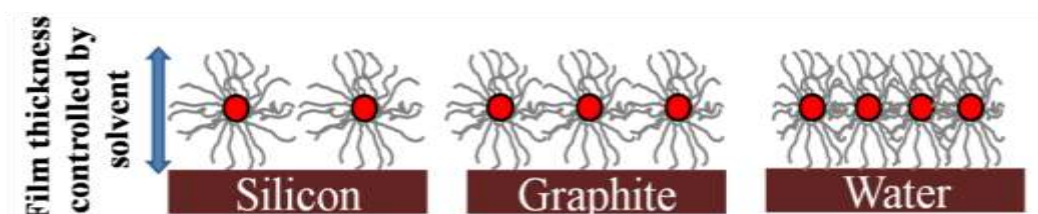


Figure **Error! No text of specified style in document..23**: Illustration summarizing the substrate effect on interparticle spacing in 2D arrays formed by drop-casting a colloidal solution of thiol-functionalized polystyrene grafted gold nanoparticles.

Mechanical properties of the nanoparticle array

The mechanical properties of the nanoparticle arrays were characterized by force spectroscopy. Representative force-displacement curves, obtained from samples cast using toluene as the solvent, are shown (Fig. 3.24). For the arrays formed on graphite and water, the hysteresis observed in the force curves (Fig. 3.24b,c) are similar to that expected for bulk polystyrene. In the other cases, the curves exhibit predominantly an elastic response, without any discernible hysteresis, similar to the response found on bare silicon and also silicon surface coated with a thin film of polystyrene thiol (Fig. 3.25). The pull-off forces were in the range of 20–40 nN in all cases, as expected for polystyrene. It is known that the elastic modulus of polymers near a free surface (length scale ~ 10 – 20 nm) is lower than that of the bulk, due to enhanced mobility of polymer segments near a free surface. The observed bulk polystyrene like mechanical behavior of

the arrays formed on water, and graphite points to a reduction in the mobility of polymer segments, as can be expected for compressed polymeric chains, which further confirms the conclusions based on FESEM data.

It was found that the substrate interactions significantly affect the interparticle spacing, ranging from 20 nm on silicon to 10 nm on a water surface, whereas, the height of the resultant thin film was found to be independent of substrate used and to correlate only with the hydrodynamic diameter of the polymer grafted nanoparticle in solution. The mechanical properties of the nanoparticle thin films are also significantly altered by such compression of the polymer ligands. The effect of substrate on altering the interparticle spacing has been reported in the case of arrays formed from diblock-copolymer micelles. However, changes in inter-micellar spacing is found to lead to corresponding changes in the height of the micellar film, and in some cases, even a loss of micellar structure is reported. This is attributed to changes in enthalpic contributions caused by a change in the polar component of the surface energy of the substrate, and the ability of the diblock copolymers to sample these configurations. The key difference between the present investigation and the aforementioned study on diblock copolymer micelles is the rigid nature of the “polar” component (i.e. gold nanoparticle). This results in a constant value for the polymer coating thickness that is proportional to the brush length in solution. The loss of configurational entropy of tethered polymer brushes near the tether point provides the driving force for overcoming unfavorable enthalpic contributions on different substrates, accounting for the observed substrate independence of the film thicknesses.

Mechanism of self-assembly of nanoparticle arrays

In order to further understand the effect of substrate on the self assembly process, a sample was prepared by transferring a partially dry film spread on a water surface (Fig. 3.26a). The representative FESEM image shows an interface (highlighted by the dashed curve in Fig. 3.26b) between two distinct domains: a disordered multilayer domain and a monolayer domain. It is postulated that this interface is the drying front formed during the evaporation of solvent, and that it is not affected by the transfer process as whatever solvent that remains in this zone is expected to be trapped within the polymer brushes and so, will be immobile. Note, the pattern formed by nanoparticles in domains where excess solvent was observed visually is mostly random in nature, and similar to multi-layered deposits reported previously as “coffee stains” (Fig. 3.26c). It is seen that nanoparticle ordering is only found in domains where the solvent has mostly evaporated, and that it is disordered on the other side of the interface with a few particles seemingly very close to one another. The closer than expected spacing is attributed to the presence of disordered multilayers, and their projection onto a 2D image. Also, the interparticle spacing is found to be slightly smaller near the perimeter of empty holes (Fig. 3.26b, inset). This is attributed to the lack of symmetric forces on the particles near the edges. All these observations indicate that ordering due to capillary forces between partially immersed nanoparticles is the probable mechanism of self-assembly (Fig. 3.27). This section described the role of substrate modulated van der Waals (vdW) interactions and substrate-solvent miscibility on the geometry and mechanical properties of the nanoparticle array, and proposes capillary interaction between partially immersed nanoparticles as the mechanism for self-assembly of polymer grafted nanoparticles.

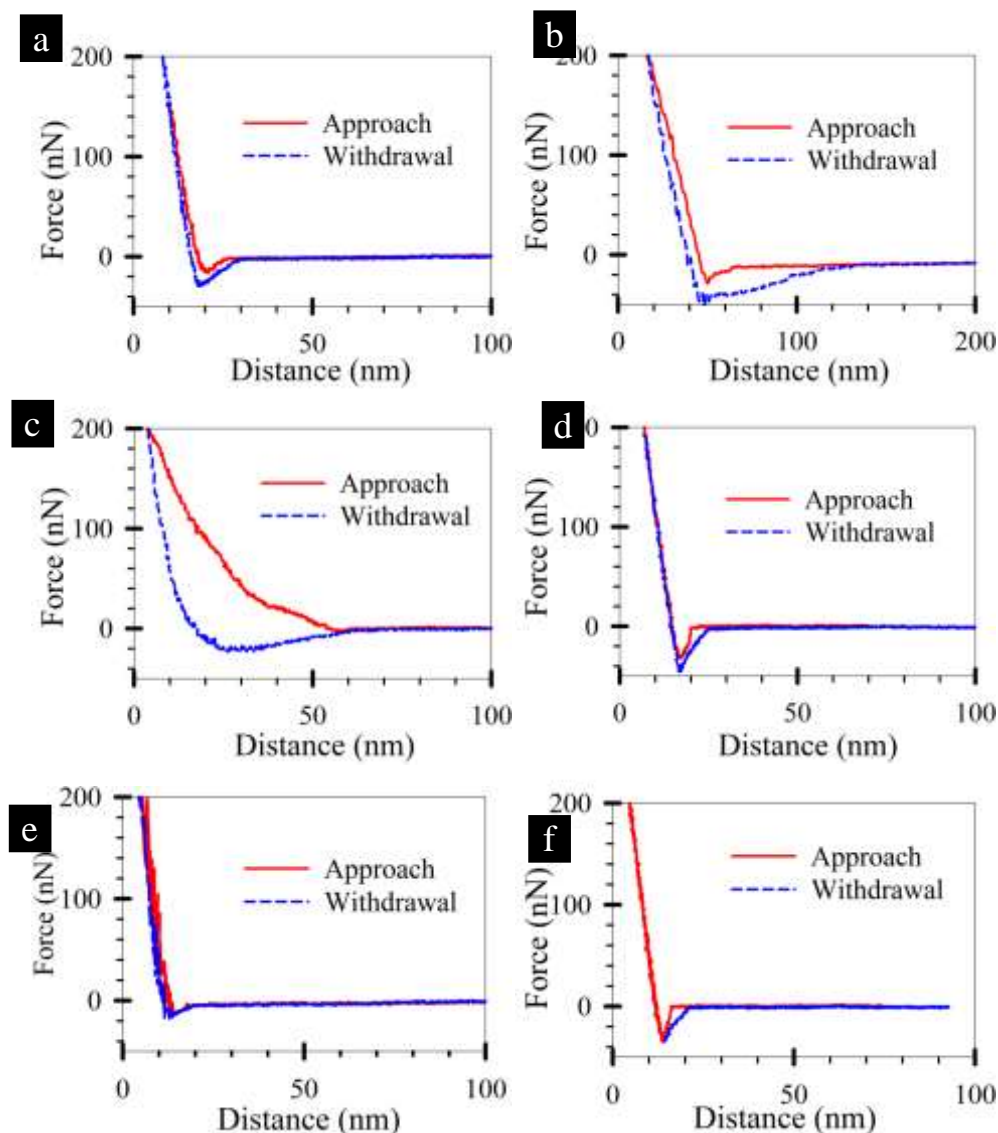


Figure **Error! No text of specified style in document.**24: Representative force-displacement curves measured on top of nanoparticle films formed by drop casting a thiol-functionalized polystyrene grafted gold nanoparticles in toluene onto: a) silicon (with native oxide), b) freshly cleaved graphite, c) water, d) water surface that was *a priori* modified with a thin film of thiol-functionalized polystyrene (average molecular weight: 3000 g/mol), (e) silicon substrate and (f) 'silicon' region presumed to be polystyrene thiol coated, due to transfer printing from the water surface modified *a priori* with polystyrene thiol molecules.

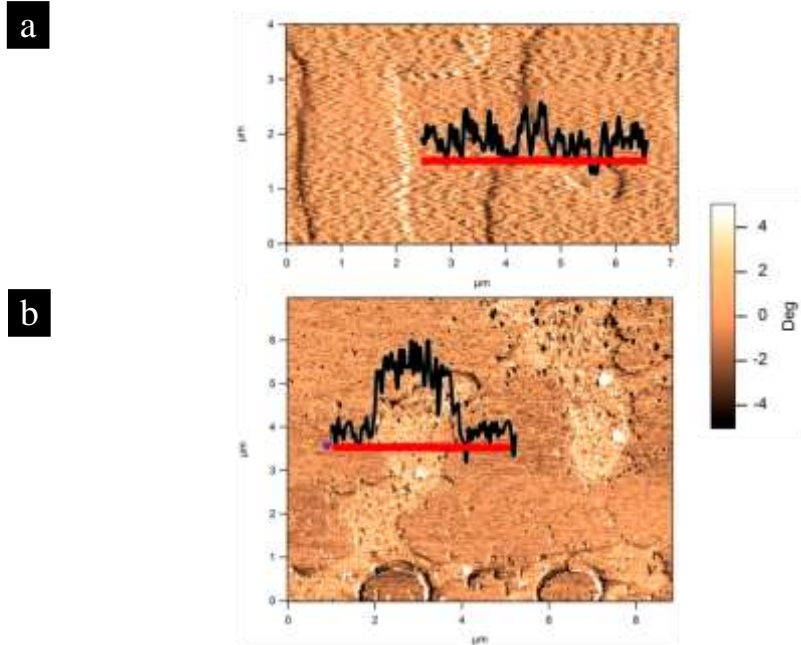


Figure **Error! No text of specified style in document.**25: Representative AFM phase scans, from the edges of self-assembled 2D arrays formed by drop-casting gold nanoparticles from (a) toluene solution onto a water surface that was *a priori* modified with a thin film of thiol-functionalized polystyrene, (b) tetrahydrofuran solution onto silicon (with native oxide). The phase profiles along the length of the corresponding straight lines are shown as overlays. Negligible phase difference in (a) clearly suggests the transfer of polystyrene thiol molecules in addition to array from the water surface.

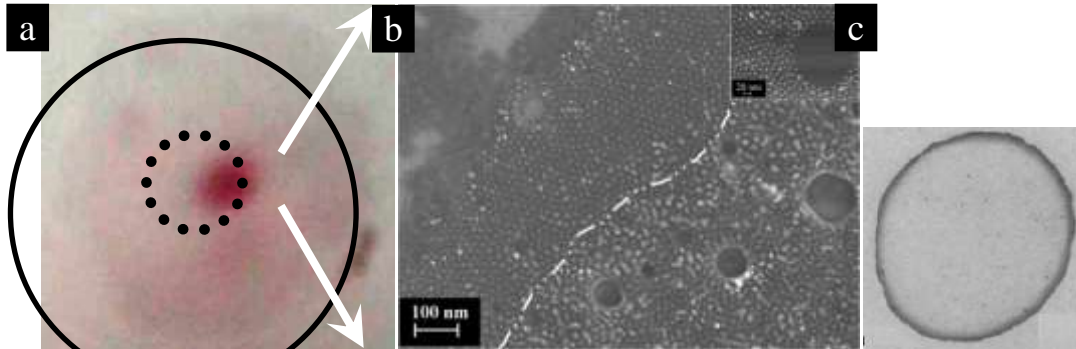


Figure **Error! No text of specified style in document.**26: (a) Digital photograph recorded during the self-assembly of gold nanoparticles on the water surface, with partial evaporation of the solvent. The region between the dotted and solid circle represent the region of partially dried film. (b) FESEM image of the nanoparticle thin film formed by transfer printing prior to complete evaporation of solvent from a colloidal solution spread on water. The dashed curve marks the putative evaporating front. The inset shows a magnified view of the arrangement of particles around a hole. (c) Optical photograph illustrating “coffee stain effect”, image reproduced from reference¹³⁶.

Capillary immersion forces - Background

Capillary forces between particles at the interface have been studied both experimentally and theoretically. Studies on the mechanism of self-assembly of 2D micron-sized, latex particles (by Nagayama’s group) have led to extensive research in this area. The deformation of the flat film surface, due to the presence of particle, is the origin of the lateral capillary force. Depending on whether the particle is floating or immersed in the liquid surface, it can be termed as capillary flotation or capillary immersion force (Fig. 3.28). Further, depending on the slope of the meniscus and the contact line, the forces can be either attractive or repulsive.

The lateral capillary force between two particles of radius R_1 and R_2 , with a centre-to-centre spacing of L is given by,

$$F = 2\pi\gamma Q_1 Q_2 q K_1(qL)[1 + O(q^2 R^2)] \quad (3.4)$$

The capillary length is given as

$$q^2 = \Delta\rho g / \gamma \quad (\text{for thick films}) \quad (3.5)$$

$$q^2 = (\Delta\rho g - \Pi') / \gamma \quad (\text{for thin films}) \quad (3.6)$$

where Π' represent the derivative of the disjoining pressure with respect to the film thickness.

Substituting the respective expression for capillary length for flotation and immersion forces for equal size particles, the following expression can be derived,

$$F \propto (R^6/\gamma)K_1(qL) \text{ for flotation force} \tag{3.7}$$

$$F \propto \gamma R^2K_1(qL) \text{ for immersion force}\tag{3.8}$$

The nomenclature of symbols used in this section is presented in Table 3-2.

So, it can be seen that in the limiting cases, for nanoparticles, floatation forces might be insignificant while the immersion forces can be two orders higher than k_BT . This functional dependence is plotted in Fig. 3.29.

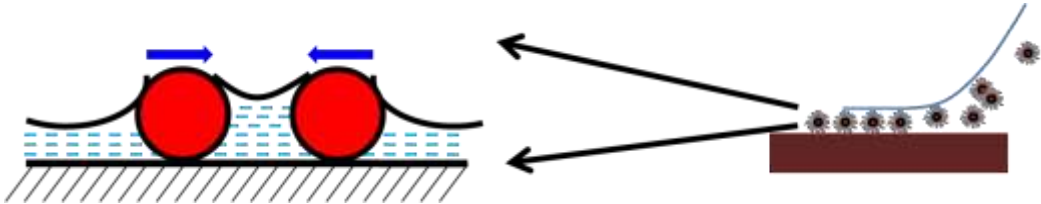
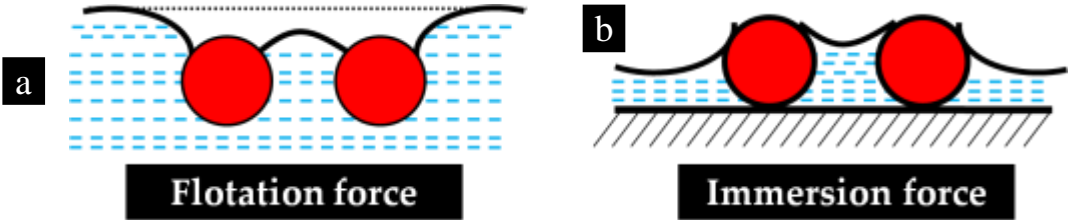


Figure **Error! No text of specified style in document.**27: Schematic representation of attractive capillary immersion forces during self-assembly of thiol-terminated polystyrene capped gold nanoparticles.



Figure**Error! No text of specified style in document.**28: Schematic representation of attractive or repulsive capillary immersion and floatation forces depending on the meniscus slope and contact line (adapted from Kralchevsky et al.).

Table **Error! No text of specified style in document.**-2: List of symbols and the respective nomenclature, used in this section.

Symbol	Nomenclature
γ	Solvent surface tension
Q	Capillary charge of particle
L	Centre-to-centre spacing
q^{-1}	Capillary length
π	Disjoining pressure
A_H	Hamaker constant of substrate with air across solvent
l_o	Film thickness
c	Core radius
λ	Thiol foot-print diameter
δ	Brush thickness
K	Bessel function

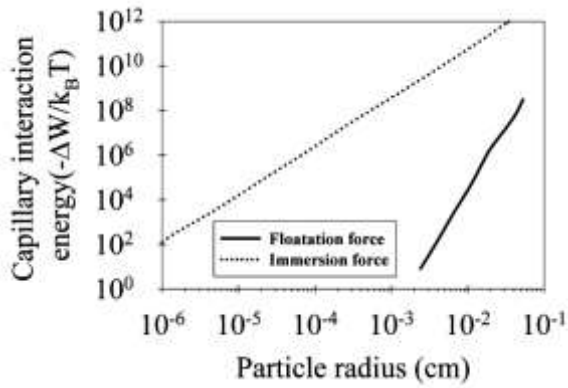


Figure **Error! No text of specified style in document.**29: Plot of capillary interaction energy, ΔW and particle size, R , at fixed interparticle distance of $L = 2R$, for capillary immersion and floatation forces (Reproduced with permission from Kralchevsky et al.. Copyright (1994) IOP Publishing).

Predictions based on model for computing capillary immersion energy show that the mechanism of lateral capillary forces due to partial immersion can account for the attractive component that bring nanoparticles into contact and order them. At the length scales involved (> 10 nm gaps between metal cores), attractive van der Waals interactions can be neglected. The limiting form of the capillary immersion energy between two equal sized spherical particles of size R is given by (proposed by Paunov and coworkers),

$$\Delta W_{cap} = 2\pi\gamma Q^2 \ln(1.78q L/2) \quad (3.9)$$

where, γ , L , Q and q^{-1} represent the solvent surface tension, centre to centre distance of the particles, capillary charge of the particle (assumed to be $0.7R$), and the capillary length respectively.

The capillary length is defined by the following relation

$$q^2 = (\Delta\rho g - \Pi'/\gamma) \quad (3.10)$$

where, $\Delta\rho$ represents the density difference between nanoparticle and solvent. For thick films, the disjoining pressure component can be neglected while for thin films, as in the current study, the derivative of disjoining pressure with respect to the film thickness l_0 has to be accounted for in estimating the capillary length.

The disjoining pressure is given by

$$\Pi = A_H/6\pi l_0^3 \quad (3.11)$$

where, A_H represents the compound Hamaker constant for the interaction of the substrate with air across the solvent. Steric repulsion between two particles due to compression of polystyrene ligands is the most significant amongst the repulsive forces opposing the capillary immersion forces. The energy required for compressing polystyrene ligands is modeled, based on the simplified form of the original expression proposed by de Gennes,

$$\Delta W_{steric} = \frac{100c\delta^2}{\pi\sigma^3} k_B T \exp\left(\frac{-\pi[L-2c]}{\delta}\right) \quad (3.12)$$

where, c , σ , and δ represent the core radius, thiol foot-print diameter, and brush thickness respectively. Experimental data (presented in section 3.4.1) were used for computing the interaction energy between equal sized spherical particles. Based on SEM measurements, core radius of 3.5 nm was used, while measured DLS hydrodynamic diameter was used for computing polymer brush thickness. The height measured by AFM (h) was used to obtain the best estimate of the immersion film thickness ($l_0 = h/2$) for computing the disjoining pressure component. Physical parameters like surface tension (26.5 mN/m for tetrahydrofuran, 28.5 mN/m for toluene), Hamaker constants (22×10^{-20} J for silicon to 4×10^{-20} J for water), and densities were collated from databases. Standard methods for estimating complex Hamaker constant were used. The thiol footprint diameter (σ) was set to be 0.9 nm (based on TGA measurements). With these values, the variation in disjoining pressure component between silicon and water ($2530 k_B T$) was found to be comparable to the elastic energy required for compressing polystyrene ligands by 50 % ($3267 k_B T$). The variation in disjoining component between silicon and graphite was estimated to be $827 k_B T$, which is comparable to the elastic energy required for compressing polystyrene ligands by 25 % ($1380 k_B T$). Given the approximate nature of some of the parameter values, the computed results for differences in capillary immersion energies and elastic energies, upon changing substrates, can be considered equal. These results confirm that capillary immersion forces are indeed responsible for the self-assembly of polymer grafted nanoparticles, unlike the case of alkanethiol protected nanoparticles that self assemble at the solvent-air interface.

A similar phenomenon can be discerned from two independent reports in the literature on the gold nanoparticles capped by thiol-terminated polystyrene molecules of molecular weight 12000 g/mol. For the arrays formed on water, the edge to edge spacing was ~ 2.5 nm, while for the arrays formed on a carbon film, the edge to edge spacing was ~ 12 nm. Chen et

al. have attributed this reduction in spacing of arrays to the enhanced core-core interaction and possible absence of substrate interactions in the case of water acting as the substrate. However, here, it has been shown unambiguously that the substrate influences particle spacing through modulation of disjoining force. The two independent results, reported in the literature, can also be accounted for by considering variations in the contribution of disjoining pressure to attractive capillary forces. Recently, Park and coworkers have demonstrated using in-situ TEM studies that indeed capillary immersion forces play a pivotal role in particle assembly.

Square packing in nanoparticle arrays

Marangoni instability using surface tension gradient (10 nm spacing)

In an attempt to modify the substrate properties of the liquid interface, an experiment was conducted by spreading a colloidal solution from toluene onto a liquid substrate comprised of 50 % ethanol–water solution. Surprisingly, square 2D lattices of nanoparticles were seen within cells that were composed of multilayer of nanoparticles (Fig. 3.30). When the ethanol-water volume ratio was decreased below 0.33, the array was found to be highly disordered (Fig. 3.31) and Marangoni cells were not observed in this case. The enhanced wetting of the polystyrene ligands, due to the presence of ethanol, leads to a nanoparticle concentration gradient in the liquid substrate that can cause Benard-Marangoni cells. Benard-Marangoni convective cells arise due to surface tension gradient on the free surface. This surface tension gradient can originate either because of thermal or concentration gradient. In the case of thermal gradient, evaporation cools the free surface, thereby leading to temperature gradient between the hot substrate and cooled free surface. The critical Marangoni number arising due to temperature gradient is given by,

$$Ma_T = \frac{(\partial\gamma/\partial T)\Delta T h_0}{\eta\alpha} \quad (3.13)$$

where γ is the surface tension, ΔT is the temperature difference between the substrate and the free surface layer, h_0 is the film thickness, η is the dynamic viscosity of the solvent and α is the thermal diffusivity.

In the case of concentration gradient, enhanced solubility of polystyrene molecules near the interface can result in surface tension gradient. In this study, due to the enhanced solubility of thiol-terminated polystyrene molecules, the concentration of nanoparticles near the region of ethanol-water interface will be high when compared to the particle concentration in the toluene region. This results initiates a convective instability in the ethanol-water interface region,

$$Ma_C = \frac{(\partial\gamma/\partial C)\Delta C h_0}{\eta D} \quad (3.14)$$

where γ is the surface tension, ΔC is concentration difference between the substrate and the free surface layer, h_0 is the film thickness, η is the dynamic viscosity of the solvent and D is the diffusivity coefficient of solvent in the polymer-solvent mixture. ΔC can be estimated using Fick's law of diffusion through diffusivity, J ,

$$J = D \frac{\Delta C}{h_0} \quad (3.15)$$

The maximum velocity, U , in the convective cell can be obtained by balancing viscous and Marangoni forces,

$$U = Ma \frac{\nu}{h_0} \quad (3.16)$$

where ν is the kinematic viscosity.

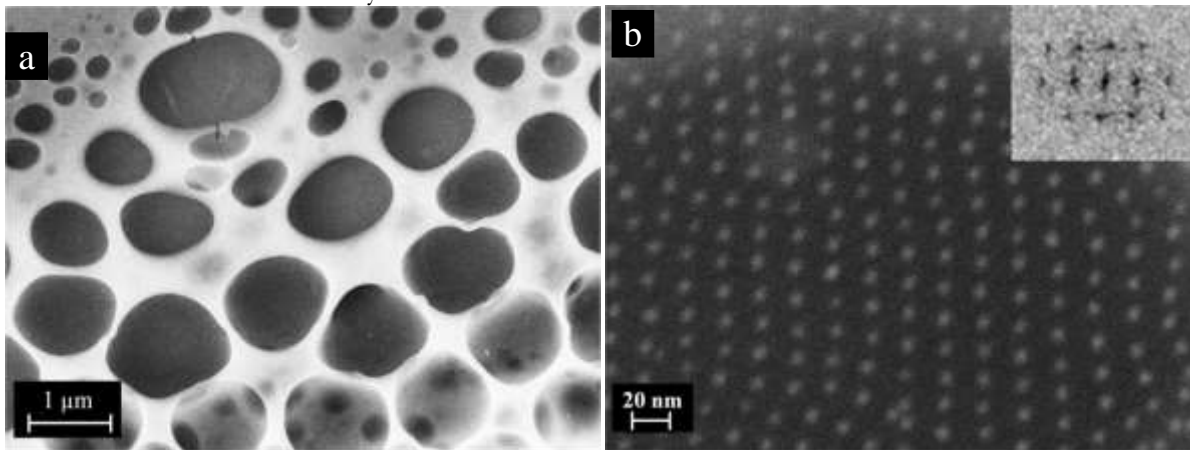


Figure 3.30: Representative FESEM image of nanoparticles forming a 2D square configuration obtained by using a 50% (v/v) solution of ethanol and water as the substrate at different magnifications; (a) low magnification image highlighting the formation of convective cells (bright regions correspond to nanoparticle multilayers with hexagonal order) and (b) high magnification image demonstrating the formation of a square lattice; the inset shows Fourier transform of the main image.

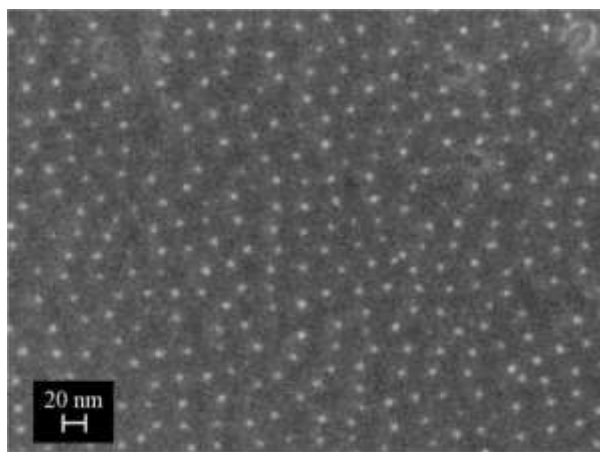


Figure **Error! No text of specified style in document.**31: Representative FESEM image of nanoparticles forming a disordered configuration by using a 1: 2 solution of ethanol and water as the substrate.

Cai and Newby have created 1D stripe like patterns of 100 nm polystyrene nanoparticles instead of 2D hexagonal patterns using Marangoni flow of ethanol into water (in lateral direction, see Fig. 3.32). This results in surface tension gradient, leading to convective instability due to water condensation, thereby driving the nanoparticles towards the receding contact line. Tang and coworkers have prepared square domains of 117 nm thick poly(ethyleneoxide)-*b*-poly(methylmethacrylate)-*b*-polystyrene (PEO-*b*-PMMA-*b*-PS) ABC triblock copolymer films after annealing under saturated benzene vapor at relative humidity of 80-90 % for 16 hours (Fig. 3.33). Sun and coworkers have assembled colloidal crystals into metastable square lattices using spin casting. The authors speculate that high shear stress generated at high spin speed (~ 6000 rpm) can result in partial melting of hexagonal packing. Bassou and Rharbi have investigated the formation of 2D ordered corrugation during solvent evaporation from polystyrene/toluene solutions. The solvent concentration difference between the surface and substrate was estimated to be $8.5 \times 10^{-4} \text{ mN m}^{-1} \text{ mol}^{-1} \text{ m}^3$. All the following parametric values were taken from the report of Bassou and Rharbi. The diffusion coefficient of pure toluene is $2.4 \times 10^{-9} \text{ m}^2 \text{ s}^{-1}$ while for toluene containing 50 % polystyrene is $0.34 \times 10^{-9} \text{ m}^2 \text{ s}^{-1}$.

In this study, the diffusion coefficient value was taken to $1 \times 10^{-9} \text{ m}^2 \text{ s}^{-1}$, while the dynamic viscosity of toluene with 10% polystyrene was taken to be 0.074 Pa s. The drying rate has been assumed to be of the order of $10^{-5} \text{ kg m}^{-2} \text{ s}^{-1}$, based on the experimental observation of polystyrene thin film drying over 100 minutes. For a film of 1 mm thickness, the critical Marangoni number was estimated to be 1.2×10^{-6} , which is equivalent to a linear velocity of 10.6 m/s, corresponding to ~ 20000 rpm (for a radial distance of 1 cm). The large shear stress within these cells is speculated to cause partial melting of shear-aligned hexagonal structures leading to the formation of metastable square lattices. This finding opens up the possibility of forming square lattices of polymer grafted nanoparticles by controlling the shear stresses during array formation, e.g. by using spin-coating, a simple and scalable manufacturing process. This possibility was tested by spinning thiol-terminated polystyrene (molecular weight: 20000 g/mol) capped gold nanoparticles suspended in toluene at ~ 8500 rpm for 1 minute (via. slowly ramping from 100 rpm to 500 rpm and then rapidly to 8500 rpm).

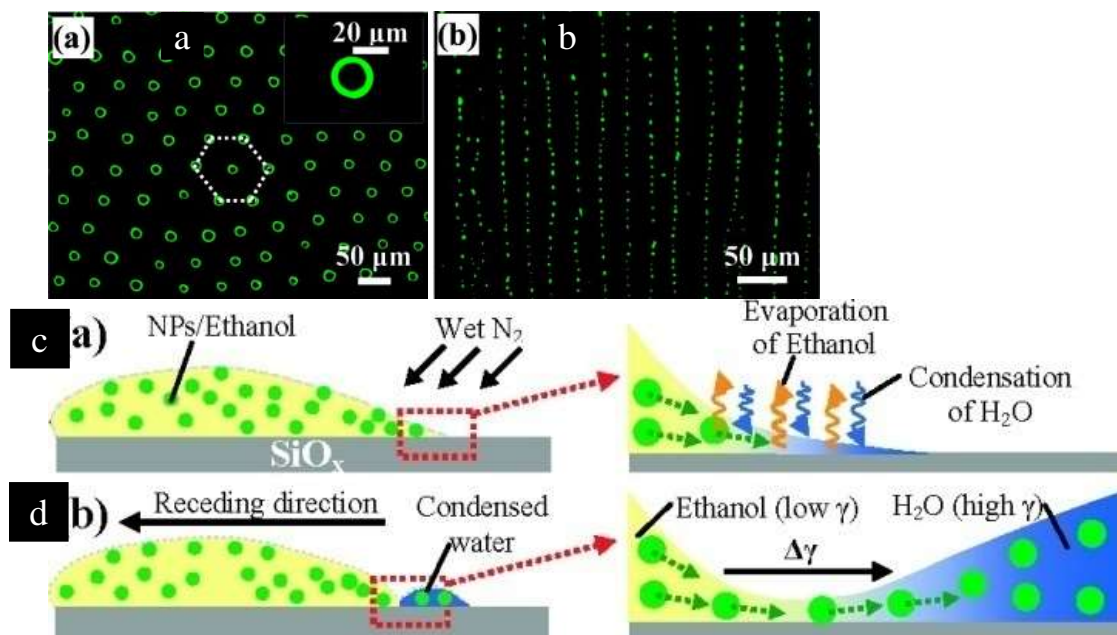


Figure **Error! No text of specified style in document..32:** (a) Fluorescent microscopic images of self-assembled hexagonal and striped patterns of polystyrene nanoparticles obtained by controlling the evaporation of solvent and inducing Marangoni flow of ethanol into water. (b) Schematic illustration of the nanoparticle self-assembly process highlighting the process of water condensation and generation of surface tension gradient, thereby driving the nanoparticles towards the receding contact line (Reproduced with permission from Cai and Newby¹⁴³. Copyright (2010) Springer).

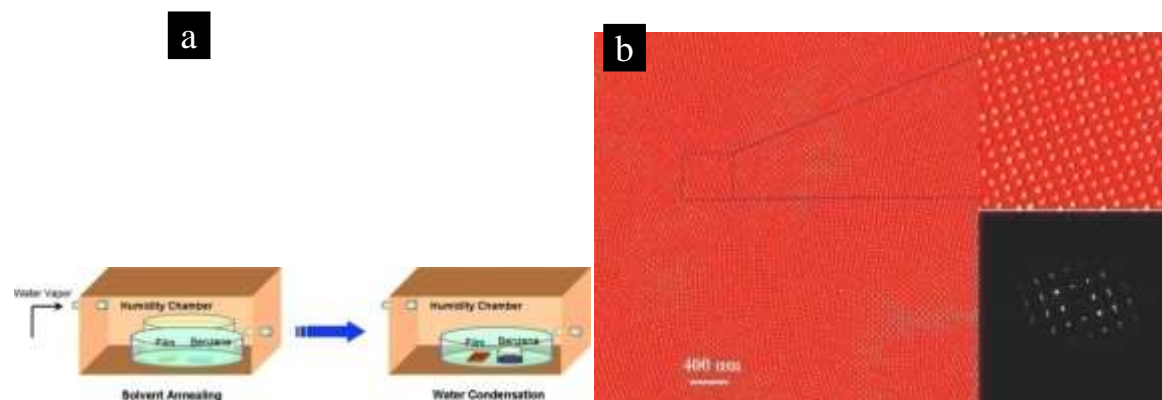


Figure **Error! No text of specified style in document..33:** Schematic illustration of poly(ethyleneoxide)-b-poly(methylmethacrylate)-b-polystyrene (PEO-*b*-PMMA-*b*-PS) ABC triblock copolymer film solvent annealing with controlled humidity. (b) Scanning Force Micrograph of square domains of 117 nm thick PEO-*b*-PMMA-*b*-PS films after annealing for 16 h under saturated benzene vapor at relative humidity of ~ 80-90 %. The top inset shows the high magnification image of the square pattern while the bottom inset represents the corresponding Fourier transform (Reproduced with permission from Tang et al.. Copyright (2008) American Chemical Society).

rpm). As expected, domains of square lattices were formed by spin coating gold nanoparticles on Si/SiO₂ substrate (Fig. 3.34). The domain size could not be extended to larger areas with the current experimental condition (maximum speed of 8500 rpm). Further efforts are needed in optimizing the formation of square arrays by spin coating, possibly using higher speeds than that feasible with the current set-up. A similar approach was attempted using dodecanethiol capped gold nanoparticles so that ultra-high density array with square lattice can be obtained. However, with ethanol-water as subphase, the particles were engulfed into the ethanol-water mixture; whereas spin-coating at speeds up to 8500 rpm did not yield any appreciable changes in the particle arrangement.

Marangoni instability using temperature gradient (2 nm spacing)

Marangoni instability can be induced in multiple ways, such as concentration gradient, temperature gradient etc. So the dodecanethiol capped gold nanoparticles precooled to ~15°C were drop-cast on a water surface which was at ~24°C (Fig. 3.35). As hypothesized, Marangoni convective cells were created resulting in domains of square lattices of gold

nanoparticles in between the domains of hexagonal packed arrays (Fig. 3.36). This suggests that square patterns can be created with an interparticle spacing of 2.2 ± 1.0 nm (Fig. 3.36d). The optical photograph of the samples also shows circular domains, similar to FESEM image (Fig. 3.37a). The optical profile across the circular pattern shows a thickness of ~ 14 nm (Fig. 3.37b), which corresponds to bilayer as single layer thickness correspond to 7 nm. For the first time, we have shown that square patterns with a pitch of < 10 nm can be obtained without the use of tedious processing to attach specific binding motifs, and thus represents an attractive opportunity. Such square packing of nanoparticle arrays, if extended uniformly over large areas, will have huge ramifications in future magnetic memory devices as read/write heads can easily address nanoparticles in a square architecture rather than hexagonal structure.

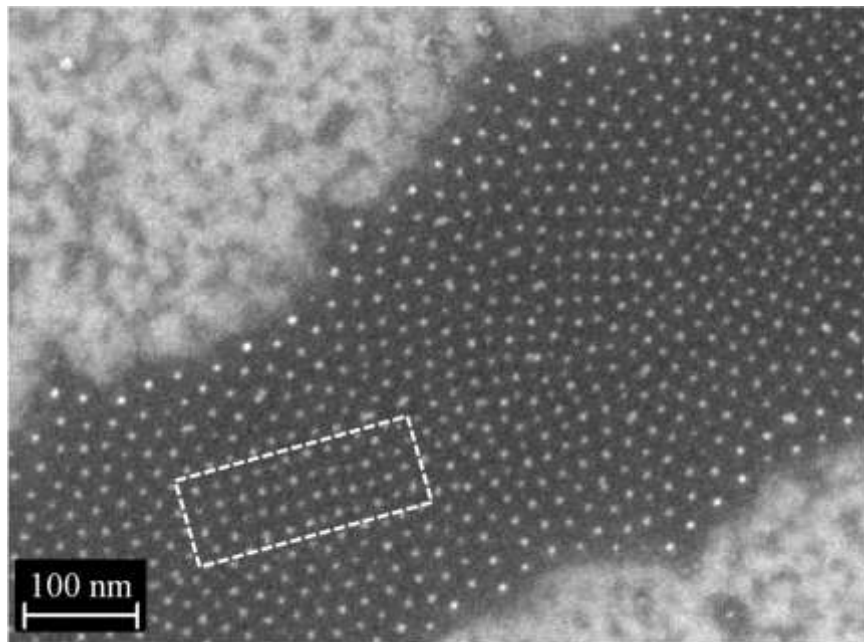


Figure **Error! No text of specified style in document.**34: Representative FESEM image of nanoparticles forming a 2D square configuration obtained by spin coating gold nanoparticles on Si/SiO₂ substrate.

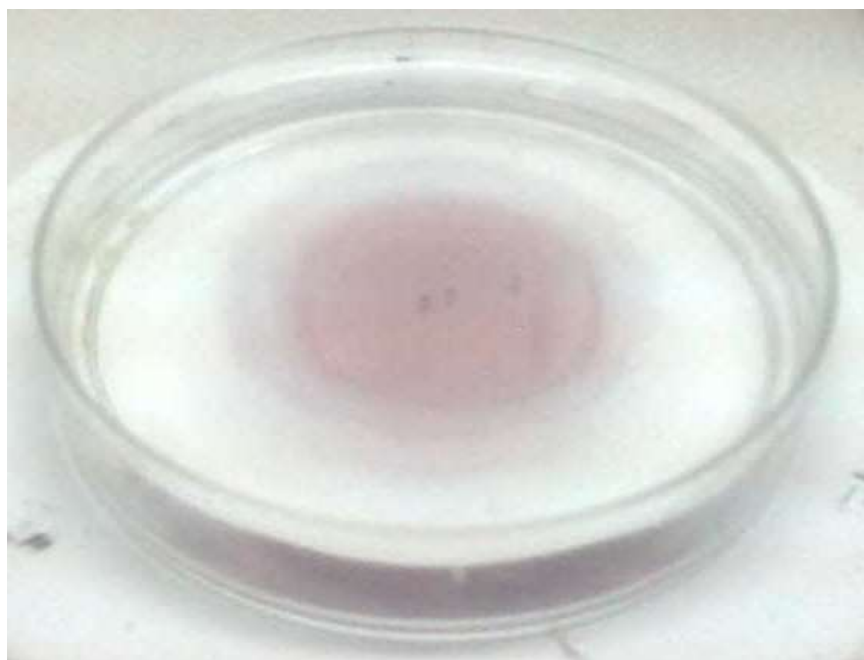
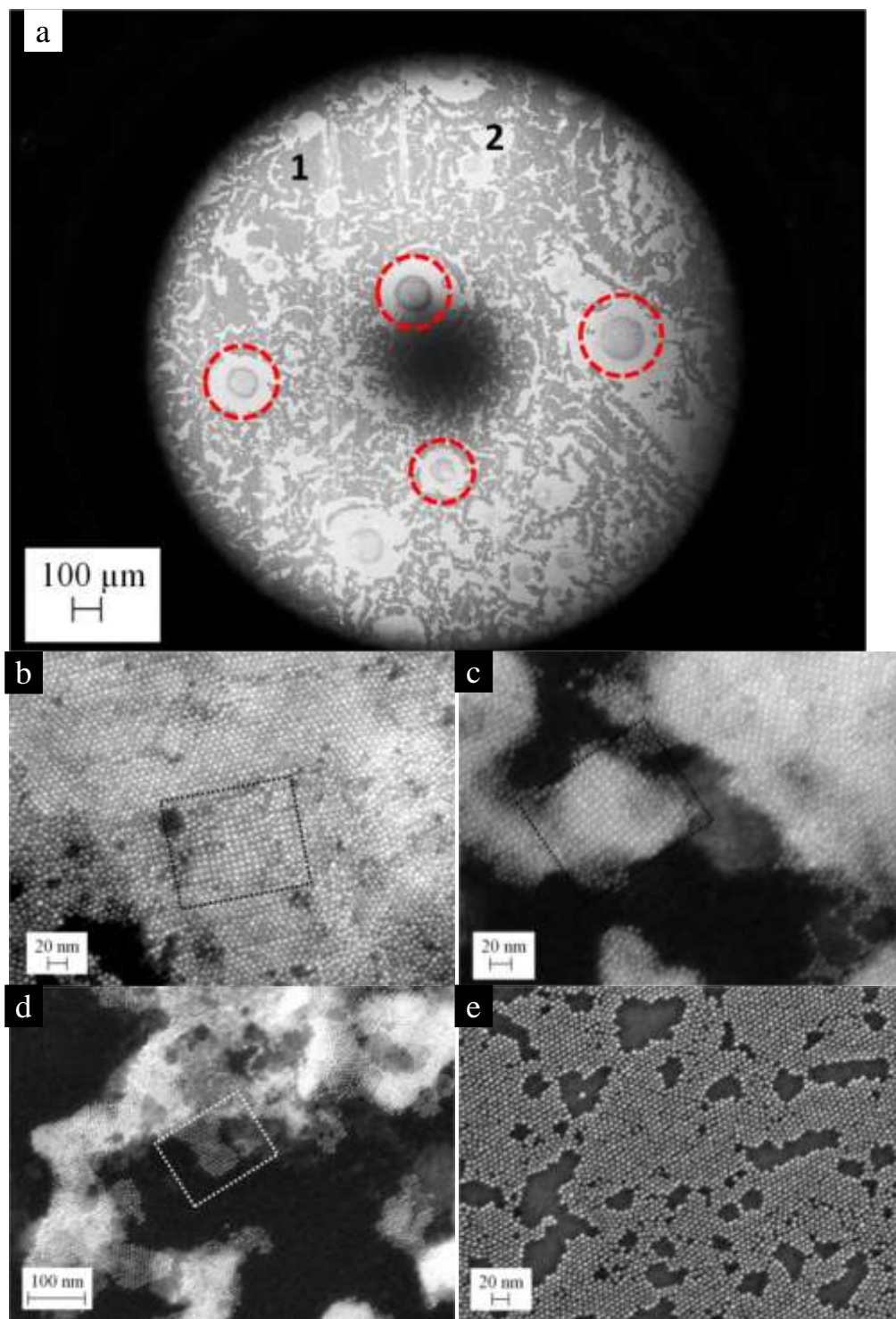


Figure **Error! No text of specified style in document.**35: Digital photograph during self-assembly of dodecanethiol capped gold nanoparticles at the air water interface. The colloidal solution contains excess thiol and maintained at ~ 15 °C before drop casting on the water surface. The water surface was maintained at room temperature (24 °C).



Error! No text of specified style in document..36: Representative FESEM images obtained by transfer printing the arrays fabricated by self-assembly of dodecanethiol capped gold nanoparticles at the air water interface, shown in Fig. 3.35. (a) Low magnification image highlighting the circular regions (dotted circles) and regions marked 1 and 2 corresponding to array and bare silicon substrate respectively. (b-d) High magnification images obtained by zooming in circular regions shown in a. The dotted rectangles represent domains of square lattice with 2.2 nm interparticle spacing. (e) High magnification image obtained by zooming in region marked 1 in a, illustrating hexagonal packing of particles.

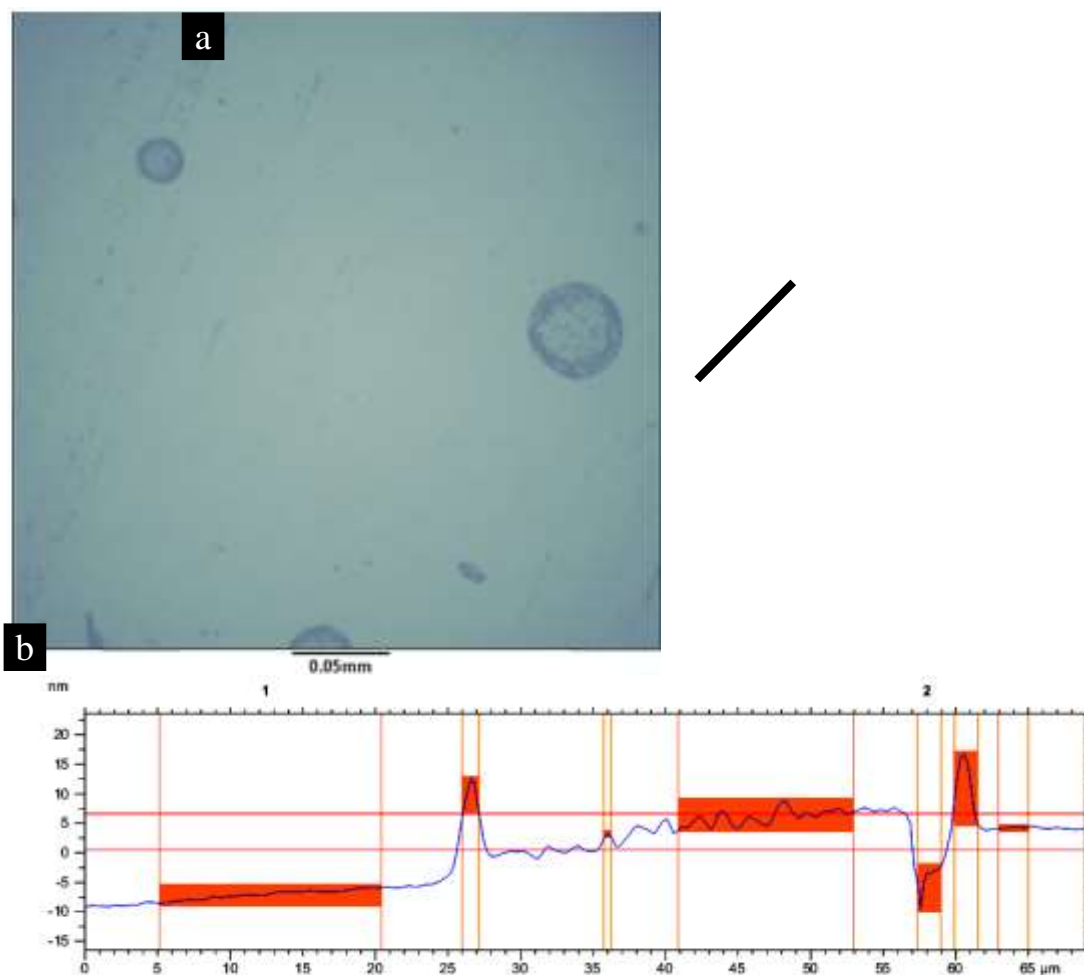


Figure **Error! No text of specified style in document..37**: (a) Optical photograph of the nanoparticle assembly created through Marangoni instability with circular patches in between the large scale monolayer. (b) Representative line scan across the circular region (marked dark line in a), indicating a thickness of ~ 14 nm, corresponding to a bilayer thickness.

Formation of nanopouches

Several techniques for the formation of 3D nanostructures by solvent-mediation have been reported in the literature. Ji et al. have proposed an approach for multi-dimensional assembly of gold nanoparticles by using a series of ionic ammonium salts, imidazolium salts, amines etc. Simple surfactant driven self-assembly has been shown to assemble gold nanoparticles from aqueous solutions into 3D nanostructures, which has significant influence on localized Surface Plasmon Resonance (SPR). Nie et al. have shown that various geometries can be obtained by incorporating water in a tetrahydrofuran (THF) solution containing metal nanorods grafted with amphiphilic triblock copolymers. Tetrahydrofuran has a special property of being soluble both in polar and apolar solvents (Table 3-1). So in a similar vein, polystyrene thiol capped gold nanoparticles being soluble in THF (good solvent), an equal volume of water was added to the colloidal solution, which resulted in the formation of circular structures having nanoparticles within the polystyrene matrix (Fig. 3.38). As water is a poor solvent for polystyrene, the particles tend to aggregate due to hydrophobic interactions. However, with the addition of water molecules, polystyrene molecules aggregate so as to expel the solvent molecules and minimize the free energy of the system. Niikura and coworkers have demonstrated similar nanoparticle vesicles, hollow nanoparticle assemblies, using gold nanoparticles capped with semi-fluorinated oligo(ethylene glycol) ligands dispersed in THF. They have reported that both ethylene glycol unit and fluorine unit are needed for observing vesicle formation. In this study, a combination of tetrahydrofuran and water was used for polymer grafted nanoparticle supra-assembly, which has potential for applications in the field of drug delivery. Interestingly, in the case of lower molecular weight polymer (thiol-terminated polystyrene, 3000 g/mol), without the addition of excess water, similar circular assemblies were formed (Fig. 3.39). The reason for this is attributed to presence of trace amounts of water in the solvent and the reduction in van der Waals interactions in the case of lower chain length when compared to the molecules of longer chain length. Such nanostructures were also obtained by drop-casting polystyrene capped nanoparticles (molecular weight: 20000 g/mol) dispersed in toluene, on a water surface that was *a priori* modified with dodecane, a bad solvent for polystyrene (Fig. 3.40).

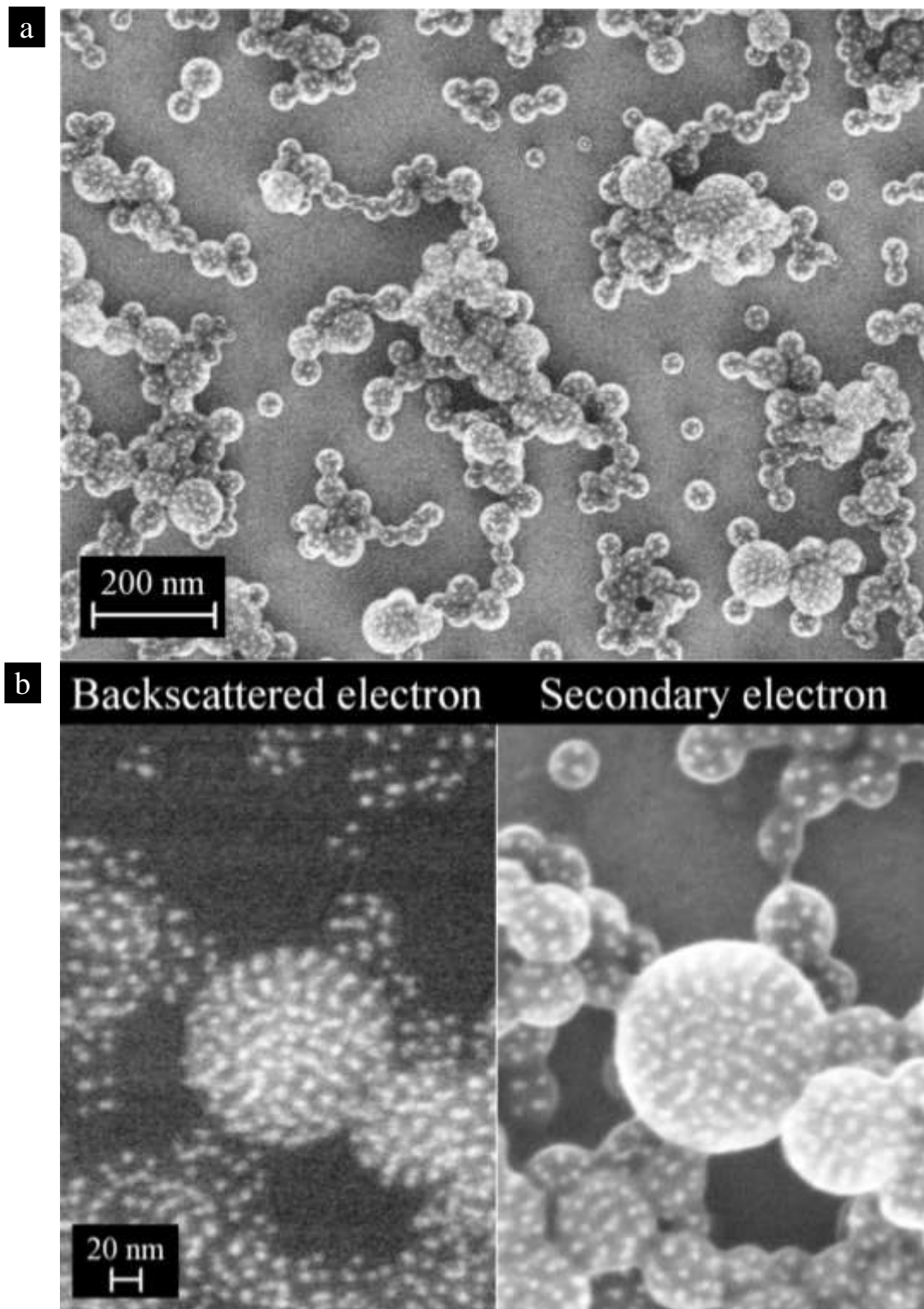


Figure **Error! No text of specified style in document..38:** (a-b) Representative FESEM images taken at different magnifications, of the polystyrene thiol-gold nanoparticle nanostructures fabricated through drop-casting polystyrene thiol capped gold nanoparticles (molecular weight: 20000 g/mol) dispersed in a solvent mixture comprising equal volumes of tetrahydrofuran and water on Si substrate. The images in b were taken using two detectors, namely, angle selective backscattered electron (left) and secondary electron (right) detector. High contrast in backscattered electrons is primarily due to the variation in atomic mass while the contrast in secondary electrons is due to surface features.

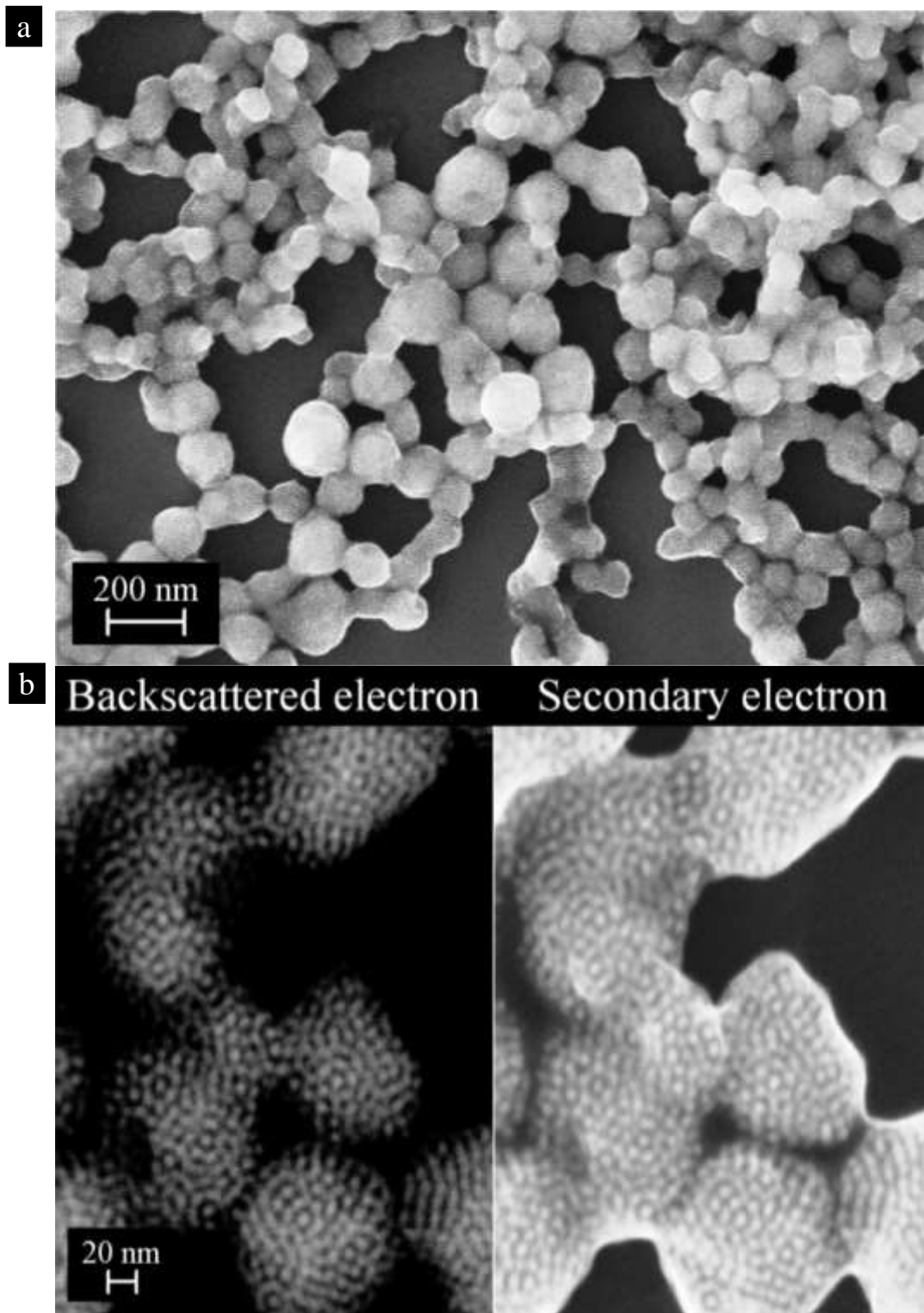


Figure **Error! No text of specified style in document..39**: (a-b) Representative FESEM images taken at different magnifications, of the polystyrene thiol-gold nanoparticle nanostructures fabricated through drop-casting polystyrene thiol capped gold nanoparticles (molecular weight: 3000 g/mol) dispersed in tetrahydrofuran on Si substrate. The images in b were taken using two detectors, namely, angle selective backscattered electron (left) and secondary electron (right) detector.

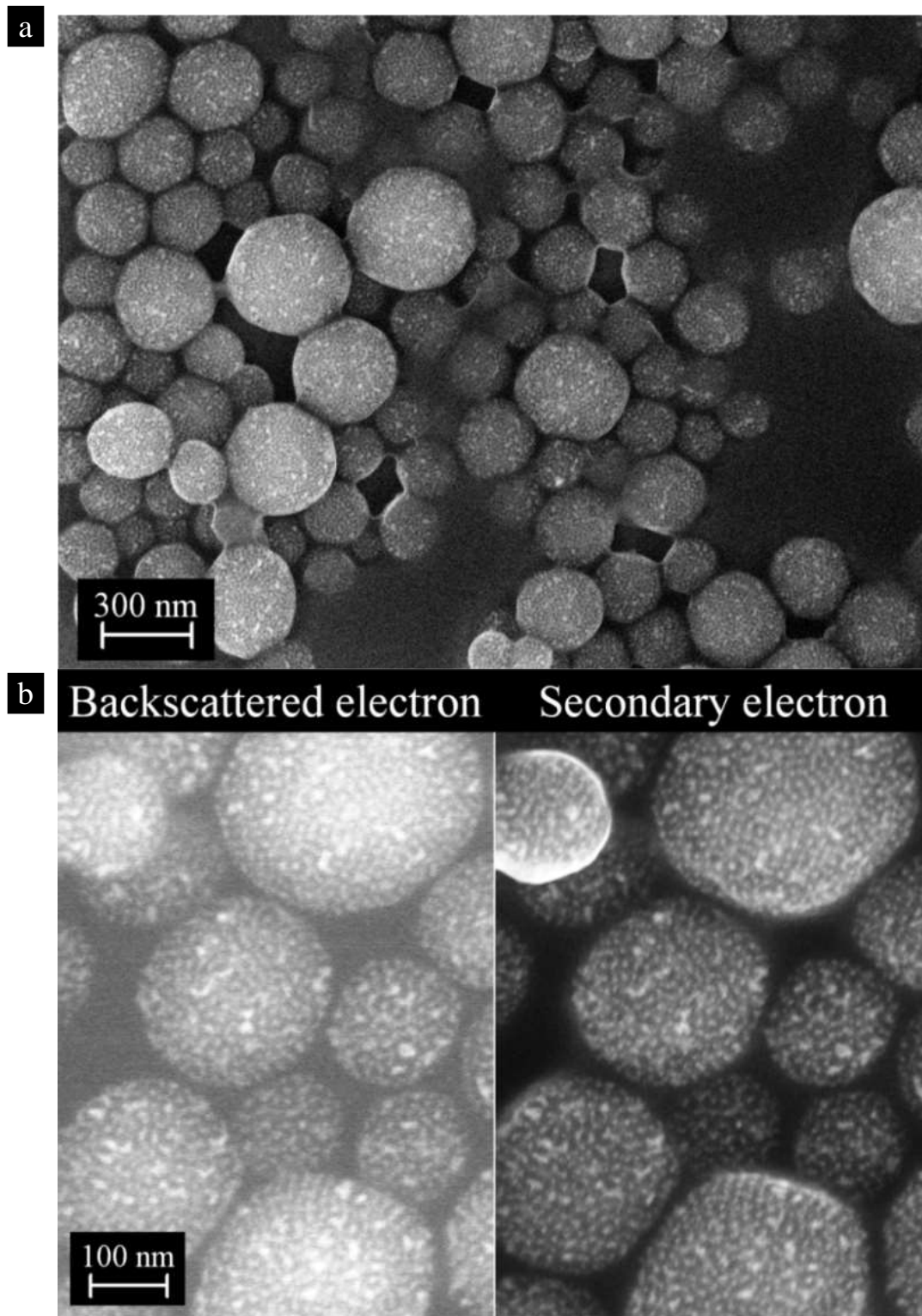


Figure **Error! No text of specified style in document.**40:(a-b) Representative FESEM images taken at different magnifications, of the polystyrene thiol-gold nanoparticle nanostructures fabricated through drop-casting polystyrene thiol capped gold nanoparticles (molecular weight: 20000 g/mol) dispersed in toluene on the water surface spread with dodecane layer. The images in b were taken using two detectors, namely, angle selective backscattered electron (left) and secondary electron (right) detector

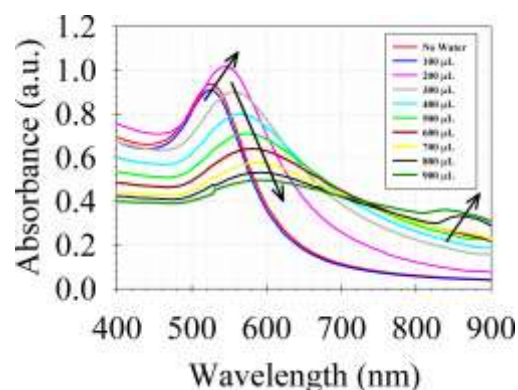


Figure **Error! No text of specified style in document.**41: UV-Visible spectra of polystyrene thiol capped gold nanoparticle in THF mixed with varying amounts of water. Remarkably, at higher water contents in the colloidal solution, nanoparticle-polystyrene assemblies have SPR in the IR region.

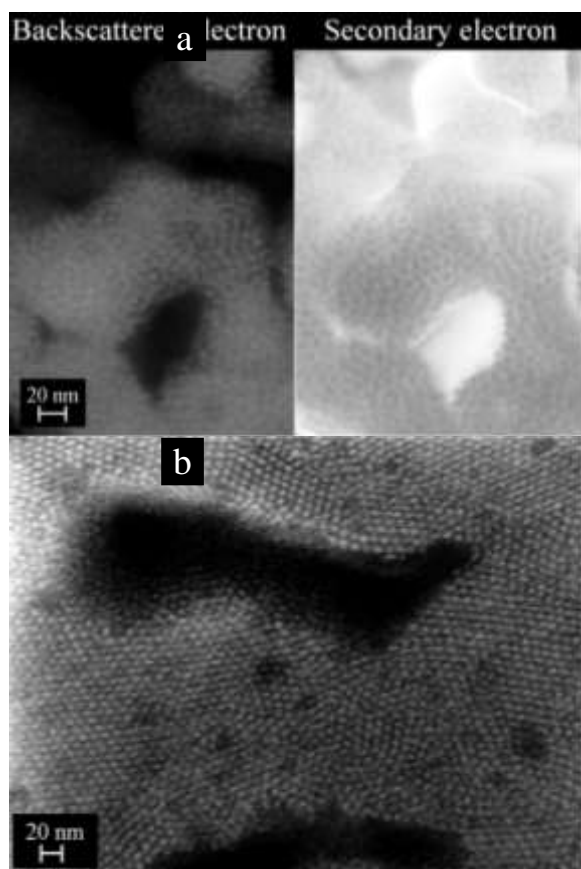


Figure **Error! No text of specified style in document.**42: (a) Representative FESEM image of the polystyrene thiol-gold nanoparticle nanostructures fabricated through drop-casting polystyrene thiol capped gold nanoparticles (molecular weight: 3000 g/mol) dispersed in THF and water (with 20% volume). The images were taken using two detectors, namely, angle selective backscattered electron (left) and secondary electron (right) detector. (b) Representative FESEM image of the polystyrene thiol-gold nanoparticle nanostructures fabricated through drop-casting polystyrene thiol capped gold nanoparticles (molecular weight: 3000 g/mol) dispersed in THF and water (with 50% volume).

Surface Plasmon Resonance (SPR) in IR region

By mixing controlled amounts of water to polystyrene thiol capped gold nanoparticles (3000 g/gmol) dispersed in THF, the peak of Surface Plasmon Resonance (SPR) band can be shifted over the visible and near-infrared (NIR) regions of the spectrum (Fig. 3.41). To 3 mL of the colloidal solution ($\sim 10^{13}$ particles per mL) dispersed in THF, small volumes of water (in the order of 100 μ L of water was added in steps. With the first addition, there was neither significant change in absorbance nor peak position in the UV-Vis spectrum. However, with the addition of another 100 μ L of water, there was a red-shift in peak position and an increase in absorbance which can be attributed to the possible interparticle coupling (as the particles might start to flocculate into small clusters) resulting in increased absorptivity. However, with next addition of water aliquot to the colloidal solution, decrease in absorbance and broadening of the red-shifted peak was

observed due to the formation of larger aggregates and solvent dilution effect. Higher percentages of water content (> 27%) in the colloidal solution results in significant enhancement of SPR in the infrared (IR) region, which can be exploited for applications in biomedical theranostics. FESEM images (at 20% and 50% water), show transformation of nanopouches to nanosheets (Fig. 3.42).

Summary

The demand for miniaturization has led to the unimagined advances in the field of nanostructure fabrication. Cost-effective bottom-up approaches are sought-after for nanostructure fabrication. In this chapter, first, a simple drop-casting approach was demonstrated for wafer-scale fabrication of an array of dodecanethiol capped gold nanoparticles. Similar process was employed to fabricate arrays with larger interparticle spacing. The underlying mechanism involving self-assembly of polymer capped nanoparticles was also investigated. The interparticle spacing and packing structure in these 2D arrays is shown to be controlled by the substrate, through modulation of the disjoining pressure in the evaporating thin film (van der Waals interaction); and by the solvent used for drop casting, through modulation of the hydrodynamic diameter. Arrays with square lattices were fabricated by exploiting Marangoni instability arising due to surface tension gradient. Finally, various other novel nanostructures were fabricated through modulation of hydrophobic interactions in the colloidal system.

9.4 Development of nanoparticle array based floating gate memory devices:-

The trend of “Data anytime, Data anywhere” has led to data storage devices being ubiquitous in personal life. Data is stored in memory devices, which can be further classified into two basic types, namely, volatile and non-volatile. Volatile memory devices are the ones where the data is lost when the power is switched off while the non-volatile memory devices are the ones where the data is retained even when the power is switched off. Flash memory, a popular type of non-volatile memory, is named after its ability to erase the data cells in a flash. It was developed from electrically erasable programmable read only memory (EEPROM).

Flash memory devices find applications in various electronic personal products such as cell phones, iPads, cameras, computers, laptops etc., and it has a multi-billion dollar market (Fig. 4.1a). Based on the 2012 report from IC Insights Inc., sales of flash memory are expected to eclipse sales of dynamic random access memory (DRAM), a volatile memory type, for the first time (Fig. 4.1b). Also, in the recent report entitled “Flash memory market to 2020”, from Electronics, CA publications, flash memory devices are projected to replace existing Hard Disk Drives (HDD). Also, it has been highlighted that flash memory will remain the most sought after devices for storage purposes.

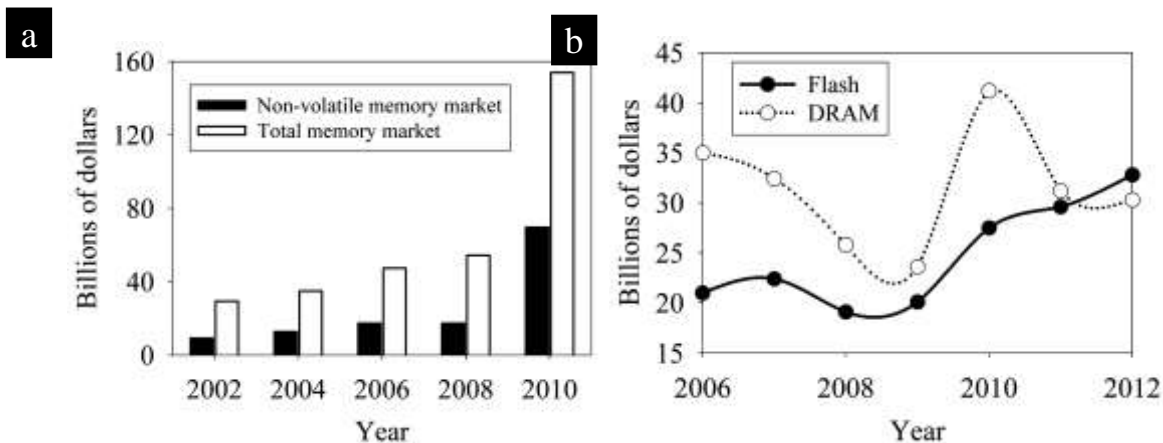


Figure Error! No text of specified style in document..43: (a) Estimate of share of non-volatile memory market in comparison with a total market (adapted from Electronics, CA publications). (b) The evolution of flash memory market in comparison with DRAM market over the last 6 years. For the first time in 2012, the flash memory business has exceeded DRAM market, adapted from IC Insights).

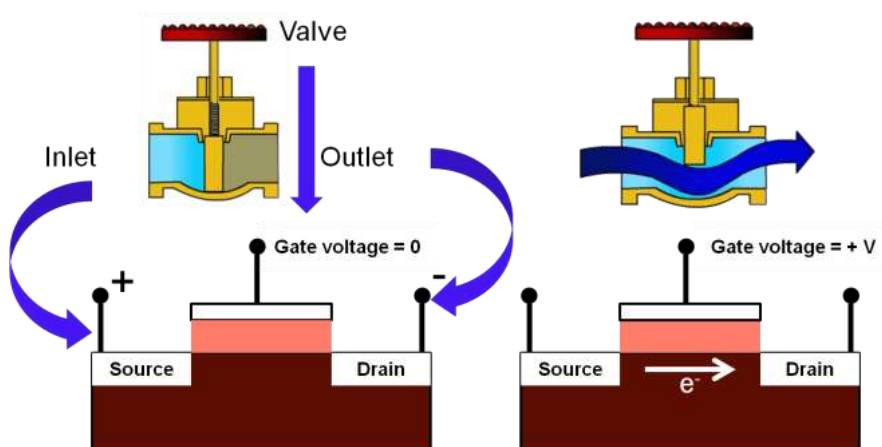
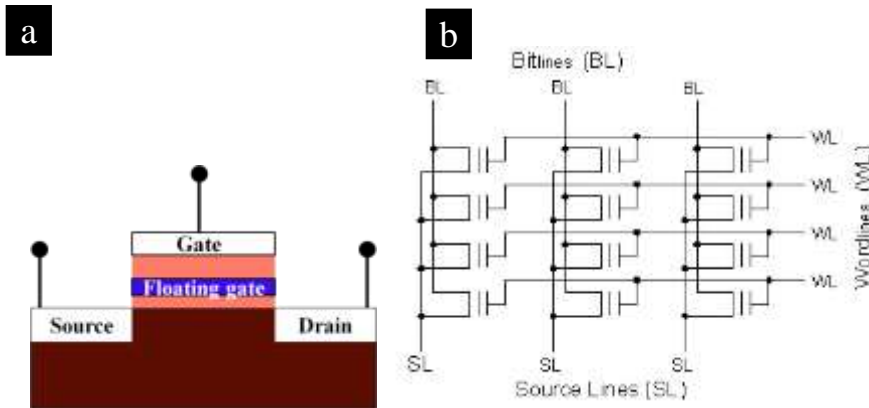


Figure Error! No text of specified style in document..44: Schematic representation of analogous behavior of flow valve and Field Effect Transistor (FET). The extent of opening of flow valve determines the liquid flow rate from inlet to outlet, analogous to the gate voltage determining the extent of conduction channel formation between source and drain.

Working principle of flash memory – Tunneling mechanism

Flash memory works on the principle of Metal-Oxide-Semiconductor Field Effect Transistor (MOSFET)¹⁵⁵. Field Effect Transistor (FET) can be treated analogous to flow valve, where in the extent of valve opening controls the flow rate of liquid from inlet to outlet analogous to the gate voltage governing the conductivity of the channel formed between source and drain (Fig. 4.2). In flash memory, the memory architecture is similar to the conventional field effect transistor except for an additional layer, a floating gate sandwiched between tunneling oxide and control oxide that traps electrons tunneled from the substrate through tunneling oxide (Fig. 4.3a). Therefore, in the literature, flash memory is also known as floating gate memory. Essentially, a field effect transistor relies on applied electric field at the gate, to control the current between two points, namely source and drain. A floating gate device can be read/written/erased depending on the applied gate voltage. Depending on the presence or absence of electrons in a floating gate, memory states can be assigned as 0 or 1. The memory chip is fabricated by assembling multiple individual memory cells. The cells are linked through bit lines, word lines and source lines (Fig. 4.3b). Control gates are connected together using word line while the bit lines unite all the drains. The source lines connect to common ground. Thus, voltage applied between word line and bit line dictates the program, erase or read operation (Fig. 4.3c). Two notable charge injection mechanisms have been employed for tunneling of charges either into or from the floating gate, namely, hot electron injection and Fowler-Nordheim (FN) tunneling. In hot electron injection mechanism, electric fields are generated in two directions, a lateral (between source and drain) one that heats up electrons, and a transversal (between the channel and control gate) one which aids in the injection of hot electrons into the floating gate. For many decades, flash memory devices have employed hot electron injection mechanism. However, this method suffers from high power consumption as a result of large currents and low injection efficiency. On the other hand, recent memory generations have started to



c

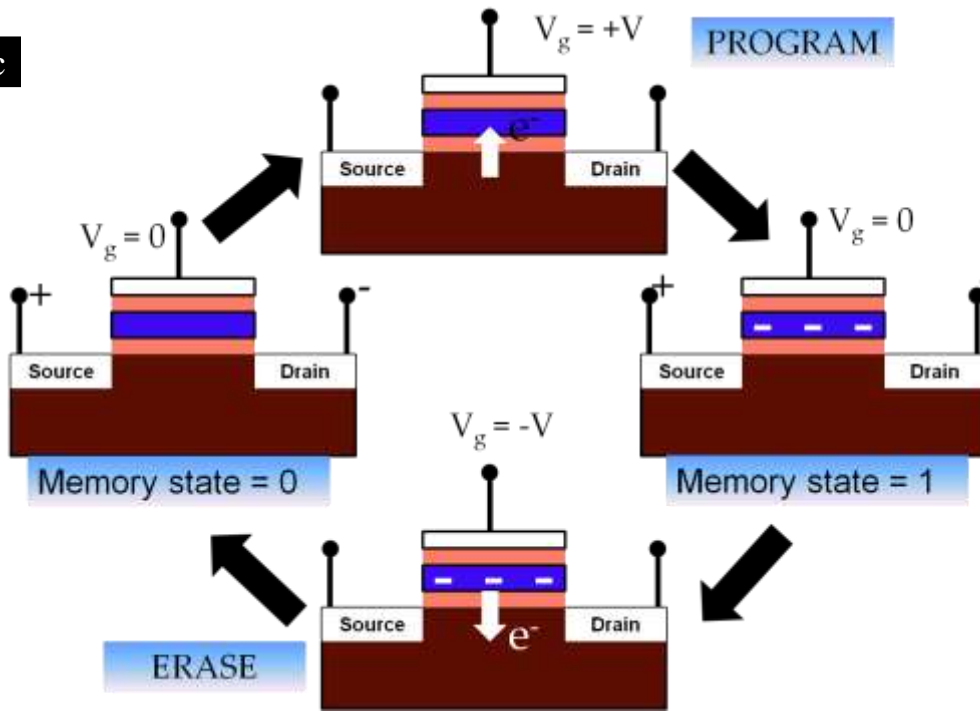


Figure Error! No text of specified style in document..45: (a) Schematic representation of field-effect floating gate transistor.(b) Each field effect transistor (FET) is connected using bit lines, word lines and source lines for program, erase and/or read operation. (c) Schematic representation of trapping/detrapping of electrons by controlling the gate voltage. Depending on the presence or absence of electrons in a floating gate, memory states are assigned as 0 or 1.

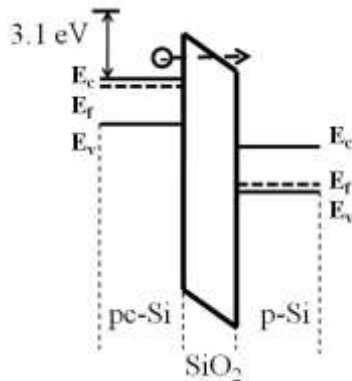


Figure Error! No text of specified style in document..46: Schematic energy-level representation of Fowler-Nordheim tunneling in a MOS capacitor.

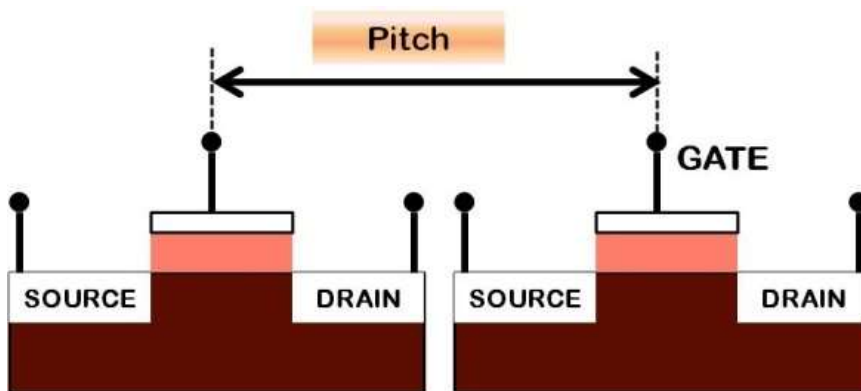


Figure Error! No text of specified style in document..47: Schematic representation of definition of “Pitch”. “Pitch” refers to the centre-centre distance between two FETs.

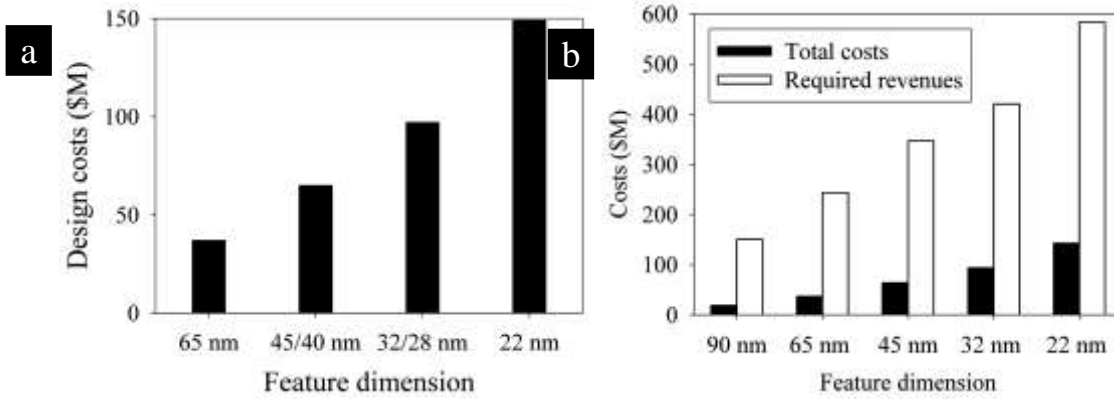


Figure **Error! No text of specified style in document.**48: (a) Estimation of increase of design cost with a decrease in feature size, adapted from reference. (b) Comparison of design cost with required revenue as the feature size decreases, for successful commercialization, adapted from reference.

exploit the alternate FN tunneling mechanism. FN tunneling involves tunneling of electrons through thin oxide, with the tunneling probability rising exponentially with the electric field (Fig. 4.4). The tunneling probability depends on shape, height and width of the potential barrier, which are governed based on thickness and nature of dielectric barrier. For a particle of mass, m and energy, E , the tunneling probability, T through a potential barrier with length, L and height, U is given by

$$T = \exp\left(-2L\sqrt{\frac{2m(U-E)}{\hbar^2}}\right) \quad (4.1)$$

Using Wentzel–Kramers–Brillouin (WKB) approximation (electronic wave function is assumed to be an exponential function of amplitude and phase) to solve Schrödinger equation. Due to exponential dependence, a small variation in oxide thickness can cause large variation in programming and erasing currents, thereby resulting in larger spread of threshold voltage distribution. On the other hand, for ultra thin oxides, electric fields of the order of 1 MV/cm can be easily reached, which can promote larger leakage currents.

Limitations of flash memory device

High design cost

Currently, the node (half-pitch of memory cell, as shown in Fig. 4.5) has reached less than 22 nm. Single pattern ultraviolet lithography (UVL) has reached its end of life at 40 nm. Extreme UltraViolet Lithography (EUVL) is projected as the next-generation lithography, with a wavelength of 13.5 nm, to progress scaling in memory devices. A decrease in feature size is typically accompanied by an order of magnitude increase in investments to build new fabrication facility (Fig. 4.6a). A lower bound to build one production site capable of achieving atomic resolution would be US \$2 Trillion, assuming no additional investments in fundamental design. For 22 nm node scaling of feature sizes, a minimum revenue of US \$583 M is needed to justify high design cost of US \$142.5 M (Fig. 4.6b). In addition, the design costs for scaling of feature sizes to sub 20 nm are projected to rise in an unpredictable manner.

Capacitive coupling between floating gates

Until now, the scaling has been realized merely by geometric shrinkage, more specifically horizontal scaling (Fig. 4.7). However, the scaling has reached a stage where it can result in capacitive coupling between the memory cells, i.e., a charge on one floating gate can cause a significant threshold voltage shift on the adjacent cell (Fig. 4.8). This demands a scaling of floating gate height to reduce the unwarranted interference between memory cells. Also, this problem can be circumvented either through vertical scaling or use of a high- k material. Currently, vertical scaling i.e., thickness of tunneling oxide has become a limiting factor for further scaling down.

Device reliability: Retention and Endurance

Flash memory devices have gained widespread acceptance due to their reliable performance. As per standard industry requirements, the current memory devices can retain data for a minimum of 10 years (charge retention) and endure over 10^4 Program/Erase (P/E) cycles (endurance). With further scaling of feature sizes below 20 nm, the devices are required to have a good reliability, i.e., to meet the standard industrial requirements of retention and endurance characteristics of 10 years and 10^4 cycles respectively. However, there are additional challenges to be surmounted in order to meet these requirements upon further scaling down of dimensions. Further feature size scaling requires a lowering of tunneling oxide

thicknesses (to the order of few nanometers), wherein direct tunneling becomes predominant leading to data loss and poor device retention characteristics. Random variations while manufacturing devices with very low oxide thicknesses are also inevitable. This non-uniformity in oxide quality also results in large variation in programming and erasing voltages - an undesirable effect. Also, for devices with low tunneling oxide thicknesses, defects are generated due to stresses induced by high electric fields. Thus, scaling down of tunneling oxide thickness affects both device retention (due to direct tunneling) and endurance (due to stress induced defects) characteristics.

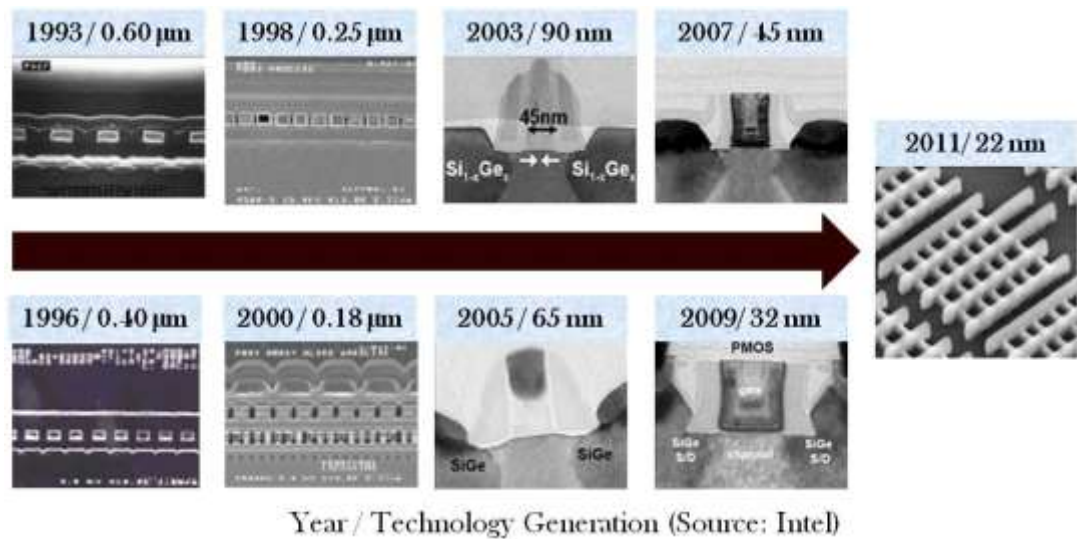


Figure Error! No text of specified style in document..49: Flash technology scaling for the last two decades, adapted from Intel¹⁶⁴.

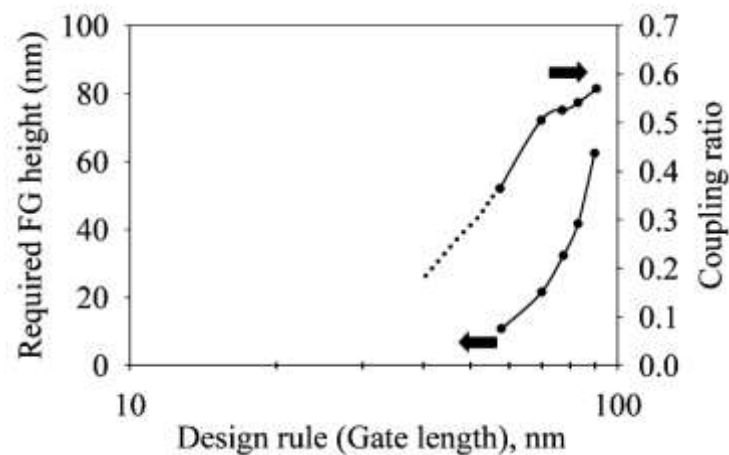


Figure Error! No text of specified style in document..50: Plot showing requirement of floating gate height for the effective suppression of gate coupling based on design rule.

Future of flash memory devices

Further improvements in flash memory performance will have to rely on electrical scaling, i.e. reducing tunneling oxide thickness and using high-k dielectrics, without compromising on reliability and endurance, as there are formidable challenges associated with physical scaling of devices, such as cell-to-cell interference, poor reliability and lower gate coupling ratio. The use of charge trapping layers, encased in a high-k dielectric, as storage nodes is the most promising route to overcome these issues (Fig. 4.9). The energy band diagram of a floating gate memory device with metal as trapping layer offers better reliability and can also enable aggressive scaling of tunneling oxide thickness below 3 nm. Charge trapping devices (Fig. 4.10), comprising of either interface traps or nanoparticles as storage nodes have been studied for a longtime, especially for military and space applications due to their enhanced radiation tolerance. ONO (oxide nitride oxide) stacks, semiconductor nanoparticles, and metal nanoparticles have been mainly studied as charge

trapping layers. The equivalent oxide thickness (EOT) scaling of ONO stacks is limited by the randomly distributed nature of charge traps in these layers. Metal nanoparticles, especially platinum and gold, have several advantages over semiconductor nanoparticles, namely: (a) a large work function leading to a deep trap level that allows for enhanced retention without sacrificing injection efficiency (Table 4-1), (b) a large density of states near the Fermi level that effectively screens out trap states formed at the nanoparticle–oxide interface, and (c) an electrostatic 3D field enhancement effect that results in improved low-voltage program/ erase (P/E) efficiencies. Even though, platinum has higher work function than gold, during device processing involving high-temperature annealing steps platinum silicide can form more easily, which will result in lowering of work function to 4.95 eV. Thus, the use of gold nanoparticles, due to its chemical inertness, as the charge trapping node is gaining in importance for fabricating next generation flash memory devices. Thin films of metal nanoparticles, for nonvolatile memory applications, have been fabricated either by top-down or bottom-up approaches. Top-down approaches include thermal evaporation, ion implantation, pulsed laser deposition, and rapid thermal annealing induced

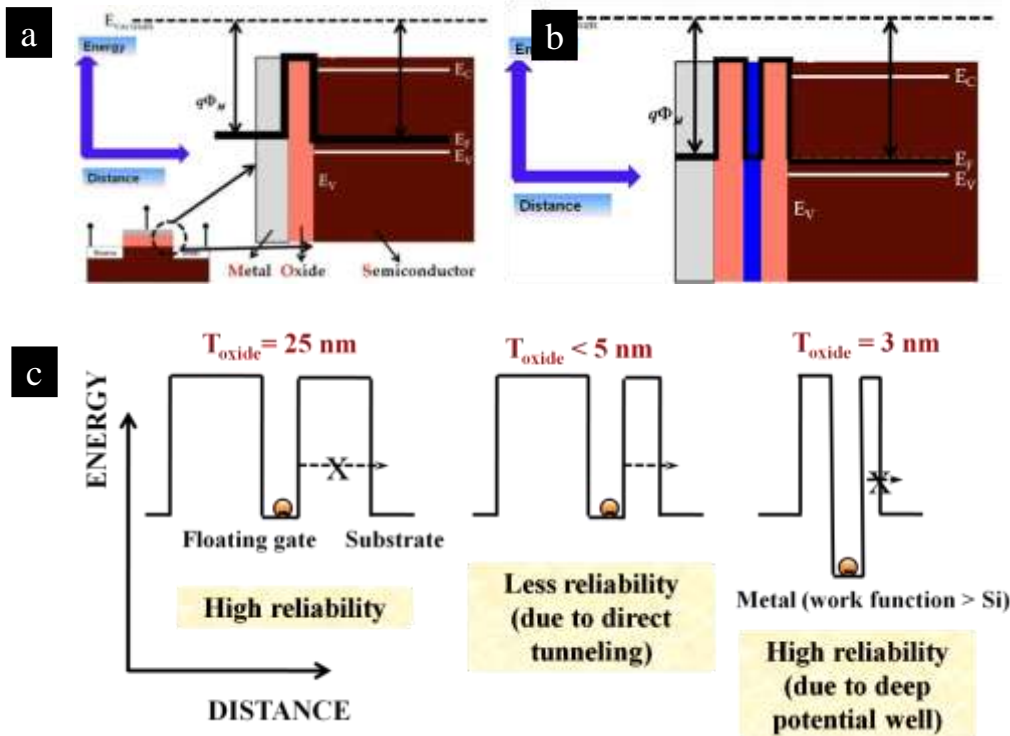


Figure **Error! No text of specified style in document..51**: (a) Schematic representation of energy band diagram of MOS capacitor (p-Si). (b) Schematic representation of energy band diagram of floating gate MOS capacitor. (c) Schematic representation of energy band diagram for (i) thick tunneling oxide highlighting negligible electron tunneling probability from floating gate to substrate. Electron trapping is necessary for reliable memory storage device. (ii) thin tunneling oxide highlighting higher electron tunneling probability. This will result in data loss. (iii) Thin metallic film sandwiched between substrate and control oxide. Metallic film offers deep potential well, thereby minimizing electron tunneling probability in comparison to semiconductor. This will aid in scaling down the tunneling oxide thickness aggressively, even down to ~ 3 nm, with higher data reliability.

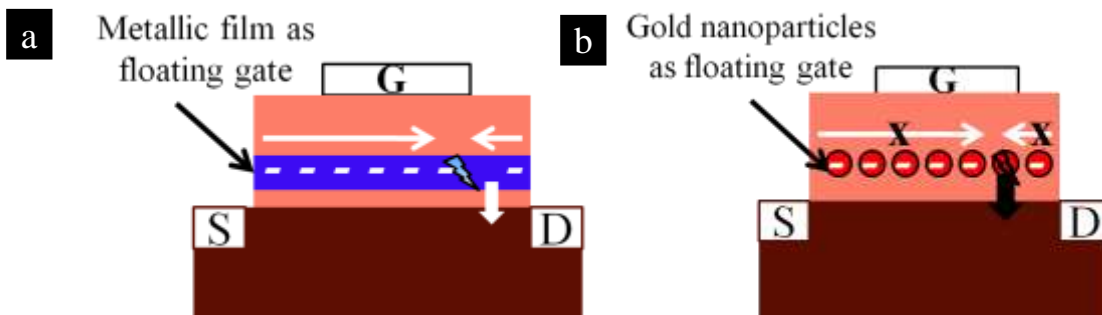


Figure **Error! No text of specified style in document..52**: Schematic representation of charge retention characteristics in the presence of defects for (a) conventional floating gate and (b) nanoparticle floating gate memory. In conventional

memory, a small leakage would cause all the stored electrons (data) to tunnel back to the substrate, while a few defects in a nanoparticle memory would not lead to complete loss of data due to charge compartmentalization.

Table **Error! No text of specified style in document.**-3: Work function of different metals that have been used as floating gates

Element	Work function, eV
Gold (Au)	5.10 ± 0.10
Silver (Ag)	4.33 ± 0.15
Platinum (Pt)	5.32 ± 0.10
Tungsten (W)	4.55 ± 0.10
Aluminium (Al)	4.24 ± 0.10

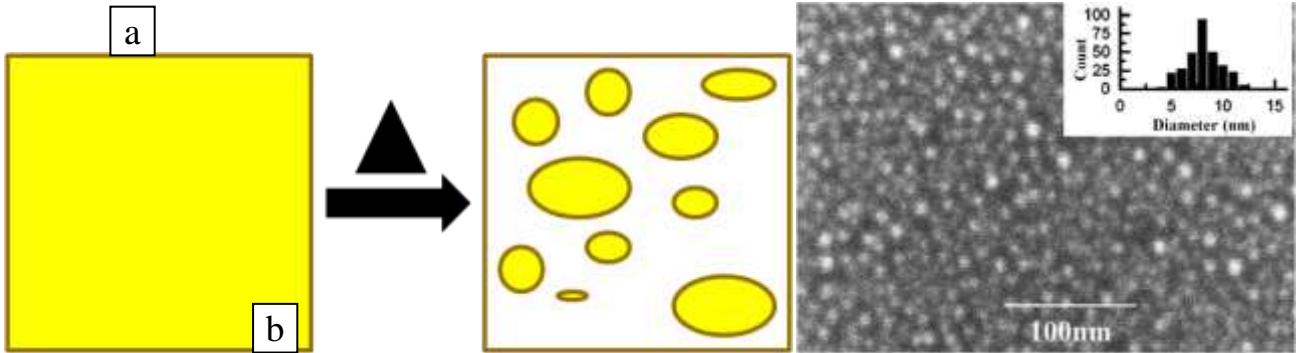


Figure **Error! No text of specified style in document.**53: (a) Schematic representation of formation of nanoparticles using annealing process. (b) Scanning electron micrograph of platinum nanoparticles obtained by annealing a thin film at 950 °C for 10 s; indicating large polydispersity (inset).

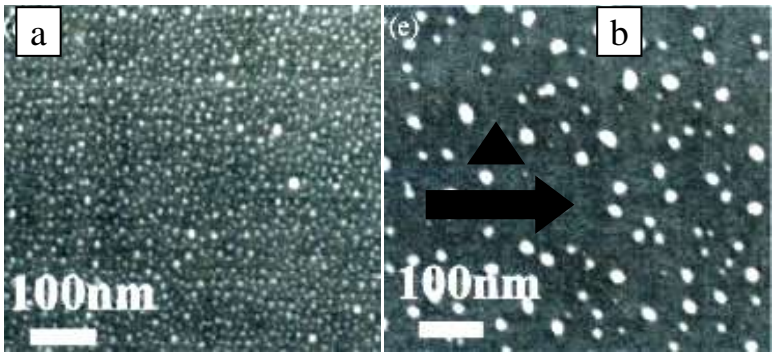


Figure **Error! No text of specified style in document.**54: (a) Representative FESEM image of gold nanoparticle array formed by spin coating .

self organization of thin films; the industrial adaptation of these approaches is limited by concerns over the ability to control the nanoparticle size and density at the sub-20 nm scale, and issues related to gold atom migration at higher annealing temperatures. For instance, the rapid thermal annealing process results in nucleation of random islands from a uniform metal film as shown in Fig 4.11. This process cannot be used to create uniform nanoparticle arrays with precision at the nanoscale, a pre-requisite for fabrication of next-generation memory devices; as otherwise it will lead to large dispersion in programming, erasing and reading voltages across devices. On the contrary, bottom-up fabrication of non-volatile flash memory devices by self-assembly of nanoparticle arrays using proteins, di-block copolymers, and covalent bonding as templates, and using LbL (layer by layer) deposition has been recently reported. Templated self-assembly routes involve tedious and costly procedures for generating the templates and are not easily scalable into the sub-20 nm range, due to limitations on the template size, particle size and spacing; whereas, the LbL route is limited by the lack of ordering of the adsorbed nanoparticles at the sub-50 nm scale. Evaporation-induced self-assembly of monolayer protected nanoparticles (MPNs) can lead to rapid formation of ordered 2D arrays over large areas, with particle size and spacing in the 1–20 nm range; thereby, promising robust device performance at the nanoscale. Translation of this promise into floating gate devices has been hampered by the inability to use CMOS (complementary metal oxide semiconductor) compatible processes for wafer-scale nanoparticle array formation, and for oxide layer deposition without disturbing nanoparticle ordering. Also, the device fabrication demands high temperature processing.

Typically, thermal annealing results in particle coalescence (Fig. 4.12), thereby affecting both particle size and ordering in the bottom-up approaches reported so far. This coalescence of nanoparticles at high temperatures is attributed to the presence of capping agents. To overcome the thermal stability issue, various groups have deposited control oxide using low temperature processes, such as spin-coating of tetra ethyl ortho silicate (TEOS), calcium arachidate, or depositing alumina using low-temperature atomic layer deposition process (ALD) process etc. The performance of many of the devices reported, thus far, is poor. For instance, the memory window decreases from 6 V to 4.2 V after 4 days due to the charge loss through TEOS oxide. In the case of low temperature ALD process, a 200 nm thick layer is deposited to ensure good charge retention. This geometry increases the programming and erasing voltages (~ 50 V), and defeats a major goal of miniaturization. Also, the highest nanoparticle density reported so far in the literature is of the order of 10^{12} particles/cm². Thus, future floating gate memory device fabrication entails process development for fabrication of large scale (wafer level), close-packed ($\sim 10^{13}$ particles/cm²), and thermally stable (up to ~ 500 °C) gold nanoparticle arrays. To summarize, the key requirements for fabrication of next-generation flash memory devices using bottom approaches are, (a) deposition of electrical-quality control oxides with low thicknesses, and (b) processes for large-scale ordered 2D arrays of nanoparticles. Fabrication of high-quality, tunneling oxide with low thicknesses is well-established in the literature. In the previous chapter, efforts to make large scale ordered arrays of gold nanoparticles was presented. Hence, the unresolved issue in fabricating future flash memory devices is to develop CMOS-compatible process for depositing control oxide, without disturbing the ordering of the nanoparticle array. Various physical and chemical deposition processes can be employed to deposit control oxide. In this study, three promising processes namely, RF magnetron sputtering, Atomic Layer Deposition (ALD) and e-beam evaporation have been used to deposit control oxide. The optimization conditions for depositing top-oxide without disturbing the array order and results of the electrical characterization of the fabricated devices are discussed in the following sections.

Device fabrication using RF sputtering

RF magnetron sputtering of dielectrics (rare earth oxides) such as Gadolinium oxide (Gd_2O_3), Europium oxide (Eu_2O_3) etc is well-established. The criteria for choosing a dielectric material for top-oxide formation in a floating-gate device is based on two factors, namely, (1) use of highest possible dielectric constant (k), and (2) presence of a high band gap offset with respect to silicon. Typically, dielectric constant and band gap of dielectrics are inversely correlated, thereby leading to a trade-off between these two parameters (Fig. 4.13). In this study, Gd_2O_3 was chosen, as it was readily available and satisfies the aforementioned parameters reasonably (Fig. 4.13).

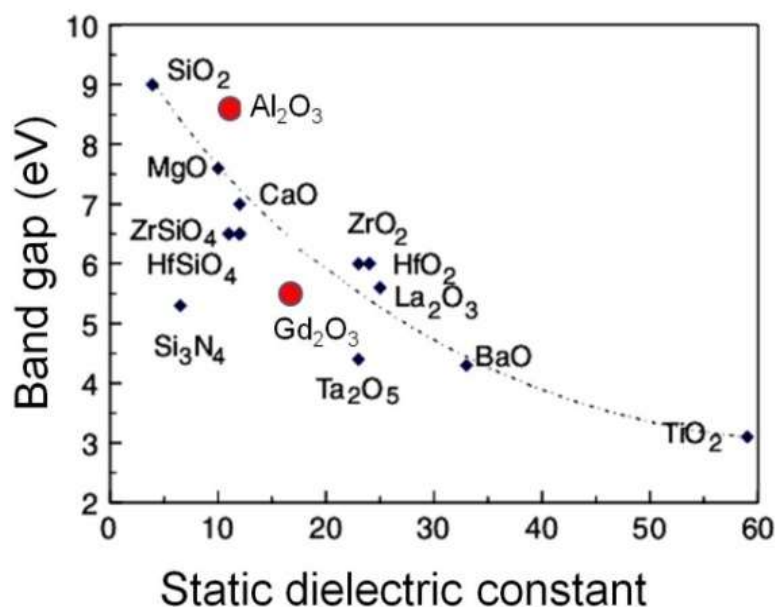


Figure 4.13: Plot showing the band gap vs. dielectric constant for typical dielectric materials (Reproduced with permission from Robertson¹⁹². Copyright (2000) AIP Publishing).

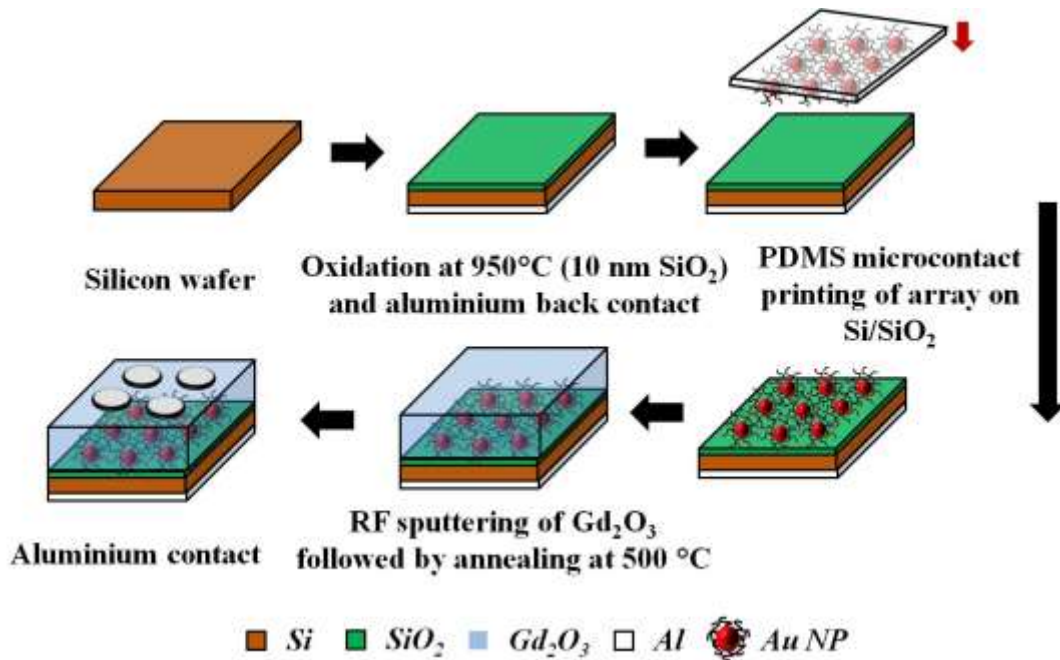


Figure Error! No text of specified style in document..56: Schematic representation of process flow sheet for fabrication of nanoparticle floating-gate memory device. Microcontact printing of gold nanoparticle array on 10 nm SiO₂/silicon wafer was done followed by gadolinium oxide deposition using RF sputtering. Aluminium contacts were deposited for device testing.

RF magnetron sputtering of gadolinium oxide (Gd₂O₃) was carried out using a commercial instrument (Anelva SPF-332H). A schematic of the proposed process flow for fabricating a silicon dioxide/gold nanoparticle array/gadolinium oxide stack is shown in Fig. 4.14. Silicon wafer (p-type, (100) orientation, resistivity of 1-2 Ω cm) was cleaned using standard RCA (Radio Corporation of America) method followed by HF (Hydrofluoric acid) dip to remove the native oxide. A 10 nm oxide layer was thermally grown on the wafer by dry oxidation at 950 °C for 5 minutes. Subsequently, the sample was annealed at 950 °C for 20 minutes under nitrogen environment, to passivate the interface traps. Ohmic back contacts were formed by thermal evaporation (HindHiVac 15F6) of ~100 nm thick aluminium (after carefully removing the native silicon dioxide film using buffered HF solution), and subsequent post-deposition annealing at 450 °C for 20 minutes in a forming gas environment. Large scale gold nanoparticle arrays with different interparticle spacing were transfer-printed onto the substrate using the optimized approaches discussed in the previous chapter. Gadolinium oxide was then deposited using RF sputtering. All these fabrication processes were carried out in a class 1000 clean room. For device characterization, 300 μm diameter aluminium contacts with ~100 nm thickness were deposited on the top surface (gate electrode) by thermal evaporation through a shadow mask, followed by post-deposition annealing at 450 °C for 30 minutes in forming gas atmosphere, for improving the contact between aluminium and top-oxide.

Process optimization

An initial experiment was carried out using the standard RF sputtering parameters for Gd₂O₃. A representative FESEM image of nanoparticle array embedded in Gd₂O₃ is shown in Fig. 4.15; indicating particle coalescence and loss of ordering. Parameters like substrate to target distance, argon gas pressure, sputtering voltage etc., dictate oxide deposition rate and energy imparted to the substrate (Fig. 4.16). This result suggested that either gadolinium ions (controlled by voltage) or argon plasma bombardment (controlled by gas pressure) could be the cause for particle coalescence and loss of ordering. A reduction in applied voltage between the substrate and target from 2 kV to 0.7 kV did not alter the results appreciably (Table 4-2).

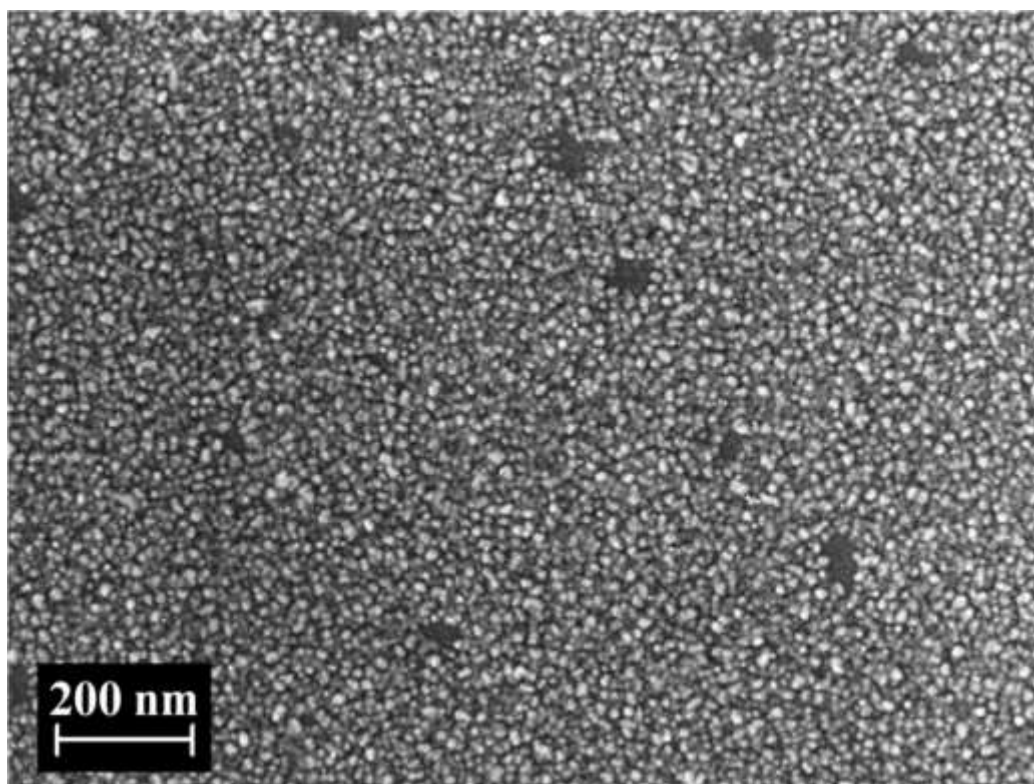


Figure **Error! No text of specified style in document..57**: Representative FESEM image of dodecanethiol capped gold nanoparticle array embedded in gadolinium oxide, which was deposited under standard conditions; particle coalescence and loss of hexagonal ordering is observed.

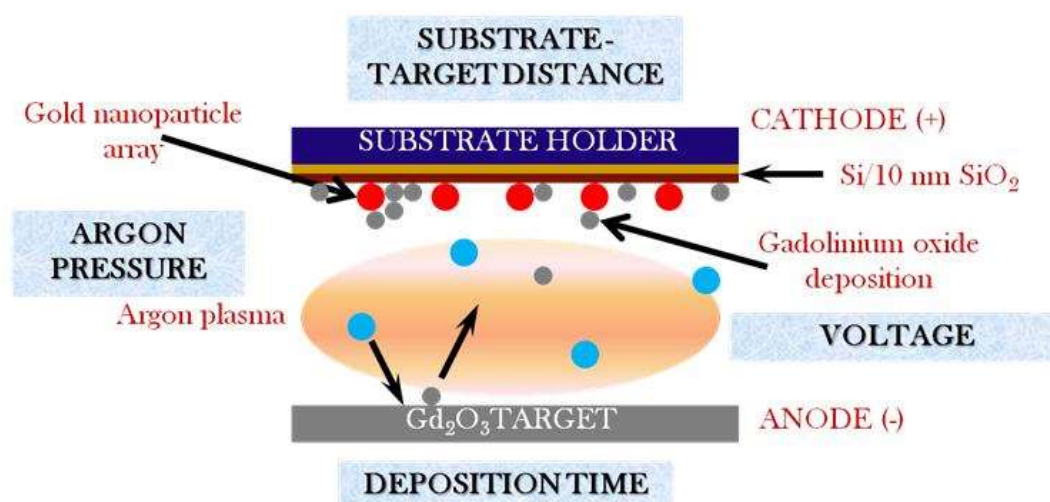
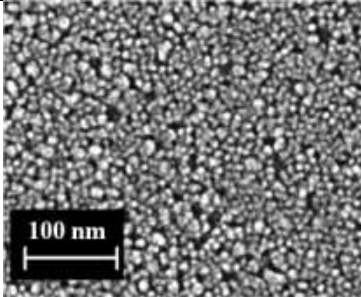
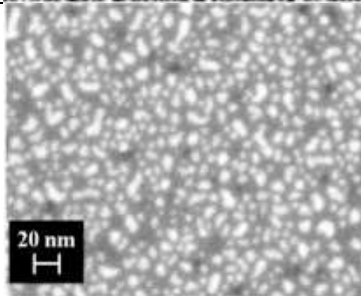
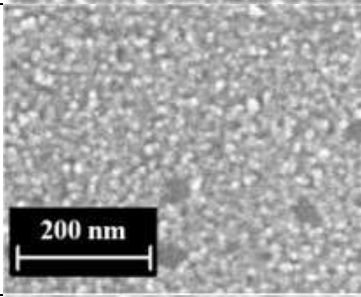
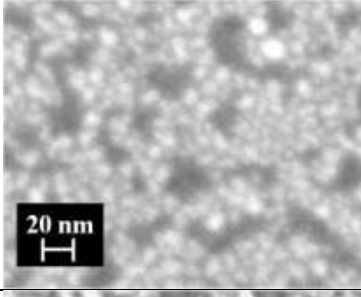
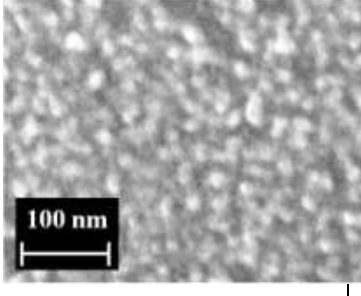
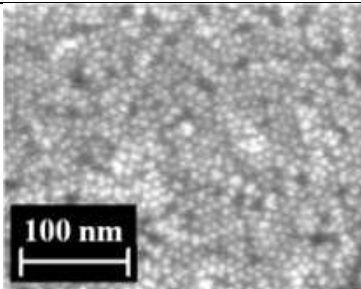
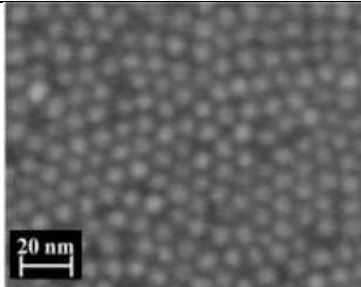


Figure **Error! No text of specified style in document..58**: Schematic of the RF magnetron sputtering process for gadolinium oxide deposition, indicating the various parameters that were optimized in this study.

Table **Error! No text of specified style in document.**-4: Effect of RF sputtering process conditions on gold nanoparticle array. The sample was annealed at 500°C for 30 min under forming gas atmosphere

Run	Process conditions	FESEM image	Remarks
1	Argon pressure: 0.01 mbar Voltage: 1 kV Substrate-target distance: 5.2 cm Deposition time: 50 minutes		Particle coalescence and loss of ordering
2	Argon pressure: 0.01 mbar Voltage: 0.7 kV Substrate-target distance: 5.2 cm Deposition time: 50 minutes		Particle coalescence and loss of ordering
3	Argon pressure: 0.007 mbar Voltage: 1 kV Substrate-target distance: 5.2 cm Deposition time: 50 minutes		Reduced coalescence of particles but extensive loss of ordering
4	Argon pressure: 0.007 mbar Voltage: 1.5 kV Substrate-target distance: 5.2 cm Deposition time: 20 minutes		Reduction in both particle coalescence and loss of ordering
5	Argon pressure: 0.007 mbar Voltage: 2 kV Substrate-target distance: 5.2 cm Deposition time: 10 minutes		Increased particle coalescence and loss of ordering by reducing the exposure time and increasing the gadolinium ion bombardment

6	<p>Argon pressure: 0.007 mbar</p> <p>Voltage: 1.5 kV</p> <p>Substrate-target distance: 4.4 cm</p> <p>Deposition time: 10 minutes</p>		<p>Particle coalescence and ordering are reasonably maintained</p>
7	<p>Argon pressure: 0.007 mbar</p> <p>Voltage: 1.25 kV</p> <p>Substrate-target distance: 4.0 cm</p> <p>Deposition time: 10 minutes</p>		<p>Optimized condition resulting in maintenance of both particle size and ordering by controlling the interplay of all the operating parameters</p>

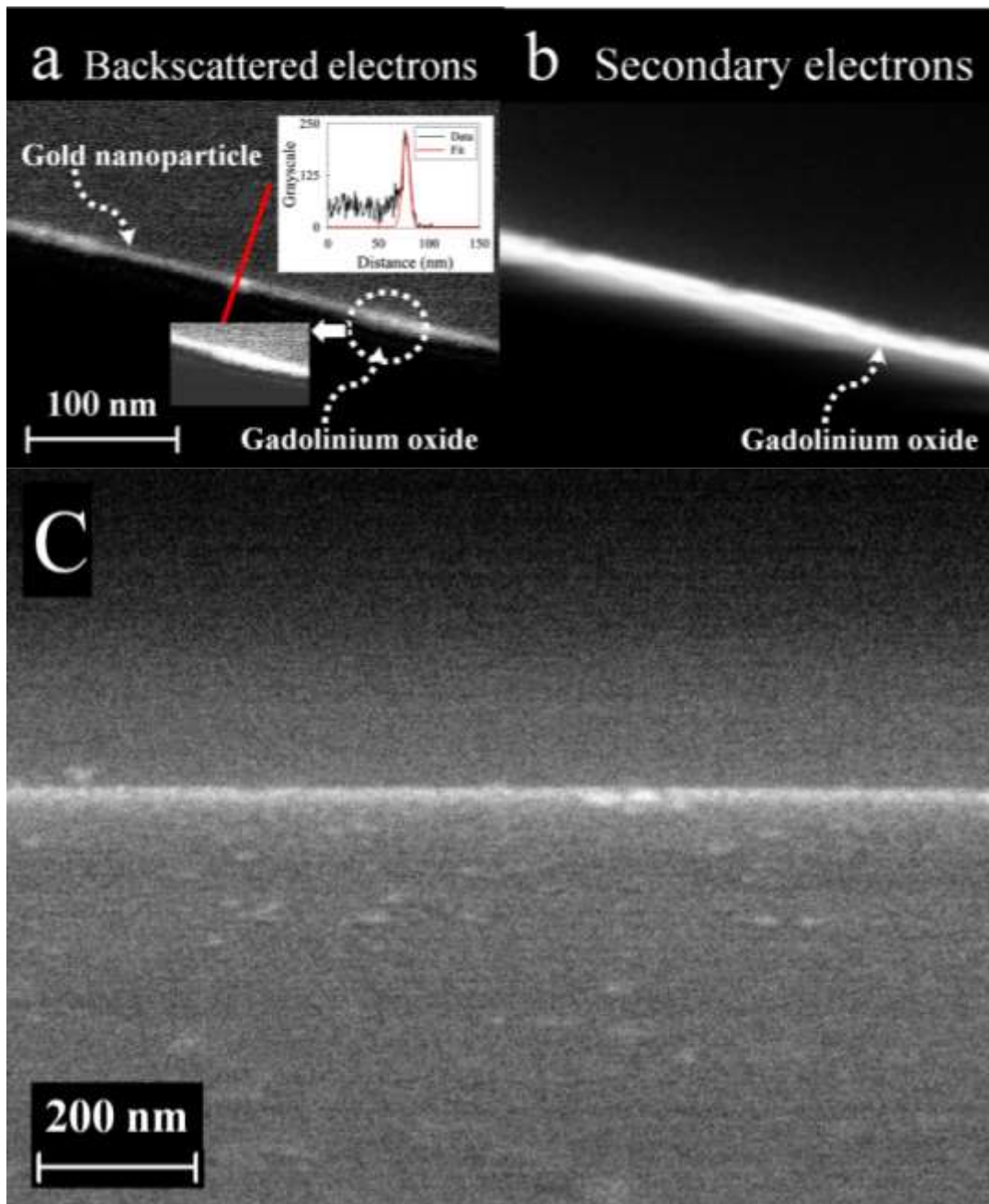


Figure **Error! No text of specified style in document.**59: Representative high magnification cross-sectional FESEM images of the MOS capacitor with gold nanoparticle arrays as charge storage nodes, obtained using (a) angle selective backscattered electron (AsB) and (b) secondary electron (SE) detector. Contrast in backscattered electron imaging is predominantly due to the difference in atomic weight (Z) while secondary electron imaging depends on surface features. Here, the sample contains both gold ($Z = 197$) and gadolinium oxide ($Z = 363.49/5=72$), hence gold nanoparticles are seen clearly in AsB and not using SE detector. The edge of the sample appears as a very faint line (indicated by the arrow labelled gadolinium oxide) in (a), while it appears very bright in (b) due to the predominance of edge effects in SE imaging. A 2-D profile plot of the grayscale values across the MOS capacitor (inset in a) indicates the thickness of array to be ~ 7 nm, based on full width at half maximum. (c) Low magnification cross-sectional FESEM image of the MOS capacitor, obtained using angle selective backscattered electron detector indicating large scale uniformity. The dense packing of the array precludes visualization of individual nanoparticles. These samples were obtained by cleaving the silicon substrate.

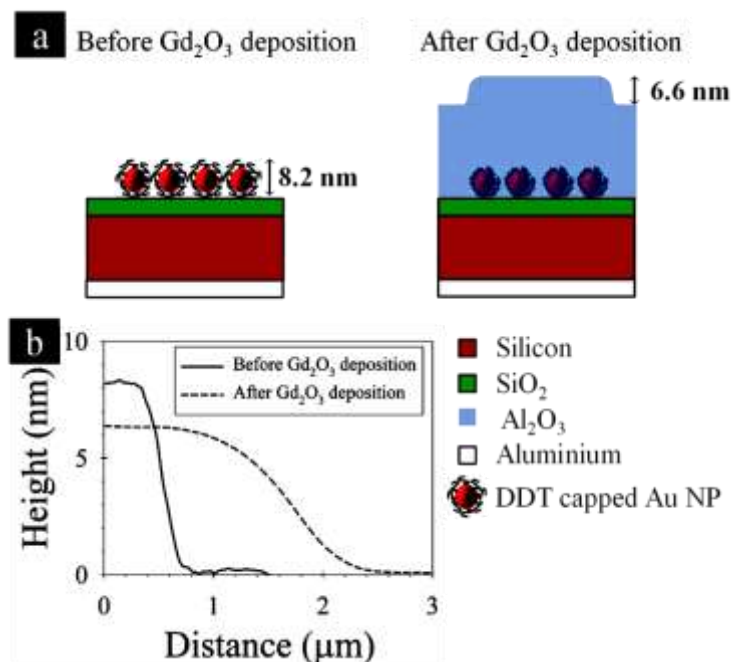


Figure **Error! No text of specified style in document..60**: (a) Schematic illustrating the expected cross-section of the device before and after RF sputter deposition, indicating that most of the ligand molecules have been removed from the ligand layer after gadolinium deposition. (b) AFM cross-sectional height profiles across the edge of the nanoparticle array before and after gadolinium oxide deposition by RF sputtering. A decrease in the difference of height from 8.2 nm to 6.6 nm indicates that most of the ligands have been removed during the RF sputtering process.

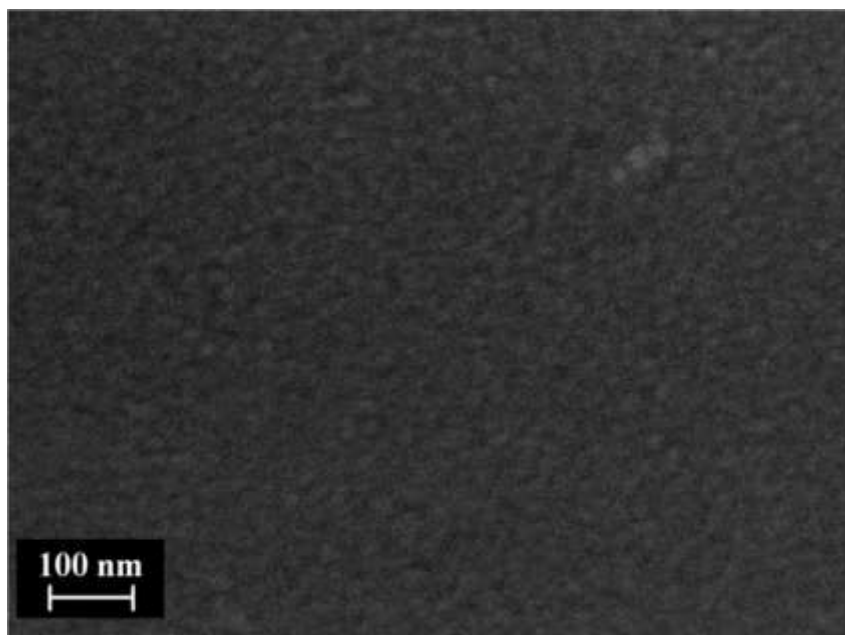


Figure **Error! No text of specified style in document..61**: Representative FESEM image of MOS capacitor fabricated with a 30 nm thick gadolinium oxide layer, indicating poor lateral resolution, which hinders the visualization of the in-plane ordering of the nanoparticle array.

However, when argon gas pressure was reduced from 0.01 mbar to 0.007 mbar, particle coalescence was minimized significantly. Further reduction in argon gas pressure had little effect on nanoparticle ordering. So, it was decided to deposit the oxide with minimal exposure time to argon plasma. This demands either a reduction in substrate to target distance or an increase in applied sputtering voltage. A tradeoff between the high deposition rate and maintaining ordering was achieved at an optimum voltage of 1.25 kV. Thus, all further studies were carried at the following optimized conditions: applied voltage 1.25 kV, argon gas pressure of 0.007 mbar, substrate to target distance of 4 cm with 10 minutes deposition time to obtain a thickness of 15 nm. The optimized sputtering conditions represent a balance between

the timescale required for plasma or ion bombardment to induce nanoparticle coalescence/disordering with the timescale for encasement of nanoparticles by gadolinium oxide. Use of higher argon pressure (increased plasma bombardment) during sputtering led to fusion of nanoparticles into percolating thin sheets, while higher sputtering voltages (increased ion bombardment) led to coarsening of nanoparticles. The substrate to target distance was minimized to the maximum extent feasible, to obtain the desired thickness of Gd_2O_3 in the shortest possible time. The sputtered oxide film, deposited under optimized conditions, was then annealed at 500°C for 30 min under forming gas atmosphere to passivate interface defects. The encasement of the nanoparticles by gadolinium oxide, under the optimized conditions, is further confirmed by the absence of particle coalescence after thermal annealing at 500°C for 30 min, as otherwise just heating to $\sim 150^\circ\text{C}$ would result in coalescence of gold nanoparticle arrays. Cross-sectional FESEM images of the oxide stack further confirmed the absence of coarsening as the thickness of the gold nanoparticle array was found to be ~ 7 nm (Fig. 4.17), equivalent to the height expected of a gold nanoparticle. Efforts to use the recently installed FIB (Helios NanoLab,) to obtain higher resolution cross-section images did not yield the desired results. Moreover, AFM line scans (Fig. 4.18) across the edge of the array, show a decrease in height of 1.6 nm after gadolinium oxide deposition. Considering that the thickness of the ligand layer coating the nanoparticles is ~ 1.5 nm, this decrease in AFM height suggests that at least 50% of the ligand molecules were removed due to the RF sputtering process. To facilitate plan-view FESEM imaging of the nanoparticle array after the various processing steps, only a 15 nm thick layer of gadolinium oxide was deposited, as higher thicknesses led to poorly resolved images of nanoparticles, caused by increased electron scattering in the gadolinium oxide layer (Fig. 4.19).

Electrical characterization

Electrical characterization of the MOS capacitors with the presence of gold nanoparticle arrays resulted in reproducible hysteresis loops in CV plots during programming and erasing cycles (Fig. 4.20a), while control devices fabricated without the gold nanoparticle layer did not show any hysteresis (Fig. 4.20b). The robust nature of the fabrication process is evident from the reproducible memory windows (flatband voltage shifts, a model estimation of flatband voltage is given in Appendix B.1) measured across several devices spread over $\sim \text{cm}^2$ area (Fig. 4.20c). The narrow spread of memory windows across devices (0.66 ± 0.05 V, $n=14$ at P/E voltages of ∓ 7 V), in conjunction with the ability to tune memory window by controlling the P/E voltages (Fig. 4.20d) will enable multilevel cell operation. The ability to store multilevel data within a single device can greatly augment the storage capacity of floating gate memory devices, and help keep pace with the expectations of the semiconductor industry. The clockwise nature of the hysteresis loop in Fig. 4.20a and the measured values of flatband voltage shifts reflect the fact that electron tunneling process during programming/erasing occurs through the gadolinium oxide rather than the silicon dioxide layer. This is attributed to the low barrier height and higher defect assisted tunneling of RF-sputtered gadolinium oxide film, as compared to thermally grown silicon dioxide film. Retention characterization were performed by ‘reading’ the capacitance at a voltage of -0.8 V (flatband voltage) for durations of 10000 seconds, after initially applying P/E voltages of ∓ 7 V. The retention characteristics were found to be reproducible across several devices (Fig. 4.21a). The large work function of gold results in a larger well depth with an asymmetric band profile (Fig. 4.21b) that enhances retention even when the Equivalent Oxide Thickness (EOT) of the fabricated device is only ~ 16 nm. The capacitance values in the programmed states show a rapid decrease within 1000 s and then stabilize to an almost constant value (about 50% of the initial charge stored has a decay time constant $> 10^8$ s). Electrostatic Force Microscopy (EFM) measurements also show a similar variation of the phase change with time (Fig. 4.21c,d). The phase change, measured by EFM is known to be proportional to the amount of stored charge which is estimated to be 2.3×10^{-7} C/ cm^2 (~ 1 e-/nanoparticle) in this case. Details of the estimation of charge storage based on EFM measurements are presented in Appendix B.2. The facts that the charge retained remains almost constant after the initial decay and that the cross-sectional profiles of phase-change show the stored charges to be bound laterally exclude a charge loss mechanism involving lateral charge dispersion. A similar trend in retention behavior has been attributed to a reduction in tunneling probability caused by lowering of the in-built electric field with charge loss; it is believed that this reasoning can also explain the trends seen in Fig. 4.21a and Fig. 4.21c,d. Significantly, endurance characterization tests show that the memory window persists even after 10^4 P/E cycles (Fig. 4.21e). The rapid shift in flatband voltages during the first 100 cycles is attributed to the generation of stress induced defects in the oxide stack. Altogether, these results confirm that it is indeed the gold nanoparticles that act as charge storage nodes in these devices. Furthermore, the reproducibility of the electrical characteristics across devices attests to the uniformity of the array of nanoparticles at the macroscopic scale, which signifies that the proposed process can be easily adopted for production of future flash memory devices. XPS spectrum of gold-4f region (Fig. 4.22a) shows the presence of gold in pure metallic form ($4f_{7/2}$ line at 84.1 eV). The absence of peaks corresponding to gold silicide formation (~ 85 eV), which degrades semiconductor device performance, highlights the compatibility of the proposed bottom-up process with CMOS technology, in contrast to approaches based on ion bombardment and annealing. XPS spectrum of gadolinium 3d and 4d levels (Fig. 4.22b) confirm the presence of gadolinium in +2 charged state, while the spectrum of oxygen 1s level (Fig. 4.22c) shows the predominant presence of gadolinium hydroxide (532.4 eV) in the stack, which is attributed to the hygroscopic nature of rare earth oxides. XPS scan of carbon 1s region (Fig. 4.22d) indicates the presence of C=O moieties (288.7 eV), possibly

formed by the decomposition of the ligands during sputtering. The presence of sulphur peaks at 162.7 eV (Fig. 4.22e) also corroborates the earlier AFM based finding that some portions of the ligands are incorporated into the oxide stack.

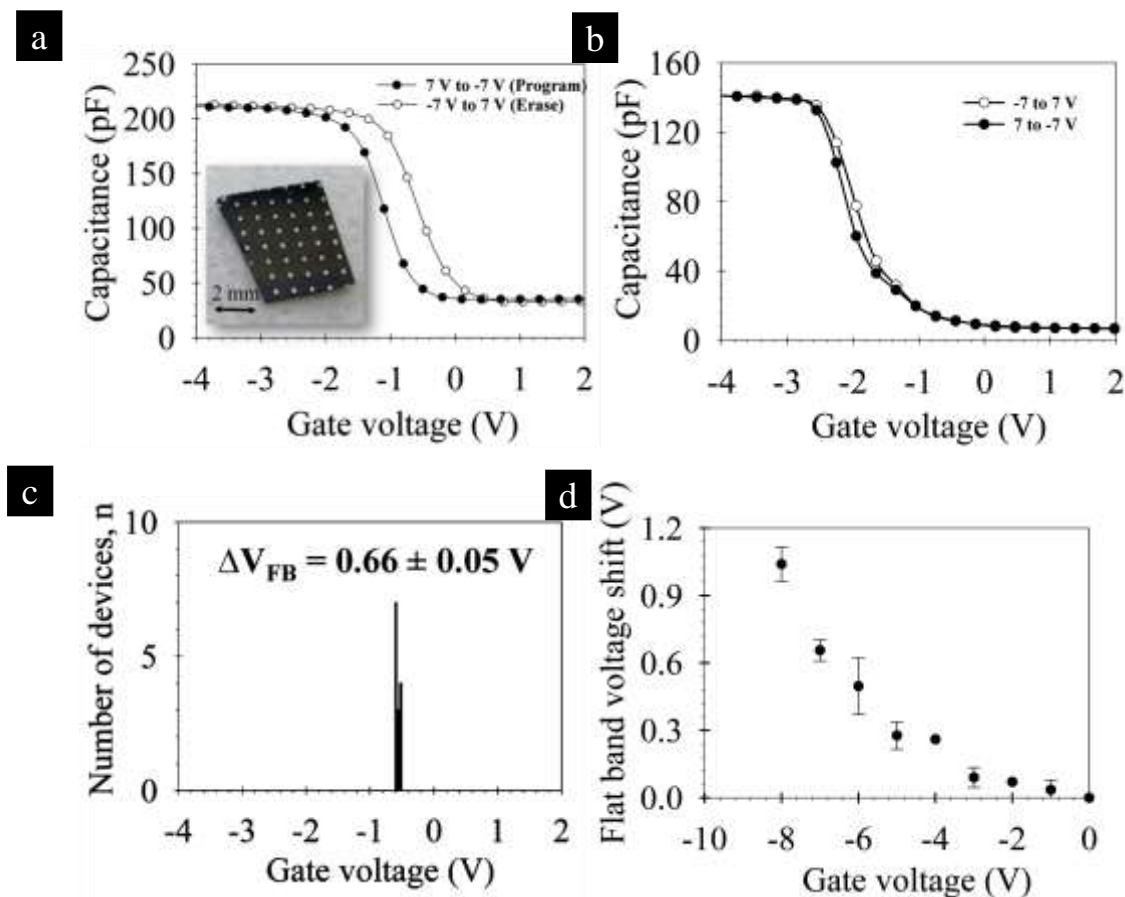


Figure **Error! No text of specified style in document.**62: (a) Capacitance-Voltage (CV) curve of a MOS capacitor with the gold nanoparticle array as floating gate, obtained by bi-directional sweep from inversion to accumulation. The appearance of a hysteresis loop indicates that gold nanoparticles act as charge storage nodes. The capacitor area is $7.07 \times 10^{-4} \text{ cm}^2$, and the measurement frequency used was 1 MHz. The inset shows an optical photograph of several MOS capacitor devices. The white dots are the aluminium top contacts. (b) Capacitance-voltage characteristics of Si/SiO₂/Gd₂O₃ (without any gold nanoparticle). The control samples do not show any hysteresis with bidirectional voltage sweeps, indicating the absence of any interface traps. (c) Histogram of flatband voltage shifts measured from 14 devices using P/E voltages of $\pm 7 \text{ V}$. The distribution of flatband voltage shifts is $0.66 \pm 0.05 \text{ V}$. (d) Variation of flatband voltage shifts as a function of P/E voltages. The points represent the average of flatband voltage shifts and the error bars represent 95% confidence interval ($n \geq 5$).

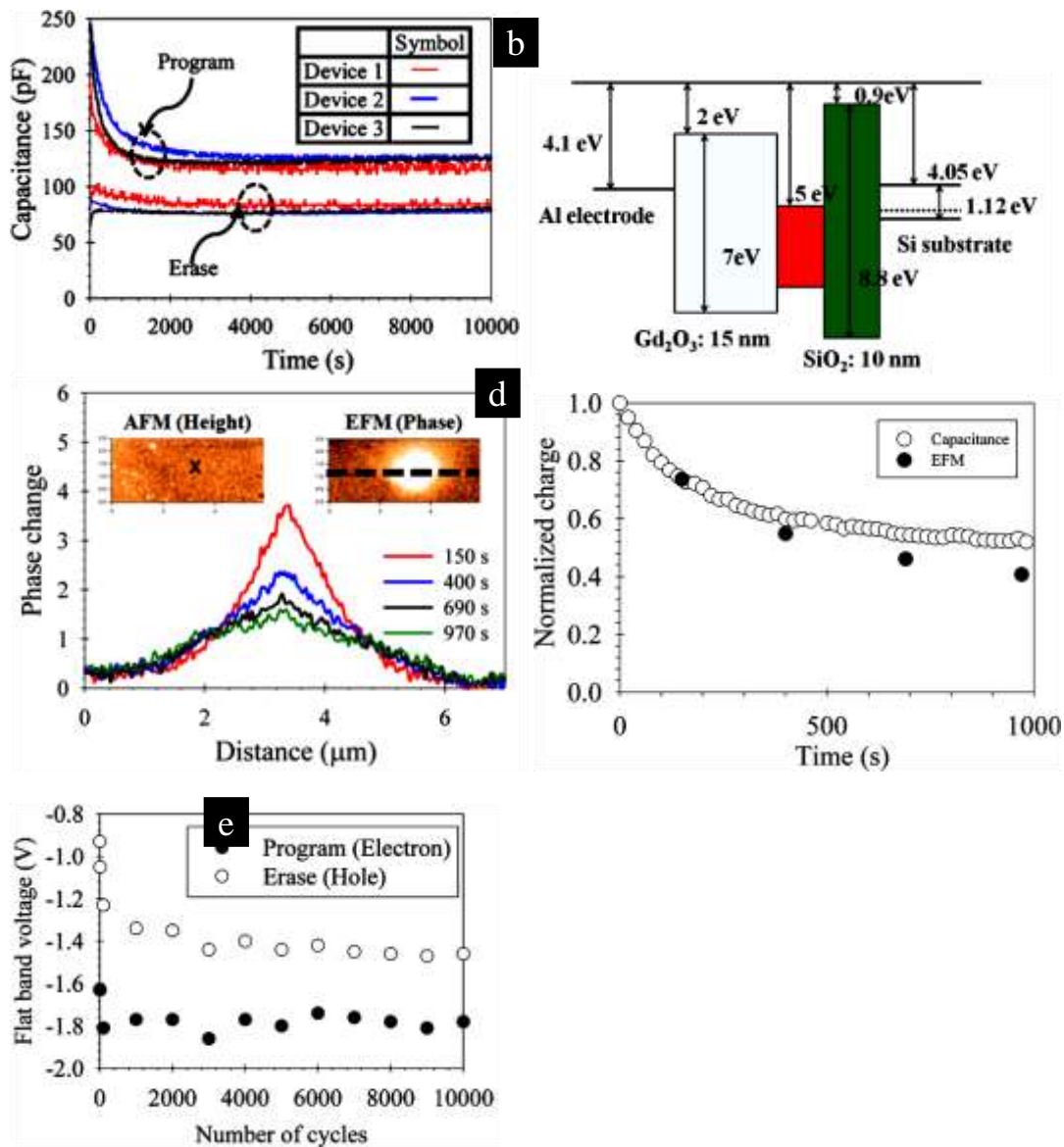


Figure **Error! No text of specified style in document..63**: (a) Representative charge retention characteristics of MOS capacitors physically spread across $\sim \text{cm}^2$ area, indicating large scale uniformity of nanoparticle array. P/E was carried out at a voltage of ± 7 V, while reading voltage was set at -0.8 V. (b) Schematic energy band diagram depicting flatband condition of the floating gate structure comprising of gold nanoparticles sandwiched between silicon dioxide and gadolinium oxide. (c) EFM phase change profiles obtained at a reading voltage of 3 V and at a height of 80 nm from the surface. Charge was injected initially, by applying -6 V from 0 to 120 s, in contact mode at the spot marked "X" in AFM topography scan (top left inset). EFM phase change image (after 150 s) is shown in the top right inset, with a line marking the cross-section along which phase change profiles were measured. (d) Comparison of normalized charge stored obtained using capacitance and EFM measurements. (e) Endurance characteristic of a device indicating a stable memory window even after 10^4 P/E cycles (by biasing at ± 7 V).

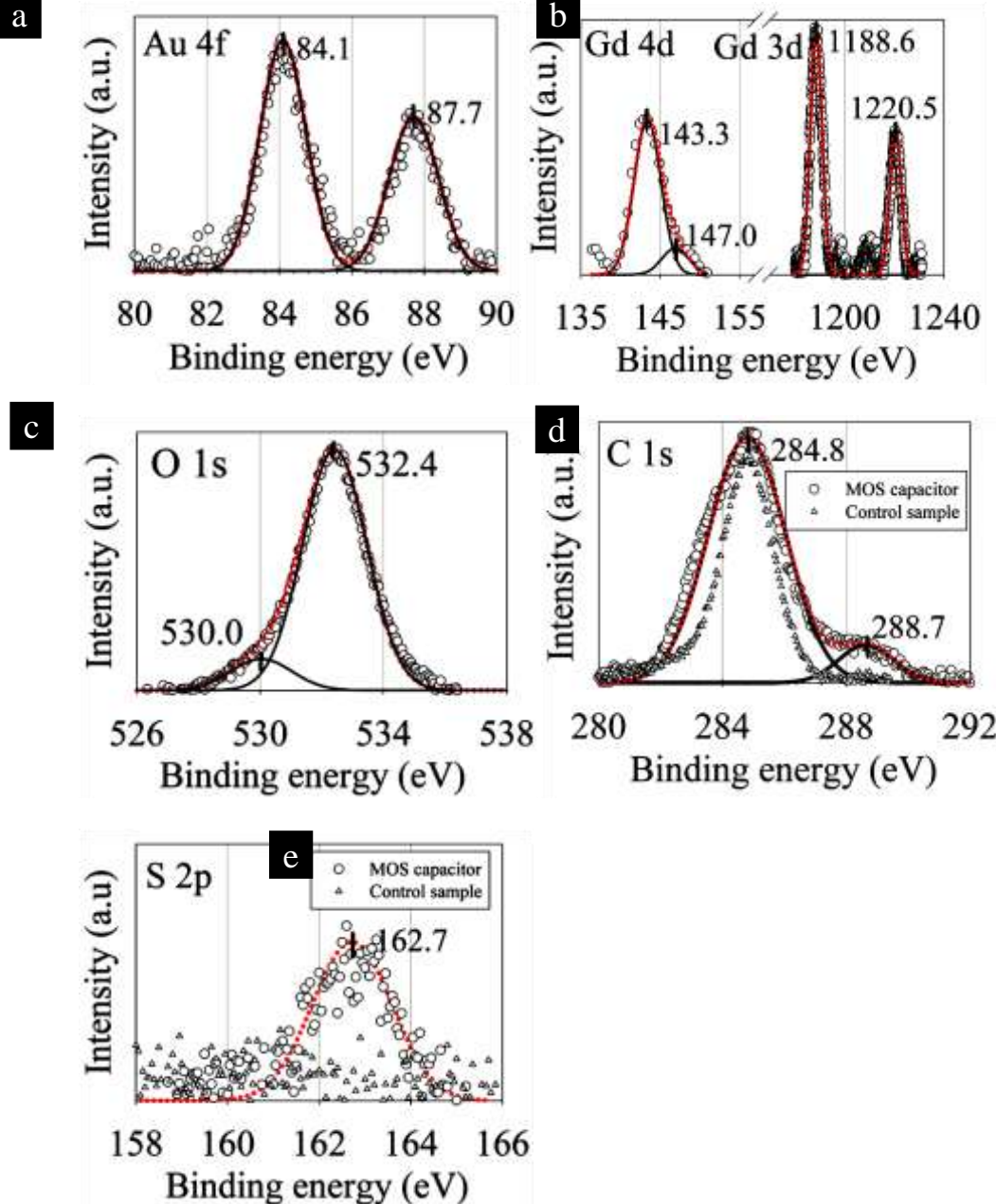


Figure **Error! No text of specified style in document..64**: (a) Au 4f core level XPS spectrum from a MOS capacitor with embedded nanoparticle array indicating the presence of gold in metallic form (84.1 and 87.7 eV). XPS spectra of (b) Gadolinium 3d and 4d levels, and (c) Oxygen 1s level indicate the predominant presence of hydroxide (532.4 eV), possibly as gadolinium hydroxide ($\text{Gd}(\text{OH})_3$) and is attributed to the hygroscopic nature of rare earth oxides. XPS spectra of (d) Carbon 1s and (e) Sulphur 2p core levels for MOS capacitors fabricated with and without (control) gold nanoparticle arrays embedded in gadolinium oxide. For MOS capacitors with the embedded nanoparticle array, the presence of C=O (288.7 eV) and trace amount of sulphur (162.7 eV) indicates that some residual ligands are trapped inside. C=O bonds are expected to have formed during the annealing steps by decomposition of the trapped ligands. In these figures, the symbols represent measured data points, the black lines represent deconvoluted peaks, and the red lines represent the overall fit. The numbers in the panels represent the peak values of the fitted curves.

Effect of interparticle spacing on memory characteristics

Control over nanoparticle ordering and spacing is necessary, as these can critically affect the performance of floating gate devices. Intuitively, smaller interparticle spacing would be considered best for increasing the storage density, while larger interparticle spacing leads to faster programming, as well as improved retention characteristics. To understand the impact of interparticle spacing at the nanoscale, the Metal-Oxide-Semiconductor (MOS) capacitors having gold nanoparticle arrays with larger (4.4 and 13.3 nm) interparticle spacings, as the floating gate were fabricated. This was accomplished by simply replacing the dodecanethiol ligand used earlier by thiol-terminated polystyrene ligands with molecular weights of 3000 and 20000 g/mol; thereby, also highlighting the versatility and ease of the developed process. Representative plan-

view FESEM image of a self-assembled 2D array of thiol-terminated polystyrene capped gold nanoparticles on top of a Si/SiO₂ substrate is shown in Fig. 4.23. Gold nanoparticles (nominally 7 nm size) form highly-ordered hexagonal arrays with interparticle spacing of 4.4 ± 0.6 nm (Fig. 4.23a) and 13.3 ± 2.3 nm (Fig. 4.23b) for thiol-terminated polystyrene of molecular weight 3000 and 20000 g/mol respectively. Representative plan-view FESEM images of samples obtained after deposition of a 15 nm thick gadolinium oxide layer onto 2D arrays of thiol-terminated polystyrene capped gold nanoparticles followed by thermal annealing at 500 °C are shown in Fig. 4.24a and Fig. 4.24b respectively. At the optimal conditions of RF sputtering found earlier, the ordering of these polystyrene-coated arrays was disturbed, but there was no evidence of particle coalescence.

Electrical characterization of devices fabricated using arrays of ligand coated gold nanoparticles (both with 4.4 nm spacing and 13.3 nm spacing) did not show any hysteresis in CV plots (Fig. 4.25a,b), despite the presence of gold nanoparticles that can serve as charge storage nodes. The loss of memory window is attributed to the possible formation of conductive carbonaceous products. Such carbonaceous products are likely formed, due to the decomposition, during the annealing steps, of polystyrene thiol ligands entrapped in the oxide stack. This aspect was further investigated using EFM studies of oxide stacks formed. In EFM measurements, the3K sample exhibited a larger phase change than the sample containing DDT coated

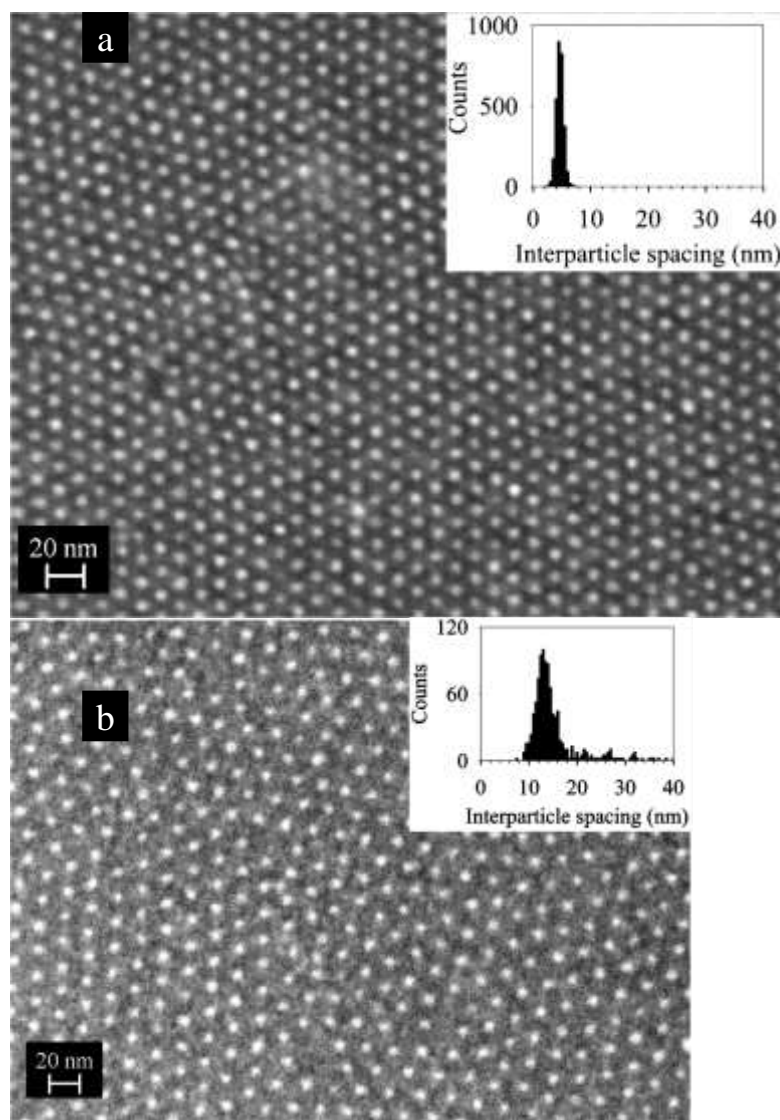


Figure **Error! No text of specified style in document..65**: Representative FESEM image of close-packed 2D array of thiol-terminated polystyrene capped gold nanoparticles (nominally 7 nm sized gold cores) with (a) 4.4 ± 0.6 nm interparticle spacing, corresponding to a number density of 7.7×10^{11} particles/cm² and (b) 13.3 ± 2.3 nm interparticle spacing, corresponding to a number density of 2.4×10^{11} particles/cm², on Si/SiO₂ prior to gadolinium oxide deposition. The insets show the corresponding histograms of interparticle spacing in these arrays.

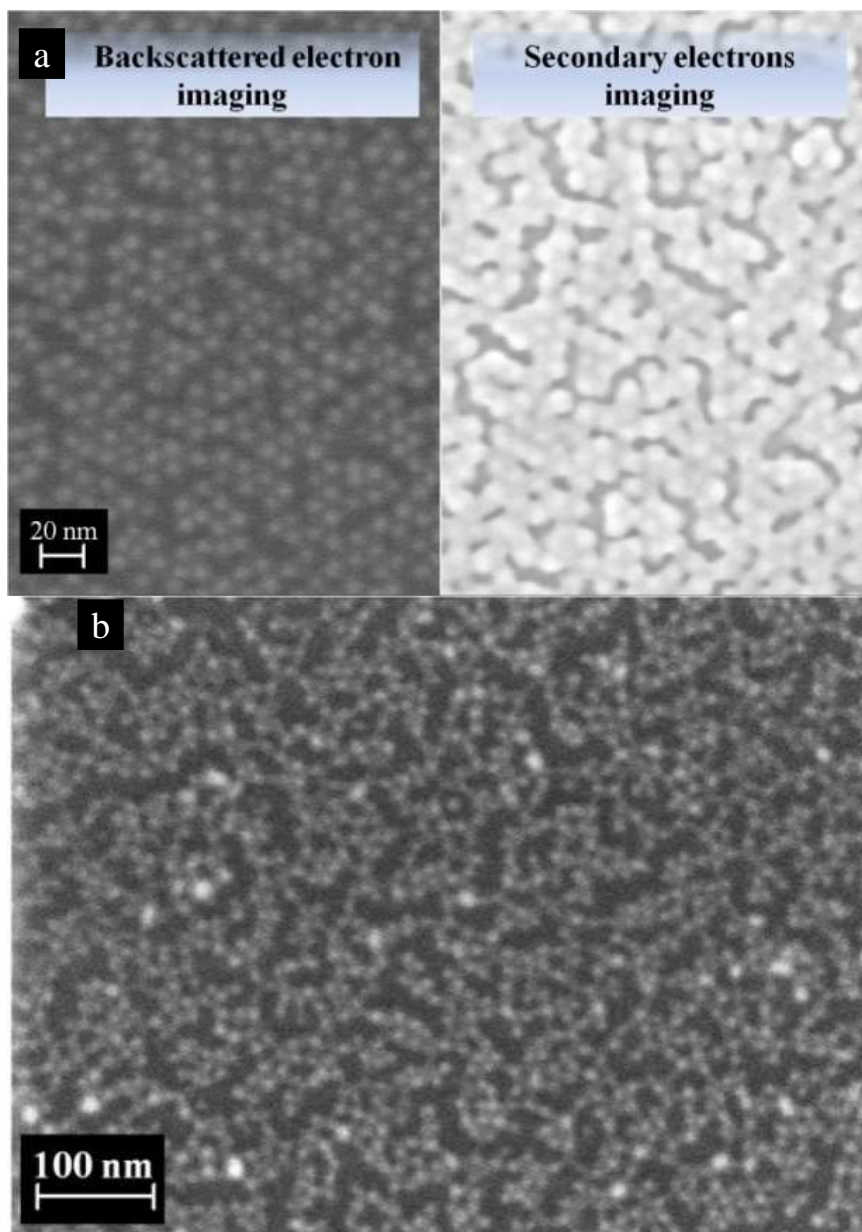


Figure **Error! No text of specified style in document.**66: (a) Representative plan-view FESEM images of samples obtained after deposition of a 15 nm thick gadolinium oxide layer onto a 2D array of thiol-terminated polystyrene capped gold nanoparticles (nominally 7 nm sized gold cores) with 4.4 nm interparticle spacing, followed by thermal annealing at 500 °C. The left hand side image was obtained using angle selective backscattered electrons, which provide information on the atomic number of the material, and the right hand side image was obtained using secondary electrons, which provide information on the surface topography. Scale bar represents 20 nm. (b) Representative plan-view FESEM images (using secondary electron detector) of samples obtained after deposition of a 15 nm thick gadolinium oxide layer onto 2D array of thiol-terminated polystyrene capped gold nanoparticles (nominally 7 nm sized gold cores) with 13 nm interparticle spacing, followed by thermal annealing at 500 °C. Scale bar represents 100 nm.

array, indicating larger storage capacity, which is attributed to the possibility of polystyrene molecules also acting as charge storage sites (Fig. 4.26a). This is unlike the CV measurements in Fig. 4.25a. This difference in observing contrasting charge storage characteristics is attributed to the differences in the two measurement techniques. In standard EFM measurement (4.26a), the sample is charged by placing the tip and sample in contact, while the reading of the stored charges, with the tip biased to the opposite polarity, takes place out of contact. However, in CV measurements the probe is always in contact with the sample and thus provides a leakage path to ground for the stored charges. To replicate this situation in EFM experiments, an intermediate step was introduced, wherein the tip remains in contact with the sample for some time after charging, prior to the reading step (Fig. 4.26b). With the intermediate step of reading in contact, the

sample showed negligible charge storage characteristics (Fig. 4.26c). These results are in accord with the hypothesis that a conductive pathway is formed in the gadolinium oxide that completely compromises its dielectric properties. The most likely cause of this is the formation of carbonaceous products by ligand decomposition. In order to circumvent the issue of presence of ligand, bare gold nanoparticle arrays were fabricated by using mild RF oxygen plasma etching, based on an earlier report. A schematic of the modified process flow for silicon dioxide/gold nanoparticle array/gadolinium oxide stack formation is shown in Fig.4.27. All the device fabrication steps remain identical except for an additional step of ligand removal using RF plasma etching. Preliminary EFM characterization showed that oxygen plasma treatment on bare Si/SiO₂ substrate results in deterioration of the electrical properties of the thin silicon dioxide layer (Fig. 4.28a,b). Thus, to reduce the amount of interface traps, the sample was subjected to forming gas annealing at 450 °C for 30 minutes. EFM measurements indicated that the charge retention properties were restored to its original condition (Fig. 4.28c). Thus, as a precaution to reduce the amount of interface traps, an additional step of forming gas annealing at 450 °C for 30 minutes was carried out after array deposition and RF oxygen plasma treatment. This processing step was not implemented in the case of the ligand coated nanoparticle array, as the nanoparticles coalesced upon annealing without top-oxide deposition. Again, this poor thermal stability is attributed to the presence of ligands. The removal of polystyrene ligands by RF oxygen of all the steps involved in device fabrication (Fig. 4.29a); this is in contrast to the earlier report on dodecanethiol coated nanoparticle arrays. This can be attributed to the ligand removal during exposure of dodecanethiol coated nanoparticle array to argon plasma during RF sputtering. In the case of the longer PSSH ligands, the ligands may not be removed during gadolinium oxide deposition process and so, are entrapped within the oxide stack. Therefore, the loss of nanoparticle ordering observed in Fig. 4.24a is attributed to the presence of ligands. A reproducible flatband voltage shift of 1.26 ± 0.17 V ($n = 8$) and 0.53 ± 0.06 ($n=3$) was obtained for the devices fabricated after incorporating the ligand removal step in the process flow for arrays with 4.4 nm and 13.3 nm interparticle spacing (Fig. 4.30a-c). Interestingly, the memory window obtained for devices with 4.4 nm spacing is larger than the memory window (0.66 V) reported earlier using dodecanethiol coated gold nanoparticle arrays with 2 nm spacing, although the number density was only 7.7×10^{11} particles/cm² in the present case, as opposed to the number density of 1.2×10^{12} particles/cm². It is to be noted that in the case of devices using dodecanethiol capped gold nanoparticles, ligand was not removed completely. To determine the role of ligand on memory characteristics, devices were made with bare nanoparticle arrays having 2 nm spacing. This was obtained by pre-treating the array with mild hydrogen plasma under optimized conditions as reported. The memory window is 0.7 V (Fig. 4.30d), which is equal to the earlier value of 0.66 ± 0.05 V obtained sing ligand coated array. This indicates that the ligand has no significant effect on memory window. Hou et al. had modeled the interaction of 3D electrostatic fields in an array of nanoparticles and found that lower particle densities lead to faster P/E times. However, the P/E times used in these measurements were found to result in saturation of flatband voltage shifts in all the cases, and so, changes in the rate of charge tunneling during P/E cannot account for the observed differences. At this juncture, it is surmised that with the increased number density of gold nanoparticles in the case of dodecanethiol sample, the limiting case of a continuous gold layer is approached, and therefore, it is more susceptible to defects in the oxide stack. As in the previous section, gadolinium oxide acts as the tunneling oxide for the devices reported herein. Because of the low barrier height and higher defect assisted tunneling compared to silicon dioxide, this results in clockwise hysteresis loops. With further increase in interparticle spacing to 13 nm, the memory window decreased to 0.53 V. This is expected because with an increase in interparticle spacing, the density of charge storage elements decreases.

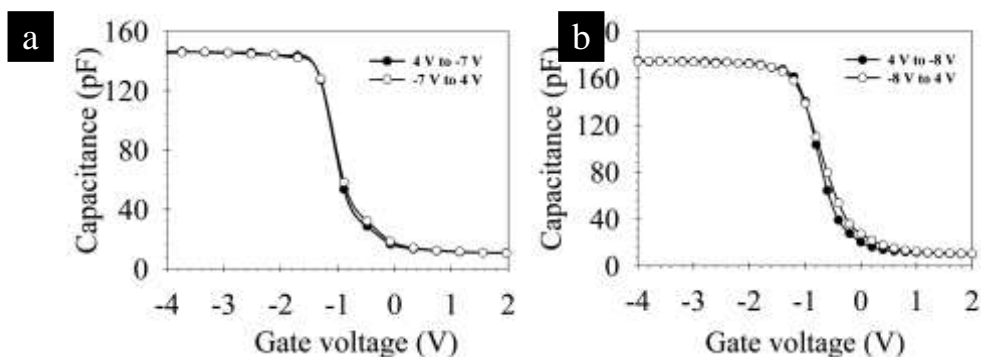


Figure Error! No text of specified style in document..67: Capacitance-voltage characteristics of MOS capacitors fabricated using arrays of gold nanoparticles capped with thiol-terminated polystyrene of molecular weight (a) 3000 g/mol and (b) 20000 g/mol, embedded in gadolinium oxide on Si/SiO₂. The samples do not exhibit any hysteresis despite the presence of gold nanoparticles that can serve as charge storage nodes. This could be possible only if thiol-terminated polystyrene molecules can be converted to carbonaceous material during annealing.

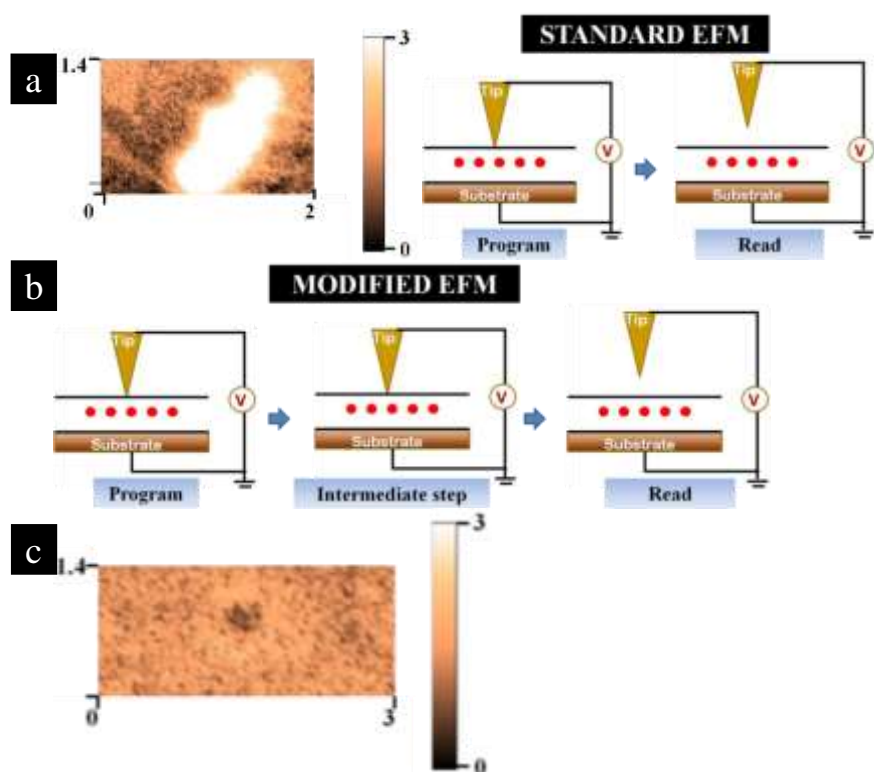


Figure Error! No text of specified style in document..68: (a) Representative EFM phase profile of MOS capacitors fabricated using arrays of gold nanoparticles capped with thiol-terminated polystyrene of molecular weight 3000 g/mol embedded in gadolinium oxide on Si/SiO₂. The units of x and y axis correspond to μm . Charge was injected initially by applying -6 V from 2 minutes while the reading voltage was fixed at 3 V at a height of 70 nm from the surface. The color coded scale bar represents the magnitude of phase change observed during EFM imaging. The EFM measurements are carried out in a standard mode (see schematic). (b) Schematic representation of modified EFM measurement with an intermediate step of contacting the tip with sample before reading. (c) EFM phase profile of modified procedure for imaging MOS capacitor incorporating gold nanoparticle arrays. Negligible presence of charge stored after reading indicates leakage paths for electrons to detrapp through the top-oxide.

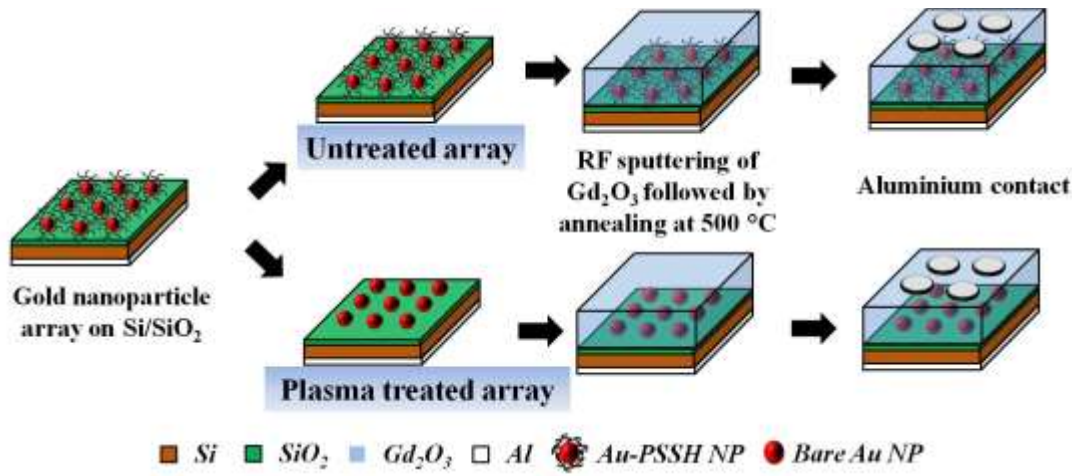


Figure **Error! No text of specified style in document..69**: Schematic representation of modified process flow sheet for nanoparticle floating-gate memory device fabrication, with an additional step of RF plasma etching to fabricate bare nanoparticle array (plasma treated array) under optimized conditions. All other steps remain identical.

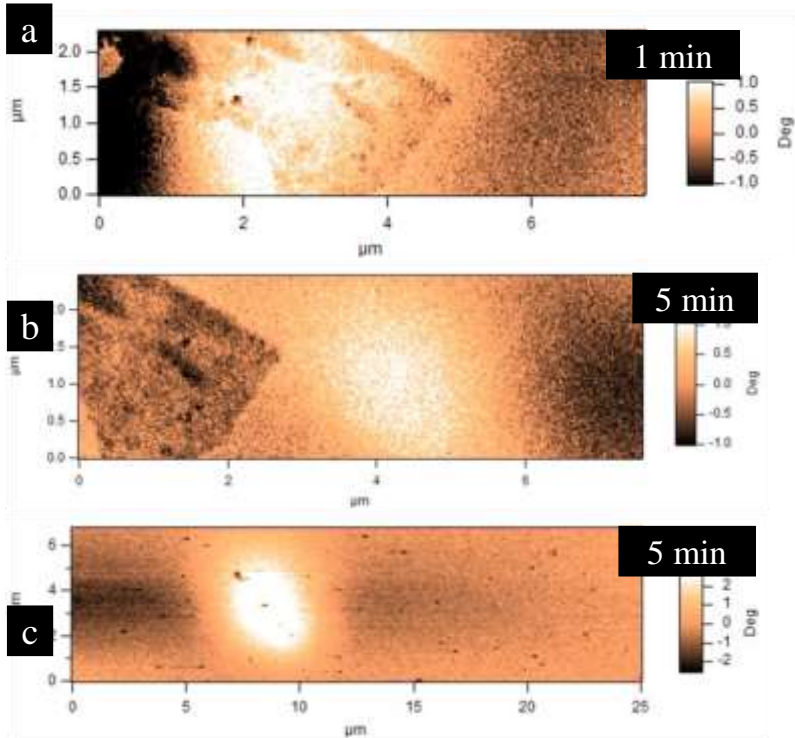


Figure **Error! No text of specified style in document..70**: Representative EFM phase profiles of charge injection on oxygen plasma treated Si/SiO₂ substrate after (a) 1 min and (b) 5 min. Plasma conditions: power - 20 W, flow rate - 50 sccm, and time - 2 minutes. Charge was injected initially by applying -8 V from 1 minute while the reading voltage was fixed at 3 V at a height of 70 nm from the surface. The color coded scale bar represents the magnitude of phase change observed during EFM imaging. The images indicate negligible charge storage after 5 minutes. (c) Representative EFM phase profile of charge injection on oxygen plasma treated Si/SiO₂ substrate, followed by forming gas annealing at 450 °C for 30 minutes. Retention of phase change in the programmed region (white region) indicates elimination of interface trap sites in the silicon dioxide film.

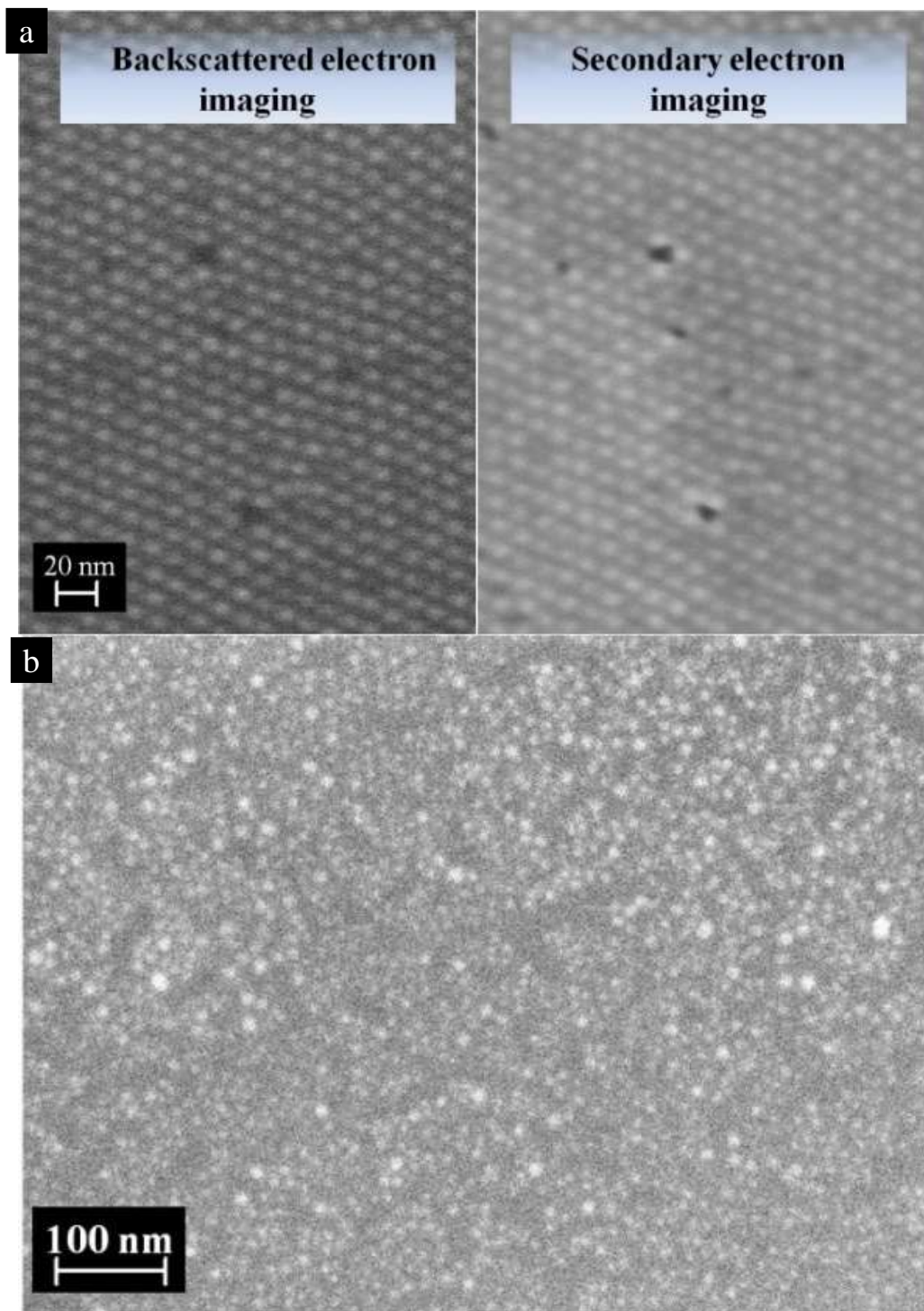


Figure **Error! No text of specified style in document.**71: Representative plan-view FESEM images of samples obtained after deposition of a 15 nm thick gadolinium oxide layer, followed by thermal annealing at 500 °C, onto plasma treated gold nanoparticle array with (a) 4.4 nm interparticle spacing and (b) 13.3 nm interparticle spacing. The polystyrene ligands were removed by RF plasma etching under optimized conditions. The left hand side image (in a) was obtained using angle selective backscattered electrons, which provide information on the atomic number of the material, and the right hand side image was obtained using secondary electrons, which provide information on the surface topography.

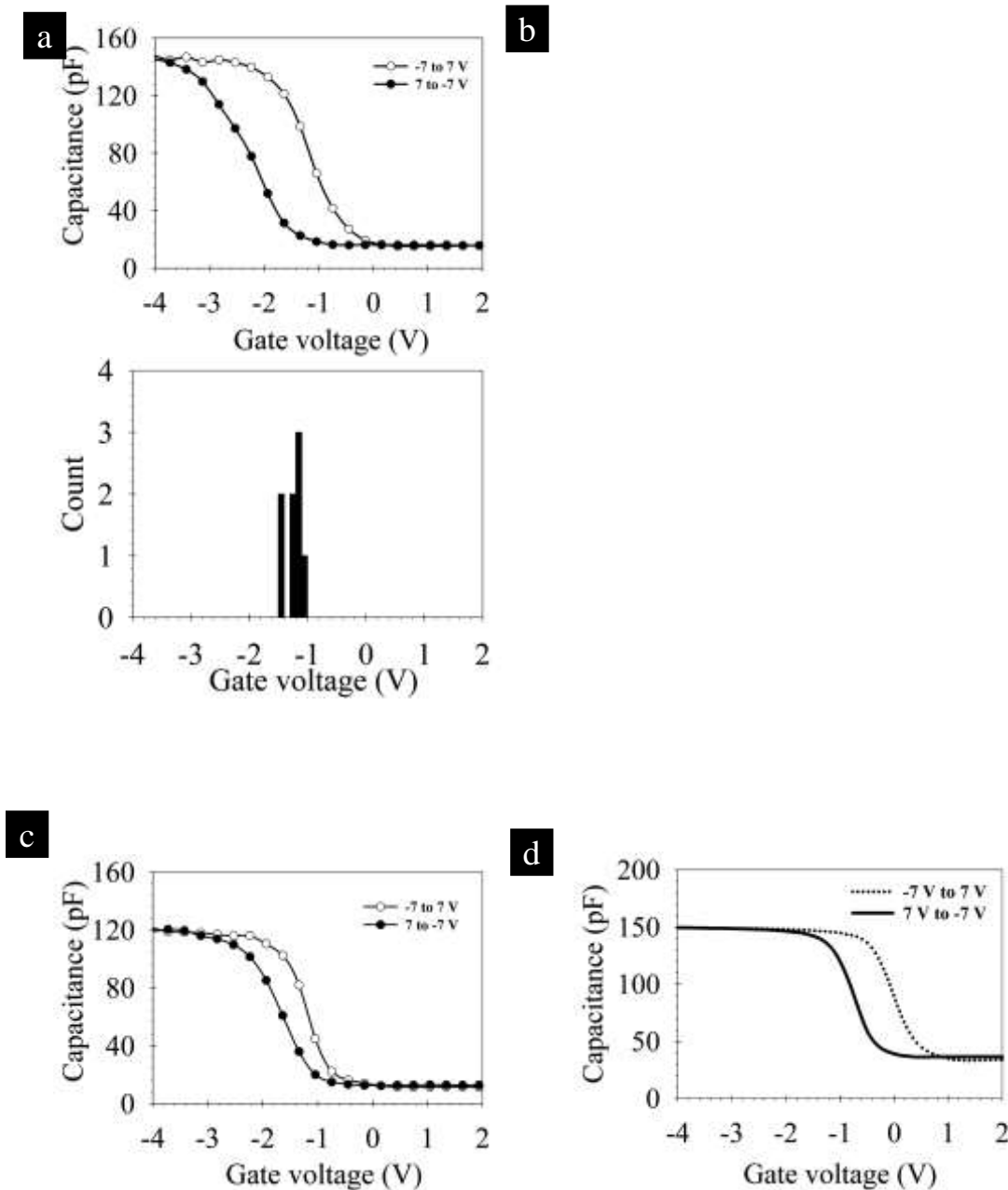


Figure **Error! No text of specified style in document.**72: (a) Capacitance–voltage curve of a MOS capacitor obtained by bi-directional sweep from inversion to accumulation with plasma treated gold nanoparticle array with 4.4 nm interparticle spacing as floating gate. (b) Histogram of flatband voltage shifts measured from 8 different devices. (c) Capacitance–voltage curve of a MOS capacitor obtained by bi-directional sweep from inversion to accumulation with plasma treated gold nanoparticle array with 13.3 nm interparticle spacing as floating gate. (d) Capacitance–voltage curve of a MOS capacitor obtained by bi-directional sweep from inversion to accumulation with plasma treated gold nanoparticle array with 2 nm interparticle spacing as floating gate.

Effect of plasma treatment on vertical leakage

Earlier it was hypothesized that the formation of conductive pathways by decomposition of entrapped ligands resulted in the loss of integrity of the oxide stack, specifically that the gadolinium oxide's insulating properties were degraded. To verify this, EFM measurements were carried out in two different configurations on the two plasma-treated samples, using standard and modified EFM techniques, as explained in Fig. 4.26. A comparison of EFM phase maps for the four scenarios involving the two samples measured by the standard and modified EFM procedures (for arrays with 4.4 nm spacing) is shown in Fig. 4.31. Clearly, without the intermediate step, both 'with ligand (untreated)' as well as 'without ligand (plasma-treated)' samples show charge storage capabilities. Moreover, the "with ligand" sample exhibits a larger phase change, indicating larger storage capacity, which is attributed to the possibility of polystyrene molecules also acting as charge storage sites. However, with the intermediate step of reading in contact, only the device fabricated using gold nanoparticle arrays without ligands retains the charge. These results are in accord with the hypothesis that a

conductive pathway is formed in the gadolinium oxide that compromises its dielectric properties. The most likely cause of this is the formation of carbonaceous products by ligand decomposition. On the contrary, characterization of retention in these devices showed that hole decay was significant, unlike devices fabricated using dodecanethiol capped nanoparticle arrays (Fig. 4.32). The quality of the RF sputtered oxide needs to be enhanced to meet standard industry requirements. The defect assisted clockwise tunneling can only be avoided by deposition of high-quality, top-oxide. Other alternative strategies namely, atomic-layer deposition and e-beam evaporation were attempted to ascertain the scope of integration of these processes with bottom-up self-assembly process. These results are discussed in the subsequent sections.

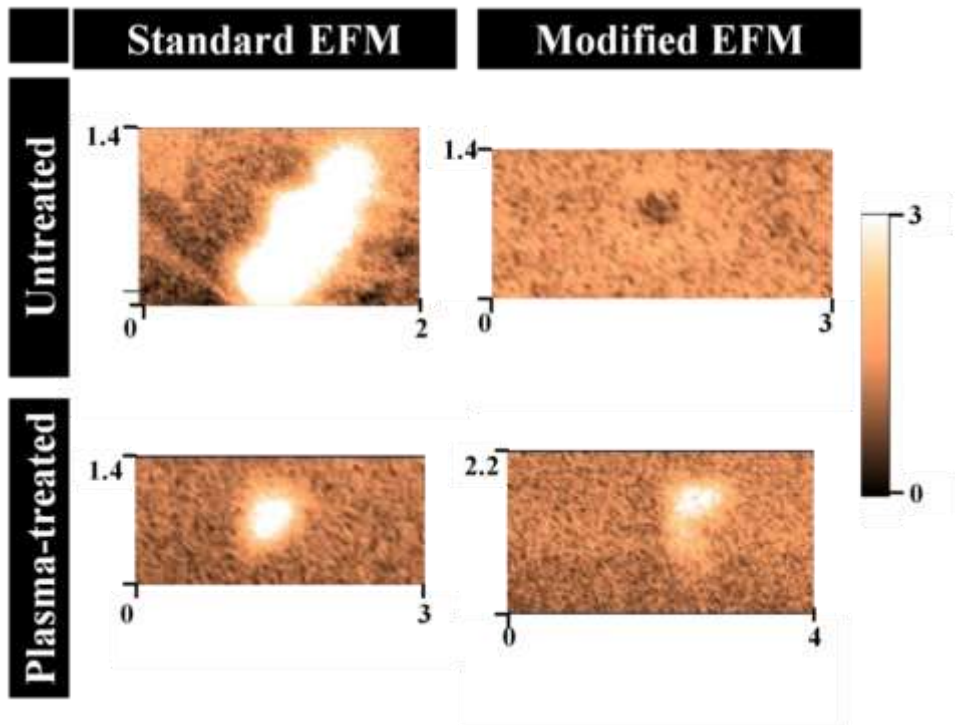


Figure **Error! No text of specified style in document..73**: Comparison of EFM phase profiles of standard and modified procedure for imaging MOS capacitors incorporating untreated and plasma treated gold nanoparticle arrays. The units of x and y axis correspond to μm . Charge was injected initially by applying -6 V from 2 minutes while the reading voltage was fixed at 3 V at a height of 70 nm from the surface. The color coded scale bar represents the magnitude of phase change observed during EFM imaging.

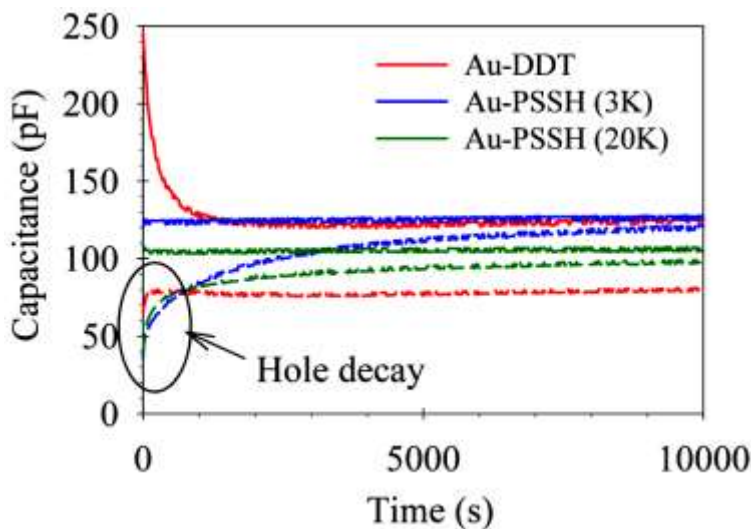


Figure **Error! No text of specified style in document..74**: Representative charge retention characteristics of MOS capacitors fabricated with 2D arrays with different interparticle spacing of 2 nm (Au-DDT), 4.4 nm (Au-PSSH (3K)) and 13.3 nm (Au-PSSH (20K)). P/E was carried out at a voltage of $\pm 7\text{ V}$, while reading voltage was set at -0.8 V for DDT capped array and -1.5 V for polystyrene thiol capped gold nanoparticle arrays. The hole decay was found to be significant for arrays with larger interparticle spacing.

Device fabrication using atomic layer deposition

Based on the 2011 International Technology Roadmap for Semiconductors (ITRS) non-volatile memory technology projection table, for 2017, the target of Effective Oxide Thickness (EOT) for tunneling and control oxide has been set at 5 nm and 10 nm respectively. This demands a precise control of not only tunneling oxide quality, but also control oxide. Atomic Layer Deposition (ALD) is an attractive avenue for fabricating next generation flash memory devices as it can control both oxide thickness and its quality, precisely at sub-nm level. Alumina (Al_2O_3) is the most extensively studied dielectric fabricated using ALD process. Since alumina has high dielectric constant (~ 8) when compared to silicon dioxide (~ 4), it is also one of the potential candidates for fabricating next-generation memory devices. In this section, investigations on the optimization of ALD set-up for Al_2O_3 deposition on nanoparticle array and the characterization of memory devices fabricated will be discussed. The effects of interparticle spacing on memory characteristics will also be presented.

Process optimization

Conventionally, ALD process has been carried out at higher temperatures, typically, greater than 250 °C. There are few reports of low temperature ALD deposition of alumina; where in the quality of oxide is comparable to the high-temperature grown oxide by modifying the process flow. With the huge demand for flexible electronics, it becomes necessary and imperative to optimize deposition process on nanoparticle array at low temperature so as to have wide applicability. First, the ALD deposition process was carried out at standard condition of 250 °C in Beneq-250 reactor, with alternate pulse cycles of trimethylaluminium (TMA) and water vapor, with intermittent nitrogen purging. The pulse times were all set at 0.2 ms. At 250 °C, alumina deposition on top of arrays fabricated using dodecanethiol capped gold nanoparticles (for untreated treated sample), led to loss of ordering and aggregation (Fig. 4.33a,b); FESEM images were obtained after annealing in forming gas atmosphere at 450 °C for 20 min. This is attributed to the melting of ligand in arrays fabricated with dodecanethiol capped gold nanoparticles, which initiates around

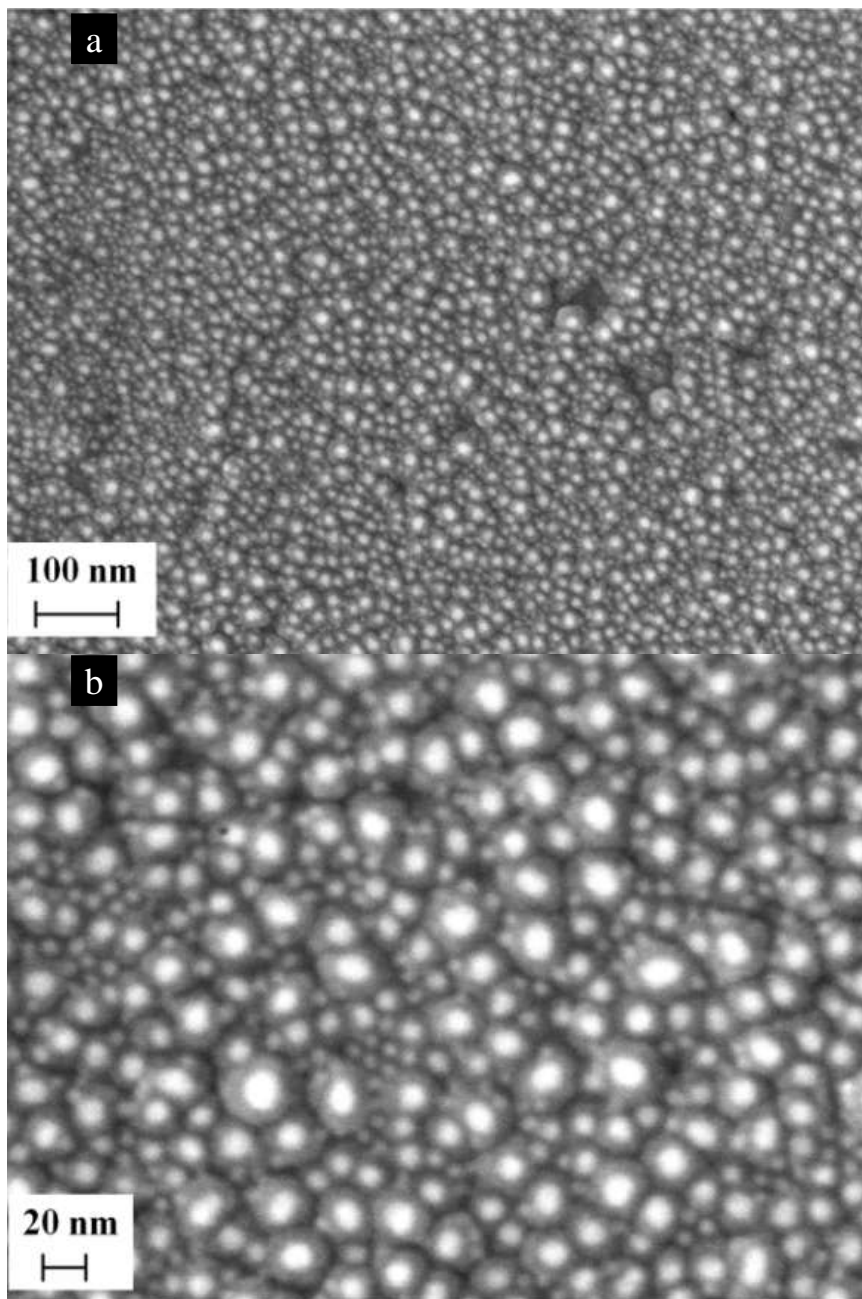


Figure **Error! No text of specified style in document..75**: Representative FESEM images of dodecanethiol capped gold nanoparticle arrays obtained after deposition of 18 nm of Al_2O_3 using ALD process at 250 °C at (a) low and (b) high magnification. Note the images were taken after annealing the sample in a forming gas atmosphere at 450 °C for 20 minutes.

200°C as reported. More severe effect of ALD deposition on untreated array can be seen in arrays formed with thiol-terminated polystyrene capped gold nanoparticles (Fig. 4.34a). An enhancement in mobility of nanoparticle upon formation of molten polymer is attributed to be the cause for the loss of ordering by particle coalescence. On the contrary, “bare” nanoparticle arrays with 20 nm (PSSH [MW: 20000 g/mol] capped gold nanoparticles) spacing was found to maintain particle ordering (Fig. 4.34b). The arrays with 20 nm spacing were prepared by drop-cast of colloidal solution on Si/SiO₂ substrate. To mitigate the effect of temperature during deposition, the ALD process was next carried out at 150 °C, with all other conditions remaining same. The samples fabricated using dodecanethiol capped gold nanoparticles was found to maintain size and ordering for both untreated sample (Fig. 4.35a) and plasma treated sample (Fig. 4.35b). Note the FESEM images were obtained after annealing the samples at 450 °C for 20 minutes in forming gas atmosphere.

Based on the work of Sivaraman and Santhanam, it can be presumed that the size of the particle do not play a major role during melting of monolayer protected nanoparticles, and that the major cause for disordering arises due to the melting of ligand. Korgel et al. have reported a pre-melting transition temperature of 140 °C, for dodecanethiol capped silver nanoparticles of size 7 nm. So as a next step, the ALD deposition process was carried at 135 °C, so as to avoid disturbing the ordering of array. In these samples, both order and size were maintained for both untreated (Fig. 4.36a,c) and plasma treated samples (Fig. 4.36b,d), for samples fabricated with 2 and 20 nm spacing. The FESEM images were obtained after forming gas annealing of samples at 450 °C for 20 minutes. FESEM of cross-section sample (prepared using FIB), shows embedding of gold nanoparticle array between Al_2O_3 and SiO_2 (Fig. 4.36e,f). This process optimization enabled us to investigate the effect of ligand, interparticle spacing on memory characteristics in addition to device performance.

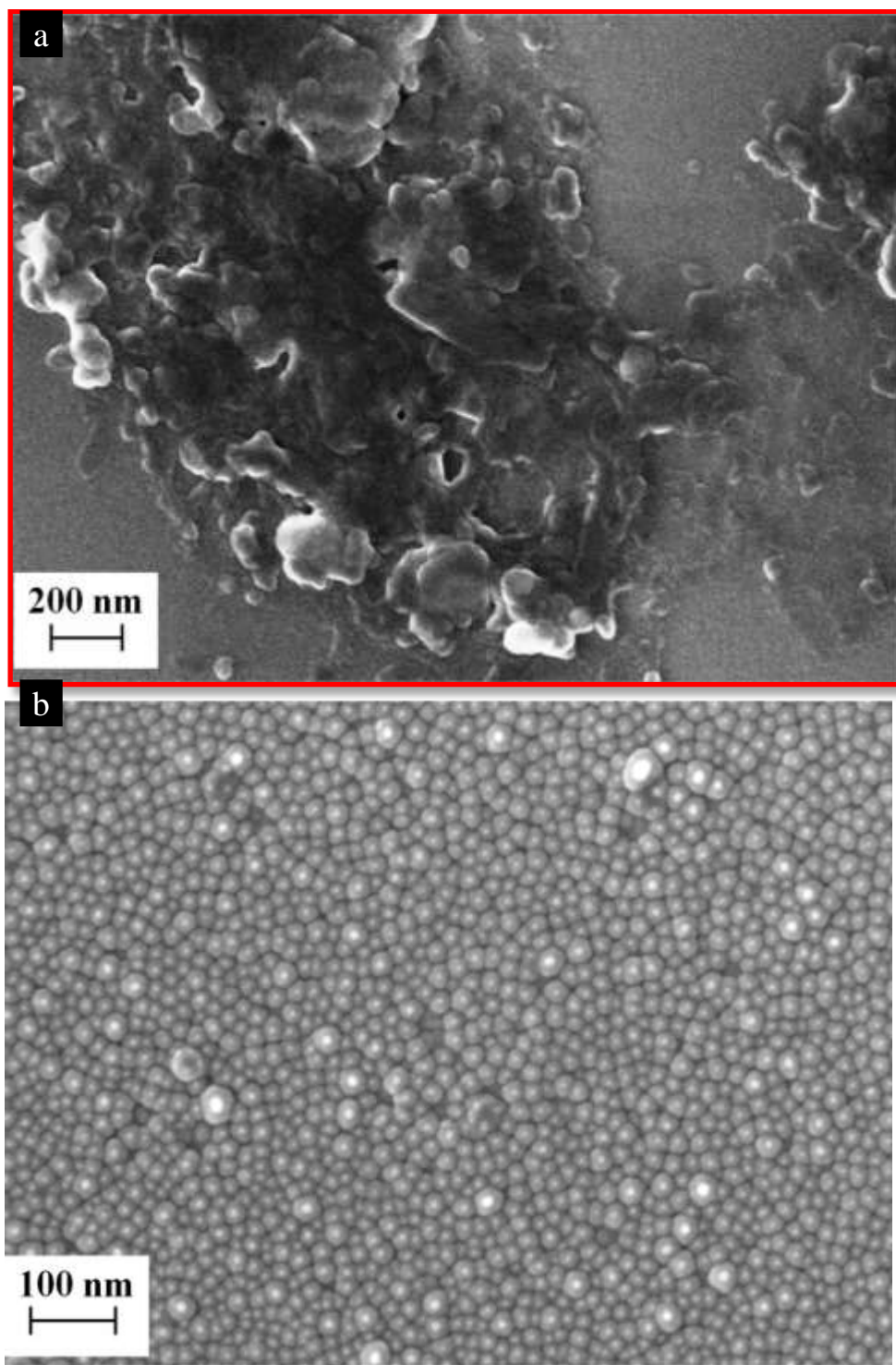


Figure Error! No text of specified style in document..76: Representative FESEM image of thiol-terminated polystyrene capped gold nanoparticle arrays (molecular weight: 20000 g/mol) obtained after deposition of 18 nm of

Al_2O_3 using ALD process at 250 °C, (a) without ligand removal and (b) with ligand removal using oxygen plasma treatment, followed by annealing of the sample in a forming gas atmosphere at 450 °C for 20 minutes.

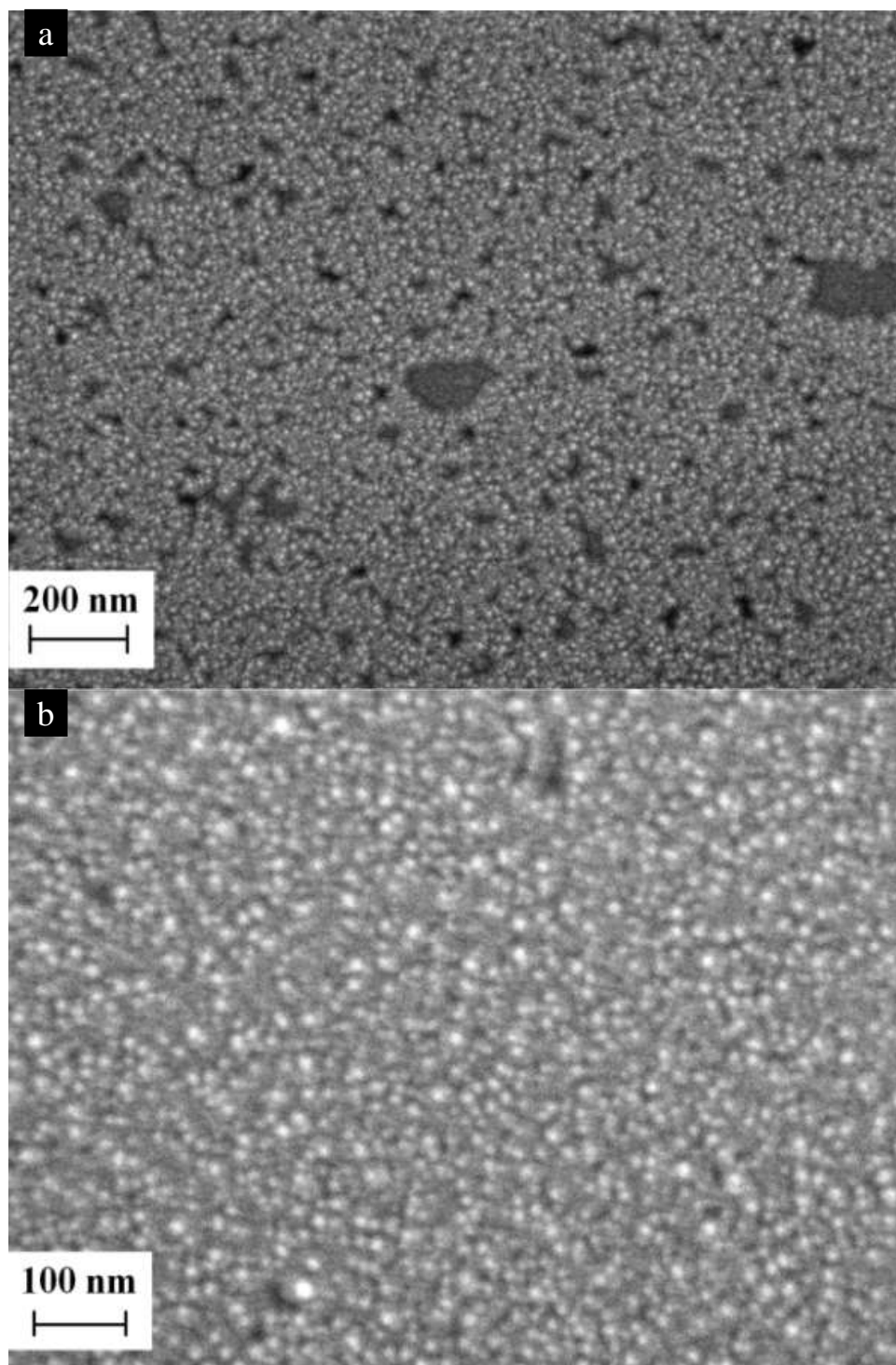


Figure **Error! No text of specified style in document..77**: Representative FESEM images of dodecanethiol capped gold nanoparticle arrays obtained after deposition of Al_2O_3 using ALD process at 150 °C, (a) without ligand removal and (b) with ligand removal using hydrogen plasma treatment followed by annealing of the sample in a forming gas atmosphere at 450 °C for 20 minutes.

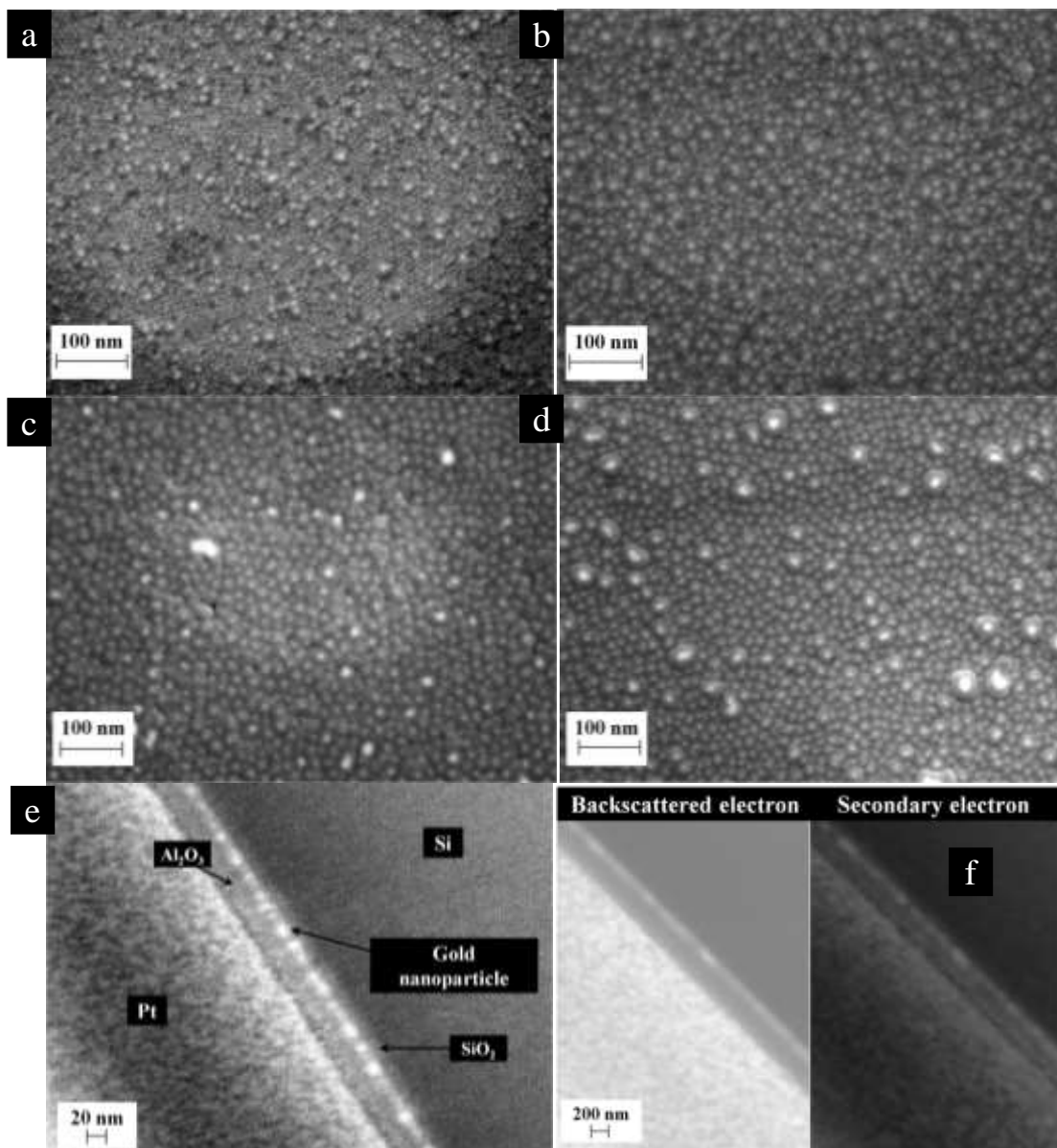
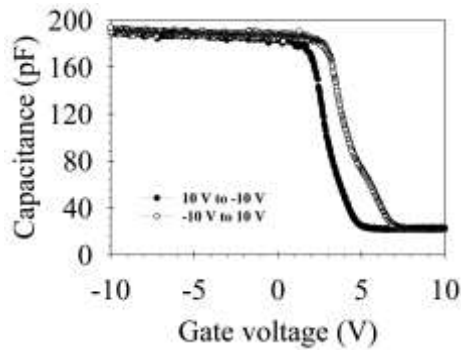


Figure **Error! No text of specified style in document.**78: Representative FESEM images dodecanethiol capped gold nanoparticle arrays obtained after deposition of Al_2O_3 using ALD process at 135°C , without ligand removal (a) and with ligand removal using hydrogen plasma treatment (b). Note, the images were taken after annealing of the sample in forming gas atmosphere at 450°C for 20 minutes. Representative FESEM image of thiol-terminated polystyrene capped gold nanoparticle arrays (molecular weight: 20000 g/mol) obtained after deposition of Al_2O_3 using ALD process at 135°C , without ligand removal (c) and with ligand removal using oxygen plasma treatment (d). Note, the images were taken after annealing of the sample in forming gas atmosphere at 450°C for 20 minutes. (e) High magnification cross-sectional FESEM image of the MOS capacitor with arrays fabricated using dodecanethiol capped gold nanoparticles as charge storage nodes. The dense packing of the array precludes visualization of individual nanoparticles. Platinum is present due to FIB sample preparation. (f) High magnification cross-sectional FESEM image of the MOS capacitor obtained using (i) backscattered electron and (ii) secondary electron detector. Contrast in backscattered electron imaging is predominantly due to the difference in atomic weight while contrast in secondary electron imaging depends on surface features.

a



b

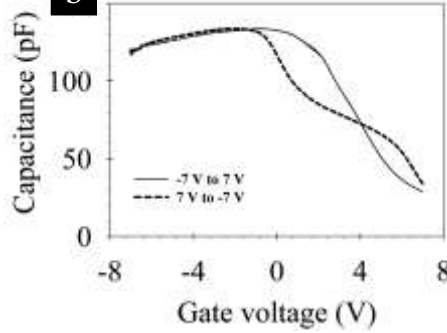


Figure **Error! No text of specified style in document.**79: (a) Capacitance-Voltage (CV) curve of a MOS capacitor without the gold nanoparticle array as floating gate obtained by depositing Al_2O_3 using ALD process at 135°C , obtained by bi-directional sweep from inversion to accumulation. The appearance of a hysteresis loop indicates the presence of interface traps in significant numbers. (b) Capacitance-Voltage (CV) curve of a MOS capacitor with the 2D arrays using dodecanethiol capped gold nanoparticles as floating gate obtained by depositing Al_2O_3 using ALD process at 135°C , obtained by bi-directional sweep from inversion to accumulation. The appearance of a hysteresis loop indicates a lot of interface traps.

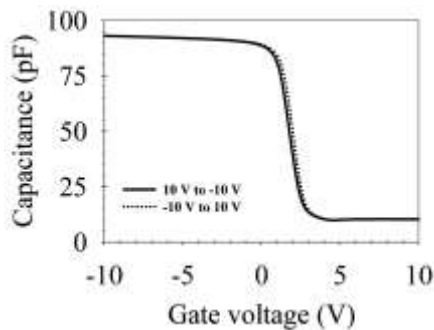
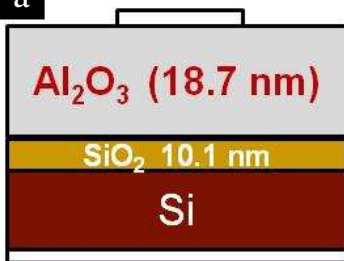


Figure **Error! No text of specified style in document.**80: Capacitance-Voltage (CV) curve of a MOS capacitor without the gold nanoparticle array as floating gate obtained by depositing Al_2O_3 using ALD process at 375°C , obtained by bi-directional sweep from inversion to accumulation. The appearance of a no hysteresis loop indicates high quality oxide without any trap charges.

a



b

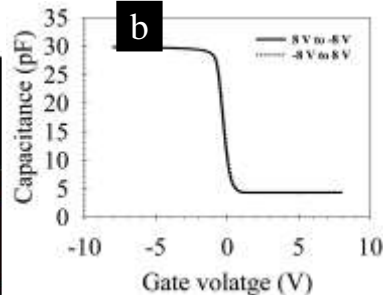


Figure **Error! No text of specified style in document.**81: (a) Schematic of the device structure of MOS capacitor with Si/ SiO_2 / Al_2O_3 . (b) Capacitance-Voltage (CV) curve of a MOS capacitor without the gold nanoparticle array as floating gate obtained by depositing Al_2O_3 using ALD process at 135°C followed by immediately annealing the sample at 400°C under nitrogen ambient for 20 minutes inside the ALD reactor. The absence of a hysteresis loop indicates the formation of high quality oxide without any trap charges.

Quality of Al_2O_3 deposited at low temperature

Capacitance-Voltage (CV) measurements of the as-fabricated devices led to irreproducible hysteresis, suggesting the presence of interface traps in the MOS capacitors. A representative CV plot of MOS capacitor is shown in Fig. 4.37a. The MOS capacitor without gold nanoparticles (control sample) also showed hysteresis in CV plot (Fig. 4.37b) unlike the MOS capacitor with just tunneling oxide, SiO_2 . This suggests that the electrical quality of alumina film deposited at 135°C and post-annealed at 450°C is poor. To investigate the effect of temperature on quality of Al_2O_3 , a control sample was fabricated with Al_2O_3 grown at 375°C . The CV plot showed no significant hysteresis (Fig. 4.38), indicating the absence of interface traps.

With post-deposition annealing of the oxide not yielding desired improvements to the quality of oxide grown at 135 °C and also as nanoparticle arrays with smaller interparticle spacing (< 2 nm) do not withstand high temperature processing, a MOS capacitor was fabricated such that the Al₂O₃ deposition takes place at 135 °C and then the sample was immediately ramped up to 400 °C (maximum permissible temperature in ALD reactor), instead of exposing the sample to the atmosphere, and then followed by forming gas annealing. The rest of the device fabrication process remained the same as before. Now, the CV plot of the control sample did not show any discernible hysteresis (Fig. 4.39) similar to the MOS fabricated using Al₂O₃ deposited at 375 °C. Thus, even a brief exposure to atmosphere (even in clean room conditions) can lead to defect formation, when oxides are deposited at low temperatures.

Effect of presence of ligand and interparticle spacing on memory characteristics

MOS capacitors were fabricated with both untreated and bare gold nanoparticle arrays using 2 nm (dodecanethiol) or 20 nm spacing (thiol-terminated polystyrene, MW: 20000 g/mol). CV plots showed significant memory window (4.4 V for 2 nm spacing and 6.2 V for 20 nm spacing, Fig. 4.40a,b) for devices fabricated with bare gold nanoparticle arrays, while it is absent for ligand-coated (unreliable charging for 2 nm spacing and < 1 V for 20 nm spacing, Fig. 4.40c,d) for a bidirectional sweep of ± 10 V. CV plot of MOS capacitor with dodecanethiol capped gold nanoparticle array exhibited continuous injection of charge behavior (as there was no clear demarcation of inversion and accumulation regions) while the devices with thiol-terminated polystyrene capped gold nanoparticle array exhibited little hysteresis. This may be attributed to the possible presence of charge trapping sites, as in the devices fabricated using RF sputtering. The observation of significant memory window for devices with bare nanoparticle arrays is in concord with the earlier study of devices fabricated using RF sputtering of gadolinium oxide, in terms of the need for removal of ligand for observing memory behavior. Therefore, it was surmised that the argon plasma in the RF sputtering chamber would have removed the dodecanethiol (shorter chain length) in the case of untreated sample while in the case of ALD chamber, as there was no additional plasma, an additional step of pre-plasma treatment is needed to remove dodecanethiol ligands similar to the longer chain length molecule of thiol-terminated polystyrene. The hysteresis was again observed as a clockwise loop, suggesting tunneling of electrons through the alumina and not silicon dioxide.

In this study, the CV measurements were carried out by applying voltage from the bottom and measurement of current from the top, so as to avoid stray signals. The voltages are then reversed to obtain gate voltage as per convention. To rule out the possibility of error occurring due to this biasing configuration, a CV measurement of MOS capacitor fabricated with bare gold nanoparticle arrays (2 nm spacing) was carried out in the opposite manner, where in the voltage bias is applied at the top and the current is measured from the bottom. There was not any significant difference in the hysteresis loop direction or in the value of capacitance. This rules out the possibility of error occurring due to the measurement configuration. This also suggests the presence of leakage paths in the control oxide, which will be discussed in the sec. 4.6.8. Also the capacitance value at accumulation decreases significantly from that of a blank sample. These indicate the possibility of leaky oxide film. This aspect will be further discussed in sec. 4.6.5 and sec.4.6.7.

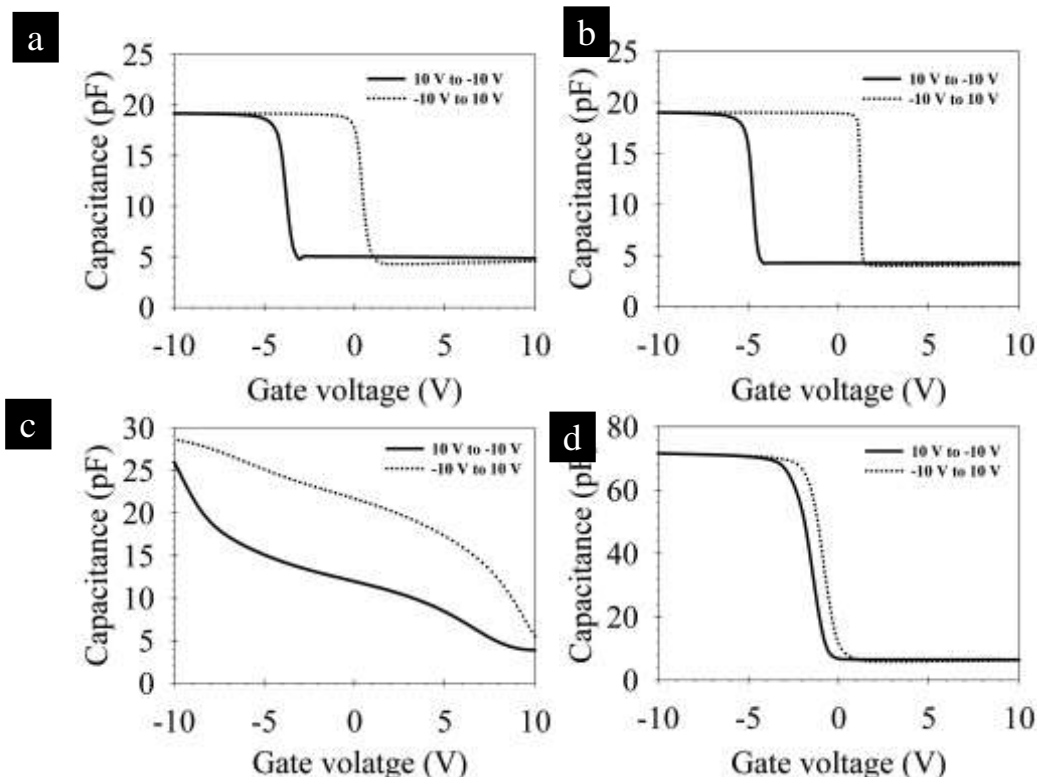


Figure **Error! No text of specified style in document..82**:Capacitance-Voltage (CV) curve of a MOS capacitor fabricated using bare gold nanoparticle arrays with (a) 2 nm interparticle spacing (DDT) and (b) 20 nm interparticle spacing (PSSH, 20000 g/mol) as floating gate. The devices were fabricated by depositing Al_2O_3 using ALD process at 135°C , followed by nitrogen annealing at 400°C for 20 minutes. The appearance of a hysteresis loop for devices fabricated using plasma treated nanoparticle array indicates the storage of electrons inside gold nanoparticles while the untreated array sample (c) 2 nm interparticle spacing (DDT capped gold nanoparticles) and (d) 20 nm interparticle spacing (PSSH capped gold nanoparticles) shows continues trapping/detrapping of charges due to the possible formation of carbonaceous product during annealing.

Effect of tunneling oxide thickness and control oxide thickness on memory characteristics

The thickness of tunneling oxide, SiO_2 was now reduced to 5 nm. As expected, CV plot showed an increase in the memory window with the reduction in tunneling oxide thickness at the same voltage, i.e., 14.8 V for 2 nm spacing and 1.3 V for 20 nm spacing (Fig. 4.41a,b). Again, significant memory window was only obtained for devices with bare gold nanoparticle arrays and not for untreated samples (Fig. 4.41c,d). Also, the control sample (without any gold nanoparticle arrays) did not show any discernible hysteresis in CV plot (Fig. 4.41e). However, device to device variability was high, as many devices did not yield any memory window. This can be attributed to the poor electrical quality of tunneling oxide. As the purge time of oxygen during dry oxidation was only 40 s, there could be a possibility of presence of pinhole defects which can act as leakage pathways for stored charges. Optimizing the quality of tunneling oxide of less than 5 nm thicknesses is a research problem on its own. On the other hand, increasing the control oxide thickness, led to lower memory window at the same voltages, which is expected as it requires higher energy to cross the barrier. However, in both cases, the hysteresis in CV plots was still clockwise, which is surprising because the physical thickness of control oxide is 3 times that of the thickness of tunneling oxide, and yet the electron tunneling during programming and erasing was found to occur only through thicker control oxide and not the thinner tunneling oxide.

Reduction in accumulation capacitance

In addition to the larger memory window for devices fabricated using ALD deposition process when compared to RF sputtering, the major difference was in the value of capacitance at accumulation (Fig. 4.41). More interestingly, the capacitance value changed very little in the presence of ligand-coated gold nanoparticles (Fig. 4.41c,d) and more significantly for bare gold nanoparticle arrays (Fig. 4.41a,b). The results have been summarized in Table 4-3. A slight increase in the case of untreated sample can be explained due to the entrapment of organic ligands. This decrease in

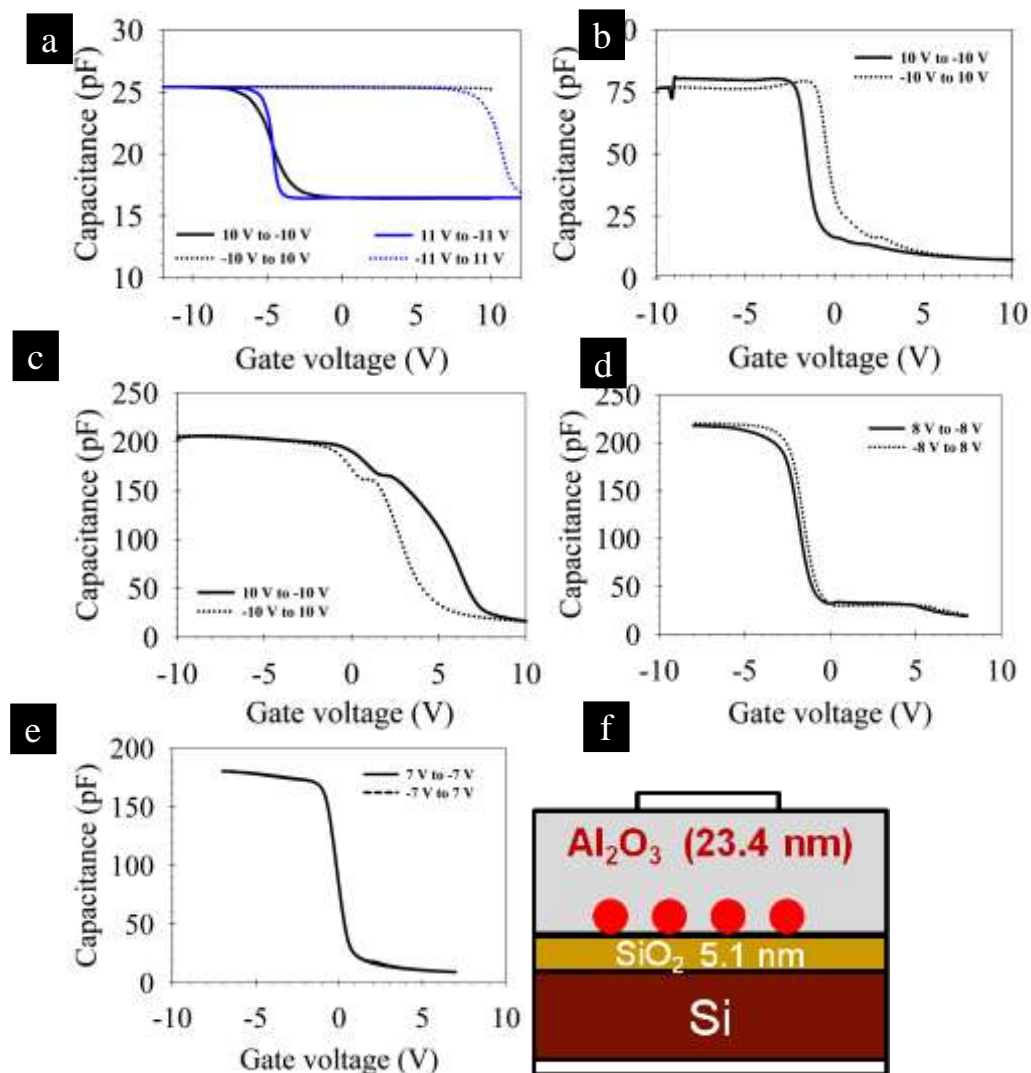


Figure **Error! No text of specified style in document..83**: Capacitance-Voltage (CV) curve of a MOS capacitor with the 2D bare gold nanoparticle arrays with (a) 2 nm interparticle spacing (DDT capped gold nanoparticles) and (b) 20 nm interparticle spacing (PSSH capped gold nanoparticles) as floating gate. The devices were fabricated by depositing Al₂O₃ using ALD process at 135°C, followed by nitrogen annealing at 400°C for 20 minutes. The appearance of a hysteresis loop for devices fabricated using plasma treated nanoparticle array sample indicates the storage of electrons inside gold nanoparticles while the devices fabricated using untreated array with (c) 2 nm interparticle spacing and (d) 20 nm interparticle spacing shows continues trapping/detrapping of charges due to the possible formation of carbonaceous product during annealing. (e) CV curve of MOS capacitor without gold nanoparticle array. (f) Schematic of the device structure of MOS capacitor.

Table **Error! No text of specified style in document.-5**: Effect of presence of ligand and nanoparticle density on the value of accumulation capacitance

Architecture	Control sample (without nanoparticle)	Spacing – 2 nm		Spacing – 20 nm	
		Untreated array	Plasma treated array	Untreated array	Plasma treated array
SiO ₂ : 5 nm & Al ₂ O ₃ : 23 nm	180 pF	207 pF	25 pF	219 pF	84pF
Al ₂ O ₃ : 11 nm & Al ₂ O ₃ : 20 nm	93 pF	78 pF	28 pF	40 pF	63 pF

Table **Error! No text of specified style in document.-6**: Effect of presence of ligand on accumulation capacitance. Devices fabricated with PECVD also showed reduction in capacitance at accumulation.

Architecture	Control sample (without nanoparticle)	Spacing – 20 nm	
		Untreated array	Plasma treated array
SiO ₂ : 9 nm & Al ₂ O ₃ : 34 nm (Two step: 135°C and 375°C)	120 pF	100pF	35 pF
SiN: 30 nm & SiO ₂ : 7 nm	90 pF	40 pF	60 pF

capacitance at accumulation was not observed for devices fabricated with RF sputtering process for deposition of top-oxide. In the case of RF sputtering process, the gadolinium oxide is sputtered directly from the target while in the case of ALD process, it involves various steps such as adsorption of precursor and purging of water vapor followed by chemical reaction. The presence of water vapor could have transformed the ligand into better trap site. Also, it has been reported that for deposition of alumina at low temperatures, sufficient time between purge cycles need to be provided so as to avoid chemical vapor deposition. So, it was decided to alter the purge timing of precursors based on the study of Groner et al. The purge times of TMA, nitrogen, water, nitrogen were set at 0.2 s, 1 s, 0.4 s, and 2 s respectively so as to avoid chemical vapor deposition. In addition, the nanoparticle arrays are thermally stable ($\sim 450^\circ\text{C}$, as tested in this study), once encapsulated in alumina matrix. In practice, the array should be stable up to the melting point of alumina, which is 2072°C . However, as the device had a back contact made of aluminum, the practical temperature up to which the devices can be annealed is limited to the melting temperature of aluminium, which is 660°C . As it is well known that the high temperature deposition of alumina is superior in terms of quality, it was decided to alter the deposition process in the following manner: the first 20 cycles ($\sim 2\text{ nm}$) were deposited at 135°C , while the remaining 320 cycles ($\sim 28\text{ nm}$) were deposited at 375°C . Even in this case, there was a significant reduction in the value of capacitance at accumulation for devices with bare gold nanoparticle arrays (Table 4-4). Also, the hysteresis loops were found to be clockwise, i.e., tunneling of charges still occurs through alumina and not silicon dioxide. To understand this effect further, memory devices were fabricated using a different process: control oxide consisting of 30 nm silicon nitride (SiN) and 7 nm silicon dioxide (SiO₂) were deposited using plasma enhanced chemical vapor deposition at 375°C . Even then, there was a reduction in the capacitance value at accumulation and the clockwise hysteresis loop was still observed (Table 4-4).

Effect of plasma treatment on device characteristics

In the literature, there are reports of plasma damage leading to poor electrical quality of ultra-thin oxides. In order to test whether the pre-plasma treatment which was used for ligand removal to fabricate bare nanoparticle arrays might be the cause for a decrease in capacitance, a control MOS capacitor without gold nanoparticles was fabricated and subjected to the RF-plasma treatment as necessary to fabricate bare nanoparticle arrays at 2 nm and 20 nm spacing. CV plots neither show discernible hysteresis nor decrease in accumulation capacitance, for the control sample subjected to the RF-plasma treatment as necessary to fabricate bare nanoparticle arrays at 2 nm (Fig. 4.42a) and 20 nm interparticle spacing (Fig. 4.42b). As shown in the previous sections, the CV plot of the MOS capacitor fabricated without gold nanoparticle (control sample) did not show any hysteresis indicating high-quality oxide without any interface traps (Fig. 4.42c) while the device fabricated with bare nanoparticle arrays with 20 nm spacing showed significant reduction in accumulation capacitance from $\sim 70\text{ pF}$ to $\sim 20\text{ pF}$ (Fig. 4.42d). These experiments showed that the mild plasma condition used for the ligand removal is not the cause for the poor electrical quality of deposited oxide film.

Current-voltage (IV) measurements were carried out on MOS capacitors, both with and without gold nanoparticles (untreated and bare nanoparticle arrays (20 nm spacing), to obtain the leakage current density. IV measurements (Fig. 4.43) highlight MOS capacitors without gold nanoparticle and bare gold nanoparticle arrays have similar leakage current densities (less than nA). The untreated sample, on the contrary, was able to withstand electric fields beyond -25 V , which can be attributed to the entrapment of thiol-terminated polystyrene molecules.

Possible causes for observed decrease in accumulation capacitance - metal in a dielectric or area screening

So far, aforementioned experiments confirm that reduction in accumulation capacitance is correlated to the presence of bare gold nanoparticle arrays in a dielectric. Also, the amount of decrease is dependent on the amount of metal inclusions, i.e., the accumulation capacitance was found to decrease with an increase in particle density. This suggests that physical presence of metal might be a cause for the decrease in capacitance value at accumulation. Capacitance is defined

as the ratio of product of dielectric constant and effective area to the distance between the plates. In this study, as the distance is identical in all the MOS capacitors (apart from ligand height), the difference in capacitance must arise either due to changes in effective dielectric constant or effective area. There are two different schools of thought for changes in effective dielectric constant namely, (i) reduction in dielectric constant, due to the metal inclusions in a dielectric, and (ii) an increase in dielectric constant due to the possible formation of percolative pathways. In the former case, various models like Bruggeman, Lorentz-Lorenz, Maxwell-Garnett etc. have been proposed.

A three layer film structure is constructed, wherein the volume fraction of metal was presumed to affect only the intermittent layer and not the dielectric constant of top and the bottom layers. Lorentz-Lorenz model was used as the effective medium approximation in this study, which is represented below,

$$\frac{\varepsilon - 1}{\varepsilon + 2} = f_a \left(\frac{\varepsilon_a - 1}{\varepsilon_a + 2} \right) + [1 - f_a] \left(\frac{\varepsilon_b - 1}{\varepsilon_b + 2} \right) \quad (4.2)$$

where, ε represents dielectric constant of the medium and f represents volume fraction. The corresponding subscript a and b represents respective properties of the two phases in the system. The effective dielectric constant changes from an initial value of 8 to 4.1 and 7.4 for an interparticle spacing of 2 nm and 20 nm respectively. This leads to capacitance values of 148 and 181 pF respectively, which do not match with the measured values of 25 and 84 pF respectively (Table 4-5). Estimation of capacitance based on the decrease in the area, obtained by extracting the free space in 2D nanoparticle array, leads to decrease in capacitance to values of 52 and 167, which again differs from the experimental value. Hence, the explanation of decrease in accumulation capacitance must lie elsewhere.

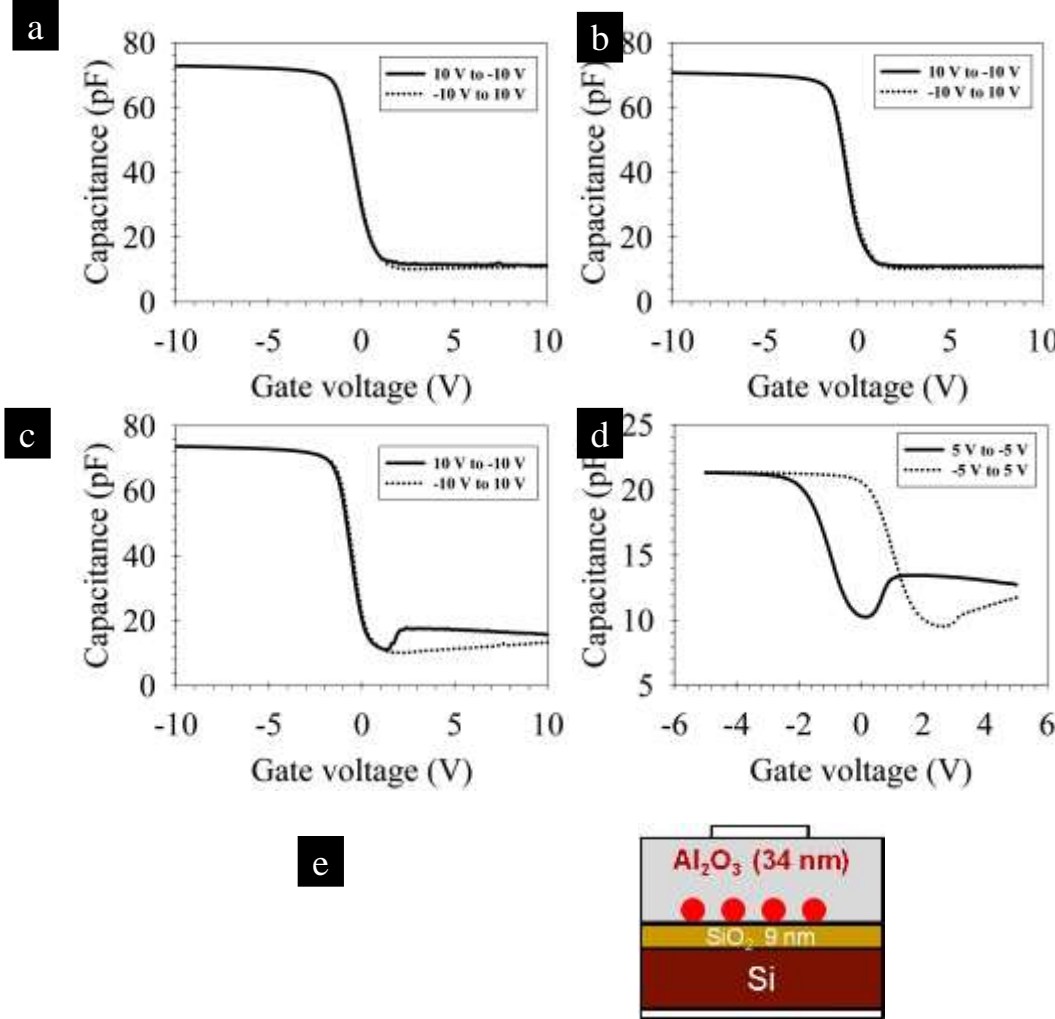


Figure **Error! No text of specified style in document.**84: Capacitance-Voltage (CV) curve of a MOS capacitor without the gold nanoparticle array subjected to the RF-plasma treatment as necessary to fabricate bare nanoparticle arrays at (a) 2 nm and (b) 20 nm spacing as floating gate. The absence of hysteresis loop and no significant reduction in capacitance at accumulation indicate plasma treatment does not cause substrate damage, similar to CV curve of a MOS capacitor without gold nanoparticle array, not subjected to any plasma treatment (c). (d) CV curve of a MOS capacitor fabricated with bare arrays with 20 nm spacing as floating gate shows significant reduction in accumulation capacitance. This experiment clearly highlights the mild plasma treatment does not cause substrate damage and the hysteresis and decrease

in accumulation capacitance arise due to the presence of bare nanoparticle arrays.(e) Schematic of the device structure of MOS capacitor.

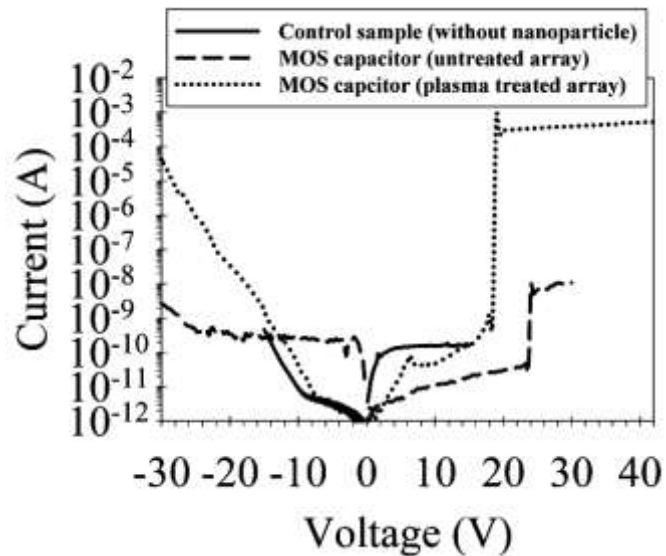


Figure **Error! No text of specified style in document.**85: Current-Voltage (IV) characteristic of MOS capacitor fabricated with (i) SiO₂ and Al₂O₃ (MOS blank), (ii) untreated and (iii) bare 2D arrays of nanoparticle with 20 nm spacing. This experiment suggests mild plasma treatment used for fabricating bare arrays does not affect the leakage current.

Table **Error! No text of specified style in document.**-7: Comparison of experimental and predicted accumulation capacitance values due to the either change in effective dielectric constant (metal in a dielectric) or effective area screening (based on nanoparticle density).

Control sample (without nanoparticle)	Spacing – 2 nm (q = 0.32)		Spacing – 20 nm (q = 0.035)	
184.5 (180)	ε = 4.1	148 pF(25pF)	ε = 7.4	181 pF(84 pF)
	A = 0.53	52 pF(25 pF)	A = 0.95	167 pF(84 pF)

Leakage characteristics in Al₂O₃

Until now, the direction of hysteresis loop observed in all the MOS capacitors has been clock-wise, suggesting injection of electrons through Al₂O₃ instead of SiO₂. This is surprising because even with 3 times the thickness of tunneling oxide, the electrons were found to tunnel through the thicker oxide. For a particle of mass, *m* and energy, *E*, the tunneling probability, *T* of the potential barrier with length, *L* and height, *U* is given by

$$T = \exp\left(-2L\sqrt{\frac{2m(U-E)}{\hbar^2}}\right) \quad (4.3)$$

using Wentzel–Kramers–Brillouin (WKB) approximation. For 10 nm SiO₂ and 30 nm Al₂O₃, the tunneling probability is computed to be exp(-41x) and exp(-70x) respectively, assuming effective mass =0.2 times the mass of an electron. This suggests electron tunneling must occur through SiO₂ rather than Al₂O₃. However this is not observed in the experiments. Another possibility is the defect assisted tunneling through alumina. To test this hypothesis, it was decided to measure the leakage currents across the alumina deposited using ALD process. For this, the alumina was deposited on 5.6 nm sputtered gold porous film using ALD (Fig. 4.44). After fabricating MOS capacitors using this substrate, a part of the substrate is immersed in 10% KOH solution to etch the alumina. This results in electrical access to the Metal-Insulator-Metal (MIM) structure, which can be utilized to measure IV characteristic across the alumina film alone. As surmised earlier, the leakage currents were found to be of the order of μA and more interestingly in some of the devices, the

breakdown voltage was found to be less than 2 V (Fig. 4.45). Note, the thickness of alumina was 34 nm. Also, a MOS capacitor was fabricated with 10 nm Al_2O_3 as tunneling oxide deposited at 375 °C. Surprisingly, the breakdown voltage of high-temperature grown oxide is very low when compared to literature report (Fig. 4.46). This demands a serious inspection of

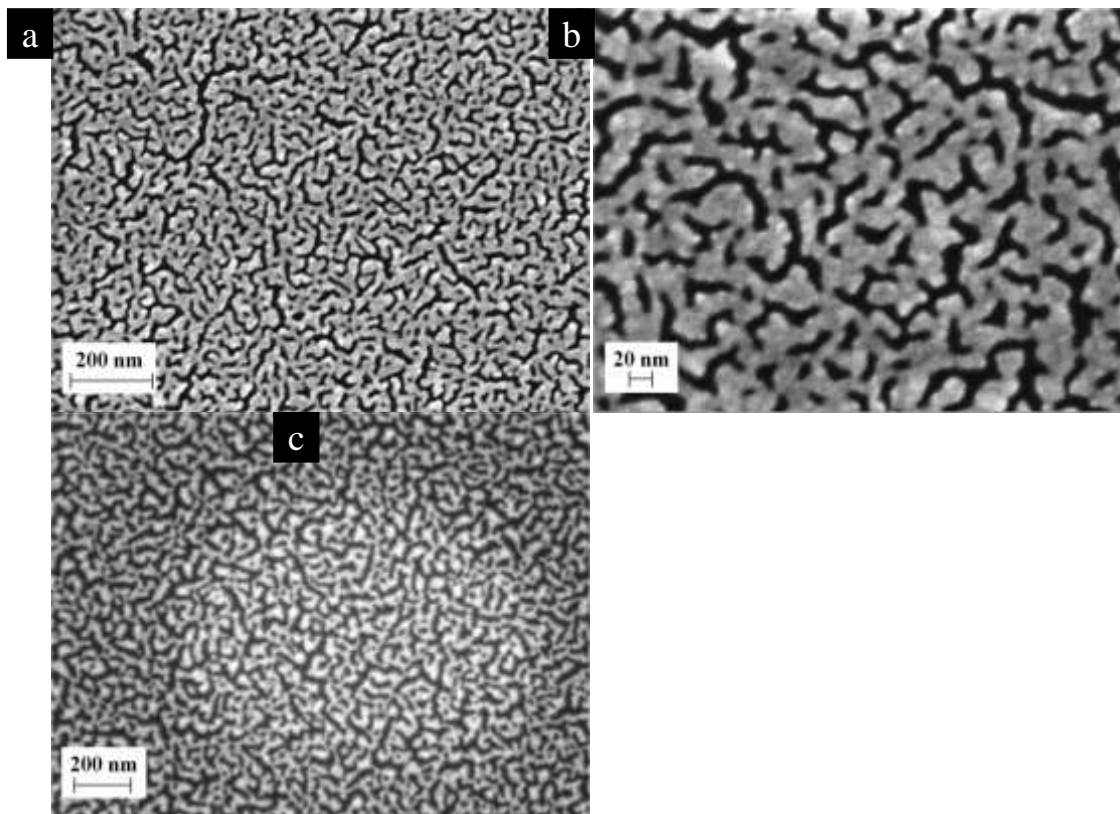


Figure **Error! No text of specified style in document.**86: (a-b) Representative FESEM images of gold porous film of thickness 5.6 nm at different magnifications. (c) Representative FESEM image of Al_2O_3 deposited on gold porous film, followed by annealing the sample at 450 °C for 20 minutes, under forming gas atmosphere.

the precursor materials used, and the reactor set-up, which is beyond the scope of this work. On the other hand, one way to reduce the leakage paths is to increasing the annealing temperature. As expected, after annealing the sample at 850 °C, no significant reduction in accumulation capacitance was observed for all the MOS capacitors (with and without nanoparticle), as shown in Fig. 4.47. This suggests that contact at the gold-alumina interface could have been an issue. FESEM images of the sample are shown in Fig. 4.48, which shows that the ordering is mostly maintained even after annealing at 850 °C, due to encasement in alumina. Now, this enables to investigate the important effect of interparticle spacing effect on memory characteristics.

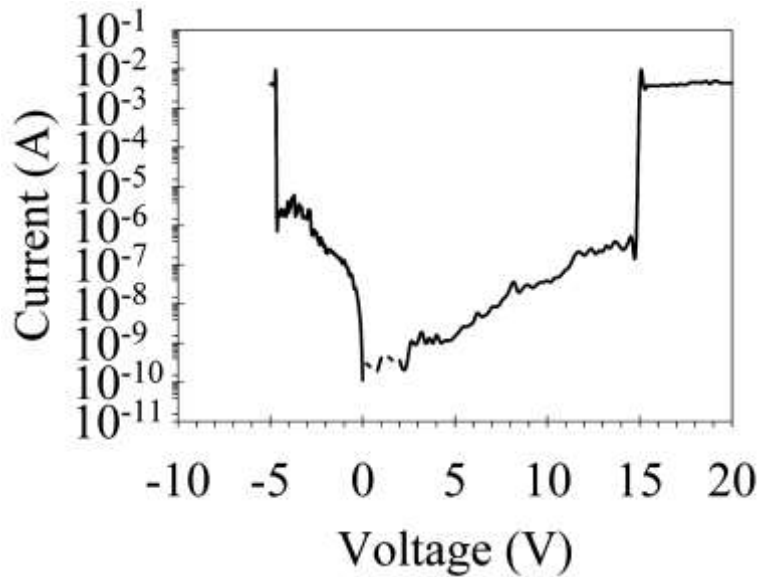


Figure **Error! No text of specified style in document.**87: Current voltage characteristic of MIM structure (with gold porous film- Al_2O_3 -Aluminium architecture), showing high leakage currents ($\sim \mu\text{A}$) in addition to very low breakdown voltage of $\sim 1\text{V}$. Note the substrate was annealed at 450°C for 20 minutes in forming gas environment.

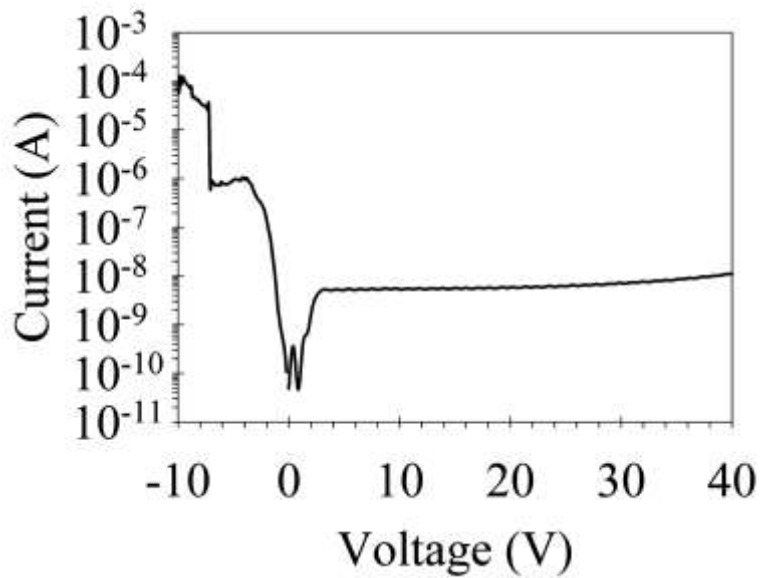


Figure **Error! No text of specified style in document.**88: Current voltage characteristic of MOS structure (with Aluminium-Si- Al_2O_3 -Aluminium) with ALD process carried out at 375°C . Even in this structure, very high leakage current and low breakdown voltage was observed.

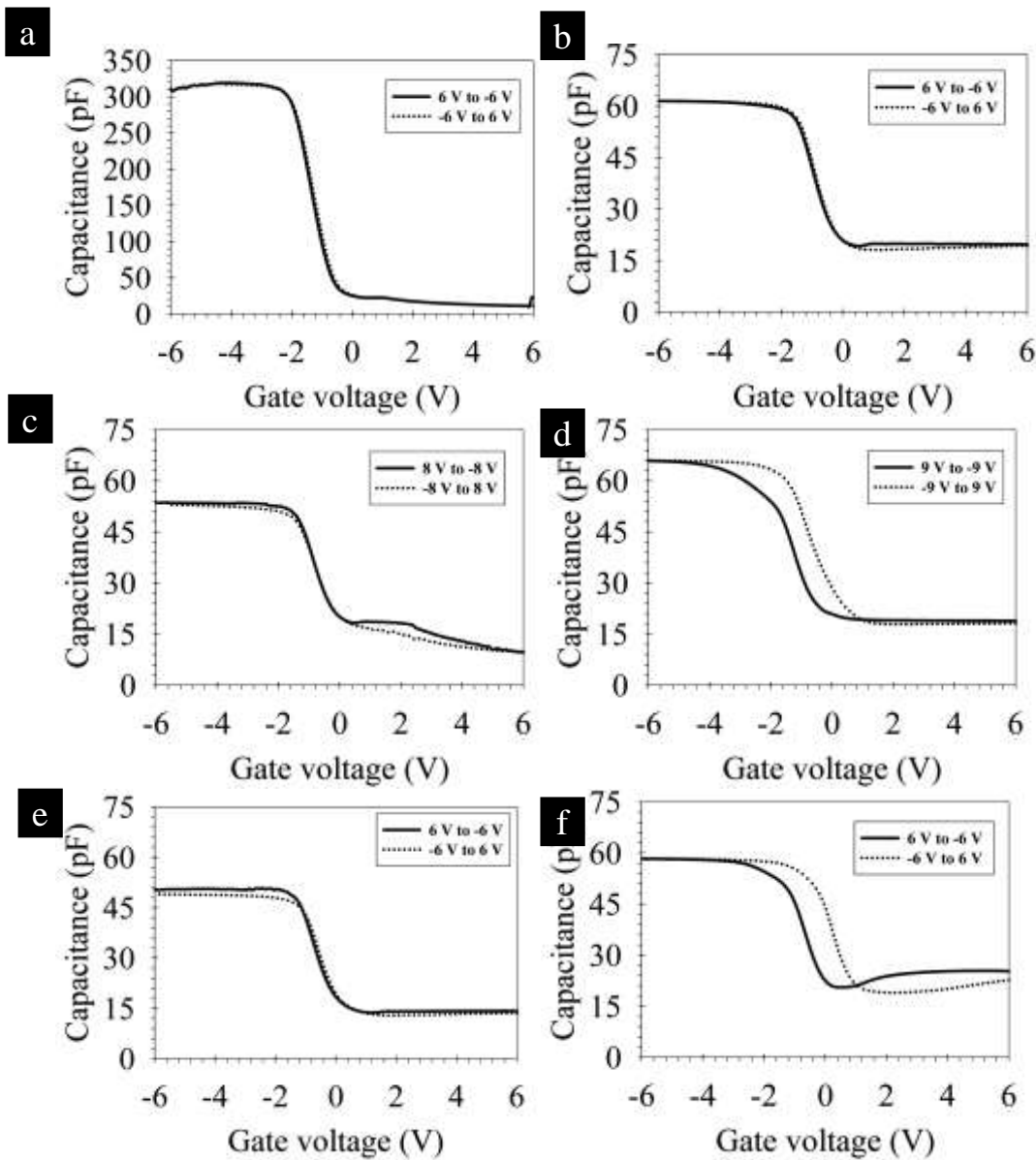


Figure **Error! No text of specified style in document.**89: (a) Capacitance-Voltage (CV) curve of a MOS capacitor with pure tunnelling oxide structure. The MOS capacitor shows no significant hysteresis, indicating negligible traps in the oxide layer. (b) Capacitance-Voltage (CV) curve of a MOS capacitor with tunnelling oxide, SiO_2 and control oxide, Al_2O_3 structure. The MOS capacitor shows no significant hysteresis, indicating negligible traps in the oxide layer. Capacitance-Voltage (CV) curve of a MOS capacitor with the 2D (c) untreated array and (d) bare gold nanoparticle array (with 2 nm spacing) as floating gate. The devices were fabricated by depositing Al_2O_3 using ALD process at 135°C , followed by nitrogen annealing at 400°C for 20 minutes. The sample was subsequently annealed under forming gas environment at 850°C for 20 minutes. The hysteresis loop is observed for devices fabricated using bare nanoparticle array (0.9 V) and not for untreated array. This can be attributed to the possible conversion of entrapped organic ligand into carbonaceous product during annealing. Capacitance-Voltage (CV) curve of a MOS capacitor with the 2D (e) untreated array and (f) bare gold nanoparticle array (with 20 nm spacing) as floating gate. The sample was subsequently annealed under forming gas environment at 850°C for 20 minutes. The hysteresis loop is observed for devices fabricated using bare nanoparticle array (0.9 V) and not for untreated array. This can be attributed to the possible conversion of entrapped organic ligand into carbonaceous product during annealing.

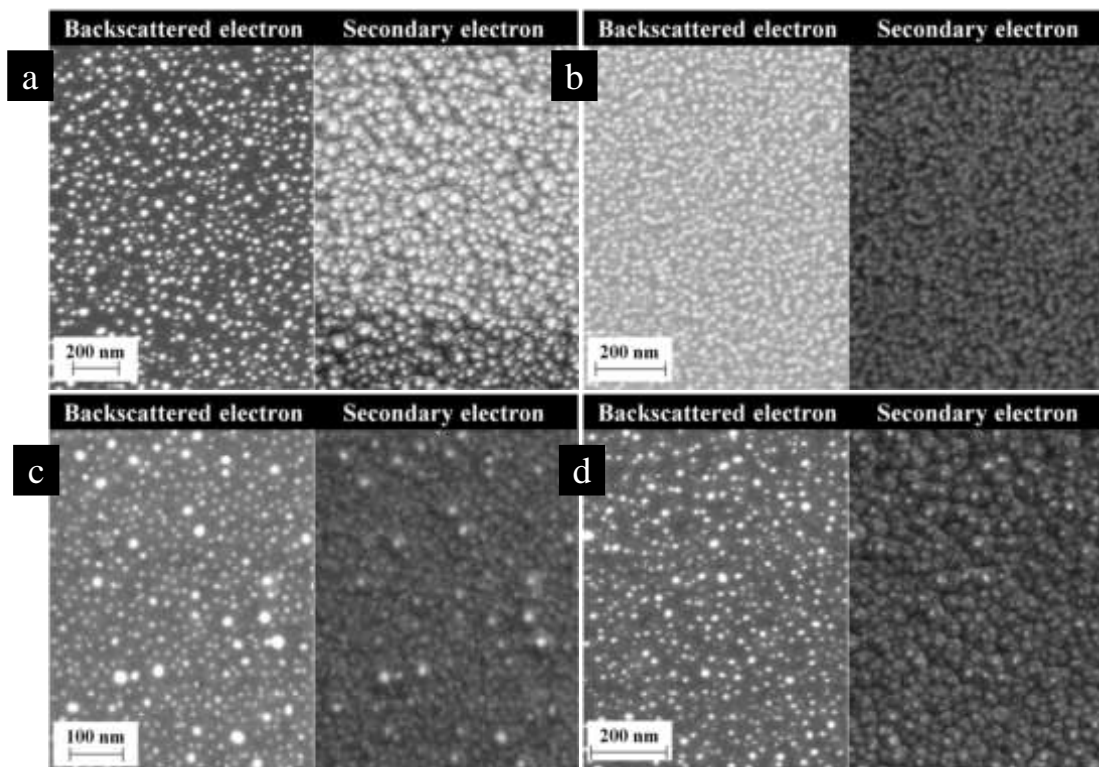


Figure **Error! No text of specified style in document..90**: Representative FESEM images of (a) untreated and (b) bare nanoparticle array with 2 nm spacing (DDT capped gold nanoparticles), after ALD deposition of Al_2O_3 followed by forming gas annealing at 850°C for 20 minutes. Representative FESEM images of (c) untreated and (d) bare nanoparticles with 20 nm spacing (using thiol-terminated polystyrene capped gold nanoparticles of molecular weight: 20000 g/mol), after ALD deposition of Al_2O_3 followed by forming gas annealing at 850°C for 20 minutes. In all the figures, left and right images were obtained using backscattered electron and secondary electron detector respectively.

Effect of interparticle spacing

Memory devices were fabricated with different interparticle spacing using dodecanethiol capped gold nanoparticle arrays ($\sim 2.2 \pm 0.8$ nm spacing) and thiol-terminated polystyrene capped gold nanoparticle arrays with different molecular weights namely, 7000, 10000 and 20000 g/mol (7.9 ± 1.8 nm, 8.9 ± 1.4 nm and 19.7 ± 3.3 nm spacing respectively), as shown in Fig. 4.49. The bare nanoparticle arrays were fabricated by exposing to plasma treatment under optimized conditions based on the report. To remove the sulphonates after hydrogen plasma treatment of dodecanethiol capped gold nanoparticle arrays, the substrate was rinsed with water followed by ethanol. FESEM images after plasma treatment are shown in Fig. 4.50a-d. The ALD process was employed to deposit alumina with thickness of 34 nm. This was followed by forming gas annealing at 850°C for 20 minutes.

More interestingly, the CV characteristic of MOS capacitors showed an optimum interparticle spacing for observing larger memory window (Fig. 4.51). The memory window followed the trend of 8.9 nm (**5.2V**) $>$ 7.9 nm (**4.5 V**) $>$ 2.2 nm (**2.9 V**) $>$ 19.7 nm (**0.8V**) with varying interparticle spacing. Values in the bracket represent the memory window. This trend is similar to the observation made in devices prepared using RF sputtering, reported earlier in this chapter. Lower memory window observed for the case of larger interparticle spacing can be explained based on the reduction in number density of particles. On the contrary, lower memory window with highest particle density can arise due to two situations, (i) more leakage paths through the oxide or (ii) inability to inject more electrons into the nanoparticle due to columbic repulsion amongst the neighboring particle. At this juncture, it is not possible to discriminate between these two explanations. The variation in inversion capacitance is attributed to the presence of residual back oxide that was found to be difficult to remove, due to the size of the sample, using buffered HF solution. This modification was adopted so as to anneal the sample at 850°C , and then deposit the back contact made of aluminium.

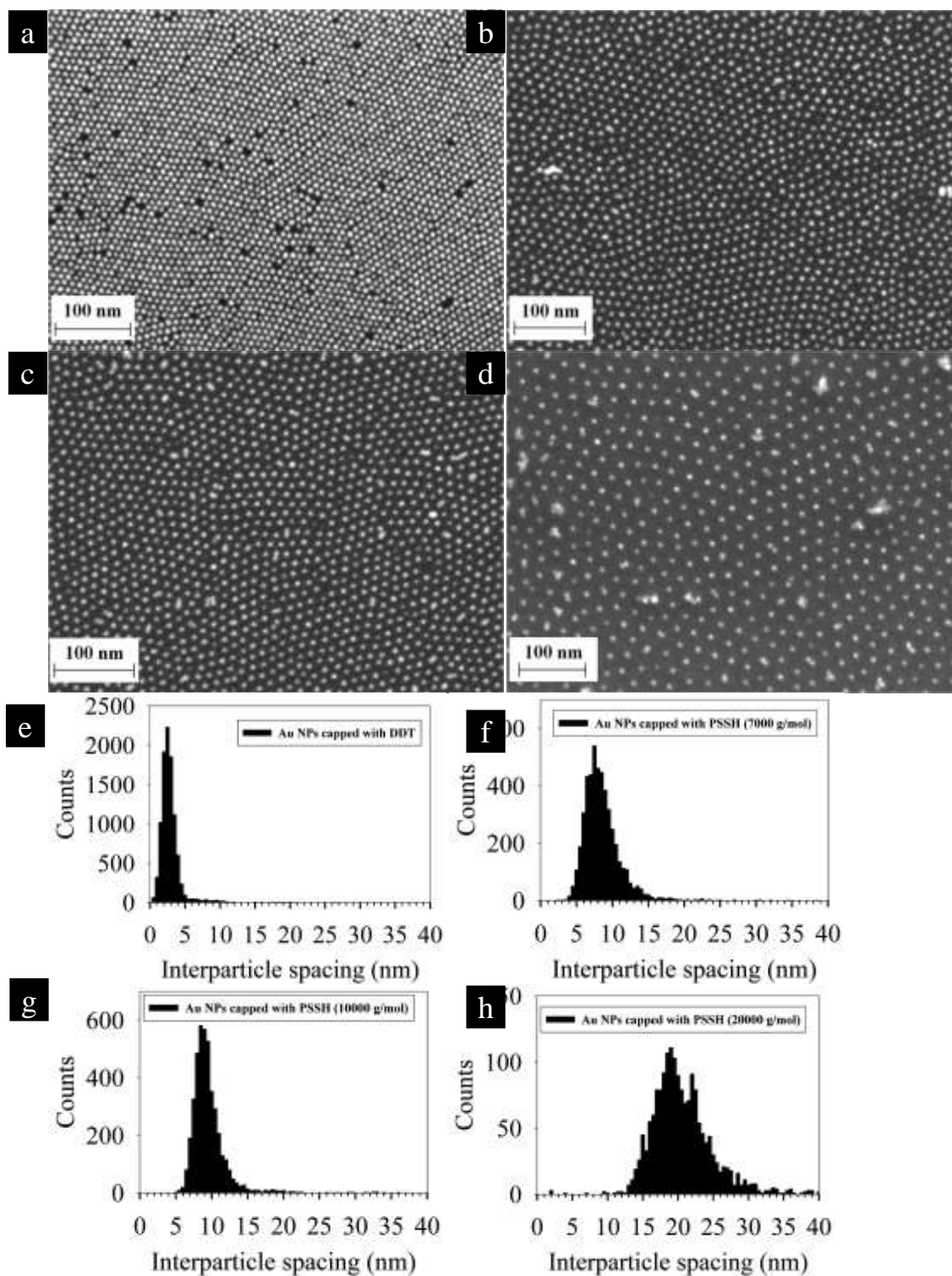


Figure **Error! No text of specified style in document.**91: Representative FESEM image of 2D arrays of gold nanoparticles capped with (a) dodecanethiol, (b) thiol-terminated polystyrene (molecular weight: 7000 g/mol), (c) thiol-terminated polystyrene (molecular weight: 10000 g/mol) and (d) thiol-terminated polystyrene (molecular weight: 20000 g/mol). The respective histograms of interparticle spacing are presented in Fig. e-h.

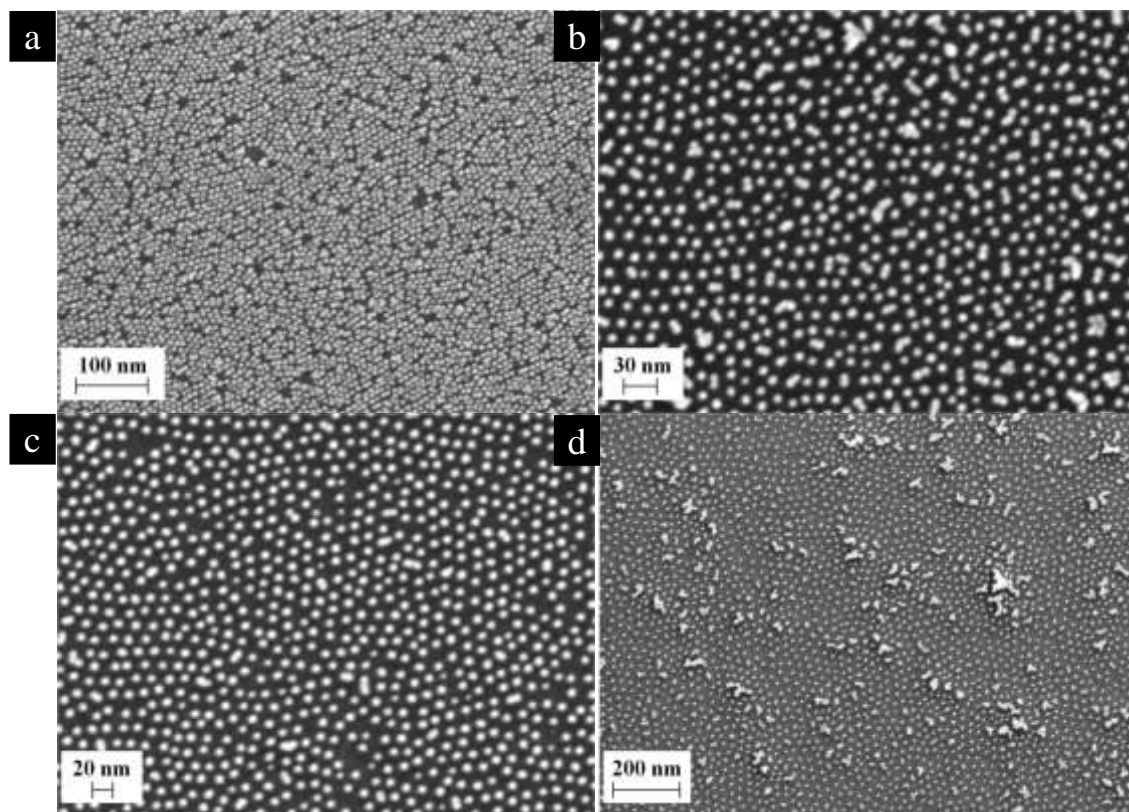


Figure **Error! No text of specified style in document..92**: Representative FESEM image of bare gold nanoparticle array with interparticle spacing of (a) 2.2 nm (dodecanethiol capped gold nanoparticle array), (b) 7.9 nm (thiol-terminated polystyrene (molecular weight: 7000 g/mol) capped gold nanoparticle array), (c) 8.9 nm (thiol-terminated polystyrene (molecular weight: 10000 g/mol) capped gold nanoparticle array), and (d) 19.7 nm (thiol-terminated polystyrene (molecular weight: 20000 g/mol) capped gold nanoparticle array); after plasma treatment under optimized conditions.

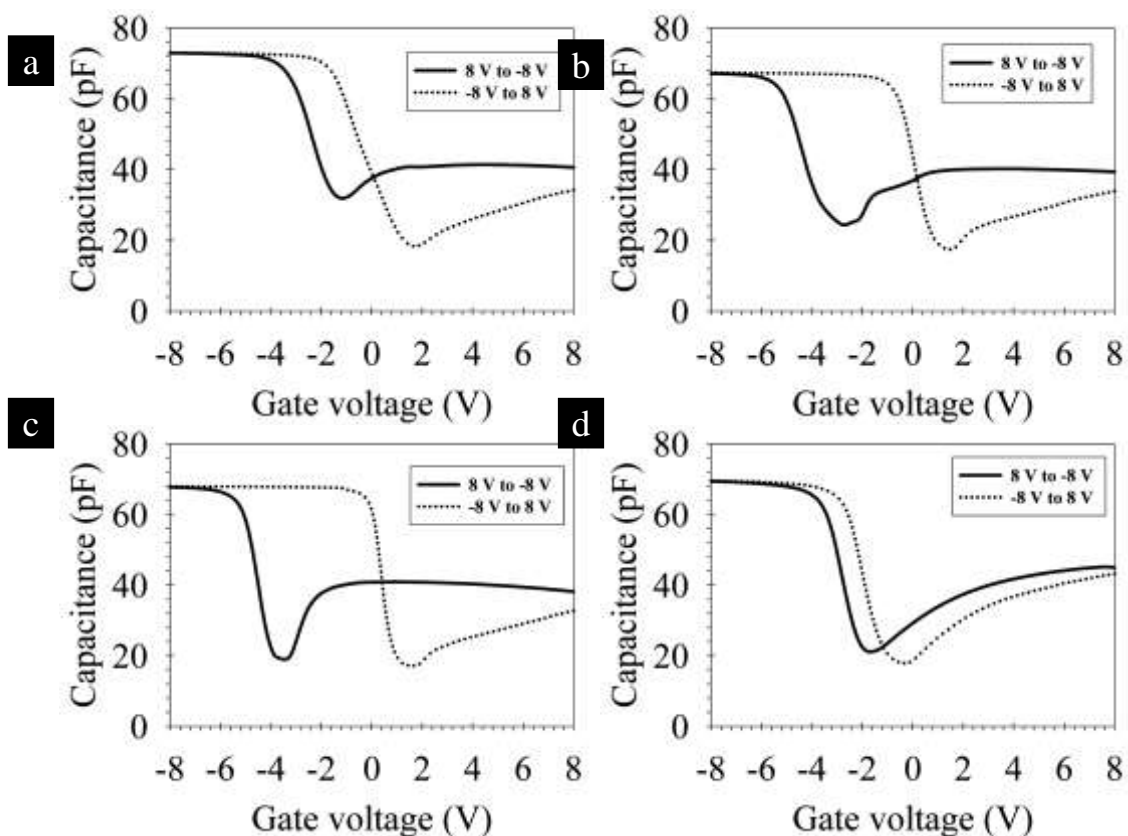


Figure **Error! No text of specified style in document.**93: Capacitance-Voltage (CV) curve of a MOS capacitor with the bare nanoparticle array with interparticle spacing of (a) 2.2 nm (dodecanethiol capped gold nanoparticle array), (b) 7.9 nm (thiol-terminated polystyrene (molecular weight: 7000 g/mol) capped gold nanoparticle array), (c) 8.9 nm (thiol-terminated polystyrene (molecular weight: 10000 g/mol) capped gold nanoparticle array), and (d) 19.7 nm (thiol-terminated polystyrene (molecular weight: 20000 g/mol) capped gold nanoparticle array); after plasma treatment under optimized conditions. The devices were fabricated by depositing Al_2O_3 using ALD process at 135°C , followed by nitrogen annealing at 400°C for 20 minutes. The sample was subsequently annealed under forming gas environment at 850°C for 20 minutes. The largest memory window was obtained for arrays prepared using thiol-terminated polystyrene molecules of molecular weight of 10000 g/mol, an intermittent spacing. The memory window followed the trend of 8.9 nm (5.2 V) > 7.9 nm (4.5 V) > 2.2 nm (2.9 V) > 19.7 nm (0.8 V) interparticle spacing. Values in the bracket represent the memory window.

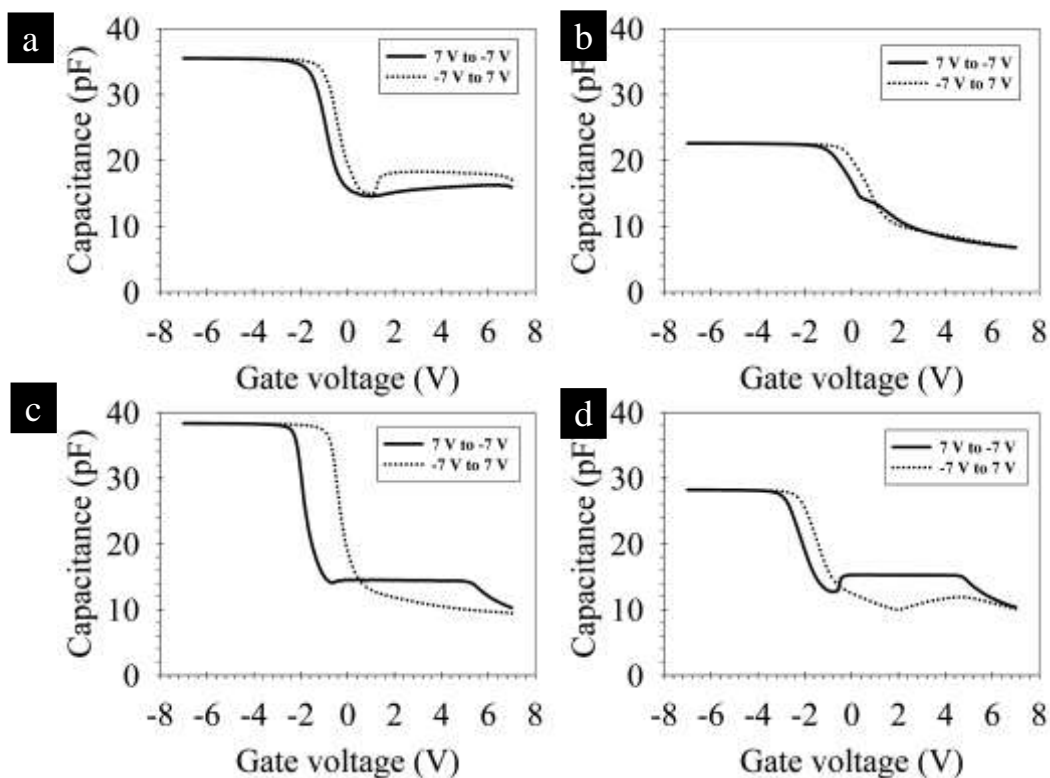


Figure **Error! No text of specified style in document.**94: Capacitance-Voltage (CV) curve of a MOS capacitor with the interparticle spacing of (a) 2.2 nm (dodecanethiol capped gold nanoparticle array), (b) 7.9 nm (thiol-terminated polystyrene (molecular weight: 7000 g/mol) capped gold nanoparticle array), (c) 8.9 nm (thiol-terminated polystyrene (molecular weight: 10000 g/mol) capped gold nanoparticle array), and (d) 19.7 nm (thiol-terminated polystyrene (molecular weight: 20000 g/mol) capped gold nanoparticle array); after plasma treatment under optimized conditions. The devices were fabricated by depositing Al_2O_3 using e-beam process at room temperature. The sample was subsequently annealed under forming gas environment at 450 °C for 20 minutes. The largest memory window was obtained for arrays prepared using thiol-terminated polystyrene molecules of molecular weight of 10000 g/mol, an intermittent spacing, similar to earlier ALD process. The memory window followed the trend of 8.9 nm (**1.5 V**) > 7.9 nm (**0.6 V**) ~ 2.2 nm (**0.6 V**) ~ 19.7 nm (**0.6 V**) interparticle spacing. Values in the bracket represent the memory window.

Table **Error! No text of specified style in document.**-8: Summary of effect of interparticle spacing in nanoparticle arrays and process parameters on memory window of the floating gate memory devices presented in this chapter

Batch Number.	Mean interparticle spacing	Top oxide (deposition route)	Memory window (average value)	Thickness
1	2 nm	Gd ₂ O ₃ (RF sputtering)	0.66 V	SiO ₂ : 10 nm Gd ₂ O ₃ : 15 nm
	4.4 nm	Gd ₂ O ₃ (RF sputtering)	1.26 V	
	13.3 nm	Gd ₂ O ₃ (RF sputtering)	0.53 V	
2	2 nm	Al ₂ O ₃ (ALD)	4.4 V	SiO ₂ : 10.1 nm Al ₂ O ₃ : 18.7 nm
	20 nm	Al ₂ O ₃ (ALD)	6.2 V	
3	2 nm	Al ₂ O ₃ (ALD)	14.8 V	SiO ₂ : 5.1 nm Al ₂ O ₃ : 23.4 nm
	20 nm	Al ₂ O ₃ (ALD)	1.3 V	
4	2.2 nm	Al ₂ O ₃ (ALD)	2.9 V	SiO ₂ : 9 nm Al ₂ O ₃ : 34 nm
	7.9 nm	Al ₂ O ₃ (ALD)	4.5 V	
	8.9 nm	Al ₂ O ₃ (ALD)	5.2 V	
	19.7 nm	Al ₂ O ₃ (ALD)	0.8 V	
5	2.2 nm	Al ₂ O ₃ (e-beam)	0.6 V	SiO ₂ : 9 nm Al ₂ O ₃ : 37 nm
	7.9 nm	Al ₂ O ₃ (e-beam)	0.6 V	
	8.9 nm	Al ₂ O ₃ (e-beam)	1.5 V	
	19.7 nm	Al ₂ O ₃ (e-beam)	0.6 V	

Device fabrication using e-beam evaporation

An alternative, attractive room temperature deposition process, namely, electron-beam evaporation was also used to deposit Al₂O₃. Arrays with four different interparticle spacing as described in the previous section for ALD deposition was employed. The thickness of the oxide deposited was 37 nm. After the deposition of alumina on top of nanoparticle arrays, the sample was annealed under forming gas environment at 450 °C for 20 minutes. The capacitance-voltage of the MOS capacitor devices are shown in Fig. 4.52. Similar to the ALD process, an optimum in spacing for obtaining larger memory window was found, i.e., 2D arrays fabricated with thiol-terminated polystyrene (molecular weight: 10000 g/mol) capped gold nanoparticles yielded the largest memory window. The memory window followed the trend of 8.9 nm (**1.5 V**) > 7.9 nm (**0.6 V**) ~ 2.2 nm (**0.6 V**) ~ 19.7 nm (**0.6 V**) with varying interparticle spacing. Again, lack of high-purity source material for e-beam evaporation led to the observation of clockwise hysteresis loops.

Summary

A CMOS-compatible process for the realization of a high-density (>10¹² particles/cm²) floating gate memory device using self-assembled 2D arrays of the gold nanoparticle as storage nodes was developed. The fabricated MOS capacitors, using RF sputtering process for top-oxide deposition, show excellent retention (decay time constant > 10⁸ s) and endurance (>10000 P/E cycles) characteristics as well as a narrow distribution of the memory window across devices. This optimized process can be readily adapted for fabricating multilevel flash memory devices at the sub-20 nm node, as it easily provides nanoscale control of the particle size and interparticle spacing. Experimental results show an optimum interparticle spacing (arrays with thiol-terminated polystyrene capped gold nanoparticles of molecular weight: 10000 g/mol) for obtaining larger memory window. Table 4-6 provides a summary of the effect of various process parameters on memory window. The quality of top-oxide deposited, using atomic layer deposition and electron-beam evaporation needs to be further improved, so as to enable commercial production of next-generation devices.

9.5 Development of a nanoparticle based catalyst layer for fuel cells:-

Polymer electrolyte (or proton exchange) membrane fuel cells (PEMFC) and direct methanol fuel cells (DMFC) are efficient, high power density, electrochemical energy devices. Pure platinum nanoparticles are used to catalyze the oxygen reduction reaction (ORR) occurring at cathode, and hydrogen oxidation reaction (HOR)/ methanol oxidation reaction (MOR) occurring at anode in PEMFC/ DMFC fuel cells, respectively. The scarcity of reserves of noble platinum metal combined with its high cost has fueled the need to reduce the platinum content in the catalyst layer of PEM/DMFC fuel cell without compromising on efficiency. Active platinum sites also suffer from CO poisoning, reducing the longevity of the catalyst layer and imposing stricter conditions on the purity of feed gases. Bimetallic nanoparticles are less susceptible to such troubles. Typically, bimetallic nanoparticles are comprised of a precious, catalytically-active metal like platinum, palladium; and a lower-cost, stable / noble metal like gold, ruthenium, cobalt, iron etc. The electrocatalytic activity of bimetallic nanoparticles has been studied extensively, and are shown to have higher efficiency and durability, in comparison with monometallic catalyst layers, especially for use in PEMFC/ DMFC. Bimetallic nanoparticles exploit the individual traits of both the metals and their enhanced activity arises from an interaction of the constituents' electronic configurations.

Experimental Section

Materials – Hydrogen tetrachloroaurate trihydrate ($\text{HAuCl}_4 \cdot 3\text{H}_2\text{O}$, purity 99.99%), tannic acid (ACS reagent), Chloroplatinic Acid Hexahydrate ($\text{H}_2\text{PtCl}_6 \cdot 6\text{H}_2\text{O}$, purity 99.99%) were purchased from Sigma Aldrich Co., potassium carbonate (K_2CO_3) from , Hydrazine hydrate, 37% sulphuric acid (H_2SO_4), 99.8% methanol, acetone, tetrahydrofuran (THF), silicon wafer,

Synthesis of Au@Pt nanoparticles – Monodispersed gold nanoparticles were synthesized at room temperature as described by Kalidas et al¹⁵. Briefly, 30 mL solution consisting of 4.5 mL tannic acid (taken from 5.88 mM stock solution), 1 mL K_2CO_3 (taken from 72.35 mM stock solution) and 24.5 mL deionized water was taken in a 100 mL beaker. pH of the 30 mL solution was 7. 20 mL solution consisting of 0.5 mL $\text{HAuCl}_4 \cdot 3\text{H}_2\text{O}$ (taken from 25.4 mM stock solution) and 19.5 mL DI water was taken in another beaker. This 20 mL chloroauric acid solution was added drop by drop over a period of 15 minutes into the 30 mL solution. The average particle diameter of gold nanoparticles determined from TEM analysis was 5.34 ± 0.62 nm. Pt shells were prepared by subsequent addition of the desired amount of platinum as chloroplatinic acid to the gold colloid, followed by reduction with Hydrazine. For example, to prepare Au@Pt nanoparticles with Pt/Au ratio of 0.09, 35 μL of $\text{H}_2\text{PtCl}_6 \cdot 6\text{H}_2\text{O}$ (taken from 19.3 mM stock solution, pH=2) was added to 25 mL of the colloidal gold solution prepared as described earlier. To this mixture, 600 μL of hydrazine was added, and the solution was stirred for a further 20 min, after which the color of the solution turned deep black. The pH of the solution was 10.5. Au@Pt nanoparticles were synthesized with different average Pt/Au ratios of 0.19, 0.39, 0.58, and 0.88 corresponding to computed platinum shell thicknesses of half atomic layer, one atomic layer, one and half atomic layer, and two atomic layer of platinum, respectively, on gold nanoparticles having a nominal size of 5 nm. The molar ratio of platinum salt to hydrazine was kept constant in all these experiments.

UV- Visible characterization. UV-Visible spectra were obtained using a Systronics double beam UV visible spectrophotometer 2201. The concentration of gold atoms in the solutions used for spectroscopic analysis, in the case of both gold and Au@Pt core shell nanoparticles, was 0.254 mM.

TEM, HRTEM and Selected area electron diffraction (SAED) characterization and sample preparation. TEM, HRTEM and SAED characterizations were carried out using either a Tecnai G2 F30 or a Tecnai G2 T20 S-Twin operating at 300 KV or 200 KV, respectively. Octadecane thiol capped Au@Pt nanoparticles were mixed in an organic solvent, which was then spread on a convex water surface bound by hydrophobic teflon boundary at its periphery. After solvent evaporation, the self-assembled nanoparticle arrays were transferred onto desired substrates using the Langmuir-Schaefer technique.

XPS characterization and sample preparation. XPS measurements were carried out using a Thermo Scientific multilab 2000 instrument with a resolution of 0.2 eV. The general scan and Au 4f and Pt 4f core level spectra were recorded with x-ray source $\text{AlK}\alpha$ (1486.6 eV). The raw data was deconvoluted using Thermo Scientific multilab software. The binding energies of the obtained spectra were calibrated using the C1s peak at 284.5 eV. Octadecane thiol capped Au@Pt nanoparticles dissolved in chloroform was drop coated onto a silicon wafer for XPS measurements.

XRD characterization and sample preparation. Octadecane thiol capped Au@Pt nanoparticles mixed in chloroform was drop coated on either a glass slide or nanoparticle bilayers, with different Pt/Au ratio, were transfer printed onto a silicon wafer substrate sputter coated with a film of Au /Cr (100 nm/7 nm).

Electrochemical characterization and sample preparation. Three electrode measurements were used for cyclic voltammetry analysis. Cyclic voltammetry (CV) was performed using DY2000 potentiostat (Digi Ivy Inc.) controlled by inbuilt software written in LabVIEW (National Instruments). The counter electrode was a platinum foil having 1 cm^2 area, and the reference electrode was standard calomel electrode (SCE) $\text{Hg}/\text{Hg}_2\text{Cl}_2$ (in saturated solution of KCl in water at 25 °C with redox potential of +0.244 V vs NHE). All voltages were measured with respect to standard calomel electrode. The working electrode was prepared as follows. Octadecane thiol capped Au@Pt nanoparticles were dissolved in an organic

solvent (50-50 volume ratio of CHCl₃-Hexane) and self-assembled into hexagonally close packed, monolayers on water surface as reported by Santhanam et al⁶. Bilayers were fabricated by transferring subsequent monolayers from the water surface to a polydimethylsiloxane (PDMS) stamp pad by the Langmuir-Schaefer (LS) technique. The bilayers were subsequently stamped on gold/chrome (100 nm/10 nm) sputtered on clean silicon wafer substrate which was used as working electrode.

Cyclic voltammetry was carried out at 300 K in 0.5 M H₂SO₄ media in order to measure the hydrogen adsorption/desorption currents. The electrolyte was purged with nitrogen gas (purity 99.998%) for 20 minutes. The CV scan on the working electrode was done for 24 scan cycles from 0V vs SHE to 1.244V vs SHE at 50mV/s scan rate. This activation treatment provided stable voltammogram profiles. The activated electrodes were then flushed with 0.5 M deaerated H₂SO₄ solution, immersed in fresh deaerated acidic electrolyte and voltammogram scans at 50mV/s scan rate was taken. The electrochemically active surface area (ESA, m² per gm Pt) was measured by calculating the area under the hydrogen-desorption curve. The ESA was obtained according to Equation (1),

$$ESA = Q_H / (W_{Pt} * 0.21) \text{ -----(1)}$$

where Q_H is the charge consumed for the electro-oxidation of adsorbed hydrogen atoms on active platinum surface, which is equivalent to the calibrated area of the hydrogen desorption peak on the CV curve (mC/cm²), 0.21 represents the charge required to oxidize a monolayer of H₂ on platinum facet (mC/cm²) and W_{Pt} is the platinum loading at the working electrode (mg/cm²)

For the study of methanol oxidation, cyclic voltammetry was conducted at a sweep rate of 50mV/s in a solution containing 2M methanol and 0.5M sulfuric acid, which was degassed by purging with nitrogen (99.998% purity) for at least 20 min prior to each measurement.

Results and discussions

Characterization of synthesized nanoparticles

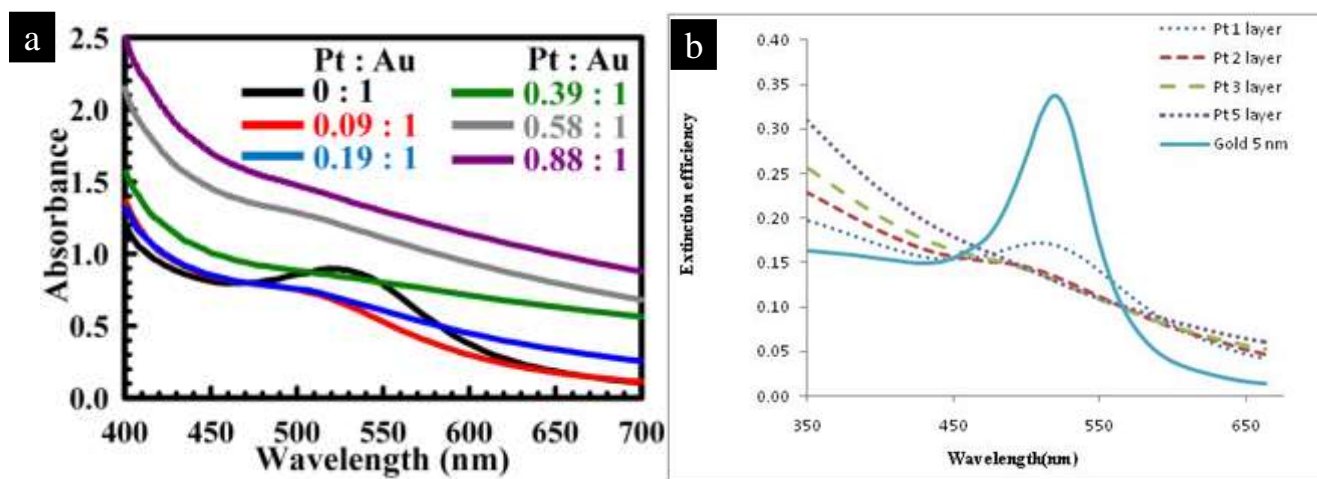


Figure 1: UV-Visible absorbance of gold seed and core shell Au@Pt nanoparticles for varying Pt/Au ratio. (a) Experimental results, (b) Simulation results.

The SPR absorbance intensity reduces gradually as the gold seed is coated with increasing number of platinum atoms. Also with increasing Pt/Au ratio, there was monotonous increase in the overall absorbance of the colloidal solution across the whole wavelength spectrum. These observations suggest that Pt atoms are coating all gold seeds uniformly. An alternative hypothesis that could explain the decrease in the plasmon peak attributed to gold could be that a sub population of the gold particles had a continuous coating of platinum atoms, while the other gold nanoparticles were relatively unchanged. However, such a hypothesis is not supported by cyclic voltammogram data, as there is no evidence for any electrocatalytic activity that could be attributed to contiguous platinum atoms. Table 1 shows the variation in the area under the surface plasmon peak with variation in Pt to Au atomic ratio. Assuming uniform distribution of platinum on nanoparticles, and partial surface coverage by continuous Pt films, only a decrease in the peak area of about 25 % and 50 % would have been expected. However, the reduction in the area under the plasmon peak attributable to gold is much higher, and was 68.7 % and 86.3% respectively. Partial/complete alloying of gold and platinum atoms in the outer shell have been attributed to similar damping of plasmon resonances in the literature. For higher Pt/Au ratios of 0.39, 0.58, and 0.88 the gold peak was completely suppressed and a monotonic increase in absorbance intensity from visible towards UV-Visible wavelength was observed. Optical properties of core-shell Au@Pt and pure gold nanoparticles were computed using discrete dipole approximation (DDA) simulations by Sureka and Santhanam for similar platinum coverages on 5 nm gold nanoparticles. With a monoatomic layer of platinum coating 5nm gold nanoparticle, the plasmon

peak reduces to half the value corresponding to a gold nanoparticle; with two atomic layers of platinum atoms coating 5nm gold nanoparticle, the extinction spectrum reduces into a shoulder which is slightly shifted towards lower wavelength; and with five layers of platinum coating 5nm gold nanoparticles, there is total disappearance of gold peak and monotonous increase of the extinction spectrum from higher towards lower wavelength. The rate of decrease of the SPR band expected, based on simulations, for a platinum shell on gold nanoparticle core is slower than what is observed experimentally. This further corroborates our earlier deduction that there is partial alloying of gold and platinum atoms in the outer shell. Such a formation of an alloy skin layer has also been reported earlier, and is attributed to be the cause of the unique electrocatalytic activity of Au@Pt nanoparticles.

Table 1: Variation of SPR area as a function of Pt/Au ratio

Pt/Au ratio	Au Plasmon area	Decrease in SPR area %
Pure gold seed	28.82	
0.09	9.014	68.72311
0.19	3.9405	86.3272

HRTEM and selected area diffraction (SAED) analysis.

Figures 2a-d show representative images of particles synthesized. The variation of the size distribution of the nanoparticles with Pt/Au ratio is shown in table 2. The core and shell are not individually differentiable because platinum and gold have atomic number of 78 and 79 respectively which lead to similar contrast in TEM images.

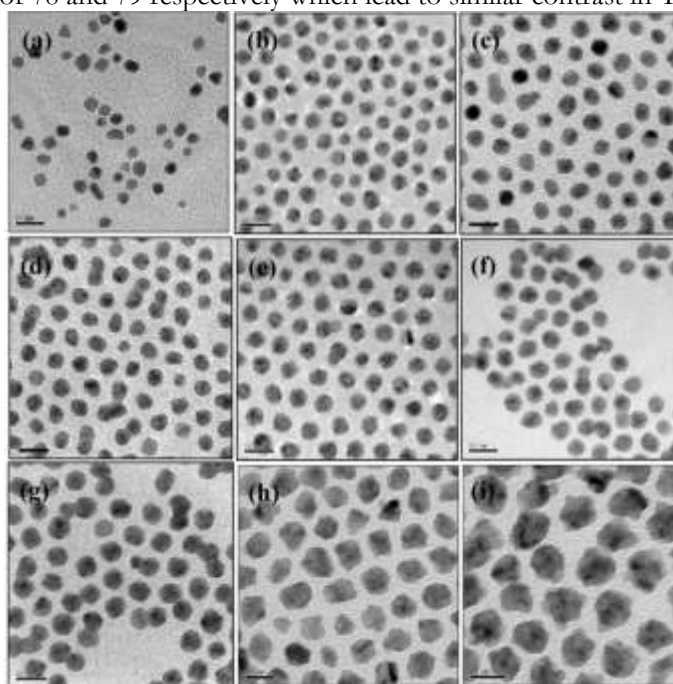


Figure 2: TEM images of Au and different ratio Pt/Au core-shell Au@Pt nanoparticles: a. gold nanoparticle b. Pt/Au 0.09, c. Pt/Au 0.19, d. Pt/Au 0.39, e. Pt/Au 0.58 and f. Pt/Au 0.88.

Table 2: TEM diameter of core gold nanoparticle and corresponding core-shell Au@Pt nanoparticles, and their shell thickness.

(Pt/Au) _{ratio}	Au seed diameter y nm	Experimental Au@Pt nps diameter x nm	Shell thickness (x- y)/2 nm	Theoretical d _{Au@Pt} nm
0.09	5.34±0.67	5.76±0.55	0.21	5.45
0.19	5.76±0.41	6.02±0.51	0.13	5.98
0.39	5.35±0.53	5.98±0.54	0.32	5.76
0.58	5.31±0.61	6.31±0.48	0.5	5.90
0.88	5.77±0.38	7.38±0.54	0.8	6.70

Ideally the shell thickness for one layer of platinum atoms uniformly covering gold nanoparticle is the diameter of platinum atom i.e 0.36nm and two layers of platinum atoms covering gold nanoparticle would have a shell thickness of 0.78nm. Experimentally the Pt/Au ratio of 0.39 corresponds to core shell Au@Pt nanoparticle of shell thickness 0.32nm as shown in table 2, which is roughly equal to the previous theoretical prediction of 0.36nm. From this it can be concluded that Pt/Au ratio of 0.39 forms uniformly wetted, one platinum atomic layer coating surface of gold nanoparticle.

Figure 3 shows the selected area diffraction (SAED) pattern and HRTEM images of Au@Pt core-shell nanoparticles of various Pt/Au ratios. There is no distinguishable separation/contrast observed in the first three concentric rings in SAED to prove the presence of platinum. This is because gold and platinum has close atomic numbers (78 for Pt and 79 for Au) and lattice constants (for fcc case 0.392nm for Pt and 0.408nm for Au). However at the fourth place two finely split concentric rings which are gold (inside one) and platinum (outside one) (311) planes were detected. The inner core of the bimetallic nanoparticles showing fcc (111) planes of pure gold and the detection of platinum (311) plane in SAED pattern suggest the fact that platinum atoms are present in the shell around core gold nanoparticles.

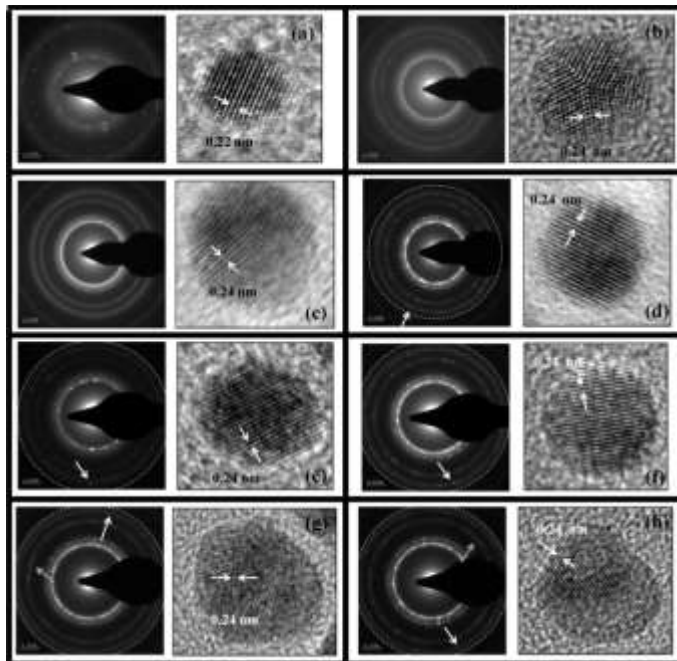


Figure 3: SAED and HR-TEM images of element Pt and Au and for different ratio Pt/Au core-shell Au@Pt nanoparticles: a. platinum nanoparticle, b. gold nanoparticle c. Pt/Au 1/10.3, d. Pt/Au 1/5.26, e. Pt/Au 1/2.56, f. Pt/Au 1/1.72, g. Pt/Au 1/1.72, h. Pt/Au 1/1.72.

Broad peaks, broadened due to presence of nanoparticles, in the XRD spectra limit the ability to deconvolute the spectra and determine the phases present in the samples using Rietveld analysis (Fig. 4). However, the peak positions corresponding to gold, and a slight shoulder present at 20 positions ascribed to Pt suggest the absence of alloy formation and also formation of Pt layers on the nanoparticles.

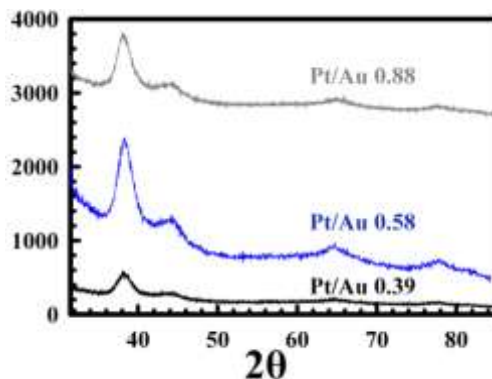


Figure 4: XRD of Au@Pt nanoparticles.

Figure 5 shows XPS spectra of octadecane-thiol coated core shell Au@Pt nanoparticles with variable Pt/Au ratios. The normalized spectra reveal an increase in platinum signal that is consistent with the increase of Pt/Au ratio. The screening of gold atoms by Pt overlayer can be neglected as the information depth in XPS is of the order of 10 nm, which is considerably higher than that of the Pt layer thicknesses and is commensurate with that of the nanoparticles' diameter.

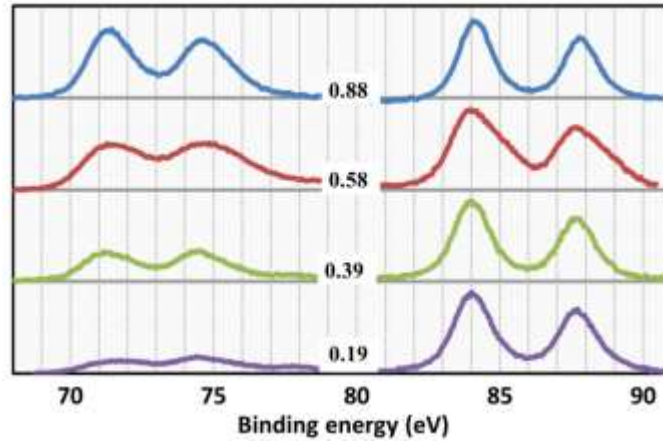


Figure 5: XPS of platinum and gold spectra for various Pt/Au ratios (Spectra have been normalized with respect to Au-4f peak).

The binding energy values of Au and Pt elements in the Au@Pt core-shell spectra were similar to that of pure Au and Pt metals. This suggests that the bimetallic nanoparticles were not alloyed as there is binding energy shift for alloy nanoparticles. The atomic Pt/Au ratio at the surface of core shell Au@Pt nanoparticles were calculated using the XPS signals of Pt and Au. This was done by integrating the area under the intensity peaks of Pt_{4f7/2}, Pt_{4f5/2}, Au_{4f7/2} and Au_{4f5/2} of both metal and oxides and then applying the formula below:

$$C_M = [I_{M(4f)} / \lambda_M \sigma_M D_M] / \sum [I_{M(4f)} / \lambda_M \sigma_M D_M] \text{ where } M = \text{Pt, Au}$$

where, I_M is the integrated intensity of M(4f) spectra, λ_M is the mean escape depths of the respective photoelectrons, σ_M is the photoionization cross section, and D_M is the geometric factor. The photoionization cross section values were taken from Scofield, and mean escape depths were taken from Penn. The geometric factor was taken as 1, since the maximum intensity in this spectrometer is obtained at 90°. The ratio calculated by (Pt/Au)_{XPS} was always greater than (Pt/Au)_{Bulk solution} as shown in table 3. This proves surface segregation of platinum on gold. Thus the bimetallic nanoparticles are concluded to be core-shell structure.

Table 3: Surface Composition measurement through XPS intensity vs Bulk sample composition

(Pt/Au) _{Bulk solution}	(Pt/Au) _{XPS}	N _{Pt} per nm ² _{Au}
0.09	0.25	3
0.19	0.31	4
0.39	0.64	8
0.58	0.84	11
0.88	1.43	18

The surface Pt/Au ratio calculated by XPS was then used to calculate the number density of platinum atoms (N_{Pt}: number of Pt atoms per nm² of the Au surface) on gold nanoparticle surface. A total number of 13 platinum atoms can cover one square nm of spherical gold nanoparticle surface (assuming the area of a single Au atom as 7.87 * 10⁻² nm² ¹³). As observed in TEM image in figure 2a, the gold seed nanoparticles are spherical. Thus the total number of platinum atoms (N_{Pt}) covering one square nm of gold would be 13*(Pt/Au)_{XPS}. The N_{Pt} values in table 1 show that for (Pt/Au)_{bulk} ratio 0.09 and 0.19 core-shell nanoparticles, there are 3 and 4 platinum atoms per nm² of the Au surface respectively. This proves that the platinum atoms segregate as 2D-rafts or small cluster islands for quarter and half platinum layer coating on gold seed. For (Pt/Au)_{bulk} ratio 0.39 and 0.58, the N_{Pt} values were 8 and 11 which are very close to the value of 13, the theoretical number of platinum atoms required to make monolayer coverage on gold nanoparticle surface. This suggests that in this (Pt/Au)_{bulk} ratio 0.39 and 0.58 range, almost a layer of platinum atoms coat the spherical gold nanoparticles. Theoretically (Pt/Au)_{bulk} ratio of 0.39 and 0.58 corresponds to one layer and 1.5 layer of platinum atoms respectively covering gold seed.

Nanoporous Electrocatalyst Layers by Self-Assembly

Combining several built-in functionalities in a single nanoporous membrane helps to overcome the weaknesses and loss of efficiency associated with multiple materials involvement in a conventional design. One such novel application is the use of a multifunctional nanoporous membrane as a substitute for the catalyst layer in fuel cell assemblies.

There are several advantages to substituting the catalyst layer (typically 4-10 microns thick) with a nanoporous membrane. The catalyst layer is a paste of nafion (for proton conduction), platinum nanoparticles (for catalytic activity) and carbon particles (for conduction) usually hot-pressed onto the nafion proton-conducting membrane. The catalyst loading in fuel cell assemblies, which is typically about 0.2-0.4 mg per square centimeter of membrane area, adds significantly to cost. In contrast, a porous catalyst layer of thickness 10 nm has a catalyst loading of only about 0.94 micro gm per square centimeter of membrane area. An important limitation in fuel cells is the mass transfer limitations through the catalyst and gas diffusion layer, which significantly reduces the potential beyond a current density of about 0.5 A/cm². The mass transfer resistance for the transport of molecules through a catalytically active, nanoporous membrane will be significantly smaller than that in a 4-10 micron thick catalyst layer.

Several challenges have to be addressed to utilize such nanomembranes in a PEMFC. Apart from porosity, it is necessary to have two additional functionalities built in to the porous membrane, catalytic activity and electrical conductivity. The catalytic activity from a membrane with thickness 10 nanometers needs to be comparable to that in the current catalyst layers with loading 0.2-0.4 mg Pt per cm² geometric area. Simultaneously, it is also necessary to ensure low electrical resistance along the plane of the membrane, so that electrons can be efficiently transported from/to the external circuit. Here, we fabricate catalytically active and conducting nanoporous membranes of thickness 10 nanometers using a bottom-up approach from platinum-gold shell-core nanoparticles. This consists of four steps, the fabrication of monodisperse core-shell nanoparticles, and assembly of the nanoparticles into layers of hexagonally ordered arrays, the stacking of multiple layers to give three-dimensional structures, and the fusion of the nanoparticles in these structures to provide a self-supporting, conducting and porous membrane..

Most procedures for assembling nanoparticles into arrays use organic ligands as spacers, in order to generate a well-defined spacing between the particles reference. These arrays can be transferred onto substrates using PDMS stamps, and multiple layers can also be fabricated by repeated stamping reference. However, membranes fabricated in this fashion cannot be used for electrocatalytic applications for two reasons; firstly, the organic ligands increase the transport resistance for reactants/products to/from the catalyst surface, and secondly, the electrical resistivity of these layers (in the range of gigaohms) does not permit electron transport along the membrane. For this reason, it is necessary to remove the organic thiols, and to fuse the particles to form a continuous, porous, metallic membrane which is also free-standing.

Here, core shell Au@Pt nanoparticles were self assembled into hexagonally close packed, monolayers on water surface as reported by Santhanam et al. Bilayers were fabricated by transferring subsequent monolayers from the water surface to a polydimethylsiloxane (PDMS) stamp pad by the Langmuir-Schaefer (LS) technique. This bilayer was subsequently stamped on a solid substrate by microcontact printing. This solid substrate was either 10nm chromium and 50nm gold sputtered on insulated silicon dioxide (1 um thick)/silicon wafers which was used as working electrode to measure the bilayers electrocatalytic activity or electrical contact pads prepared by sputtering 7 nm chrome followed by 50nm gold on silicon dioxide (1 um thick)/silicon substrate. Across these electrical contact pads, sheet resistance of gold nanoparticle bilayer and trilayer was measured for different time of argon plasma treatment. The minimum resistance of gold nanoparticle bilayer was 2914 Ω /sq and trilayer was 82 Ω /sq. For pure gold nanoparticle bilayers the sheet resistance varied within 30% of its minimum sheet resistance with two variable electron conduction lengths of 92um and 200um which prove that there is negligible contact resistance between the bilayer and contact pad junctions. For gold nanoparticle trilayers sheet resistance was exactly same for channel widths of 92 um and 200 um. All CV curves were recorded in N₂-saturated 0.5M H₂SO₄ from 0V to 1.244V (vs RHE). The nanoparticle bilayer was then exposed to 100W argon plasma at room temperature for various durations. For plasma exposures of 60s duration, the hexagonal packing was not disturbed as observed in SEM. There was reduction of sheet resistance to 3.7 G Ω /sq and signs of electrocatalytic activity of the bilayer. The bilayer was subsequently treated to different time of argon plasma exposure. From 240s to 960s time range the core-shell nanoparticles coalesced to increasing extent with their nearest neighbors in the adjacent layer as shown in SEM and by schematic. In this time window, the electrocatalytic activity of the bilayer reaches its maxima and sheet resistance decreases to 9.84 k Ω /sq. From 960s to 1920s time frame the bilayer transforms into laterally fused, continuous, nanoporous metallic sheet as shown in SEM. The electrocatalytic activity of the bilayer reduces (shown by CV in figure 1h) and sheet resistance decreases further to minima of 3.6 k Ω /sq. Above 1920s the bilayer breaks up into segregated islands shown in SEM. The electrocatalytic activity of the bilayer reduces further and sheet resistance start increasing slowly to a value of 4.7 k Ω /sq at 2400s. The gold oxide reduction peak was shifted to a lower potential of 0.97V vs SHE and platinum oxide reduction peak was also shifted to a lower potential of 0.45V vs SHE. This suggests that the surface is nanoporous which results in this negative shift. Another feature of nanoporosity is the high charging current leading to broad double layer region. This arises due to the high surface area of the nanoporous membrane.

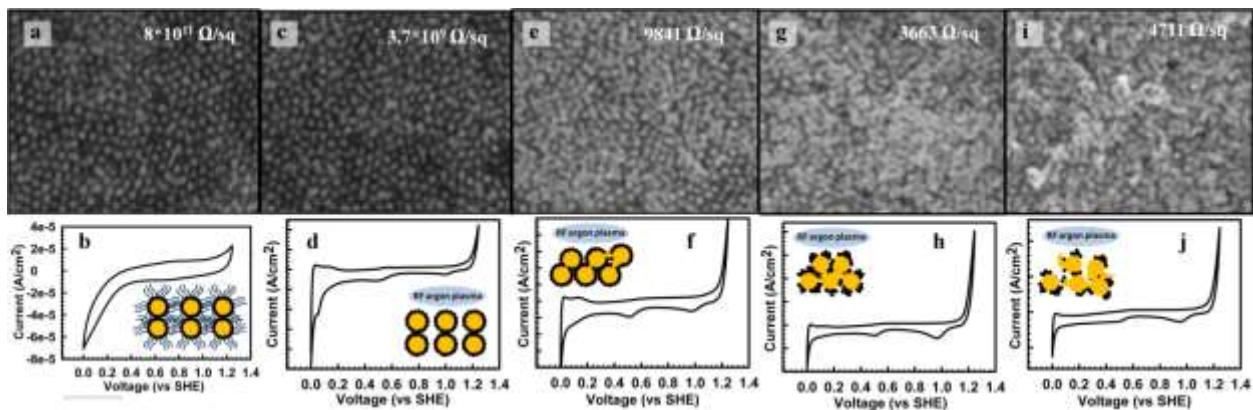


Figure 6: SEM images and corresponding CVs (with schematics in inset) at different time intervals of argon plasma exposure on a bilayer of core shell Au@Pt nanoparticles (Pt/Au 1/2.56) are shown in figures (a,b) 0s, (c,d) 60s, (e,f) 960s, (g,h) 1500s, (i,j) 2400s.

Hexagonally close packed 2D-bilayers were subsequently prepared with pure platinum nanoparticle and different Pt/Au ratio core shell nanoparticle building blocks with theoretical half monolayer of platinum atoms on gold core (1/5.26), one monolayer of platinum atoms on gold core (1/2.56), one and half monolayer of platinum atoms on gold core (1/1.72), and two monolayers of platinum atoms on gold core (1/1.13) respectively. Figure 7b shows the relationship between electrochemical active areas (ECSAs) versus time of argon plasma exposure for these nanoparticle bilayers at different Pt/Au ratios. The theoretical platinum loading calculated for the different Pt/Au ratio bilayers were $0.47 \mu\text{g}/\text{cm}^2$ (Pt/Au 1:5.26), $0.94 \mu\text{g}/\text{cm}^2$ (Pt/Au 1:2.56), $1.39 \mu\text{g}/\text{cm}^2$ (Pt/Au 1:1.72), $2.11 \mu\text{g}/\text{cm}^2$ (Pt/Au 1:1.13), and $5.92 \mu\text{g}/\text{cm}^2$ (Pt/Au 1:0). Bilayer with Pt/Au ratio 1/5.26 reaches maximum catalytic activity at 480s of plasma exposure to $31.7 \text{ m}^2/\text{gm}$. For Pt/Au ratio with lower platinum content the catalytic activity is negligible. Bilayer with Pt/Au ratio 1/2.56, 1/1.72, and 1/1.13 reaches maximum catalytic activity at plasma exposure of 480s, 1500s, and 960s respectively to $106.3 \text{ m}^2/\text{gm}$, $89 \text{ m}^2/\text{gm}$, and $86.3 \text{ m}^2/\text{gm}$. This lead to the conclusion that most catalytically efficient bilayers are those whose building units comprise of one monolayer of platinum covering 5nm gold nanoparticle. For bilayers with Pt/Au ratio 1/2.56, 1/1.72, 1/1.13 and 1/0, there were two independent maxima observed in the ECSA curve which were the lower maxima (one which sets at lower time interval) and higher maxima (one which sets at higher time interval). Figure 7c shows the relationship between sheet resistances versus time of argon plasma exposure for these nanoparticle bilayers at different Pt/Au ratios. Figure 7d shows the HRTEM image of the fused bilayer and it has through holes of magnitude $2\text{nm} - 7\text{nm}$ laterally.

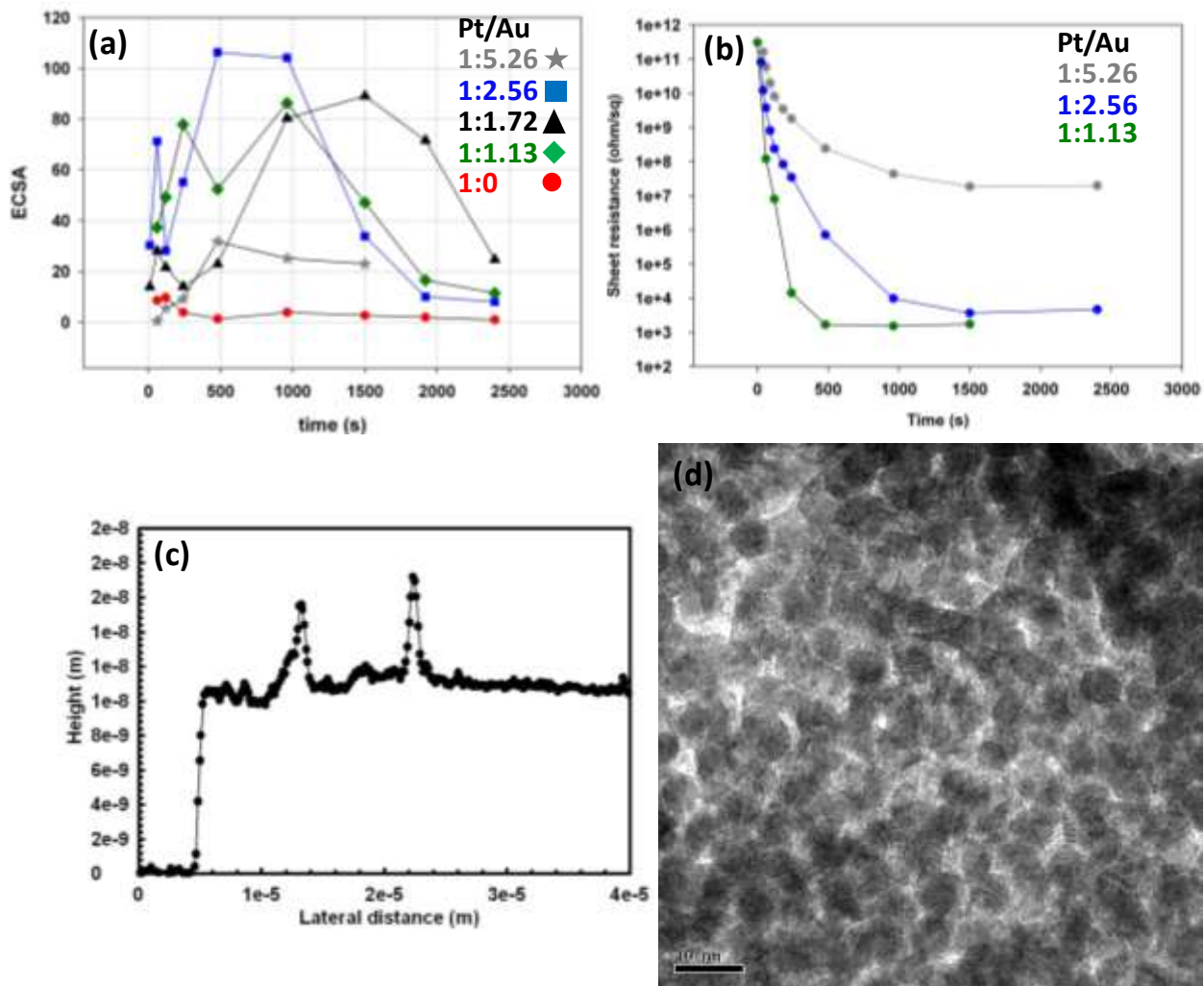


Figure 7: (a) Electrochemical surface area (ECSA) of different Pt/Au ratio core-shell nanoparticles bilayer for different time of argon plasma exposure (b) Sheet resistance of self assembled nanoparticle bilayers at different time of argon plasma exposure for variable Pt/Au ratio core-shell nanoparticle building blocks. The AFM height (c) and HRTEM image (d) of the completely fused nanoparticle bilayer.

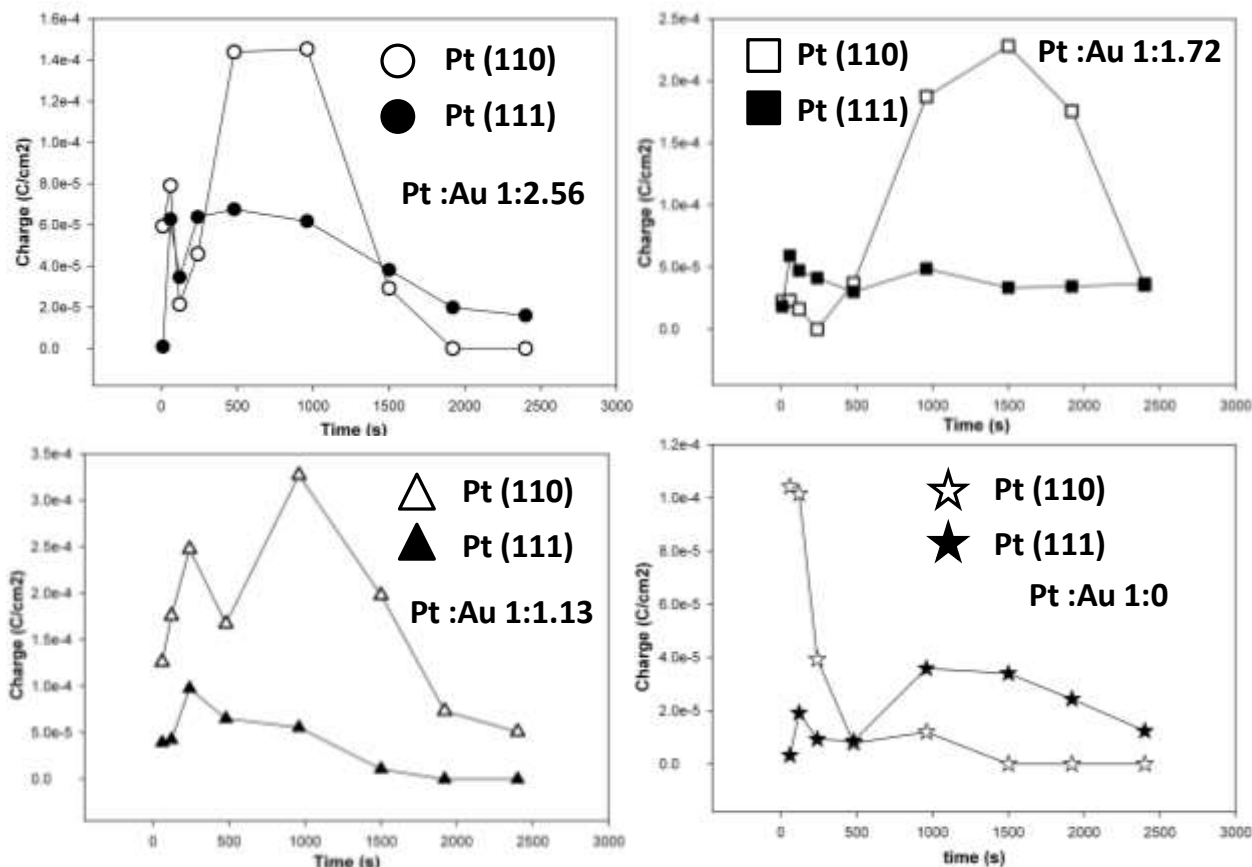


Figure 8: Charge under the hydrogen desorption region and different time of argon plasma exposure for Pt/Au ratios (a) 1/2.56, (b) 1/1.72, (c) 1/1.13 and (d) 1/0.

The cyclic voltammogram features two distinct peaks at 0.05V and 0.15V vs. SHE in hydrogen desorption region for nanoparticle bilayers with Pt/Au ratio 1/2.56, 1/1.72, 1/1.13 and 1/0 and one distinct peak at 0.05V vs. SHE with Pt/Au ratio 1/5.26. The peak at 0.05V vs. SHE signify formation of Pt(111) facet and peak at 0.15V vs. SHE signify formation of Pt(110) facets on core gold nanoparticle. Figure 8 (a-d) shows charge associated with hydrogen desorption (oxidation) on Pt(111) and Pt(110) facets for varying Pt/Au ratio nanoparticle bilayers across different time of argon plasma exposure. The Pt(110) facet has highest exchange current density of $0.65 \times 10^{-3} \text{ A/cm}^2$ and Pt(111) has an exchange current density of $0.21 \times 10^{-3} \text{ A/cm}^2$. So the hydrogen oxidation reaction (HOR) is most efficient when a large number of Pt(110) facets exist. Core shell nanoparticle bilayer structure has minimal platinum loading of $0.94 \mu\text{g}_{\text{Pt}}/\text{cm}^2$ (for Pt/Au 1/2.56), $1.39 \mu\text{g}_{\text{Pt}}/\text{cm}^2$ (for Pt/Au 1/1.72), $2.11 \mu\text{g}_{\text{Pt}}/\text{cm}^2$ (for Pt/Au 1/1.13) which is expended to create Pt(110) and Pt(111) facets amongst which Pt(110) facets proliferate with increasing time of argon plasma exposure. Contrarily for a pure platinum nanoparticle bilayer with high platinum loading of $5.92 \mu\text{g}_{\text{Pt}}/\text{cm}^2$ (Pt/Au 1/0), although initially both Pt(110) and Pt(111) facets are present but at large time scale of argon plasma exposure it is only the Pt(111) facets which remain stable and Pt(110) facets are completely diminished. Thus core shell Au@Pt nanoparticle bilayers are more electrocatalytically active than pure platinum nanoparticle bilayers with increasing time of argon plasma exposure.

For nanoparticle bilayers with Pt/Au ratio 1/5.26 the peak at 0.15V vs. SHE is completely absent. For this reason they have low electrocatalytic activity as compared to others. With Pt/Au ratio 1/2.56 and 1/1.72, at 2400s of argon plasma exposure the peak at 0.05V vs SHE is most prominent and peak at 0.15V vs SHE is partially visible to being absent. With Pt/Au ratio 1/1.13, the peak at 0.05V vs. SHE is absent at lower argon plasma exposures and appears as a hint at larger intervals when the platinum shell atoms undergo surface restructuring prior to imminent nanoparticle bilayer fusion. At 2400s of argon plasma exposure the peak at 0.15V vs SHE is most prominent and peak at 0.05V vs SHE is partially visible. For pure platinum nanoparticle bilayers, both peaks at 0.05V and 0.15V vs. SHE are present at first maxima signifying dominant presence of Pt(110) and Pt(111) facets. However as the bilayer fuse the peak at 0.15V vs. SHE slowly disappears signifying loss of Pt(110) facets. At 2400s of argon plasma exposure the peak at 0.15V vs SHE is absent and peak at 0.05V vs SHE is only visible.

Thus evolution of Pt(110) and Pt(111) facets in the bilayer give rise to the lower and higher electrochemically active states at lower and higher times of argon plasma exposure of the core-shell Au@Pt nanoparticle bilayer. The peak at 0.15V vs. SHE becomes distinct as the core-shell Au@Pt bilayer proceeds from primary to secondary ECSA maxima and then

slowly disappears post observation of the secondary ECSA maxima signifying that Pt(110) facets are disappearing. The formation of Pt(110) facets can be explained by restructuring of the platinum shell atoms. After very long plasma exposures, the underlying gold covers the platinum facets. For pure platinum nanoparticle bilayer from 0s to 1000s there is no gold oxide reduction peak observed and it proves the fact that the bilayer has not disintegrated. Post 1000s there is disintegration of the platinum nanoparticle bilayer and exposure of the gold base below which gives rise to the gold oxide reduction charge. For Au@Pt core-shell nanoparticle bilayer with Pt/Au ratio 1/5.26, 1/2.56, and 1/1.72 they show gold oxide reduction charge at 0-500s plasma exposure. This is because their surface is not fully covered with platinum atoms which form 2D rafts and clusters on gold nanoparticle surface. For Pt/Au ratio 1/1.13, there is no gold reduction signal from 0-1500s which first signifies that these nanoparticles are fully covered platinum atoms on gold and that these bilayer membranes are stable and did not fragment till 1500s of plasma exposure. For Pt/Au ratio 1/1.72, there is initial signal of gold reduction but it reduces to 0 from 500s-1500s because here the nanoparticles bilayer gets laterally coalesced into planar 2D-structure. In that way the exposed gold atoms are overshadowed by restructured platinum atoms. Above 1500s base substrate gold becomes partially exposed to plasma as the membrane starts to disintegrate negligibly till 2400s. For Pt/Au ratio 1/5.26 and 1/2.56, there is a lot of exposed gold in the core-shell nanoparticle bilayer. Hence the gold oxide reduction charge shows monotonic increase in magnitude.

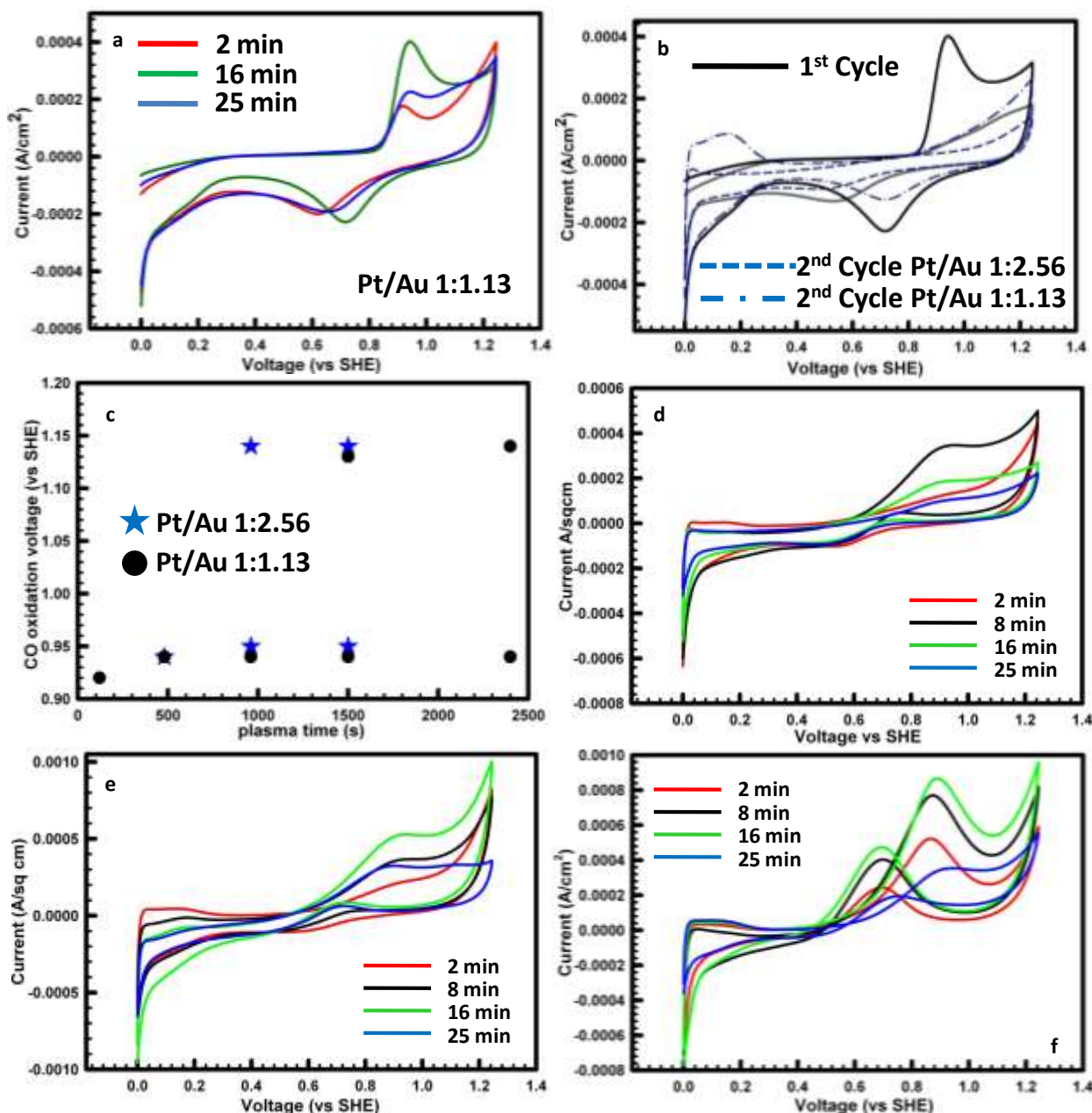


Figure 9: CO oxidation and methanol oxidation.

Figure 9a shows electrooxidation of irreversibly adsorbed CO monolayer on Pt/Au 1:1.13 bilayer exposed to 2min, 16min and 25min of argon plasma. The CO adlayer was formed by purging CO gas in 0.5M H₂SO₄ solution holding the working electrode at 0.064V vs RHE for 10 min. Then the acidic solution was purged with nitrogen for 10min to remove excess CO molecules dissolved. CO stripping voltammograms were collected in range 0V to 1.244V vs SHE. Figure 4a shows CO oxidation potential peak of Pt/Au 1/1.13 bilayer varying with 120s, 960s and 1500s of argon plasma exposure to 0.94V, 0.96V and two separate peaks at 0.96V and 1.15V vs SHE respectively. Thus the singular CO oxidation peak shifts to positive potential with higher time of argon plasma exposure and after an optimum exposure time a secondary new peak appears at 1.15V vs SHE along with primary peak at 0.94V-0.94V vs SHE. Figure 9c plots the CO oxidation peak potential of Pt/Au 1/2.56 and 1/1.13 bilayer for different time of argon plasma exposure. Initially both bilayers on being treated to low time scale of argon plasma yield CO oxidation at peak potential of 0.94V-0.96V vs SHE. Then at higher time of argon plasma exposure, CO oxidation has a primary peak and a secondary peak at 0.94V-0.96V vs SHE and 1.15V vs SHE respectively. The onset of secondary CO oxidation peak at 1.15V vs SHE appears earlier for Pt/Au 1/2.56 bilayer. Rincon. et al. report CO oxidation potential for varying platinum thickness on gold nanoparticles. They report that for 3ML-10ML of platinum atoms on gold nanoparticle, there were two CO oxidation peaks, one at 0.75V and other at 1V vs SHE. For 1ML-2ML of platinum atoms on gold nanoparticle, a single broad peak at 1V vs SHE was observed. Thus with decreasing platinum thickness the magnitude of peak at 0.75V vs SHE reduces and onset of a secondary peak at 1V vs SHE was observed. Comparing with their report it can be concluded that with increasing time of exposure to argon plasma, there is thinning down of the platinum shell thickness coating gold nanoparticles in the bilayer. This phenomenon can be corroborated by the SEM image morphology where the surface topology changes from spherical nanoparticles bilayer to laterally coalesced, planar 2D-structure where atomic mass is transported from the outer circumference of spherical shaped metal nanoparticles to give rise to the horizontally connected structures. Figure 4b shows that in the first scan the cyclic voltammogram show complete absence of hydrogen adsorption-desorption features from 0V to 0.4V vs SHE due to chemisorbed CO on its active sites. CO oxidation occurs in the first scan without any trace of CO left in the second scan and complete recovery of active platinum sites. Figures 9d,e and f represent methanol oxidation profiles of bilayers prepared with Pt/Au ratio 1/2.56, 1/1.72 and 1/1.13 respectively for different time of argon plasma exposure. CVs were measured in a solution mixture consisting of 0.5M H₂SO₄ and 2M CH₃OH. Figure 4d shows the methanol oxidation reduction reaction occurring on Pt/Au ratio 1/2.56 bilayer for 2min, 8min, 16min and 25min. The methanol oxidation reduction peaks at 2min is negligible, achieves maxima at 8min and decreases again on subsequent treatments at 16min and 25min. The geometric area normalized activity of Pt/Au ratio 1/2.56 bilayer (figure 4d), as reported by the peak current density in the forward scan, is 0.13 (2min), 0.34 (8min), 0.19 (16min) and 0.10 mA/cm²(25min) for varying plasma treatment time of the bilayer. The geometric area normalized activity of Pt/Au ratio 1/1.72 bilayer (figure 4e), as reported by the peak current density in the forward scan, is 0.23 (2min), 0.36 (8min), 0.53 (16min) and 0.31 mA/cm²(25min) for varying plasma treatment time of the bilayer. The geometric area normalized activity of Pt/Au ratio 1/1.13 bilayer (figure 4f), as reported by the peak current density in the forward scan, is 0.51 (2min), 0.76 (8min), 0.87 (16min) and 0.35 mA/cm²(25min) for varying plasma treatment time of the bilayer. Du et al reported that an optimum number of neighbouring platinum atoms are required for methanol oxidation. For the bilayers with 2 min argon plasma treatment there happens to be a dearth of such efficient group of platinum atoms and thus they have low magnitude of methanol oxidation current. All the bilayers have maximum magnitude of methanol oxidation current in the time range of argon plasma exposure where their ECSAs are at the higher maxima. In the forward scan of methanol oxidation the CH₃OH adsorbs to active platinum sites to give rise to several intermediates like PtCH₂OH, Pt₂CHOH and Pt₃COH species which get oxidized combining with Pt-OHads. Among these intermediate species some rearrange to form PtCO which is a poisonous carbonaceous species. In the reverse scan of the reaction these poisonous carbonaceous species are removed. The ratio of the forward anodic peak current (I_f) to reverse anodic peak current (I_b), I_f/I_b, can be used to evaluate the bilayer's tolerance to carbonaceous species accumulation. If the value is greater than 1, then the catalyst layer has high conversion efficiency of methanol to CO₂ and has low amount of accumulated carbonaceous groups. In the above cases the I_f/I_b ratio are 6.8(Pt/Au 1/2.56), 6(Pt/Au 1/1.72), and 1.85(Pt/Au 1/1.13) respectively making them efficient and highly selective catalyst bilayer membranes.

In summary we have proposed a novel method for synthesis and fabrication of membranes with significant electrocatalytic activity, in-plane conductivity and porosity for use as nanoporous catalyst layers in PEMFCs.

9.6 Nanostructured films on paper using inkjet printing for low-cost sensing/diagnostic applications:-

Paper is an inexpensive and easily available material that is rapidly emerging as a substrate of choice for the fabrication of disposable electronic circuits and point-of-care diagnostic devices. Batteries, field-effect Transistors, RFID antennas, sensors, and solar cells have been fabricated on paper, wherein paper functions primarily as a mechanical support and sometimes as an active part of a device. Significant efforts are underway, in the field of paper electronics, to develop additive manufacturing techniques in order to reduce material consumption and lower costs. Digital inkjet printing is a widely available technological platform that allows complete flexibility during pattern designing while also being compatible with the use of paper, attributes that can promote rapid penetration of lab-scale innovations in the developing world.

The development of flexible and portable electronic circuits in a cost-effective manner relies on the fabrication of conductive films in desired patterns. In particular, there is a need to develop fabrication processes that are compatible with roll-to-roll processing, to facilitate large-scale manufacturing of RFID based tags/sensors for diagnostic devices and for 'ubiquitous' sensor networks. The use of paper as a low-cost and 'green' alternative to flexible polymer substrates for fabricating electronic circuits has been actively pursued for the last two decades. Conductive patterns on paper-based substrates have been fabricated using techniques such as physical vapor deposition, chemical modification, rod coating, screen printing, spray painting etc. However, all these techniques require an additional subtractive process to remove unwanted material and form desired patterns.

The use of inkjet printing, an additive technique, for fabricating conductive patterns is actively pursued, especially to meet the requirements of low-cost, high-volume applications such as RFID tags, as it offers the added advantage of being compatible with roll-to-roll processing. Using nanoparticle-based ink solutions necessitates tedious and expensive processing during nanoparticle ink formulation to ensure ink-stability during storage, and also require subsequent thermal or chemical annealing steps to eliminate organic components and become conductive. The need for such complicated processing renders inkjet printing of nanoparticle inks unsuitable for cost-effective production of conductive patterns on paper. Alternatively, the use of reactive inkjet printing technique, wherein precursor solutions are sequentially printed and react in situ on a substrate to form nanoparticles, can help overcome issues with ink formulation; thereby, paving the way towards low-cost applications. However, conductive features can only be formed after several hundred repetitive cycles of printing precursor solutions and intermittent drying, hindering its adaptation as a large-scale manufacturing process. To overcome the requirement for sintering of nanoparticle inks, conductive features have been fabricated on plastic substrates using a combination of inkjet deposition of nanoparticle inks and electroless deposition; wherein, the nanoparticles act as catalytic sites for electroless deposition. However, material and capital costs, associated with nanoparticle ink formulation and use of specialty printers, are still prohibitive for development of ubiquitous sensors or low-cost diagnostics. A simpler approach of forming catalyst patterns for electroless deposition by using a desktop printer to deposit palladium salt solution and then dipping the substrate in a bath of reducing agent to form palladium nanoparticles was reported earlier. However, challenges related to material costs, precursor stability, hazardous nature of the reducing agent used, and losses due to detachment of colloidal particles during reduction have to be overcome for using such an approach to fabricate low-cost, paper-based circuits. To surmount this barrier, we formed silver nanoparticles by reactive inkjet printing of stable and non-hazardous reagents, used them as catalysts for electroless deposition of conductive and thick copper films on paper, and further demonstrated their utility as RF antennas. This communication describes the rapid, in situ formation and characterization of silver nanoparticles on paper at room temperature using stable, non-hazardous reagents, and their subsequent development into conductive copper films using an electroless plating process. The results of characterization of RF antennas fabricated on paper and their performance comparison with similar antenna designs on a copper-clad Kapton® substrate, fabricated using conventional lithographic processes, are presented next. To our knowledge, this is the first successful demonstration of the use of an office Inkjet printer to fabricate paper-based RF antennas.

MATERIALS AND METHODS

All the chemicals used were of analytical grade or higher, and used as received. DeIonised (DI) water, from a MilliPore MilliQ system, was used to prepare the required solutions. Printer and black cartridges were procured from an hP retail outlet in Bangalore, India.

Fabrication of conductive copper patterns

An inkjet printer (hP deskjet 1000 J 110 series, Rs 1,100/-), using thermal inkjet technology, and black cartridges (hP 802) were used in these experiments. After prying open the lids of the cartridges, the ink and sponge used for ink storage were removed, and the cartridges were thoroughly rinsed with tap water. The cartridges were then used to print 'black' pages using DI water and isopropanol a few times to flush ink solution out of the channels and aid in drying of the channels within the cartridges, respectively. Printing was carried out in grayscale mode using a resolution of 600 dpi x 600 dpi. The amount of water deposited varied from 4 to 5 $\mu\text{L}/\text{cm}^2$ per print. As a precaution, all precursor solutions were printed

three times to overcome non-uniformities in spatial deposition. Overall, a line resolution of 0.3 mm and positioning accuracy < 0.5 mm, for manual duplex printing, could be routinely achieved using this printer.

Silver nanoparticles were formed on paper (A4 size commercial printer paper, 80 g/m²) by sequential printing of silver nitrate (470 mM solution, metal precursor) and tannic acid (25 mM solution, reducing agent) from two separate cartridges, to avoid inadvertent contact within a cartridge. The pH of the tannic acid solution was adjusted to 10, just prior to printing. The process conditions are based on a rapid, room temperature synthesis protocol that was developed earlier in our group using tannic acid, an environmentally-benign reagent derived from plants. The desired patterns were created and saved as .pdf files with appropriate resolution and printed from a standard computer. The amount of silver deposited was ~ 0.7 mg/cm² of printed area. The silver nitrate printed paper was allowed to dry under ambient conditions and then manually placed in the feed tray before printing tannic acid solution. The formation of silver nanoparticles was evident as the paper reached the output tray of the printer. The same process could be repeated to form silver nanoparticles on both sides of the paper.

Copper films were formed on paper using the silver nanoparticles as catalyst for electroless deposition. A standard recipe [20] was modified to increase the rate of deposition. Briefly, the printed paper was placed in a plastic tray and immersed in 60 mL of copper plating solution containing CuSO₄·5H₂O (3 g), Ethylenediaminetetraacetic acid (EDTA, 6.5 g), NaOH (4.2 g), formaldehyde (2 mL) and Potassium ferrocyanide (K₄Fe(CN)₆·3H₂O, 2.5 mg). The pH of the electroless plating solution was maintained between 12.5 to 13. Potassium ferrocyanide acts as a stabilizer preventing formation of copper oxide as the reaction begins, but it also lowers the deposition rate. The reported recipe was modified to avoid blistering and increase the rate of deposition, by adding 0.5 mL of formaldehyde to the plating solution at a regular interval of 2 minutes. For the samples reported here, the plating solution was maintained at 60° C for 8 minutes and then the paper was rinsed in DI water and dried. These conditions were determined to be optimal for forming copper films, which remained conductive even after prolonged exposure to ambient conditions. Further increase in plating rates by adding more formaldehyde led to fragile powdery deposits, which were easily dusted off and rendered the patterns non-conductive. Copper-clad Kapton® films were coated with a photoresist film that was patterned using photolithography. The exposed copper film was then etched away and the photoresist stripped off to form the flexible antennas needed for performance comparison.

Characterization Techniques

Field Emission Scanning Electron Microscope (Ultra 55, Zeiss GmbH) operated at 2 kV was used for structural and morphological characterization of the samples on paper. An optical profilometer (Zeta 20, True color 3D) was also used to measure the thickness of the copper film deposited on paper fiber. X-Ray Diffraction (XRD) spectra were recorded using a Siemens Diffractometer (AXS D5005, Cu source). X-ray Photoelectron Spectroscopy (XPS) spectra were recorded using a Thermo Scientific Multilab-2000 instrument with Al-K α (energy of 1486.6 eV) as the X-ray radiation source. The antenna performance was characterized using a vector network analyzer from Agilent (2-port PNA-N5320A).

Ultra Wide Band (UWB) Antenna Design

The design of the dual monopole RF antenna was adapted from Wang and Huang. Since substrates used were thin and have relatively similar values of dielectric constants (Kapton® substrate: $\epsilon_r = 3.85$, (loss tangent) ' $\tan \delta$ ' ≤ 0.004 , thickness = 1.1 mm; b) Paper substrate: $\epsilon_r = 3.2$, $\tan \delta = 0.07717$ [23], thickness = 1.2 mm), antenna design parameters were first optimized for paper based on simulations carried out using CST microwave studio®, and used in both cases. The dimensions and the layout of the UWB antenna used for printing are shown in Figure 6.1.

RESULTS AND DISCUSSIONS

Figure 6.2 shows digital photographs of the UWB antennas fabricated on paper using the proposed process and on Kapton® using conventional lithographic processing. To ensure good mechanical and electrical contact between the RF connector and the printed antenna structure, the patterns corresponding to the two sides were printed on different areas of a sheet of paper; after copper deposition the two patterns were cut and glued onto opposite sides of a cardboard support (1 mm thick). Similarly, two sheets of Kapton were pasted onto another cardboard. The photograph clearly shows that copper film is deposited only on the areas defined during inkjet printing of the silver nanoparticle precursor solutions. Also, the electrodeposited film has a rough microstructure (vide infra) and appears black, while the commercially available copper cladding has a lustrous sheen. The copper patterns deposited on the paper substrate are robust and adhere well even after being flexed or rubbed using fingers.

Structural Characterization

Microscopic (FESEM) and spectroscopic characterization (XPS, XRD) of a paper-based sample after reactive inkjet printing, and after electroless plating confirmed the reduction of silver salt in situ on paper to form silver nanoparticles, and the formation of uniform copper plating over the paper-fibers, respectively (Fig. 6.3). XPS, being a surface-sensitive technique with a penetration depth of ~10 nm, indicated that 30% of copper was in oxidized state after exposure to air. XRD, with a penetration depth of ~0.2 μm , also showed the presence of copper oxide phases, but the extent was only 5% suggesting that oxide phases were formed mainly at the exposed surface. XRD measurements on the silver

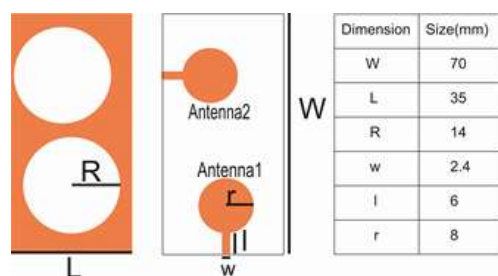


Fig. 6.1. Design layout of the fabricated antenna structures along with antenna dimensions.

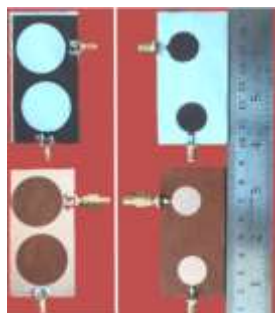


Fig. 6.2. Digital photographs of the two sides of UWB antennas fabricated on paper (top) by using reactive inkjet printing and electroless deposition, and on Kapton® (bottom) by using lithographic processes. The electrodeposited copper has a much rougher microstructure and appears black in color, while the copper cladding on Kapton® has a lustrous metallic sheen.

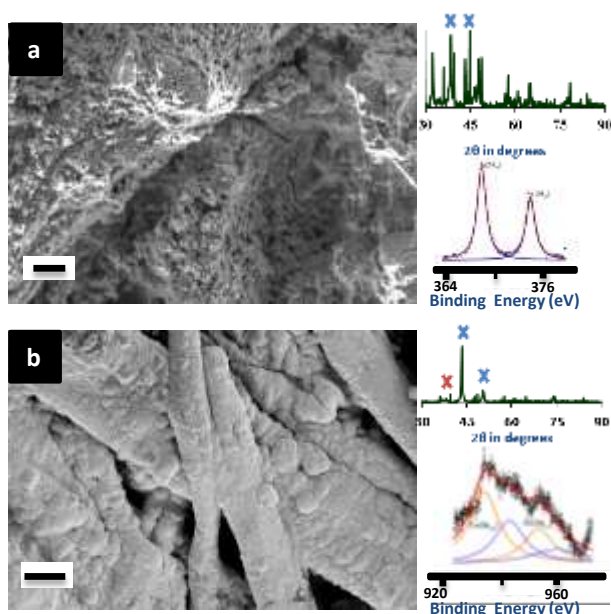


Fig. 6.3. Structural characterization of paper samples. (a) after silver nanoparticle formation– FESEM image shows that silver nanoparticles are uniformly distributed over the fibers along with some organic matrix (presumed to be excess tannic acid). Scale bar corresponds to 1 μm . XPS analysis (bottom-right in (a)) shows the presence of silver in reduced form only and XRD (top-right in (a)) further confirms the presence of metallic silver. Peaks corresponding to FCC (111) and (200) planes of silver are marked with a blue 'x'. (b) after copper plating– FESEM image shows that all fibers are uniformly coated with copper and that copper film is interconnected at the microscopic scale. Scale bar corresponds to 10 μm . XPS analysis (bottom-right in (b)) shows the presence of copper in oxidized form along with reduced copper. XRD (top-right in (b)) confirms the presence of both copper ((111) and (200) planes-blue 'x') and copper oxide (red 'x') phases.

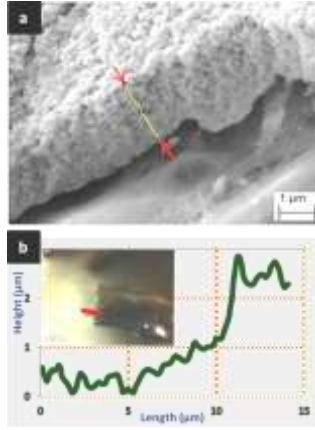


Fig. 6.4. Thickness of electrodeposited copper film. (a) Cross-section FESEM image shows that copper nanoparticles have aggregated to form the film. The thickness of the film was estimated to be 1.8 μm . (b) Height profile, using an optical profilometer, along a paper-fiber and across the edge of the copper film (corresponding to the red line in the inset). The average thickness estimated from this profile corresponds well with FESEM measurements.

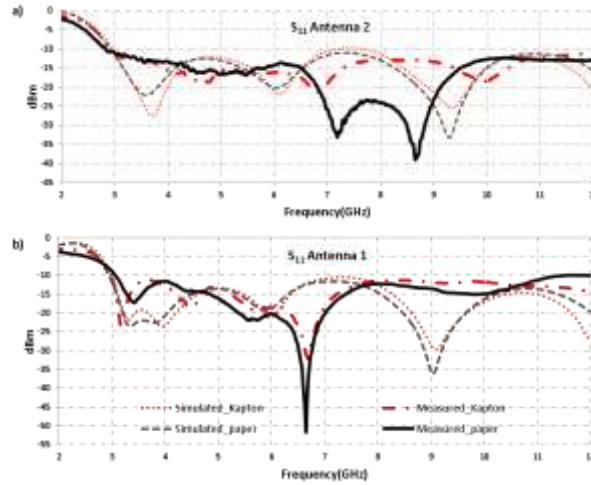


Fig. 6.5. Measured transfer characteristics (S_{11}) of fabricated antennas. (a) Antenna 2, (b) Antenna 1. The -10 dB bandwidth of both antennas on paper span from 3 GHz to 11 GHz, covering the entire UWB spectrum. The performance of paper and Kapton® based antennas are comparable.

nanoparticle film also indicate the presence of other metal-organic complexes, presumably silver atoms dispersed in a matrix of tannic acid residues. The presence of cracks in FESEM images of silver nanoparticle coated paper is also suggestive of the formation of such complexes.

The thickness of the deposited copper film was estimated to be 1.8 μm based on cross-sectional FESEM images, and this estimate was further corroborated by optical profilometer measurements (Fig. 6.4). The cross-sectional FESEM image shows that the electroless film is composed of nanoparticles, which are uniformly spread over the depth of the film. Together, the results of structural characterization clearly demonstrate that silver nanoparticles formed in situ using an office inkjet printer catalyzed the formation, by electroless plating, of copper films on paper.

Electrical Characterization

The sheet resistance of the copper film deposited on paper was measured to be 9 Ω/\square using four-point probe measurements. This corresponds to a resistivity of $4.5 \times 10^{-5} \Omega\text{m}$, considering paper to have 70% porosity. This resistivity estimate is $\sim 1\%$ of typical values reported, and reflects the absence of a thermal annealing step to sinter the deposited copper nanoparticles. The transfer characteristics (S_{11}) of the two antennas in the design were measured and compared with simulations for both paper-based antennas as well as those fabricated on a Kapton® substrate (Fig. 6.5). The measured and simulated characteristics are similar for both substrates, deviations are attributable to contact impedance variations. The performance of paper-based antennas was comparable to that of antennas fabricated on a Kapton® substrate; thereby, demonstrating the capability of fabricating low-cost RFID tags using an office inkjet printer.

SUMMARY

Silver nanoparticles were formed in situ on paper using a simple office inkjet printer. Electroless plating of copper on these silver nanoparticles was used to fabricate conductive copper patterns on paper. The performance of UWB antennas fabricated using the proposed process was found to be equivalent to that of similar antennas fabricated using conventional lithographic processes. These results are promising for low-cost, high-volume manufacturing of RFID tags, as both inkjet printing and electroless plating are both amenable for roll-to-roll processing. The simplicity of using an office inkjet printer for defining conductive patterns should enable the advent of flexible, low-cost devices for applications in diverse areas, such as biomedical diagnostics, flexible electronics, ubiquitous sensing platforms etc.

In Situ Silver nanowire Formation

Conductive layers, either as interconnects or active elements, are an integral part of all electrical and electronic circuits. As such, there is significant research on printing conductors using different materials. Amongst them, silver has emerged as the material of choice since it is the best conductor that is also stable under normal operating conditions. Functional inks for printing silver can be classified into three main categories, namely organometallic inks, complexed silver-salt based ink formulations, and nanoparticle based inks. Organometallic inks form silver on the substrate by decomposition of the deposited ink upon heating. The considerable energy input required to decompose organometallic inks limits their usefulness for paper based applications. Ink formulations containing silver salts in complexed form along with appropriate reducing agents can form overlapping silver nanostructures in situ upon drying. Such inks can be used for either printing or ‘writing’. The high conductivities, equivalent to that of bulk silver, achieved using such inks are promising for various applications; however, the tedious processing and short shelf-life of these inks limit their suitability for low-cost applications. Silver nanoparticle inks are the most widely prevalent form of conductive inks that are also commercially available. Curing of these inks to form conductive traces by chemical or physical processing is a crucial step in obtaining conductive traces. Significant efforts have been undertaken to develop rapid curing techniques; recently, desktop printing compatible ink-substrate packs have become available. Despite such efforts, the technologically-intensive processing required to formulate these inks and the smooth substrates required remain prohibitively expensive for widespread adaptation.

During a preliminary search for a simple, low-cost process to form conductive patterns on paper using reactive inkjet printing, we realized that a key step for success would be the ability to avoid leaving by-products of the metallization reaction as a solid residue within the film. Photographic processing is one such metallization scheme that relies on forming silver halide layers on a substrate, exposing silver halides to light to form a latent image, followed by ‘development’ in an appropriate chemical bath to amplify the latent image. ‘Salt Printing’ is a silver-based photographic process that relies on *in situ* formation of silver halide layers on paper and is the precursor of the modern photographic-film based process. Therefore, we hypothesized that overexposing densely-packed silver halide layers formed *in situ* on paper using a desktop printer, followed by development could be a simple solution for forming patterned and conductive silver layers on paper while also avoiding unwanted residues. To test this hypothesis, we used an office inkjet printer for defining patterns of silver halide layers on paper by sequentially printing aqueous solutions of potassium halide and silver nitrate. After sufficient light exposure and development, we discovered that dense percolating networks of silver nanowires were formed on paper and that conductive layers with sheet resistances of the order of a few Ω/\square could be easily obtained using this method. In this communication, we report the results of structural characterization of the silver

nanowire networks formed on paper using such a 'print-expose-develop' process, posit a plausible mechanism for the formation of inter-connected silver nanowires, and demonstrate the percolating nature of the conductive films formed on paper. Recently, formation of conductive films on smooth polymer or paper substrates starting with silver nanowire containing pastes/inks have been reported³¹⁻³²; while, silver grains generated within photographic film after light exposure and development have also been used as seeds to form metallic structures. However, for the first time, *in situ* formation of conductive silver nanowire networks on paper is reported herein.

Materials and Methods

Materials used- DI water was used to prepare all the solutions. All chemicals used were of analytical grade or higher purity. The molar ratio of KX to AgNO₃ printed was 2:1, to ensure complete conversion to AgX on the paper. For the results reported here, a Bromide: Iodide = 95:5 %w composition was used as the halide (X) source, as addition of Iodide ions enhances photosensitivity²⁹. Typically, 3.3 M KX and 1.67 M AgNO₃ solutions (corresponding to a silver nitrate loading of 1.04 mg/cm² after three prints) were used to prepare the samples reported in this paper, except for figure 3 in which the AgNO₃ concentration was varied from 0.167 M to 1.67 M while KX values were varied from 0.33 to 3.3 M, correspondingly. The developer solution was prepared according to a standard recipe for making D-76. Briefly, 100 g of sodium sulphite was dissolved in hot water (50 °C) and then 2 g of Metol (monomethyl-p-aminophenol hemisulfate) along with 5 g of hydroquinone were added and mixed thoroughly. To this solution, 2 g of Borax was added. Finally, cold water was added to make the solution volume 1000 mL. The pH of the D-76 developer was found to be 8.5 (Note – Use of ascorbic acid also led to the formation of nanowire films, but with conductivity values that were half of the films formed using D-76). The washing or 'fixing' solution consisted of 0.5 M Hypo solution (Sodium thiosulphate).

Pattern formation- A HP Deskjet 1000 printer was used for printing the precursor salt solutions. Two separate HP 802 black ink cartridges were used for printing KX and AgNO₃ solutions. The cartridges were thoroughly cleaned by making a hole in their lids, removing the sponge holding the black ink and rinsing the reservoir in flowing tap water. Finally, DI water was filled in the reservoir and some test patterns were printed on paper until there was no evidence of black ink on paper. Black and white designs were generated using a vector graphics editor (Inkscape, an open source graphics editor) and printed at 600 dpi resolution. By weighing the cartridges before and after printing DI water, the volume of solution deposited was found to be 1.2 µL/cm² of the printed area. To ensure spatial uniformity of the printed material, all patterns were generated using three consecutive prints of the salt solutions. After printing desired amounts of potassium halide and silver nitrate solutions, the paper (A4 copier paper, 80 gsm) was kept at a distance of 50 cm under a 500 W halogen lamp (Crompton Greaves J240V 500W R7S, 9500 Lumens) for 10 minutes (Note - exposure to either sunlight on a summer afternoon in Bangalore for 1.5 hours or an UV lamp [8 W, 254 nm] for 10 minutes also produced films with similar conductivities). Longer exposure times did not affect the measured conductivity appreciably, while shorter exposures (5 minutes) led to films with non-uniform conductivities and large fluctuations in measured resistance values over length scales of a few millimetres. The samples were placed in a plastic tray containing a standard developer solution (D-76, containing Metol) for 10 minutes, followed by washing in a tray containing a fixer for 10 minutes to remove unreacted silver ions, if any. (Note – Fixing does not alter the conductivity of the features). The paper was then rinsed in water and allowed to dry under ambient conditions or dried using a hair drier.

Solution synthesis- For the solution synthesis of silver nanowires, 1 mL silver nitrate solution (0.25 M) was mixed with 2 mL KBr/KI solution (0.25 M). After desired extent of light exposure, 3 mL of D-76 developer was added and the solution was left standing for 10 min. If the solution had been previously exposed to light, the solution turned greenish brown in colour indicating the formation of silver nanostructures. The excess developer was then removed by decantation following a centrifugation step. The precipitate was then soaked in hypo solution for 10 minutes to remove unreacted silver ions and then rinsed with DI water. Finally, the precipitate was dispersed in DI water using a sonicator followed by drop casting on a silicon wafer for FESEM analysis.

Microstructural and Electrical Characterization- Field Emission Scanning Electron Microscope (FESEM) images were obtained using the Everhart-Thornley SE detector of a Zeiss Ultra-55. The operating voltage was typically 5 kV, and working distance was 6 to 7 mm. Movies were collected as a series of scanned frames using an add-on in the FESEM software. XRD characterizations of the samples were carried out using a Philips X'pert Pro diffractometer. The scan range was 20 to 80° (2θ values). Photographs of samples and movie on capacitive switching were captured using a digital camera. A Model 280DI four point probe station (Four Dimensions Inc.) was used to determine the sheet resistance of the samples. Samples for sheet resistance measurement consisted of two 6 cm squares printed on an A4 paper. The averaged value of the readings taken at different positions on the two squares is reported. For the bending tests, one bending cycle consisted of manually flexing the paper up and down (i.e. into ∩ and U shape), The resistance data was measured after every 50 such cycles till a total of 1000 cycles. The test sample consisted of two squares (side length of 14 mm each) that acted as contacts to three conductive lines (1 mm width x 12 mm length). The minimum radius of curvature during the bending cycles was nominally 3 mm.

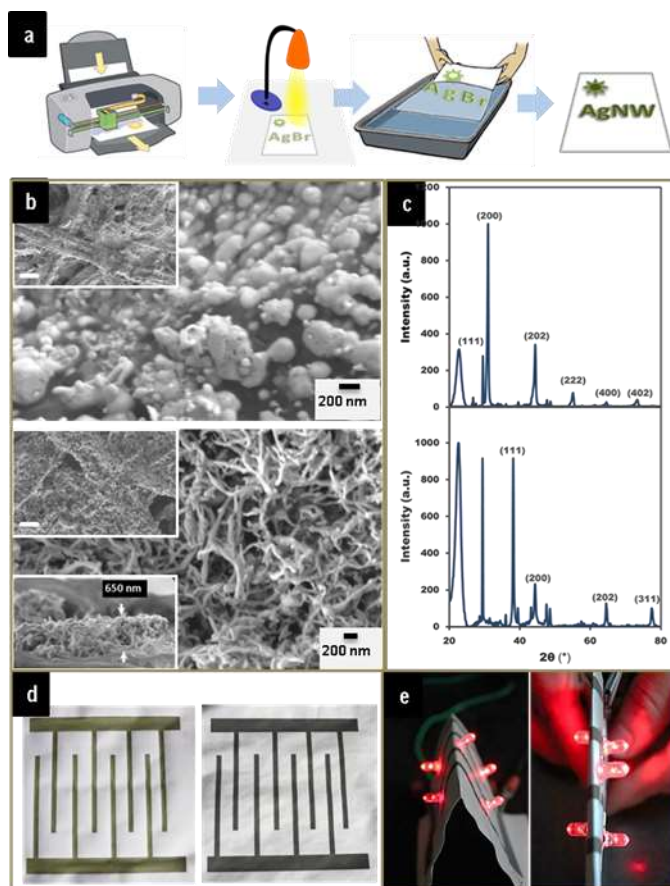


Figure 6.6. (a) Schematic representation of the print-expose-develop cycle. (b) FESEM images of the film after printing (top panel) and after light exposure and development (bottom panel). The insets in the top-left of these images are lower magnification images showing coated paper-fibres. The scale bars in these insets correspond to 10 μm . The lower inset in the bottom panel is a cross-sectional view of the conductive film. (c) XRD of the films formed on paper after printing (top panel) and after developing and fixing (bottom panel). (d) Digital photographs of a printed electrode pattern after salt printing (left) and after developing and fixing (right). The distance between the thicker horizontal electrodes is 15 cm. (e) The paper substrate could be bent or folded flat without losing connectivity. The LED pins were ‘stapled’ to make electrical contact.

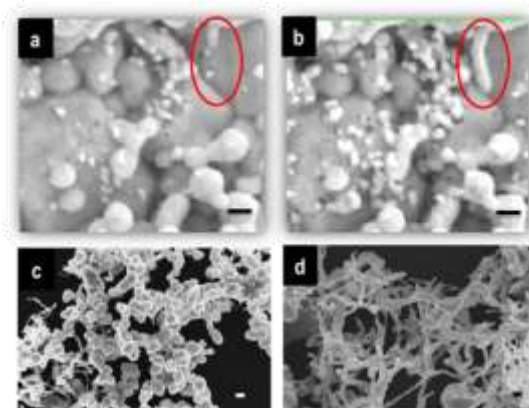


Figure 6.7. Effect of light exposure on nanowire growth. (a) & (b) FESEM images from subsequent scans ($\Delta t = 5\text{s}$) during imaging of an AgBr sample on paper that was exposed to light from a halogen lamp. The oval outline highlights the growth of a nanowire during imaging. (c) silver nanostructures formed in solution after exposure to ambient light. (d) silver nanostructures formed in solution after 10 minutes of exposure to light from a halogen lamp. All scale bars correspond to 200 nm.

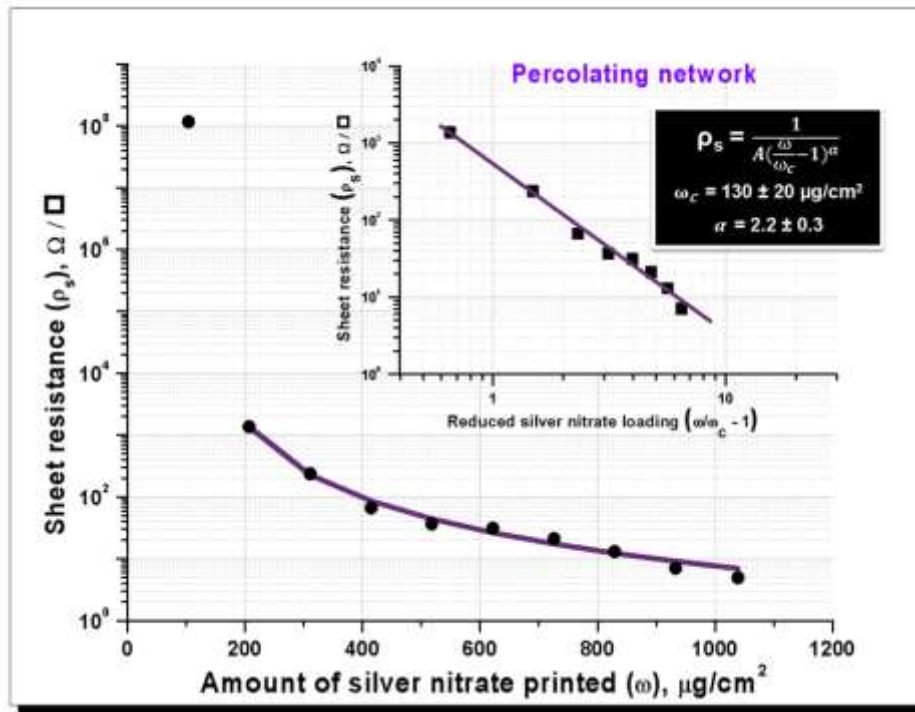


Figure 6.8. Variation of the measured sheet resistance (ρ_s) as a function of the amount of silver nitrate printed (ω). The sharp decline in sheet resistance between the first two data points indicates the presence of a critical threshold value for silver nitrate loading (ω_c) to form a percolating conductive network. The inset shows a log-log plot of the sheet resistances as a function of reduced silver nitrate loading (i.e. silver nitrate loading normalized with respect to the critical value). Only data points beyond the threshold are considered in the inset plot. The points represent the measured data while the curves represent a model fit (based on a non-linear curve fit) to the equation based on percolation theory. The model used as well as the estimated parameter values (mean \pm standard error) for critical loading and scaling exponent are shown.

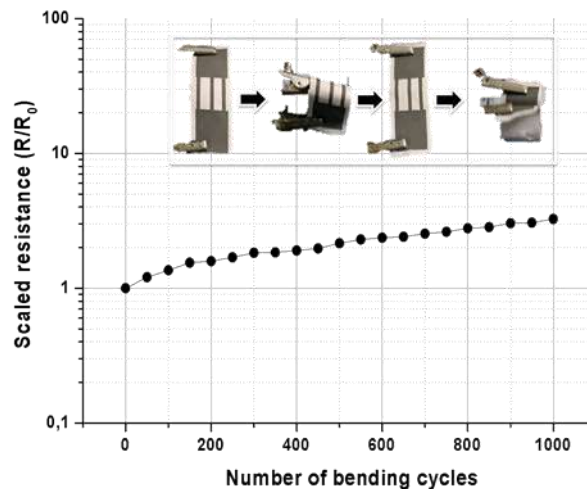


Figure 6.9. Variation of the scaled resistance (R/R_0) as a function of the number of bending cycles. The points represent the data collected after every 50 cycles. The line is a guide to the eye. The inset shows digital photographs of the sample under test being bent during one complete cycle.

A desktop inkjet printer was used to sequentially deposit potassium halide and silver nitrate solutions on paper in desired patterns (Fig. 6.6a). Polygonal crystals were found to be dispersed evenly on all the fibres in the printed portions of the paper (Fig. 6.6 b, top panel). XRD analysis of the film formed on paper, prior to light exposure, indicates the presence of FCC crystals, whose major reflections could be assigned to AgBr as shown (ICCD: 04-006-5963, Fig. 6.6c, top panel). The other reflections could be assigned to CaCO₃ (ICCD: 04-007-2808), which is attributed to the use of calcite as a filler in office paper. The printed film on paper has a greenish tint (Fig. 6.6d, left) and there was no evidence of electrical connectivity on a macroscopic scale in these features. The printed film on paper was then exposed to light from a halogen lamp for 10 minutes, which should lead to the formation of silver clusters within the halide crystals. The paper was then sequentially immersed in a developing bath and a fixing bath. Interconnected network of silver nanowires, whose diameters ranged from 30 to 100 nm, were found on all the printed portions of the paper (Fig. 6.6b, lower panel). The tangled network morphology was observed in both planar and cross-sectional views, and the thickness of the nanowire film was similar to that of the polygonal crystals found prior to development suggesting that AgBr crystals had disintegrated into this tangled network after light exposure and development. XRD analysis of these films of nanowires showed reflections that were assigned to FCC silver (ICCD: 04-006-2775, Fig. 6.6c, lower panel), alongside the reflections attributable to calcite. Remarkably, the film showed excellent conductivity over macroscopic length scales. It had a dull brown appearance, due to the rough texture of the film and penetration into the paper. The as-fabricated silver films showed excellent adhesion to the paper fibres and could not be scraped or peeled off without damaging the underlying paper fibres. The excellent connectivity across the conductive film is further demonstrated by creasing to form a flatly folded electrode (Fig. 6.6e).

Silver nanowires were found to emanate from the surface of AgBr crystals during FESEM imaging of silver halide films that were earlier exposed to light from the halogen lamp (Fig. 6.7a & b). The AgBr films remained unchanged under similar imaging conditions if they were not exposed to light prior to imaging. AgBr crystals are known to have highly mobile Ag⁺ species within their lattice. During photographic development, the silver clusters formed upon light exposure act as an electron reservoir that help reduce mobile silver ions in the lattice, thereby, amplifying the 'latent image'. We hypothesize that a similar process occurs during the print-expose-develop process presented here, as well as during FESEM imaging. Clearly, the electrons used for imaging have reduced the silver ions within the polygonal AgBr crystals to form nanowires; a process catalysed by the creation of 'latent silver clusters' during light exposure. Similar filamentous outgrowth of wire-like silver offshoots has been reported in an earlier electron microscopic observation of AgBr films. To understand the effect of the substrate and the extent of light exposure on nanowire formation, we carried out three experiments in solution, as described earlier, by adding developing and fixing agent sequentially to freshly made silver bromide solutions that had been kept - a) in a covered vial during the experiment which was carried out in a dark room, b) in a vial exposed to ambient fluorescent lighting during the experiment, and c) in a vial that was exposed to light from the halogen lamp for 10 minutes, prior to the addition of developing solution. Silver nanowires formed in solution only upon being exposed to light from the halogen lamp. In the sample exposed to ambient light, polyhedral particles were predominantly formed; whereas, in the sample kept in the dark, washing in 'hypo' solution led to complete dissolution of the precipitate, indicating that reduction of silver had not taken place at all. These results confirm that higher dosage of light exposure is the key for nanowire formation, while also dispelling doubts regarding the role of unknown chemical species present in the office paper. An earlier study on the formation of silver nanowires from silver bromide crystals after exposure to ambient light found that nanowires were only formed if gelatin was used to stabilize the AgBr emulsion and when excess silver nitrate was also present in the solution. The role of gelatin has been speculated to be similar to that of PVP, which acts as a template that controls crystal growth by passivating certain crystal facets. However, such a mechanism cannot account for either the fact that nanowires were formed in the absence of gelatin or the role of light exposure in nanowire formation. Given that several 'latent sites' can be formed upon intense light exposure, we postulate that reduction of mobile silver ions at multiple sites on a grain leads to breakup of the parent AgBr crystal into silver nanowires, some of which can also grow and span across crystals. Silver nanowires bridging across to touch neighbouring AgBr crystals can induce metallization of the neighbouring crystals, and thus explain the creation of macroscopically interconnected networks from silver bromide layers that were non-overlapping at the microscopic scale. This mechanism is also consistent with earlier reports on the formation of silver filaments from individual silver bromide crystals under conditions similar to that used in our study (i.e. chemical development, wherein only silver ions from the parent silver bromide crystal are reduced). Interestingly, a recent report demonstrates the formation of silver chloride crystals decorated with silver nanoparticle nuclei during the 'waiting period under ambient light conditions' that is part of the standard high-temperature polyol route. Our results on the dosage of light exposure suggests that controlling light exposure may be a fruitful avenue towards room temperature silver nanowire synthesis in the polyol process. A percolation threshold for macroscopic electrical connectivity was observed in the variation of sheet resistance as a function of silver nitrate loading (Fig. 6.8). Beyond a threshold value of the amount of silver nitrate printed, the sheet

resistance dropped sharply by five orders of magnitude from 10^8 to $10^3 \Omega/\square$. The post-threshold behaviour of the sheet resistance data could be fit reasonably well using a model based on percolation theory (Eq. 1), which describes the creation of long-range conductive channels in randomly dispersed systems.

$$\rho_s = \frac{1}{A(\frac{\omega}{\omega_c} - 1)^\alpha} \quad [1]$$

wherein, ρ_s represents the sheet resistance (Ω/\square) beyond the percolation threshold, A is a proportionality constant, ω represents the amount of silver nitrate printed, ω_c denotes a critical threshold value for the amount of silver nitrate ($130 \pm 20 \mu\text{g}/\text{cm}^2$, as estimated using a non-linear curve fit), and α is a scaling exponent that depends on the dimensionality of the system (estimated to be 2.2 ± 0.3). The estimated range of the scaling exponent (95% confidence levels) encompasses the value of 1.94 expected of a 3D percolating network. This result is in accord with the entangled nanowire features observed throughout the depth of the conductive film. The inset in figure 6.8 demonstrates the power-law scaling of the sheet resistance values close to the threshold. An implicit assumption in deriving equation 1 is that an increase in the amount of silver nitrate printed does not change the film thickness; a breakdown of this assumption at higher values of silver nitrate loading could be the cause of the deviations observed. The specific conductivity of the as-fabricated sub-micron thick silver films is in the range of 1-10 % of the bulk silver value of $6.3 \times 10^7 \text{ S/m}$, a range that depends on the estimates of porosity of the system as well as the amount of silver present on the top surface of paper. We believe that macroscopic conductivity can be enhanced by further optimizing the salt concentrations to form 2-3 μm sized tabular crystals of AgBr on paper, such that the resultant nanowires can more efficiently span the regions where large cellulose fibres (5-10 μm dia.) cross over each other. In comparison, films fabricated using inkjet printing of a specially-formulated silver nanoparticle ink followed by plasma and microwave sintering are reported to have 60% of the bulk specific conductivity, albeit on smooth plastic substrates²⁷. Finally, figure 6.9 shows the variation of the resistance (scaled to the initial value) as a function of the number of bending cycles. It is seen that the resistance varies only by a factor of three over 1000 cycles, which attests to the excellent adhesion and conformal coverage of the silver nanowires.

In conclusion, a simple process, comprising of print-expose-develop sequence, for the *in situ* formation of silver nanowire networks on paper has been demonstrated. The process does not require any surface modification of the paper and the inherent characteristic of standard office paper to absorb aqueous ink has been leveraged to form highly conductive patterned features within minutes. The fact that two simple and widely used processes, inkjet printing and photographic development can be combined to form conductive patterns on paper without requiring substantial capital or running costs should encourage the widespread adaptation of low-cost, disposable diagnostic and electrical devices, especially in the developing world. Furthermore, the discovery of the importance of light exposure in forming nanowires from AgBr crystals will be useful in optimizing the process of silver nanowire formation in solution.

10. Conclusions summarising the achievements and indication of scope for future work:

Summary of achievements:

The objectives of the proposal (given above) have been met and groundwork in terms of process development for solar energy conversion has been undertaken. Characterization of RF plasma processing by TEM, SEM, DLS, AFM, FTIR and contact angle measurements have been carried out, and have helped in elucidating the salient features of the process. A green protocol for the rapid, room-temperature synthesis of metal nanoparticles has been developed. The main conclusions are:

- Size-controlled, monodisperse gold nanoparticles in the range of 1-10 nm were synthesized within 10 minutes at room temperature using a green reducing agent.
- RF plasma has been used to selectively remove the ligands (FTIR, AFM characterizations) in an MPN array without disturbing the lateral ordering, and both chemical stability and thermal stability is seen to be greatly enhanced post processing, and is only limited by interparticle spacing and nanoparticle melting point.
- Under optimal processing conditions, AFM characterization indicates that the ligand layers are removed as if a uniform reaction front (AFM cross-section profiling) is progressing downwards. There are two probable mechanisms for explaining such a result: a) the thiol ligands are mobile and diffuse on the surface at a rapid rate to maintain a homogeneous coverage on the particle, b) the particles are rotating to expose all sides evenly. The actual mechanism can only be probed using sophisticated x-ray characterization tools.
- Overexposure of closely packed nanoparticle arrays clearly show signs of aggregation at length scales corresponding to 3-4 nanoparticle diameters. However, based on projected area (TEM characterization) and AFM height analysis, there is no indication of three-dimensional agglomeration in these plasma irradiated films.
- By varying the ligand size, the interparticle spacing has been varied from 2 -15 nm and the core diameter was varied independently from 5-10 nm. It was found that larger interparticle spacing leads to greater thermal stability.

Innovations:

A simple and robust, room-temperature, aqueous phase protocol for size and shape-controlled nanoparticle synthesis has been developed. This is currently being used to characterize various reactor designs for continuous-flow synthesis of monodisperse nanoparticles.

RF plasma based processing of MPN arrays to form chemically and thermally stable bare metal nanoparticle arrays with interspacings of the order of particle diameters.

Scope for future work:

The batch protocol shows great promise for the development of a green, economically-viable continuous flow process for large scale synthesis of size-controlled metal nanoparticles. Such size-controlled gold nanoparticles are useful for bioconjugation of proteins in rapid assay tests based on Localised Surface Plasmon Resonance (LSPR). Forming ordered templates for growth of nanowire arrays by VLS process for further application in nanostructured solar cell architectures, and fabrication of nanoporous, conducting, electro-catalytically active membranes for fuel cell applications are being actively pursued in our group. Apart from these, bare metal nanoparticle arrays are also being characterized as the active layers in floating gate based memory devices.

11. S&T benefits accrued:

i. List of Research publications

S No	Authors	Title of paper	Name of the Journal	Volume	Pages	Year
1	S.K. Sivaraman, I.Elango, Sanjeev Kumar, V. Santhanam	A green protocol for room temperature synthesis of silver nanoparticles in seconds	Current Science	97(7)	1055-1059	2009
2	S. K. Sivaraman, Sanjeev Kumar, and V. Santhanam	Room temperature synthesis of gold nanoparticles -- Size-control by slow addition	Gold Bulletin	43(4)	275-286	2010
3	G. Muralidharan, S. K. Sivaraman, and V. Santhanam	Effect of substrate on particle arrangement in arrays formed by self-assembly of polymer grafted nanoparticles	Nanoscale	3(5)	2138-2141	2011
4	G. Muralidharan, L. Subramanian, S. K. Nallamuthu, V. Santhanam, and Sanjeev Kumar	Effect of reagent addition rate and temperature on synthesis of gold nanoparticles in microemulsion route	Ind. Eng. Chem. Res.	50(14)	8786-8791	2011
5	S. K. Sivaraman, Sanjeev Kumar, and V. Santhanam	Monodisperse sub-10 nm gold nanoparticles by reversing the order of addition in Turkevich method – The role of chloroauric acid	J. Colloid Interf. Sci.	361(2)	543-547	2011
6	G. Muralidharan, N. Bhat, and V. Santhanam	Scalable processes for fabricating flash memory devices using self-assembled 2D array of gold nanoparticles as charge storage nodes	Nanoscale	3(11)	4575-4579	2011
7	S. K. Sivaraman, and V. Santhanam	Realization of thermally durable close-packed 2D gold nanoparticle arrays using self-assembly and plasma etching	Nanotechnology	23	255603	2012
8	S. Kumar, V.Bhat, K.J. Vinoy, and V. Santhanam	Using an office inkjet printer to define conductive patterns on paper	IEEE Trans. Nanotechnol	13(1)	160-164	2014

ii. *Manpower trained on the project*

a) *Research Scientists or Research Associates:* 1

b) *No. of Ph.D. produced:* 3

c) *Other Technical Personnel trained:* 12

iii. *Patents taken, if any*

✓ S. Sankar Kalidas, V. Santhanam, "A method for preparing metal or metal oxide nanoparticles", US 8361188.

12. *Financial Position:*

No	Financial Position/ Budget Head	Funds Sanctioned	Expenditure	% of Total cost
<i>I</i>	<i>Salaries/ Manpower costs</i>	25,08,000	25,19,219	5.2
<i>II</i>	<i>Equipment</i>	4,40,39,000	4,33,08,271	89.4
<i>III</i>	<i>Supplies & Materials</i>	15,00,000	14,56,218	3.01
<i>IV</i>	<i>Contingencies</i>	5,00,000	5,00,918	1.04
<i>V</i>	<i>Travel</i>	2,00,000	1,56,583	0.32
<i>VI</i>	<i>Overhead Expenses</i>	5,00,000	5,00,000	1.03
	Total			100%

13. Procurement/ Usage of Equipment

a)

S No	Name of Equipment	Make/Model	Cost (Rs. In Lakhs)	Date of Installation	Utilisation Rate (%)	Remarks regarding maintenance/ breakdown
1	Class 10000 Cleanroom	Four-C-Tron	20	Jul, 2008	100%	Requires constant maintenance, and we are reliant on the expertise of a local refrigeration cycle mechanic for upkeep Requires about 10-15 lakhs over a three year period for maintenance and upkeep
2	Field Emission Scanning Electron Microscope	Ultra-55, Zeiss	300	Nov, 2008	75%	
3	Maskless Laser Writer	uPG 101, Heidelberg Instruments	70	Sept, 2008	30%	
4	e-beam evaporator	Univex 300, Oerlikon-Leybold	65	May, 2009	25%	Turbo pump needs to be replaced to achieve better results
5	Electrical characterization System	MMR-4, MMR technologies SCS-4200, Keithley, and DY200, DigiIVY inc	45	2009	25%	

b) Plans for utilising the equipment facilities in future

The infrastructure developed under the IRHPA scheme is the enabling tool for most of the nanotechnology related research being undertaken in our department.

Name and Signature with Date

14-04-2014

a. _____
(Sanjeev Kumar, Principal Investigator)

14-04-2014

b. _____
(V. Kumaran, Principal Investigator)

14-04-2014

c. _____
(S. Venugopal, Principal Investigator)